



# Formation et exhumation des granulites permienues : établir les conditions pré-rift et déterminer l'histoire d'exhumation syn-rift

Benoît Petri

## ► To cite this version:

Benoît Petri. Formation et exhumation des granulites permienues : établir les conditions pré-rift et déterminer l'histoire d'exhumation syn-rift. Sciences de la Terre. Université de Strasbourg, 2014. Français. NNT : 2014STRAH012 . tel-01145262

**HAL Id: tel-01145262**

<https://theses.hal.science/tel-01145262>

Submitted on 23 Apr 2015

**HAL** is a multi-disciplinary open access archive for the deposit and dissemination of scientific research documents, whether they are published or not. The documents may come from teaching and research institutions in France or abroad, or from public or private research centers.

L'archive ouverte pluridisciplinaire **HAL**, est destinée au dépôt et à la diffusion de documents scientifiques de niveau recherche, publiés ou non, émanant des établissements d'enseignement et de recherche français ou étrangers, des laboratoires publics ou privés.

**École Doctorale des Sciences de la Terre et de l'Environnement (ED 413)**

*Institut de Physique du Globe de Strasbourg (UMR 7516)*

**Thèse** présentée par :

**Benoît PETRI**

soutenue le : 2 décembre 2014

pour obtenir le grade de : **Docteur de l'université de Strasbourg**

Discipline/ Spécialité : Sciences de la Terre – Géologie

**Formation et exhumation des granulites permianes**

*Établir les conditions pré-rift et déterminer l'histoire de l'exhumation syn-rift*

**THÈSE dirigée par :**

Dr. ŠTÍPSKÁ Pavla  
Pr. MANATSCHAL Gianreto  
Pr. WIJBRANS Jan R.

Université de Strasbourg  
Université de Strasbourg  
Vrije Universiteit, Amsterdam

**RAPPORTEURS :**

Pr. MANCKTELOW Neil S.  
Pr. WEINBERG Roberto F.

Eidgenössische Technische Hochschule, Zürich  
Monash University, Melbourne

**EXAMINATEUR :**

Pr. BALLÈVRE Michel

Université de Rennes 1



# RÉSUMÉ ÉTENDU

Une des questions majeures en Sciences de la Terre concerne la compréhension des phénomènes liés au démantèlement d'une chaîne de montagne, menant à la construction d'une croûte continentale équilibrée. La fin d'une phase tectonique compressive ayant mené à la construction d'un orogène est généralement marquée par une intense activité tectonique, magmatique et métamorphique. L'ensemble de ces processus post-orogéniques vont élaborer une « nouvelle » croûte continentale équilibrée à partir d'une croûte orogénique par définition sur-épaisse. Cette nouvelle architecture crustale influencera la localisation, la structure et le mode de déformation des systèmes de rifts intracontinentaux postérieurs. Ce travail vise ainsi à comprendre certains phénomènes post-orogéniques et leurs implications pour les événements tectoniques ultérieurs (c.-à-d. les riftings).

## *Contexte de l'étude*

En Europe de l'Ouest, le stade terminal de l'orogénèse dévono-carbonifère dite varisque a lieu de la fin du Carbonifère au début du Permien. A cette époque, de grands décrochements extensifs traversent l'ancien domaine orogénique et sont associés à la formation de bassins sédimentaires et volcano-sédimentaires dont la dynamique d'ouverture est modifiée par rapport aux bassins syn-orogéniques. Dans tous les niveaux crustaux se mettent en place des intrusions magmatiques mafiques et felsiques, très fréquemment associées à un métamorphisme de contact de haute température enregistrant les températures et pressions de ces intrusions.

Cependant, de nombreuses questions persistent concernant cette période d'extension post-orogénique et sont développées dans cette thèse. Comment et dans quel contexte géodynamique se forment ces intrusions magmatiques et plus particulièrement celles de la croûte moyenne ? Combien de temps perdurent les conditions de leur formation ? Est-ce que les granulites sont toujours produites par métamorphisme de contact ? Résident-elles aux profondeurs de leur genèse avant d'être exhumées lors d'un deuxième épisode tectonique ou bien sont-elles exhumées immédiatement après leur formation ? Grâce à l'enregistrement des conditions de leurs formations, ces roches peuvent devenir un excellent marqueur structural, permettant de retracer l'évolution des différents niveaux crustaux durant les phases tectoniques postérieures, à condition de répondre à ces incertitudes.

Ce travail de thèse a pour but d'étudier et de caractériser un système magmatique et métamorphique Permien dans les nappes austroalpines (sud-est de la Suisse, nord de l'Italie) par une approche pluri-disciplinaire couplant des méthodes de pétrologie métamorphique,

de géologie structurale et de géochronologie. Ce principal chantier d'investigations a pour avantage de présenter à l'affleurement tous les niveaux d'une croûte continentale permienne. Ces différents niveaux crustaux, auparavant superposés, ont été juxtaposés lors de l'ouverture très bien documentée au Jurassique de la Téthys alpine. De plus, les terrains n'ont été que peu déformés lors de la phase compressive ayant abouti à l'éduction des Alpes. En particulier, les unités de Campo et de Grosina montrent des évidences d'une histoire polyphasée de l'orogénèse varisque à l'orogénèse Alpine, préservant remarquablement les évènements post-orogéniques et de rifting Jurassique. Elles permettent ainsi d'élucider bon nombre de questions.

### ***L'évolution P-T-t-d de l'unité de Campo***

Une grande partie du travail de thèse se focalise sur des niveaux crustaux intermédiaires qui n'ont été que peu étudiés alors qu'ils ont le mérite d'enregistrer potentiellement plusieurs évènements successifs. Ainsi, les micaschistes de l'unité de Campo sont intrudés par le gabbro de Sondalo au Permien. L'évolution en pression (*P*), en température (*T*), en temps (*t*) et en déformation (*d*) des roches encaissant le gabbro ainsi que des xénolites de roches encaissantes pris dans le gabbro est contrainte grâce à une étude couplant cartographie, géologie structurale et pétrologie métamorphique.

La présence de paragénèses à grenat et staurotide dans les micaschistes portant les fabriques Sc1 et Sc2 témoigne d'un chemin prograde barrovien pré-Permien atteignant 6 kbar/600°C. L'unité de Campo subit ensuite un réchauffement quasi-isobare, sans déformation apparente, autour de 4 kbar/540°C, menant à la cristallisation d'andalousite et de cordiérite. Le gabbro de Sondalo intrude l'unité de Campo à ~5,5 kbar/930°C en produisant des xénolites composés de granulites à grenat, sillimanite, cordiérite et spinelle. Les roches sont immédiatement décomprimées menant à une mise en place finale à ~4 kbar lors du développement d'une nouvelle fabrique Sc3 localisée autour du pluton. Les échantillons se trouvant dans l'auréole de contact composée de migmatites portant la fabrique Sc3 montrent une évolution contrastée subissant soit uniquement une exhumation de 6 kbar/750°C à 5 kbar/725°C, soit un enfouissement de 4,5 kbar/500°C à 5,2 kbar/800°C suivi d'une exhumation à 4,8 kbar/770°C.

Les résultats de cette première partie indiquent que seuls le gabbro et son auréole immédiate ont été exhumés de 18 à 12 km (2 kbar) lors de son intrusion, mais que l'unité encaissante n'a pas suivi la même évolution, restant dans le même niveau structural. Intégrés aux résultats d'autres études du domaine Austroalpin, ils permettent de proposer un modèle d'évolution pendant l'extension post-orogénique Permienne.

### ***Le mode de mise en place du gabbro de Sondalo***

Les résultats obtenus lors de la première partie de la thèse posent la question du mode de mise en place d'une intrusion mafique dans les niveaux intermédiaires de la croûte continentale, question développée dans la deuxième partie de la thèse. Ainsi, la caractérisation de la structure du pluton ainsi que des fabriques magmatiques et magnétiques (par *Anisotropie de Susceptibilité Magnétique – ASM*) est couplée à des datations U–Pb sur zircon (LA-ICPMS) de roches magmatiques et métamorphiques.

Les fabriques magmatiques et magnétiques du pluton – qui préserve son orientation originelle – sont essentiellement verticales (foliations et linéations), indiquant un transfert vertical de magma au travers la croûte continentale, alimentant des systèmes magmatiques plus superficiels. L'intrusion s'est mise en place en deux étapes. (1) L'ascension de magma s'est tout d'abord réalisée au moyen de fractures ouvertes parallèlement à la fabrique Sc2 de l'encaissant métasédimentaire. Ceci est indiqué par la présence d'une foliation magmatique parallèle à la foliation Sc2 de l'encaissant métasédimentaire dans le centre du pluton, ainsi que par l'allongement des xénolites n'ayant pas été inclinés lors de l'intrusion. Les datations U–Pb nous permettent de contraindre cette phase intrusive à 289–288 Ma. (2) La deuxième partie de l'ascension est marquée par un changement de rhéologie de l'encaissant vis-à-vis du magma. La résistance mécanique de la roche encaissante diminue suite à une augmentation de température dans l'auréole métamorphique, causant sa fusion partielle et donc la production de migmatites. La déformation devient à ce moment plastique, déclenchant la formation de la fabrique Sc3 dans l'auréole métamorphique, ainsi que d'une seconde fabrique magmatique assez peu développée dans le pluton. Cette phase de remontée magmatique a lieu entre 288 et 285 Ma et explique l'évolution contrastée de roches se trouvant dans l'auréole métamorphique de contact. Les modélisations thermiques de l'intrusion montrent que pendant le cisaillement associé à la deuxième phase de remontée magmatique, l'auréole métamorphique est amincie.

### ***Refroidissement et exhumation des unités de Campo et de Grosina***

Le refroidissement et l'exhumation de l'unité de Campo et de l'unité sus-jacente de Grosina séparée par la zone de cisaillement d'Eita sont explorés par l'acquisition d'âges par la méthode  $^{40}\text{Ar}/^{39}\text{Ar}$  sur hornblende, muscovite et biotite. Les nouvelles données géochronologiques sur Grosina montrent des âges  $^{40}\text{Ar}/^{39}\text{Ar}$  sur muscovite entre 273 et 261 Ma, et entre 248 et 246 Ma pour la biotite. L'unité de Campo montre des datations sensiblement plus jeunes avec un âge entre 210 et 177 Ma (mal constraint) sur hornblende, entre 182 et 176 Ma sur muscovite et entre 174 et 171 Ma sur biotite. Bon nombre de datations réalisées dans l'unité

de Campo ont dû être éliminées pour cause d'excès en  $^{40}\text{Ar}$  systématique pour les amphiboles, probablement causé par l'intrusion mafique au Permien. Ces nouveaux âges, couplés à une compilation des datations multi-méthodes (U–Pb, Sm–Nd, Rb–Sr, K–Ar,  $^{40}\text{Ar}/^{39}\text{Ar}$ ) réalisées sur les deux unités nous donnent un jeu de données conséquent, permettant d'estimer les vitesses de refroidissement. Ainsi, les unités de Campo et Grosina refroidissent à raison de  $\sim 10^\circ\text{C/Ma}$  lors du Permien. L'unité de Grosina étant située dans des niveaux plus faibles que l'unité de Campo, elle n'enregistra pas les refroidissements Jurassiques atteignant plus de  $50^\circ\text{C/Ma}$  dans l'unité de Campo. La différence notable de vitesse atteste d'un refroidissement sans exhumation tectonique au Permien, alors qu'au Jurassique, l'unité de Campo est exhumée et placée dans des niveaux crustaux suffisamment superficiels pour permettre son refroidissement rapide. Ce dernier événement tectonique s'est probablement réalisé grâce à des cisaillements au toit de l'unité de Campo, dans l'unité de Grosina et le long de la zone de cisaillement d'Eita. Ces résultats apportent de nouvelles contraintes sur la formation ainsi que sur le budget thermique d'une marge continentale riftée.

En conclusion, les résultats de cette étude ont montré qu'au moins certaines des granulites Permianes sont issues d'un métamorphisme de contact causé par des intrusions magmatiques, jusque dans des niveaux crustaux intermédiaires. Ce magma, produit dans le manteau sous-continentale, est très probablement issu d'un épisode d'amincissement lithosphérique marquant la fin de l'orogénèse varisque. Les roches sont restées dans leur niveau crustal de formation avant d'être éventuellement exhumées lors d'un épisode tectonique postérieur et indépendant de leur formation, en particulier lors des phases de rifting mésozoïques. D'une manière générale, les granulites post-orogéniques intimement associées à un sous-plaquage mafique peuvent constituer un bon marqueur pour la reconstruction de l'architecture crustale pré-tectonique.

# ***EXTENDED ABSTRACT***

One of the major questions in Earth Sciences concerns phenomena associated to the dismantling of mountain chains, leading to the construction of an equilibrated continental crust. The end of a compressive tectonic phase that led to the building of an orogen is generally marked by an intense tectonic, magmatic and metamorphic activity. All of these post-orogenic processes will form a “new” equilibrated continental crust from an orogenic crust that is by definition over-thickened. This new crustal architecture will influence the localization, the structure and the mode of deformation of subsequent intracontinental rift systems. Therefore, this work aims to understand some of the post-orogenic processes and their implications for subsequent tectonic events (i.e. riftings).

## ***Context***

In Western Europe, final stages of the Devono-Carboniferous orogeny, the so-called Variscan orogeny, occurred in Late Carboniferous to Early Permian time. At that time, transtensive faults crosscut the former orogenic domain and are associated to the formation of sedimentary and volcano-sedimentary basins, with contrasted opening dynamics with respect to the syn-convergent basins. Mafic and felsic magmatic intrusions are emplaced at all crustal levels, frequently associated to contact metamorphism recording the temperature and pressure conditions of these intrusions.

Nevertheless, numerous questions persist concerning this extensive post-orogenic period, questions that are developed in this thesis. How and in which geodynamic context are these intrusions emplaced, especially those of mid-crustal level? How long do the conditions of their formation persist? Are the granulites always produced by contact metamorphism? Are they stalled at the depth of their formation before being exhumed during a subsequent tectonic episode independent of their formation? Or are they immediately exhumed after their formation? Thanks to the record of their formation conditions, these rocks may be an excellent structural marker, allowing to track the evolution of different structural levels during subsequent tectonic phases, on the condition that we elucidate these uncertainties.

This thesis aims to study and characterize a Permian magmatic and metamorphic system in the Austroalpine nappes (South-East of Switzerland, North of Italy), following a pluri-disciplinary approach coupling metamorphic petrology, structural geology and geochronology. The main study area is fortunately preserving all structural levels of a pre-rift continental crust, notably affected by the Permian event. These different levels, previously superposed, were

juxtaposed during the well-documented opening of the Alpine Tethys during Jurassic. Moreover, these rocks were only poorly overprinted during compressional phases that led to the rise of the Alps. Notably, the Grosina and Campo units present evidences of a polyphased history from the Variscan orogeny to the Alpine orogeny, remarkably preserving post-orogenic and Jurassic rifting events. Therefore, they may provide keys to answer the above mentioned questions.

### ***The P–T–t–d evolution of the Campo unit***

The first part of the thesis focused on intermediate crustal levels that were poorly studied, despite their potential to record multiple stages. Thus, micaschists from the Campo unit were intruded by the Sondalo gabbro in Permian times. The evolution in pressure ( $P$ ), temperature ( $T$ ), time ( $t$ ) and deformation ( $d$ ) of the country-rock of the gabbro and the country-rock xenoliths in the gabbro is constrained thanks by coupling cartography, structural geology and metamorphic petrology.

The presence of paragenesis bearing garnet and staurolite in micaschists with the Sc1 and Sc2 planar fabrics attests of a pre-Permian barrovian prograde path, reaching 6 kbar/600°C. Subsequently, the Campo unit undergoes a near-isobaric heating around 4 kbar/540°C, with no apparent deformation, leading to the crystallization of andalusite and cordierite. The Sondalo gabbro intrudes the Campo unit at ~5.5 kbar/930°C, forming granulitic xenoliths made of garnet, sillimanite, cordierite and spinel. The rocks are immediately decompressed leading to a final emplacement at ~4 kbar during the development of a new Sc3 planar fabric localized around the pluton. Samples in the metamorphic contact aureole bearing the Sc3 fabric present a contrasted evolution, being exhumed from 6 kbar/750°C to 5 kbar/725°C, or being buried from 4.5 kbar/500°C to 5.2 kbar/800°C followed by an exhumation to 4.8 kbar/770°C.

The results of this first section indicate that only the gabbro and its immediate aureole were exhumed from 18 to 12 km (2 kbar), but the country-rock did not follow the same evolution and stayed in the same structural level. Integrated to results of other studies performed in the Austroalpine domain, these results allows to propose an evolutionary model during the Permian post-orogenic extension.

### ***The emplacement mechanism of the Sondalo gabbro***

The results obtained in the first section of the thesis ask the question of the emplacement mechanism of a mafic intrusion in intermediate crustal levels, question developed in the second section of the thesis. Thus, the characterization of the structure of the pluton and the magmatic and magnetic (by *Anisotropy of Magnetic Susceptibility – AMS*) fabrics is coupled to U–Pb on zircon dating (LA-ICPMS) from magmatic and metamorphic rocks.

The magmatic and magnetic fabric of the pluton – who preserves its original orientation – are essentially vertical (foliations and lineations), indicating a vertical magma transfer through the continental crust, feeding more superficial systems. The intrusion was emplaced in two phases. (1) The first magma ascent phase occurred through fractures open parallel to the Sc2 fabric of the metasedimentary country-rock. This is indicated by the presence of a magmatic foliation parallel to the Sc2 fabric of the host-rock in the center of the pluton, and by the alignment of the elongated xenoliths that were not tilted during the intrusion. U–Pb dating brackets this intrusive phase between 289 and 288 Ma. (2) The second magma ascent phase is marked by a rheological switch of the country-rock with respect to the magma. A temperature increase in the metamorphic contact aureole is responsible for its partial melting and associated formation of migmatites, decreasing the mechanical strength of the country-rock. At that time, the deformation became plastic, triggering the formation of the Sc3 fabric in the metamorphic aureole along with a second magmatic foliation that is poorly developed in the pluton. This ascent phase occurs between 288 and 285 Ma and explains the contrasted evolution of rocks in the metamorphic contact aureole. Thermal models of the intrusions indicate that during the shearing associated to the second phase of ascent, the metamorphic contact aureole is thinned.

### ***Cooling and exhumation of the Campo and Grosina units***

The cooling and exhumation of the Campo unit and the overlying Grosina unit, separated by the Eita shear zone are explored by the acquisition of  $^{40}\text{Ar}/^{39}\text{Ar}$  ages on hornblende, muscovite and biotite. New geochronological data on the Grosina unit present  $^{40}\text{Ar}/^{39}\text{Ar}$  ages between 273 and 261 Ma for muscovite, and between 248 and 246 Ma for biotite. The Campo unit shows clearly younger ages between 210 and 177 Ma on hornblende (poorly constrained), spanning between 186 and 176 Ma on muscovite and between 174 and 171 Ma on biotite. Numerous data were discarded due to frequent excess  $^{40}\text{Ar}$  on amphiboles, probably associated to the emplacement of the gabbro in Permian times. These new ages, associated to a compilation of ages obtained with different chronometers from the literature (U–Pb, Sm–Nd, Rb–Sr, K–Ar,  $^{40}\text{Ar}/^{39}\text{Ar}$ ) performed on different lithologies from both units allows to estimate their cooling rates. Thus, both Campo and Grosina units underwent a cooling rate around 10°C/Ma in Permian times. The Grosina unit, being in shallower crustal levels, did not record the Jurassic cooling rates, reaching up to 50°C/Ma in the Campo unit. The notable difference in cooling rate attests of a cooling without being associated to an exhumation in Permian times, whereas the Campo unit cooled rapidly in Jurassic times, associated to an exhumation and an emplacement in shallow crustal levels. The latter tectonic event was probably achieved through shearing at the top of the Campo unit, in the Grosina unit and along the Eita shear zone. These results bring

new constrains on the formation and the thermal budget of rifted continental margins.

To conclude, results of this study showed that at least part of the Permian granulites are caused by contact metamorphism due to the intrusion of mafic magmas, up to intermediate crustal levels. This magma, produced in the sub-continental mantle, is probably due to a lithospheric thinning episode at the end of the Variscan orogeny. The rocks staid in their crustal level of formation. Eventually, they may be exhumed during a subsequent tectonic event, especially during Mesozoic rifting phases. In general, post-orogenic granulites intimately associated to mafic magmas may be a good marker for the reconstruction of pre-tectonic crustal architecture.

---

## *REMERCIMENTS*

---



## ***REMERCIEMENTS***

Voilà le moment de mettre la touche finale à ce manuscrit avec ces dernières lignes, lignes qui au final ne sont pas les plus faciles à rédiger. Au cours de ces trois années et quelques mois, de nombreuses personnes ont participé de près ou de loin à mon travail, et je souhaite qu'elles soient ici remerciées.

Mes premiers remerciements vont naturellement à mes trois directeurs de thèse. Je remercie Pavla Štípská pour m'avoir transmis ses méthodes de travail rigoureuses et pour avoir supervisé mes travaux sur la pétrologie métamorphique. Je désire souligner l'enthousiasme et l'optimisme débordant de Gianreto Manatschal, sur des sujets qui sont certainement loin de ses thèmes de prédilection. Il a toujours su trouver le temps pour toutes sortes de requêtes, et je lui en suis grandement reconnaissant. Et enfin je salue Jan R. Wijbrans pour sa sympathie et sa bonne volonté, Jan qui a toujours été opérationnel pour répondre à mes questions, même à distance lorsque les valves et les pompes de la ligne argon s'emballaient. À tous les trois, sincèrement merci.

Ce travail a bénéficié d'une collaboration plus qu'active avec Geoffroy Mohn, homme de l'ombre à la référence cinématographique certes adaptée à chaque situation, mais parfois douteuse. J'ai pu compter sur toi sur le terrain, du fond des vallées jusqu'aux sommets – parfois un peu moins entre les deux – mais également de retour du terrain. Je te remercie pour tout ce que tu as fait, qui vaut un bon nombre de paquets de *lardo*, de *Mulino Bianco* ou de *Felix*.

Je remercie également Karel Schulmann et Etienne Skrzypek, qui depuis le master m'ont toujours suivi d'un œil, transmis une partie de leurs connaissances, et ont toujours été ouverts à la discussion. J'ai également pu retrouver cette bienveillance à Lausanne auprès d'Othmar Müntener et de Federico Galster, qui m'ont invité à utiliser les infrastructures de Lausanne pour les analyses des zircons. Je veux également souligner la contribution de Philippe Robion sur le magnétisme des roches et enfin je remercie Marco Beltrando pour les nombreuses discussions, idées partagées, et pour cette semaine dans le bush Corse.

Je remercie les membres du jury, Michel Ballèvre, Roberto Braga, Neil S. Mancktelow et Roberto F. Weinberg d'avoir pris le temps de lire et d'évaluer ce manuscrit, mais également d'avoir fait le déplacement jusque Strasbourg pour la soutenance, et d'y avoir partagé leurs idées.

Certaines parties de ce manuscrit ont profité des relectures d'Anne-Marie Karpoff, et des discussions diverses avec Dominique Frizon de Lamotte et d'Andrea Galli, et je tiens ici à les en remercier.

Derrière un travail de thèse, il y a certes l'étudiant et les collaborateurs, mais il y a également les infrastructures et les expertises présentes dans les universités de Strasbourg, d'Amsterdam, de Lausanne et de Stuttgart. Ainsi, je souhaiterais sincèrement remercier Amélie Aubert et Roel van Elsas pour leur aide à la préparation des échantillons et la séparation des minéraux, John Moine pour la confection des lames minces et Gilles Morvan et Pierre Vonlanthen pour leur coup de main quant à l'utilisation des divers instruments des microscopes électroniques. Je suis également reconnaissant envers Juan Carlos González et Thomas Theye pour l'utilisation des microsondes, Alexey Ulyanov, Klaudia Kuiper et Christel Bontje pour leur aide à l'acquisition et au traitement des différentes données isotopiques, et enfin Tsvetomila Mateeva et Aubéry Longeau pour les mesures des différentes propriétés magnétiques des roches.

Je remercie chaleureusement Betty Kieffer pour avoir à maintes reprises redoublé d'efforts pour trouver des références obscures, et Annie Bouzeghaia pour ses coups de crayons aux divers travaux d'illustrations. Je remercie également Ghenima Begriche, Joëlle Jelaca, Didier Baumann et David Palmis pour leur aide administrative et logistique à tout moment. J'ai pu retrouver cette même sympathie sur le terrain auprès de la famille Ricetti et d'Emanuele Spicuglia, *grazie mille* ! Au détour d'un couloir, j'ai également rencontré la bienveillance de Jean-Claude Horrenberger, toujours soucieux de prendre de mes nouvelles.

Enfin, il y a toute la troupe de ± jeunes du labo, ou anciennement du labo, qui ont participé à la bonne ambiance de travail. Je garderai de bons souvenirs et mon bureau portera toujours les stigmates de leurs attaques répétées, allant jusqu'à la nuit suivant la soutenance en rentrant récupérer mes affaires. Je liste ici tous les accusés, mais j'en profite bien évidemment pour les remercier de la bonne ambiance quasi-quotidienne : Victor do Brasil, Mick du terroir, Pau, Isa et Momo, les tortionnaires de patates, Bruno leur libérateur (hé oui...), Pierre le roi du farniente sur les rives canadiennes, Médé le tombeur, Pauline la bretonne, Yann le géophysicien, Marie-Éva que je remercie également pour m'avoir accompagné en compagnie de Pauline W. pour une campagne d'échantillonnage assez tard dans la saison. Je salue également les plus anciens avec Francis le Chon, mon mentor de master 1 aux conseils souvent précieux, Julie, Manu, Alexis le lorrain, Mimile le vosgien, Alessandro, Natasha do Brasil aussi, Suzon, Alexandra et enfin Fabulous Fab. Je n'oublie pas les anciens collègues de licence et master qui ont quitté Strasbourg : Peter Müller et ses fameux waters, Marine, Antoine, Martin, Lio et les nudistes croates.

## *Remerciements*

---

Je tiens également à remercier les trois compères de Schwin, Francky, Guitoune et Vince, avec qui les soirées ont toujours été... intéressantes.

Je remercie très chaleureusement ma famille et plus particulièrement mes parents et mon frère qui m'ont toujours soutenu.

Finalement, mes dernières pensées vont à Aurélie, qui m'a supporté tous les jours, la fin devait être assez ardue pour toi. Il y a tant de choses pour lesquels je devrais te remercier donc pour tout, merci infiniment.



---

## ***SOMMAIRE***

---

## **SOMMAIRE**

RÉSUMÉ ÉTENDU	5
EXTENDED ABSTRACT	9
REMERCIEMENTS	13
SOMMAIRE	19
INTRODUCTION	23
1. Les processus tardi- à post-orogéniques	25
2. Implications pour l'architecture de la croûte continentale	28
3. Les éléments clés	29
CHAPITRE I: CONTEXTE	31
1. Orogénèse varisque	33
2. Évolution tardi- à post-orogénique	36
CHAPITRE II: CADRE ET MÉTHODOLOGIE	45
1. Questions soulevées	47
2. Où y répondre ?	47
3. Comment y répondre	49
4. Plan du mémoire de thèse	50
CHAPITRE III: MÉTAMORPHISME POST-VARISQUE DANS LES ALPES	53
Abstract	55
1. Introduction	56
2. Geological setting	57
3. Structural evolution	62
4. Petrography and mineral chemistry	65
5. Mineral equilibria modelling	76
6. Discussion	84
7. Conclusion	90
Acknowledgments	90
CHAPITRE IV: MISE EN PLACE D'UN GABBRO EN CROÛTE MOYENNE	91
Abstract	93
1. Introduction	94
2. Geological setting	96
3. Petrology and structure of the Campo unit	99
4. Petrography and magmatic structures of the Sondalo gabbro	100
5. Geochronology	104
6. Anisotropy of Magnetic Susceptibility	119
7. Discussion	129
8. Conclusions	141

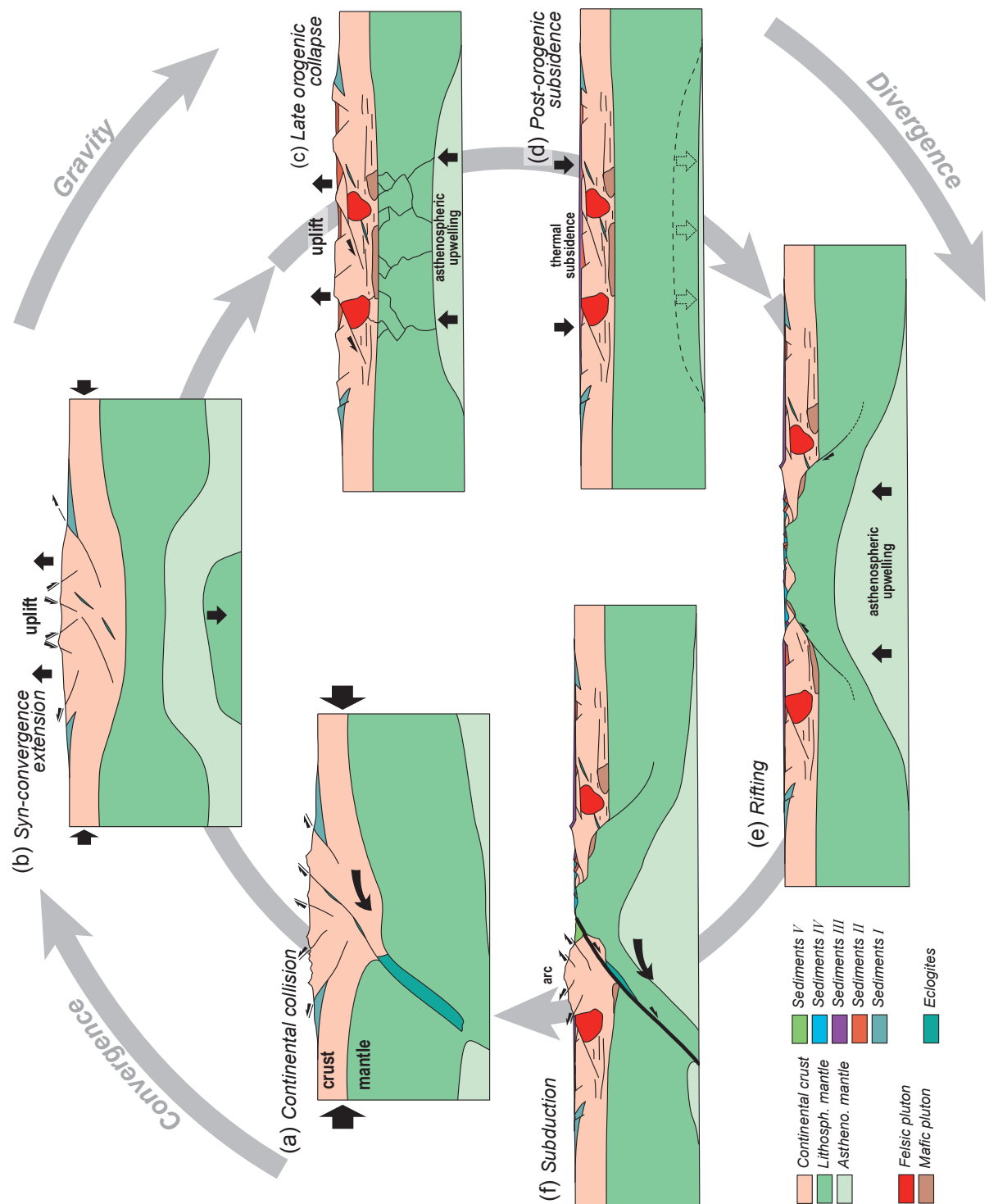
<b>CHAPITRE V: EXHUMATION ET REFROIDISSEMENT PENDANT LE RIFTING</b>	147
<b>Abstract</b>	149
<b>1. Introduction</b>	150
<b>2. Tectonic, geochronological and geological framework</b>	151
<b>3. <math>^{40}\text{Ar}/^{39}\text{Ar}</math> geochronology</b>	159
<b>4. Discussion on ages</b>	175
<b>5. Evolutionary model of the formation of necking zone</b>	184
<b>6. Conclusion</b>	189
<b>Acknowledgments</b>	189
<b>Appendix: Photomicrographs of dated samples</b>	190
<b>CHAPITRE VI: DISCUSSION GÉNÉRALE</b>	193
<b>1. Quel est le lien entre magmatisme et métamorphisme ?</b>	196
<b>2. Quelle est la dynamique de mise en place des intrusions mafiques ?</b>	199
<b>3. Quels sont les systèmes d'exhumation ?</b>	202
<b>4. L'extension post-orogénique permienne : quel contexte géodynamique ?</b>	204
<b>5. Quelle est l'influence de l'architecture lithosphérique sur les rifts ?</b>	209
<b>Conclusion</b>	211
<b>RÉFÉRENCES</b>	217
<b>ANNEXES</b>	247
<b>GUIDE D'EXCURSION</b>	265
<b>Abstract</b>	267
<b>1. Introduction</b>	268
<b>2. Logistics</b>	270
<b>3. Field observations</b>	271
<b>4. Tectono-metamorphic evolution</b>	282
<b>5. Conclusion</b>	284
<b>Acknowledgments</b>	284
<b>References</b>	285
<b>LISTE DES FIGURES</b>	288
<b>LISTE DES TABLEAUX</b>	291
<b>TABLE DES MATIÈRES</b>	292
<b>RÉSUMÉ</b>	298
<b>ABSTRACT</b>	298



---

# *INTRODUCTION*

---



La théorie de la tectonique des plaques décrit des cycles au cours desquels des périodes de convergence des continents alternent avec des périodes de divergence continentale. Alors que les uns façonnent les chaînes de montagnes (ou orogènes), les autres sont à l'origine de la formation des océans. Chaque étape modifie de manière plus ou moins intense et plus ou moins pérenne l'architecture de la lithosphère continentale (Fig. 1). Ces cycles ont été identifiés par Wilson (1966), en montrant que l'océan Atlantique a réutilisé une limite de plaque préexistante, potentiellement affaiblie par une ancienne phase orogénique (Dewey, 1988). Ainsi, la compréhension des phénomènes d'océanisation ou plus généralement de rifting passe, en partie, par la connaissance des phénomènes transformant une croûte continentale orogénique, par définition sur-épaisse, en une croûte continentale équilibrée sur laquelle se développeront des rifts continentaux.

## 1. LES PROCESSUS TARDI- À POST-OROGÉNIQUES

La dynamique d'un orogène peut être résumée par une compétition entre les forces horizontales aux limites du système, d'origine tectonique ( $\sigma(\text{lim})$ ), et les forces verticales de volume d'origine gravitaire ( $\sigma(\text{vol})$ ). Lors de phases convergentes ( $\sigma(\text{lim}) \gg \sigma(\text{vol})$ ), la croûte continentale est épaisse par chevauchements d'unités et raccourcissements horizontaux, menant à une élévation de la topographie (Fig. 2ab). En profondeur, l'épaisseissement est induit par l'enfouissement du Moho ainsi que par la limite entre le manteau lithosphérique et asthénosphérique. Ainsi, la croûte continentale sur-épaisse, peu dense, est stabilisée par l'épaisseissement du manteau lithosphérique dense. En revanche, les stades finaux de l'évolution orogénique sont souvent gouvernés par des processus extensifs (Dewey, 1988), lors desquels la topographie est progressivement réduite (voir Rey *et al.*, 2001 pour synthèse). Les reliefs créés au cours de la subduction et de la collision sont érodés (effondrement par érosion, Avouac & Burov, 1996), mais la principale source d'atténuation de l'épaisseur de la croûte orogénique est d'origine tectonique.

---

**Fig. 1:** Modèle d'évolution simplifié de la croûte continentale et du manteau lithosphérique au cours d'un cycle de Wilson. (a) La croûte continentale et le manteau lithosphérique sont épaisse lors d'un épisode de collision continentale. (b) Les forces tectoniques diminuent, la racine lithosphérique se détache, en surface le système commence à s'effondrer, déclenchant (c) l'effondrement gravitaire de l'orogène, accompagné d'une remontée asthénosphérique. En profondeur, le fluage de la croûte inférieure s'associe à des intrusions mafiques ; plus en surface des granites se mettent en place et des bassins sédimentaires se forment. (d) Après cet épisode de haute température, la lithosphère se refroidit par conduction et subside, formant un bassin sag. (e) Un rift se développera sur cet ancien domaine orogénique, qui se refermera par exemple (f) au moyen d'une subduction. Les trois premiers inserts sont modifiés d'après Malavieille *et al.* (1990).

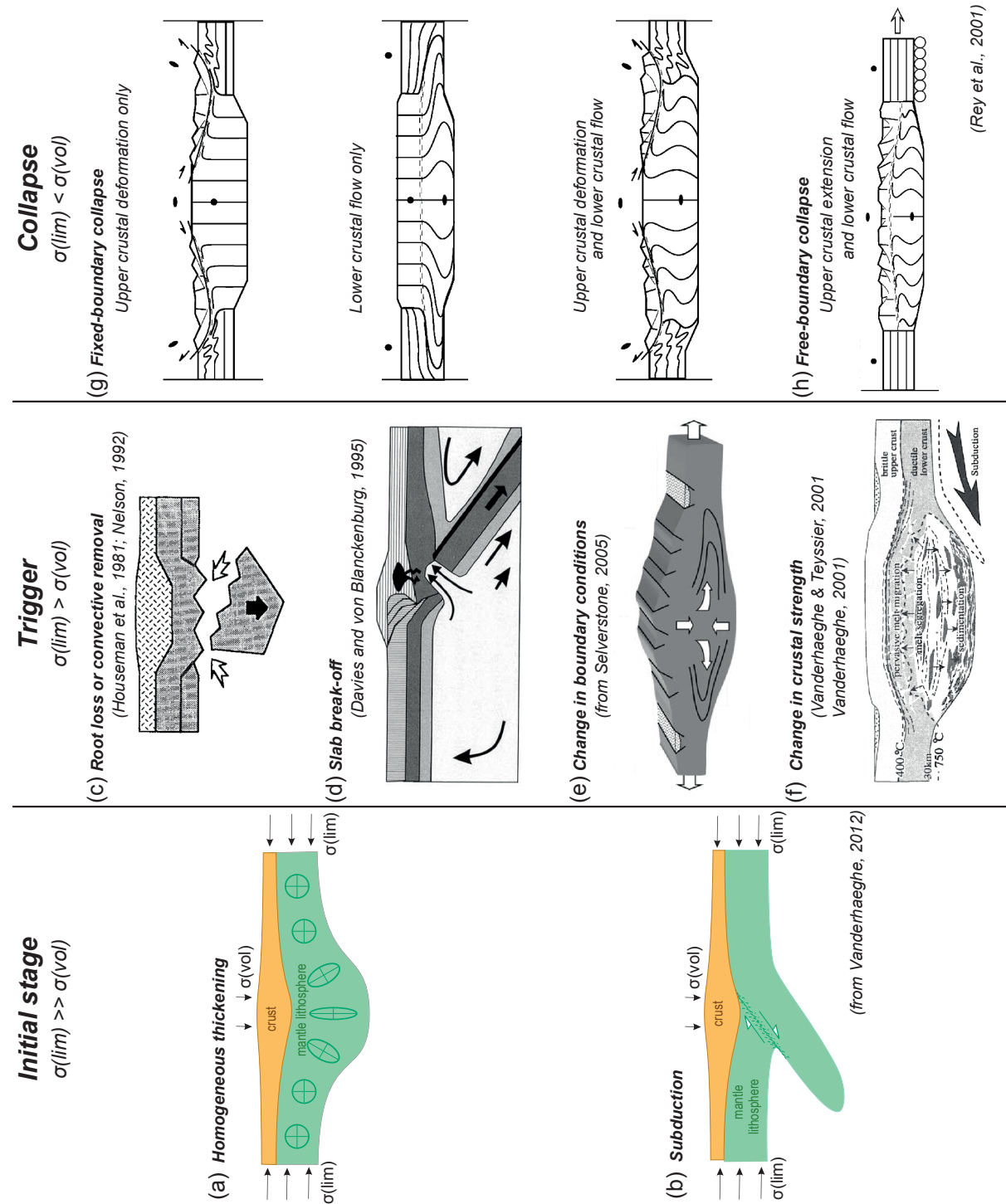
« L'équilibre » du domaine orogénique peut être perturbé de plusieurs manières ( $\sigma(\text{lim}) \geq \sigma(\text{vol})$ ). Soumises à des conditions de pression différentes de celles de leur formation, les roches de la racine crustale et mantellique de l'orogène vont se rééquilibrer et augmenter en densité, principalement au moyen de « l'éclogitisation » (p. ex. Leech, 2001; Meissner & Mooney, 1998). L'ensemble des parties denses a de fortes probabilités d'être perdu soit :

- (1) par « délamination », au cours de laquelle l'ensemble de la racine est détaché avec ou sans portion de croûte continentale (Fig. 2c, Bird, 1979; Nelson, 1992), ou simplement aminci progressivement par « érosion » mécanique et thermique (Fig. 2c, Houseman *et al.*, 1981; Platt & England, 1993)
- (2) soit par rupture uniquement de la plaque plongeante (Fig. 2d, Davies & von Blanckenburg, 1995).

L'effondrement peut également être généré par une diminution des forces tectoniques appliquées aux marges du système lors d'un changement de la dynamique des plaques (Fig. 2e), lors d'une chute de la résistance mécanique de l'orogène causée par exemple par la fusion partielle de la croûte épaisse (Fig. 2f, Vanderhaeghe & Teyssier, 2001), ou lorsque la topographie devient trop importante pour être supportée par les forces tectoniques. De fait, l'effondrement gravitaire ( $\sigma(\text{lim}) < \sigma(\text{vol})$ ) d'un orogène peut être déclenché alors que les forces tectoniques demeurent compressives (Armijo *et al.*, 1986; Gapais *et al.*, 1992; Selverstone, 2005), ou deviennent extensives (p. ex. Henk, 1999). Dès lors, bien que les facteurs déclencheurs de l'effondrement sont loin de faire consensus, ces conséquences sont certaines : l'orogène va subir une extension qui peut être localisée à différents niveaux crustaux et lithosphériques (Fig. 2gh, Rey *et al.*, 2001).

---

**Fig. 2:** Évolution théorique d'un orogène, où la croûte continentale et le manteau lithosphérique sont épaisse soit de manière homogène, soit au moyen d'une subduction (modifié d'après Vanderhaeghe, 2012). L'édifice est destabilisé par (c) détachement ou érosion thermique progressive de la racine lithosphérique (Houseman *et al.*, 1981; Nelson, 1992), (d) détachement de la plaque plongeante (Davies & von Blanckenburg, 1995), (e) changement des conditions aux limites, p. ex. changement de cinéétique des plaques continentales (d'après Selverstone, 2005), ou bien (f) changement de la résistance mécanique de la croûte orogénique p. ex. suite à la fusion partielle de la croûte orogénique sur-épaisse (Vanderhaeghe, 2001; Vanderhaeghe & Teyssier, 2001). Ces mécanismes déclenchent l'effondrement gravitaire de l'orogène (g) sans divergence continentale, ou bien (h) en étant accompagné de divergence continentale (Rey *et al.*, 2001).



## **2. IMPLICATIONS POUR L'ARCHITECTURE DE LA CROÛTE CONTINENTALE**

### **2.1 Modifications thermiques**

L'effondrement d'une chaîne de montagnes a une conséquence majeure sur l'architecture thermique de la lithosphère. En effet, qu'ils soient accompagnés de la perte d'une portion profonde de l'orogène ou simplement d'un amincissement de la lithosphère orogénique sur-épaisse, les modèles d'effondrement prévoient une élévation de l'asthénosphère, c'est-à-dire une augmentation du gradient géothermique (Fig. 3, p. ex. Platt & England, 1993). Bien que transitoire, cette dernière peut causer une élévation brutale de la topographie (ou *uplift*), dont le retour à l'équilibre est caractérisé par une subsidence thermique permettant le développement d'un bassin *sag*. Ainsi, l'extension géographique et la puissance de cet amincissement du manteau lithosphérique peuvent être estimées qualitativement grâce à l'analyse de la subsidence et du remplissage sédimentaire de ces bassins.

### **2.2 Modifications lithologiques**

Le retour à l'équilibre de la croûte orogénique a de nombreuses conséquences sur l'architecture de la croûte continentale. L'extension qui affecte le domaine orogénique, chaud et sur-épaissi, produit un *rifting diffus* (Buck, 1991; Buck *et al.*, 1999). Typiquement, des dômes migmatitiques (ou *metamorphic core complexes*) sont développés dans ces domaines (p. ex. Vanderhaeghe & Teyssier, 2001; Whitney *et al.*, 2012) et sont associés à un fluage latéral de la croûte inférieure pendant le développement d'une foliation horizontale dans la croûte inférieure (Block & Royden, 1990; Brun *et al.*, 1994; Malavieille, 1993; Sandiford, 1989). L'atténuation des reliefs de l'orogène permet aux sédiments d'être déposés dans l'ancien domaine orogénique, dans les nombreux bassins intra-montagneux bordés par des failles normales (Buck, 1991). Éventuellement, les roches enregistrent une exhumation identifiable grâce à des géochronomètres et à leur évolution en pression et en température.

Précédemment enrichi lors des subductions océaniques et continentales, le manteau sera partiellement fondu en raison de l'augmentation du gradient géothermique (Fig. 3cd), ce qui causera son appauvrissement. Des magmas mafiques d'affinité calco-alcaline à tholéitique (Bonin *et al.*, 1998) sont alors produits. Leur ascension au travers du manteau sous-continentale sera stoppée à la limite de rhéologie et de densité que constitue le Moho (Huppert & Sparks, 1988; Rudnick & Fountain, 1995; Voshage *et al.*, 1990). Ainsi, les corps mafiques sous-plaqués, typiques de la croûte inférieure, vont se constituer (Fountain, 1989; Fountain & Salisbury, 1981; Rudnick & Fountain, 1995). Leur structure va participer à la foliation horizontale de la croûte

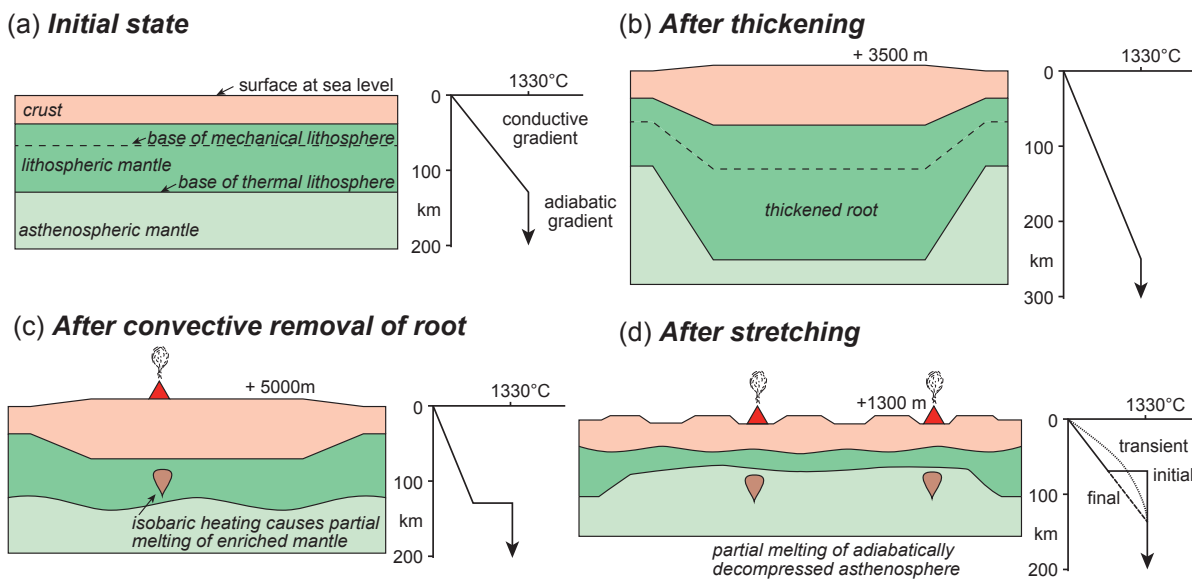


**Fig. 3:** Évolution théorique du géotherme lors d'un cycle orogénique à post-orogénique (modifié d'après Platt & England, 1993).

inférieure (Fountain, 1989). Ces liquides magmatiques advectent de la chaleur responsable de la fusion partielle de la croûte continentale (p. ex. Clark *et al.*, 2011; Clark *et al.*, 2014; Wells, 1980). Des liquides granitiques vont ainsi être produits (Annen *et al.*, 2006). Le magmatisme associé au démantèlement sera donc typiquement bimodal, où des plutons mafiques et felsiques seront mis en place de manière synchrone (Turner *et al.*, 1992).

Le métamorphisme de contact cause la fusion partielle de la croûte inférieure à moyenne en rééquilibrant les roches du faciès supérieur des amphibolites au faciès des granulites. Selon Harley (1989), les granulites ainsi produites se différencient des granulites de type orogénique (p. ex. O'Brien & Rötzler, 2003) par la nature de leur chemin rétrograde, qui va suivre une décompression isotherme (*ITD – near-isothermal decompression*, Harley, 1989) dans le cas des granulites orogéniques, à la différence des granulites post-orogéniques qui vont rester en profondeur en suivant un refroidissement isobarique (*IBC – near-isobaric cooling*, Bohlen, 1991; Harley, 1989).

### 3. LES ÉLÉMENTS CLÉS

Les processus tardi- à post-orogéniques ont donc la capacité de remodeler la croûte continentale dont l'architecture contiendra typiquement : en surface des bassins sédimentaires plus ou moins associés à des épisodes volcaniques et en profondeur de nombreuses intrusions mafiques et felsiques. Ces intrusifs sont associés à un métamorphisme de contact pouvant atteindre le faciès des granulites, suivis d'un refroidissement isobarique. La fin de l'épisode tectonique est marquée par la formation de bassins *sags* causée par une subsidence thermique.



---

# *CHAPITRE I*

---



# ÉVOLUTION EN EUROPE DE L'OUEST : DE L'OROGÈNE VARISQUE À L'EXTENSION POST-OROGÉNIQUE

Cette étude est focalisée sur l'Europe de l'Ouest et plus particulièrement sur la manière dont l'architecture de la croûte continentale européenne est modifiée par les processus actifs à la fin de l'orogénèse varisque, pendant le Permo-Carbonifère. De manière intéressante, les phases mésozoïques de rifting, qui ont permis l'ouverture de plusieurs domaines océaniques (voir les synthèses de Handy *et al.*, 2010; Mohn *et al.*, 2010; Schmid *et al.*, 2008; Stampfli *et al.*, 1998), ont amené proche de la surface, voire à l'affleurement, les roches composant cette lithosphère pré-rift, du manteau sous-continentaux aux bassins sédimentaires superficiels. Ces reliques de marges continentales sont désormais à l'affleurement dans les chaînes alpines *sensu lato*. Bien que certaines portions ont subi un métamorphisme important lors des stades de subduction et de collision (p. ex. Lardeaux & Spalla, 1991), certains domaines y ont échappé, permettant par conséquent d'étudier leur évolution pré-alpine et même pré-mésozoïque (p. ex. von Raumer & Neubauer, 1993).

Ainsi, l'évolution de l'orogène varisque en Europe de l'Ouest et plus particulièrement dans les Alpes peut se résumer en trois phases : son initiation lors de convergences et subductions du Dévonien au Carbonifère, son apogée marquée par une collision continentale au Carbonifère et son démantèlement de la fin du Carbonifère au début du Permien.

## 1. OROGÉNÈSE VARISQUE

### 1.1 Convergences et subductions dévono-carbonifères

L'orogénèse varisque est initiée par l'accrétion sur la marge sud du continent Laurussia (comprenant Laurentia et Baltica, accolés pendant l'orogénèse cadienne) de terrains (ou « micro-continents ») dérivés de la marge nord du Gondwana (Fig. I-1ab). La migration de ces terrains (p. ex. Armorica) est associée à des fermetures d'océans (Rheic, Galicia-Massif Central, Matte, 1986; Matte, 2001) lors d'épisodes de subduction initiés de la fin du Silurien au Dévonien (p. ex. Ballèvre *et al.*, 2014; Faure *et al.*, 2009). Leur nombre exact demeure en discussion (voir p. ex. Franke, 2014). Ces subductions sont associées à un métamorphisme de haute pression dont les reliques sont documentées par exemple dans le Massif Central (Faure *et al.*, 2009). Elles sont également observées dans les Alpes avec la présence d'éclogites (p. ex. Godard *et al.*, 1996; Schulz & Von Raumer, 1993) et de granulites de haute pression

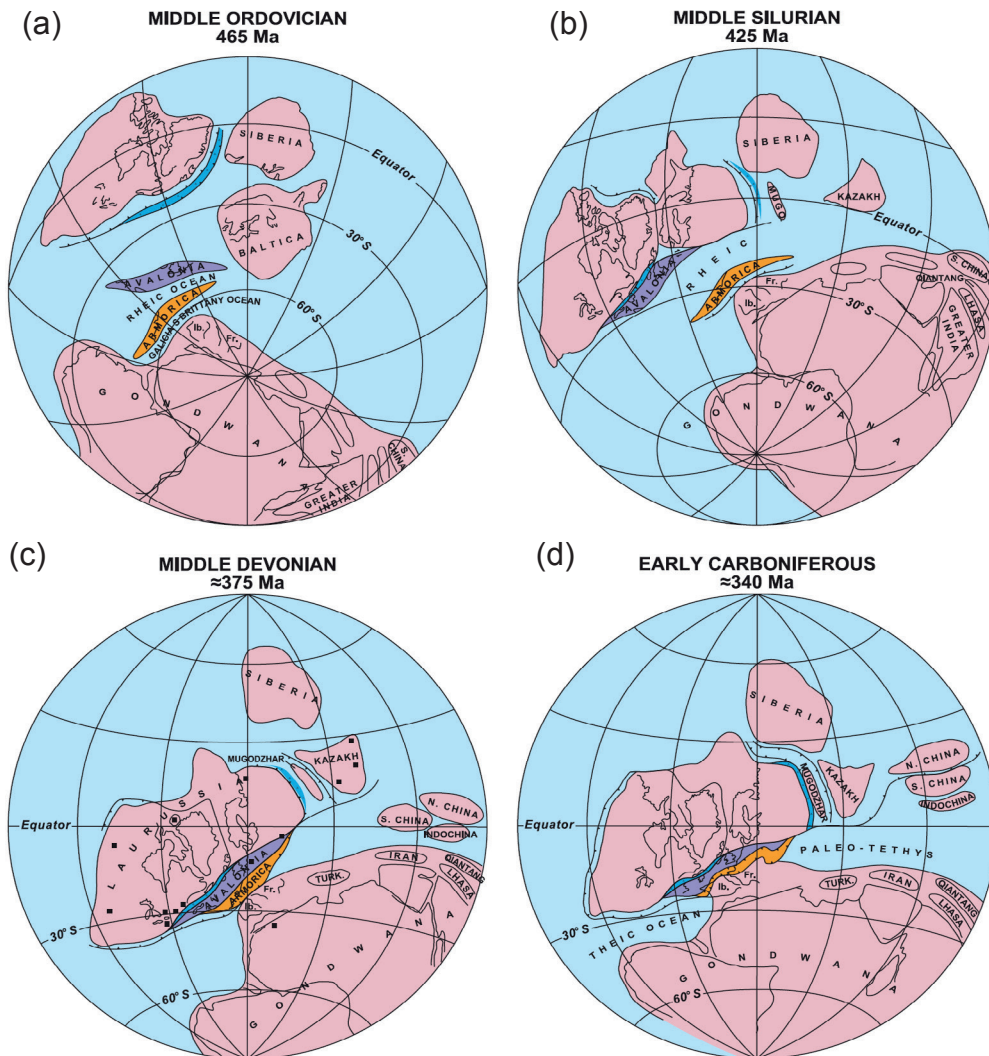


**Fig. I-1:** Reconstruction palinspatique de la marge nord du Gondwana et des continents Laurentia et Baltica (rose) formant le continent Laurussia à partir du Dévonien moyen, et sur lequel viennent s'accréter des arcs insulaires associés aux systèmes de subduction océanique (bleu) et des rubans continentaux (violet : Avalonia ; orange : Armorica) lors de la construction de l'orogénèse varisque. Modifié d'après Matte (2001).

(Ferrando *et al.*, 2008) datées entre 370 et 330 Ma (Ladenhauf *et al.*, 2001; Miller & Thöni, 1995; Rubatto *et al.*, 2010; Rubatto *et al.*, 2001; Tumiati *et al.*, 2003). Les phases compressives sont interrompues par des phases extensives formant des bassins d'arrière arc du Dévonien jusqu'au début du Carbonifère, de nature fréquemment marine (p. ex. Skrzypek *et al.*, 2012). Ainsi, le domaine orogénique subit des transgressions marines répétées (voir Franke, 2014 et références citées).

## 1.2 Collision carbonifère

La fin des épisodes de subduction est marquée par la fermeture de tous les bassins océaniques lors de la collision continentale entre Gondwana et Laurussia, formant la Pangée du Dévonien au Carbonifère moyen (Fig. I-1cd, Matte, 2001). Le long de la marge active sud-est de Laurussia, l'océan Paléotéthys est préservé. La chaîne orogénique varisque ainsi formée s'étend à la fin du Carbonifère du Caucase à l'est, jusqu'aux Appalaches à l'ouest, et est composée des nombreux blocs accrétés lors des subductions et séparés par des sutures (p. ex. Matte, 2001). La collision continentale convertit le domaine Rheno-Hercynien en bassin flexural d'avant-pays au nord de la chaîne (Fig. I-2, Oncken *et al.*, 2000). La structure de l'avant-pays sud demeure peu contrainte à cause des intenses remaniements dus à la tectonique méditerranéenne (p. ex. Alvarez *et al.*, 1974). Ainsi, les bassins d'avant-pays entourent le domaine orogénique et sont documentés, en plus du domaine Rheno-Hercynien, en Bohême (Hartley & Otava, 2001), dans les Alpes carniaques (Krainer, 1993; Läufer *et al.*, 2001) et éventuellement le long de la marge ibérique (Manatschal *et al.*, 2001; Whitmarsh *et al.*, 1998).

Le cœur du domaine orogénique subit un métamorphisme de haute température et moyenne pression, causé par la décroissance d'éléments radioactifs (Gerdes *et al.*, 2000) associée à une « maturation thermique » due à la relaxation des isothermes (England & Thompson, 1986). La croûte fond partiellement et un important magmatisme granitique est développé (Fig. I-2, voir p. ex. Henk *et al.*, 2000). De manière synchrone, les intrusions de magmas magnésio-

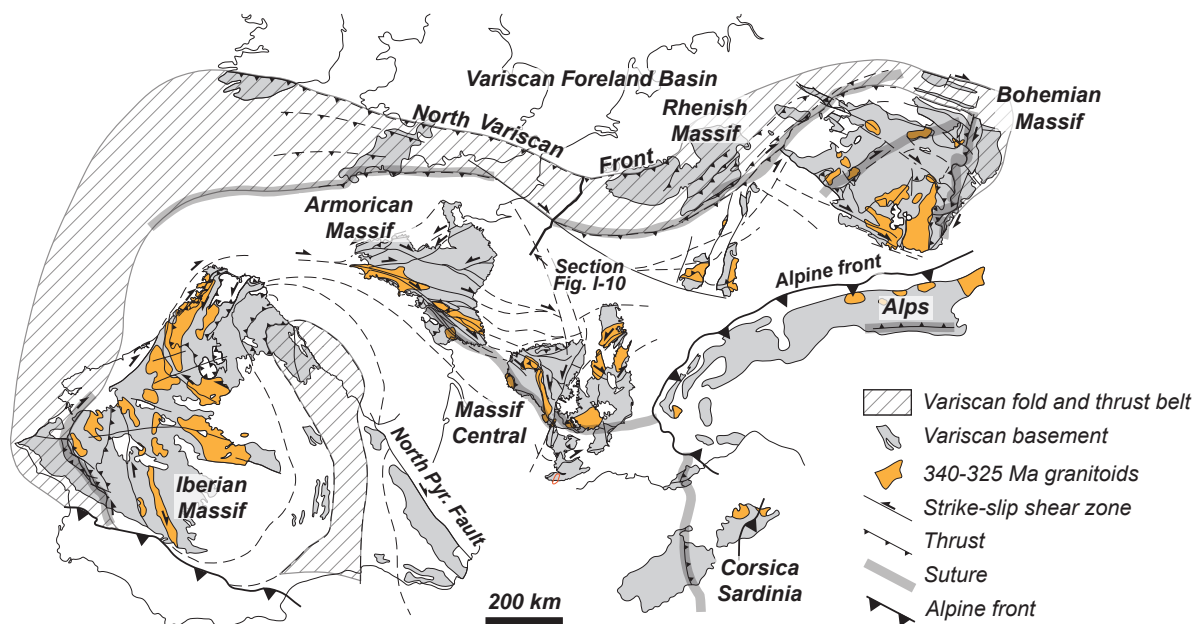


**Fig. I-2:** Schéma de la chaîne varisque en Europe de l'ouest modifié d'après Martínez Catalán (2011) et Ballèvre *et al.* (2014). Distribution des granitoïdes datés de 340 à 325 Ma d'après Henk *et al.* (2000). La localisation de la coupe sismique présentée en Fig. I-7 est indiquée.

potassiques entre 340 et 335 Ma (vaugnérites et durbachites, p. ex. von Raumer *et al.*, 2014) indiquent que l'état thermique du manteau est assez élevé (Henk *et al.*, 2000). Dans le domaine alpin, les roches ayant subi un métamorphisme barrovien (jusque 12 kbar et 650°C; Braga *et al.*, 2007; Frei *et al.*, 1995; Maggetti & Flisch, 1993; Schaltegger & Gebauer, 1999; Thélin *et al.*, 1993) subissent un pic thermique entre 330 et 310 Ma (Bussy & Hernandez, 1997; Bussy *et al.*, 1996; Langone *et al.*, 2011; Maggetti & Flisch, 1993; Rubatto *et al.*, 2010; Rubatto *et al.*, 2001; Schaltegger, 1994; Spalla *et al.*, 1999; Thöni, 1999) alors que le domaine est intrudé par des magmas magnéso-potassiques à ultra-potassiques (Bonin *et al.*, 1993; Debon *et al.*, 1998; Debon & Lemmet, 1999; Spillmann & Büchi, 1993; von Raumer *et al.*, 2014).

## **2. ÉVOLUTION TARDI- À POST-OROGÉNIQUE**

La fin de la phase convergente est marquée par l'activité de grandes structures de décrochements dextres d'orientation NO-SE, le long des marges nord du Gondwana et sud de Laurussia au travers de tout le domaine orogénique (Fig. I-3, Arthaud & Matte, 1977; Muttoni *et al.*, 2003). Ces décrochements sont relayés par de plus petites structures senestres NNE-SSO. Ces structures, également identifiées dans les Alpes (p. ex. Padovano *et al.*, 2012), retracent un déplacement dextre entre les deux plaques continentales, entrant désormais en collision en Oural au NE (p. ex. Matte, 2006), en Mauritanie et dans Appalaches au SO (p. ex. Chopin *et al.*, 2014). Éventuellement, ces décrochements sont responsables (ou ont au moins participé) à la formation de l'orocinal Cantabre entre 304 et 295 Ma (Martínez Catalán, 2011; Weil *et al.*, 2013). À cette époque, le système fonctionne toujours en convergence (Denèle *et al.*, 2014), mais les directions de linéation d'étirement et les déformations des plutons syn-cinématiques indiquent une extension de la chaîne parallèlement à son élongation (voir Burg *et al.*, 1994; Faure, 1995). À partir du Carbonifère moyen, de rares bassins intra-continentaux commencent à s'ouvrir dans la chaîne, alors que les bassins d'avant-pays sont encore sous le niveau de la mer (Fig. I-4).

À partir de 300 Ma en Europe de l'Ouest, les conditions tectoniques, auparavant principalement compressives, deviennent transtensives et la lithosphère entière voit son architecture profondément modifiée, de la croûte supérieure au manteau. Les éléments en sont synthétisés ci-dessous.

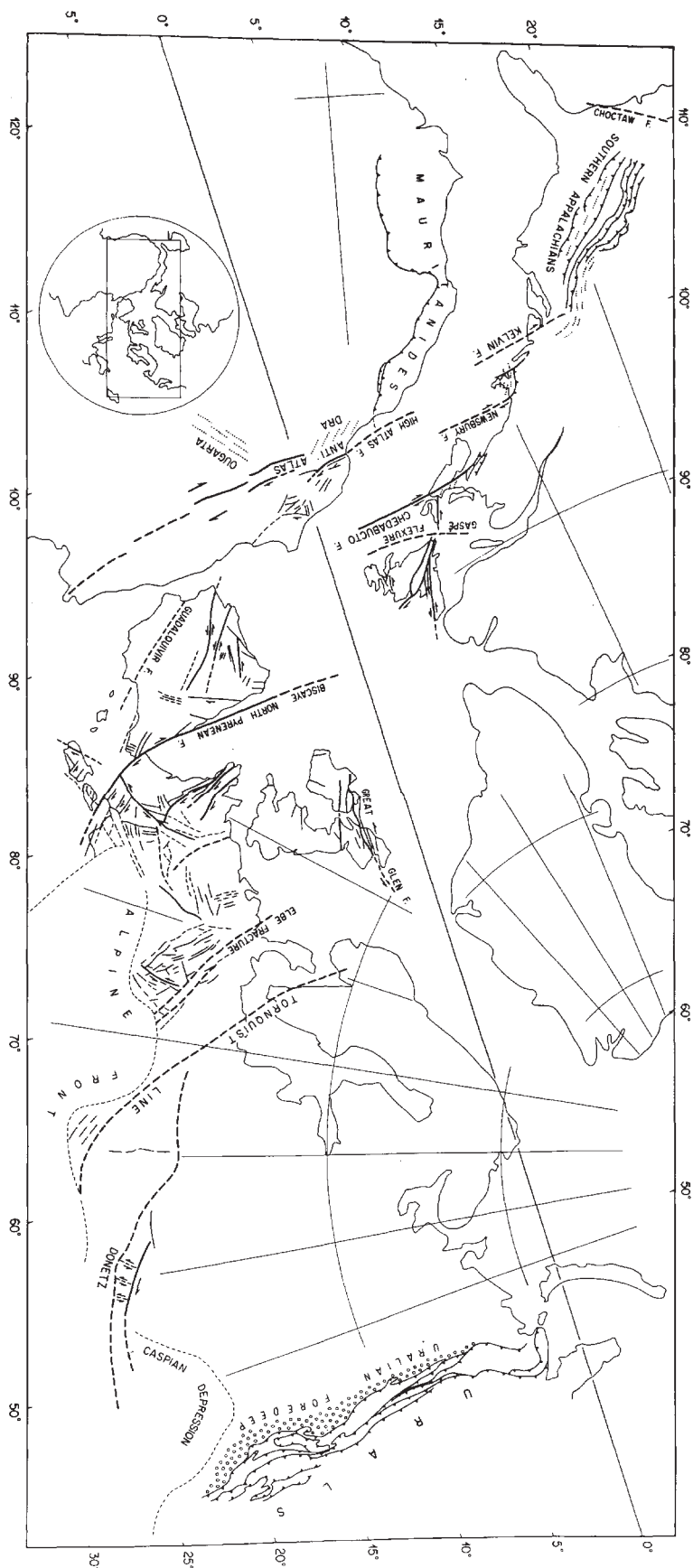


**Fig. I-3:** Carte des structures tardi-varisques de l'Oural aux Appalaches d'après Arthaud & Matte (1977).

## **2.1 Évolution des bassins sédimentaires**

La tectonique transtensive généralisée au début du Permien permet l'ouverture de nombreux bassins au travers de tout le domaine orogénique et de son avant-pays désormais émergé (Fig. I-5, McCann *et al.*, 2006), lors d'un épisode de soulèvement étendu à toute l'Europe de l'Ouest (Ziegler *et al.*, 2004).

Dans les parties internes, des dômes extensifs migmatitiques (Ledru *et al.*, 2001) ou non migmatitiques (Froitzheim *et al.*, 2008) se forment, tandis que les dômes compressifs pyrénéens (p. ex. Denèle *et al.*, 2014) sont inversés par une extension principalement NE-SO (p. ex. Pitra *et al.*, 2012; Van Den Driessche & Brun, 1991-1992). Ces directions varient fortement d'un bloc à l'autre à l'échelle de l'orogène (Burg *et al.*, 1994). Le jeu des failles permet la formation de bassins petits et allongés (Fig. I-5), dans lesquels se déposent des grès et conglomérats entrecoupés par des passées limniques (Becq-Giraudon & Van Den Driessche, 1994; Cassinis *et al.*, 1995). Les dépôts de ces bassins deviennent progressivement fluvio-lacustres en haut de la séquence, mais demeurent continentaux pendant le Permien. La topographie du domaine orogénique au début de cette phase tectonique demeure incertaine : certains auteurs suggèrent que l'altitude est supérieure à 4500 m dans la chaîne (Becq-Giraudon & Van Den Driessche, 1994), tandis que d'autres proposent un relief plus modéré (essentiellement des « collines », Franke, 2012; Franke, 2014; Roscher & Schneider, 2006).

Au nord de l'ancienne chaîne orogénique se forment de nombreux bassins dont en particulier les bassins permianes nord (dont une partie constitue le rift d'Oslo) et sud (Nord de l'Allemagne, Fig. I-5b, p. ex. van Wees *et al.*, 2000). En particulier, le bassin sud permien se développe sur l'ancien domaine d'avant-pays orogénique, où les dépôts du Paléozoïque au Cénozoïque atteignent jusque 12 km d'épaisseur (Oncken *et al.*, 2000). Ces bassins utilisent des structures lithosphériques préexistantes d'ordre majeur (Ebbing *et al.*, 2005; McCann *et al.*, 2006). Le remplissage de ces bassins est essentiellement clastique, mais à la différence des bassins intra-orogéniques, ils subissent des transgressions marines répétées dès la fin du Carbonifère, indiquant qu'ils se situent proche ou au niveau de la mer.

Dans les Alpes, les grabens ou demi-grabens sont également petits et allongés, à remplissage clastique à volcano-clastique. Ces bassins sont déjà ouverts au Carbonifère (Capuzzo & Wetzel, 2004; Trümpy, 1980) et les dépôts peuvent atteindre une épaisseur de 2500 m (p. ex. dans le domaine Briançonnais, Courel *et al.*, 1986). Soumis principalement à des dynamiques fluviales à lacustres, ils voient rapidement leurs dépôts devenir évaporitiques à marins peu profonds dans l'avant-pays sud varisque échantillonné dans les Alpes carniques (Krainer, 1993; Läufer *et al.*, 2001).

Progressivement, les petits bassins individualisés se connectent sans jeu de failles, indiquant une période de subsidence thermique qui perdurera pendant une bonne partie du Mésozoïque, pour former par exemple le bassin de Paris. Les modélisations suggèrent que cette phase est initiée dès la fin du Permien inférieur, autour de 285 Ma (Ziegler *et al.*, 2004; Ziegler *et al.*, 2006). Alors que l'activité tectonique se stabilise progressivement en Europe, le domaine sud- et est-alpin demeure actif avec l'ouverture de la Néotéthys et de Meliata-Vardar (p. ex. Stampfli & Kozur, 2006).

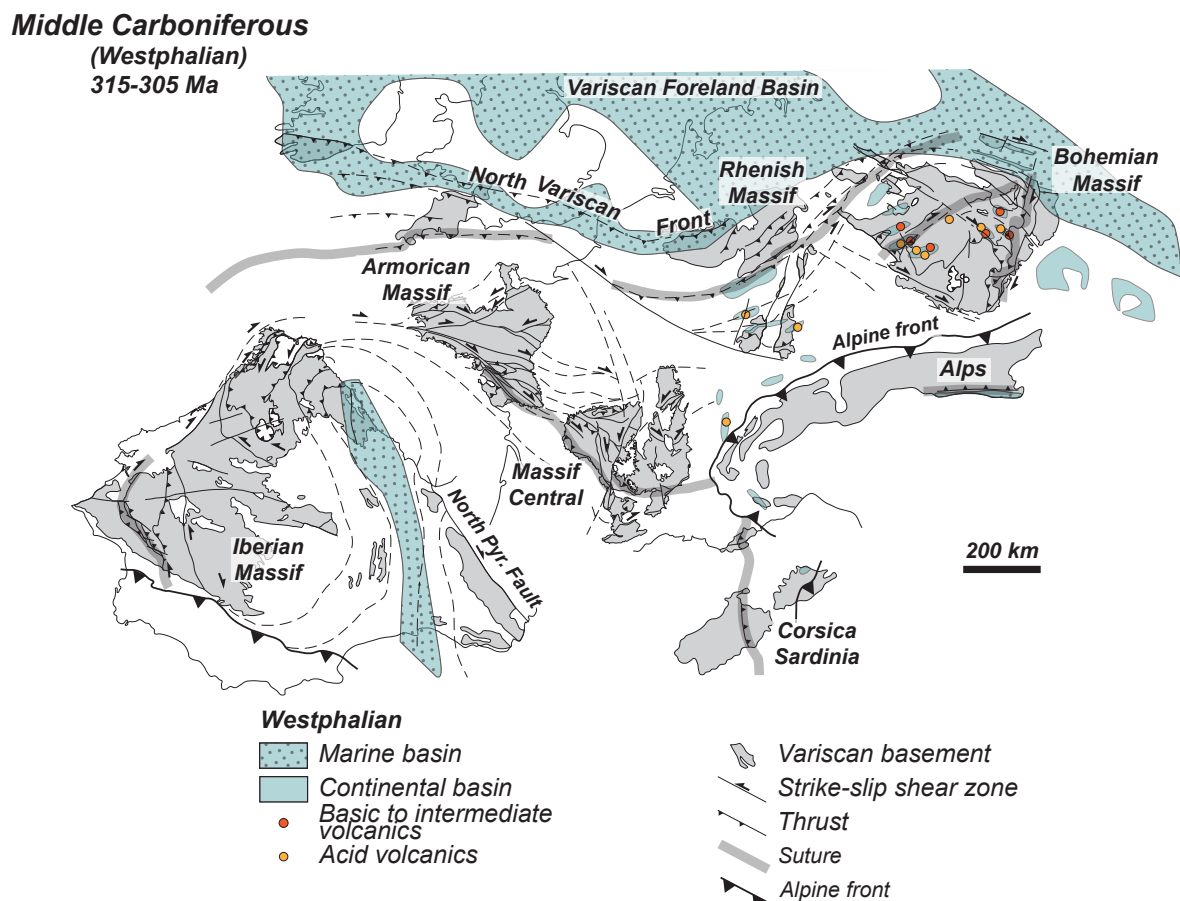


**Fig. I-4:** Carte des bassins sédimentaires et des roches volcaniques datés du Carbonifère moyen (315 – 305 Ma) d'après Lorenz & Nicholls (1976). Schéma de la chaîne varisque modifié d'après Martínez Catalán (2011) et Ballèvre *et al.* (2014).

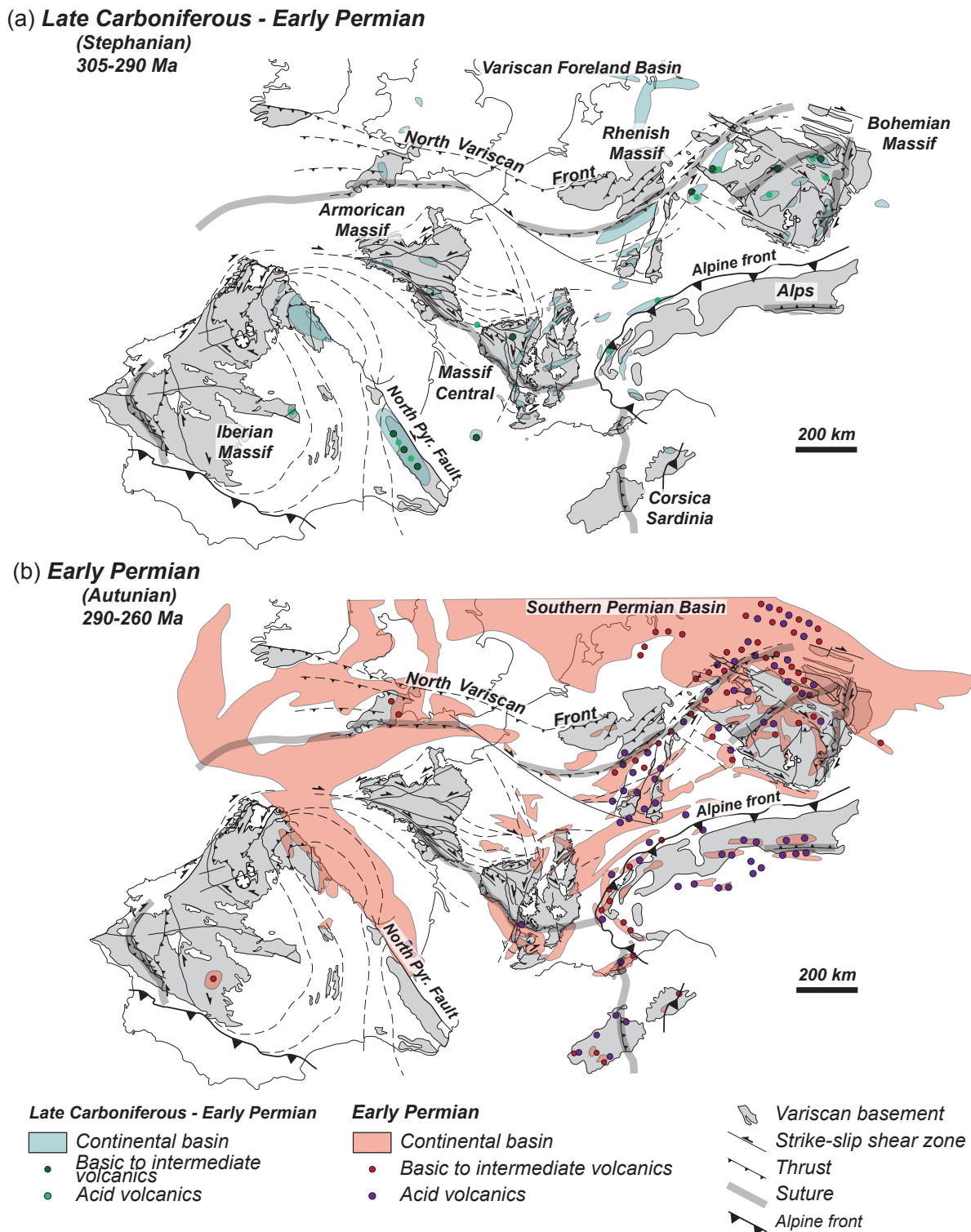


**Fig. I-5:** Carte des bassins sédimentaires et des roches volcaniques. (a) Carbonifère supérieur à Permien inférieur (305 – 290 Ma) d'après Feys (1989), Läufer et al. (2001) et Lorenz & Nicholls (1976). (b) Permien inférieur (290-260 Ma) d'après Burg et al. (1994), Cassinis et al. (2012), Châteauneuf (1989), Feys (1989) et Lorenz & Nicholls (1976). Schéma de la chaîne varisque modifié d'après Martínez Catalán (2011) et Ballèvre et al. (2014).

## 2.2 Évolution magmatique

La tectonique transtensive vue dans tout le domaine européen est associée à un magmatisme mafique et felsique, dont l'expression entre les anciens domaines orogéniques et non orogéniques est contrastée (p. ex. Timmerman, 2004).

En dehors de la chaîne, les dépôts clastiques des bassins nord et sud permiens sont entrecoupés par des passées volcaniques (Fig. I-5b, Heeremans *et al.*, 2004a). Débutant vers 310 Ma, le volcanisme est principalement actif vers 290 Ma (Heeremans *et al.*, 2004b; Timmerman *et al.*, 2009). Les magmas expulsés sont majoritairement mafiques dans le bassin permien nord, alors qu'ils deviennent principalement felsiques vers le sud (Fig. I-5b). De nombreux dykes sont également documentés en Grande-Bretagne et en Irlande (Heeremans *et al.*, 2004a; Kirstein *et al.*, 2006). Cependant, la présence de corps mafiques sous-plaqués dans ces domaines externes est incertaine (voir p. ex. Ebbing *et al.*, 2005; Timmerman *et al.*, 2009).

Alors que le volcanisme permien à l'extérieur de la chaîne est plutôt alcalin, dans le centre de la chaîne il est tout d'abord calco-alcalin, puis évolue progressivement (mais pas de manière synchrone) vers un magmatisme alcalin (Bonin, 1988; Bonin *et al.*, 1998; Spillmann & Büchi, 1993; Von Quadt *et al.*, 1994). De nombreux niveaux de tuffs et coulées felsiques tardi-carbonifères à permiens se déposent dans les bassins intra-montagneux (Fig. I-5, voir synthèse de Timmerman, 2004), particulièrement visibles dans les Alpes avec la mise en place de granites et de rhyolites (p. ex. Schaltegger & Brack, 2007; Von Quadt *et al.*, 1994).

Des plutons mafiques permiens, d'affinité tholéitique, sont exhumés tectoniquement dans les domaines de rift mésozoïques plus ou moins réactivés par les compressions alpines (marge ibérique, Pyrénées, Alpes, Corse, voir Fig. I-6). Ces plutons permiens sont documentés dans tous les niveaux crustaux (Fig. I-6 & II-1) : en croûte inférieure (Hermann *et al.*, 1997; Libourel, 1988; Vielzeuf & Pin, 1991; Voshage *et al.*, 1987), en croûte moyenne (p. ex. Tribuzio *et al.*, 1999) et en croûte supérieure (Monjoie *et al.*, 2007; Tribuzio *et al.*, 2009). La différenciation magmatique et l'assimilation de liquides d'origine crustale produisent un magmatisme felsique, intimement lié au magmatisme mafique (Schaltegger & Brack, 2007; Sinigoi *et al.*, 2011). La majeure partie de ces intrusifs est datée entre 290 et 280 Ma (Hansmann *et al.*, 2001; Paquette *et al.*, 2003; Peressini *et al.*, 2007). Dans les Alpes, le manteau subit à cette époque un épisode de fusion partielle majeur (Müntener *et al.*, 2004; Rampone *et al.*, 1996; Rampone *et al.*, 1998), alors que dans la chaîne ibérique, les signatures isotopiques des magmas felsiques à intermédiaires mis en place au début du Permien montrent un remplacement progressif de la source mantellique (Gutiérrez-Alonso *et al.*, 2011).

En dehors des zones de rifting mésozoïques où la croute inférieure n'est pas accessible, les volcans tertiaires et quaternaires échantillonnent des portions de croûte inférieure,

fréquemment – mais pas systématiquement – mafique. En particulier, la croûte inférieure sous le Massif Central, le massif de l’Eiffel, et le « Système Central Espagnol » est – au moins en partie – composée de roches mafiques litées (Downes *et al.*, 1990; Féménias *et al.*, 2005; Loock *et al.*, 1990; Villaseca *et al.*, 2007). Dans le Massif Central, ces roches mafiques litées (Berger *et al.*, 2007) se sont mises en place avant ou autour de 257 Ma (Féménias *et al.*, 2003). Certains auteurs étendent ce magmatisme sous-plaqué tardi-carbonifère à début-permien à l’ensemble des parties internes de l’orogène varisque (Costa & Rey, 1995; Rey, 1993), car les caractéristiques sismiques de la croûte inférieure sont homogènes à l’échelle de l’ancien domaine et que son litage recoupe les structures varisques (Fig. I-7, Bois *et al.*, 1989).

Alors que l’activité magmatique se réduit au court du Permien, elle reste particulièrement active dans les Alpes du sud et est maintenue jusqu’au Trias, voire au Jurassique (p. ex. Cassinis *et al.*, 2008; Zanetti *et al.*, 2013).

### **2.3 Évolution métamorphique**

De manière synchrone, l’augmentation du géotherme est responsable d’un métamorphisme de haute température, équilibrant les roches du faciès des schistes verts aux granulites et principalement documenté dans les Alpes (voir la compilation de Schuster & Stüwe, 2008). La plupart des granulites permianes est associée à des corps mafiques mis en place à des conditions similaires que celles du métamorphisme des roches encaissantes (Barboza & Bergantz, 2000; Braga *et al.*, 2001; Lardeaux & Spalla, 1991; Libourel, 1985; Müntener *et al.*, 2000). En revanche, le métamorphisme de contact de certains intrusifs semble localement se superposer à un métamorphisme de haute température préexistant (p. ex. Barboza *et al.*, 1999). Ainsi, la relation exacte entre le métamorphisme et le magmatisme reste discutée. Bien que sa position au cours du Paléozoïque est peu contrainte, la Calabre enregistre également cet épisode magmatique et métamorphique (Caggianelli *et al.*, 2013; Schenk, 1981). Des unités de granulites felsiques sont également documentées dans les Pyrénées. Bien que leur âge ne soit que peu contraint (Vielzeuf, 1984), elles semblent reprises par un événement de haute température mésozoïque (Clerc & Lagabrielle, 2014). De rares dômes migmatitiques extensifs datés du début du Permien se créent dans le Massif Central (Ledru *et al.*, 2001).

En dehors des domaines affectés par les phases de rifting mésozoïques, des granulites felsiques et des granulites mafiques (dérivées des corps mafiques sous-plaqués) sont également échantillonnées dans des xénolithes par des volcans tertiaires et quaternaires. Elles sont principalement équilibrées à des conditions de croûte inférieure, dont le métamorphisme est contraint entre 312 et 277 Ma par exemple dans la chaîne ibérique (Fernández-Suárez *et al.*,

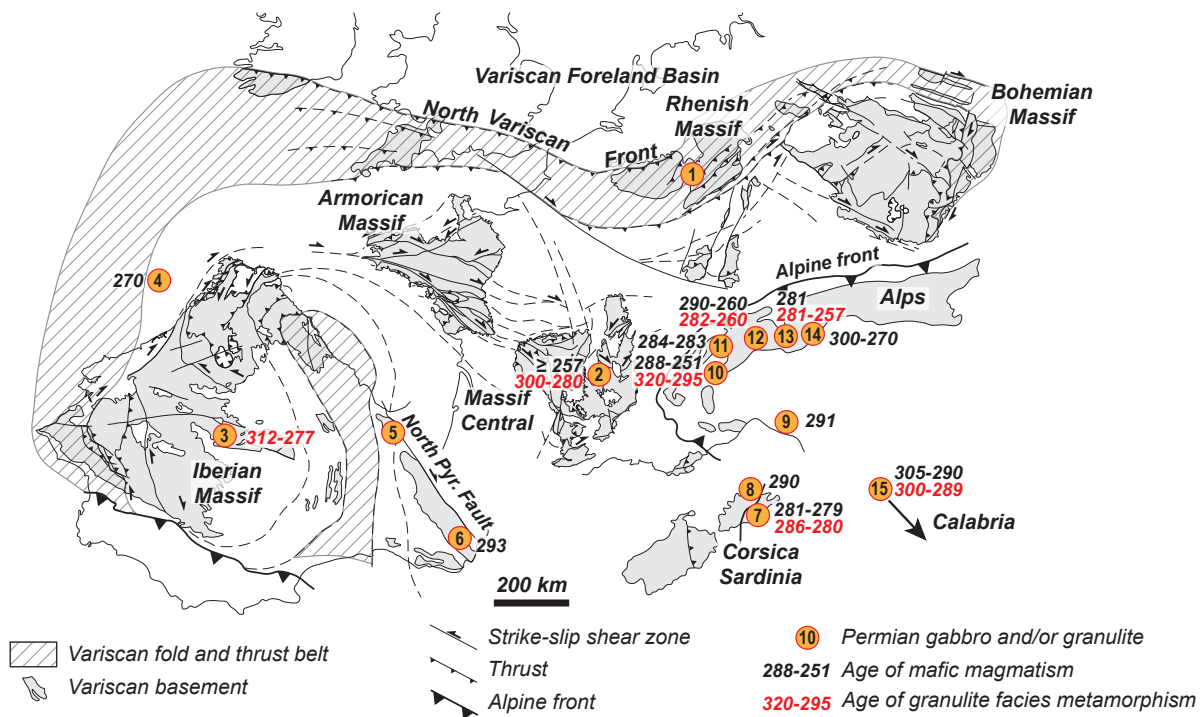


**Fig. I-6:** Synthèse non exhaustive des affleurements présentant gabbros permiens et granulites permienues échantillonnes par les volcans tertiaires (xénolithes) ou par les processus tectoniques. Xénolithes : 1 – Massif de l'Eifel (e.g. Loock *et al.*, 1990) ; 2 – Massif Central (Beaunit, Costa & Rey, 1995; Downes *et al.*, 1991; Féminias *et al.*, 2003) ; 3 – Système Central Espagnol (Fernández-Suárez *et al.*, 2006; Villaseca *et al.*, 2007) ; 4 – Marge Ibérique (site ODP 1069, Manatschal *et al.*, 2001) ; 5 – Massif d'Ursuya (Vielzeuf, 1984; Vielzeuf & Kornprobst, 1984) ; 6 – Norite de Treilles (Vielzeuf & Pin, 1991) ; 7 – Massif de Santa Lucia (Paquette *et al.*, 2003; Rossi *et al.*, 2006) ; 8 – Gabbro de Bocca di Tenda (Cocherie *et al.*, 2005; Tribuzio *et al.*, 2009) ; 9 – Monte Ragola (Meli *et al.*, 1996) ; 10 – Ivrea (Peressini *et al.*, 2007; Pin, 1986) ; 11 – Sassa, Sermenta et Mont Collon (Baletti *et al.*, 2012; Bussy *et al.*, 1998; Monjoie *et al.*, 2007) ; 12 – Complexe de Gruf (Galli *et al.*, 2012) ; 13 – Malenco (Hansmann *et al.*, 2001; Hermann & Rubatto, 2003) ; 14 – gabbro de Sondalo (Bachmann & Grauert, 1981; Tribuzio *et al.*, 1999) ; 15 – Calabre (Caggianelli *et al.*, 2013; Schenk, 1981).

2006). Dans le Massif Central, les datations U–Pb sur zircon et monazite des granulites felsiques sont concordantes entre 300 et 280 Ma (Costa & Rey, 1995; Downes *et al.*, 1991).

Typiquement, la majeure partie des terrains enregistrant ce métamorphisme présente l'association de roches métamorphiques de haut degré et de roches magmatiques mafiques plus ou moins métamorphiques. Elles suivent un refroidissement isobarique (p. ex. Müntener *et al.*, 2000) typique des granulites post-orogéniques (Harley, 1989) et qui diffère des granulites dites « orogéniques » également documentées ailleurs dans l'orogène (p. ex. Vielzeuf & Pin, 1989). Ainsi, ceci indique que les roches ont séjourné pendant une période plus ou moins longue dans leur niveau de formation, avant d'être éventuellement exhumées lors d'un cycle tectonique ou volcanique postérieur.

## 2.4 Cadre géodynamique

La province cénozoïque du *Basin and Range* à l'ouest des États-Unis a été considérée comme un analogue actuel des stades tardi- à post-orogéniques varisques (Lorenz & Nicholls, 1976; Lorenz & Nicholls, 1984), en raison de similitudes de topographie (hauts topographiques formés par le socle, bordés par des bassins contemporains ou plus jeunes, Ménard & Molnar, 1988), de géométrie des bassins (étroits et allongés, Lorenz & Nicholls, 1984), de magmatisme (Schaltegger & Corfu, 1995), ou bien simplement tectoniques (Malavieille, 1993). Cependant, les causes géodynamiques des évènements tardi- à post-orogéniques varisques demeurent moins contraintes. En effet, la plupart des modèles pouvant provoquer le déclenchement de l'effondrement gravitaire d'une chaîne orogénique, listés dans la section précédente, a été proposée pour l'orogène varisque :

- la perte de la racine orogénique (Gutiérrez-Alonso *et al.*, 2011) ;
- une diminution des forces tectoniques compressives (Malavieille *et al.*, 1990) par un rifting se propageant au travers de l'orogène (Schuster *et al.*, 2001; Schuster & Stüwe, 2008), éventuellement aidé par la subduction de la dorsale Paléotéthysienne (Stampfli, 1996) ;
- une rupture de plaque plongeante (p. ex. Ziegler *et al.*, 2006) ;
- un diapir mantellique profond (Doblas *et al.*, 1998).

Henk (1999) propose que les forces tectoniques et gravitaires ont toutes deux causé cet évènement, par effondrement gravitaire couplé à une divergence entre Gondwana et Laurussia, déclenchant ainsi l'extension dans et en dehors de la chaîne varisque. Cependant, tous les modèles mentionnés ci-dessus impliquent que la lithosphère a été épaisse lors de la collision continentale. Ce phénomène est remis en cause p. ex. par Franke (2014) qui conclut que l'orogène varisque, exceptionnellement chaud, était voué à l'échec.

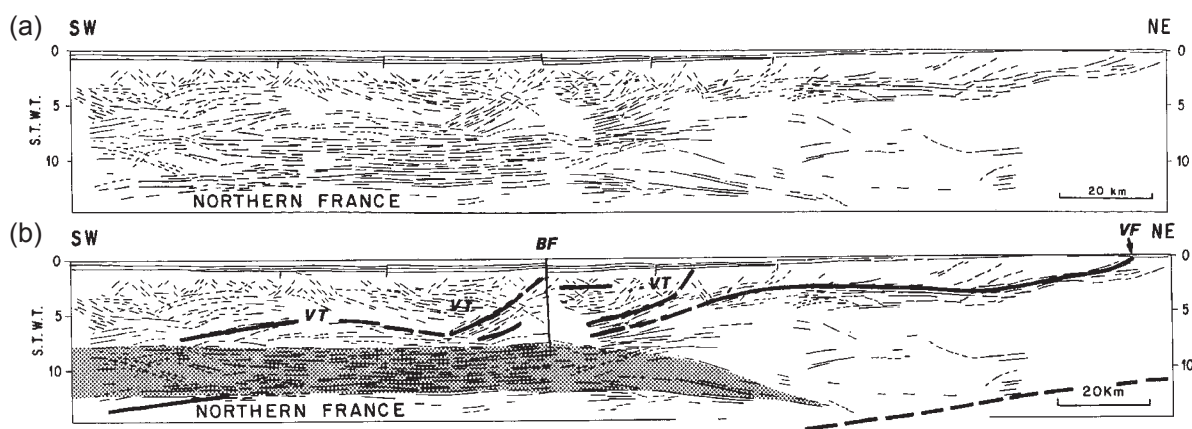


**Fig. I-7:** (a) Coupe sismique profonde du nord de la France avec (b) son interprétation. BF – Faille de Bray ; VF – Front Varisque ; VT – Chevauchement varisque. Voir localisation de la coupe sismique sur la Fig. I-2. Gris : croûte inférieure litée. D'après Bois *et al.* (1989).

---

## *CHAPITRE II*

---



## CADRE, MÉTHODOLOGIE ET PLAN DE LA THÈSE

### 1. QUESTIONS SOULEVÉES

La synthèse géologique présentée dans le *chapitre I* montre que les événements tectoniques, magmatiques et métamorphiques permiens modifient profondément l'architecture de la croûte continentale européenne. Une grande partie de ces modifications est associée au magmatisme mafique. Ainsi, ce travail de thèse a pour but de contraindre les phénomènes post-orogéniques permiens, et plus particulièrement la relation entre magmatisme, métamorphisme et tectonique. Les principales questions formulées dans cette thèse sont :

- A) *Quel est le lien entre magmatisme et métamorphisme lors de l'évolution tardive à post-orogénique ? (Chapitre III)*
- B) *Quels est la dynamique de mise en place des intrusions mafiques permiennes ? (Chapitres III & IV)*
- C) *Quels sont les systèmes d'exhumation des intrusions permiennes, de leur formation au rifting mésozoïque ? (Chapitres III, IV & V)*
- D) *L'extension post-orogénique permienne : quel contexte géodynamique ? (Chapitre VI)*
- E) *Quelle est l'influence de l'architecture crustale ou lithosphérique héritée des événements post-orogéniques sur les rifts mésozoïques ? (Chapitre VI)*

### 2. OÙ Y RÉPONDRE ?

La plupart des études portant sur les problématiques soulevées se focalise sur les unités de croûte inférieure, mais ces études sont fréquemment confrontées à des problèmes de superposition d'événements tectoniques, magmatiques et métamorphiques, rendant leur individualisation souvent difficile. En revanche, les systèmes magmatiques et métamorphiques permiens dans les niveaux intermédiaires (comprendre « la croûte moyenne ») peuvent éviter les inconvénients présents dans la croûte inférieure. Ces niveaux intermédiaires ne sont documentés que le long des chaînes alpines. Cependant, afin de pouvoir contraindre au maximum la dynamique de mise en place des intrusions permiennes dans la croûte moyenne, il est essentiel de contraindre au maximum les événements tectoniques ultérieurs, comme l'ouverture de la Téthys alpine et l'orogénèse alpine. Ainsi, la zone d'étude devra avoir échappé aux fortes déformations et rééquilibrages métamorphiques lors des phases de collision.

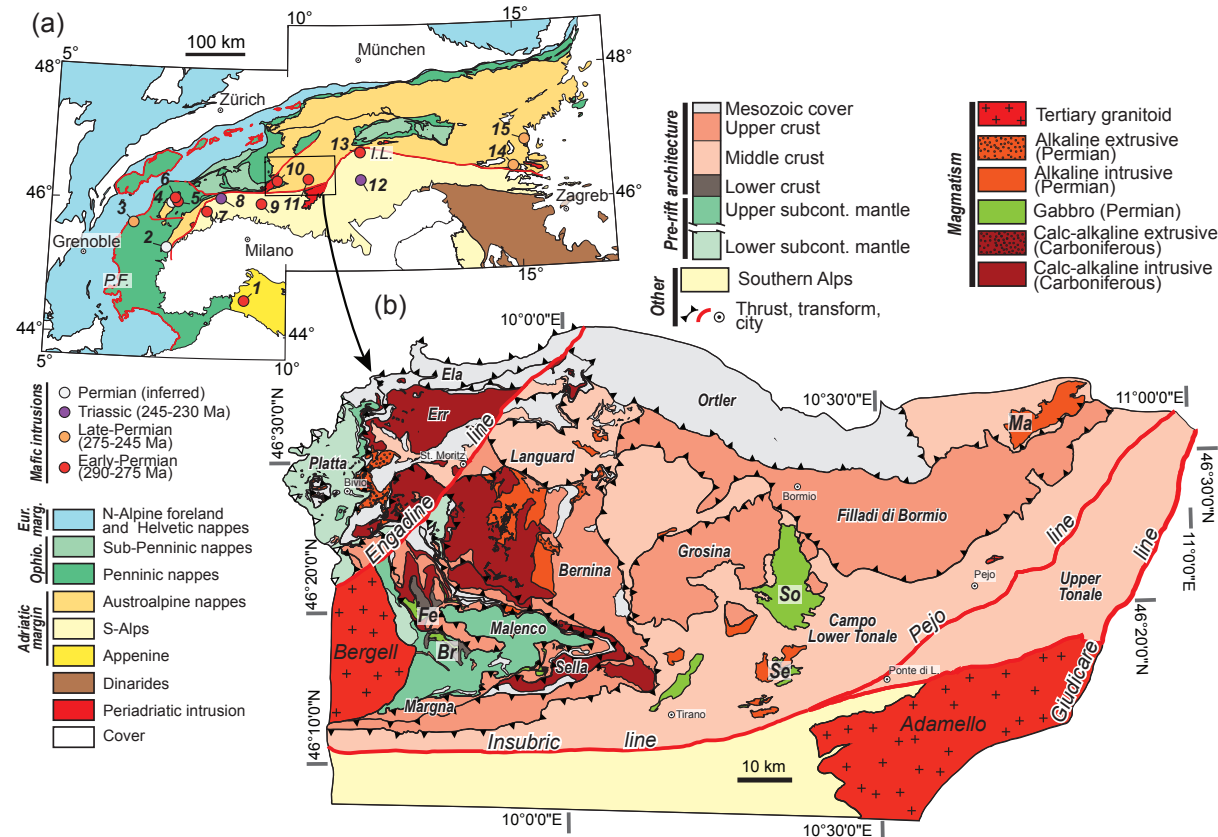


**Fig. II-1:** (a) Carte tectonique du domaine alpin, modifiée d'après Schmid *et al.* (2004), et position des intrusifs mafiques permianes et triassiques d'après Spalla *et al.* (2014) : 1 – Monte Ragola (Meli *et al.*, 1996); 2 – Corio/Monastero (Rebay & Spalla, 2001); 3 – unité du Versoyen (Beltrando *et al.*, 2007); 4 – Sassa (Baletti *et al.*, 2012); 5 – Sermenza (Bussy *et al.*, 1998); 6 – Mont Collon (Monjoie *et al.*, 2007); 7 – corps principal d'Ivrée (e.g. Pin, 1986); 8 – Finero (Zanetti *et al.*, 2013); 9 – Val Biandino (Pohl *et al.*, 2014; Thöni *et al.*, 1992); 10 – Fedoz/Braccia (Hansmann *et al.*, 2001); 11 – Sondalo (Tribuzio *et al.*, 1999); 12 – Monzoni – Predazzo (Borsi *et al.*, 1968; voir références dans Mundil *et al.*, 2010); 13 – Bressanone/Brixen (Del Moro & Visonà, 1982); 14 – Eisenkappel (Miller *et al.*, 2011); 15 – Bärofen/Gressenberg (Miller & Thöni, 1997; Thöni & Jagoutz, 1992).. I.L.: Ligne Insubrienne, P.F.: Front Pennique. (b) Carte litho-tectonique du domaine austroalpin au SE de la Suisse et au N de l'Italie, représentant les différents niveaux crustaux pré-rift. La carte est une compilation de Del Moro & Notarpietro (1987), Del Moro *et al.* (1999), Goso *et al.* (2004), Mohn *et al.* (2011), Staub (1946), des cartes géologiques de la Suisse à l'échelle 1:25 000, des cartes géologiques de l'Italie aux échelles 1:10 000 et 1:25 000 et d'observations personnelles. Fe, gabbro de Fedoz; Br, gabbro de Braccia; So, gabbro de Sondalo; Se, intrusifs du Serottini; et Ma, granite de Martell sont les principaux intrusifs permianes.

De fait, la zone d'étude se situe dans les nappes austroalpines, au nord de l'Italie et au sud-est de la Suisse. Plus d'un siècle de travaux sur la formation de la Téthys alpine ont mené à une connaissance approfondie des systèmes formant la marge adriatique jurassique, avant tout grâce à l'évolution en surface de la dynamique d'ouverture des bassins sédimentaires. Plus récemment, l'évolution du socle a été versée à l'histoire du rift, permettant de proposer un modèle de fonctionnement d'une marge continentale à l'échelle lithosphérique (Mohn *et al.*, 2012; Müntener & Hermann, 2001). En effet, les processus de rifting au Jurassique, puis l'orogénèse alpine du Crétacé supérieur au Tertiaire, ont permis l'échantillonnage de tous les niveaux de la croûte pré-rift, du manteau sous-continentale à la surface (Fig. II-1). En particulier l'unité de Campo, positionnée entre la marge proximale et distale, se trouvait en position de croûte moyenne avant l'initiation du rifting. Dans cette unité ont été décrits plusieurs corps magmatiques permiens, dont le gabbro de Sondalo qui est associé à des roches métamorphiques équilibrées dans le faciès des granulites. Les faibles surimpressions tectoniques et métamorphiques de ces unités pendant l'orogénèse alpine en font un lieu approprié au développement de la problématique.

### 3. COMMENT Y RÉPONDRE

Les thématiques mises en avant dans cette introduction sont très variées. Ainsi, tenter de répondre à ces questions nécessite une approche pluridisciplinaire. Par conséquent, cette étude associe cartographie des terrains métamorphiques et magmatiques et analyse structurale par mesure de terrain et par caractérisation des fabriques magnétiques par *Anisotropie de Susceptibilité Magnétique* (ASM), en particulier pour les roches dont les structures sont peu exprimées. Ces données de terrain sont ensuite couplées à la caractérisation de l'évolution en pression et en température des roches métamorphiques, quantifiée par modélisation d'équilibres des minéraux (*pseudosections*). L'évolution temporelle du système est contrainte grâce à des méthodes de géochronologie de haute température avec les datations U–Pb sur zircons, ainsi que des méthodes de plus basse température avec les datations  $^{40}\text{Ar}/^{39}\text{Ar}$  sur amphiboles, muscovites et biotites.

Cependant les données de terrain et les méthodes souffrent de quelques limites. Dans un premier temps, les déformations et transformations dues à l'orogénèse ne sont parfois pas négligeables. Ainsi, les conditions métamorphiques alpines, allant jusqu'au faciès des schistes verts, inhibent toute reconstruction de l'histoire métamorphique et géochronologique mésozoïque de ces terrains. Les déformations alpines peuvent avoir démantelé et basculé plus ou moins profondément les structures pré- et syn-rift, rendant parfois les positions exactes des unités avant et pendant le rifting peu contraintes.

## **4. PLAN DU MÉMOIRE DE THÈSE**

Le premier chapitre a permis de synthétiser de manière non exhaustive mais nécessaire les processus théoriques et l'évolution du domaine ouest-européen à la fin du Paléozoïque, mettant en place le cadre géodynamique général de ces travaux de thèse, dont la problématique et la démarche sont présentés dans ce deuxième chapitre. La suite du manuscrit est organisée en trois chapitres successifs présentés sous forme d'articles en préparation, suivis d'une discussion générale (*chapitre VI*).

Le troisième chapitre présente l'évolution en pression, en température et en déformation (*P-T-d*) de l'unité de Campo préservant le gabbro permien de Sondalo. Ainsi, l'évolution métamorphique de l'unité de Campo avant, pendant et après l'intrusion du gabbro est contrainte au moyen d'un travail de terrain puis d'une description détaillée des épisodes de cristallisation et de déformation, description couplée à des modélisations thermodynamiques. L'article en préparation associé à ce chapitre, intitulé « *Évolution magmatique et métamorphique permienne dans les Alpes : apports de l'unité de Campo (Nappes austroalpines, est des Alpes centrales)* » sera soumis à la revue *Contributions to Mineralogy and Petrology*.

Le quatrième chapitre étudie le mode de mise en place et l'âge du gabbro de Sondalo, en couplant géologie structurale, géochronologie et pétrologie magmatique. La structure du gabbro est déterminée dans un premier temps par un travail de terrain puis grâce à la caractérisation des fabriques magmatiques et magnétiques (par *Anisotropie de Susceptibilité Magnétique – ASM*), tandis que son âge est contraint avec des datations par la méthode U–Pb sur zircon (LA-ICPMS) de roches magmatiques et métamorphiques. Couplés à l'évolution métamorphique des roches encaissantes, ces résultats permettent de contraindre les mécanismes de mise en place du gabbro, qui feront l'objet d'un article intitulé « *Ages et mécanismes d'ascension et de mise en place dans la croûte continentale moyenne de magmas mafiques : l'exemple du complexe gabbroïque permien de Sondalo* », qui sera soumis à la revue *Tectonics*.

Le cinquième chapitre de ce travail détaille le refroidissement et l'exhumation des unités de Campo et de Grosina au moyen de datations  $^{40}\text{Ar}/^{39}\text{Ar}$ , réalisées sur plusieurs minéraux, et leurs implications sur les processus du le rifting jurassique. Associés à une synthèse des âges fournis par la bibliographie, ces résultats permettent de proposer un modèle d'évolution tectonique de la zone d'étude, de l'extension post-orogénique au rifting jurassique. Cet article est intitulé « *Histoire de l'exhumation, du refroidissement et de la déformation dans la zone d'étranglement adriatique : la section Campo/Grosina (SE de la Suisse, N de l'Italie)* ».

L'ensemble des résultats obtenus est enfin mis en relief et confronté à l'évolution à plus grande échelle du système étudié. La sixième et dernière section du corps de ce manuscrit synthétise les résultats, et discute du cadre géodynamique de cette étude, ainsi que de l'importance

de ces évènements post-orogéniques permiens sur les phases de rifting postérieures.

De plus, en annexe se trouve une proposition d'excursion dans la zone d'étude. Elle propose au lecteur une visite en une journée des principaux éléments de terrain facilement accessibles. Cette annexe au travail est intitulée « *L'évolution des unités de Campo et Grosina dans les nappes austroalpines (Italie du N) : de l'orogénèse varisque au rifting jurassique* », sera soumise au *Journal of the Virtual Explorer*.



---

## *CHAPITRE III*

---

Le *chapitre III* a pour but de déterminer l'évolution en température ( $T$ ), en pression ( $P$ ), en déformation ( $d$ ) et éventuellement en temps ( $t$ ) de l'unité de Campo, avant, pendant et après l'intrusion du gabbro de Sondalo. Pour ce faire, des campagnes de cartographie, de mesures structurales et d'échantillonnage ont été réalisées lors des étés 2011, 2012 et 2013. Ce travail se base sur l'établissement des relations cristallisation/déformation des différentes phases, ainsi que sur l'étude leur chimie. Cette dernière a été obtenue par analyse sur microsonde lors de séjours à la Vrije Universiteit d'Amsterdam ainsi qu'à l'Institut für Mineralogie und Kristallchemie de Stuttgart.

La présentation des données est organisée en trois sections :

- une description des différentes structures déterminées par relations de terrain et observations microscopiques ;
- une synthèse détaillée des relations cristallisation/déformation des différents minéraux et de leur chimie ;
- la modélisation thermodynamique de l'équilibre des minéraux, à l'aide du logiciel THERMOCALC. Ces modélisations ont profité des bénéfices d'une interface graphique, développée en collaboration avec E. Skrzypek (Kyoto University) sous MATLAB® (TCWizard, Petri & Skrzypek, 2013).

Enfin, l'ensemble de ces données a été confronté pour proposer un modèle d'évolution de l'unité de Campo lors de l'orogénèse varisque et des évènements tectoniques, magmatiques et métamorphiques ayant eu cours avant, pendant et après l'intrusion du gabbro de Sondalo au Permien.

L'article adossé à ce chapitre, intitulé « *Évolution magmatique et métamorphique permienne dans les Alpes : apports de l'unité de Campo (Nappes austroalpines, est des Alpes centrales)* », est en préparation pour la revue *Contributions to Mineralogy and Petrology*.

# **PERMIAN MAGMATIC AND METAMORPHIC EVOLUTION IN THE ALPS: INSIGHTS FROM THE CAMPO UNIT (AUSTROALPINE NAPPES, EASTERN CENTRAL ALPS)**

B. Petri<sup>1,2</sup>, G. Mohn<sup>3</sup>, P. Štíspká<sup>1,4</sup>, G. Manatschal<sup>1</sup>

<sup>1</sup>*Ecole et Observatoire des Sciences de la Terre, Institut de Physique du Globe de Strasbourg – CNRS UMR7516,  
Université de Strasbourg, 1 rue Blessig, F–67084, Strasbourg Cedex, France*

<sup>2</sup>*Vrije Universiteit, Department of Geology and Geochemistry, de Boelelaan 1085, 1081HV Amsterdam, The  
Netherlands*

<sup>3</sup>*Département Géosciences et Environnement, Université de Cergy-Pontoise, 5, mail Gay Lussac, Neuville-sur-  
Oise, 95031 Cergy-Pontoise Cedex*

<sup>4</sup>*Center for Lithospheric Research, Czech Geological Survey, 11821 Praha 1, Czech Republic*

## **ABSTRACT**

We investigate the contact aureole of the Sondalo gabbro emplaced in a mid-crustal position during the Permian, exposed in the Austroalpine Campo unit (N-Italy) using structural geology, metamorphic petrology and geochronology. The presence of paragenesis bearing garnet and staurolite in micaschists hosting the Sondalo Gabbro attests to a pre-Permian barrovian prograde path, reaching 6 kbar/600°C associated with the formation of a sub-vertical NW dipping foliation (Sc1) and its overprint by a NE-dipping sub-vertical foliation (Sc2). Subsequently, the Campo unit underwent a near-isobaric heating around 4 kbar/540°C, with no apparent deformation, leading to the crystallization of andalusite and cordierite. The Sondalo Gabbro intrudes the Campo unit at ~5.5 kbar/930°C, forming granulitic xenoliths made of garnet, sillimanite, cordierite and spinel. The xenoliths are subsequently decompressed leading to a final emplacement at ~4 kbar during the development of a new foliation (Sc3) that is localized around the pluton and moderately dips away from the center of the pluton. Samples in the metamorphic contact aureole bearing the Sc3 fabric present a contrasted evolution, being either exhumed from 6 kbar/750°C to 5 kbar/725°C, or being buried from 4.5 kbar/500°C to 5.2 kbar/800°C followed by an exhumation to 4.8 kbar/770°C.

Our results indicate that only the gabbro was exhumed to around 12 km (4 kbar) during its intrusion, but the country-rock did not follow the same evolution and stayed in the same structural level. The combination of these new results with existing results allows to propose an evolutionary model to explain the magmatic evolution during the Permian post-orogenic extension.

## 1. INTRODUCTION

The final stage of an orogenic cycle is generally associated with extension and thinning of an over-thickened continental crust, classically explained as the collapse of an orogen due to gravitational reequilibration (e.g. Rey *et al.*, 2001). Such an orogenic collapse is often associated with high temperature – low pressure (HT-LP) metamorphism where heat can be: (1) inherited from the migmatitic orogenic middle crust heated by radioactive decay (e.g. Gerdes *et al.*, 2000) and thermal “maturation” (England & Thompson, 1986) as e.g. expressed in core complexes (Vanderhaeghe, 2001; Vanderhaeghe & Teyssier, 2001), (2) result from distributed lithospheric extension (wide rift mode of Buck, 1991; Royden & Keen, 1980), and/or (3) advected by mafic magmatism derived from mantle partial melting (e.g. Annen *et al.*, 2006; Clark *et al.*, 2011; Clark *et al.*, 2014; Wells, 1980). All these processes can interact and overlap in time and space, leading to complex overprinting relationships, characterizing the post-orogenic deformation style (Whitney *et al.*, 2012).

In Western Europe and in the Alpine realm in particular, the succession of two orogenic cycles, the Variscan and the Alpine cycles are preserved. The Devono-Carboniferous Variscan orogeny was followed by Mesozoic rifting leading to the opening of several oceanic basins (Stampfli *et al.*, 2013; Stampfli & Kozur, 2006). Mesozoic rifting is preceded by a widespread Permian post-orogenic (post-Variscan) extension that is characterized by transtensional tectonics (Arthaud & Matte, 1977) associated with the formation of sedimentary basins and intense bimodal magmatic activity (see Fig. III-1a for the mafic magmatism in the Alpine realm). Because this event affected mainly the former Variscan orogenic lithosphere (Burg *et al.*, 1994; Lorenz & Nicholls, 1976; Wilson *et al.*, 2004), this transitional period was either interpreted as a post-orogenic collapse, comparable to the Basin and Range province (Dewey, 1988; Malavieille, 1993; Ménard & Molnar, 1988; Wilson *et al.*, 2004), and/or as being related to the westward propagation of the Neotethys rifting (e.g. Schuster *et al.*, 2001). Eventually, parts of the Permian lithosphere, affected by the post-Variscan extensional event, were exhumed and emplaced during Mesozoic rifting and Alpine orogeny in their present-day position.

Previous studies investigating the Permian metamorphic event were mainly concentrated on the Ivrea lower crustal body (e.g. Fountain, 1976; Schmid & Wood, 1976 and subsequent studies). However, its deep crustal position during Permian times and the repeated magma injections led to complex relations between magmatism and metamorphism (e.g. Barboza *et al.*, 1999). In fact, lower crustal levels are likely pervasively overprinted by the latest thermal event, erasing the previous history (e.g. Harley, 1989). On the opposite, upper-crustal levels are mostly intruded by felsic but rarely mafic plutons. Therefore, a key crustal portion to investigate the different heating processes is the middle crust. In this paper we will show that preserved

Permian mid-crustal level in Austroalpine domain offers a window that enables us to investigate the different heating processes recorded due to repeated but partial deformation/metamorphic events resulting from the Variscan orogenic collapse.

The Austroalpine domain in SE Switzerland and adjacent N Italy preserves a polyphase tectonic history spanning the Carboniferous Variscan orogeny, the Late Carboniferous - Early Permian post-Variscan extension, the Jurassic rifting and eventually the Alpine orogeny. This domain underwent only minor Alpine deformation and metamorphism (Bousquet *et al.*, 2012; Mohn *et al.*, 2011) enabling us to investigate rocks and structures that constituted the different crustal and mantle levels of the pre-rift Permian lithosphere (Mohn *et al.*, 2010; Müntener & Hermann, 2001). We focused our study on the Sondalo gabbro emplaced in the Campo unit at a mid-crustal level during the Permian (Braga *et al.*, 2001; Tribuzio *et al.*, 1999). The weak Alpine overprint in the Campo unit enables us to investigate the relationships between the Sondalo mafic intrusion and the Campo metasedimentary host rocks. This study aims to (1) provide the  $P-T-t-d$  evolution of the metasediments hosting the mafic intrusion using crystallization-deformation relationships associated to mineral equilibria modeling, (2) unravel the complex tectono-magmatico-metamorphic evolution recorded in the Austroalpine domain during post-Variscan extension, and (3) give insights on the behavior of mid-crustal levels during post-orogenic extension.

## 2. GEOLOGICAL SETTING

The Austroalpine domain, located in SE Switzerland and N Italy (Fig. III-1ab), consists essentially of a Late-Cretaceous nappe-stack sampling remnants of the Adriatic passive margin formed during the Jurassic rifting (e.g. Trümpy, 1975). Notably, Jurassic rifting processes led to the exhumation of pre-rift Permian upper, middle, lower crust and sub-continental mantle rocks to shallow levels, as indicated by their  $P-T-t$  evolution and their contacts with Mesozoic sediments (Mohn *et al.*, 2011; Mohn *et al.*, 2010; Müntener *et al.*, 2000). The portions of the Permian lithosphere exhumed during the Jurassic rifting were subsequently incorporated in the Austroalpine nappe stack. The low imprint of the Alpine, pressure-dominated metamorphism observed in the Austroalpine units enables us to investigate and characterize different portions of the basement affected by Variscan and post-Variscan events.

### 2.1 Evidence for Variscan orogeny

The pressure-dominated Variscan metamorphism in the Austroalpine domain is testified by the presence of eclogites in the Upper Tonale unit (Ulten zone) at 15-25 kbar for 750-800°C (Hauzenberger *et al.*, 1996; Tumiati *et al.*, 2003) associated to Grt-peridotites preserving UHP

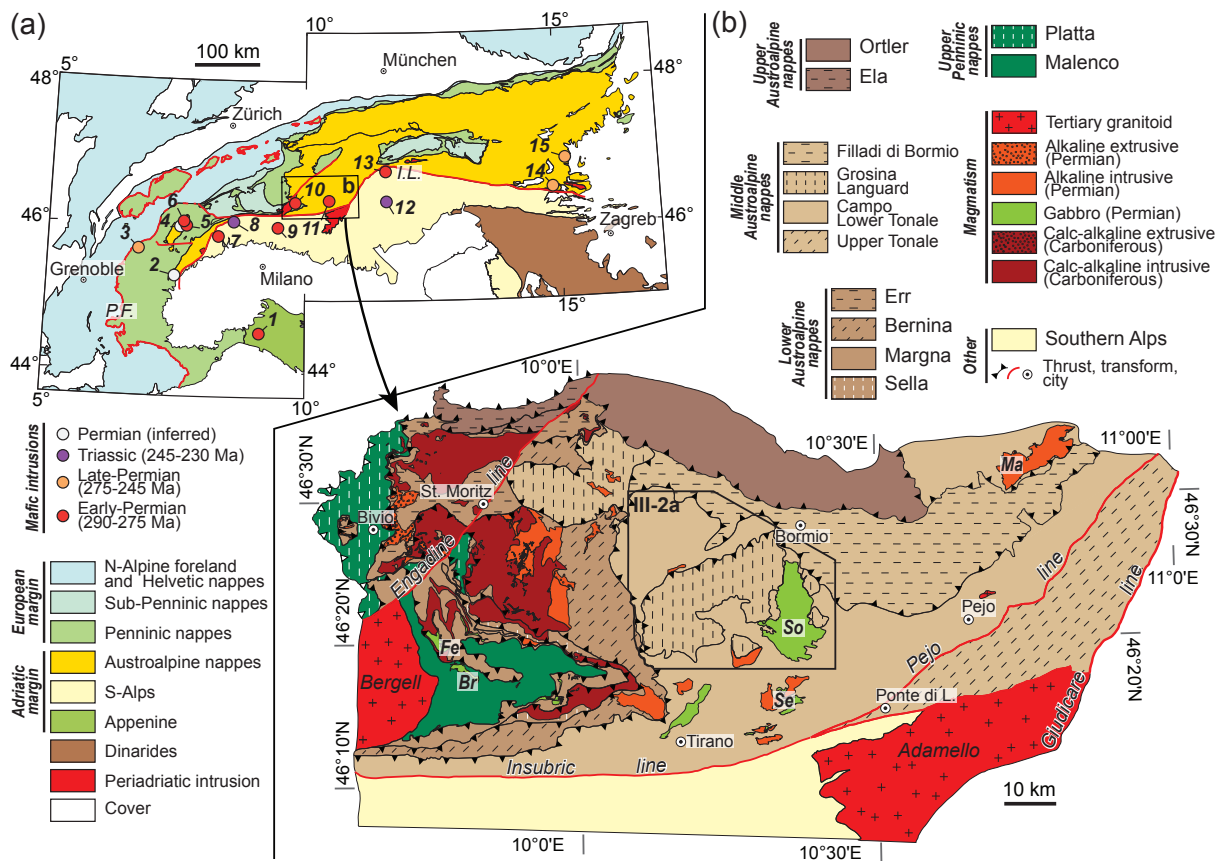


**Fig. III-1:** (a) Tectonic map of the Alpine realm based on Schmid *et al.* (2004) with Permian to Triassic mafic intrusions modified after Spalla *et al.* (2014): 1—Monte Ragola (Meli *et al.*, 1996); 2—Corio/Monastero (Rebay & Spalla, 2001); 3—Versoyen unit (Beltrando *et al.*, 2007); 4—Sassa (Baletti *et al.*, 2012); 5—Sermenza (Bussy *et al.*, 1998); 6—Mont Collon (Monjoie *et al.*, 2007); 7—Ivrea main gabbro (e.g. Pin, 1986); 8—Finero (Zanetti *et al.*, 2013); 9—Val Biandino (Pohl *et al.*, 2014; Thöni *et al.*, 1992); 10—Fedoz/Braccia (Hansmann *et al.*, 2001); 11—Sondalo (Tribuzio *et al.*, 1999); 12—Monzoni—Predazzo (Borsi *et al.*, 1968; see references in Mundil *et al.*, 2010); 13—Bressanone/Brixen (Del Moro & Visonà, 1982); 14—Eisenkappel (Miller *et al.*, 2011); 15—Bärofen/Gressenberg (Miller & Thöni, 1997; Thöni & Jagoutz, 1992). I.L. refers to the Insubric Line, P.F. to the Pennic Front. (b) Litho-tectonic map of the Austroalpine and upper-Penninic nappes in N-Italy and SE-Switzerland compiled from Del Moro & Notarpietro (1987), Del Moro *et al.* (1999), Goso *et al.* (2004), Mohn *et al.* (2011), Staub (1946), the 1:25,000 geological maps of Switzerland, the 1:10,000 and 1:25,000 geological maps of Italy and personal observations. Black rectangle in (b) reports location of the map in Fig. III-2a. Main Permian intrusives are reported and correspond to Fe, Fedoz gabbro; Br, Braccia gabbro; So, Sondalo gabbro; Se, Serottini intrusives; and Ma, Martell granite.

evidence reaching 27 kbar for 850°C (Nimis & Morten, 2000). These HP-rocks are associated in the field to Grt-Ky migmatites to a P-peak at 11 kbar/750 °C at 351–343 Ma (U-Pb on Mnz), followed by a T-peak at 750–800 °C for 8.5–12.5 kbar at 330–326 Ma (U-Pb on Mnz; Braga *et al.*, 2007; Braga & Massonne, 2008; Langone *et al.*, 2011). Variscan amphibolite facies metamorphism is documented for Grt-St micaschists of the Campo unit at ~5–9 kbar and 550–600°C (Bianchi Potenza *et al.*, 1978a; Braga *et al.*, 2001; Notarpietro & Gorla, 1981; Pace, 1966), in the Err and Bernina units (Büchi, 1994; Halmes, 1991), and inferred in the Margna unit (Guntli & Liniger, 1989). Calc-alkaline diorites and granodiorites were emplaced in the Bernina unit at 338–324 Ma (Rageth, 1984; Spillmann & Büchi, 1993; Von Quadt *et al.*, 1994)

but do not present evidence of Variscan deformation (Spillmann & Büchi, 1993). In the Margna unit, lithologies geochemically similar to intrusive rocks of the Bernina unit (Guntli & Liniger, 1989) are pervasively deformed (orthogneiss and mylonites) during the Alpine orogenic cycle (Spillmann & Büchi, 1993). The surface expression of these intrusive rocks is likely related to the undated calc-alkaline volcanics documented in the Err unit (Mercolli, 1989).

## 2.2 Evidence for the post-Variscan evolution in the upper and lower crust

During the Permian and after the Variscan orogeny, the complete lithosphere was strongly affected by magmatism and metamorphism. At upper crustal levels, alkaline felsic magmatic rocks were emplaced. In the Bernina unit, the Carboniferous calc-alkaline suite is intruded by an alkaline syenite-granite (Spillmann & Büchi, 1993) at 295–292 Ma (Von Quadt *et al.*, 1994) at  $P < 3$  kbar (Al in magmatic hornblende, Büchi, 1987) and a granodiorite at 285 Ma at  $P < 4.5$  kbar (Brusio granite with andalusite-bearing contact aureole; Boriani *et al.*, 1982). Both calc-alkaline and alkaline intrusive rocks and their host rocks are unconformably overlain by younger alkaline rhyolites of  $288 \pm 7$  Ma (Rageth, 1984; Staub, 1946; Von Quadt *et al.*, 1994) occurring also as discordant dykes in few areas (Spillmann & Büchi, 1993). The overall rock association is cross-cut by basic dykes of unknown age but affected by a strong Alpine recrystallization (Rageth, 1984; Spillmann & Büchi, 1993).

Notably, the Permian lower crust was intruded by magmas of tholeiitic affinity such as the Fedoz and the Braccia gabbros in the Malenco unit (Fig. III-1b) at 281–278 Ma (U-Pb on Zrn, Hansmann *et al.*, 2001; Spillmann & Büchi, 1993). The latter emplaced at the crust-mantle transition zone around 10 kbar (Hermann *et al.*, 2001; Hermann *et al.*, 1997).

The Braccia gabbro is overlain by HT-MP felsic granulites in the Malenco unit (Hermann *et al.*, 1997). The felsic granulites consist of Grt-Ky bearing restites equilibrated at 10 kbar for 800–850°C (Hermann *et al.*, 1997; Müntener *et al.*, 2000). Monazite dating shows that HT conditions lasted ~20 Ma between 280 and 257 Ma (Hermann & Rubatto, 2003). Crystallization of hydrous phases at ~9 kbar and 600°C (Müntener *et al.*, 2000) was dated to late-Triassic early-Jurassic times (Villa *et al.*, 2000), related to the onset of rifting leading to its exhumation (Müntener & Hermann, 2001; Trommsdorff *et al.*, 2005).

## **2.3 Evidence for the post-Variscan evolution in the middle crust**

The middle Austroalpine Campo unit (following the nomenclature of Mohn *et al.*, 2011) was thrust westwards over the lower Austroalpine units and was overprinted at its southern part by the Tertiary Insubric line. The Campo unit is separated from the overlying Grosina unit along a Jurassic shear zone (Fig. III-2a; Eita shear zone; Mohn *et al.*, 2012). Both Grosina and Campo were thrust during Late-Cretaceous by the Filladi di Bormio unit (e.g. Gorla & Potenza, 1975).

The Campo unit consists of amphibolite-facies micaschist, paragneiss and minor amphibolite and calc-silicate of Ordovician protolith age (Bergomi & Boriani, 2012) presenting a variable eo-Alpine and Alpine overprint at its borders (Gazzola *et al.*, 2000; Schmid & Haas, 1989).

The Campo unit was sporadically intruded by Permian granitoids (Bockemühl & Pfister, 1985; Gazzola *et al.*, 2000; Guglielmin & Notarpietro, 1997; Notarpietro & De Capitani, 1985a; Notarpietro & De Capitani, 1985b) at  $\sim$ 285–259 Ma based on Rb–Sr dating on muscovite and biotite (Boriani *et al.*, 1982; Del Moro & Notarpietro, 1987; Del Moro *et al.*, 1981). Their emplacement occurred at  $P < 4.5$  kbar indicated by the presence of andalusite and sillimanite in the contact aureole (e.g. Del Moro & Notarpietro, 1987). The Campo unit is crosscut by pegmatites bearing Qtz–Pl–Ms–Bt–Grt–Ap±Dum±Chryso–Brl±Tur (Fig. III-4c; Linck, 1899) of 255–250 Ma Sm–Nd on garnet ages, 257–251 Rb–Sr on muscovite ages and 217–187 Ma K–Ar on muscovite ages (Hanson *et al.*, 1966; Sölvä *et al.*, 2003; Thöni, 1981). The pegmatites have a common origin with the Tur-bearing Martell granite (Fig. III-1b), emplaced between 275 and 260 Ma (Bockemühl, 1988; Grauert *et al.*, 1974a; Mair & Schuster, 2003). K–Ar ages of pegmatites coincide with the  $^{40}\text{Ar}/^{39}\text{Ar}$  ages on biotite and muscovite from the Campo unit ranging between 184 and 189 Ma (Meier, 2003; Mohn *et al.*, 2012; Thöni, 1981) interpreted to be related to Jurassic exhumation and cooling during rifting (Mohn *et al.*, 2012). Rare trachytic dykes crosscut the Campo unit at *ca.* 32  $\pm$  1 Ma (K–Ar on groundmass, Bianchi Potenza *et al.*, 1985) and are related to the Periadriatic intrusion suite (e.g. Callegari & Brack, 2002; von Blanckenburg, 1992).

The Sondalo gabbroic complex is a  $\sim$ 40 km<sup>2</sup> mafic pluton derived from tholeiitic parental liquids (Tribuzio *et al.*, 1999) emplaced at 4–6 kbar in the Campo unit (Braga *et al.*, 2003; Braga *et al.*, 2001). The pluton is concentrically zoned with an Ol-gabbro core surrounded by Opx–Cpx-bearing gabbro with a dioritic to granodioritic rim of a variable thickness (Campiglio & Potenza, 1964; Campiglio & Potenza, 1966; Campiglio & Potenza, 1967; Koenig, 1964; Potenza, 1973). The pluton incorporated roof pendants (kinzigitic and granulitic metapelitic xenoliths) up to 300m in thickness and 1km in length during its emplacement whereas migmatites are localized in the contact aureole. Sm–Nd mineral-isochron dating performed on troctolite and

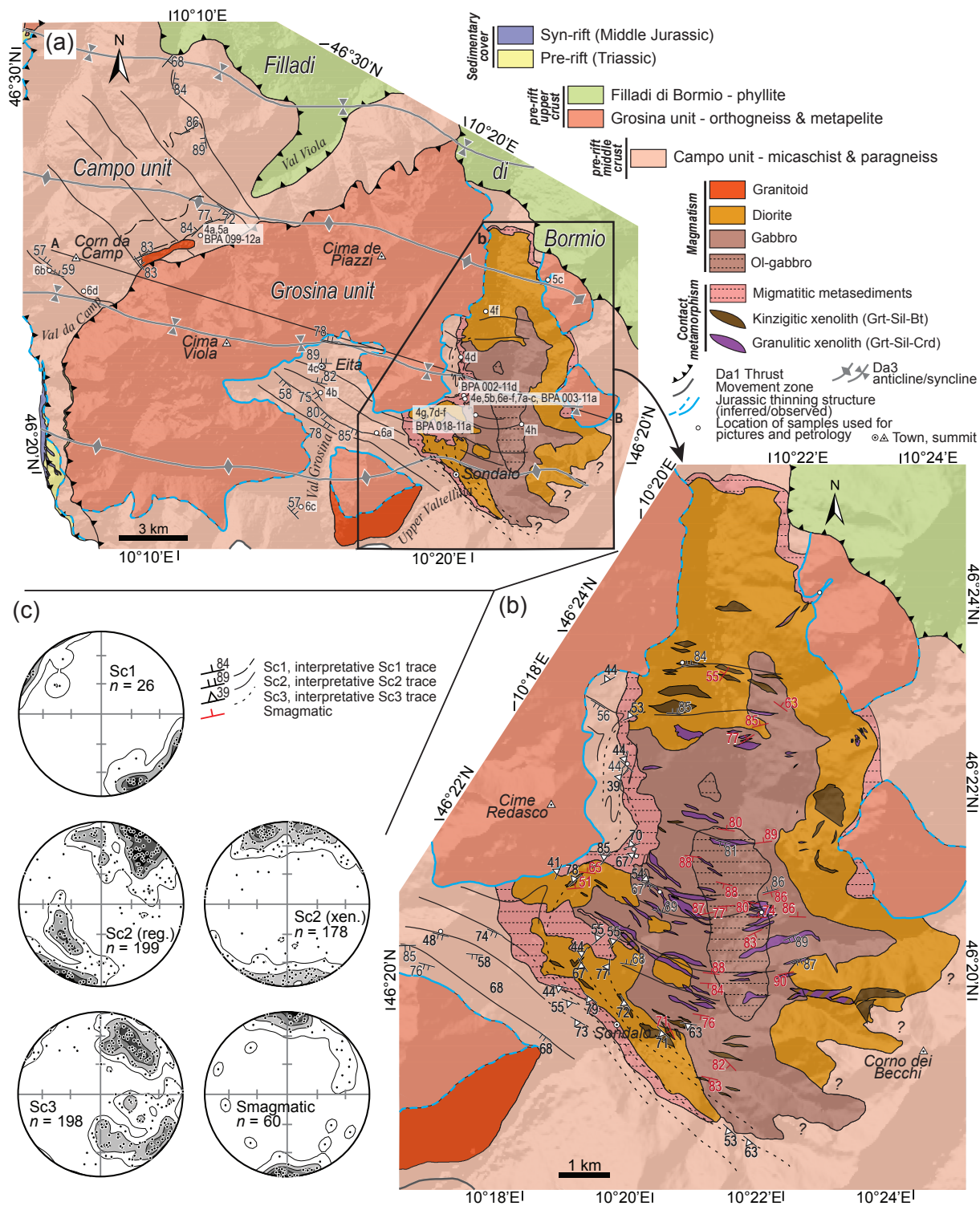


**Fig. III-2:** Geological and structural maps of the study area. (a) The study area of the Campo/Grosina. Location of field photographs (Figs III-4 & III-5), samples used for petrology (labelled BPA) and location of the A–B transect presented in Fig. III-3 are indicated. (b) The Sondalo gabbro. Maps are compilation of Mohn et al. (2011), Campa et al. (1997), Koenig (1964), Braga et al. (2003), 1:10,000 geological maps of Italy and personal observations. (c) Stereonets of planar structures Sc1, Sc2 from the host-rock and from xenoliths of the Sondalo gabbro, Sc3 and magmatic foliation (equal-area, lower hemisphere projection).

norite from the Sondalo gabbro *s.l.* gave respectively  $300 \pm 12$  and  $280 \pm 10$  Ma whereas Rb–Sr isochron ages are  $266 \pm 10$  and  $269 \pm 16$  Ma (Tribuzio *et al.*, 1999) identical to a U–Pb zircon age from a diorite ( $\sim 270$  Ma; Bachmann & Grauert, 1981).

### **3. STRUCTURAL EVOLUTION**

The area of interest, preserving the pre-Alpine structures encompasses the Campo unit W of the Sondalo gabbro and N of the Grosina unit (Figs III-1b & III-2a). Structural framework is described as follows: “D” stands for a deformation event responsible for the development of folds “F” and schistosity “S”, “c” refers to the Campo unit, “g” to the Grosina unit and “a” to alpine structures and numbering refers to the relative chronological sequence of deformations/fabrics determined from field and microstructural observations

#### **3.1 Regional Sc1 and Sc2 fabrics**

In the Campo unit, a first macroscopically visible fabric is a NE-SW trending steep Sc1 foliation (Fig. III-2ac), preserved mainly in the north of the study area. Sc1 is marked by compositional layering, alternation of mica- and quartz-rich bands (Fig. III-4ab) and by preferential orientation of muscovite and biotite in micaschists. Few folded quartz segregations within the Sc1 foliation represent pre-Sc1 quartz veins (Fig. III-4a & III-5a).

Sc1 fabric is affected by open to isoclinal Fc2 folds with steeply plunging fold axis and steep NW-SE trending axial planes. The Fc2 folding leads to development of a Sc2 cleavage (Fig. III-4a) and in most places to almost complete transposition into a Sc2 foliation (Fig. III-4b). Thus, the main structure in the Campo unit is the steep NW-SE trending Sc2 fabric (Figs III-2abc & III-3) defined by compositional layering, alternation of mica- and quartz-rich layers, alignment of elongated quartz segregations as well as probable rare leucosomes, and by preferential orientation of biotite and muscovite (Fig. III-4bc). The Sc2 fabric is crosscut by undeformed to weakly deformed mid-Permian pegmatites (Fig. III-4c).

Within the Sondalo gabbro, metapelitic septa are preferentially oriented parallel to the Sc2 fabric of the Campo unit (Fig. III-2b). At the outcrop scale, Sc2 within the septa is defined by compositional layering (Fig. III-4h), elongated quartz segregations (Fig. III-4g), and by shape-preferred orientation of biotite and sillimanite.

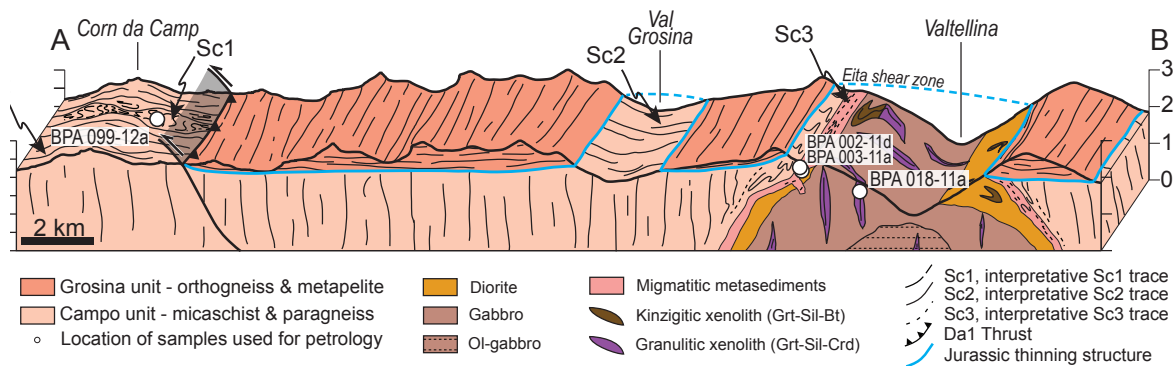


**Fig. III-3:** Synthetic block along the transect A–B indicated on Fig. III-2a showing relationships between fabrics in the Campo unit around the Sondalo gabbro. Grosina unit in the upper part is modified from Mohn et al. (2012).

### 3.2 Regional Sc2 fabric preserved in the pluton

The Sondalo gabbro displays locally a magmatic foliation marked by preferred orientation of pyroxene, amphibole and plagioclase, and in places by an alternation of pyroxene and amphibole rich layers with plagioclase rich layers. The magmatic foliation is parallel to the Sc2 foliation of the metapelitic septa and of the Campo unit (Fig. III-2bc).

### 3.3 Syn-intrusion Sc3 fabric

The Sc2 planar fabric is reworked in the contact aureole of the pluton by Dc3 deformation phase, in a zone ranging in thickness from meter- to few hundred meters and with intensity increasing towards the gabbro. In zones of weak Dc3 deformation, the Sc2 foliation is affected by plurimetric open Fc3 folds, with moderately plunging fold axis and axial planes dipping moderately away from the pluton centre (Fig. III-4d). In zones of strong Dc3 deformation, the Fc3 folds are tight to isoclinal with rare relicts of the Sc2 fabric (Fig. III-4e). Sc2 fabric is in places completely transposed into the Sc3 foliation parallel to the pluton margins and dipping moderately away from the center of the pluton (Fig. III-2bc). The Sc3 fabric is defined by shape preferred orientation of elongated quartz segregations and leucosomes and preferred orientation of biotite and sillimanite.

Dc3 is present in the few xenoliths close to the pluton boundary. It has a variable intensity from open microfolds (Figs III-4g & III-7e) to complete transposition of the previous foliation (Fig. III-4f). In both the contact aureole and in the xenoliths, leucosome are present in necks of boudins (inter-boudin partitions). Moreover, there is no solid-state recrystallization in the xenoliths and surrounding gabbroic and other magmatic rocks do not present sub-solidus deformation.

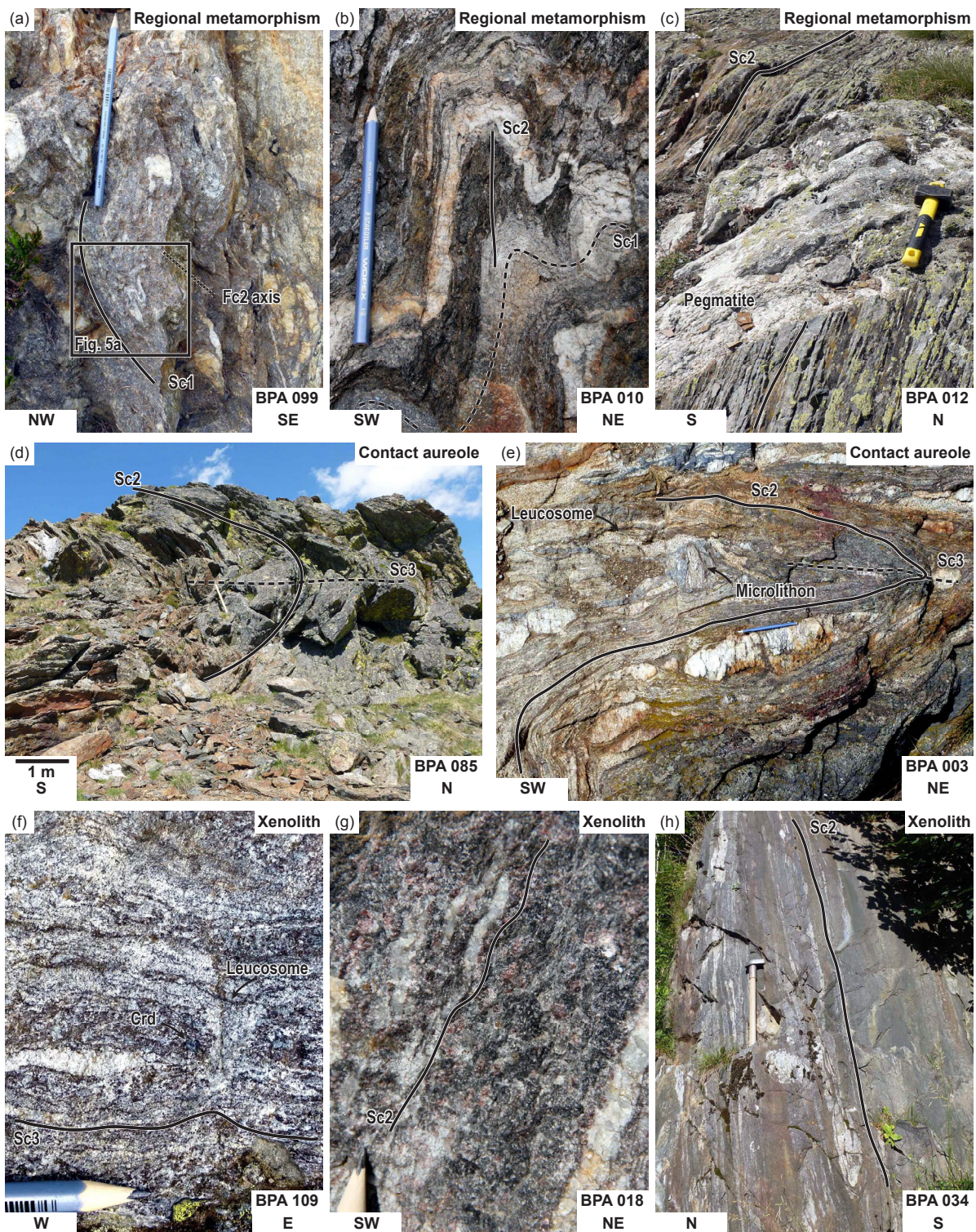


**Fig. III-4:** Field photographs of macroscopic structures. Regional structures: (a) micaschists with Sc1 fabric weakly affected by Fc2 folds and preserving pre-Sc1 quartz veins, location in Fig. III-5a; (b) paragneiss and micaschist folded by Fc2, micas are reoriented along Sc2 in the hinge zone; (c) steeply dipping Sc2 fabric crosscut by undeformed Permian pegmatite. Contact aureole: (d) Plurimetric Fc3 folds; (e) metataxite where melanosome preserves Sc2 fabric in Fc3 hinge. Metapelitic xenoliths: (f) melanosome boudins with leucosome-filled neck zones; (g) felsic granulite (Grt-Sil-Crd) with quartz lenses elongated in Sc2; (h) felsic granulite alternating with Qtz-rich layers along the Sc2 fabric, the yellowish color is due to abundant staurolite.

### 3.4 Evidence for rift-related and Alpine deformations

In the Campo unit, a greenschist facies deformation overprints Carboniferous and Permian amphibolite facies structures approaching the rift-related shear zone separating the Campo and the Grosina units (Fig. III-2, Eita shear zone, see Mohn *et al.*, 2012). It consists of sub-horizontal recumbent open folds affecting the Campo metapelites and Permian pegmatites, and localized shear-zones at the top of the Sondalo gabbro that transpose fabrics (described hereafter) only few meters below the contact with the Grosina unit.

Late Cretaceous Alpine thrusts (Da1) are localized at the top and the bottom of the Campo unit and consist of a few meters thick shear zone retrogressed to greenschist facies conditions. Locally, few normal faults (Da2) were described such as the “Mortirolo” fault of Late-Cretaceous age (Meier, 2003). During the Tertiary, Alpine deformation was responsible for large-scale gentle folds with ENE–SWS trending fold axis (Da3, Fig. III-2a) visible in the Val Grosina, but this deformation is not pervasive enough to disturb pre-Permian fabrics. The youngest deformation involves only few meters displacements along NW–SE oriented normal faults (Sistema della Piatta Grande, Corradini *et al.*, 1973) associated to localized shear zones and pseudotachylites (see Meier, 2003 for description).

## 4. PETROGRAPHY AND MINERAL CHEMISTRY

Several oriented thin-sections of micaschists, metapelitic migmatites and granulites in and around the Sondalo gabbro were studied in order to characterize the  $P$ – $T$ – $d$  evolution of the Campo unit. One sample from regional Campo micaschists, two melanosomes (kinzigite) from the migmatitic contact aureole and one granulite from a metapelitic xenolith in the pluton were selected for a detailed study. Location of samples is indicated in Figs III-2a & III-3. Petrographic observations are summarized in Figs III-5, III-6 & III-7 and interpreted in terms of crystallization/deformation relationship in Fig. III-8. Mineral and end-member abbreviations follow IUGS recommendations (Siivola & Schmid, 2007) plus Dum for dumortierite. Mineral analyses were carried out at the Faculteit der Aard- en Levenswetenschappen (Vrije Universiteit, Amsterdam) on a JEOL JXA-8800 Superprobe equipped with four WDS detectors with operating conditions of 15 kV and 15 nA, and at the Institut für Mineralogie und Kristallchemie (Universität Stuttgart) on a Cameca SX 100 equipped with four WDS detectors with operating conditions of 15 kV and 15 nA decreased to 10 nA for feldspars and micas. Compositional X-ray maps of garnet were performed at the Stuttgart Universität with analytical conditions of 10 s counting-time, 15 kV, 60 nA and 5  $\mu\text{m}$  beam-size. Representative mineral analyses

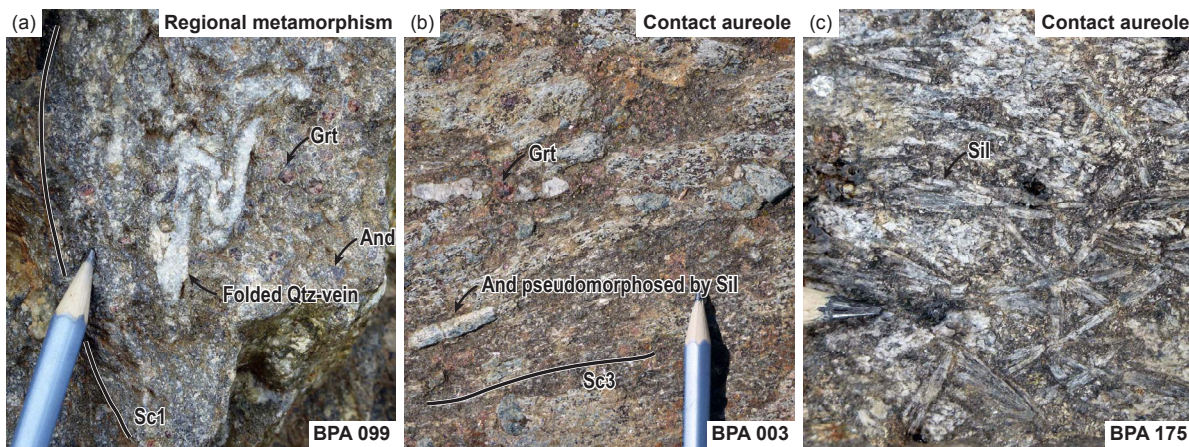


**Fig. III-5:** Macroscopic mineral relationships. Regional metamorphism: (a) Detail of the micaschist in the Fc2 hinge zone indicated in Fig. III-4a. Contact aureole: (b) melanosome from metatexite with andalusite porphyroblasts (pseudomorphed by sillimanite); (c) metatexite with randomly oriented prismatic sillimanite.

are reported in Tables III-1 & III-2 and garnet chemical profiles and maps in Fig. III-9. Ferric iron is estimated by charge balance. Compositional variables are defined as:  $X_{\text{Fe}} = \text{Fe}/(\text{Fe} + \text{Mg})$ ,  $\text{Alm} = \text{Fe}^{2+}/(\text{Fe}^{2+} + \text{Mg} + \text{Ca} + \text{Mn})$ ,  $\text{Prp} = \text{Mg}/(\text{Fe}^{2+} + \text{Mg} + \text{Ca} + \text{Mn})$ ,  $\text{Grs} = \text{Ca}/(\text{Fe}^{2+} + \text{Mg} + \text{Ca} + \text{Mn})$ ,  $\text{Sps} = \text{Mn}/(\text{Fe}^{2+} + \text{Mg} + \text{Ca} + \text{Mn})$ ,  $\text{Ab} = \text{Na}/(\text{Na} + \text{Ca} + \text{K})$ ,  $\text{An} = \text{Ca}/(\text{Na} + \text{Ca} + \text{K})$  and  $\text{Or} = \text{K}/(\text{Na} + \text{Ca} + \text{K})$  for measured compositions;  $x(\text{Grt}, \text{St}, \text{Crd}, \text{Bt}) = \text{Fe}/(\text{Fe} + \text{Mg}) \times 100$ ,  $\text{alm} = \text{Fe}^{2+}/(\text{Fe}^{2+} + \text{Mg} + \text{Ca} + \text{Mn}) \times 100$ ,  $\text{prp} = \text{Mg}/(\text{Fe}^{2+} + \text{Mg} + \text{Ca} + \text{Mn}) \times 100$ ,  $\text{grs} = \text{Ca}/(\text{Fe}^{2+} + \text{Mg} + \text{Ca} + \text{Mn}) \times 100$ ,  $\text{sps} = \text{Mn}/(\text{Fe}^{2+} + \text{Mg} + \text{Ca} + \text{Mn}) \times 100$  for modelled isopleths.

#### 4.1 Regional micaschists and paragneiss

In micaschist and paragneiss from the Campo unit, alternation of quartz-rich and mica-rich layers defines the Sc1 fabric. This foliation is pervasively folded and transposed into the main Sc2 fabric. Numerous quartz segregations chiefly preserve an elongation along Sc1 and Sc2. Rare Qtz–Fsp aggregates are preferentially elongated along Sc2 and may represent leucosomes. Micaschists contain Grt–St–Ms–Bt–Pl–Qtz±Sil±And±Crd whereas paragneisses contain Ms–Bt–Pl–Qtz. Muscovite, biotite and quartz-plagioclase aggregates are aligned along both Sc1 and Sc2. In micaschists, porphyroblastic garnet (up to 1 cm in diameter) bears inclusions of ilmenite and quartz, oriented along Sc1 in the core and occasionally along Sc2 in the rim (Fig. III-6a). Poikiloblastic to porphyroblastic staurolite (up to few cm in length) and its Ilm–Qtz±Chl±Tur inclusions are parallel to Sc2 (Fig. III-6b). Sillimanite lies in the Sc2 foliation and is sometimes associated to biotite in pressure shadows around garnet generated during Dc2 (Fig. III-6c). Sporadic small cordierite (<1 mm in size) occurs in quartz aggregates and does not present any preferential orientation and pressure shadow. Local andalusite blades (up to 10 cm in length) do not present pressure shadows associated to Dc2 and preserve muscovite,

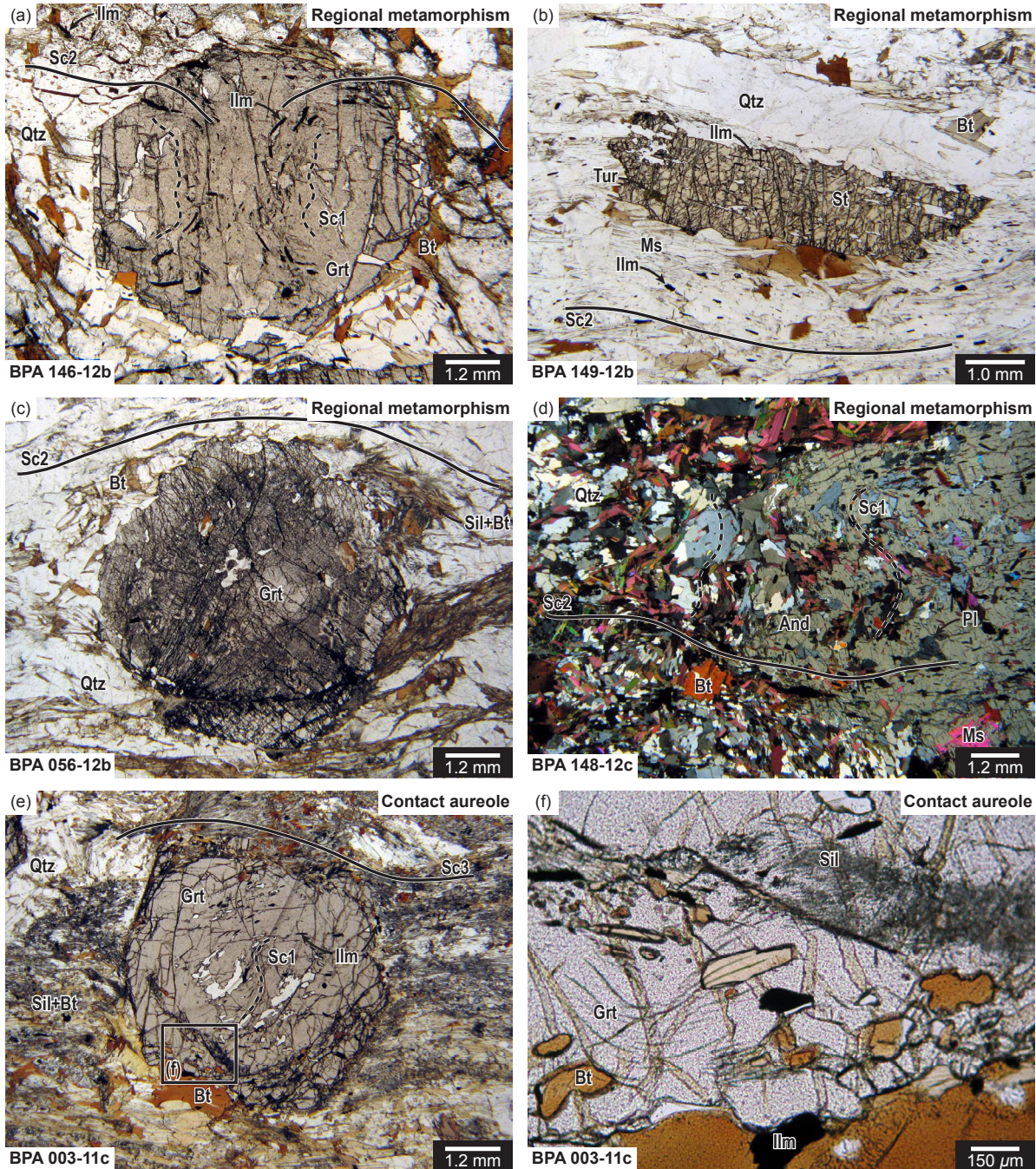


**Fig. III-6:** Microphotographs showing the paragenetic relationships in metapelites. Regional metamorphism: (a) garnet porphyroblast with Ilm–Qtz inclusions aligned along Sc1 and Sc2 with a millipede microstructure; (b) staurolite porphyroblast with ilmenite inclusion trails parallel to the Sc2 foliation; (c) Sil–Bt nests in Sc2 pressure shadows around garnet; (d) muscovite and biotite aligned in both Sc1 and Sc2 in the matrix and included in post-kinematic andalusite. Contact aureole: (e) garnet with Ilm–Qtz inclusions in the core and Sil–Bt–Ilm inclusions in the rim, sillimanite and biotite from the matrix are aligned along Sc3, black rectangle indicates location of the microphotograph (f); (f) detail of garnet external rim with abundant inclusions of sillimanite, biotite and ilmenite.

biotite, plagioclase, quartz and ilmenite inclusions aligned parallel to both Sc1 and Sc2 (Fig. III-6d). Rare kyanite was described in the literature (Bianchi Potenza *et al.*, 1978a; Pace, 1966) but was never observed in during this study. Ilmenite and tourmaline are accessory and present in both Sc1 and Sc2. Tourmaline is also concentrated along pegmatitic dykes cross-cutting the Sc2 fabric.

The micaschist BPA 099-12a was collected in an open Fc2 fold hinge (similar to Figs III-4a & III-5a) and therefore presents Sc1 foliation affected by Fc2 crenulation. The rock contains Grt–St–Ms–Bt–Pl–Qtz–Ilm with andalusite porphyroblasts. Garnet (few mm in diameter) is rimed by a  $\sim 100 \mu\text{m}$  thick biotite corona and contains arcuate inclusion trails of ilmenite parallel to Sc1 interpreted as syn-Dc1 flattening pattern (Zwart, 1962). It shows a bell-shape compositional zoning (Fig. III-9a) with an increase of Alm and Prp, a decrease of XFe and Sps and a constant Grs content from core (Alm = 0.72, Prp = 0.05, Grs = 0.06, Sps = 0.17, XFe = 0.94) to inner rim (Alm = 0.82, Prp = 0.07, Grs = 0.05, Sps = 0.07, XFe = 0.93). The  $\sim 100 \mu\text{m}$  outermost rim shows either Sps decrease associated to Alm increase when in contact with biotite (Alm = 0.86, Prp = 0.09, Grs = 0.02, Sps = 0.03, XFe = 0.91) or Sps increase and Alm decrease when in contact with quartz (Alm = 0.82, Prp = 0.09, Grs = 0.02, Sps = 0.07, XFe = 0.90). Yellow staurolite (up to 0.5 in size) lies in Ms–Bt aggregates, bears rarely biotite and ilmenite inclusions and shows a sharp XFe increase from unzoned core (XFe = 0.86–0.88) to few  $\mu\text{m}$  thick rim (XFe = 0.91). Muscovite (Si = 2.97–3.05 a.p.f.u., Al = 2.75–2.85 a.p.f.u., Na = 0.18–0.22 a.p.f.u.) and biotite (XFe = 0.58–0.63, Ti = 0.09–0.13 a.p.f.u.) are stable in both Sc1 and Sc2 without significant compositional differences. Rare albitic plagioclase (Ab = 0.92, An = 0.08, Or = 0.00) lies in Qtz–Pl aggregates. Andalusite porphyroblasts (up to 1 cm in length) contain Bt–Ms–Ilm inclusions preserving Fc2 crenulations seen in the surrounding Ms–Bt matrix and does not deflect the foliation. It is therefore interpreted as a post-Dc2 static crystallization. Ilmenite occurs in the matrix and is included in numerous minerals.

## 4.2 Migmatitic metapelite in contact aureole

Metapelites from the contact aureole range from stromatitic metatexite to schollen diatexite with rare micaschist. In the migmatites, alternation of Grt–Sil–Bt-rich melanosome (kinzigite) and well-segregated leucosomes made of Fsp–Qtz define both Sc2 and Sc3. The melanosome presents shape-preferred orientation of its constituents whereas the leucosome is rarely foliated. The leucosome is made of Grt–Bt–Pl–Kfs–Qtz with minor sillimanite, pinitized cordierite and muscovite.

The melanosome has commonly the assemblage of Grt–Sil–Bt–Qtz with subordinate plagioclase, K-feldspar, pinitized cordierite, spinel, muscovite and ilmenite. Garnet (up to 1 cm in diameter) bears inclusions of quartz and ilmenite preserving Sc1 orientation in the core (Fig. III-6e) and a rim with Sil–Bt–IIm rounded inclusions (Fig. III-6f). Fibrolitic sillimanite and biotite intergrowth lies in three different structural position: parallel to Sc2, in the Fc3 hinge zone and parallel to Sc3. Randomly oriented prismatic sillimanite (up to 2 cm in length) crosscuts Sil–Bt nests (Fig. III-5c). Andalusite with biotite inclusions is rarely present (Fig. III-5b), and interpreted to be pseudomorphosed by Sil–Spl–Crn aggregates due to their particular shape (elongated with a square cross sections; Fig. III-7ab). Andalusite polycrystalline aggregates occur in quartz layers in Sil-bearing rocks and are interpreted to be post-kinematic (Fig. III-7c). Quartz textures present numerous triple-points, no dynamic recrystallization textures and sometimes weak undulose extinction. In some places, muscovite (<2 mm in size) contains oriented inclusions of fibrolitic sillimanite and is interpreted to be post-kinematic. Ilmenite is the only oxide. Two samples with different paragenesis were selected.

Sample BPA 003-11a has an assemblage of Grt–Sil–Crd–Spl–Bt–Kfs–IIm. Kfs–Qtz layers, sillimanite and biotite show a moderate shape-preferred orientation defining a weakly developed Sc3 foliation. Garnet often presents a core with ilmenite and quartz inclusions elongated along a pre-Sc3 orientation with a compositional profile evolving from the core ( $\text{Alm} = 0.66$ –,  $\text{Prp} = 0.13$ ,  $\text{Grs} = 0.15$ ,  $\text{Sps} = 0.06$ ,  $X\text{Fe} = 0.83$ ) to an internal rim by presenting a slight increase of Prp balanced by a slight decrease of Sps and  $X\text{Fe}$  ( $\text{Alm} = 0.73$ ,  $\text{Prp} = 0.21$ ,  $\text{Grs} = 0.04$ ,  $\text{Sps} = 0.02$ ,  $X\text{Fe} = 0.76$ , Fig. III-9b). The outermost rim is characterized by Sil–Bt±Crn inclusions, decrease of Prp, increase of Alm and  $X\text{Fe}$  ( $\text{Alm} = 0.82$ ,  $\text{Prp} = 0.12$ ,  $\text{Grs} = 0.04$ ,  $\text{Sps} = 0.02$ ,  $X\text{Fe} = 0.88$ ). Locally, matrix biotite ( $X\text{Fe} = 0.50$ – $0.53$ ,  $Ti = 0.08$ – $0.13$  a.p.f.u.) presents lamellar intergrowth with quartz. Few corundum grains (up to 300  $\mu\text{m}$ ) lie in sillimanite aggregates (see Fig. III-7a). Green spinel ( $X\text{Fe} = 0.83$ – $0.85$ ,  $Zn = 0.00$ – $0.10$  a.p.f.u.) is massively present in these aggregates (Fig. III-7b) as symplectitic intergrowth with sillimanite and as bigger grains (<100  $\mu\text{m}$ ) with frequent sillimanite inclusions. The Sil–Spl±Crn aggregates (Figs III-5b & III-7ab) are interpreted as pseudomorphs after porphyroblastic andalusite with biotite inclusions described in the eastern contact aureole (Giacomini, 1997). Plagioclase is slightly zoned from core ( $\text{Ab} = 0.67$ ,  $\text{An} = 0.33$ ,  $\text{Or} = 0.00$ ) to rim ( $\text{Ab} = 0.82$ ,  $\text{An} = 0.18$ ,  $\text{Or} = 0.00$ ). Cordierite is largely pinitized and associated to K-feldspar in few leucosomes. Rare tiny muscovite (<100  $\mu\text{m}$ ,  $\text{Si} = 3.01$ – $3.03$  a.p.f.u.,  $\text{Al} = 2.85$  a.p.f.u.,  $\text{Na} = 0.15$  a.p.f.u.) are randomly orientated in quartz aggregates. Ilmenite occurs either in the matrix or as inclusions whereas uncommon late

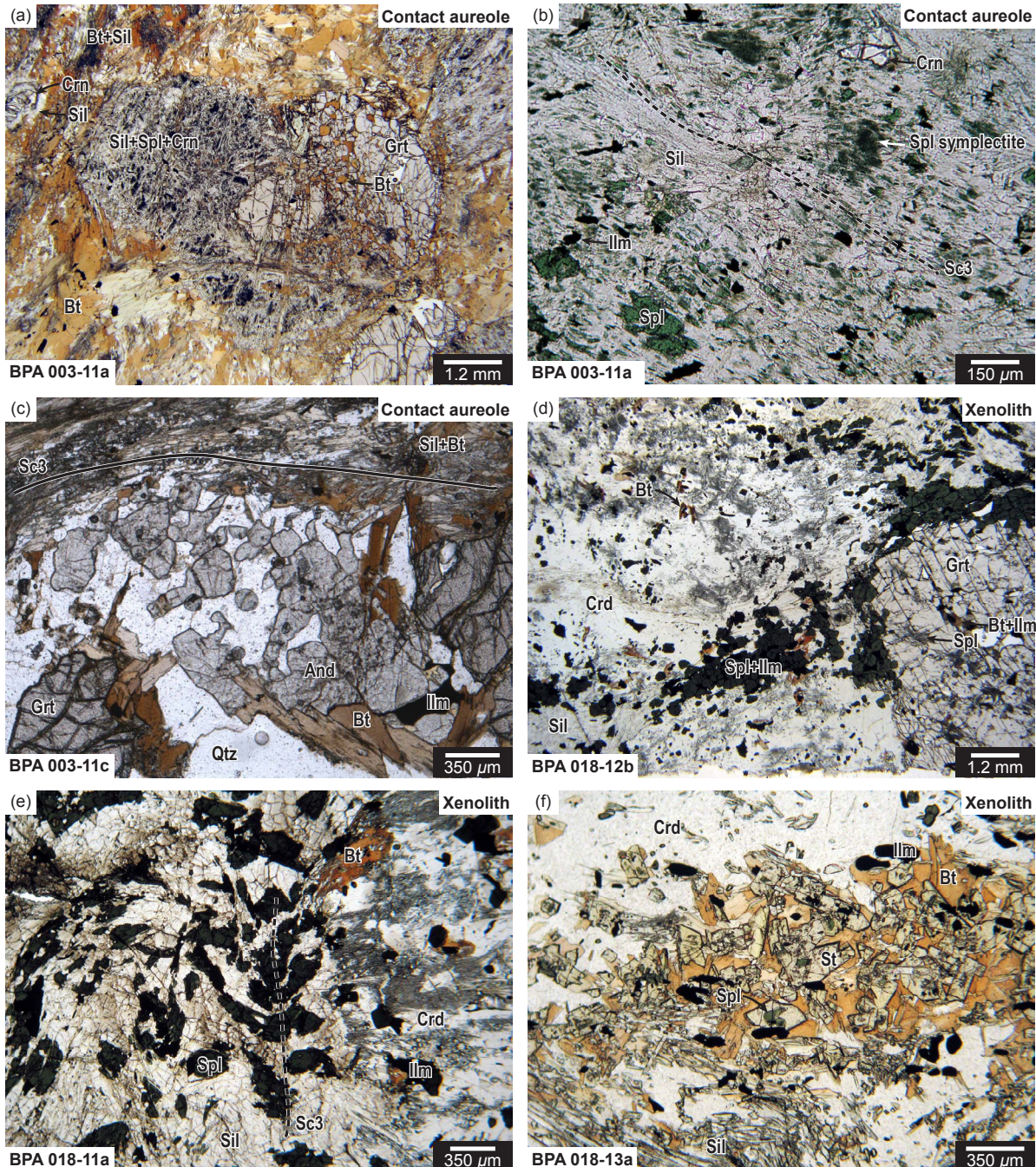


**Fig. III-7:** Microphotographs showing the paragenetic relations in metapelites. Contact aureole: (a) garnet around  $\text{Sil-Spl-Ilm} \pm \text{Crn}$  nest interpreted as a pseudomorph after andalusite, corundum in matrix surrounded by sillimanite; (b) detail of  $\text{Sil-Spl-Ilm} \pm \text{Crn}$  nest; (c) andalusite in a quartz aggregate. Metapelitic xenoliths: (d) felsic granulite with cordierite aggregates and garnet partly surrounded by spinel; (e)  $\text{Sil-Spl}$  aggregates in  $\text{Fc3}$  open microfolds; (f) felsic granulite has aggregates of biotite and euhedral staurolite with spinel inclusions.

cracks are filled with rutile.

The melanosome BPA 002-11d contains Grt–Sil–Bt–Pl–Qtz–Ilm. Sillimanite and brown-red biotite display a strong shape-preferred orientation defining the Sc3 foliation. The Sc3 fabric is also marked by elongation of Pl–Qtz aggregates and is deflected around garnet prophyroblasts. Garnet has a poikiloblastic core with Bt–Pl–Qtz–Ilm inclusions and shows decreasing Grs from core ( $\text{Alm} = 0.61$ ,  $\text{Prp} = 0.04$ ,  $\text{Grs} = 0.24$ ,  $\text{Sps} = 0.11$ ,  $X\text{Fe} = 0.94$ ) to rim ( $\text{Alm} = 0.78$ ,  $\text{Prp} = 0.12$ ,  $\text{Grs} = 0.07$ ,  $\text{Sps} = 0.04$ ,  $X\text{Fe} = 0.87$ , Fig. III-9ce). The Prp-rich rim (~1 mm thick) has fewer inclusions and shows a decrease in Prp and an increase of Alm, Sps and  $X\text{Fe}$  from the Bt–Qtz-bearing internal part ( $\text{Alm} = 0.74$ ,  $\text{Prp} = 0.19$ ,  $\text{Grs} = 0.05$ ,  $\text{Sps} = 0.02$ ,  $X\text{Fe} = 0.80$ ) to the Sil–Bt-bearing external part ( $\text{Alm} = 0.79$ ,  $\text{Prp} = 0.14$ ,  $\text{Grs} = 0.03$ ,  $\text{Sps} = 0.04$ ,  $X\text{Fe} = 0.85$ ) and presents a slight Grs oscillatory zoning (Fig. III-9e). In the matrix, fibrolitic sillimanite and biotite ( $X\text{Fe} = 0.50\text{--}0.52$ ,  $\text{Ti} = 0.10\text{--}0.14$  a.p.f.u.) aggregates are crosscut by prismatic sillimanite not deflecting Sc3 foliation or presenting a shape-preferred orientation. It rarely bears fine-grained spinel symplectite. Plagioclase is oligoclase zoned from core ( $\text{Ab} = 0.70$ ,  $\text{An} = 0.30$ ,  $\text{Or} = 0.00$ ) to rim ( $\text{Ab} = 0.78$ ,  $\text{An} = 0.21$ ,  $\text{Or} = 0.01$ ), no K-feldspar is observed. Decussate aggregates of muscovite lie in Qtz-rich layers and have  $\text{Si} = 2.97\text{--}3.03$  a.p.f.u.,  $\text{Al} = 2.85\text{--}2.96$  a.p.f.u. and  $\text{Na} = 0.10\text{--}0.14$  a.p.f.u. Both prismatic sillimanite and muscovite are interpreted as post-kinematic. Ilmenite is the dominant Ti-bearing mineral; rutile is only present in rare cracks.

### 4.3 Migmatitic and granulitic metapelites in xenoliths

Metapelitic xenoliths, located in the external part of the pluton (see Fig. III-2b), range from stromatitic metatexite to schollen diatexite, similar to rocks from the contact aureole. Grt–Sil–Bt melanosome is rarely associated to Grt–Kfs–Pl–Qtz leucosome; the latter is often mixed with mafic magmas, responsible for magma hybridization (e.g. Braga *et al.*, 2001; McCarthy & Patiño Douce, 1997). Progressive disappearance of biotite balanced by an increase of cordierite and sillimanite is observed inward the pluton. As a result, granoblastic dark-blue granulites (Fig. III-4g) form most of the xenoliths and have a Grt–Sil–Spl–Crd–Ilm assemblage with variable amount of staurolite, biotite, Mg-chlorite and rare orthopyroxene (~100  $\mu\text{m}$ ), corundum, sapphirine and prismatic. In xenoliths, compositional layering such as leucosome/melanosome alternation still preserves the Sc2 orientation whereas shape-preferred orientation of minerals along Sc2 is only well developed in melanosome. The Sc3 fabric is observed in few external xenoliths (e.g. Fig. III-4f) but in granulitic xenoliths, the Dc3 deformation effect is usually restricted to Fc3 microfolds of Sil–Spl–Ilm aggregates (Fig. III-7e). In granulite, garnet (up to 1 cm in diameter) commonly bears inclusions of green spinel, sillimanite, biotite

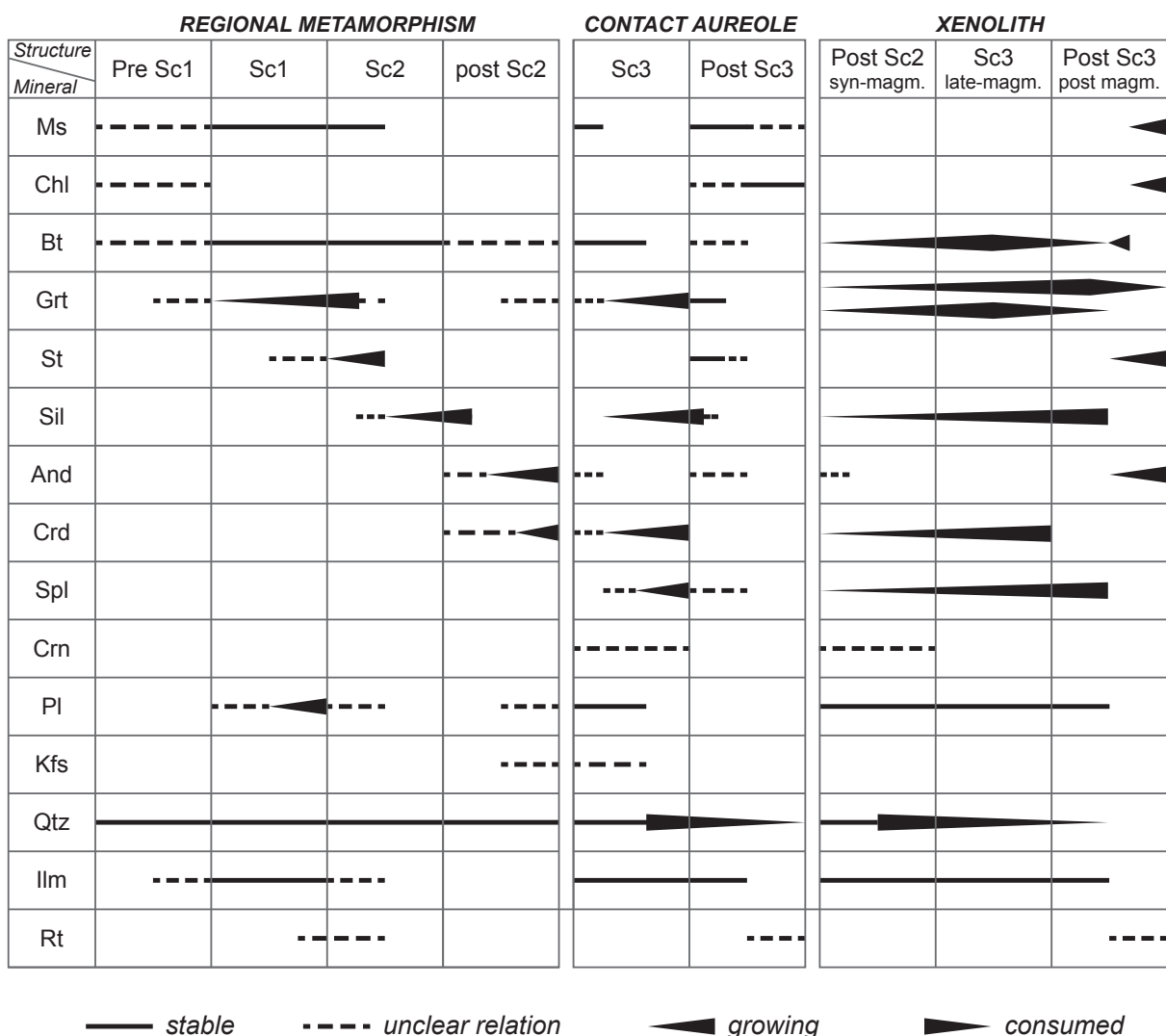


**Fig. III-8:** Crystallization-deformation relationships of the metapelites from the Campo unit far from the intrusion, in the contact aureole and in metapelitic xenoliths in the gabbro. See text for details.

and ilmenite and occasionally a core rich in quartz and ilmenite similar to core of the garnet in Fig. III-6e. Locally, garnet is mantled by a green to dark-green spinel rim (Fig. III-7d). Spinel also lies in the matrix with sillimanite needles as inclusions. Cordierite in centimetre-scale and isometric aggregates bears sillimanite, spinel and zircon inclusions. Euhedral yellow staurolite (<1 mm in size) occasionally with green-spinel inclusions occurs in different locations: (1) in small pockets associated with biotite (Fig. III-7f) and more often with pale-green chlorite; (2) in bands along the leucosome/melanosome border; (3) along cracks crosscutting cordierite; and (4) in the matrix in retrogressed xenolith still preserving corundum, garnet and rarely spinel and cordierite (e.g. rocks from Fig. III-4h). Ilmenite occurs in the matrix and no rutile was observed.

The sample BPA 018-11a has a felsic granulite assemblage of Grt–Sil–Crd–Spl–Irm. Garnet porphyroblast (1 cm in diameter) bears Sil–Spl–Bt–Irm inclusions and Sil–Bt pockets. The compositional profile is flat ( $\text{Alm} = 0.72$ ,  $\text{Prp} = 0.23$ ,  $\text{Grs} = 0.03$ ,  $\text{Sps} = 0.01$ ,  $X\text{Fe} = 0.76$ ) with a 1 mm thick rim with many Spl inclusions and showing Prp decrease balanced by Alm

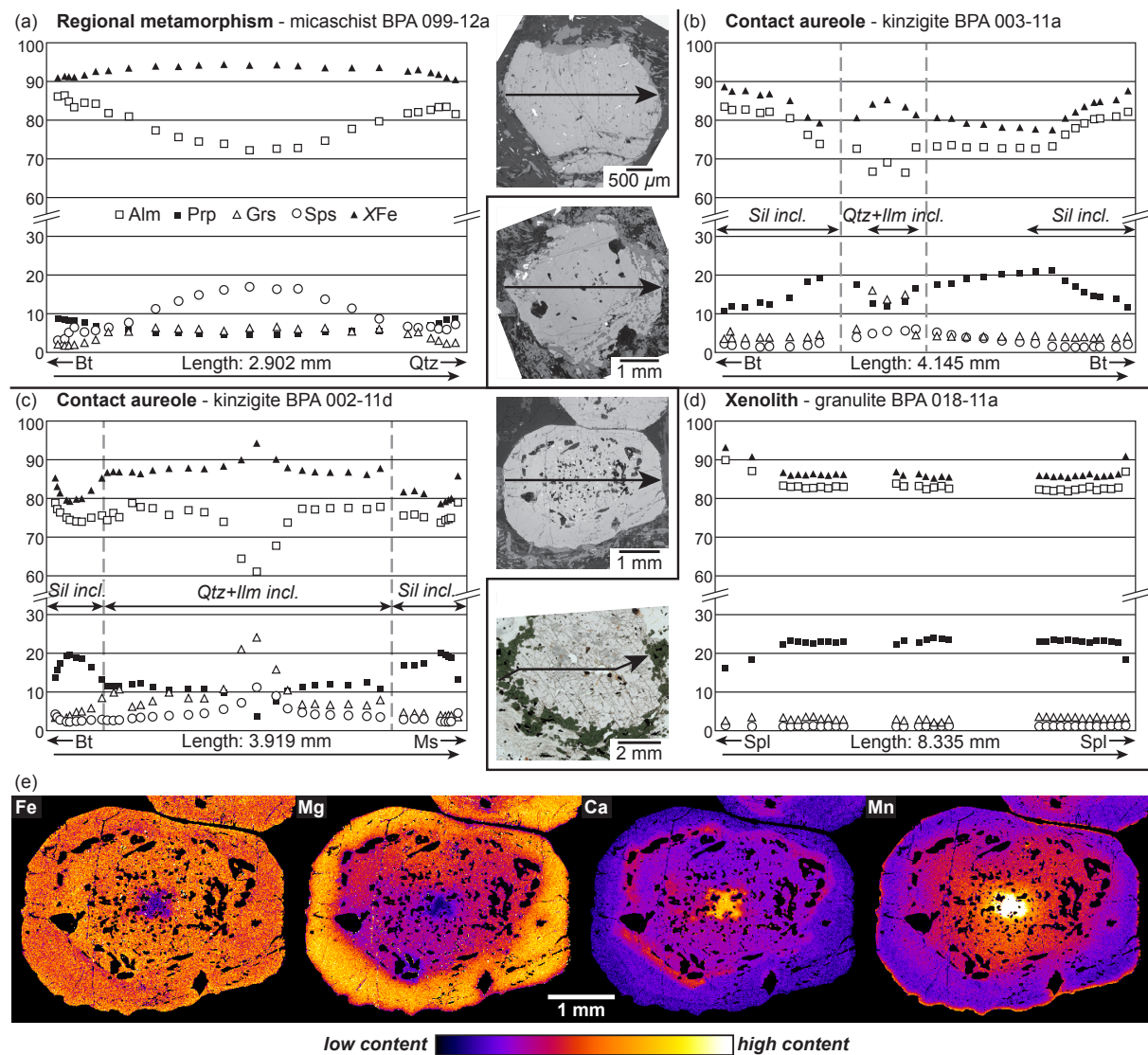


**Fig. III-9:** Garnet compositional profiles for the samples from (a) micaschist from regional metamorphism, (b) and (c) kinzigite from the contact aureole and (d) granulitic xenolith. Compositional maps are for kinzigite sample BPA 002-II d (contact aureole) presented in (c). (e) Note the presence of inherited core and the Prp-rich rim with light Grs oscillatory zoning.

and  $X\text{Fe}$  increase ( $\text{Alm} = 0.80$ ,  $\text{Prp} = 0.16$ ,  $\text{Grs} = 0.03$ ,  $\text{Sps} = 0.01$ ,  $X\text{Fe} = 0.83$ ). It is sometimes rimmed by green spinel with hercynite chemistry ( $X\text{Fe} = 0.76\text{--}0.83$ ,  $\text{Zn} = 0.02$  a.p.f.u.) with sillimanite inclusions, the latter also occurring in the matrix. Fibrolitic sillimanite is aligned along cordierite polycrystalline aggregates (up to 1 cm,  $X\text{Fe} = 0.37\text{--}0.40$ ,  $\text{Na} = 0.01\text{--}0.02$  a.p.f.u.,  $\text{K} = 0.00$  a.p.f.u.) and is sometimes crenulated during Dc3 deformation (Fig. III-7e). Cordierite has prismatic and fibrolitic sillimanite, ilmenite and rare zircon inclusions. Sil–Spl aggregates sometimes display Fc3. Few brown-red biotite lies along grain boundaries, includes all matrix minerals and have  $X\text{Fe} = 0.43\text{--}0.51$  and  $\text{Ti} = 0.09\text{--}0.16$  a.p.f.u. It is therefore interpreted as retrograde.

**Table III-1:** Representative mineral analysis from samples BPA 099-12a (micaschist from regional metamorphism) and BPA003-11a (kinzigite from the contact aureole).

Lithology	Micaschist BPA 099-12a										Kinzigite BPA 003-11a								
	Grt		St		Ms		Bt		Pl		Grt		Spl		Ms		Bt		Pl
Mineral	core	int.	rimext.	rim	core	rim	mat.	mat.	mat.	core	int.	rimext.	rim	in Sil	mat.	mat.	rim	core	
Position	core	int.	rimext.	rim	core	rim	mat.	mat.	mat.	core	int.	rimext.	rim	in Sil	mat.	mat.	rim	core	
An. Name	p90e	p96e	p101e	p1e	p4e	p35e	p27e	p31e	p64a	p73a	p81a	p47a	p85a	p48a	p89a	p88a			
Wt%																			
SiO <sub>2</sub>	36.10	36.12	36.37	27.27	25.82	45.85	34.63	65.26	36.60	36.88	36.54	0.00	45.31	35.37	58.91	62.82			
TiO <sub>2</sub>	0.07	0.03	0.03	0.48	0.49	0.26	1.89	0.00	0.03	0.06	0.05	0.06	0.43	1.64	0.00	0.00			
Cr <sub>2</sub> O <sub>3</sub>	0.00	0.01	0.00	0.03	0.02	0.03	0.03	0.00	0.03	0.02	0.01	0.09	0.02	0.03	0.00	0.00			
Al <sub>2</sub> O <sub>3</sub>	21.28	21.21	21.06	56.01	56.19	35.76	19.15	21.14	21.84	21.99	21.97	60.00	36.34	19.91	26.04	23.45			
FeO	32.79	37.38	37.62	11.04	12.45	1.04	21.37	0.02	31.23	34.50	37.06	33.05	1.12	19.21	0.03	0.00			
MnO	7.19	2.87	3.11	0.23	0.19	0.02	0.06	0.01	2.42	0.67	0.48	0.06	0.00	0.00	0.00	0.00			
NiO	0.00	0.00	0.01	0.00	0.02	0.02	0.10	0.00	0.00	0.03	0.00	0.07	0.00	0.05	0.02	0.02			
MgO	1.09	1.60	2.13	0.63	1.14	0.60	7.99	0.02	3.24	5.25	3.75	3.49	0.60	10.20	0.00	0.00			
CaO	2.12	1.65	0.84	0.00	0.01	0.00	0.00	1.72	5.04	1.37	1.27	0.00	0.00	0.01	6.88	3.80			
Na <sub>2</sub> O	0.05	0.01	0.01	0.00	0.00	1.65	0.19	11.04	0.00	0.00	0.01	0.00	1.16	0.20	7.86	9.77			
K <sub>2</sub> O	0.00	0.00	0.01	0.03	0.01	9.34	9.02	0.05	0.00	0.01	0.00	0.00	9.91	9.32	0.02	0.05			
ZnO	0.00	0.00	0.00	3.05	2.62	0.08	0.14	0.00	0.00	0.00	0.00	4.39	0.00	0.12	0.00	0.00			
Total	100.69	100.87	101.18	98.76	98.94	94.65	94.57	99.26	100.43	100.78	101.13	101.21	94.88	96.05	99.76	99.91			
Cations/Charge	8/24	8/24	8/24	30/48	30/48	7/24	8/24	5/16	8/24	8/24	8/24	3/8	7/24	8/24	5/16	5/16			
Si	2.92	2.92	2.93	7.69	7.26	3.05	2.76	2.87	2.91	2.90	2.90	0.00	3.02	2.73	2.62	2.77			
Ti	0.00	0.00	0.00	0.10	0.10	0.01	0.11	0.00	0.00	0.00	0.00	0.00	0.02	0.10	0.00	0.00			
Cr	0.00	0.00	0.00	0.01	0.00	0.00	0.00	0.00	0.00	0.00	0.00	0.00	0.00	0.00	0.00	0.00			
Al	2.03	2.02	2.00	18.63	18.63	2.81	1.80	1.10	2.04	2.04	2.05	1.98	2.85	1.81	1.37	1.22			
Fe <sup>3+</sup>	0.12	0.14	0.15	0.00	0.00	0.06	0.00	0.00	0.14	0.15	0.14	0.01	0.06	0.00	0.00	0.00			
Fe <sup>2+</sup>	2.10	2.38	2.38	2.61	2.93	0.00	1.42	0.00	1.93	2.13	2.32	0.76	0.00	1.24	0.00	0.00			
Mn	0.49	0.20	0.21	0.05	0.05	0.00	0.00	0.00	0.16	0.04	0.03	0.00	0.00	0.00	0.00	0.00			
Ni	0.00	0.00	0.00	0.00	0.00	0.00	0.01	0.00	0.00	0.00	0.00	0.00	0.00	0.00	0.00	0.00			
Mg	0.13	0.19	0.26	0.27	0.48	0.06	0.95	0.00	0.38	0.62	0.44	0.15	0.06	1.17	0.00	0.00			
Ca	0.18	0.14	0.07	0.00	0.00	0.00	0.00	0.08	0.43	0.12	0.11	0.00	0.00	0.00	0.33	0.18			
Na	0.01	0.00	0.00	0.00	0.00	0.21	0.03	0.94	0.00	0.00	0.00	0.00	0.15	0.03	0.68	0.83			
K	0.00	0.00	0.00	0.01	0.00	0.79	0.92	0.00	0.00	0.00	0.00	0.00	0.84	0.92	0.00	0.00			
Zn	0.00	0.00	0.00	0.63	0.54	0.00	0.01	0.00	0.00	0.00	0.00	0.09	0.00	0.01	0.00	0.00			
H	0.00	0.00	0.00	2.00	2.00	2.00	2.00	0.00	0.00	0.00	0.00	0.00	2.00	2.00	0.00	0.00			
Total	8.00	8.00	8.00	30.00	30.00	7.00	8.00	5.00	8.00	8.00	8.00	3.00	7.00	8.00	5.00	5.00			
XFe/Ab	0.94	0.93	0.90	0.91	0.86		0.60	0.92	0.83	0.78	0.84	0.84		0.51	0.67	0.82			
Alm/An	0.72	0.82	0.82					0.08	0.66	0.73	0.80				0.33	0.18			
Prp/Or	0.05	0.07	0.09					0.00	0.13	0.21	0.15				0.00	0.00			
Grs	0.06	0.05	0.02						0.15	0.04	0.04								
Sps	0.17	0.07	0.07						0.06	0.02	0.01								

Analysis names ended by \* were performed in Amserdam, otherwise in Stuttgart

**Table III-2:** Representative mineral analysis from samples BPA 002-11d (kinzigit from the contact aureole) and BPA 018-11a (granulitic xenolith).

Lithology	Contact aureole (BPA 002-11d)							Xenolith (BPA 018-11a)					
	Grt			Ms		Bt		Pl		Grt		Crd	Spl
Mineral	core	int. rim	ext. rim	mat.	mat.	core	rim	core	rim	mat.	mat.	mat.	mat.
Position	p21b	p6b	p1b	p1a	p8a	p10a	p11a	p54a*	p27a*	p20a*	p1a*	p12a*	
An. Name													
Wt%													
SiO <sub>2</sub>	36.89	36.35	36.59	44.62	34.12	58.48	61.34	38.23	37.60	48.10	0.01	36.17	
TiO <sub>2</sub>	0.05	0.02	0.06	0.22	2.29	0.01	0.02	0.08	0.06	0.01	0.00	2.72	
Cr <sub>2</sub> O <sub>3</sub>	0.02	0.05	0.02	0.00	0.04	0.00	0.01	0.00	0.00	0.02	0.15	0.04	
Al <sub>2</sub> O <sub>3</sub>	21.33	21.93	22.26	35.55	18.46	24.71	23.22	21.90	21.54	32.20	60.52	17.81	
FeO	28.82	35.92	34.48	1.02	19.45	0.05	0.21	33.41	36.61	9.41	33.82	17.67	
MnO	4.84	1.80	1.05	0.00	0.03	0.01	0.00	0.49	0.60	0.02	0.03	0.00	
NiO	0.05	0.04	0.00	0.01	0.07	0.00	0.04	0.00	0.00	0.00	0.00	0.00	
MgO	0.92	3.31	4.61	0.57	10.21	0.00	0.00	5.95	4.09	7.75	5.62	11.83	
CaO	8.28	1.12	1.64	0.02	0.01	6.52	4.53	1.22	0.90	0.00	0.00	0.01	
Na <sub>2</sub> O	0.00	0.02	0.00	0.83	0.15	8.24	9.17	0.01	0.00	0.11	0.03	0.29	
K <sub>2</sub> O	0.01	0.02	0.00	10.19	9.41	0.05	0.07	0.00	0.00	0.00	0.00	8.75	
ZnO	0.00	0.00	0.00	0.00	0.00	0.00	0.00	0.00	0.00	0.00	0.76	0.00	
Total	101.20	100.57	100.72	93.03	94.22	98.08	98.60	101.29	101.38	97.62	100.93	95.29	
<b>Cations/Charge</b>													
	8/24	8/24	8/24	7/24	8/24	5/16	5/16	8/24	8/24	11/36	3/8	8/24	
Si	2.93	2.91	2.89	3.03	2.69	2.64	2.75	2.98	2.97	5.00	0.00	2.80	
Ti	0.00	0.00	0.00	0.01	0.14	0.00	0.00	0.01	0.00	0.00	0.00	0.16	
Cr	0.00	0.00	0.00	0.00	0.00	0.00	0.00	0.00	0.00	0.00	0.00	0.00	
Al	2.00	2.07	2.07	2.85	1.72	1.32	1.23	2.01	2.01	3.95	1.97	1.63	
Fe <sup>3+</sup>	0.13	0.12	0.14	0.06	0.00	0.00	0.01	0.02	0.04	0.06	0.03	0.00	
Fe <sup>2+</sup>	1.79	2.28	2.14	0.00	1.28	0.00	0.00	2.16	2.38	0.76	0.75	1.14	
Mn	0.33	0.12	0.07	0.00	0.00	0.00	0.00	0.03	0.04	0.00	0.00	0.00	
Ni	0.00	0.00	0.00	0.00	0.00	0.00	0.00	0.00	0.00	0.00	0.00	0.00	
Mg	0.11	0.40	0.54	0.06	1.20	0.00	0.00	0.69	0.48	1.20	0.23	1.37	
Ca	0.71	0.10	0.14	0.00	0.00	0.32	0.22	0.10	0.08	0.00	0.00	0.00	
Na	0.00	0.00	0.00	0.11	0.02	0.72	0.80	0.00	0.00	0.02	0.00	0.04	
K	0.00	0.00	0.00	0.88	0.95	0.00	0.00	0.00	0.00	0.00	0.00	0.86	
Zn	0.00	0.00	0.00	0.00	0.00	0.00	0.00	0.00	0.00	0.00	0.02	0.00	
H	0.00	0.00	0.00	2.00	2.00	0.00	0.00	0.00	0.00	0.00	0.00	2.00	
Total	8.00	8.00	8.00	7.00	8.00	5.00	5.00	8.00	8.00	11.00	3.00	8.00	
XFe/Ab	0.94	0.80	0.85		0.52	0.70	0.78	0.76	0.83	0.41	0.77	0.46	
Alm/An	0.61	0.74	0.79			0.30	0.21	0.72	0.80				
Prp/Or	0.04	0.19	0.14			0.00	0.00	0.23	0.16				
Grs	0.24	0.05	0.03					0.03	0.03				
Sps	0.11	0.02	0.04					0.01	0.01				

Analysis names ended by \* were performed in Amsterdam, otherwise in Stuttgart

## 5. MINERAL EQUILIBRIA MODELLING

### 5.1 Modelling strategy

Pseudosections were calculated using THERMOCALC 3.33 (Powell *et al.*, 1998, 2009 version) using the dataset 5.5 (Holland & Powell, 1998, November 2003 upgrade) in the system MnO–Na<sub>2</sub>O–CaO–K<sub>2</sub>O–FeO–MgO–Al<sub>2</sub>O<sub>3</sub>–SiO<sub>2</sub>–H<sub>2</sub>O–TiO<sub>2</sub>–O<sub>2</sub> (MnNCKFMASHTO) and assembled using the TCWizard package (Petri & Skrzypek, 2013). Used *a–x* models are after: White *et al.* (2005) for garnet, biotite and ilmenite; Mahar *et al.* (1997) and Holland & Powell (1998) for cordierite and staurolite; White & Powell (2002) for orthopyroxene and spinel; Coggon & Holland (2002) for white micas; Holland & Powell (2003) for feldspar; and White *et al.* (2007) for silicate melt. Pseudosections were calculated using whole-rock compositions obtained by ICP–AES analyses at Acme Laboratories (Vancouver, Canada) and reported in Table III-3 corrected of the CaO content of apatite. Fe<sub>2</sub>O<sub>3</sub> content (O value) was set to 0.01 to reproduce the reduced oxidation state of pelitic rocks. Molar and compositional isopleths were plotted for selected phases of interest.

For the micaschist sample representing the regional metamorphism (BPA 099-12a), the presence of quartz segregation lenses and muscovite, and absence of leucosome indicates that H<sub>2</sub>O was present. Therefore, pseudosection is calculated under saturated conditions with respect to water and quartz. On the other hand, presence of leucosome associated to melanosome for migmatites of the contact aureole and anhydrous assemblage for the granulitic xenoliths indicates that rocks suffered partial melting and therefore granitic melt was present. Modelling strategy for such conditions follows the approach developed in Hasalová *et al.* (2008) that assumes a continuous assemblage equilibration until melt becomes absent (Guiraud *et al.*, 2001; Powell *et al.*, 2005; Štípská & Powell, 2005). Therefore, H<sub>2</sub>O content is determined using *T–M(H<sub>2</sub>O)* sections so that the solidus is located in the field corresponding to the observed matrix assemblage and garnet compositional isopleths at solidus are close to garnet measured composition.

**Table III-3:** Major element concentration of samples (in wt. %) obtained from whole rock analyses by ICP-AES and used for mineral equilibria modelling.

	wt%	SiO <sub>2</sub>	Al <sub>2</sub> O <sub>3</sub>	Fe <sub>2</sub> O <sub>3</sub>	MgO	CaO	Na <sub>2</sub> O	K <sub>2</sub> O	TiO <sub>2</sub>	MnO
Micaschist	BPA 099-12a	46.65	26.64	10.53	2.93	0.22	0.81	6.82	1.15	0.16
Kinzigite	BPA 003-11a	42.61	30.29	13.38	4.67	0.33	0.52	4.51	1.54	0.07
	BPA 002-11d	50.67	23.67	12.84	3.82	0.63	0.81	4.16	1.14	0.18
Granulite	BPA 018-11a	35.59	35.60	19.85	5.86	0.20	0.01	0.15	2.17	0.12

## 5.2 Regional metamorphism: pseudosection for micaschist sample BPA 099-12a far from the pluton

The pseudosection for micaschist BPA 099-12a (Fig. III-10) is calculated for sub-solidus conditions, i.e. at  $T < 650^\circ\text{C}$  with  $\text{H}_2\text{O}$  and quartz in excess using whole rock composition presented in Table III-3. Major characteristics for the pseudosection are garnet stability for  $T > 510^\circ\text{C}$  and  $P > 3$  kbar and chlorite stable till staurolite field ranging between 2.7 kbar/535 °C and 8–9 kbar/670°C. Aluminosilicate are present at  $T > 600$ – $650^\circ\text{C}$  for  $P < 6$  kbar, plagioclase below 4–6 kbar and cordierite below 3 kbar. Biotite is always stable. Rutile replaces ilmenite above 9 kbar/600°C.

The paragenetic relations involve garnet with ilmenite inclusions, muscovite, biotite, plagioclase, quartz and ilmenite aligned along the Sc1 foliation. Staurolite has an unclear structural situation in this sample but grows with Ms–Bt–Pl–Qtz matrix minerals affected by the Dc2 deformation. Garnet is compositionally zoned and presents a decrease in Sps balanced by an increase in Alm mostly from core ( $\text{Alm} = 0.72$ ,  $\text{Prp} = 0.05$ ,  $\text{Grs} = 0.06$ ,  $\text{Sps} = 0.17$ ,  $X\text{Fe} = 0.94$ ) to inner rim ( $\text{Alm} = 0.82$ ,  $\text{Prp} = 0.07$ ,  $\text{Grs} = 0.05$ ,  $\text{Sps} = 0.07$ ,  $X\text{Fe} = 0.93$ ). In the outermost rim ( $\text{Alm} = 0.82$ ,  $\text{Prp} = 0.09$ ,  $\text{Grs} = 0.02$ ,  $\text{Sps} = 0.07$ ,  $X\text{Fe} = 0.90$ ), a decrease in Grs is balanced by an increase in Prp (Fig. III-9a). Staurolite has an unzoned core ( $X\text{Fe} = 0.86$ – $0.88$ ) and a few

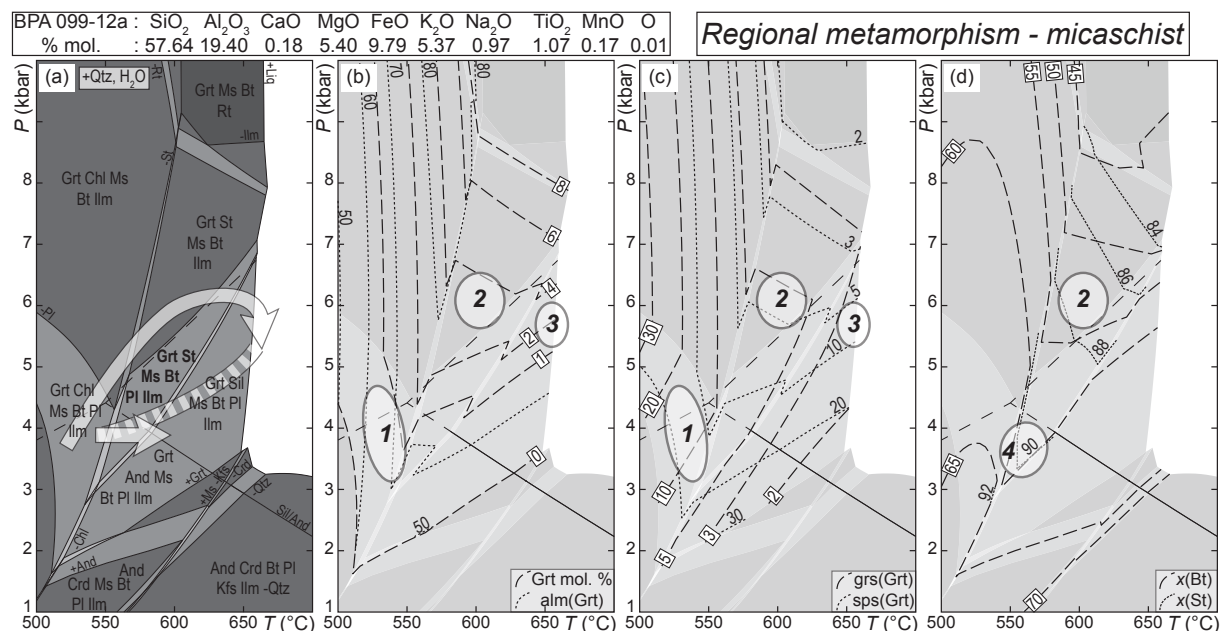


**Fig. III-10:** (a) P-T pseudosection for micaschist sample BPA 099-12a from the regional metamorphism (whole rock composition in mol. % normalized to 100%). The white arrows represent the P-T evolution deduced from paragenetic relations, matrix assemblage (in bold) and chemistry of garnet, staurolite and biotite. See text for details. (b, c, d) Simplified pseudosection contoured with garnet molar and compositional isopleths and biotite and staurolite compositional isopleths. Ellipses indicate probable equilibration of garnet (from core to rim circles 1, 2 and 3), staurolite (circle 2 for core and circle 4 for rim) and biotite (circle 2).

$\mu\text{m}$  thick rim ( $X\text{Fe} = 0.91$ ). Biotite has  $X\text{Fe} = 0.58\text{--}0.63$ . Porphyroblastic andalusite lies over both Sc1 and Sc2 fabrics.

This pattern points to two successive and independent prograde evolutions separated by a decompression event (white arrows and circles 1, 2, 3 and 4 in Fig. III-10). The initiation of the first path is indicated by the garnet core chemistry which is similar to modelled isopleths around 4 kbar/540°C (circle 1 in Fig. III-10bc). It follows a mid-pressure gradient to reach 6 kbar/600°C as pointed by the garnet internal rim chemistry, by the core of staurolite blasts and the biotite compositions (circles 2 in Fig. III-10bcd). The garnet external rim chemistry matches modelled isopleths around 5.6 kbar/650°C (circle 3 in Fig. III-10bc), nearby the solidus, which is in agreement with presence of sillimanite and rare leucosome in some other samples. Staurolite rim chemistry (circle 4 in Fig. III-10d) and growth of andalusite blades point to a second  $P\text{--}T$  prograde evolution occurring between 3 and 4.5 kbar from 540 to maximum 585°C. This near isobaric heating leads to cordierite crystallization in some other samples. The two stages are separated by a decompression that is not recorded by the paragenetic relations.

### 5.3 Contact metamorphism: pseudosection for kinzigite sample BPA 003-11a from the contact aureole

The pseudosection for the sample BPA 003-11a (Fig. III-11) is build using  $\text{H}_2\text{O} = 5.66$  mol. % for whole-rock chemistry listed in Table III-3. It allows the observed matrix assemblage Grt–Sil–Crd–Spl–Bt–Kfs–Ilm–Liq field to be bounded by the solidus while satisfying the garnet rim chemistry associated to this assemblage. A lower  $\text{H}_2\text{O}$  value shifts the solidus to higher temperature and lowers alm(Grt) that would not satisfy measured compositions. Conversely, a higher  $\text{H}_2\text{O}$  content lowers the solidus temperature and garnet and spinel would not be stable together close to the liquid-in line. The major features of the pseudosection include a solidus at  $T = 750\text{--}850^\circ\text{C}$  and the garnet-out line between 1 kbar/460°C and 5 kbar/785°C. Cordierite is stable below 1 kbar/450°C and 7 kbar/850°C and spinel ~1 kbar below. Aluminosilicate-out line ranges from 1 kbar/660°C to 6.2 kbar/850°C. Biotite and K-feldspar are always stable whereas muscovite only above ~6.2 kbar for sub-solidus conditions. Ilmenite–rutile transition lies between 7 and 9 kbar.

Crystallization–deformation relationships for this sample imply garnet core growth ( $\text{Alm} = 0.66\text{--}0.73$ ,  $\text{Prp} = 0.12\text{--}0.17$ ,  $\text{Grs} = 0.04\text{--}0.16$ ,  $\text{Sps} = 0.04\text{--}0.06$ ,  $X\text{Fe} = 0.81\text{--}0.85$ ) with ilmenite and quartz inclusions well oriented along a pre-Sc3 fabric. This type of inclusions associated to such high Grs-values are not reproducible with the  $\text{H}_2\text{O}$ -undersaturated pseudosection, which indicates that garnet core may have grown under a  $\text{H}_2\text{O}$ -saturated path, occurring before melting and associated melt-loss. The garnet core is overgrown by a rim ( $\text{Alm}$

$= 0.73$ ,  $\text{Prp} = 0.21$ ,  $\text{Grs} = 0.04$ ,  $\text{Sps} = 0.02$ ,  $X\text{Fe} = 0.76$ ) with randomly orientated sillimanite, biotite and ilmenite inclusions. External rim shows a decrease of  $\text{Prp}$  with an increase of  $X\text{Fe}$  and  $\text{Alm}$  ( $\text{Alm} = 0.82$ ,  $\text{Prp} = 0.12$ ,  $\text{Grs} = 0.04$ ,  $\text{Sps} = 0.02$ ,  $X\text{Fe} = 0.88$ ). Andalusite porphyroblasts lie in an unconstrained structural position, almost totally replaced by  $\text{Sil}-\text{Spl}\pm\text{Crn}$  during the reequilibration of the rock weakly deformed during Dc3. Matrix biotite has  $X\text{Fe} = 0.50\text{--}0.53$  and spinel has  $X\text{Fe} = 0.83\text{--}0.85$ . Rare oligoclase ( $\text{Ab} = 0.92$ ,  $\text{An} = 0.08$ ,  $\text{Or} = 0.00$ ) lies in the

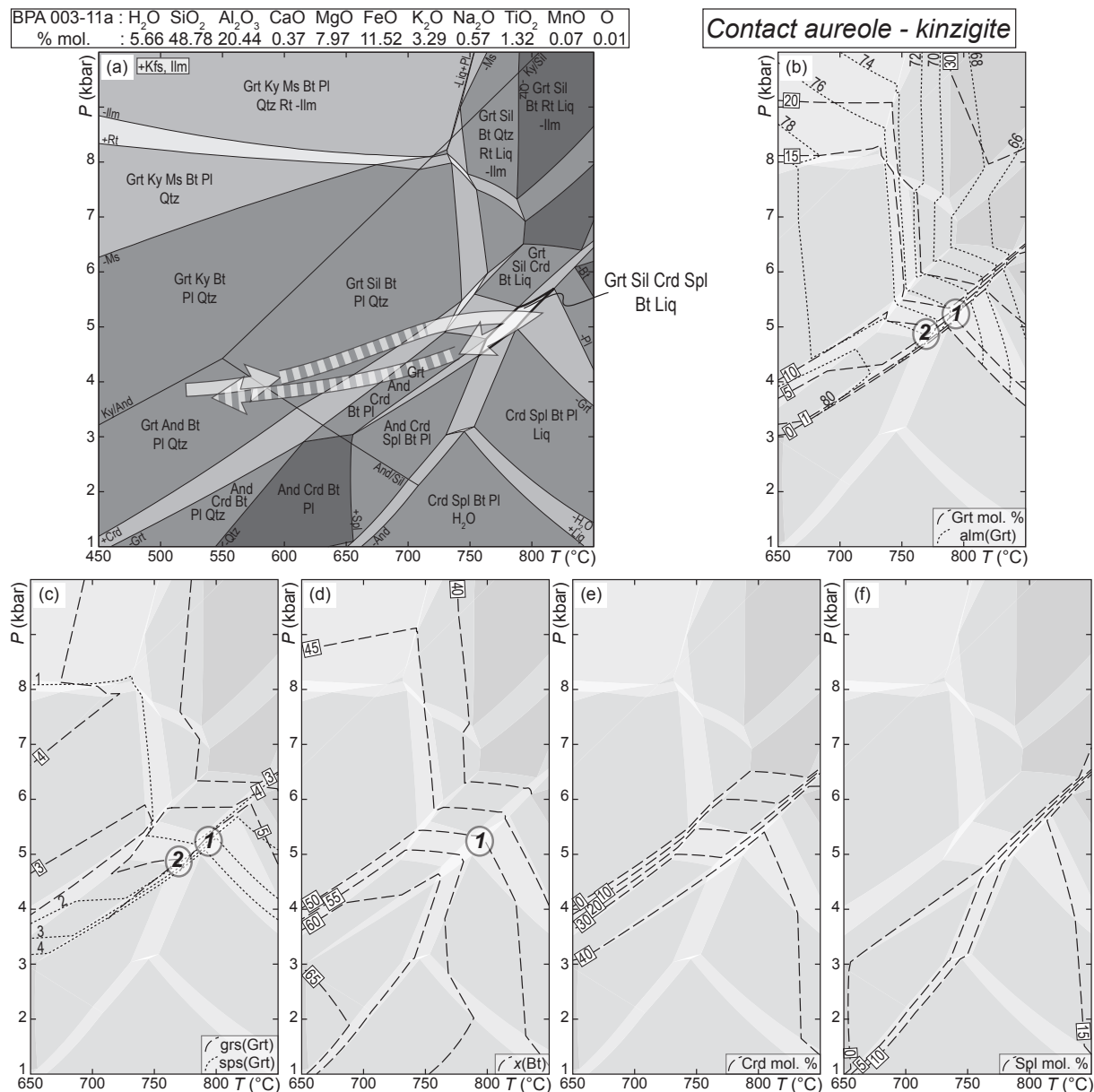


**Fig. III-11:** (a)  $P$ - $T$  pseudosection for kinzigitic sample BPA 003-11a from the contact aureole (whole rock composition in mol. % normalized to 100%). The white arrows represent the  $P$ - $T$  evolution deduced from paragenetic relations, matrix assemblage (in bold) and chemistry of garnet and biotite. See text for details. (b, c, d, e, f) Simplified part of the pseudosection contoured with garnet molar and compositional isopleths, biotite compositional isopleths and cordierite and spinel molar isopleths. Ellipses indicate probable equilibration of garnet (from core to rim circles 1 for inner rim and 2 outermost rim), biotite (circle 2) with the matrix.

BPA 002-11d :	$H_2O$	$SiO_2$	$Al_2O_3$	$CaO$	$MgO$	$FeO$	$K_2O$	$Na_2O$	$TiO_2$	$MnO$	O
% mol.	: 5.66	56.22	15.48	0.65	6.32	10.72	2.94	0.87	0.95	0.17	0.01

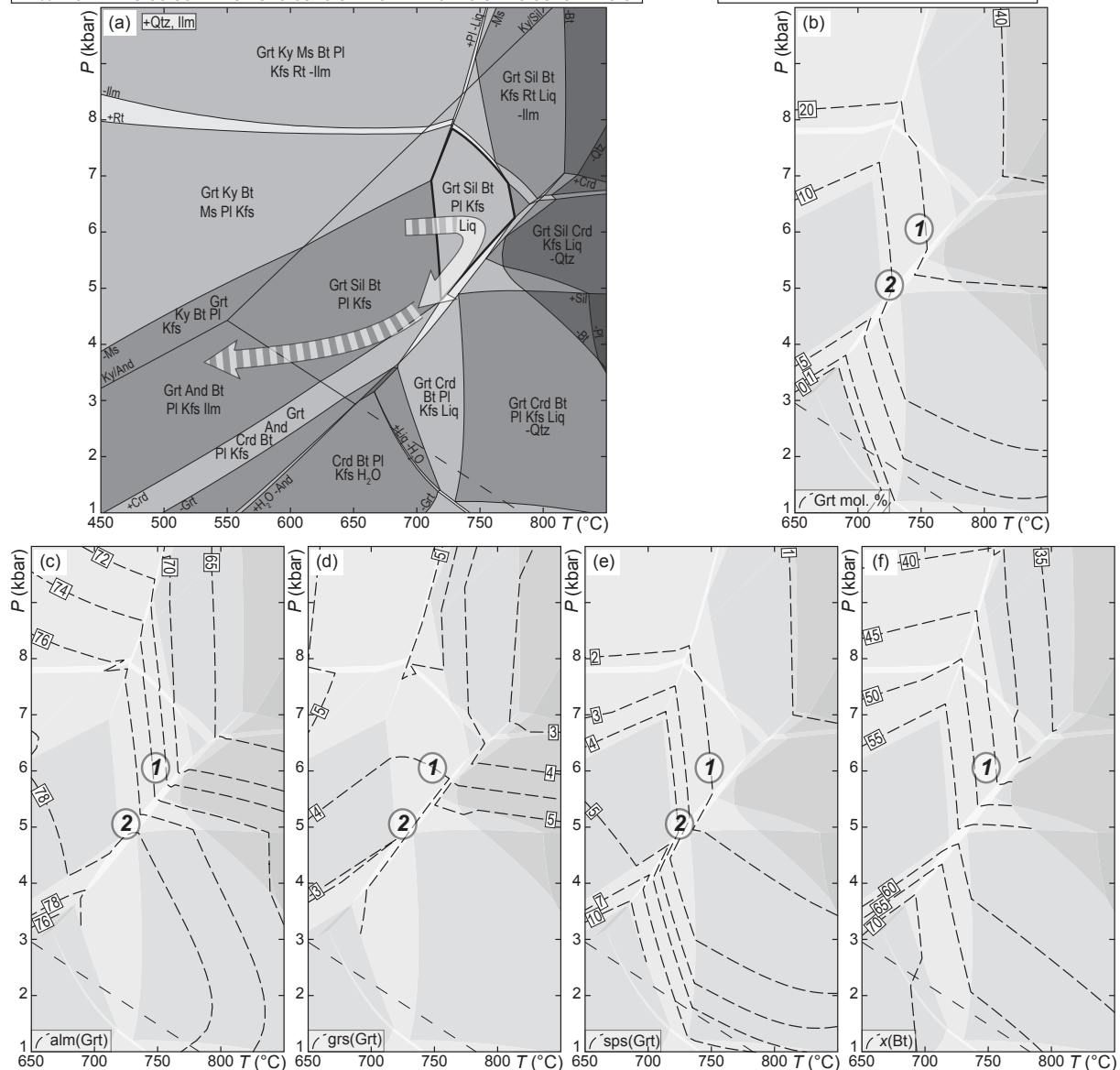


**Fig. III-12:** (a)  $P$ - $T$  pseudosection for kinzigite sample BPA 002-11d from the contact aureole (whole rock composition in mol. % normalized to 100%). The white arrow represents the  $P$ - $T$  evolution deduced from paragenetic relations, matrix assemblage (in bold) and chemistry of garnet and biotite. See text for details. (b, c, d, e, f) Simplified part of the pseudosection contoured with garnet molar and compositional isopleths, biotite compositional isopleths. Ellipses indicate probable equilibration of garnet (from core to rim circles 1 for inner rim and 2 outermost rim), biotite (circle 2) with the matrix.

matrix whereas few K-feldspar and pinitized cordierite form leucosome. Ilmenite is located in the matrix and in minerals as inclusions. After equilibration of the dominant matrix assemblage, the sequence is ended by post-tectonic growth of small muscovite.

The  $P$ - $T$  path deduced from mineralogical relationships (white arrows in Fig. III-11a) is characterized by a preliminary near-isobaric heating responsible for the growth of porphyroblastic andalusite around 3–4 kbar/525–585°C. It is followed by matrix equilibration in the Grt–Sil–Crd–Spl–Bt–Kfs–Ilm–Liq field during a higher temperature stage synchronous with Dc3 deformation. Presence of spinel and cordierite indicates heating or exhumation, as

modal isopleths are  $P$ - and  $T$ -dependent (Fig. III-11ef). However, near-isobaric heating in this field is supported by the absence of quartz inclusions in garnet rim and no evidence of garnet consumption that may be due to decompression. Measured biotite, spinel and garnet compositions for the internal rim match modelled isopleths around 5.2 kbar/800°C (circle 1 in Fig. III-11bcd for garnet and biotite). Higher temperature/lower pressure unstabilizes garnet and sillimanite whereas higher pressure does not allow spinel to be present. Garnet rim is re-equilibrated during cooling by diffusion close to the liquid-out line at 4.8 kbar/770°C (circle 2 in Fig. III-11bc). A second andalusite generation visible in some other samples from the same outcrop indicates a cooling path reaching andalusite stability field (Fig. III-7c).

#### 5.4 Contact metamorphism: pseudosection for kinzigite sample BPA 002-11d from the contact aureole

The pseudosection for the second kinzigite sample from the contact aureole (BPA 002-11d, Fig. III-12) is constructed using the whole-rock chemistry listed in Table III-3.  $H_2O$  is set to 5.66 mol. % that allows the solidus within the Grt–Sil–Bt–Pl–Kfs–Qtz–Liq field with modelled isopleths satisfying measured garnet composition. Higher  $H_2O$  content would shift the solidus to higher temperature, lower  $H_2O$  content would shift the solidus to lower temperature and garnet modelled isopleths would not reproduce the measured composition. K-feldspar is present in all fields but in very low modal proportion (<0.01 mol. % for the field of interest). The pseudosection is similar to the kinzigite from the contact aureole (Fig. III-11) except that spinel is never present; aluminosilicate are unstable below a line from 1 kbar/560°C to 7 kbar/850°C; biotite is not stable between 5.8 to 10 kbar/770°C and 3.5 kbar/850°C; muscovite is stable at  $P > 4$  kbar and  $T < 700^\circ C$ ; and quartz-out line lies between 1 kbar/730°C and 7.9 kbar/850°C.

Crystallization–deformation relations involve growth of a garnet core ( $Alm = 0.61–0.79$ ,  $Prp = 0.04–0.12$ ,  $Grs = 0.06–0.24$ ,  $Sps = 0.03–0.11$ ,  $XFe = 0.86–0.94$ ) with numerous Bt–Qtz–Ilm inclusions with high  $Grs(Grt)$  and  $Sps(Grt)$  in the center that is not reproducible with the  $H_2O$ -undersaturated pseudosection. As for the previous sample, we suggest that the core grew during a previous  $P–T$  loop, possibly on a prograde  $P–T$  path in  $H_2O$ -saturated conditions, inaccessible in this pseudosection. The core is surrounded by an aureole ( $Alm = 0.74$ ,  $Prp = 0.19$ ,  $Grs = 0.05$ ,  $Sps = 0.02$ ,  $XFe = 0.80$ ) with Sil–Bt inclusions, a high  $Prp$  value and a slight  $Grs$  oscillatory zoning (Fig. III-9ce). Garnet outermost rim presents a decrease of  $Prp$  and an increase of  $XFe$ ,  $Alm$  and  $Sps$  ( $Alm = 0.79$ ,  $Prp = 0.14$ ,  $Grs = 0.03$ ,  $Sps = 0.04$ ,  $XFe = 0.85$ ). Quartz and plagioclase are present in aggregates elongated along Sc3. Biotite ( $XFe = 0.50–0.52$ ) with sillimanite are aligned parallel to the Sc3 fabric. Post-tectonic growth of muscovite marks the end of the crystallization sequence.

Abundant sillimanite, absence of cordierite and garnet textural features are compatible with a heating path in the Grt–Sil–Bt–Pl–Kfs–Qtz–Ilm–Liq field (white arrow in Fig. III-12a), involving increase in garnet molar isopleths. Modelled isopleths are close to measured compositions for the internal rim of the garnet and biotite (circle 1 in Fig. III-12bcdef) indicating a near-isobaric heating up to 6 kbar/750°C. The outermost rim of garnet matches the modelled isopleths at 5 kbar/725°C (circles 2 in Fig. III-12bcde) and is interpreted as diffusionally reequilibrated on retrograde path. The late growth of andalusite in other samples indicates that the retrograde  $P$ – $T$  path went through andalusite stability field.

## 5.5 Contact metamorphism: pseudosection for granulite sample BPA 018-11a from a xenolith

The whole rock chemistry used for modelling is listed in Table III-3 (Fig. III-13). H<sub>2</sub>O is set to 1.96 mol % using garnet core composition. Such a value allows the Grt–Sil–Crd–Spl–Ilm–Liq to lie just ~10°C apart from the solidus. A lower value shifts the solidus to higher temperatures; alm(Grt), grs(Grt) and sps(Grt) would decrease and would not fit the measured garnet compositions. A higher H<sub>2</sub>O content shifts both the solidus and K-feldspar-out line to lower temperatures, but also the quartz-in line to higher pressure: modelled garnet isopleths would satisfy measured compositions only for Qtz-bearing assemblages. The pseudosection is characterized by solidus around 900°C for  $P$  < 6 kbar becoming near-isobaric at 6 kbar for  $T$  < 900°C. Garnet-out line heads from 1 kbar/740°C to 6 kbar/1100°C and sillimanite-out line from 3.3 kbar/700°C to 7.8 kbar/1100°C. Opx is stable below 1–3 kbar and 1000°C and cordierite below ~8 kbar where ilmenite/rutile transition occurs. Spinel is always stable except for  $P$  > 6.5 kbar and  $T$  < 820°C. Plagioclase and K-feldspar have similar compositions and are stable below 6 kbar and 1040°C. Qtz-bearing assemblages are restricted to a 2.5 kbar window at higher temperatures than 5.5 kbar/930°C.

Crystallization relationships involve growth of garnet over Sil–Bt pockets, ilmenite and green spinel. Garnet has a constant composition in the core (Alm = 0.72, Prp = 0.23, Grs = 0.03, Sps = 0.01, XFe = 0.76) but Prp decreases and Alm and XFe increase in tight association with included spinel at rim (Alm = 0.80, Prp = 0.16, Grs = 0.03, Sps = 0.01, XFe = 0.83). Sil–Spl aggregates squeezed between cordierite aggregates present Fc3 microfolds (Fig. III-7e). Cordierite has XFe = 0.37–0.40 and spinel has XFe = 0.76–0.83. The sequence ends with post-tectonic crystallization of biotite (XFe = 0.43–0.51). In some other samples, biotite is associated with staurolite and in places replaced by pale-chlorite.

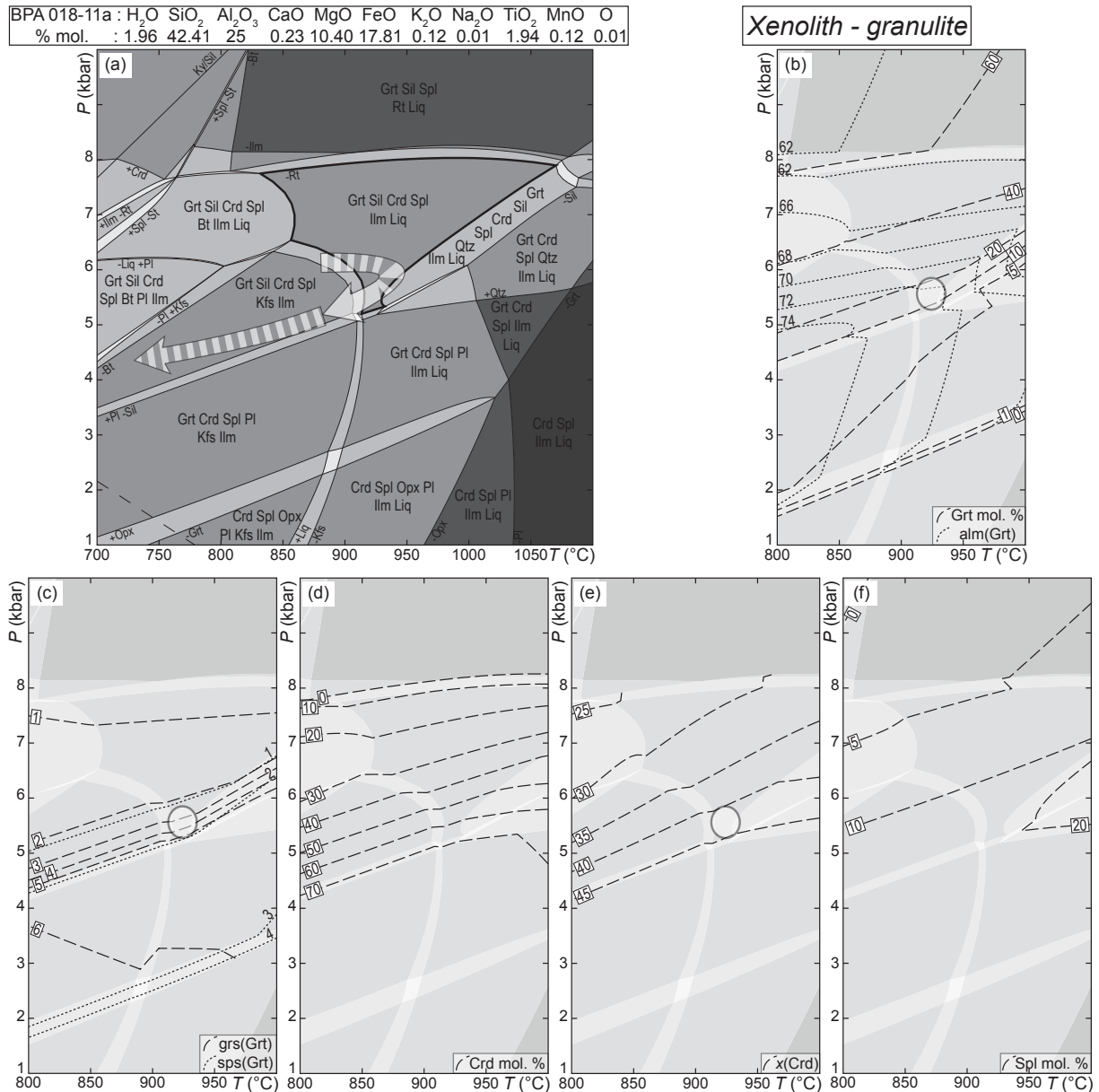


**Fig. III-13:** (a)  $P$ - $T$  pseudosection for granulite sample BPA 018-11a from a metapelitic xenolith (whole rock composition in mol. % normalized to 100%). The white arrow represents the  $P$ - $T$  evolution deduced from paragenetic relations, matrix assemblage (in bold) and chemistry of garnet and cordierite. See text for details. (b, c, d, e, f) Simplified part of the pseudosection contoured with garnet molar and compositional isopleths, cordierite molar and compositional isopleths and spinel molar isopleths. Ellipse indicates probable equilibration of garnet core and cordierite with the matrix.

$P$ - $T$  path deduced from this paragenetic sequence is indicated by the white arrow in Fig. III-13a. The rock assemblage indicates pervasive re-equilibration in the field Grt–Sil–Crd–Spl–IIm–Liq. The constant composition of the garnet core is interpreted as diffusional equilibration at 5.5 kbar/930 °C (white circle in Fig. III-13bc), supported also by the cordierite composition (white circle in Fig. III-13e). Moat structure of spinel around garnet and large cordierite aggregates suggest crossing modal isopleths of cordierite and spinel (Fig. III-13df) during decompression. Late crystallization of biotite occurred during cooling.

## 6. DISCUSSION

### 6.1 *P–T–d evolution of the Campo unit*

#### 6.1.1 *Regional evolution*

The sample BPA 099-12a displays evidence of a medium-pressure Barrovian prograde path for the Campo unit (Fig. III-14a). These involve growth of garnet in Sc1 and of garnet and staurolite during Sc2, both in the presence of muscovite and biotite. Initiation of the prograde path is marked by garnet core chemistry that fits with modelled isopleths around 4 kbar/540°C (circle 1 in Fig. III-10bc) and the peak pressure is reached at 6 kbar/600°C as indicated by garnet internal rim chemistry (circle 2 in Fig. III-10bcd). Garnet external rim composition indicates diffusion at 5.6 kbar/650°C (circle 3 in Fig. III-10bc). Crystallization of sillimanite in pressure-shadows of garnet due to Dc2 deformation in some samples (Fig. III-6c) also attests of such *P–T* conditions. Since muscovite remains usually stable and only rare leucosomes are present in the Campo unit far from the intrusion, maximal temperature may be slightly higher than muscovite-out/liquid-in line that lies around 650°C. The Barrovian *P–T* loop is followed by a decompression path that is not recorded by textural relationship but that should occur before the onset of the second prograde evolution. This second prograde path consists of an isobaric heating constrained by the growth of andalusite porphyroblasts (blades up to 10 cm in length) and by diffusion in staurolite rim at  $P \approx 4$  kbar and  $T < 580^\circ\text{C}$  as no sillimanite is observed (circle 4 in Fig. III-10d). Such prograde path questions the eclogite-facies conditions described in the literature (20 kbar/800°C, Gosso *et al.*, 1995).

#### 6.1.2 *Evolution of metasediments in and around the pluton*

In the contact aureole, the sample BPA 003-11a (Fig. III-14b) preserves evidence of the prograde evolution: (1) presence of garnet cores that could be identified by their compositional zoning (Fig. III-9b) and their textures indicating a growth in a pre-Sc3 structure (similar to Fig. III-6e) where *P–T* conditions can hardly be constrained; (2) by the pseudomorphs of Sil–Spl–Ilm±Crn after pre-Sc3 andalusite with Bt–Ilm inclusions (Figs III-5b & III-7ab). The presence of pre-Sc3 leucosomes indicates that before Dc3, rocks were already partially molten. This sample presents striking similarities with the sample BPA 099-12a lying far from the intrusion. However, andalusite pseudomorph points to a heating initiation below the aluminosilicate triple point at 4.5 kbar/500°C. This 4.5 kbar/550°C point contains a significant error bar, as it may be influenced by the minerals involved (e.g. fibrolitic/prismatic sillimanite, Kerrick, 1990). The sample reaches 5.2 kbar/800°C where the matrix equilibrated during Dc3 (circle 1 in Fig. III-

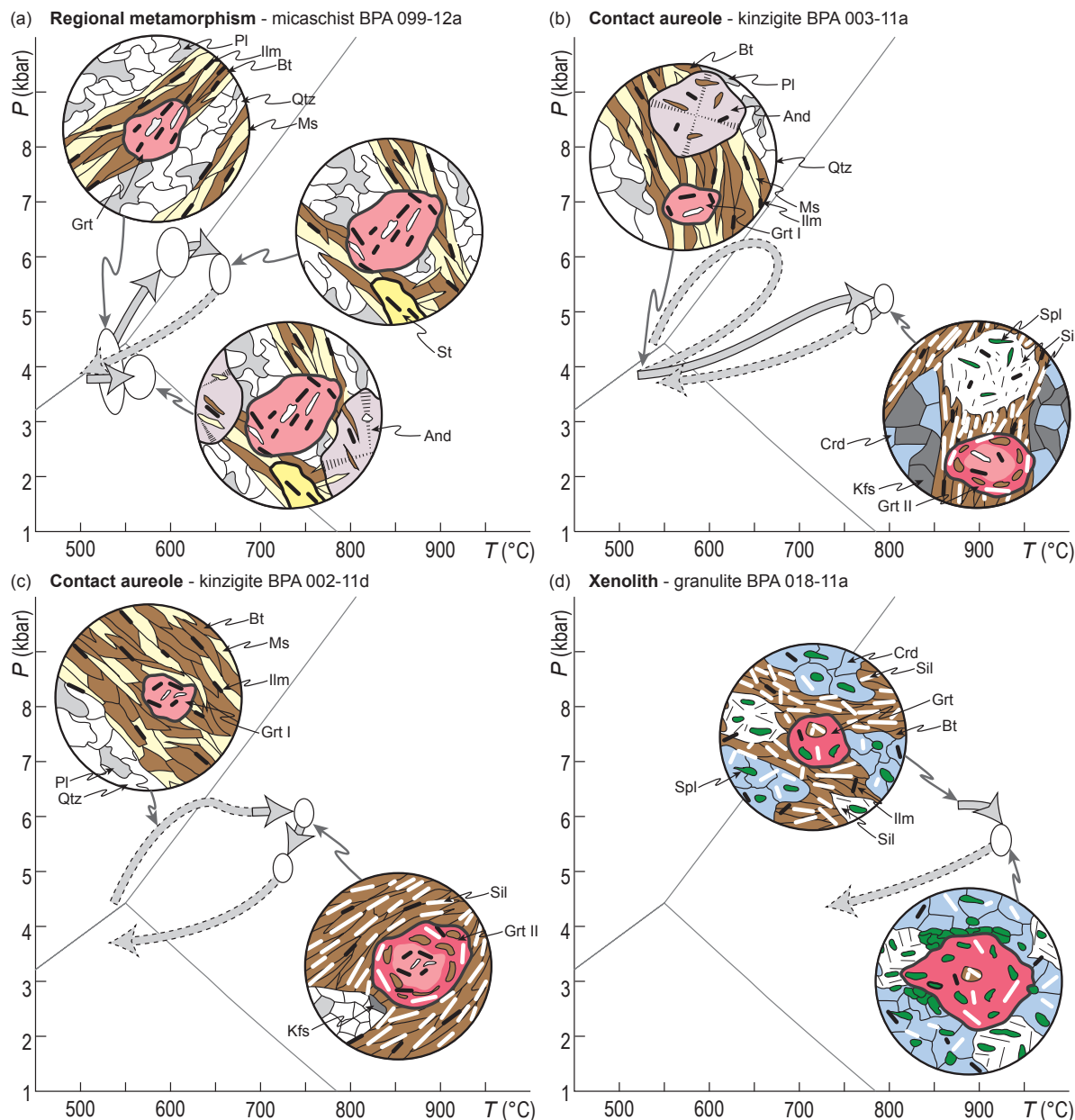


**Fig. III-14:** Sketches summarizing the inferred P-T path and associated crystallization/deformation relationships for (a) regional metamorphism, (b, c) samples in the contact aureole and (d) metapelitic xenoliths. See text for details.

11bcd) and where the garnet grew while incorporating sillimanite, biotite and ilmenite grains (similar to Fig. III-6f). Garnet external rim was partially re-equilibrated by late-diffusion at 4.8 kbar/770°C during retrogression (circle 2 in Fig. III-11bc).

Sample BPA 002-11d (Fig. III-14c) from the contact aureole presents few similarities with the other sample. The low Prp-core of garnet (Fig. III-9ce) with quartz and ilmenite inclusions (similar to Fig. III-6e) grew early during  $\text{H}_2\text{O}$ -saturated conditions not modelled by our pseudosection. Locally, this garnet present variations in Grs-content probably associated to an incorporation of calcium set free by the apatite consumption at the onset of partial melting (e.g. Indares *et al.*, 2008). Prp-rich garnet rim with light oscillatory Grs zoning (Fig. III-9ce) and Sil–Bt–IIm inclusions (similar to Fig. III-6ef) constrains conditions of 6 kbar/750°C where

garnet diffused in presence of melt (circle 1 in Fig. III-12bcdef). Under these conditions, the matrix reequilibrated and produced pressure shadows around garnet associated to Sc3. Finally, garnet rim chemistry diffused at 5 kbar/725°C during the retrograde path (circle 2 in Fig. III-12bcde).

The granulite BPA 018-11a sampled in a metapelitic xenolith presents a higher  $T$  evolution (Fig. III-14d). Whereas it is not visible in this sample, garnet in xenoliths sometimes preserves inherited cores with textural features similar to the samples from the regional metamorphism (core of garnet in Fig. III-6e) and from the contact aureole, indicating a pre-HT prograde evolution. Most of the matrix minerals and inclusions of sillimanite, spinel and ilmenite in garnet do not present shape-preferred orientations or pressure shadows indicating that matrix equilibration and garnet growth occurred under static conditions.  $P-T$  conditions are constrained to 5.5 kbar/930°C (circle in Fig. III-13bce) by a matrix assemblage and a garnet flat compositional profile (Fig. III-9d) produced by diffusion. Such conditions are in agreement with stability of Bt-free assemblages during partial melting experiments (Patiño Douce & Johnston, 1991; Vielzeuf & Montel, 1994). Dc3 deformation reorienting Sil–Spl grains remains weak and is limited to Fc3 microfolds of Sil–Spl grains (Fig. III-7e). K-feldspar that should appear during cooling before melt crystallization is not visible probably because of the low amount predicted by the modelling (around 0.01 mol. %). Diffusion affected garnet outermost rim and is characterized by a Fe–Mg exchange, Ca and Mn remaining constant (Fig. III-9d). This indicates a partial re-equilibration of garnet by diffusion during cooling associated to slight decompression below 4.5 kbar.

In some samples collected in xenoliths, biotite presents lamellar intergrowth with quartz and is interpreted as back-reactions with melt or aqueous fluids (Waters, 2001). Staurolite stable in HT assemblages is described up to 1050°C if  $X_{\text{Fe}}$  is low (high Mg content, Grevel *et al.*, 2002; Sato *et al.*, 2010) or could be stabilized in supra-solidus conditions by a high Zn content (e.g. Ganguly, 1972). In our case, low Zn and Mg content, spinel inclusions (Fig. III-7f), occurring in biotite or Mg-chlorite pockets indicate that staurolite occurs late in the prograde sequence or is retrograde. Therefore, we interpret these St-pockets to be a product of back-reaction with melt (e.g. Ashworth, 1975; Kriegsman & Hensen, 1998). Retrogression for the two samples from the contact aureole and the sample from a xenolith in andalusite stability field points to decompression below 4.5 kbar. In the samples from the contact aureole, it is testified by the presence of a second generation of andalusite that grows statically (Fig. III-7c), therefore after the end of Dc3 deformation. Dc3 deformation seems to be restricted to supra-solidus conditions, as quartz presents no recrystallization and occasionally only a weak undulose extinction.

## 6.2 Implications for the geodynamic evolution of the Austroalpine domain

### 6.2.1 Variscan tectono-metamorphic evolution

The Campo unit records a pre-Permian Barrovian metamorphism reaching amphibolite to upper-amphibolite facies (Fig. III-15a), in agreement with previous qualitative estimations (~5–9 kbar and 550–600°C, Bianchi Potenza *et al.*, 1978a; Braga *et al.*, 2001; Notarpietro & Gorla, 1981; Pace, 1966). It is also the case for numerous lithologies in the Err and Bernina units (Büchi, 1994; Halmes, 1991) and inferred in the Margna unit (Guntli & Liniger, 1989). In particular, the yet undated pre-Permian history of the Campo unit shares similarities with the Variscan prograde metamorphism dated in the Ulten area (the Upper Tonale unit) to the lower Carboniferous (U–Pb on Mnz, Langone *et al.*, 2011). Using the similarities with the Ulten area, we interpreted the Dc1 deformation phase of the Campo unit as related to the Variscan crustal thickening during the Lower Carboniferous. It is followed by the Dc2 deformation stage during the thermal peak, bracketed in the Ulten zone to Middle Carboniferous times. This evolution is fairly consistent with the Variscan evolution of the Alpine realm (see e.g. Schaltegger *et al.*, 2003).

### 6.2.2 Late-Variscan tectono-metamorphic evolution

The end of the Variscan evolution in the Austroalpine domain is characterized by an extensional phase associated with exhumation and cooling of basement rocks (Fig. III-15b, e.g. at 310 Ma, Rb–Sr ages in Silvretta, Thöni, 1981). Evidence for exhumation between *ca.* 310 and *ca.* 290 Ma are preserved in the Bernina unit where alkaline intrusive rocks, emplaced at  $P < 3$  kbar and 295 Ma, are crosscut by alkaline rhyolites dated at 288 Ma (Büchi, 1987; Spillmann & Büchi, 1993; Von Quadt *et al.*, 1994). Decompression of the Campo unit to  $P < 4.5$  kbar occurs after the Variscan burial and exhumation, before the onset of HT regime associated with the emplacement of the Sondalo gabbro (samples BPA 099-12a and BPA 003-11a, Figs III-10, III-11 & III-14ab). But, no evidence of retrograde deformation could be found in the Campo unit. Therefore, we suggest that the Campo unit was tectonically unroofed during late-Carboniferous/Permian times, by a shear zone at the top of the unit.

From 290 to 270 Ma, the Permian post-Variscan extension is interpreted as characterized by a shallow lithosphere-asthenosphere boundary, responsible for the mantle partial melting and associated emplacement of mafic intrusion at all crustal level. In the Austroalpine domain mafic intrusions are emplaced in the lower crust (e.g. the Braccia gabbro, Hermann *et al.*, 1997) and middle crust (e.g. the Sondalo gabbro, Braga *et al.*, 2001; Tribuzio *et al.*, 1999). In the case of the Campo unit, near-isobaric heating due to the intrusion (samples BPA 099-12a and BPA

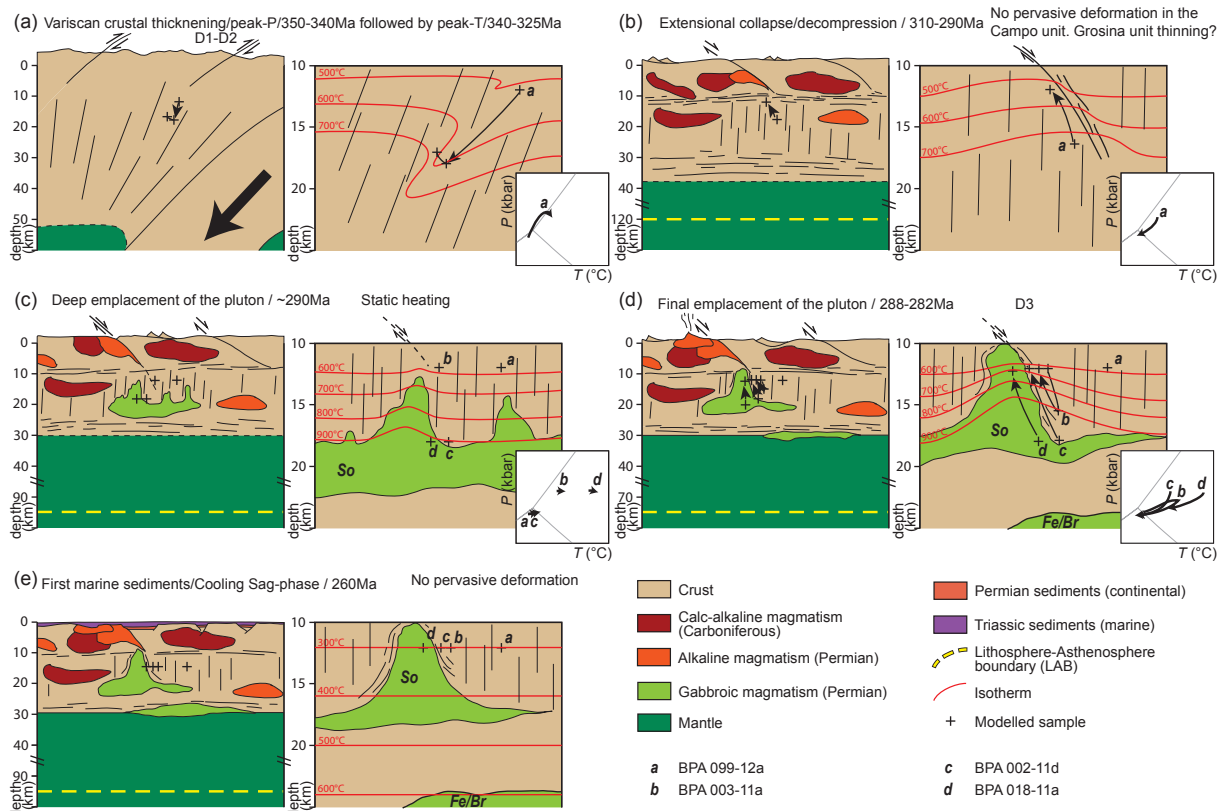


**Fig. III-15:** Model representing a schematic evolution of the area during (a) Variscan tectonics in Carboniferous times; (b) extensional collapse of the orogenic crust associated with calc-alkaline to alkaline magmatism; (c) intrusion of the Sondalo gabbro in deep levels; (d) emplacement of the Feddoz and Braccia gabbros, final emplacement of the Sondalo gabbro in shallower crustal levels and associated contact metamorphism; and (e) post-tectonic cooling of the crust with formation of a sag-basin. See text for detailed explanations. Approximate position of the lithosphere-asthenosphere boundary is taken from the thermal model of Schuster & Stüwe (2008). So refers to Sondalo gabbro, Fe/Br to Feddoz/Braccia gabbros.

003-11a, Figs III-10, III-11 & III-14ab) occurred when the Campo present-day surface exposure was already lying at  $P < 4.5$  kbar (Fig. III-15c), as attested by the static growth of andalusite and staurolite rim equilibration of samples BPA099-12a and BPA003-11a (labelled *a* and *b* on Fig. III-15). From a thermal point of view, it implies that rocks were re-equilibrated before the initiation of the heating. Similar  $P-T$  paths with a pre-Permian “orogenic” evolution followed by a Permian HT metamorphism are documented in the South Alpine realm (e.g. Barboza & Bergantz, 2000; Benciolini *et al.*, 2006). But contrary to Barboza & Bergantz (2000), who suggested that the Permian HT phase recorded in the basement occurs in continuity of the Variscan collapse, our data suggest that in some cases, crustal portions were (at least partially) thermally re-equilibrated before the onset of heating.

The intrusion of the Sondalo gabbro is responsible for HT metamorphism in the contact aureole and in metapelitic xenoliths before and during Dc3. A 2 kbar pressure gap occurs between samples far from the pluton (Fig. III-14ab) and samples in the pluton (Fig. III-

14cd) at the initiation of the near-isobaric heating path. These two end-member samples are geographically separated by the contact aureole affected by the supra-solidus Dc3 deformation. This points to a two stage intrusion. The mafic magma emplaced at ~18 km (~6 kbar) with few pipes rising up to ~12 km (~4 kbar) that are the Sondalo gabbro, but also other Permian intrusives in the Campo unit (Fig. III-15c) responsible for the development of pre-Sc3 static metamorphism. This was followed by a magma rise where deep xenoliths equilibrated at ~18 km are exhumed to ~12 km using Dc3 shearing (Figs III-13, III-14d & III-15d). During this exhumation, samples from the contact aureole have a contrasted *P-T* evolution being either exhumed (BPA 002-11d, labelled c on Fig. III-15) or buried and latter exhumed (BPA 003-11a). These *P-T-d* evolutions can give insights on the emplacement dynamics of the pluton, but needs to be constrained with more detailed characterization of magmatic fabrics.

The Permian HT-phase ended at *ca.* 260 Ma (Hermann & Rubatto, 2003). This event was followed by the deposition of thick Triassic succession (> 1km), passing from fluvial to shallow marine conditions. The deposition of these sediments is interpreted as related to thermal subsidence and possibly to tectonic subsidence in relation with the opening of the Neo-Tethys (Schuster & Stüwe, 2008). Geochronological arguments and field relations of the Austroalpine area in SE-Switzerland and N-Italy but also in the Alps in general, indicates that Permian HT rocks reach the surface only during Jurassic rifting (Mohn *et al.*, 2012; Villa *et al.*, 2000).

## 7. CONCLUSION

The study of the metamorphic evolution of the Campo unit allowed us to constrain a polyphase Permo-Carboniferous  $P-T-d$  evolution that can be summarized as following:

- After a period of crustal thickening when rocks of the Campo unit reached 6 kbar/600°C resulting from Carboniferous Dc1 and Dc2 deformation stages, the Campo unit was exhumed before being intruded by Permian plutons.
- The mid-crustal gabbro intrusion in the Campo unit is responsible for host-rock partial melting and granulite facies metamorphism in metapelitic xenoliths in the pluton.
- Contrasted  $P-T$  paths from migmatites from the contact aureole indicate that the emplacement of the gabbro occurred in two steps. First, the gabbro intruded the deep Campo unit at 6 kbar. Second, an exhumation through Dc3 shearing in the migmatitic contact aureole placed the gabbro at 4kbar in the already shallower Campo unit.
- This HT-Permian evolution ends with formation of sag-basin and deposition of first marine sediments at *ca.* 260 Ma.

## ACKNOWLEDGMENTS

We acknowledge J.C. Corona, T. Theye and G. Morvan for guidance on microprobe from Amsterdam, Stuttgart and Strasbourg, respectively. K. Schulmann and E. Skrzypek are thanked for discussions.

---

## *CHAPITRE IV*

---

Le *chapitre IV* vise à contraindre les mécanismes ayant permis l'intrusion du gabbro de Sondalo dans l'unité de Campo, afin de comprendre comment se développe le magmatisme mafique dans des niveaux crustaux superficiels pour les magmas mafiques. Ainsi, ce travail est basé sur la cartographie des lithologies et les mesures des structures des roches magmatiques mais également de leur encaissant métasédimentaire. Ces campagnes de cartographie et d'échantillonnage ont eu lieu au cours des étés 2011, 2012 et 2013.

Cette section du manuscrit est axée sur trois parties :

- Les datations U–Pb de zircons extraits de roches magmatiques et métamorphiques, couplées aux analyses d'éléments en traces. La préparation et la séparation des minéraux ont été réalisées avec le concours de T. Mateeva, partiellement à la Vrije Universiteit d'Amsterdam, partiellement à l'Université de Strasbourg. Les mesures isotopiques U–Pb sur zircons ont été réalisées lors de séjours à l'Université de Lausanne avec l'aide de F. Galster, qui a par la suite complété les datations par des analyses des éléments en traces.
- La caractérisation des fabriques magmatiques et magnétiques. Cette section s'appuie sur des mesures de terrain, elles-mêmes couplées à une étude des structures magmatiques par Anisotropie de Susceptibilité Magnétique réalisée sur les roches magmatiques, en particulier sur celles dont les structures macroscopiques sont peu visibles. L'échantillonnage nécessaire a été effectué lors d'une campagne de forage en compagnie de G. Mohn, E. Skrzypek et T. Mateeva. La plupart des mesures ASM a été réalisée par T. Mateeva, ainsi que quelques-unes par A. Longeau (Université de Cergy-Pontoise).
- Une discussion des mécanismes d'intrusion du magma mafique dans l'unité de Campo, s'appuyant en partie sur un modèle thermique simple de l'intrusion.

Le contenu de ce chapitre fait l'objet d'un article en préparation, « *Ages et mécanismes d'ascension et de mise en place dans la croûte continentale moyenne de magmas mafiques : l'exemple du complexe gabbroïque permien de Sondalo* », qui sera soumis à la revue *Tectonics*.

# **TIMING AND MECHANISMS OF MAFIC MAGMA ASCENT/EMPLACEMENT IN THE CONTINENTAL MIDDLE CRUST: AN EXAMPLE FROM THE PERMIAN SONDALO GABBROIC COMPLEX (EASTERN CENTRAL ALPS, N-ITALY)**

B. Petri<sup>1,2</sup>, G. Mohn<sup>3</sup>, E. Skrzypek<sup>4</sup>, T. Mateeva<sup>5</sup>, F. Galster<sup>6</sup>, Ph. Robion<sup>3</sup>,  
O. Müntener<sup>6</sup>, K. Schulmann<sup>1,7</sup>, G. Manatschal<sup>1</sup>

<sup>1</sup>Ecole et Observatoire des Sciences de la Terre, Institut de Physique du Globe de Strasbourg – CNRS UMR7516,  
Université de Strasbourg, 1 rue Blessig, F–67084, Strasbourg Cedex, France

<sup>2</sup>Vrije Universiteit, Department of Geology and Geochemistry, de Boelelaan 1085, 1081HV Amsterdam, The Netherlands

<sup>3</sup>Département Géosciences et Environnement, Université de Cergy-Pontoise, 5, mail Gay Lussac, Neuville-sur-Oise, 95031 Cergy-Pontoise Cedex

<sup>4</sup>Department of Geology and Mineralogy, Graduate School of Science, Kyoto University, Kitashirakawa Oiwake-cho, Sakyo-ku, 606–8502 Kyoto, Japan

<sup>5</sup>Department of Earth and Ocean Sciences, University of Liverpool, Liverpool L69 3BX, United Kingdom

<sup>6</sup>Institut of Mineralogy and Geochemistry, University of Lausanne, 1015 Lausanne, Switzerland

<sup>7</sup>Center for Lithospheric Research, Czech Geological Survey, 11821 Praha 1, Czech Republic

## **ABSTRACT**

We explore the mechanisms of mafic magma ascent and emplacement in the continental crust by studying the Permian Sondalo gabbroic complex which is exposed in the Austroalpine Campo unit (Eastern Central Alps, N-Italy). First, we characterize the structure and anisotropy of magnetic susceptibility (AMS) fabric of the concentric gabbroic to dioritic intrusions. Second, we constrain the timing and depth of intrusion by using U–Pb zircon dating on magmatic and metamorphic rock samples, trace element geochemistry in zircon and existing  $P$ – $T$  estimates. Petrological and geochemical observations provide insights on the crystallization sequence in the magmatic rocks, and facilitate the interpretation of the AMS record.

The magmatic and magnetic fabrics of the pluton reflect its original orientation and are essentially vertical (foliations and lineations), indicating a vertical magma transfer through the crust. The intrusion was emplaced in two phases. (1) The concordant orientation between the magmatic foliation and the host-rock xenoliths in the centre of the pluton suggest that the first magma ascent phase occurred through fracture opening parallel to the vertical fabric of the host metasedimentary rocks. Trace element analyses in zircon point to a late-magmatic zircon crystallization and are used to interpret the associated U–Pb results of 289–288 Ma as the age of this initial emplacement stage. (2) The second magma ascent phase is marked by a

rheological change in the host-rock. The temperature increase generated in the contact aureole is responsible for partial melting and decreasing mechanical strength in the metasediments. This resulted in the formation of a vertical foliation in the metamorphic aureole and a weaker but concordant magmatic foliation at the rim of the pluton. This ascent phase occurred at 288–285 Ma and accounts for the contrasted  $P$ – $T$  evolutions of metasedimentary rocks in the contact aureole. Thermal models of the intrusion indicate that the contact aureole was finally thinned by shearing during the second ascent phase.

## 1. INTRODUCTION

The ascent mechanisms of magma through the continental crust remain a long standing controversy. The pathway of intermediate to felsic magmas can be continuously traced through the crust: magma is sourced in a lower-crustal granite-migmatite complex and rises through mid-crustal sheeted conduits (Mahan *et al.*, 2003; Miller & Paterson, 2001) up to upper-crustal batholiths and eventually volcanic structures (e.g. Sawyer *et al.*, 2011). This is explained by the lower density of felsic melt with respect to the surrounding continental crust. By contrast, mafic magmas pond in the lower crust and form underplated complexes as a consequence of density and rheological barriers (Huppert & Sparks, 1988; Rudnick & Fountain, 1995; Voshage *et al.*, 1990). Mafic magmatism has also been documented in upper crustal levels in the form of small scale dyke swarms to massive flood basalts (e.g. Coffin & Eldholm, 1994). However, mafic magma transfer between the lower and upper crustal levels remains less well understood than for felsic melts.

Intra-crustal transfer and emplacement of magma in general could be achieved in several ways (e.g. Brown, 1994). For granitic magmas, three end-members were proposed (e.g. Paterson & Miller, 1998; Petford *et al.*, 2000): (1) *dyking* where magma flows in fractures which opened by elastic cracking of the country rock (e.g. Clemens & Mawer, 1992; Lister & Kerr, 1991), (2) *diapirism* where the *en-masse* displacement of buoyant magma is accommodated through host-rock ductile deformation (e.g. Ramberg, 1981), and (3) *pervasive flow* that can be expressed on a mesoscale by forming magma sheets along the host rock anisotropy (foliation, bedding; Collins & Sawyer, 1996; Weinberg, 1999) or on a microscale by flow through grain boundaries (e.g. Hasalová *et al.*, 2011; Scott & Stevenson, 1986). However, most of these mechanisms are based on the physical properties of felsic melts. Therefore, the transfer and emplacement of mafic magmas in the middle crust is less understood.

Indeed, the pervasive flow mechanisms imply that the host-rock temperature is close to, or lies above the solidus temperature of the rising melt. For mafic magma, this mechanism can be achieved in high temperature settings ( $> 1000^{\circ}\text{C}$ ) such as (1) in the mantle (e.g. McKenzie,

1984; Müntener & Piccardo, 2003) or (2) in an already built crystal mush column/channel (e.g. Jagoutz *et al.*, 2006; Solano *et al.*, 2014). Therefore, this mechanism is unlikely to occur for mafic magma propagation through non-intruded crustal rocks. Whether the diapiric rise of granitic magma is a viable mechanism is still a matter of debate (see e.g. Brown, 2007), mafic diapirs may not exist in the continental crust as they will be drained by dykes at early stages of their formation (Weinberg, 1996). Finally, fracture-controlled ascent will produce either dykes or sills depending on the structural relation with the country-rock anisotropy, but will need fast ascent in order to avoid freezing of the magma (Annen & Sparks, 2002; Menand, 2011; Petford *et al.*, 1993). In any case, several ascent mechanisms may be competing and the dominant mechanism may change through space and time (e.g. Weinberg, 1996). Since the different ascent mechanisms are also controlled to some degree by host-rock composition and structure, constraining the structural and metamorphic evolution of both the country-rock and intrusive rocks will help to identify the dominant process (Paterson *et al.*, 1991).

In the Alps, the Variscan continental crust was intruded by numerous mafic and granitic plutons during Early-Permian post-orogenic extension (see Fig. IV-1a and Spalla *et al.*, 2014 for references) and was exhumed during the subsequent Jurassic rifting and Alpine convergence (Galli *et al.*, 2013; Mohn *et al.*, 2012; Müntener *et al.*, 2000). However, only the lower-crustal Ivrea body was studied in terms of emplacement dynamics/mechanisms and was used to propose two models. On the one hand, the “gabbro glacier” model of Quick *et al.* (1992; 1994) was inspired by magmatic processes active at mid-ocean ridges and is characterized by the permanently replenished magmatic lens at the top of the gabbro. In this model, the mafic body grows by cumulate formation and syn-magmatic extension at the base of the lens. On the other hand, Rutter *et al.* (1993) developed an emplacement model that is based on successive sub-horizontal sills along the country-rock foliation. In this model, the magmatic body inflates due to locking at the tips of the sill during continuous injection of mafic magma from the mantle.

The Austroalpine Campo unit represents a part of the middle crust during Permian times, and was intruded by the mafic Sondalo gabbro at a depth between 12 and 20 km. The weak Alpine deformation and metamorphic overprint offers an opportunity to document the structure and emplacement dynamics of a mid-crustal pluton. The metamorphic and structural evolution of the country-rock of the Sondalo gabbro was described in an earlier work (*chapter III*), but the structural evolution and the precise intrusion age of the Sondalo gabbro itself remains to be depicted.

In this contribution, we (1) document the intrusion structure of a mafic pluton at mid-crustal depth, (2) discuss the ascent mechanism(s) through the continental crust considering the role and behavior of the country-rock during magmatism. Eventually, these results may provide

critical insights for the understanding of the magmatic system associated with Permian post-orogenic extension in the Alps. The structure of the pluton and the host rock will be investigated by combining field mapping with the study of Anisotropy of Magnetic Susceptibility (AMS) in magmatic rocks, in particular for rocks where the magmatic fabric is poorly visible. The timing of intrusion will be constrained by U–Pb dating on zircon from magmatic and metamorphic rocks and trace element geochemistry in zircon, bringing also insights on the conditions of its crystallization and the sequence of crystallization of minerals in the rocks.

## **2. GEOLOGICAL SETTING**

The study area is located in the Austroalpine domain, SE-Switzerland and N-Italy (Fig. IV-1ab), which preserves a polyphase tectonic history spanning the Carboniferous Variscan orogeny, the Permian post-orogenic extension, the Jurassic rifting and eventually the Alpine convergence. Due to Jurassic rifting and subsequent Alpine convergence, the Austroalpine domain exposes a complete, but presently disrupted, pre-rift lithospheric section (Fig. IV-1b, Mohn *et al.*, 2010).

The Campo unit preserves a portion of middle crust intruded by numerous Permian intrusions. The unit is separated from the overlying Grosina orthogneiss unit by a sub-horizontal shear zone inferred to be Jurassic in age and only weakly reactivated during Alpine compression (Eita shear zone, Fig. IV-2a, Meier, 2003; Mohn *et al.*, 2012). To the north, the Campo unit is overthrust by the Filladi di Bormio phyllites, whereas to the south it is cut by the Insubric line (Fig. IV-1b).

The Campo unit is made of Variscan Ordovician sediments (Bergomi & Boriani, 2012) affected by amphibolite-facies metamorphism (Bianchi Potenza *et al.*, 1978a; Meier, 2003; Notarpietro & Gorla, 1981; Pace, 1966). This unit was intruded during the Permian by numerous dioritic to granodioritic plutons and notably by a gabbroic intrusion, the Sondalo gabbro (Bockemühl & Pfister, 1985; Boriani *et al.*, 1982; Del Moro & Notarpietro, 1987; Del Moro *et al.*, 1981; Guglielmin & Notarpietro, 1997; Mair & Schuster, 2003; Notarpietro & De Capitani, 1985a; Notarpietro & De Capitani, 1985b; Tribuzio *et al.*, 1999).

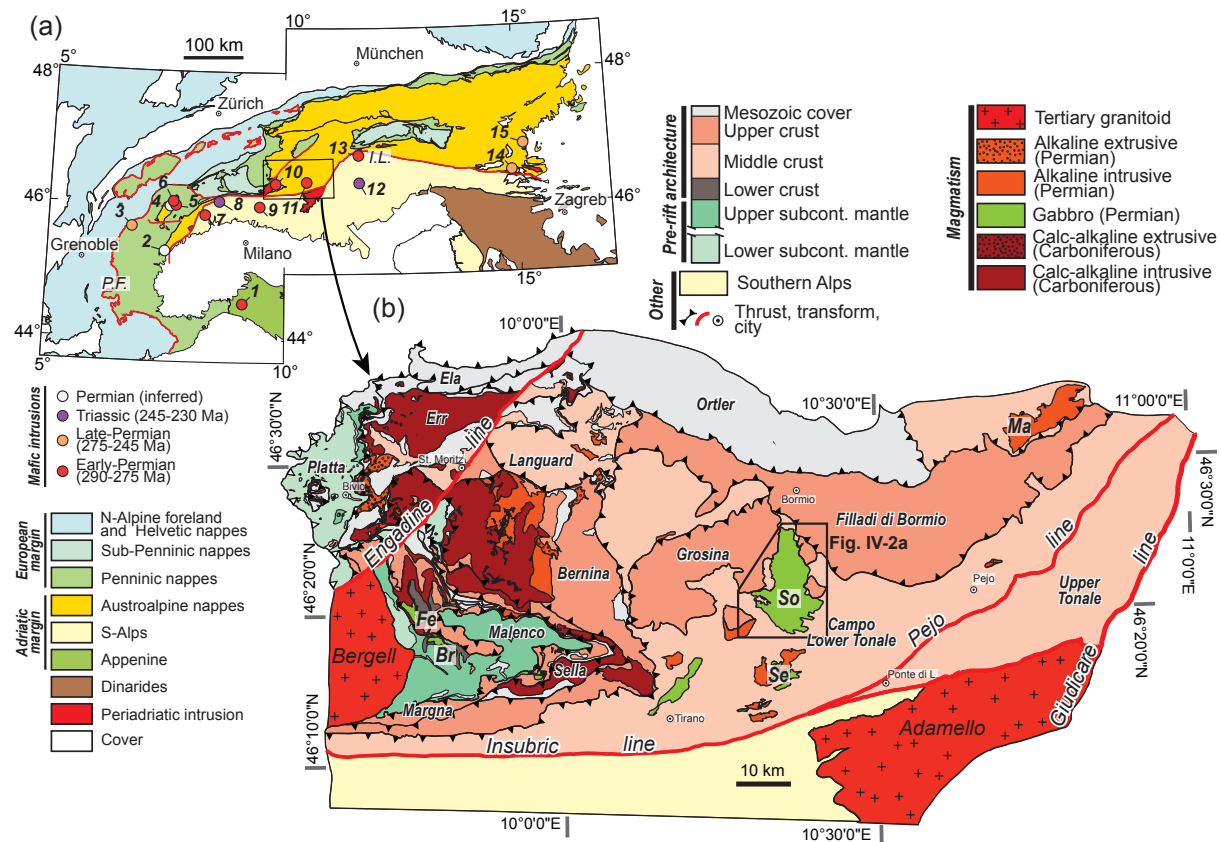


**Fig. IV-1:** (a) Tectonic map of the Alpine realm, modified after Schmid et al. (2004) and location of Permian and Triassic mafic intrusives after Spalla et al. (2014): 1-Monte Ragola (Meli et al., 1996); 2-Corio/Monastero (Rebay & Spalla, 2001); 3-Versoyen unit (Beltrando et al., 2007); 4-Sassa (Baletti et al., 2012); 5-Sermenza (Bussy et al., 1998); 6-Mont Collon (Monjoie et al., 2007); 7-Ivrea main gabbro (e.g. Pin, 1986); 8-Finero (Zanetti et al., 2013); 9-Val Biandino (Pohl et al., 2014; Thöni et al., 1992); 10-Fedoz/Braccia (Hansmann et al., 2001); 11-Sondalo (Tribuzio et al., 1999); 12-Monzoni-Predazzo (Borsi et al., 1968; see references in Mundil et al., 2010); 13-Bressanone/Brixen (Del Moro & Visonà, 1982); 14-Eisenkappel (Miller et al., 2011); 15-Bärofen/Gressenberg (Miller & Thöni, 1997; Thöni & Jagoutz, 1992).. I.L.: the Insubric Line, P.F.: Penninic Front. (b) Litho-tectonic map of the Austroalpine domain in SE-Switzerland and N-Italy representing the different pre-rift crustal domains. The map is a compilation of Del Moro & Notarpietro (1987), Del Moro et al. (1999), Goso et al. (2004), Mohn et al. (2011), Staub (1946), the 1:25,000 geological maps of Switzerland, the 1:10,000 and 1:25,000 geological maps of Italy and personal observations. Black rectangle in (b) reports location of the map in following figures. Main Permian intrusives are reported and correspond to Fe, Fedoz gabbro; Br; Braccia gabbro; So, Sondalo gabbro; Se, Serottini intrusives; and Ma, Martell granite.

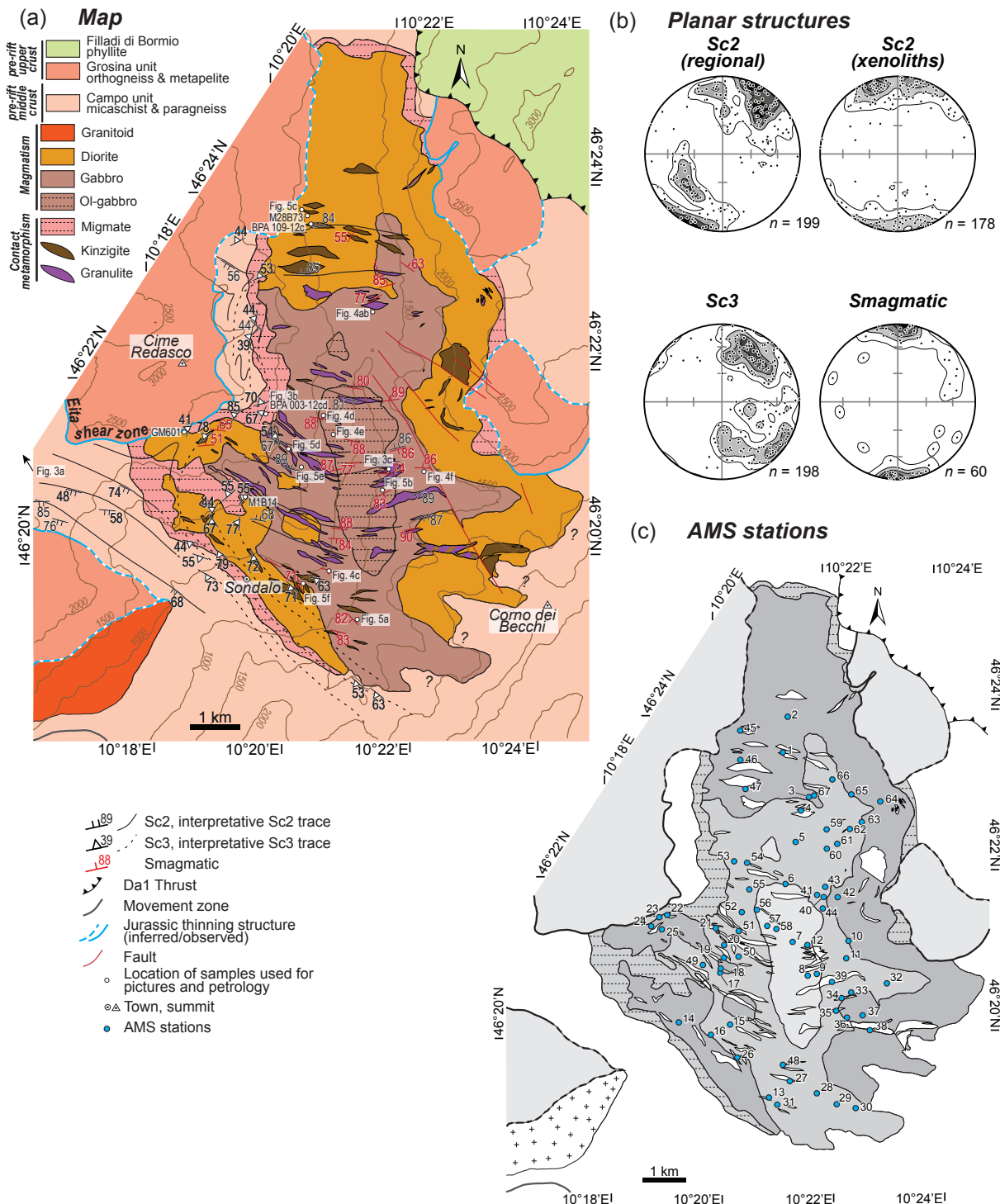


**Fig. IV-2:** (a) Geological and structural map of the Sondalo gabbro and the host-rock Campo unit. Location of field photographs (Fig. IV-3 and IV-4), microphotographs (Fig. IV-5) and samples used for geochronology is indicated. Contour lines are plotted each 500 m. (b) Stereonet plot (equal area, lower hemisphere projection) of Sc2 and Sc3 foliations poles (metasediments) and magmatic foliation. (c) Location of stations used for the AMS study.

### 3. PETROLOGY AND STRUCTURE OF THE CAMPO UNIT

The metasedimentary Campo unit represents the host-rock of the Sondalo gabbro. Its structural succession involves four structures, described in details in the *chapter III*. The first visible fabric is a NE-SW trending steep foliation Sc1 (not visible on Fig. IV-2a). Sc1 is affected by open to isoclinal Fc2 folds with steeply plunging and steep NW-SE trending axial planes, leading in most places to almost complete transposition of the Sc1 fabric into a NW-SE trending Sc2 planar fabric (Fig. IV-2ab). This Sc2 foliation is crosscut by weakly deformed to undeformed Permian pegmatites (Fig. IV-3a), and is often preserved in metapelitic septa within the Sondalo gabbro (Fig. IV-2a & IV-3c). The Sc2 planar-fabric is transposed into a Sc3 foliation parallel to the margin of the pluton and moderately dipping away from the pluton by Dc3 deformation (Fig. IV-2a & IV-3b).

The metasediments of the Campo unit consist essentially of Grt-St micaschists and paragneiss indicating a prograde path in the amphibolite facies reaching 6 kbar/600°C during the formation of Sc1. This foliation is pervasively reworked by a NE trending sub-vertical Sc2 fabric made of Ms-Bt-Sil metasediments around 6 kbar/650°C (Figs IV-2ab & IV-3a). This Sc2 fabric represents the main structure observed in the Campo unit. This fabric is also found in metapelitic xenoliths (slices up to few hundred meters in length) in the core of the Sondalo gabbro (Fig. IV-3c).

In the narrow (500–700 m thick) contact aureole a steeply to moderately dipping Sc3 fabric is developed all around the pluton (Figs IV-2ab & IV-3b). From host-rock to the core of the intrusion, increasing metamorphism lead to the transformation of micaschists into Grt-Sil-Crd-Spl granulites, equilibrated at 5.5 kbar/930°C (Fig. IV-18c). In the contact aureole, the Sc3 foliation is associated with the formation of migmatites with Grt-Sil-Bt melanosomes showing contrasted  $P-T$  paths during Dc3 (*chapter III*). Migmatites are either (1) exhumed from 6 kbar/750°C to  $P < 4.5$  kbar, (2) buried from ~4 kbar/500°C up to 5.2 kbar/800°C and exhumed to  $P < 4.5$  kbar (Fig. IV-18cd). Both remain finally at  $P < 4.5$  kbar (Fig. IV-18cd) before being exhumed close to the surface during Jurassic rifting. The presence of pre-Sc3 andalusite and leucosome affected by Fc3 folds indicates that the contact metamorphism and associated partial melting of the metasedimentary host-rock occurred already before the development of Sc3.

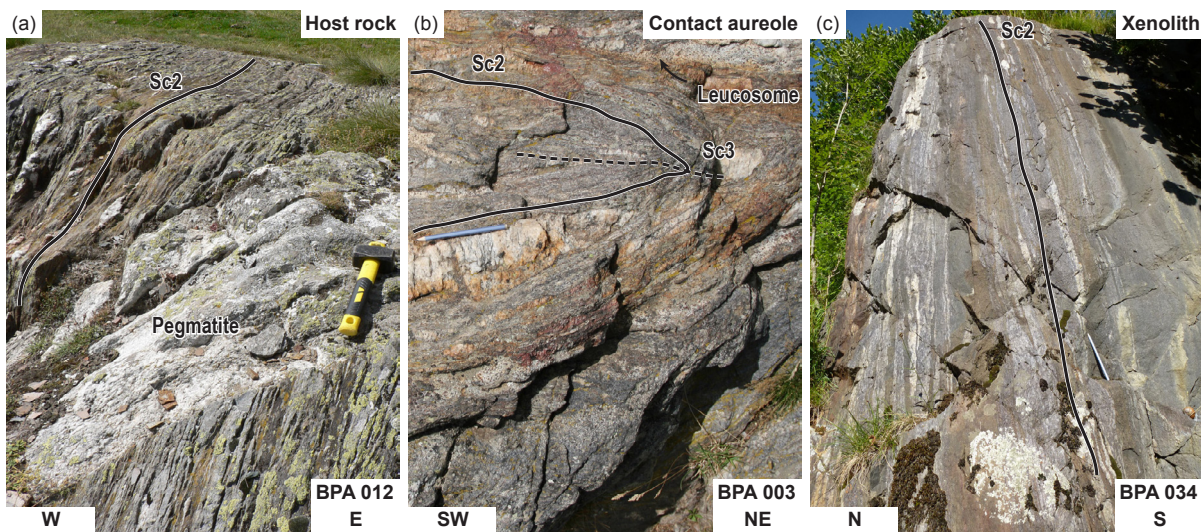


**Fig. IV-3:** Field photographs of metasediments. (a) Steeply dipping foliation of host-rock micaschists far from the Sondalo gabbro (direction indicated on Fig. IV-2a). (b) Moderately inclined Fc3 fold located in the migmatitic contact aureole of the pluton. (c) Granulite-facies metasedimentary xenolith in the core of the gabbro preserving the Sc2 fabric. Location of photographs is indicated on Fig. IV-2.

## 4. PETROGRAPHY AND MAGMATIC STRUCTURES OF THE SONDALO GABBRO

### 4.1 The Sondalo gabbro

The Sondalo gabbro is a ~40 km<sup>2</sup> pluton exposed in the N-S oriented Adda Valley (Fig. IV-2a). The pluton is concentrically zoned and composed of Ol-gabbros in the Central Zone (hereafter referred to as CZ), gabbros in Intermediate Zone (IZ) and a diorites to granodiorites in a Border Zone (BZ) of a variable width (Campiglio & Potenza, 1964; Campiglio & Potenza, 1966; Campiglio & Potenza, 1967; Koenig, 1964; Potenza, 1973; Rasch, 1911). Contacts between units are rarely visible. All different facies are thought to be derived from a basaltic parental liquid of tholeiitic affinity, differentiated through fractional crystallization and affected by crustal assimilation (Tribuzio *et al.*, 1999).

Sm–Nd mineral-isochrons on troctolite and norite samples gave ages of  $300 \pm 12$  and  $280 \pm 10$  Ma, respectively. Rb–Sr isochron ages for the same samples are respectively  $266 \pm 10$  and  $269 \pm 16$  Ma (Tribuzio *et al.*, 1999). Zircon from a diorite collected in the BZ was dated at 270 Ma (Concordia age, Bachmann & Grauert, 1981). Rare trachytic dykes dated at  $32 \pm 1$  Ma cross-cut the gabbro (K–Ar on ground-mass, Bianchi Potenza *et al.*, 1985).

## 4.2 Petrography

The CZ and IZ of the gabbroic complex consist of Ol–gabbros, troctolites and gabbros to norites (Fig. IV-5ab) mainly composed of euhedral to subhedral plagioclase, olivine and orthopyroxene, with higher amount of olivine in Ol–gabbros. Plagioclase is labradoritic and often zoned with higher anorthite content in the core. Olivine is often replaced by pseudomorphs of talc and magnetite. Clinopyroxene is poikilitic, sometimes rimmed by red-brown Ti–pargasite that may also be poikilitic. Both pyroxene and pargasite are sometimes transformed into brown-green hornblende (uralite facies of Rasch, 1911). Biotite is rare interstitial mineral in (olivine-) gabbro and norite. In the gabbro, ilmenite is the main opaque phase with minor poikilitic Fe-sulfides (pyrrhotite) and magnetite. Ilmenite and magnetite are sometimes intergrown and usually interstitial to plagioclase (Fig. IV-5e). Numerous magnetite and ilmenite lamellae are frequently exsolved from pyroxene (with up to 1 wt% of TiO<sub>2</sub>; Tribuzio *et al.*, 1999) crystals along their cleavage planes (Fig. IV-5f). Rutile is also found as inclusion in pyroxene, but not exsolved from it (Fig. IV-5f).

In the BZ, diorites and granodiorites have a hypidiomorphic structure with euhedral to subhedral plagioclase and green-brown hornblende (Fig. IV-5c). Zoned plagioclase has a labradorite core and an andesine rim. Hornblende may contain inclusions of clino- and orthopyroxene. Interstitial quartz is frequent. Opaque minerals are mostly ilmenite and rare pyrrhotite and magnetite, in the same textural position than in gabbro and Ol–gabbro.

## 4.3 Magmatic fabric

Ol–gabbro, gabbro and diorite are generally medium-grained showing a weakly to strongly developed fabric defined by the shape-preferred orientation of euhedral to subhedral and elongated plagioclase, pyroxene and amphibole (Figs IV-4cde & IV-5ac). This foliation is usually steeply dipping to the north or to the south (Fig. IV-2ab). Locally, fine-grained gabbro rhythmically alternates with coarse-grained gabbro (Fig. IV-4ab). Rare pyroxenite compacted layers are elongated parallel to the sub-vertical foliation (Fig. IV-4c). Under the microscope, pyroxenes are aligned parallel to the compacted layers elongation (Fig. IV-5a), locally included in poikilitic plagioclase, indicating mineral sorting during magma flow (Tobisch *et al.*, 1997). The absence of solid-state deformation (dynamic recrystallization) indicates that the mineral foliation is magmatic (for criteria, see e.g. Paterson *et al.*, 1989; Vernon, 2000). Exceptionally, close to the Eita shear zone, magmatic foliations are affected by deformation in greenschist facies.



**Fig. IV-4:** Field photographs of mafic rocks. Sheeted dykes with (a) sub-vertical rhythmic grain-size layering in the center of the pluton and (b) close-up view of the structure, location indicated in (a). (c) In-situ sub-vertical layering and foliation produced by compaction and felsic liquid extraction. (d) Strong foliation defined by shape-preferred orientation of plagioclase and amphibole. (e) Patchy pegmatites due to late-stage accumulation of interstitial liquid. Note the modal lamination of the fine-grained and foliated gabbro. (f) Foliated diorite intruded by a pegmatitic dyke with a sharp contact. Location of photographs is indicated on Fig. IV-2.

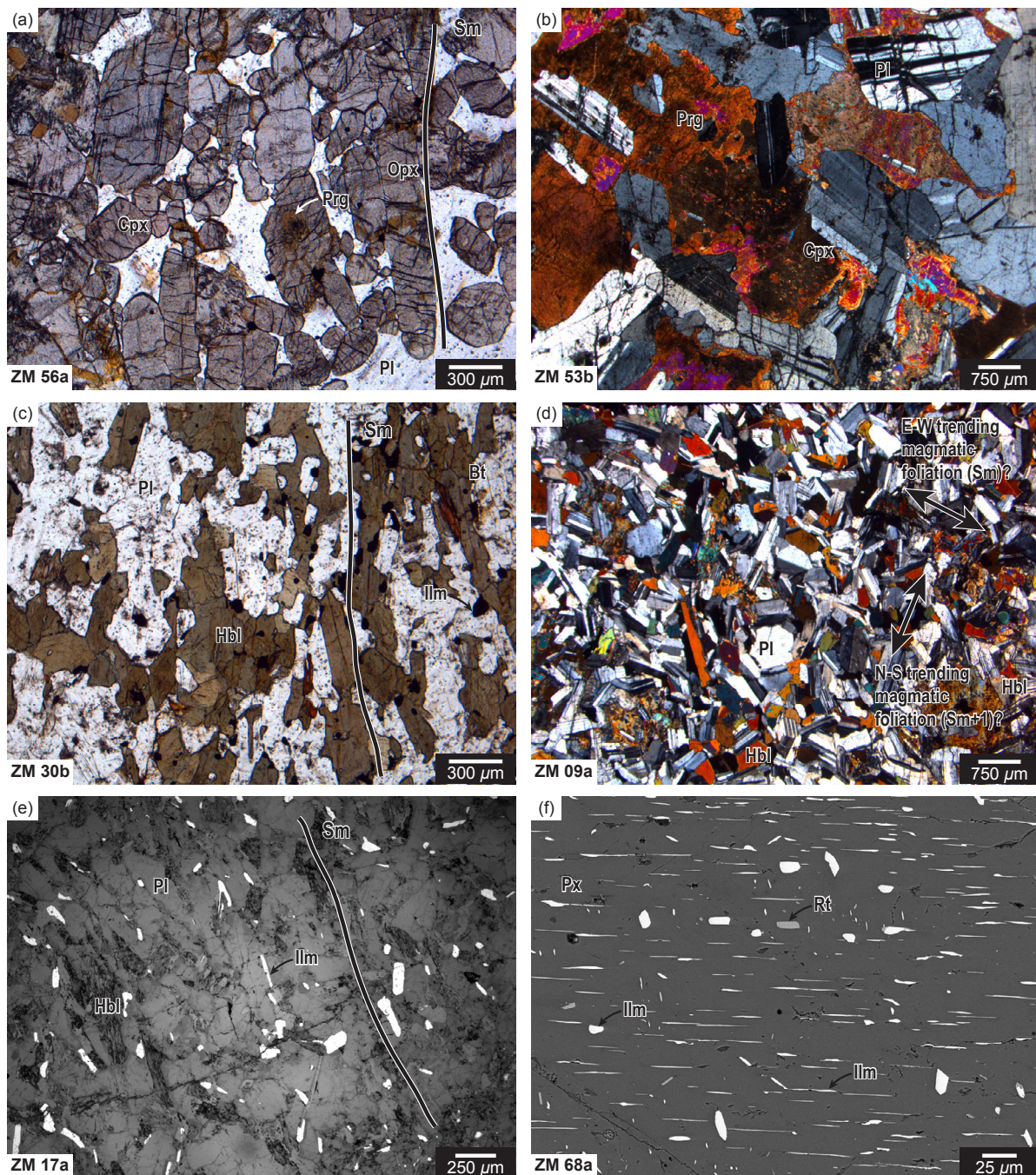


**Fig. IV-5:** Photomicrographs of magmatic rocks (a–d: transmitted light; e: reflected light; f: back-scattered electron (BSE) image). (a) Oriented Opx–Cpx grains in a mafic cumulate, surrounded by a poikilitic plagioclase monograins. (b) Pegmatitic gabbro with weakly oriented plagioclase and poikilitic Cpx. (c) Diorite with a strong shape-preferred orientation of subhedral plagioclase and hornblende. (d) Diorite showing superposition of two magmatic fabrics. (e) Ilmenite along oriented plagioclase crystals. (f) Lamellar exsolution of ilmenite along the cleavages of the pyroxene. Location of samples is indicated on Fig. IV-2.

Locally in the BZ, a different foliation is visible and lies at high angle with respect to the principal magmatic fabric of the gabbro, especially at the western margin of the pluton (Fig. IV-2a). This fabric is roughly parallel to the pluton margins and to the Sc3 foliation in the contact aureole. On the outcrop scale, no evidence of magmatic fabric transposition can be detected as rocks in this area are apparently isotropic. Moreover, no folds of magmatic foliation or cumulates are visible. Under the microscope, the magmatic foliation is poorly developed, with plagioclase and ferromagnesian minerals forming a “mesh” structure (Fig. IV-5d).

Late-stage magma accumulation formed patchy pockets with no apparent foliation, cross cutting the magmatic foliation (Fig. IV-4e). Syn-magmatic mafic dykes cross cut the weakly to well foliated gabbro, sometimes with a sharp contact (Fig. IV-4f). Both usually display pegmatitic textures with up to 5 cm long plagioclase and hornblende crystals. Subhedral plagioclase defines a very weak shape-preferred orientation, whereas hornblende is poikilitic and locally includes clinopyroxene. Occasionally in the BZ, magma mingling between a leucocratic and a more mafic magma is indicated by pillow structures with chilled margins.

## 5. GEOCHRONOLOGY

In order to constrain the emplacement age of the Sondalo gabbro and of the timing of the associated contact metamorphism, we performed U–Pb isotopic dating of zircon on six samples. Three igneous rocks (M28B73, GM601 and M1B14) were collected across the pluton (location indicated on Fig. IV-2a). In addition, three migmatitic metasediments were selected in the contact aureole; one migmatite (BPA 003-12c) and one leucosomes from the contact aureole (BPA 003-12d) and one leucosome from a xenolith close to the margin of the pluton (BPA 109-12c, location indicated on Fig. IV-2a).

U–Pb isotopic measurements and trace element analysis on zircon were performed at the Institute of Mineralogy and Geochemistry of the University of Lausanne using a LA–ICP mass spectrometer. Spot location was guided by transmitted and reflected light observation as well as back-scattered electrons (BSE) and cathodoluminescence (CL) images (Fig IV-7 and IV-8). Detailed isotopic ratios and ages are reported in Table IV-1 and Table IV-2. Results were plotted in conventional and inverse Concordia diagrams (Fig IV-7 and IV-8) using Isoplot/Ex 3.75 (Ludwig, 2012) with a  $2\sigma$  level of confidence ellipses. For igneous rocks and leucosomes, discordant and outlier ages (radiogenic Pb loss, initial Pb incorporation or inherited cores) were discarded for the Concordia age determination. For the migmatite sample, the Discordia line was anchored to the initial Pb ratio of 0.8534 (following Stacey & Kramers, 1975), outliers ages were discarded for age determination. Detailed analytical conditions are reported in Appendix A.

## 5.1 Samples description

### 5.1.1 Magmatic rocks

*Diorite M28B73* [46.39551°N; 10.34243°E] was collected at ~10 m from a Sil–Bt metapelitic xenolith in the dioritic rim north of the pluton. It contains Bt–Pl–Kfs–Qtz with minor garnet, muscovite and ilmenite. The sample is phaneritic (up to 5 mm in size) and preserves its original magmatic texture with weak solid-state deformation attested by discrete undulose extinction in quartz. Plagioclase (andesine) hosts fine-grained muscovite inclusions and is preferentially oriented along a weakly developed magmatic foliation that in the field is steeply dipping to the north. Interstitial biotite (~1 mm) contains ilmenite and zircon inclusions and is occasionally chloritized. Zircon is also included in quartz. K-feldspar is represented by microcline with some patchy exsolution lamellae of albite. Tiny garnet (<1 mm in size) has rare quartz inclusions and becomes more frequent towards the xenolith.

*Deformed diorite GM601* [46.36016°N; 10.31110°E] is sampled few meters away from the contact with the overlying Grosina unit in the vicinity (~5 m) of the Eita Shear zone, at the south-western margin of the pluton. This deformed diorite is cutting through the metapelitic host-rock at high angle with respect to the Sc3 foliation of the migmatitic aureole. The magmatic structure is pervasively overprinted by a mylonitic foliation. The sample contains Ms–Bt–Pl–Kfs–Qtz. Porphyroclastic plagioclase and K-feldspar phenocrysts (up to 2.5 mm in size) are dismembered by numerous brittle cracks. Small porphyroclastic muscovites (~0.5 mm) recrystallize into fine-grained muscovite, whereas biotite occurs only as fine-grained aggregates. Quartz is totally recrystallized into fine grains (few µm) by the bulging recrystallization mechanism bracketing the deformation temperature to between 300 and 400°C (Stipp *et al.*, 2002) at greenschist facies conditions. The quartz aggregates contains occasionally zircon grains.

*Leucocratic diorite MIB14* [46.34483°N; 10.32495°E] was sampled close to a large roof pendant in the pluton, in contact with very-fine grained gabbro pillows with chilled margins. This sample still preserves its magmatic texture with no sub-solidus deformation but without presenting clear magmatic foliation. It is essentially made of subhedral plagioclase (few mm in length) and K-feldspar, with common fine-grained interstitial hornblende, biotite rarely chloritized and quartz with rare zircon inclusions. Small garnet (up to 100 µm in diameter) contains inclusions of plagioclase and ilmenite whereas ilmenite in the matrix is usually associated to hornblende.

### 5.1.2 Migmatitic metasediments

*Leucosome BPA 003-12d* [46.35977°N; 10.33070°E] comes from a metatexite collected in the western part of the metamorphic contact aureole of the pluton. The rock contains Bt–Grt–Pl–Kfs–Qtz with minor muscovite, sillimanite and ilmenite. The weak shape-preferred orientation of euhedral plagioclase causes a preferential orientation of interstitial biotite, all aligned along Sc3, without presenting any sub-solidus recrystallization. Euhedral to subhedral biotite contains zircon. Atoll to euhedral garnet (up to 3 mm in diameter) is frequent and includes tiny biotite, plagioclase, quartz and ilmenite. Muscovite and partially chloritized biotite form nests with polygonal borders, probably after cordierite. Ilmenite from the matrix contains rare rutile inclusions. This sample comes from the same outcrop than kinzigite BPA 003-11a studied in *chapter III*.

*Leucosome BPA 109-12c* [46.39400°N; 10.34333°E] is extracted from a migmatite forming a xenolith in the pluton. K-feldspar phenocrysts (up to 1 cm in length) lie in finer-grained matrix made of plagioclase, quartz and biotite, the latter two containing few zircon inclusions. K-feldspar, plagioclase and biotite present a weak preferred orientation parallel to the Sc2 foliation of the melanosome that is steeply dipping to the north. Tiny muscovite (<1 mm) is rare, whereas garnet is totally absent from the sample. In contact with the melanosome, such leucosomes are richer in biotite and quartz, as well as in garnet and cordierite.

*Migmatite BPA 003-12c* [46.35977°N; 10.33070°E] is a metasedimentary metatexite. It presents alternation of leucosome and melanosome layers parallel to the moderately NW-dipping Sc3 foliation. The neosome is made of Ms–Grt–Crd–Kfs–Qtz±Bt±Sil±IIm whereas the melanosome bears Grt–Sil–Crd–Bt–Kfs–Qtz±Spl±Pl. Red-brown biotite from the melanosome contains numerous zircon inclusions. Ilmenite is the only opaque phase in the rock. Zircon is included in biotite in the melanosome, and occasionally in quartz in the neosome. This sample comes from the same outcrop than kinzigite BPA 003-11a studied in *chapter III*.

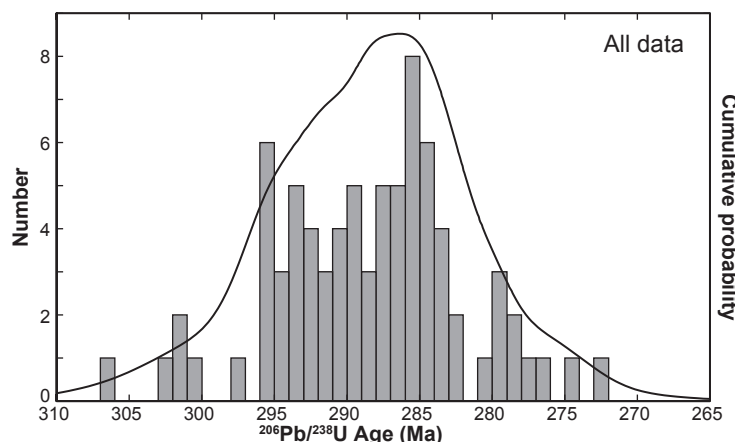


**Fig. IV-6:** Histogram and cumulative probability plots of single-spot  $^{206}\text{Pb}/^{238}\text{U}$  ages on zircon from diorites and migmatites.

## 5.2 Zircon morphology and internal structure

Zircons from magmatic rocks (samples M28B73, GM 601 and M1B14, Fig. IV-8bcd) are up to 300 µm in length and 100 µm in width. They present elongated shapes, are prismatic, euhedral to sub-euhedral, with slightly rounded outlines. Rare zircon from sample M1B14 shows irregular outlines pointing to late-magmatic chemical corrosion without or with low recrystallization/overgrowth. CL images reveal frequently oscillatory zoned internal structure with rarely homogenous cores. Zoning is sometimes disrupted and overgrown by a zoned rim. Rare sub-solidus recrystallization due to late to post magmatic processes are attested by heterogeneous patchy patterns (brecciated) or by thin homogenous and bright rim (up to 10 µm in thickness) or crack.

Zircon extracted from migmatitic metasediments (samples BPA 003-12d, BPA 003-12c and BPA 109-12c, Fig. IV-8bce) are up to 300 µm in length and 100 µm in width, a little smaller for the migmatite BPA 003-12c. They are usually elongated and prismatic, with slightly rounded outlines. Cores present a well-developed oscillatory zoning sometimes disrupted by a bright and homogeneous rim (> 10 µm in thickness) penetrating occasionally deeply into the grain (up to 20 µm from the rim for sample BPA 003-12c). Xenocrystic cores were observed only in sample BPA 109-12c, and are overgrown by a patchy and dark rim (up to 150 µm).

## 5.3 U–Pb results

*Diorite M28B73* (Fig. IV-7a): twenty-nine analyses were carried out on twenty-six zircon grains. Most of the analyses are concordant to sub-concordant, the main population ranging between 284 and 302 Ma, with a maximum at *ca.* 292 Ma. A rather homogeneous age population defines a Concordia age of  $289 \pm 4$  Ma (MSWD = 0.22) constrained by thirteen spot analyses. Sub-concordant analyses are slightly marginal with respect to the main population, probably due to younger lead loss. Between core and rim analyses, no significant age difference could be observed.

*Deformed diorite GM601* (Fig. IV-7b): thirty spot analyses were performed on twenty-five zircons. Analyses of zircon cores point to slightly older ages than rim analyses. The main age population spans between 282 and 298 Ma, with a maximum probability at *ca.* 287 Ma. A homogeneous population of thirteen analyses defines an age of  $285 \pm 2$  Ma (MSWD = 0.33) on a conventional Concordia diagram. The older age population visible on the histogram is mainly composed of discordant ages, probably due to a younger lead-loss event.

*Leucocratic diorite M1B14* (Fig. IV-7c): nine analyses were performed on eight grains.  $^{206}\text{Pb}/^{238}\text{U}$  ages ranges from 283 to 291 Ma, with a peak at *ca.* 284 Ma. After discarding

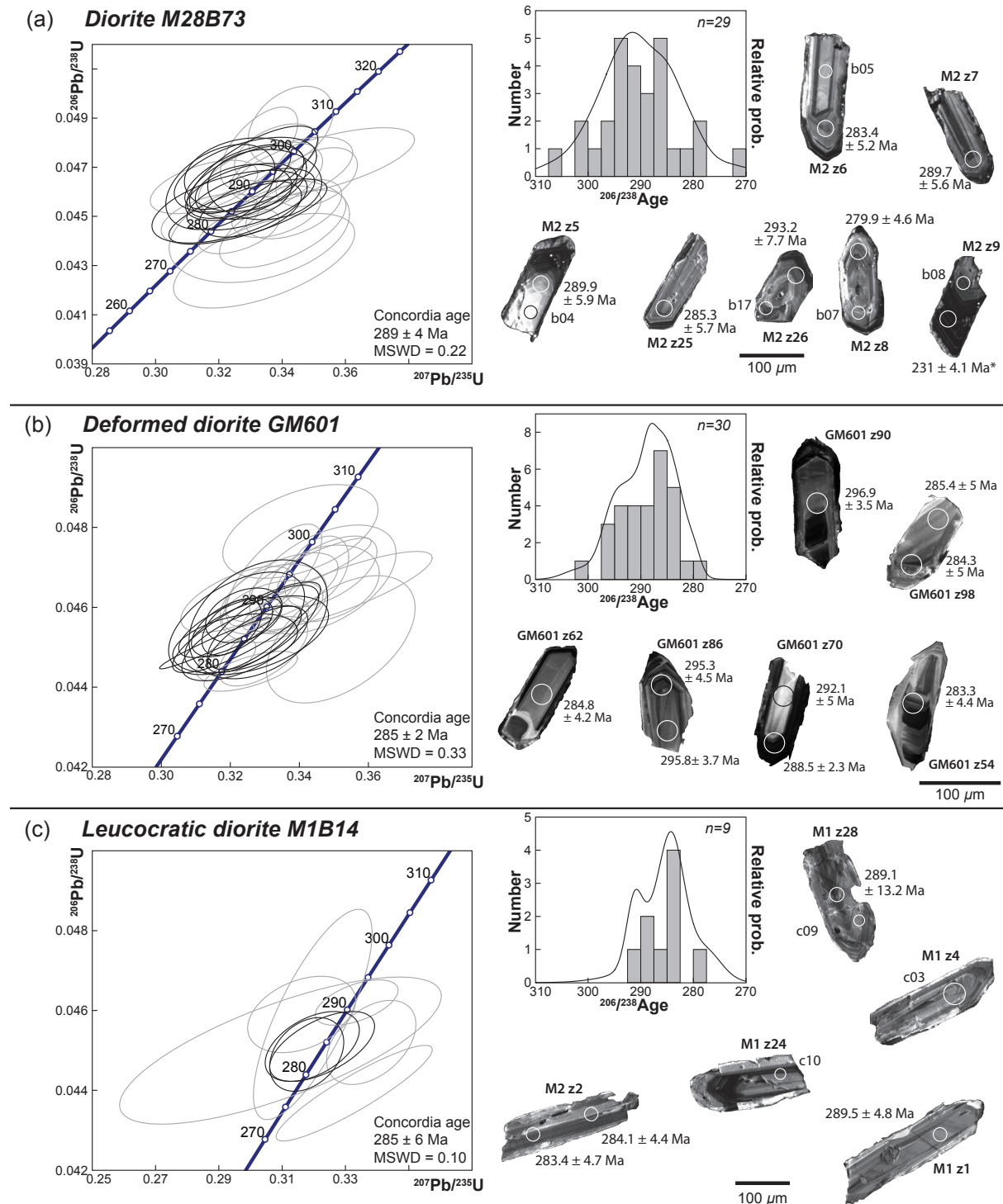


**Fig. IV-7:** Conventional Concordia age diagrams of U-Pb ages on zircon from LA-ICPMS analyses performed on diorites, histograms of single-spot  $^{206}\text{Pb}/^{238}\text{U}$  ages and CL images of zircons for diorites (a) M28B73, (b) GM601 and (c) M1B14. Concordia diagrams were calculated using Isoplot/Ex 3.75 (Ludwig, 2012), grey ellipses were not used for age calculation, ellipses are plotted at 95% level of confidence and age errors are reported at a  $2\sigma$  level. Spot location for U-Pb and trace element analyses are indicated along with  $^{206}\text{Pb}/^{238}\text{U}$  ages. \* indicates discordant ages.

discordant and outlier ages, three concordant analyses yields a Concordia age of  $285 \pm 6$  Ma (MSWD = 0.10).

*Leucosome BPA 003-12d* (Fig. IV-8ab): five spot analyses were carried out on 4 zircon grains. One spot from a zircon core yielded an inherited age of  $854 \pm 5$  Ma. The remaining four spots lies between 282 and 292 Ma showing a poorly constrained peak around 286 Ma. They define a Concordia age of  $288 \pm 5$  Ma (MSWD = 0.037).

*Leucosome BPA 109-12c* (Fig. IV-8ac): six analyses were carried out on four zircons. Four concordant analyses from two different grains define the main age population ranging between 274 and 279 Ma clustered at *ca.* 276 Ma and defines an age of  $277 \pm 3$  Ma (MSWD = 0.20) on a Concordia diagram. Two analyses performed on two different grains are slightly older with a concordant age of  $288 \pm 3$  Ma or present lead loss.

*Migmatite BPA 003-12c* (Fig. IV-8de): out of four spot analyses performed on 3 zircons, only one is strictly concordant at  $288 \pm 3$  Ma. Three spots lies in a mixing line between initial Pb defining a Discordia line with a lower intercept at  $289 \pm 4$  Ma (MSWD = 0.01) on an inverse Concordia diagram.

## 5.4 U, Th, Hf and trace element geochemistry of zircon

U, Th, Hf and trace element composition of zircon was analyzed to constrain the conditions of zircon growth. Raw analytical results and parameters are provided in Table IV-3 for zircon from magmatic rocks and Table IV-4 for zircon from migmatitic metasediments. Parameters are reported in Figs IV-9, IV-10 and IV-11. REE composition diagrams, Eu/Eu\* (Eu-anomaly,  $\text{Eu}_{\text{n}} / ((\text{Sm}_{\text{n}} + \text{Gd}_{\text{n}}) / 2)$ ) and  $\text{Yb}_{\text{n}} / \text{Gd}_{\text{n}}$  (slope of the REE pattern) are normalized by the C1-chondrite composition of Sun & McDonough (1989).

### 5.4.1 Magmatic rocks

Most of magmatic zircons present typically a steep HREE pattern (Fig. IV-9a), with a positive Ce-anomaly, a negative Eu-anomaly, and Th/U ratios  $> 0.01$ , characteristic for magmatic zircons (Murali *et al.*, 1983; Rubatto, 2002; Schaltegger *et al.*, 1999).

Zircons from sample M28B73 present a relatively high Th/U ratio (0.036–0.338). A decrease of the HREE content ( $\text{Yb}_{\text{n}} / \text{Gd}_{\text{n}} \approx 40$  to  $\text{Yb}_{\text{n}} / \text{Gd}_{\text{n}} \approx 0–10$ ) is balanced by a reduction of the Eu-anomaly, with Eu/Eu\* varying from 0.023 up to 0.160, with younger zircon ages having a low  $\text{Yb}_{\text{n}} / \text{Gd}_{\text{n}}$  and a high Eu/Eu\* value (Fig. IV-9a). The slope of the HREE diagram is inversely correlated to the Nb/Ta ratio due to a decreasing Ta content while  $\text{Yb}_{\text{n}} / \text{Gd}_{\text{n}}$  decrease and Nb/Ta increase (Fig. IV-9b). Similarly, Hf and U-contents weakly decreases with lower  $\text{Yb}_{\text{n}} / \text{Gd}_{\text{n}}$  values (Fig. IV-9c).

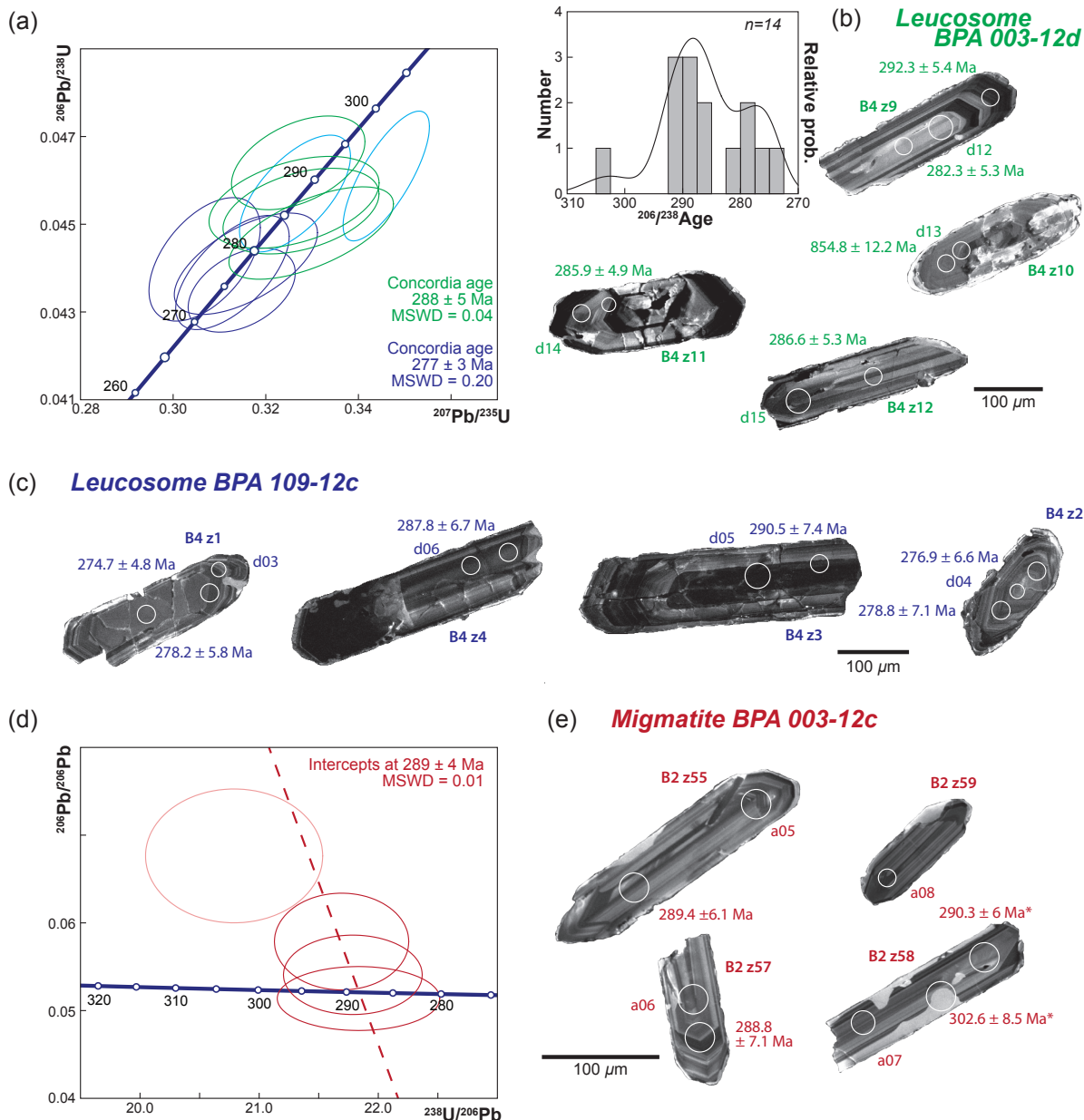


**Fig. IV-8:** (a,d) Conventional and inverse Concordia age diagrams of U-Pb ages on zircon from LA-ICPMS analyses performed on migmatitic metasediments, histograms of single-spot  $^{206}\text{Pb}/^{238}\text{U}$  ages and CL images of zircons for (b) leucosome BPA 003-12d, (c) leucosome BPA 109-12c and (d) migmatite BPA 003-12c. Concordia diagrams were calculated using Isoplot/Ex 3.75 (Ludwig, 2012), light colored ellipses were not used for age calculation, ellipses are plotted at 95% level of confidence and age error are reported at a  $2\sigma$  level. Spot location for U-Pb and trace element analyses are indicated along with  $^{206}\text{Pb}/^{238}\text{U}$  ages. \* indicates discordant ages.

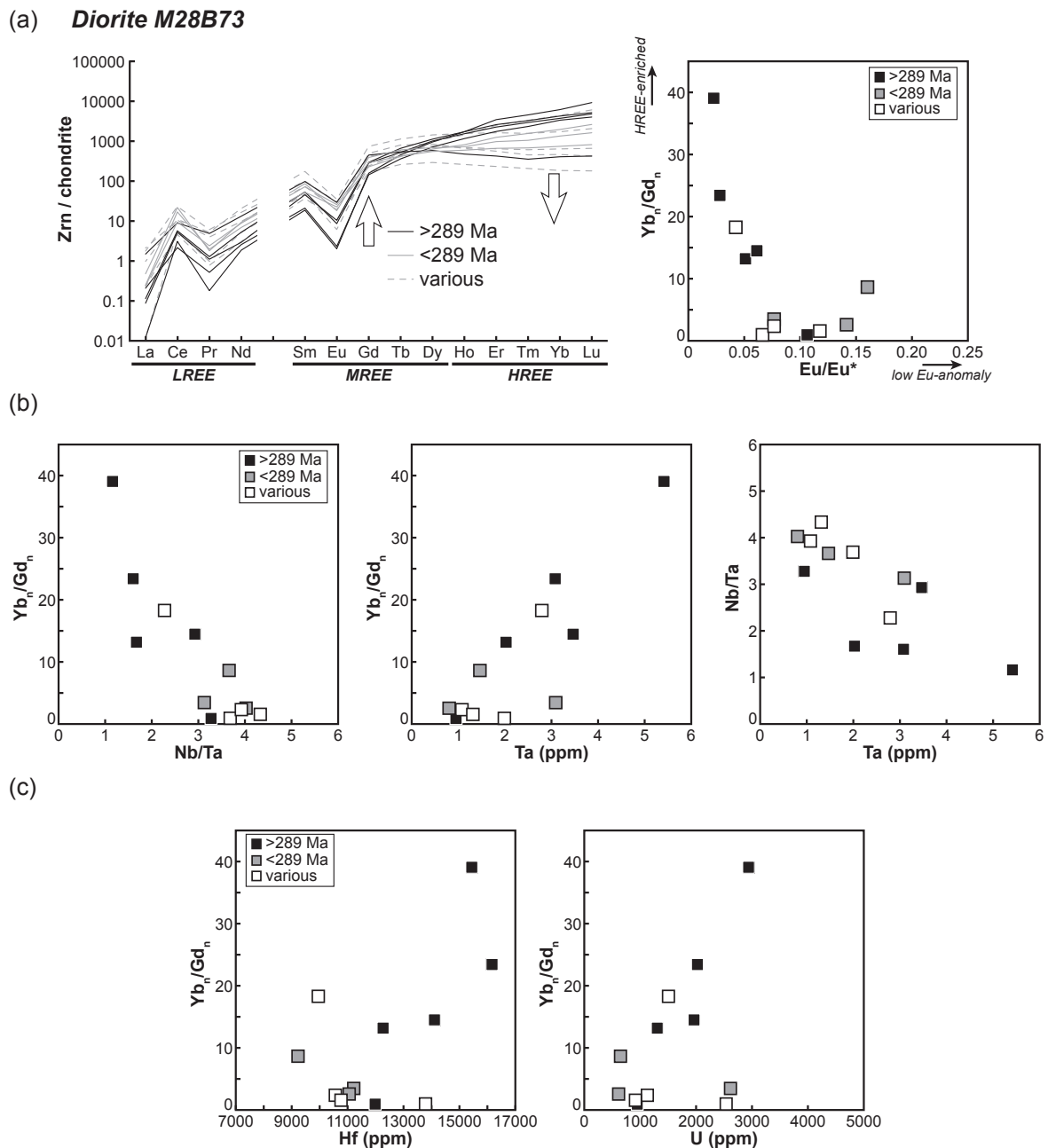


**Fig. IV-9:** REE and trace element composition for diorite M28B73. Spot locations are indicated on Fig. IV-7. REE composition and ratios are normalized to the C1-chondrite composition of Sun & McDonough (1989).

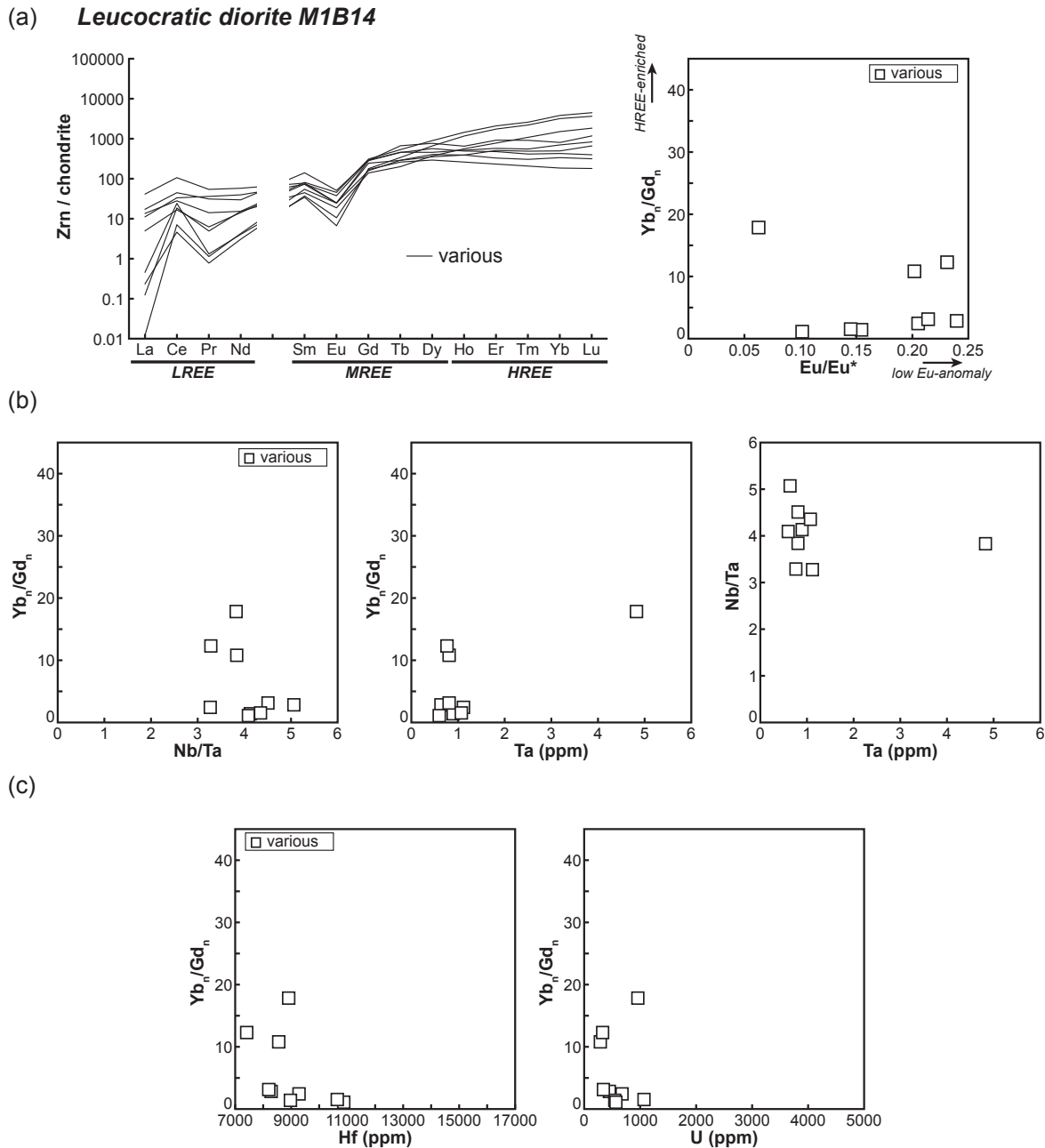
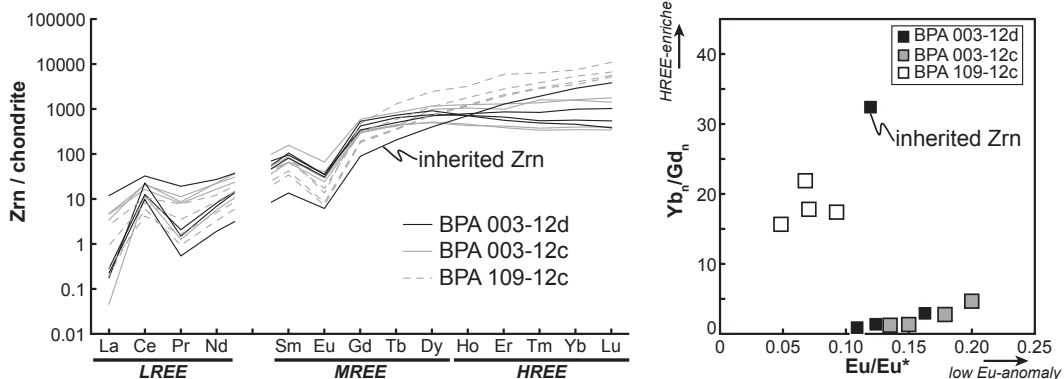
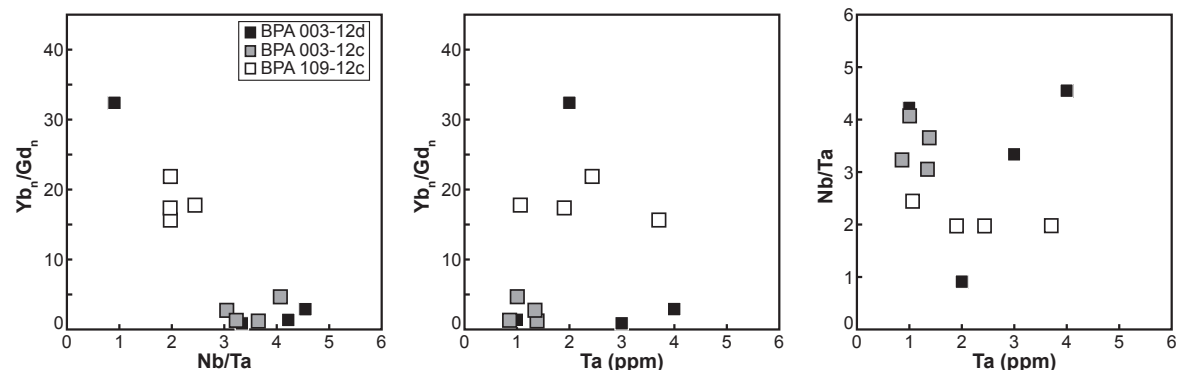


**Fig. IV-10:** REE and trace element composition for diorite M1B14. Spot locations are indicated on Fig. IV-7. REE composition and ratios are normalized to the C1-chondrite composition of Sun & McDonough (1989).

(a) **Leucosomes & migmatites**



(b)



(c)

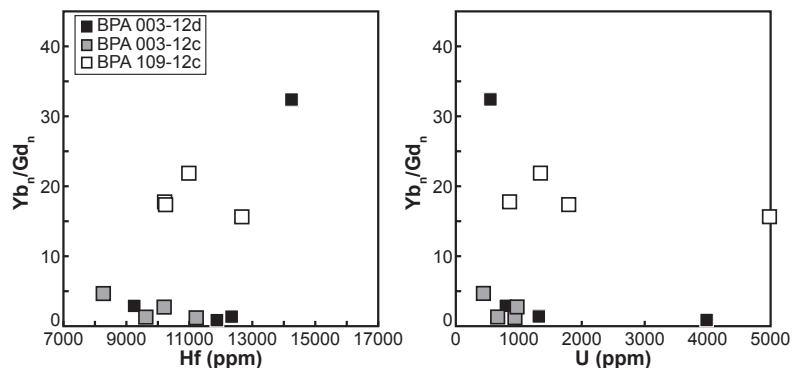


**Fig. IV-11:** REE and trace element composition for metasediments (leucosome and migmatite). Spot locations are indicated on Fig. IV-8. REE composition and ratios are normalized to the C1-chondrite composition of Sun & McDonough (1989).

**Table IV-1:** U-Pb isotopic data for zircon from magmatic samples (diorites) analyzed by LA-ICPMS.  
M28B73 - Diorite [46.39551°N; 10.34243°E]

Mnt.	Zrn	Pos.	Tex.	Radiogenic ratios				Age (Ma)				Conc. (%)	
				$^{207}\text{Pb}/^{235}\text{U}$	$\pm 1\sigma$	$^{206}\text{Pb}/^{238}\text{U}$	$\pm 1\sigma$	$\rho$	$^{206}\text{Pb}/^{238}\text{U}$	$\pm 2\sigma$	$^{207}\text{Pb}/^{235}\text{U}$	$\pm 2\sigma$	
M1	z30	co	os	0.3327	1.5	0.0478	1.41	0.61	301.0	8.3	291.7	7.8	290
<b>M1</b>	<b>z30</b>	<b>ri</b>	<b>ho</b>	<b>0.3345</b>	<b>2.2</b>	<b>0.0463</b>	<b>1.26</b>	<b>0.05</b>	<b>292.0</b>	<b>7.2</b>	<b>293.0</b>	<b>11.0</b>	<b>348</b>
<b>M1</b>	<b>z31</b>	<b>co</b>	<b>os</b>	<b>0.3284</b>	<b>2.8</b>	<b>0.0467</b>	<b>1.33</b>	<b>0.50</b>	<b>294.5</b>	<b>7.7</b>	<b>288.3</b>	<b>14.1</b>	<b>322</b>
M1	z31	co	os	0.3382	1.6	0.0476	1.00	0.44	300.0	5.9	295.8	8.1	304
<b>M1</b>	<b>z32</b>	<b>co</b>	<b>os</b>	<b>0.3205</b>	<b>2.2</b>	<b>0.0462</b>	<b>1.53</b>	<b>0.40</b>	<b>290.8</b>	<b>8.7</b>	<b>282.3</b>	<b>11.1</b>	<b>278</b>
<b>M1</b>	<b>z32</b>	<b>co</b>	<b>os</b>	<b>0.3284</b>	<b>2.3</b>	<b>0.0464</b>	<b>1.30</b>	<b>0.58</b>	<b>292.2</b>	<b>7.4</b>	<b>288.3</b>	<b>11.5</b>	<b>266</b>
<b>M2</b>	<b>z5</b>	<b>co</b>	<b>os</b>	<b>0.3271</b>	<b>2.2</b>	<b>0.0460</b>	<b>1.03</b>	<b>0.52</b>	<b>289.9</b>	<b>5.9</b>	<b>287.3</b>	<b>10.8</b>	<b>260</b>
M2	z6	ri	os	0.3173	2.0	0.0449	0.93	0.45	283.4	5.2	279.8	9.6	258
<b>M2</b>	<b>z7</b>	<b>ri</b>	<b>os</b>	<b>0.3278</b>	<b>1.9</b>	<b>0.0460</b>	<b>0.99</b>	<b>0.24</b>	<b>289.7</b>	<b>5.6</b>	<b>287.9</b>	<b>9.6</b>	<b>252</b>
M2	z8	ri	os	0.3263	1.6	0.0444	0.84	0.51	279.9	4.6	286.7	8.2	310
M2	z9	ri	os	0.3235	1.1	0.0365	0.91	0.52	231.0	4.1	284.6	5.2	298
<b>M2</b>	<b>z11</b>	<b>co</b>	<b>ho</b>	<b>0.3234</b>	<b>3.1</b>	<b>0.0454</b>	<b>1.33</b>	<b>0.53</b>	<b>286.0</b>	<b>7.4</b>	<b>284.5</b>	<b>15.6</b>	<b>304</b>
M2	z13	co	os	0.3153	2.2	0.0462	0.96	0.52	291.0	5.5	278.3	10.7	238
M2	z16	co	os	0.3430	2.3	0.0469	1.16	0.51	295.3	6.7	299.5	11.8	298
<b>M2</b>	<b>z23</b>	<b>co</b>	<b>ho</b>	<b>0.3260</b>	<b>2.1</b>	<b>0.0466</b>	<b>1.15</b>	<b>0.64</b>	<b>293.8</b>	<b>6.6</b>	<b>286.5</b>	<b>10.6</b>	<b>244</b>
<b>M2</b>	<b>z25</b>	<b>co</b>	<b>os</b>	<b>0.3300</b>	<b>2.0</b>	<b>0.0453</b>	<b>1.03</b>	<b>0.48</b>	<b>285.3</b>	<b>5.7</b>	<b>289.5</b>	<b>10.0</b>	<b>316</b>
M2	z26	ri	os	0.3332	2.4	0.0465	1.34	0.49	293.2	7.7	292.0	12.3	288
<b>M2</b>	<b>z28</b>	<b>co</b>	<b>ho</b>	<b>0.3310</b>	<b>2.5</b>	<b>0.0469</b>	<b>1.55</b>	<b>0.71</b>	<b>295.7</b>	<b>8.9</b>	<b>290.3</b>	<b>12.6</b>	<b>292</b>
<b>M2</b>	<b>z30</b>	<b>co</b>	<b>ho</b>	<b>0.3284</b>	<b>2.4</b>	<b>0.0467</b>	<b>1.31</b>	<b>0.19</b>	<b>294.3</b>	<b>7.5</b>	<b>288.4</b>	<b>12.2</b>	<b>224</b>
M2	z31	co	os	0.3533	3.3	0.0472	1.22	0.66	297.6	7.1	307.2	17.3	344
<b>M2</b>	<b>z32</b>	<b>co</b>	<b>os</b>	<b>0.3301</b>	<b>2.5</b>	<b>0.0457</b>	<b>1.12</b>	<b>0.58</b>	<b>287.9</b>	<b>6.3</b>	<b>289.6</b>	<b>12.4</b>	<b>324</b>
M2	z34	ri	os	0.3427	1.6	0.0487	1.34	0.36	306.4	8.0	299.2	8.5	210
M2	z35	co	ho	0.3509	1.5	0.0466	1.05	0.42	293.4	6.0	305.4	8.2	364
M2	z36	co	ho	0.2959	1.0	0.0278	0.99	0.48	176.8	3.4	263.2	4.6	458
M2	z38	co	os	0.3402	2.4	0.0445	1.45	0.60	280.9	8.0	297.3	12.3	424
M2	z40	co	ho	0.3328	3.5	0.0444	1.92	0.33	279.7	10.5	291.7	17.9	352
M2	z41	co	ho	0.3343	3.5	0.0432	1.82	0.58	272.4	9.7	292.8	17.8	406
M2	z42	ri	os	0.3437	1.8	0.0453	1.09	0.49	285.4	6.1	300.0	9.3	422
<b>M2</b>	<b>z44</b>	<b>co</b>	<b>os</b>	<b>0.3292</b>	<b>3.1</b>	<b>0.0452</b>	<b>1.20</b>	<b>0.71</b>	<b>285.0</b>	<b>6.7</b>	<b>289.0</b>	<b>15.8</b>	<b>320</b>
													<b>110</b>
													<b>99</b>

**GM601 - Deformed diorite [46.36016°N; 10.31110°E]**

Mnt.	Zrn	Pos.	Tex.	Radiogenic ratios				Age (Ma)				Conc. (%)	
				$^{207}\text{Pb}/^{235}\text{U}$	$\pm 1\sigma$	$^{206}\text{Pb}/^{238}\text{U}$	$\pm 1\sigma$	$\rho$	$^{206}\text{Pb}/^{238}\text{U}$	$\pm 2\sigma$	$^{207}\text{Pb}/^{235}\text{U}$	$\pm 2\sigma$	
GM	z46	co	os	0.3239	1.4	0.0458	0.61	0.35	288.6	3.4	284.9	7.0	256
<b>GM</b>	<b>z50</b>	<b>co</b>	<b>os</b>	<b>0.3214</b>	<b>2.3</b>	<b>0.0451</b>	<b>0.67</b>	<b>0.40</b>	<b>284.2</b>	<b>3.7</b>	<b>283.0</b>	<b>11.5</b>	<b>316</b>
<b>GM</b>	<b>z53</b>	<b>co</b>	<b>os</b>	<b>0.3199</b>	<b>1.9</b>	<b>0.0455</b>	<b>0.68</b>	<b>0.69</b>	<b>286.9</b>	<b>3.8</b>	<b>281.8</b>	<b>9.5</b>	<b>258</b>
GM	z54	co	os	0.3295	1.6	0.0449	0.79	0.61	283.3	4.4	289.2	7.9	290
GM	z61	co	os	0.3188	1.1	0.0447	0.49	0.57	282.0	2.7	280.9	5.6	298
<b>GM</b>	<b>z61</b>	<b>ri</b>	<b>ho</b>	<b>0.3205</b>	<b>1.5</b>	<b>0.0455</b>	<b>0.66</b>	<b>0.54</b>	<b>286.9</b>	<b>3.7</b>	<b>282.3</b>	<b>7.6</b>	<b>234</b>
<b>GM</b>	<b>z62</b>	<b>co</b>	<b>ho</b>	<b>0.3270</b>	<b>1.7</b>	<b>0.0452</b>	<b>0.75</b>	<b>0.74</b>	<b>284.8</b>	<b>4.2</b>	<b>287.3</b>	<b>8.5</b>	<b>286</b>
<b>GM</b>	<b>z63</b>	<b>co</b>	<b>os</b>	<b>0.3218</b>	<b>2.5</b>	<b>0.0456</b>	<b>1.15</b>	<b>0.53</b>	<b>287.5</b>	<b>6.5</b>	<b>283.3</b>	<b>12.5</b>	<b>286</b>
GM	z63	ri	os	0.3450	1.1	0.0469	0.77	0.41	295.6	4.4	300.9	5.6	306
GM	z64	co	os	0.3222	2.1	0.0462	0.73	0.61	291.4	4.2	283.6	10.2	278
GM	z65	co	os	0.3403	2.7	0.0479	1.00	0.47	301.8	5.9	297.4	14.2	242
GM	z66	co	os	0.3470	1.9	0.0466	0.84	0.27	293.3	4.8	302.5	9.8	318
GM	z68	co	os	0.3348	2.0	0.0465	0.76	0.58	293.2	4.3	293.2	10.2	248
GM	z70	co	ho	0.3510	3.2	0.0464	0.88	0.84	292.1	5.0	305.5	17.0	366
GM	z70	ri	os	0.3345	1.0	0.0458	0.41	0.36	288.5	2.3	293.0	5.1	314
<b>GM</b>	<b>z71</b>	<b>co</b>	<b>os</b>	<b>0.3295</b>	<b>2.0</b>	<b>0.0455</b>	<b>0.95</b>	<b>0.71</b>	<b>287.0</b>	<b>5.3</b>	<b>289.2</b>	<b>10.0</b>	<b>280</b>
<b>GM</b>	<b>z73</b>	<b>co</b>	<b>os</b>	<b>0.3281</b>	<b>2.5</b>	<b>0.0457</b>	<b>1.33</b>	<b>0.36</b>	<b>287.9</b>	<b>7.5</b>	<b>288.1</b>	<b>12.4</b>	<b>310</b>
GM	z74	co	os	0.3259	1.7	0.0444	0.46	0.65	279.8	2.5	286.4	8.3	288
GM	z75	co	os	0.3325	1.9	0.0461	0.87	0.34	290.7	4.9	291.5	9.7	288
GM	z81	ri	os	0.3326	1.7	0.0468	1.12	0.71	294.8	6.4	291.5	8.7	246
GM	z86	co	ho	0.3432	2.1	0.0470	0.64	0.88	295.8	3.7	299.6	10.7	354
GM	z86	ri	os	0.3480	1.7	0.0469	0.77	0.56	295.3	4.5	303.2	9.1	380
<b>GM</b>	<b>z88</b>	<b>co</b>	<b>os</b>	<b>0.3242</b>	<b>2.3</b>	<b>0.0451</b>	<b>0.85</b>	<b>0.64</b>	<b>284.4</b>	<b>4.7</b>	<b>285.1</b>	<b>11.4</b>	<b>330</b>
<b>GM</b>	<b>z90</b>	<b>co</b>	<b>ho</b>	<b>0.3204</b>	<b>1.1</b>	<b>0.0455</b>	<b>0.63</b>	<b>0.49</b>	<b>286.9</b>	<b>3.5</b>	<b>282.2</b>	<b>5.4</b>	<b>254</b>
<b>GM</b>	<b>z98</b>	<b>co</b>	<b>ho</b>	<b>0.3276</b>	<b>2.6</b>	<b>0.0453</b>	<b>0.89</b>	<b>0.51</b>	<b>285.4</b>	<b>5.0</b>	<b>287.8</b>	<b>12.9</b>	<b>364</b>
<b>GM</b>	<b>z98</b>	<b>ri</b>	<b>os</b>	<b>0.3157</b>	<b>2.1</b>	<b>0.0451</b>	<b>0.58</b>	<b>0.97</b>	<b>284.3</b>	<b>3.2</b>	<b>278.6</b>	<b>10.0</b>	<b>312</b>
GM	z76	co	os	0.3520	2.5	0.0452	1.44	0.49	285.0	8.0	306.2	13.3	424
GM	z77	co	os	0.3468	2.5	0.0467	1.19	0.48	294.5	6.8	302.3	13.0	336
GM	z96	co	os	0.3322	1.8	0.0460	0.60	0.43	290.2	3.4	291.2	9.1	312
<b>GM</b>	<b>z95</b>	<b>co</b>	<b>os</b>	<b>0.3247</b>	<b>2.7</b>	<b>0.0455</b>	<b>1.02</b>	<b>0.84</b>	<b>286.8</b>	<b>5.7</b>	<b>285.5</b>	<b>13.6</b>	<b>218</b>
													<b>90</b>
													<b>100</b>

**Table IV-1: (Continued)**
**MIB14 - Leucocratic diorite [46.34483°N; 10.32495°E]**

Mnt.	Zrn	Pos.	Tex.	Radiogenic ratios					Age (Ma)					Conc. (%)	
				$^{207}\text{Pb}/^{235}\text{U}$	$\pm 1\sigma$	$^{206}\text{Pb}/^{238}\text{U}$	$\pm 1\sigma$	$\rho$	$^{206}\text{Pb}/^{238}\text{U}$	$\pm 2\sigma$	$^{207}\text{Pb}/^{235}\text{U}$	$\pm 2\sigma$	$^{206}\text{Pb}/^{207}\text{Pb}$		
M1	z1	co	ho	0.3161	2.2	0.0459	0.85	0.36	289.5	4.8	278.9	10.6	236	94	104
M1	z3	co	os	0.3335	1.6	0.0462	0.50	0.54	291.3	2.9	292.2	8.2	290	64	100
<b>M1</b>	<b>z20</b>	<b>co</b>	<b>ho</b>	<b>0.3195</b>	<b>1.9</b>	<b>0.0451</b>	<b>0.79</b>	<b>0.47</b>	<b>284.4</b>	<b>4.4</b>	<b>281.6</b>	<b>9.5</b>	<b>288</b>	<b>78</b>	<b>101</b>
M1	z28	co	os	0.3197	2.4	0.0459	2.34	0.77	289.1	13.2	281.7	11.7	246	72	103
M2	z1	co	ho	0.3330	3.0	0.0440	1.10	0.91	277.5	6.0	291.8	15.4	442	94	95
<b>M2</b>	<b>z2</b>	<b>co</b>	<b>os</b>	<b>0.3178</b>	<b>1.5</b>	<b>0.0449</b>	<b>0.84</b>	<b>0.33</b>	<b>283.4</b>	<b>4.7</b>	<b>280.2</b>	<b>7.4</b>	<b>264</b>	<b>68</b>	<b>101</b>
<b>M2</b>	<b>z2</b>	<b>co</b>	<b>os</b>	<b>0.3226</b>	<b>2.1</b>	<b>0.0451</b>	<b>0.79</b>	<b>0.58</b>	<b>284.1</b>	<b>4.4</b>	<b>283.9</b>	<b>10.3</b>	<b>264</b>	<b>80</b>	<b>100</b>
M2	z3	co	ho	0.3095	6.7	0.0450	1.67	0.74	283.5	9.3	273.8	32.0	198	258	104
M2	z4	co	ho	0.3382	1.7	0.0452	0.95	0.43	285.1	5.3	295.8	8.9	342	72	96

Notes:

Spot location: co = core; ri = rim

Zircon texture: ho = homogenous; os = oscillatory; in = inherited core

Conc. is the percentage of concordancy, 100% denotes a concordant analysis

Analyses in bold were used for age calculation

**Table IV-2: U-Pb isotopic data for zircon from metamorphic samples (leucosomes and migmatites) analyzed by LA-ICPMS.**
**BPA 003-12d - Leucosome [46.35977°N; 10.33070°E]**

Mnt.	Zrn	Pos.	Tex.	Radiogenic ratios					Age (Ma)					Conc. (%)	
				$^{207}\text{Pb}/^{235}\text{U}$	$\pm 1\sigma$	$^{206}\text{Pb}/^{238}\text{U}$	$\pm 1\sigma$	$\rho$	$^{206}\text{Pb}/^{238}\text{U}$	$\pm 2\sigma$	$^{207}\text{Pb}/^{235}\text{U}$	$\pm 2\sigma$	$^{206}\text{Pb}/^{207}\text{Pb}$		
B4	<b>z9</b>	co	ho	<b>0.3298</b>	2.2	<b>0.0448</b>	<b>0.96</b>	<b>0.63</b>	282.3	<b>5.3</b>	<b>289.4</b>	<b>11.2</b>	<b>350</b>	<b>82</b>	<b>98</b>
B4	<b>z9</b>	ri	os	<b>0.3270</b>	<b>1.8</b>	<b>0.0464</b>	<b>0.94</b>	<b>0.45</b>	292.3	<b>5.4</b>	<b>287.3</b>	<b>8.8</b>	<b>310</b>	<b>72</b>	<b>102</b>
B4	z10	co	in	1.3271	1.7	0.1418	0.76	0.93	854.8	12.2	857.6	19.6	866	42	100
B4	<b>z11</b>	ri	os	<b>0.3276</b>	<b>2.1</b>	<b>0.0453</b>	<b>0.88</b>	<b>0.40</b>	285.9	<b>4.9</b>	<b>287.7</b>	<b>10.6</b>	<b>350</b>	<b>88</b>	<b>99</b>
B4	z12	co	os	0.3261	2.3	0.0455	0.94	0.42	286.6	5.3	286.6	11.7	302	96	100

**BPA 003-12c - Migmatite [46.35977°N; 10.33070°E]**

Mnt.	Zrn	Pos.	Tex.	Radiogenic ratios					Age (Ma)					Conc. (%)	
				$^{207}\text{Pb}/^{235}\text{U}$	$\pm 1\sigma$	$^{206}\text{Pb}/^{238}\text{U}$	$\pm 1\sigma$	$\rho$	$^{206}\text{Pb}/^{238}\text{U}$	$\pm 2\sigma$	$^{207}\text{Pb}/^{235}\text{U}$	$\pm 2\sigma$	$^{206}\text{Pb}/^{207}\text{Pb}$		
B2	<b>z55</b>	co	os	<b>0.3422</b>	2.3	<b>0.0459</b>	<b>1.08</b>	<b>0.48</b>	289.4	<b>6.1</b>	<b>298.9</b>	<b>11.8</b>	<b>376</b>	<b>90</b>	<b>97</b>
B2	<b>z57</b>	co	os	<b>0.3244</b>	<b>1.6</b>	<b>0.0458</b>	<b>1.26</b>	<b>0.44</b>	288.8	<b>7.1</b>	<b>285.3</b>	<b>7.9</b>	<b>320</b>	<b>70</b>	<b>101</b>
B2	<b>z58</b>	co	os	<b>0.3678</b>	<b>2.8</b>	<b>0.0461</b>	<b>1.05</b>	<b>0.27</b>	290.3	<b>6.0</b>	<b>318.0</b>	<b>15.2</b>	<b>510</b>	<b>118</b>	<b>91</b>
B2	z58	ri	ho	0.4485	3.1	0.0481	1.44	0.03	302.6	8.5	376.2	19.5	796	142	80

**BPA 109-12c - Leucosome [46.39400°N; 10.34333°E]**

Mnt.	Zrn	Pos.	Tex.	Radiogenic ratios					Age (Ma)					Conc. (%)	
				$^{207}\text{Pb}/^{235}\text{U}$	$\pm 1\sigma$	$^{206}\text{Pb}/^{238}\text{U}$	$\pm 1\sigma$	$\rho$	$^{206}\text{Pb}/^{238}\text{U}$	$\pm 2\sigma$	$^{207}\text{Pb}/^{235}\text{U}$	$\pm 2\sigma$	$^{206}\text{Pb}/^{207}\text{Pb}$		
B4	<b>z1</b>	co	ho	<b>0.3157</b>	2.0	<b>0.0441</b>	<b>1.07</b>	<b>0.61</b>	278.2	<b>5.8</b>	<b>278.6</b>	<b>9.7</b>	<b>280</b>	<b>72</b>	<b>100</b>
B4	z1	ri	os	<b>0.3148</b>	<b>1.5</b>	<b>0.0435</b>	<b>0.90</b>	<b>0.41</b>	274.7	<b>4.8</b>	<b>277.9</b>	<b>7.4</b>	<b>342</b>	<b>64</b>	<b>99</b>
B4	<b>z2</b>	co	os	<b>0.3068</b>	<b>1.6</b>	<b>0.0442</b>	<b>1.30</b>	<b>0.51</b>	278.8	<b>7.1</b>	<b>271.7</b>	<b>7.8</b>	<b>258</b>	<b>68</b>	<b>103</b>
B4	<b>z2</b>	co	os	<b>0.3128</b>	<b>1.6</b>	<b>0.0439</b>	<b>1.21</b>	<b>0.63</b>	276.9	<b>6.6</b>	<b>276.3</b>	<b>7.8</b>	<b>272</b>	<b>60</b>	<b>100</b>
B4	z3	co	os	0.3460	1.1	0.0461	1.31	0.76	290.5	7.4	301.7	5.7	468	38	96
B4	z4	co	in,os	0.3263	1.5	0.0457	1.19	0.64	287.8	6.7	286.7	7.5	328	54	100

Notes:

Spot location: co = core; ri = rim

Zircon texture: ho = homogenous; os = oscillatory; in = inherited core

Conc. is the percentage of concordancy, 100% denotes a concordant analysis

Analyses in bold were used for age calculation

**Table IV-3:** U, Th and trace element (REE) concentration of zircon from magmatic samples (diorites) analyzed by LA-ICPMS.

**M28B73 - Diorite [46.39551°N; 10.34243°E]**

An.	Mnt.	Nb											Zr											Nb/Gd <sub>n</sub>		Eu/Eu*		$A_{\text{ge}}^{(1)}$ (Ma)			
		Hf	Ta	Th	U	La	Ce	Pr	Nd	Sm	Eu	Gd	Dy	Ho	Er	Tm	Yb	Lu	Nb/U	Yb <sub>n</sub> /Gd <sub>n</sub>	Eu/Eu*										
b04	M2	25	3.39	12271	2.03	164	1307	0.027	3.48	0.122	2.45	8.20	0.499	58.1	256	86.4	372	74.8	632	122	0.125	1.7	13.2	0.051	289.9						
b05	M2	26	3.24	11063	0.805	160	618	0.057	5.76	0.228	4.11	11.0	1.49	59.8	140	33.6	109	17.3	126	20.8	0.259	4.0	2.5	0.142	283.4						
b07	M2	28	5.38	9231	1.47	193	649	0.059	10.3	0.188	3.22	8.08	1.31	46.8	161	46.0	206	39.6	334	66.3	0.297	3.7	8.6	0.160	279.9						
b08	M2	29	9.69	11224	3.09	885	2615	0.114	13.4	0.171	4.31	13.2	1.06	80.3	175	40.9	161	26.8	229	41.1	0.338	3.1	3.4	0.077	231.0						
b10	M2	214	6.36	9954	2.79	172	1507	bdl	3.37	0.093	2.39	7.32	0.36	49.4	245	82.0	412	85.0	746	154	0.114	2.3	18.3	0.043	na						
b11	M2	215	7.35	13791	1.99	338	2539	0.500	6.42	0.376	4.56	11.3	1.10	102	216	37.2	92.5	11.5	78.9	10.7	0.133	3.7	0.9	0.067	na						
b12	M2	216	6.29	15443	5.42	116	2942	bdl	1.90	0.017	0.872	2.85	0.117	32.5	240	97.3	572	11.6	1048	233	0.039	1.2	39.0	0.023	295.3						
b13	M2	217	4.25	10564	1.08	380	1132	0.231	6.75	0.495	9.61	26.7	2.04	152	365	88.3	268	40.2	293	52.3	0.336	3.9	2.3	0.077	na						
b14	M2	220	5.70	10768	1.32	299	917	0.421	14.2	0.580	7.72	15.3	1.75	84.7	192	39.4	107	15.6	108	16.8	0.326	4.3	1.5	0.118	na						
b15	M2	223	10.2	14108	3.47	176	1966	0.021	3.19	0.106	1.37	6.98	0.606	60.5	285	97.0	428	83.5	723	132	0.090	2.9	14.5	0.061	293.8						
b17	M2	226	4.95	16169	3.08	72.1	2027	0.049	1.32	0.049	1.20	3.24	0.135	29.5	181	65.4	290	59.6	571	102	0.036	1.6	23.4	0.028	293.2						
b18	M2	228	3.12	11987	0.951	177	951	0.353	5.49	0.465	6.15	14.9	1.68	92.1	148	27.0	69.9	9.01	68.9	10.8	0.186	3.3	0.9	0.106	295.7						

**MI-B14 - Leucocratic diorite [46.34483°N; 10.32495°E]**

An.	Mnt.	Nb											Zr											Nb/Gd <sub>n</sub>		Eu/Eu*		$A_{\text{ge}}^{(1)}$ (Ma)			
		Hf	Ta	Th	U	La	Ce	Pr	Nd	Sm	Eu	Gd	Dy	Ho	Er	Tm	Yb	Lu	Nb/U	Yb <sub>n</sub> /Gd <sub>n</sub>	Eu/Eu*										
c03	M1	24	3.23	8282	0.638	154	450	4.084	27.3	2.952	13.8	21.5	2.97	58.8	195	36.7	152	23.3	137	29.9	0.341	5.07	2.83	0.240	285.1						
c04	M1	29	3.11	8559	0.810	161	289	3.223	17.2	1.340	7.16	6.86	1.08	28.7	94.0	31.8	130	27.7	256	46.7	0.557	3.84	10.80	0.202	na						
c05	M1	z11	3.66	9281	1.12	142	679	1.177	10.1	0.595	6.64	11.3	2.18	60.0	116	29.3	94.9	14.0	119	21.2	0.209	3.27	2.41	0.205	na						
c06	M1	z12	2.51	7416	0.764	197	330	0.029	11.3	0.467	7.15	12.4	2.63	63.9	227	81.8	347	66.1	649	113	0.597	3.28	12.27	0.231	na						
c07	M1	z24	3.70	8976	0.896	116	548	9.770	64.8	5.127	27.0	11.9	1.44	50.2	90.0	22.1	54.5	7.76	57.3	7.98	0.211	4.13	1.38	0.155	na						
c08	M1	z20	2.44	10877	0.598	77.5	566	0.056	2.81	0.074	1.44	5.67	0.612	35.0	74.5	14.8	38.5	5.29	31.3	4.56	0.137	4.09	1.08	0.102	284.4						
c09	M1	z28	3.65	8202	0.810	83.9	345	2.635	20.4	3.423	18.4	11.1	1.44	32.7	103	22.1	84.2	12.5	84.0	16.8	0.243	4.51	3.11	0.214	289.1						
c10	M1	z24	4.67	10647	1.07	167	1068	bdl	4.34	0.108	2.00	8.32	1.42	58.2	144	27.7	78.7	10.5	72.7	10.1	0.156	4.35	1.51	0.145	na						
c11	M1	z22	18.5	8915	4.83	542	959	0.108	14.8	0.125	1.90	5.24	0.387	36.6	168	65.9	288	56.0	540	92.7	0.565	3.83	17.83	0.063	na						

Notes:

bdl: below detection limit

na: not analyzed

$\text{Yb}_{\text{n}}/\text{Gd}_{\text{n}}$  and Eu/Eu\*: normalised to chondrite after Sun and McDonough (1989)

<sup>(1)</sup> $\text{^{206}\text{U}/^{238}\text{U}$  ages, see Table IV-1 and Table IV-2 for details

Table IV-4: U, Th and trace element (REE) concentration of zircon from metamorphic samples (leucosomes and migmatite) analyzed by LA-ICPMS.

<b>BPA 003-12d - Leucosome /46.35977°N; 10.33070°E/</b>												
An.	Mnt.	Zrn	Nb	Hf	Ta	Th	U	La	Ce	Pr	Nd	Sm
		(ppm)										
d12	B4	z9	6.90	12341	1.64	256	1318	0.067	7.70	0.198	3.81	12.5
d13	B4	z10	76.4	14245	84.2	26.3	549	0.054	5.96	0.051	0.899	2.08
d14	B4	z11	13.4	11879	4.01	1343	3985	0.042	13.9	0.141	3.25	16.2
d15	B4	z12	6.46	9253	1.42	208	796	2.82	19.9	1.81	12.7	14.4

<b>BPA 003-12c - Migmatite /46.35977°N; 10.33070°E/</b>												
An.	Mnt.	Zrn	Nb	Hf	Ta	Th	U	La	Ce	Pr	Nd	Sm
		(ppm)										
a05	B2	z55	5.05	11223	1.38	192	942	0.011	7.21	0.120	2.68	9.9
a06	B2	z57	4.10	8270	1.01	273	438	1.09	10.0	0.759	7.74	10.0
a07	B2	z56	4.10	10199	1.35	313	976	0.814	13.2	0.819	10.7	23.9
a08	B2	z59	2.78	9623	0.862	172	667	1.12	12.6	1.06	10.4	12.2

<b>BPA 109-12c - Leucosome /46.39400°N; 10.34333°E/</b>												
An.	Mnt.	Zrn	Nb	Hf	Ta	Th	U	La	Ce	Pr	Nd	Sm
		(ppm)										
d03	B4	z1	4.80	10987	2.43	179	1344	0.046	3.70	0.089	1.55	5.24
d04	B4	z2	2.60	10219	1.06	130	856	0.070	2.55	0.157	2.35	6.42
d05	B4	z3	7.32	12666	3.71	278	4986	0.617	6.48	0.734	5.67	13.4
d06	B4	z4	3.75	10245	1.90	287	1794	0.219	4.92	0.333	4.09	10.1

<b>BPA 109-12c - Leucosome /46.39400°N; 10.34333°E/</b>												
An.	Mnt.	Zrn	Nb	Hf	Ta	Th	U	La	Ce	Pr	Nd	Sm
		(ppm)										
d03	B4	z1	4.80	10987	2.43	179	1344	0.046	3.70	0.089	1.55	5.24
d04	B4	z2	2.60	10219	1.06	130	856	0.070	2.55	0.157	2.35	6.42
d05	B4	z3	7.32	12666	3.71	278	4986	0.617	6.48	0.734	5.67	13.4
d06	B4	z4	3.75	10245	1.90	287	1794	0.219	4.92	0.333	4.09	10.1

Notes:

bdl: below detection limit

na: not analyzed

 Yb<sub>n</sub>/Gd<sub>n</sub> and Eu/Eu\*: normalized to chondrite after Sun and McDonough (1989)

 (1) <sup>206</sup>U/<sup>238</sup>U ages, see Table IV-1 and Table IV-2 for details

A high Th/U ratio (0.137–0.597) is found for zircons of sample M1B14 (Fig. IV-10a). They present a relatively low HREE-enrichment ( $\text{Yb}_{\text{n}}/\text{Gd}_{\text{n}} < 20$ ) and a negative Eu-anomaly ( $\text{Eu}/\text{Eu}^* = 0.063–0.240$ ). No clear trend between  $\text{Yb}_{\text{n}}/\text{Gd}_{\text{n}}$  or  $\text{Eu}/\text{Eu}^*$  is observed. Zircons have commonly a low tantalum concentration (~ 0.8 ppm) that is not correlated with the Nb/Ta ratio (Fig. IV-10b). Similarly, they are poor in hafnium and uranium, around 9000 and 600 ppm, respectively. Both element concentrations do not present any peculiar trend with  $\text{Yb}_{\text{n}}/\text{Gd}_{\text{n}}$  (Fig. IV-10c).

#### **5.4.2 Migmatitic metasediments**

Metasediments sampled in the contact aureole (leucosome BPA 003-12d and migmatite BPA 003-12c, Fig. IV-11a) present a homogeneous REE pattern, with the exception made for inherited cores. They have a high Th/U ratio (0.194–0.624), are depleted in HREE ( $\text{Yb}_{\text{n}}/\text{Gd}_{\text{n}} \approx 2$ ) and present a medium Eu-anomaly ( $\text{Eu}/\text{Eu}^* \approx 0.14$ , Fig. IV-11a). The Ta-content commonly varies between 0.9 and 4.0 ppm without being correlated to the  $\text{Yb}_{\text{n}}/\text{Gd}_{\text{n}}$  and Nb/Ta ratios (Fig. IV-11b). The hafnium and uranium concentration in zircon is weakly but inversely correlated to the slope of the REE diagram (Fig. IV-11c).

Zircons from the leucosome BPA 109-12c have a high Th/U ratio (~ 0.12) medium HREE enrichment ( $\text{Yb}_{\text{n}}/\text{Gd}_{\text{n}} \approx 18$ ). The quite low  $\text{Eu}/\text{Eu}^*$  value (~ 0.07) indicates a strongly negative europium anomaly (Fig. IV-11a). The variable Ta-concentration (1.06 to 3.71 ppm) is not correlated to Nb/Ta or  $\text{Yb}_{\text{n}}/\text{Gd}_{\text{n}}$  (Fig. IV-11b). The similar hafnium and variable uranium concentration in zircon, around 10000 ppm and between 856 and ~5000 ppm, respectively, does not present a trend with respect to HREE-slope (Fig. IV-11c).

## 6. ANISOTROPY OF MAGNETIC SUSCEPTIBILITY

In contrast to granitic rocks and migmatites, the application of the Anisotropy of Magnetic Susceptibility (AMS) in mafic rocks to estimate the rock fabric is not straightforward. Such rock types may often have inverse to abnormal (intermediate) magnetic fabrics with respect to the petrofabric (e.g. Geoffroy *et al.*, 2002) due to various processes. First, in mafic rocks, the AMS may be a result of paramagnetic minerals such as pyroxene and amphibole that both have variable long axis ( $K_1$ ) orientation that can lie at high angle to the crystallographic  $c$ -axis (e.g. Borradaile & Jackson, 2010; Rochette *et al.*, 1999). Second, mineral orientations may sometimes differ from the magmatic flow with e.g. mineral imbrications or variations of the velocity gradient (Cañón-Tapia & Chávez-Álvarez, 2004). Pyroxene in general is known for magnetite inclusions or exsolutions (Lagroix & Borradaile, 2000; Renne *et al.*, 2002). This can sometimes mimic and enhance the magnetic signal of pyroxene, if growing along the  $c$ -axis of the host mineral (e.g. Yaouancq & MacLoed, 2000), but can also induce a third perturbation type if growing randomly or along structures independent of the rock fabric (Clark & Tonkin, 1994; Rochette, 1987; Rochette *et al.*, 1999). A fourth perturbation may be due to magnetite itself. Depending on its grain size, magnetite can be either mono- or poly-domain and present intrinsic axis permutations (Rochette *et al.*, 1992). Despite these caveats, the AMS method was successfully applied to mafic rocks (Pearce & Fueten, 1989; Richter *et al.*, 1996; Yaouancq & MacLoed, 2000).

### 6.1 AMS Methods

Samples were collected using a portable drilling machine at the stations indicated on Fig. IV-2c. AMS was measured with a MFK1-A Kappabridge (AGICO, Inc.) operating in low field at the University of Strasbourg. Raw data are reported in Table IV-5. The magnetic susceptibility  $K_m$  is usually controlled by the relative proportion of diamagnetic, paramagnetic and ferromagnetic minerals. Rocks with  $K_m$  on the order of  $10^{-4}$  SI have an AMS signal carried by paramagnetic minerals (e.g. pyroxene and amphibole with intrinsic  $K_m = 0.5\text{--}5 \text{--} 10\text{--}6$  SI; Hrouda, 1982; Rochette *et al.*, 1992) whereas rocks with susceptibilities around  $10^{-3}$  SI may contain ferromagnetic minerals (Hrouda & Kahan, 1991; Rochette *et al.*, 1992). In order to qualitatively prevent the variability of AMS fabric due to the variability of ferromagnetic (*s.l.*) minerals in rocks, we performed identification of magnetic mineralogy by investigating coercivity-unblocking temperature spectra of ferromagnetic minerals (following the method of Lowrie, 1990) at the University of Cergy-Pontoise. Analytical conditions and parameters description are reported in Appendix B.

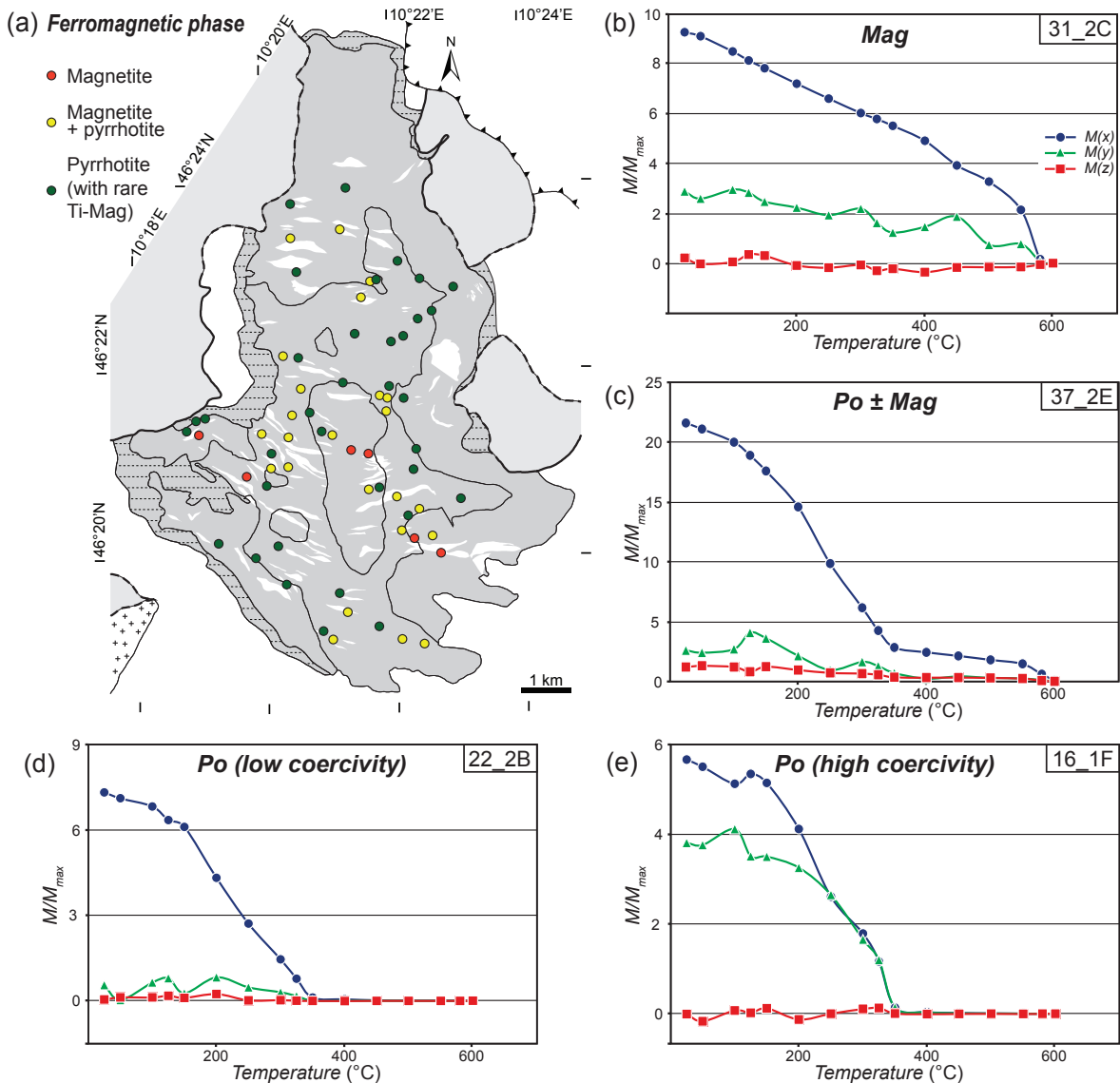


**Fig. IV-12:** (a) Synthesis of magnetic mineralogy determination with 3axes-IRM and (b–e) representative experiments representing  $M$  normalized by  $M_{max}$  in function of temperature for low coercivity ( $M(x)$ , blue circles), medium coercivity ( $M(y)$ , red squares) and high coercivity axes ( $M(z)$ , green triangles). (b) Magnetite-, (c) pyrrhotite- and magnetite-, (d) low coercivity pyrrhotite- and more rarely (e) high coercivity pyrrhotite-bearing samples.

## 6.2 Magnetic mineralogy results

Following results of the stepwise thermal demagnetization 3axes-IRM, three different rock types can be defined according to their variable amounts of ferromagnetic phases. (1) The first group presents a progressive decrease of the magnetization from the ambient temperature to reach an unblocking temperature around 580°C pointing to the presence of near pure magnetite mainly carried by the low coercivity axis  $M(x)$  (titanomagnetite with low Ti-content; Lattard *et al.*, 2006) (Fig. IV-12b). (2) The second group (Fig. IV-12c) presents a sharp decrease of the signal from the beginning of the experiment until 350°C, followed by a progressive decrease

until 580°C. This points to a two-phase composition with an unblocking temperature around 350°C that could be either titanomagnetite or pyrrhotite, but the low magnetization of the medium coercivity axis  $M(y)$  values indicate the presence of a lower coercivity phase that can preferentially be a low coercivity pyrrhotite or a titano-magnetite. The second phase of higher unblocking temperature around 580°C can be magnetite. (3) The third and last group presents a sharp decrease from the beginning of the experiment until 350°C mainly carried by the low coercivity axis  $M(x)$  indicating a low coercivity pyrrhotite or titanomagnetite (Fig. IV-12d). In rare cases, signal of the medium coercivity axis  $M(y)$  indicates the presence of a higher coercivity pyrrhotite (Fig. IV-12e). These 3axes-IRM results does not allow to make the distinction between pyrrhotite and titanomagnetite, but as pyrrhotite was observed in thin section (see petrographic decription), we favor the presence of pyrrhotite. Nevertheless, minor occurrence of titanomagnetite cannot be excluded.

### 6.3 Bulk susceptibility

The bulk susceptibilities of the rocks from the Sondalo gabbro range from 448 up to  $3540 \times 10^{-6}$  SI (Fig. IV-13a) with most of values below  $10^{-3}$  SI. Such high values attest of a mixed contribution to the AMS signal of paramagnetic and ferromagnetic minerals. For the rare values on the order of  $10^{-3}$  SI, the signal is carried essentially by ferromagnetic minerals. Despite textural heterogeneities of magmatic rocks, bulk susceptibility is usually consistent at the outcrop scale (Fig. IV-15a) but occasionally extremely variable indicating that ferromagnetic minerals may not be homogeneously distributed (outcrop 7 for instance).

In a map view, the highest susceptibility values ( $K_m > 1.5 \times 10^{-3}$  SI) lie close to the Ol-gabbro core (Fig. IV-14). In contrast, towards the margin of the complex, no specific trend can be described and  $K_m$  values are generally lower than  $10^{-3}$  SI.

The distribution of the bulk susceptibilities over the pluton (Fig. IV-14a) corroborates generally well with the three mineralogical groups (Fig. IV-12a). Low susceptibility samples usually do not contain magnetite, whereas high susceptibility samples do. This is not the case for few stations (e.g. stations 25, 29 and 30), probably due to strong differences in the distribution of ferromagnetic phases in samples.

**Table IV-5: Anisotropy of Magnetic Susceptibility data**

Stn.	Lat	Lon	$K_m$	$N$	$(10^{-6} \text{ SI})$	$T$	$P$	$P_j$	$K_1 d$	$K_1 i$	$K_1 \sigma$	$K_2 d$	$K_2 i$	$K_2 \sigma$	$K_3 d$	$K_3 i$	$K_3 \sigma$
	(°N)	(°E)	(deg)						(deg)	(deg)	(max/min)	(deg)	(deg)	(max/min)	(deg)	(deg)	(max/min)
1	46.392	10.354	11	840	0.246	1.031	1.031	282.8	66.4	13.5/6.3	44.2	12.8	15/5.4	138.8	19.5	12.8/4.6	
2	46.399	10.355	16	448	-0.086	1.016	1.016	143.6	44.2	60.9/27.6	32.8	20.1	61.5/40.1	285.5	39.0	45/24	
3	46.383	10.361	14	824	-0.208	1.049	1.050	63.9	56.8	9.3/4.8	252.1	32.9	12.9/6.3	159.6	3.7	11.2/4.6	
4	46.380	10.359	19	753	0.250	1.034	1.034	263.3	35.8	26.1/7.4	56.1	50.9	26.3/9.7	163.3	13.5	13.2/5.8	
5	46.373	10.357	15	632	-0.448	1.010	1.010	282.8	81.5	18.3/6.6	139.8	6.8	37.9/15.4	49.2	5.1	37.2/6.3	
6	46.365	10.354	11	962	0.400	1.079	1.081	79.4	50.5	12.6/4.5	262.6	39.5	13.4/6.1	171.3	1.6	8.5/2.7	
7	46.352	10.356	16	2720	-0.366	1.082	1.084	131.2	71.2	22.8/8.6	15.2	8.5	34.7/21.4	282.7	16.7	34.8/9.5	
8	46.345	10.360	16	2830	-0.029	1.107	1.107	84.3	34.2	22/10.1	225.1	48.8	27.9/17.3	339.9	20.2	25.3/9.1	
9	46.346	10.363	19	593	0.364	1.061	1.063	244.7	49.5	26.9/4	73.4	40.2	27.2/6.8	339.7	4.3	8.5/4.7	
10	46.352	10.373	16	538	0.146	1.023	1.023	317.3	59.1	31.2/16.4	69.0	12.5	33.3/24.2	165.8	27.7	29.4/10.7	
11	46.349	10.372	20	455	-0.441	1.032	1.033	83.5	45.6	9.9/7.7	239.0	41.7	29.5/7.7	340.5	12.5	29.4/9.5	
12	46.352	10.360	17	1940	0.170	1.065	1.065	76.3	51.0	7.7/3	203.7	26.1	11.5/4.8	307.9	26.7	9.9/2.8	
13	46.320	10.348	17	1380	0.204	1.090	1.091	251.3	24.6	14/6.3	147.6	27.4	13.6/5.3	16.6	51.6	8.6/5.6	
14	46.336	10.321	16	769	0.555	1.028	1.029	219.6	12.8	76.4/48.4	98.5	66.1	76.4/52.9	314.3	19.8	54.6/47.3	
15	46.335	10.337	17	1290	-0.582	1.057	1.061	260.8	28.6	10.4/5.9	14.6	36.5	33.3/8.5	143.4	40.3	33/6.3	
16	46.333	10.331	11	887	0.106	1.048	1.048	303.4	28.4	11.9/7.3	89.8	57.0	12/7.3	204.8	15.4	9.7/5.1	
17	46.346	10.334	17	1020	0.432	1.056	1.058	77.0	67.8	52.1/32.3	260.0	22.2	51.7/27.4	169.6	1.0	36.4/25.1	
18	46.348	10.329	20	638	0.825	1.035	1.039	197.0	38.2	54.9/11	301.4	17.5	55/8.9	50.9	46.5	11.1/10.3	
19	46.349	10.335	16	702	0.176	1.012	1.012	9.1	23.0	30.8/8.8	240.2	55.9	32/15.1	109.8	23.7	18.3/8.9	
20	46.352	10.335	13	1050	-0.585	1.015	1.016	321.4	62.0	17.3/8.5	221.9	5.0	30.4/15.4	129.3	27.5	30.6/10	
21	46.356	10.333	16	620	-0.498	1.026	1.027	215.4	47.8	23.7/7.8	316.9	10.2	48/17	55.7	40.3	47.3/10.1	
22	46.358	10.318	22	861	0.242	1.019	1.019	222.5	35.3	13.9/11.3	69.1	51.6	25.3/12.8	322.0	13.2	26.3/8.7	
23	46.358	10.316	14	1170	0.405	1.011	1.011	207.0	6.9	42.6/6.9	116.0	8.9	44.6/15.3	334.3	78.8	31.7/8.9	
24	46.356	10.313	16	820	0.544	1.022	1.023	181.3	76.2	33.2/4.2	68.7	5.4	33.2/10.2	337.5	12.6	10.6/5.4	
25	46.356	10.316	16	837	0.568	1.015	1.016	252.8	46.9	28.2/14.8	351.7	8.3	28.2/15.9	89.3	41.9	16/14.8	
26	46.329	10.339	22	770	0.298	1.011	1.011	161.5	39.1	20.6/8.6	333.5	50.6	20.4/13.7	68.3	3.9	14.2/9.3	
27	46.323	10.354	15	1270	-0.335	1.017	1.018	267.7	68.1	26.9/18.5	26.1	10.8	48.6/25	119.8	18.8	48.8/15.2	
28	46.321	10.362	14	693	-0.589	1.013	1.013	270.7	77.0	36.3/24.5	25.6	5.5	58.8/27	116.8	11.7	58.6/33.6	
29	46.319	10.368	10	448	-0.359	1.019	1.019	10.8	57.8	23.6/13.5	103.3	1.5	50.5/19.2	194.2	32.1	50.3/10.5	
30	46.318	10.374	12	672	0.250	1.059	1.059	125.2	16.4	10.4/8.7	17.7	45.6	11.7/7.5	229.4	39.8	9.5/8.4	
31	46.319	10.350	14	1340	-0.661	1.039	1.042	9.8	80.7	32.9/16	208.8	8.8	69.1/23	118.4	3.0	68.7/15.8	
32	46.343	10.384	17	1330	-0.391	1.078	1.080	172.5	79.1	18.3/3	44.4	6.8	55.4/10.8	313.3	8.5	54.9/3	
33	46.342	10.373	15	1090	0.518	1.019	1.020	225.1	8.7	14.6/5.5	32.1	81.0	14.1/8.2	134.8	2.0	8.4/6.9	
34	46.341	10.370	16	963	0.521	1.100	1.104	150.9	64.3	31.7/10.3	57.9	1.5	31.8/5.2	327.2	25.7	10.5/5.7	

**Table IV-5: (Continued)**

Stn.	Lat	Lon	$K_m$	$N$	$(10^{-6} \text{ SI})$	$T$	$P$	$P_j$	$K_1 d$	$K_1 i$	$K_1 \sigma$	$K_2 d$	$K_2 i$	$K_2 \sigma$	$K_3 d$	$K_3 i$	$K_3 \sigma$
	(°N)	(°E)	(deg)						(deg)	(deg)	(max/min)	(deg)	(deg)	(max/min)	(deg)	(deg)	(max/min)
35	46.338	10.368	14	2310	-0.093	1.021	1.021	6.1	75.4	15.9/12.6	136.6	9.6	26.9/13.1	228.4	10.9	27.1/13.3	
36	46.336	10.372	17	1000	0.163	1.014	1.014	62.4	53.8	33.1/10.4	194.3	26.0	33.2/17.9	296.4	23.3	19.8/12.6	
37	46.337	10.376	16	1210	0.471	1.022	1.023	112.9	65.3	12.7/3.5	257.2	20.5	13/7.5	352.2	13.2	8.1/3.5	
38	46.334	10.379	11	1100	0.152	1.042	1.042	61.7	27.7	12.3/9	283.0	55.1	12.6/6.6	162.5	19.5	9.3/7.6	
39	46.344	10.367	13	1100	0.570	1.019	1.019	240.5	50.8	17.9/7.1	51.2	38.8	19.4/4.3	144.9	4.6	10.8/5.8	
40	46.362	10.363	18	3540	0.115	1.058	1.058	71.4	52.5	13.8/8	240.1	37.0	16.8/10.7	334.3	5.5	14.7/8.1	
41	46.362	10.365	15	542	-0.104	1.023	1.023	100.4	3.6	20.8/7.7	9.9	8.5	26.9/19	213.1	80.8	27.1/7.7	
42	46.362	10.370	18	959	0.273	1.008	1.008	65.0	60.1	48.2/17.3	228.8	28.9	48.3/29	322.7	7.0	30.5/18.2	
43	46.364	10.366	16	658	-0.273	1.013	1.013	94.2	39.6	17.4/13.4	1.0	3.9	28.6/16.7	266.4	50.1	28.8/13.9	
44	46.359	10.365	16	694	-0.292	1.009	1.010	90.1	71.0	15.2/6.5	235.8	15.9	27.1/13.4	328.8	10.1	27.9/6	
45	46.397	10.341	16	912	0.014	1.151	1.151	15.2	88.3	12.1/3.7	114.2	0.3	11.6/7.3	204.2	1.7	8/5.8	
46	46.391	10.341	15	508	0.481	1.038	1.039	111.3	82.7	34.6/3.3	275.4	7.0	34.6/8	5.6	2.0	8.6/4.1	
47	46.384	10.342	12	931	0.483	1.014	1.014	132.0	73.0	38.9/9	227.3	1.6	38.9/8.7	317.8	16.9	11.7/8.4	
48	46.327	10.352	18	847	-0.074	1.023	1.023	311.0	57.6	57.4/16.8	52.3	7.1	57.4/27.4	146.7	31.4	29/18.5	
49	46.347	10.334	17	945	-0.171	1.028	1.028	190.3	26.7	32.1/26.9	314.3	48.1	48.5/25.8	83.7	29.7	47.9/30.6	
50	46.350	10.339	18	896	-0.532	1.012	1.012	228.6	49.5	13.1/4.2	323.0	3.7	34.9/6	56.1	40.2	34.9/12.4	
51	46.355	10.340	14	1710	-0.311	1.089	1.091	61.9	84.0	24.9/9.1	203.0	4.7	38.7/21.1	293.3	3.8	37.3/10.1	
52	46.359	10.341	13	671	0.710	1.011	1.012	232.9	24.8	50.5/18.9	66.0	64.6	50.5/15.2	325.2	5.1	19.2/15.1	
53	46.369	10.339	16	1020	-0.127	1.018	1.018	320.2	50.9	10.6/7.8	76.2	19.6	16.3/8.7	179.2	32.3	15.8/8.3	
54	46.369	10.342	14	798	-0.056	1.020	1.020	65.8	78.2	37.7/8.7	253.3	11.7	46.1/19.2	163.0	1.5	43.8/14.8	
55	46.364	10.343	16	1160	0.351	1.060	1.061	253.1	68.0	17.5/7.1	53.3	20.8	17.7/5.6	145.9	6.8	8.2/6.5	
56	46.359	10.345	17	1310	0.529	1.089	1.093	250.5	56.8	15.3/7.9	82.5	32.6	16.5/8.1	349.0	5.5	12.6/5.2	
57	46.356	10.348	24	687	-0.084	1.024	1.024	297.2	63.3	14/7.9	88.8	23.9	24/13.5	183.9	11.3	24.1/7.9	
58	46.355	10.351	16	656	-0.020	1.022	1.022	318.5	72.9	13/9.1	82.9	9.9	25.9/6.6	175.4	13.9	24.3/8.8	
59	46.376	10.367	11	642	-0.164	1.036	1.036	32.7	55.8	12.5/4.8	293.1	6.5	25.9/10.3	198.7	33.4	25.6/6.1	
60	46.372	10.367	16	514	-0.526	1.009	1.009	55.7	54.0	35.4/20.2	273.0	30.1	58.1/34.2	172.2	17.9	58.1/22.7	
61	46.373	10.370	13	1100	0.689	1.050	1.053	82.2	7.5	31.5/10.3	328.4	72.0	31.5/14.1	174.3	16.3	16.9/6.2	
62	46.376	10.374	12	856	-0.358	1.006	1.006	267.4	57.6	32/18.6	88.0	32.4	37.9/19.8	357.8	0.3	38.1/29.4	
63	46.377	10.377	15	857	-0.383	1.010	1.011	331.3	52.7	17.1/13.2	81.1	14.4	28.7/15.5	180.9	33.5	30.3/9.8	
64	46.381	10.383	16	883	0.724	1.031	1.034	58.8	37.9	58.8/8.8	312.9	19.4	58.9/14.6	201.8	45.7	15.9/8.6	
65	46.383	10.374	21	1170	-0.176	1.034	1.034	338.7	66.4	21.5/13.1	100.2	12.8	34.6/12.8	194.8	19.4	35.8/16.8	
66	46.386	10.369	15	1030	-0.232	1.023	1.024	53.0	58.5	32.4/12	286.5	20.0	36.8/26.9	187.5	23.2	34.9/10.4	
67	46.383	10.363	39	733	0.269	1.016	1.016	60.2	27.2	30.7/8.1	291.8	50.4	31.9/18.5	165.0	26.4	21.2/8.4	

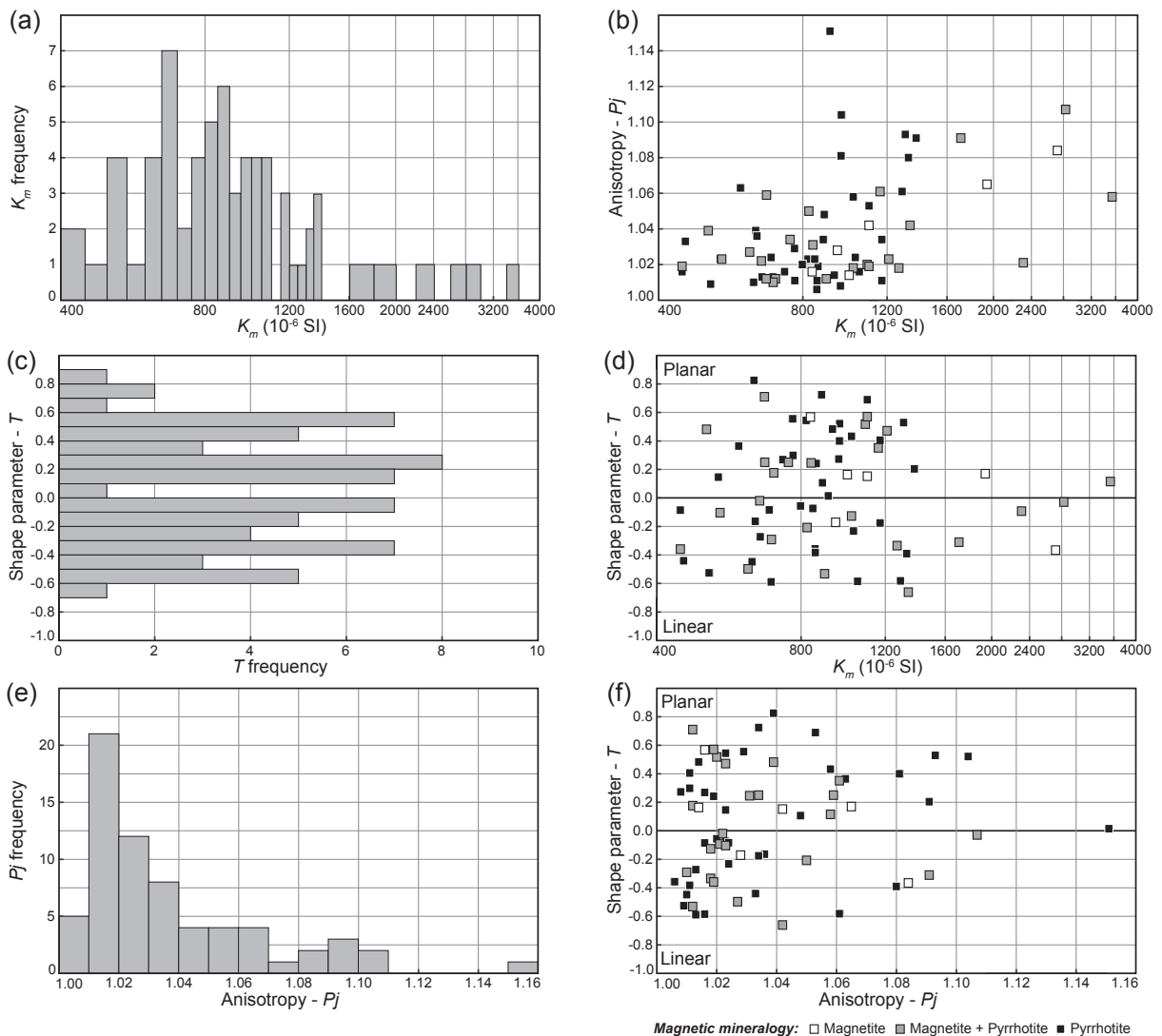
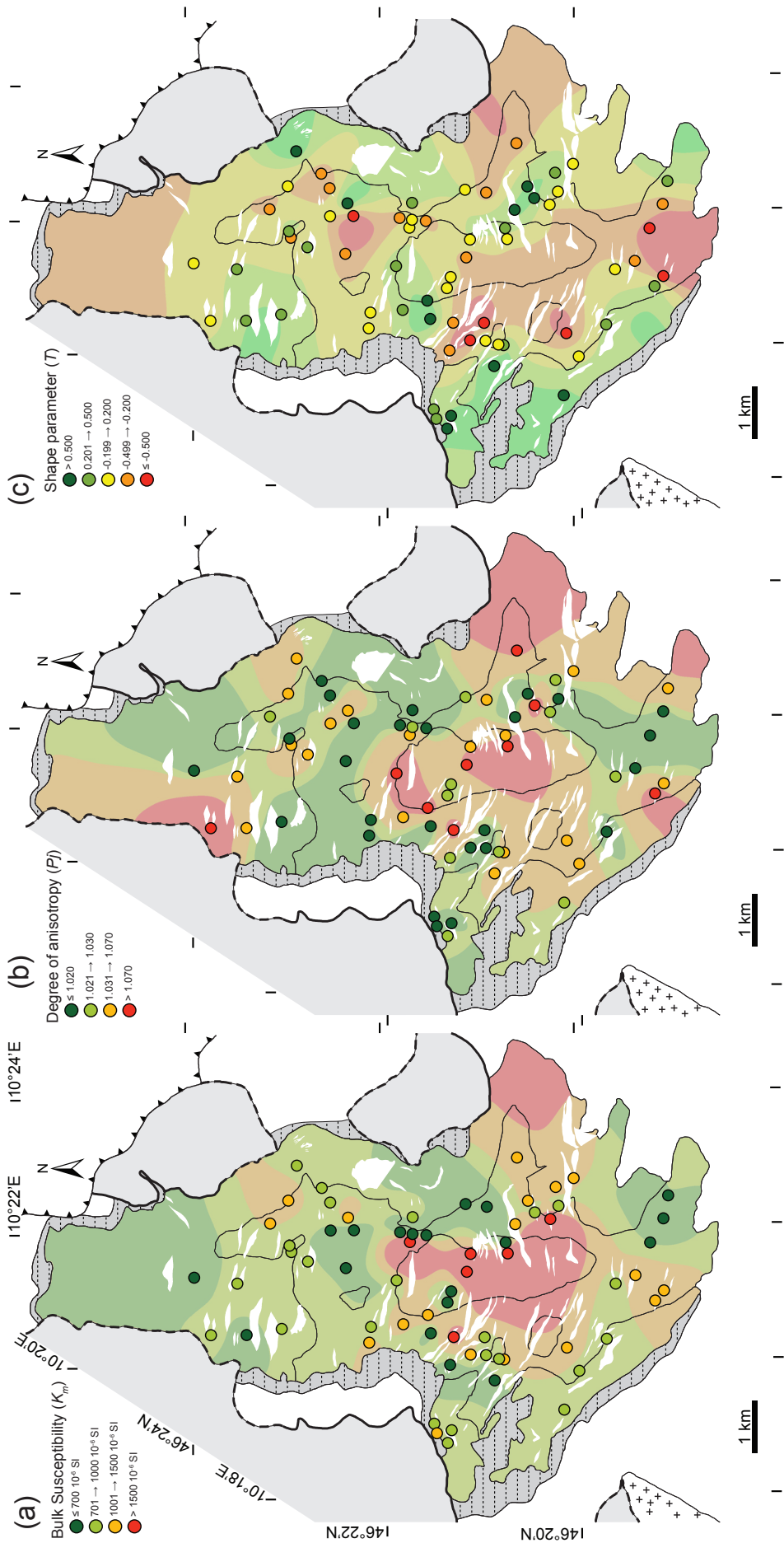


**Fig. IV-13:** (a)  $K_m$  frequency plot; (b)  $Pj$ - $K_m$  diagram; (c)  $T$  frequency plot; (d)  $T$ - $K_m$  diagram; (e)  $Pj$  frequency plot; (f)  $T$ - $Pj$  diagram. Plotted values and histograms represent average value per site.

## 6.4 Magnetic fabric parameters

The magnetic anisotropy  $Pj$  (see definition in Appendix B) ranges from 1.006 up to 1.151 with a mean value around 1.037. The spread of the anisotropy increases progressively with increasing  $K_m$  values up to  $10^{-3}$  SI where it reaches a maximum of 1.11 (Fig. IV-13b). At the sample core and outcrop scale,  $Pj$  is quite low but seems to be constant (Fig. IV-15ab). Averages between cores of different textures from the same outcrop indicates that in general, specimens presenting a macroscopic mineral foliation are more anisotropic and pull the mean  $Pj$  to higher values (Fig. IV-15a).  $Pj$  is not correlated to the magnetic mineralogy (Fig. IV-13bf).

**Fig. IV-14:** Maps with (a) bulk susceptibility  $K_m$ , (b) degree of anisotropy  $P_j$  and (c) the shape parameters  $T$  averaged value. Colored background map is obtained through spline interpolation method.



Most of analyzed sites have a shape parameter  $T$  lying in the linear, planar to plano-linear or plato-linear field, with an average value of 0.055 (Fig. IV-13c).  $T$  is not dependent of the magnetic mineralogy (Fig. IV-13df). Only rare sites are strictly linear whereas many more sites are strictly planar (Fig. IV-13cdef), but no spatial trend can be seen in a map view (Fig. IV-14c).  $T$  does not seem to be correlated with the bulk susceptibility of rocks but seems to be more plato-linear for high  $P_j$  values (Fig. IV-13 cdef).  $T$  can vary from one extreme to the other in specimens from the same core especially for cores with pegmatitic textures (Fig. IV-15b).

## 6.5 Magnetic foliation and lineation

The magnetic foliation corresponds to the plan containing the maximum ( $K_1$ ) and the intermediate ( $K_2$ ) axis of susceptibility. The pole of the magnetic foliation corresponds to the minimum axis of susceptibility ( $K_3$ ). The magnetic lineation corresponds to the orientation of the maximum axis of susceptibility ( $K_1$ ).

At the outcrop scale, the orientation of the main axis of the magnetic ellipsoid is rather constant, except for pegmatitic specimens. Nevertheless, the mean declination and mean inclination of  $K_1$  and  $K_3$  are usually similar between cores with different textures. Exceptions are represented by sites 31, 54, 58, 23 and 41 for the orientation of  $K_1$ , where variations of more than 30 degrees of inclination and up to 90° for declination are measured between cores of different textures from the same outcrop (Fig. IV-15ce). For such cores,  $T$ -values indicate that the shape of the AMS ellipsoid is plato-linear to planar and therefore  $K_1$  orientation is not representative (Fig. IV-15e). Conversely, the orientation of the short magnetic axis ( $K_3$ ) is highly variable for a few sites that are plato-linear to linear, i.e. where the  $K_3$  orientation is meaningless (Fig. IV-15df).

At the scale of the pluton, the orientation of the principal susceptibilities is rather constant in the CZ and IZ (Fig. IV-16). The magnetic foliation pole for sites with planar and planar to plato-linear magnetic ellipsoid is usually sub-horizontal and gently plunges to the north or to the south. As a consequence, magnetic foliation poles define two maxima which correspond to a ENE-WSW striking vertical magnetic foliation steeply dipping to the north or south (Figs IV-16a & IV-17a). For sites with linear and linear to plato-linear ellipsoid,  $K_1$  (the magnetic lineation) shows a well-defined sub-vertical maximum (Fig. IV-16b). A few sites lying close to metapelitic xenoliths are slightly shifted major susceptibility axis with respect to surrounding sites (e.g. stations 35 and 36).

Approaching the margins of the pluton,  $K_1$  and  $K_3$  have different orientations but still preserve locally the similar orientations than to the pluton core (e.g. station 49). It corresponds to a poorly defined foliation (linear magnetic ellipsoid) that is moderately dipping to the NW,

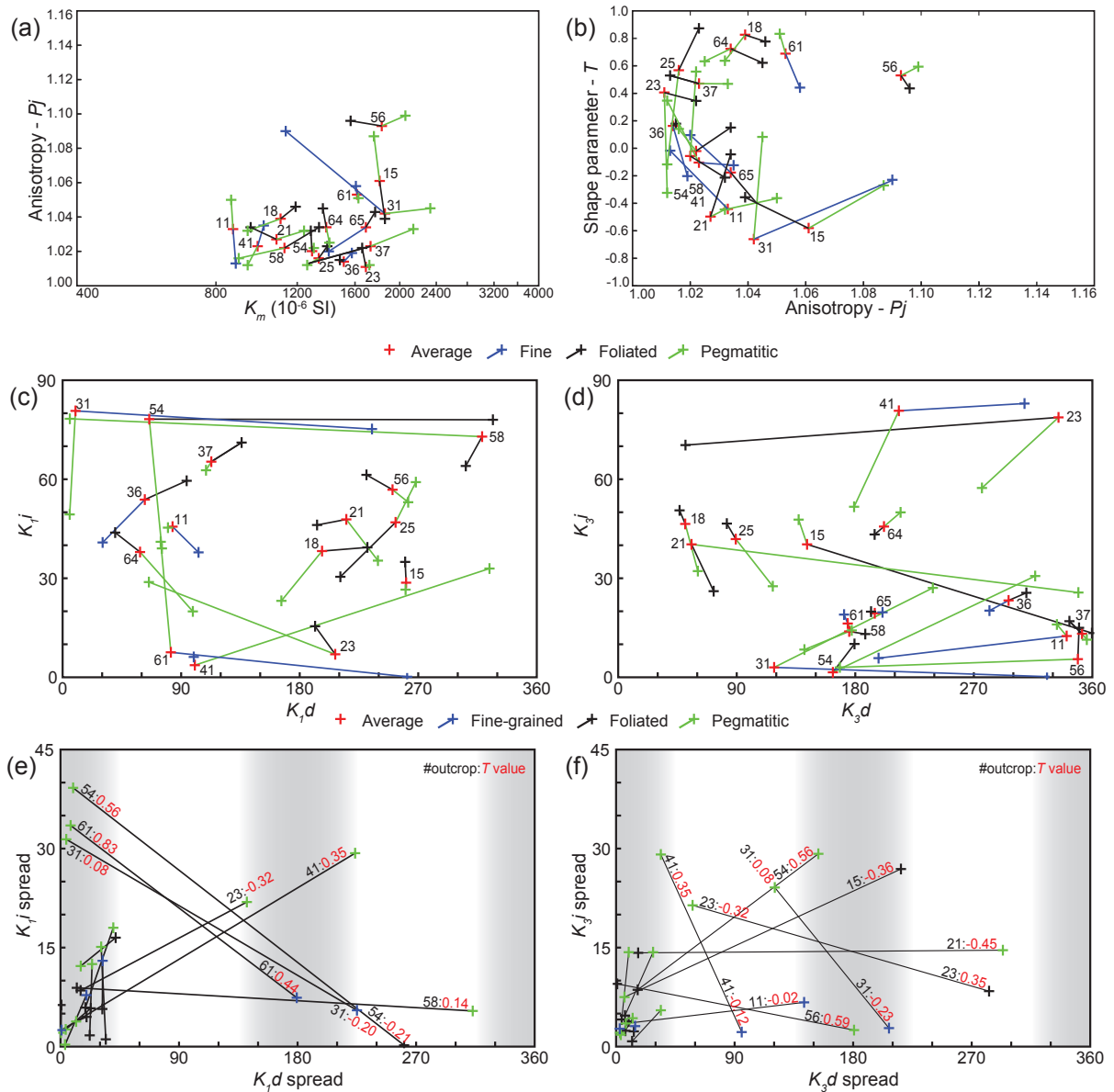


**Fig. IV-15:** Averaged AMS parameters / textures relationship for cores and outcrops with different magmatic textures (fine-grained, foliated and pegmatitic). (a)  $P_j$ - $K_m$  and (b)  $T$ - $P_j$  diagrams. Inclination-declination diagrams for the (c) long axis  $K_i$  and (d) the short axis  $K_j$ . Difference between mean outcrop value and different textural groups for (e) the long axis  $K_i$  and (f) the short axis  $K_j$ . Mean  $T$ -value for each textural group is indicated. Light grey background indicates  $\sim 180^\circ$  variations in declination.

at high angle with respect to the foliation of the core. The magnetic lineation is moderately plunging parallel to the foliation trend. In the outermost part of the pluton, the ellipsoid is planar, with foliation trend parallel to the pluton margin steeply to and moderately dipping out of the pluton (e.g. to the W in the western rim). There, one outcrop has a sub-horizontal foliation (station 23). This group of data defines outliers values in Fig. IV-17a.

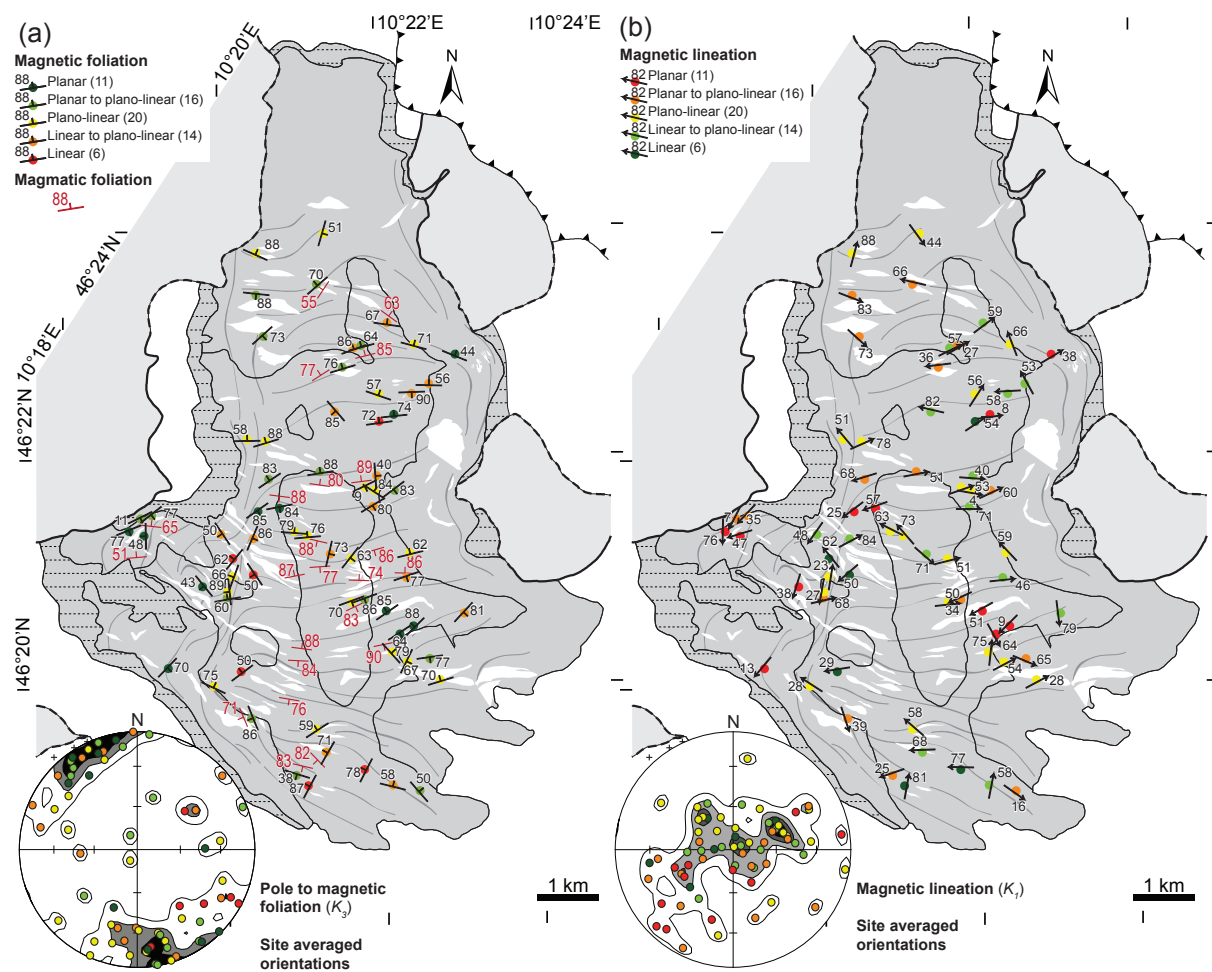


**Fig. IV-16:** Maps of (a) magnetic and magmatic foliations and (b) magnetic lineations. Color code indicates shape categories defined by the shape parameter  $T$  from red (not reliable orientation, linear for  $K_f$  orientation and planar for  $K_l$  orientation) to green (reliable orientation, planar for  $K_f$  orientation and linear for  $K_l$  orientation). Stereonet of poles to magnetic foliation ( $K_f$ ) and magnetic lineations ( $K_l$ ) are plotted with equal area on lower hemisphere projection.

## 7. DISCUSSION

### 7.1 Timing of pluton emplacement and contact metamorphism

#### 7.1.1 Magmatic rocks

U–Pb ages on magmatic zircons from the Sondalo gabbro are similar within error, ranging from *ca.* 289 ± 4 Ma to 285 ± 6 Ma. These results are in line with previous Sm–Nd dating of 300–280 Ma (± 10–12 Ma, Tribuzio *et al.*, 1999) and the U–Pb zircon age of 270 Ma (Bachmann & Grauert, 1981).

The oldest concordant age in magmatic rocks is found in a diorite sample (M28B73) at *ca.* 289 ± 4 Ma. Notably, most of the oldest zircon grains from this sample display steep slopes of HREE and high Eu anomalies, which may indicate the initial crystallization of a garnet-free magma associated with well crystallized plagioclase (Rubatto, 2002). In contrast, the reduction of negative Eu- anomaly in younger zircon grains (Fig. IV-9a) indicates a mixing with a less evolved liquid where plagioclase had not completely crystallized. The associated lower  $\text{Yb}_n/\text{Gd}_n$  values point to a progressive depletion of the residual liquid, generally interpreted as reflecting a progressive crystallization of garnet, a mineral which is observed in the sample. Ilmenite and biotite are the main hosts for Nb and Ta, but biotite incorporates preferentially Nb over Ta in contrast to ilmenite (Stepanov & Hermann, 2013; Xiong *et al.*, 2011). The inverse correlation between the Nb/Ta ratio and the Ta content coupled with the decrease of Ta with decreasing  $\text{Yb}_n/\text{Gd}_n$  (Fig. IV-9b) thus indicates that magmatic ilmenite is the main phase that fractionates Nb over Ta during crystallization. The weak decrease of Hf content (Fig. IV-9c) is not consistent with its expected increase during magmatic differentiation (Hoskin & Schaltegger, 2003; Linnen & Keppler, 2002). This may be explained by the crystallization of magmatic ilmenite synchronously with zircon crystallization, during or after the crystallization of plagioclase.

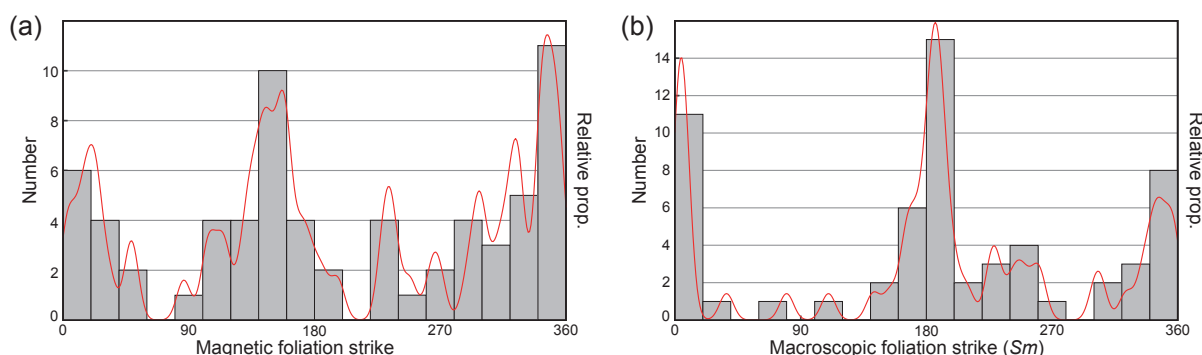


**Fig. IV-17:** Histograms and relative probability of (a) magnetic foliation strike and (b) macroscopic foliation strike.

Field observations point to an increasing garnet content in magmatic rocks towards the metapelitic xenoliths, indicating an increasing magma hybridization by crustal assimilation. This is supported by the decreasing  $\text{Yb}_{\text{n}}/\text{Gd}_{\text{n}}$  ratio in the presence of garnet, a phase generally enriched in HREE (diorite sample M28B73). In the absence of magma mingling structures, it is proposed that the mafic magma is contaminated by the liquid derived from the partially molten metapelites. In such case, a progressive enrichment in LREE, Hf and U is expected in the residual liquid and therefore in zircon. The decreasing Hf and U contents (Fig. IV-9c) may be due to the lack of resorption of Hf and U-rich phases, respectively biotite and zircon, in migmatites of the BZ, i.e. where the diorite sample was collected. The residual liquid might be progressively depleted in Hf during the crystallization of magmatic ilmenite. Alternatively, magma contamination is recorded in trace element compositions of gabbros and Ol-gabbros from the CZ and IZ (Tribuzio *et al.*, 1999).

The slightly younger concordant ages of the two diorites sampled at the western margin of the pluton lie at  $285 \pm 2$  Ma and  $285 \pm 6$  Ma. The moderately steep to flat HREE profiles (low  $\text{Yb}_{\text{n}}/\text{Gd}_{\text{n}}$  values) combined with strong to moderate Eu anomalies indicate that zircons crystallized in the presence of garnet and plagioclase. The apparently increasing Hf concentration in zircon indicates fractionation during crystallization (Hoskin & Schaltegger, 2003; Linnen & Keppler, 2002).

### 7.1.2 Metamorphic rocks

Leucosome and migmatite samples collected at the same outcrop have similar characteristics. The concordant age of  $288 \pm 4$  Ma for leucosome sample BPA 003-12d is similar (within error) to the lower intercept age of  $289 \pm 4$  Ma in the migmatite. The very low  $\text{Yb}_{\text{n}}/\text{Gd}_{\text{n}}$  coupled to a moderate negative Eu-anomaly attest the presence of garnet and plagioclase during the crystallization of zircon in both samples. In agreement with the Sil–Bt assemblage in restitic parts of the migmatites, the commonly low U value indicates that partial melting of the metapelites did not reach the biotite-out reaction and/or zircon dissolution.

Finally, zircons in sample BPA 109-12c point to a concordant age of  $277 \pm 3$  Ma that is poorly constrained by only four concordant analyses on 2 grains. One older and concordant age is similar to the main magmatic pulse around 288 Ma. All analyses have a coherent REE signature with a moderate HREE-enrichment and a moderate negative Eu-anomaly indicating that zircon crystallization occurs in presence of feldspar but with low garnet content. The higher  $\text{Yb}_{\text{n}}/\text{Gd}_{\text{n}}$  in this leucosome compared to the two previous samples may indicate a mixing with mafic magmas. The younger age of this sample with respect to the other dated rocks may be due to (1) late-crystallization of zircon grains in this metamorphic sample in agreement with

their higher Eu-anomaly, (2) younger lead loss, or (3) younger and minor magma injection that may be related to the pegmatitic dykes around the pluton, coeval with the tourmaline-bearing Martell granite (275–260 Ma; Bockemühl, 1988; Grauert *et al.*, 1974b; Mair & Schuster, 2003).

### 7.1.3 Synthesis

To sum up, ages from both magmatic and metamorphic rocks are similar within error, ranging between  $289 \pm 4$  and  $285 \pm 6$  Ma. In plutonic rocks zircon crystallizes after plagioclase (presence of Eu-anomalies). Thus, we stress that it records the final crystallization of the magmatic melt, and not older processes associated to magma ascent or post-emplacement alteration.

## 7.2 Magmatic and magnetic fabrics

The petrofabric of the rocks from the Sondalo gabbro are defined by the shape-preferred orientation of plagioclase, pyroxene, hornblende and rarely biotite. This fabric corresponds to a mineral preferred orientation coherent from the outcrop to the thin-section scale. This fabric is considered to be of magmatic origin based on the following observations: (1) the presence of sheeted zones with rhythmic layering (Fig. IV-4ab), (2) the strong shape preferred orientation of euhedral and subhedral crystals with no sub-solidus recrystallization (Figs IV-4d & IV-5c), and (3) the presence of vertical mafic compacted levels with a preserved preferred orientation of the mafic minerals (pyroxenes) intergrown by undeformed poikilitic plagioclase (Figs IV-4c & IV-5a). Minerals were therefore oriented during magma flow due to numerous processes such as velocity gradients (e.g. Benn & Allard, 1989; Cañón-Tapia & Chávez-Álvarez, 2004), compaction and extraction of felsic liquids (e.g. Higgins, 1991; Nicolas, 1992).

In the Sondalo gabbro, the variation of the magnetic susceptibilities is correlated to both the lithology and the magnetic mineralogy. The AMS signal is mostly dominated by ferromagnetic magnetite and pyrrhotite for samples with the highest  $K_m$  values, whereas both ferromagnetic and paramagnetic (e.g. pyroxene, amphibole) minerals contribute to the signal for samples with the lowest  $K_m$ . The measured magnetic foliation orientations are remarkably similar to the observed macroscopic magmatic fabrics (compare Figs IV-17a and IV-17b). This is due to mineral alignment in the magmatic foliation (Fig. IV-5e) or late crystallization of opaque minerals along already crystallized and oriented minerals (e.g. pyrrhotite with poikilitic texture) that can form a template in which ferromagnetic minerals will grow (Hrouda *et al.*, 1971). Such a late-crystallization of opaque minerals is also indicated by zircon trace element compositions (see above section). A second important process is the growth of exsolved magnetite along lattice anisotropies of pyroxene typically represented by the [110] cleavage

planes (in similar position to ilmenite in Fig. IV-5f). Their small size indicates that they are single-domain minerals where AMS is controlled by the shape of the grain (Bouchez, 2000). Consequently, the  $K_z$  axis will be defined by the intersection of [110] cleavage planes in pyroxene, which is parallel to the crystallographic  $c$ -axis. Both mechanisms indicate that ferromagnetic grains mimic the orientation of the frame constituted of silicate minerals, explaining the high concordance between the petrofabric and the magnetic fabric orientations (e.g. Yaouancq & MacLoed, 2000).

In the CZ, the magmatic and magnetic foliations are steeply N- or S-dipping. These structures are parallel to the elongated metapelitic rafts and their internal foliation, and are in continuity with the host-rock planar structure Sc2. Therefore, we assume that magma flowed vertically along the host metapelitic foliation, and the progressive lateral widening of the pluton left xenolithic rafts. The position of rafts in the western part of the pluton indicates that these were not strongly re-oriented during emplacement of mafic magmas. There, the AMS parameters are highly variable and agree with local perturbations of the structural trend, suggesting that the flow field is wrapping around the xenoliths. Moreover, considering a late/secondary growth of ferromagnetic minerals, the parameters probably do not fully reflect the magnitude of strain and symmetries (Borradaile & Henry, 1997).

In the BZ, both magnetic and magmatic foliations are moderately to steeply dipping with a trend roughly following the margin of the pluton. Notably in the western BZ, the foliations are steeply NE- or SW-dipping. In this region, shape parameters indicate a planar ellipsoid. This foliation is parallel to the Sc3 planar structures of the migmatitic contact aureole (Fig. IV-16a) and is rarely found in metapelitic xenoliths or farther from the pluton margin. In *chapter III*, we showed that this Dc3 deformation was active at supra-solidus conditions. In this western part, one outcrop (station 23) presents a shallow-dipping foliation highly contrasting with the overall steep structures. Due to the fabric orientation and the location of the outcrop close to the Eita shear zone (separating the Grosina unit from the Campo unit, Fig. Iv-2a), and the slight retrogression of the sample at greenschist-facies conditions, the AMS fabric is likely associated to deformation produced by the sub-horizontal Eita shear zone (Meier, 2003; Mohn *et al.*, 2012) rather than syn-magmatic processes.

The transition between both foliations is hard to decipher. A first scenario could involve the development of both foliations at the same time due to different primary flow field in the CZ and BZ. Differences in the shape of the AMS ellipsoid may be due to local variations. For example, a planar ellipsoid may be due to a higher flattening component in the rim of the pluton due to lateral compaction during magma flow.

Alternatively, the mesh texture of magmatic rocks in the transitional zone may point to partial transposition of the E-W trending foliation (Sm) into the subsequent N-S trending foliation (Sm+1, Fig. IV-5d; Žák *et al.*, 2008). In such a case, the overprinting relationships between the two fabrics are documented in the western margin of the central part, between stations 15 and 52 (Fig. IV-16a). The magnetic foliation (moderately dipping to the west) is poorly constrained because of quite systematic linear magnetic ellipsoid due to the superposition of the two magmatic fabrics leading to prolate magnetic ellipsoid (Schulmann & Ježek, 2012). On the grain scale, the transposition occurs without kinking or folding of the previous fabric indicating that crystals were still separated by a liquid fraction (crystal mush). The late and secondary crystallization of ferromagnetic minerals will mimic this petrofabric and probably have an elongated shape, resulting in an elongated (linear) AMS ellipsoid.

Foliated rocks are crosscut by syn-magmatic and pegmatitic dykes which locally lie at high angle to the main magmatic fabric. In spite of the absence of a clear magmatic fabric for such textures, AMS parameters and orientation of the main susceptibility axis are quite consistent with the surrounding foliated rocks. This is true except for the  $K_1$  orientations of planar ellipsoids and the  $K_3$  orientations of linear ellipsoids. Therefore we assume that the pegmatitic dykes sometimes use the host anisotropy or constitute late crystallization pockets that solidify at the end of the principal magmatic flow.

### 7.3 Magma ascent mechanisms

We assume that the gabbro is still in its original orientation and was not tilted during subsequent tectonic events based on the following arguments: (1) the Campo unit record a weak Alpine overprint without evidence of major structures that may accommodate the tilting, (2) the top of the Sondalo gabbro and Campo unit is cross-cut by a sub-horizontal Jurassic shear zone over more than 20 km, (3)  $P-T$  conditions are similar all along the shear zone and apparently around the pluton, and finally (4) the Campo unit crops out continuously over more than 40 km with always similar regional  $P-T$  conditions (see *chapter III*). The Sondalo gabbro documents essentially sub-vertical magmatic foliations with sub-vertical magmatic lineations pointing to a vertical magmatic flow. Using structural, metamorphic and geochronological data, we propose a three-stage model for mafic magma ascent in the middle crust.

#### 7.3.1 Stage 1: magma flow along host-rock anisotropy

The Sondalo gabbro was emplaced during the Permian in the Campo unit. This unit is characterized by a well-developed, pre-intrusion, regional Sc2 fabric steeply dipping either to the northeast or southwest (Fig. IV-2a). During its intrusion, the gabbro incorporated numerous

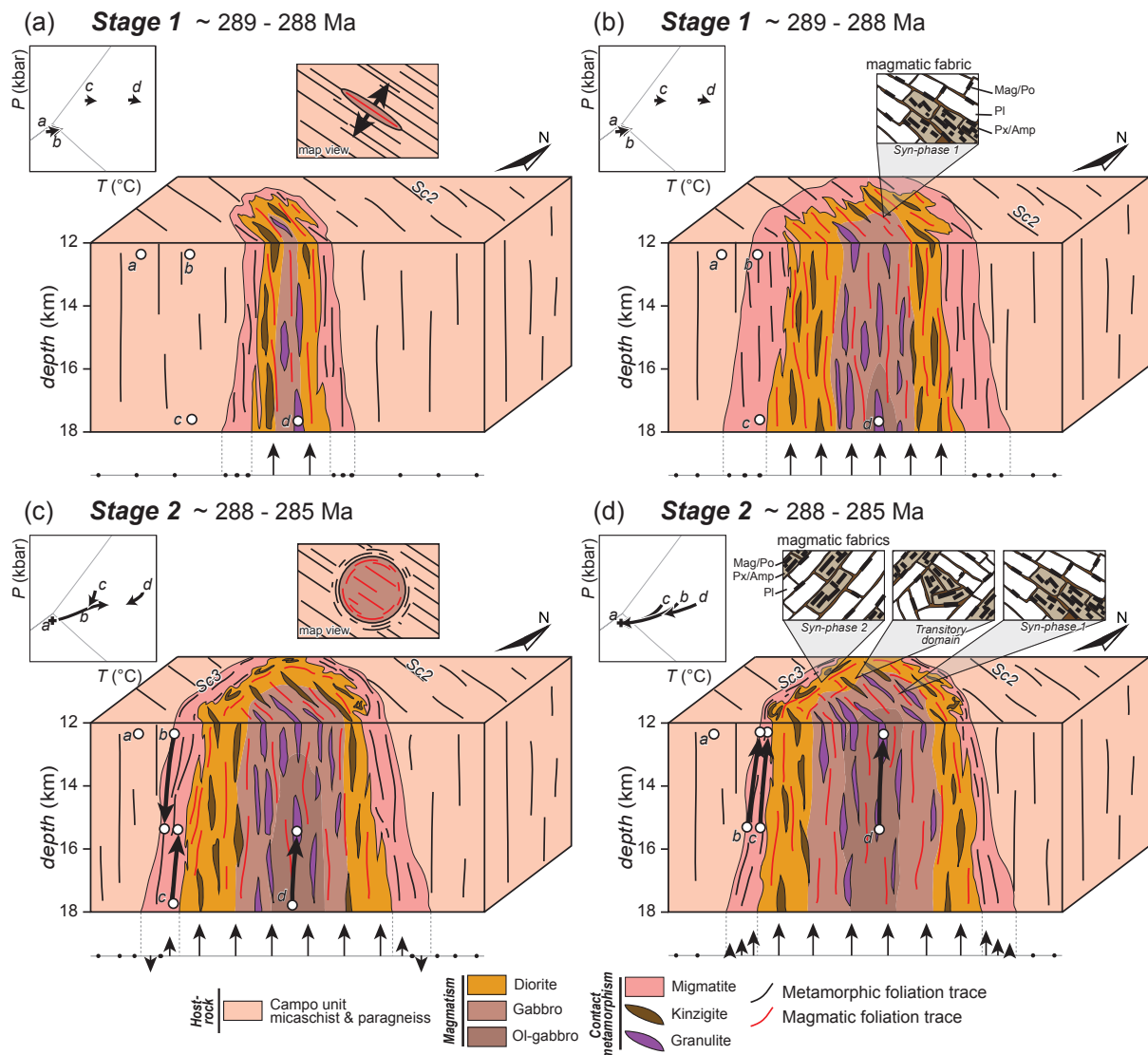


**Fig. IV-18:** Evolutionary model depicting the emplacement mechanism during the multi-stage intrusion of the Sondalo gabbro. (a,b) Fracture-controlled magma ascent and (c,d) en-masse ascent of the core. Insets illustrate the P-T evolution of metasediments (see chapter III for details), map view synthetic model and microstructures of magmatic rocks and position of ferromagnetic minerals. See text for details.

xenoliths of the host-rock. The present-day shape preferred orientation of the xenoliths, which is parallel to the regional Sc<sub>2</sub> fabric, indicates that most of them preserve their orientations and were not tilted during the intrusion (Fig. IV-3c). In the core of the pluton, the magmatic foliation is parallel to the xenolith orientation, with a mostly vertical magnetic lineation. Therefore, magmatic flow occurred vertically in between the metapelitic screens without a significant deformation of the host-rock at this stage. Locally, the magma flow may wrap around the xenoliths and eventually the margins of the pluton, but is probably unable to significantly deform the host-rock.

The presence of pre-Sc3 andalusite, that are statically growing far from the intrusion, as well as pre-Sc3 leucosomes in the contact aureole indicates that HT metamorphism occurred before the subsequent Sc3 deformation. In contact with the fertile metapelites, mafic magma caused HT contact metamorphism grading from upper amphibolite conditions in the contact aureole to granulite facies conditions in the core of the pluton (*chapter III*). Granitic melt segregated from the migmatites contaminated the mafic magma, as indicated by the trace element composition of zircon, and the LREE enrichment of the magma with respect to a parental N-MORB liquid (Tribuzio *et al.*, 1999). The highest metamorphic conditions are recorded in the core of the pluton, where Grt–Sil–Crd granulites equilibrated at 5.5 kbar/930°C, indicating that the presently exposed xenoliths in the core of the pluton were located at around 18 km depth during this intrusion stage. Conversely, the presence of andalusite in the host-rock and the contact aureole indicates a shallower depth of ~15 km ( $P < 4.5$  kbar) during the intrusion. The emplacement of mafic magmas occurred around  $289 \pm 4$  Ma. It is in agreement with the similar age obtained in two migmatite samples of the contact aureole (BPA 003-12c and d) dated at  $289 \pm 4$  Ma and  $288 \pm 5$  Ma.

### 7.3.2 Stage 2: rise of the core of the pluton and material transfer in the aureole

The second intrusion stage is indicated by a change in the rheological behavior of the host-rock with respect to the magma. The steeply north-dipping magmatic foliation which originated during phase 1 is transposed into a sub-vertical to vertical magmatic foliation that follows the border of the pluton. This process is essentially documented in the western margin of the pluton, where the strike of this new fabric lies at high angle to that of the foliation in the CZ. The new magmatic foliation is concordant with the Sc3 foliation which is essentially present in the contact aureole and in few marginal xenoliths. This relation is interpreted as the deformation of the host rock during a second phase of the pluton emplacement. The pluton is still increasing in size, as indicated by the incorporation of a few folded and deformed xenoliths (e.g. in the westernmost part of the pluton, Fig. IV-2a). Eventually, the end of the intrusion may be marked by compaction in the rim of the pluton, explaining the planar AMS ellipsoid in the BZ.

Notably, the host Campo unit away from the intrusion is unaffected by the deformation (Fig. IV-18ab). In the *chapter III*, we showed that during Dc3, parts of the contact aureole are buried from ~4 kbar to 5.2 kbar and then exhumed back to 4 kbar (Fig. IV-18cd), whereas originally deeper rocks are exhumed from 6 kbar to the final emplacement depth of around 4 kbar (Fig. IV-18). Synchronously, internal xenoliths are exhumed and therefore transported from 5.5 kbar to the same final emplacement depth of 4 kbar. Consequently, the syn-emplacement

Dc3 is associated to pervasive and ductile deformation associated to burial and exhumation of the host-rock in the contact aureole (Fig. IV-18cd). Alternatively, the requested burial and exhumation may be lowered by tectonic overpressure processes due to magmatic efforts or shearing in the contact aureole (e.g. Mancktelow, 2008). As xenoliths are exceptionally parallel, aligned along the host-rock foliation and does not seem to present different  $P-T$  evolutions, we suggest that all xenoliths were exhumed during the *en-masse* magma ascent episode (Fig. IV-18cd). We suggest that shearing also occurred at the margin of the pluton and produced the magmatic foliation in the BZ while the core of the pluton remained only poorly affected.

An upper age limit for this process is given by the  $ca.$   $288 \pm 5$  Ma of migmatites showing evidence for supra-solidus Dc3 deformation (BPA 003-11c and d). A lower limit is  $285 \pm 2$  Ma, given by diorite sample GM601 apparently cross-cutting the Sc3 deformation of the migmatites. Given the lack of evidence for sub-solidus deformation, we propose that the activity of Dc3 is restricted to supra-solidus conditions, and therefore unrelated to the activity of a shear zone as documented for some Permian lower crustal magmatic bodies (Zibra *et al.*, 2012).

### 7.3.3 Stage 3: late-magmatic activity

The magmatic activity in the Sondalo gabbro continues after the final ascent with minor syn-magmatic dyking, as indicated by the  $285 \pm 6$  Ma diorite and the  $285 \pm 2$  Ma diorite cross-cutting the Sc3 foliation in the migmatitic contact aureole. Finally, a later and minor magmatic pulse seems to occur around  $277 \pm 3$  Ma, but this age needs to be better constrained. Alternatively, this age could correspond to the late crystallization of zircon in metamorphic rocks related to the main magmatic intrusion.

## 7.4 Discussion with a simple thermal model

We apply a simple 1D thermal model of the intrusion to estimate the thermal effect on the host-rock and model the expected thickness of the migmatitic aureole. Here, we will only consider the thermal diffusion as heat input and no other additional heat source following the approach of Spear (1993). Model setup description can be found in Appendix C.

### 7.4.1 Results

We consider a total thickness of 3.6 km accounting for the middle of the pluton, where the migmatitic aureole has a thickness ranging from 500 to 700 m, inferred from field observations (considering an average dip of  $70^\circ$  of the aureole). After Cermak & Rybach (1982), a randomly oriented schist has a thermal conductivity  $K = 3.14 \text{ W.m}^{-1}\text{K}^{-1}$ , a specific heat of  $c$

$= 800 \text{ J} \cdot \text{kg}^{-1} \cdot \text{K}^{-1}$  and garnet-micaschists have a mean density of  $\rho = 2700 \text{ kg} \cdot \text{m}^{-3}$ . The initial temperature of the magma is constrained to  $T_0 = 1100^\circ\text{C}$ , a mean value for a mafic magma whereas the host-rock temperature  $T_s$  is calculated for different geothermal gradients using at a depth of 12 km (4 kbar estimated for the final emplacement of the pluton; *chapter III*). The maximum thickness of the migmatitic aureole is bounded at  $\sim 650^\circ\text{C}$ , corresponding to the solidus temperature of water-saturated granites (e.g. Spear *et al.*, 1999; Vielzeuf & Holloway, 1988; White *et al.*, 2004).

Results of the thermal modeling are represented in Fig. IV-19 for five different geothermal gradients between 30 and  $50^\circ\text{C} \cdot \text{km}^{-1}$ . The estimated thickness of the migmatitic aureole and the delay between intrusion and peak temperature are reported in Fig. IV-19. For a geothermal gradient of about  $30^\circ\text{C}/\text{km}$ , the migmatitic aureole is around 400 m thick and the maximal temperature is achieved at the aureole external margin at 0.04 Ma. In contrast, for a very high geothermal gradient of  $50^\circ\text{C}/\text{km}$ , the expected migmatitic aureole is 6.9 km thick, and  $T_{max}$  occurs at 0.82 Ma for the external margin of the aureole. Base on petrological data from the Eastern Alps, Schuster *et al.* (2001) proposed a geothermal gradient of  $35^\circ\text{C}/\text{km}$  during late-Variscan stages, followed by a reheating reaching a geothermal gradient of  $45^\circ\text{C}/\text{km}$  after the magmatic intrusions. Similarly, we estimated the geothermal gradient to  $35\text{--}40^\circ\text{C}/\text{km}$  before the magmatic intrusion using petrological data from the study area (*chapter III*). In such conditions, the modelled migmatitic aureole is 0.8–1.4 km thick and the peak temperature is achieved around 0.06–0.10 Ma (Fig. IV-19).

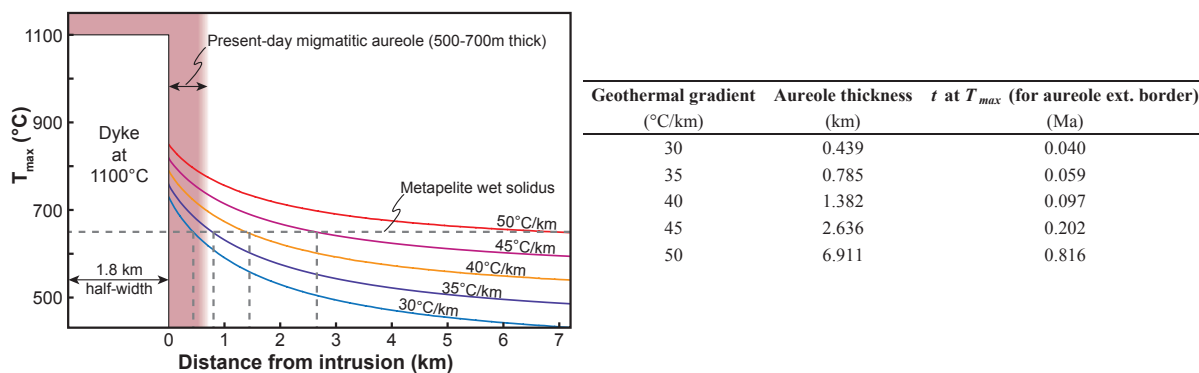


**Fig. IV-19:** Evolution of the maximal temperature experienced by the host-rock due to the intrusion of a 3.6 km wide dyke intruding at  $1100^\circ\text{C}$  as a function of distance from the intrusion. The maximal temperature is calculated for different geothermal gradients.

#### **7.4.2 Implication of the intrusion mechanism on the contact aureole**

The estimated thickness of the migmatitic metapelites ring around the pluton has to be considered as a minimum value as (1) the modelled thickness of the pluton was taken at its thinnest part, (1) numerous heat inputs are not considered such as magma convection or upward flow (Brown, 1994), and (3) the instantaneous intrusion is likely replaced under natural conditions by incremental emplacement of magma, that may increase the thickness of the thermal aureole (Annen, 2011).

The model suggests that, except for the coldest geothermal gradient – which is possible in Early Permian times – the calculated thickness is thicker than the real migmatitic aureole of 500 to 700 m. Although the thermal model needs to be more developed in terms of emplacement dynamics (e.g. small and repetitive magma injection), we attribute the discrepancy to Dc3 shearing along the margins of the pluton during the stage 2 ascent of the core of the pluton. This shearing thinned the migmatitic aureole (Fig. IV-18d) in a similar way than presented by Flood & Vernon (1978).

### **7.5 Implications for intrusion dynamics**

With the exception of the late-magmatic evolution that is not dominant, the intrusion and emplacement of the Sondalo gabbro can be divided into mainly two stages with contrasted magma/host rock relationships.

#### **7.5.1 Stage 1**

The first stage of the magma ascent used the mechanical anisotropy of the host-rock without deforming it. Therefore, the mode of ascent is likely to be controlled by fracture opening along the pre-existing host-rock foliation that constitutes a mechanical anisotropy (Fig. IV-18ab). Usually crack orientation during dyking is controlled by  $\sigma_1$  and  $\sigma_3$  orientations (Lister & Kerr, 1991). However, in case of small deviatoric stresses that may occur in the middle and lower crust, cracks could open using the host-rock anisotropy such as bedding or main foliation (Lucas & St-Onge, 1995). The magma flow can occur through dykes opened either by the hydrostatic pressure generated by the magma, or by tensional tectonic forces or passive invasion of the host-rock generating xenolithic blocks referred in the literature to as the “stoping” process. This “stoping” process may play a minor role in the magma ascent because it is more frequently active in the upper-crust than in the middle-crust (Paterson *et al.*, 1991) and less likely to create enough space for the magma to ascent (Glazner & Bartley, 2006). As

modelled by Gerya & Burg (2007), the formation of pluton through dyking is possible without being tectonically assisted. Therefore the relative role of the magma hydrostatic pressure and the tectonic forces in the first stage of emplacement is hard to decipher.

### 7.5.2 Stage 2

The ascending magma is expected to switch from diapirism to dyking as it meets colder and stiffer rocks upward (Weinberg, 1996). The early intrusion of the gabbro occurred in the cold and stiff metasediments of the Campo unit that consequently favored the formation of dykes parallel to the pre-existing steep Sc2 foliation of the metasediments. Bringing heat into fertile metasediments, the migmatitic contact aureole was developed around the dyke system. With a reasonable melt-content, the strength of metasediments drastically decreases (e.g. Arzi, 1978), migmatites started to flow and the structural aureole around the pluton was developed. The lubrication of the aureole of the crystallizing pluton inverted the rheology of the magma with respect to the host-rock. It allowed the magma to rise a few kilometers more by shearing and probably thinning of the contact aureole while preserving the structure of the core of the pluton, maybe already behaving as a solid-state body (Weinberg & Podladchikov, 1995). This change in deformation style is an example showing that the thermal effect of the intrusion may be used at late stages of magma ascent (Weinberg & Podladchikov, 1994).

The vertical displacement/exchange of material in the contact aureole, referred to as (near-field) material transfer processes (Paterson & Fowler Jr, 1993), minors the role of the model of in-situ growth of pluton by lateral displacement of the host-rock referred in the literature as “ballooning” (e.g. Ramsay, 1989), disputed e.g. by Paterson & Vernon (1995). Eventually, this may occur in the latest stages of the magma ascent (Gerya & Burg, 2007), but is only a minor contribution to the emplacement process. The required architecture for the development of a diapir, with a density inversion between the light underlying magma and the heavy overlying host rock (e.g. van den Eeckhout *et al.*, 1986), implicit in the term diapir, is unlikely here as the mafic magma is denser than the metasedimentary hot-rock. Braga *et al.* (2001) argue that extraction of anatetic melts from surrounding and xenolithic migmatites produce a dense melanosome able to sink in the mafic magma. This may trigger a potential relative motion of sinking xenoliths in the magma, but does not account for magma ascent over long distances (Glazner & Bartley, 2006). Eventually, fractional crystallization and assimilation of crustal-derived melts has the ability to buffer magma buoyancy, helping its ascent and entraining more mafic and dense magma (e.g. Cruden *et al.*, 1995).

## 7.6 Implications for the Permian post-Variscan extension

In the Permian post-orogenic magmatic system, numerous authors have proposed a genetic link between lower crustal mafic magmas (e.g. Ivrea-Verbano mafic complex) and upper crustal granitoids (e.g. Serie dei Laghi, Schaltegger & Brack, 2007; Sinigoi *et al.*, 2011). The main arguments are the comparable ages (Schaltegger & Brack, 2007), geochemical affinities (see e.g. Boriani & Giobbi, 2004) and close field associations (e.g. Hansmann *et al.*, 2001; Müntener *et al.*, 2000). In this study, we suggest that the Sondalo gabbro may represent a feeding system, transferring magma through the middle crust and therefore providing a link between magmatic systems in the lower and upper crust.

Evidence of how magmas are extracted from lower crustal bodies to reach shallower levels are documented in the Ivrea-Verbano zone (e.g. Handy & Streit, 1999; Schaltegger & Brack, 2007). The mafic complex is unfortunately truncated at its top by the Permian Cossato-Mergozzo-Brissago line/shear zone (CMB; Snock *et al.*, 1999). Nevertheless, the CMB is often “decorated” by syn-kinematic intrusions of mafic melts (the so-called appinites; Boriani *et al.*, 1990) supposed to be extracted from the underlying mafic body (Handy & Streit, 1999; Mulch *et al.*, 2002). Therefore, mafic melts may be extracted from lower crustal magmatic systems along shear zones (Fig. IV-20). Such structures may trigger the movement of mafic magma from high hydrostatic pressure areas to lower pressure ones, i.e. to mid-crustal levels. This suggests a strong link between tectonics and mafic magma ascent, and suggest that if no shear zone is developed, mafic magma will remain trapped in the lower crust, as modelled by Gerya & Burg (2007). The Sondalo gabbro may represent the continuation of the ascent of mafic magma in the

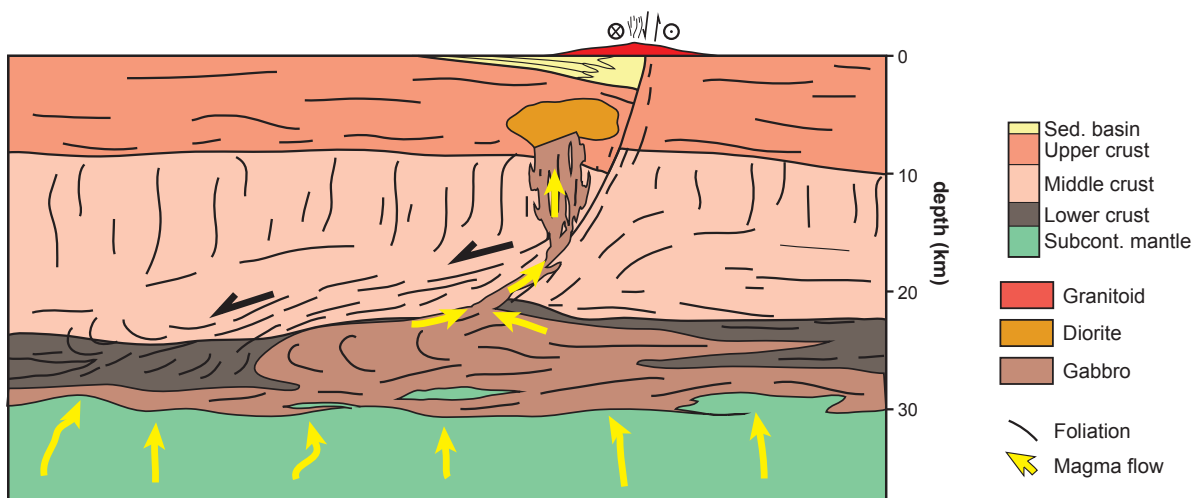


**Fig. IV-20:** Synthetic model of ascent of magma through the crust. The magma is extracted from lower-crustal mafic bodies thanks to crustal-scale shear zones. Modified after Handy & Streit (1999) and Rutter *et al.* (1993). See text for details.

continental crust linked to major shear zones although no evidence for such a structure has been documented in our study area. Eventually, mafic magma may evolve and differentiate before reaching upper crustal levels, where it eventually forms felsic intrusions.

## **8. CONCLUSIONS**

The intrusion of the Permian Sondalo Gabbro occurred in two stages, between 289 and 285 Ma. During the first stage, magma flowed upward along the sub-vertical foliation of the metasedimentary Campo unit, without apparent deformation. Synchronously, a migmatitic aureole was developed, while granulitic xenoliths were left behind by the magma progression. The second stage is characterized the *en-masse* rise of the core of the pluton, during which xenoliths equilibrated at 18 km were juxtaposed with the host-rock that remained at 12 km. The exhumation of the core occurred by shearing in the migmatitic contact aureole and in the border zone of the pluton, transposing the pre-existing magmatic and metamorphic foliations. Apparently, the intrusion is not directly associated to a shear zone or any other large-scale deformation structure. Therefore, the mechanical reasons for the magma ascent remain unclear.

## **ACKNOWLEDGMENTS**

R. van Elsas and A. Aubert are thanked for the help with mineral separation, and P. Vonlanthen and G. Morvan for the BSE and CL imaging, A. Ulianov for the help with the LA-ICPMS, and A. Longeau for the 3axes-IRM measurements.

## **APPENDIX A: GEOCHRONOLOGY: METHODS**

Zircons were separated from samples after crushing, sieving (50–250 µm) and cleaned ultrasonically. Zircons were carefully selected by handpicking under a binocular microscope and mounted in epoxy after concentration of zircon using a gold pan, hand magnet and Frantz magnetic separator. U–Pb isotopic measurements were performed at the Institute of Mineralogy and Geochemistry of the University of Lausanne using a ThermoFischer Element XR ICP–MS coupled to a NewWave UP-193 ArF excimer laser ablation system. Analytical conditions are identical to those described by Ulianov *et al.* (2012). Zircon grains were ablated with a 25–35 µm spot size at 2.2–2.5 J.cm<sup>-2</sup> with a 5 Hz repetition rate. Isotopic ratios were normalized after each ten spot analyses by the GEMOC GJ-1 primary standard (CA-ID-TIMS <sup>206</sup>Pb-<sup>238</sup>U age of 600.5 ± 0.4 Ma; Schaltegger *et al.*, unpubl. In: Boekhout *et al.*, 2012) and with the 91500 secondary standard (1065.4±0.3 Ma, Wiedenbeck *et al.*, 1995). Ages were calculated using LAMTRACE (Jackson, 2008). Additional data reduction methods can be found in Ulianov *et al.* (2012).

Zircon trace element analyses were also carried out at the University of Lausanne on an Element XR ICP–MS with a NewWave laser ablation system and normalized to the SRM 612 glass reference material (Pearce *et al.*, 1997) after each ten analyses. Apart from a spot size of 35 µm, analytical conditions are identical to those used for U–Pb dating. Data were regressed using SILLS (Guillong *et al.*, 2008).

## **APPENDIX B: ANISOTROPY OF MAGNETIC SUSCEPTIBILITY: METHODS**

At least 2 cores per site were collected, with a minimum of 10 standard specimens (23 mm in diameter and 22 mm in height) and oriented with a magnetic compass. AMS was characterized for all samples whereas magnetic mineralogy was determined for one specimen per site following the methods described below.

AMS was measured with a MFK1–A Kappabridge (AGICO, Inc operating in low field at the University of Strasbourg. Data were regressed using Anisoft 4.2 (AGICO, Inc.). To infer the magnetic susceptibility tensor ( $K$ ), the specimen is slowly rotated in a coil with an applied field of 80 A.m<sup>-1</sup> and magnetic susceptibility is measured in 48 directions. This operation is repeated for three mutually perpendicular directions. This procedure allows a very precise determination of magnetic susceptibility tensor  $K$  by least square inversion (Jelinek, 1977). The susceptibility tensor can be decomposed into three eigenvalues (principal susceptibilities,  $K_1 \geq K_2 \geq K_3$ ) and three associated orthogonal eigenvectors. While the eigenvectors are represented on a stereogram (equal area lower hemisphere projection), eigenvalues are usually combined to

infer the shape of the ellipsoid. We use the shape parameter  $T$  defined as:

$$T = \frac{\ln(K_2/K_3) - \ln(K_1/K_2)}{\ln(K_2/K_3) + \ln(K_1/K_2)} \quad (\text{Eq. IV-1})$$

and the anisotropy parameter  $Pj$  defined as:

$$Pj = \exp \sqrt{2 \left[ \left( \ln \left( \frac{K_1}{K_m} \right) \right)^2 + \left( \ln \left( \frac{K_2}{K_m} \right) \right)^2 + \left( \ln \left( \frac{K_3}{K_m} \right) \right)^2 \right]} \quad (\text{Eq. IV-2})$$

The shape parameter is interpreted as reflecting the shape of the ellipsoid: linear ( $-1 < T < -0.5$ ), linear to plano-linear ( $-0.5 < T < -0.2$ ), plano-linear ( $-0.2 < T < 0.2$ ), planar to plano-linear ( $0.2 < T < 0.5$ ) or planar ( $0.5 < T < 1$ ). The  $Pj$  parameter increases from 1 (isotropic) up to values depending on the magnetic constituents of the rocks. A third useful parameter is the mean susceptibility  $K_m = (K_1 + K_2 + K_3)/3$ , which generally relates to the magnetic phases of the rock (Rochette *et al.*, 1992).

Two ways of combining these parameters are commonly used in the AMS studies. The first one links  $Pj$  vs  $K_m$  and gives information on the influence of the magnetic mineralogy on the measured anisotropy (Fig. IV-13b). The second, which links  $T$  vs  $Pj$  (Fig. IV-13f), shows the relationship between the measured anisotropy and the shape of the ellipsoids (see e.g. Borradaile, 1988).

The investigation of coercivity-unblocking temperature spectra of ferromagnetic minerals was obtained by applying decreasing isothermal remanent magnetization saturation in three perpendicular directions (so-called 3axes-IRM) on a standard cylindrical sample, which was then stepwise thermally demagnetized in a paleomagnetic furnace, free of external magnetic fields. The isothermal remanent magnetization (IRM) in each direction is provided by an ASC impulse magnetizer (ASC Model IM-10) enabling a high field up to 1.1 T. Stepwise demagnetization was obtained in a home-made oven with a residual field of 100 nT. At each step, the magnetization was measured with a JR6-A spinner magnetometer (Agico, Inc.). The three saturation magnetizations are determined by both technical considerations and rock magnetic properties. The first applied magnetic field (associated to  $M(z)$ ) corresponds to the maximum 1.1 T provided by the device and is supposed to magnetize the high coercivity minerals. This is the high coercivity axis. The second field of 0.5 T (associated to  $M(y)$ ), applied perpendicular to the first one, magnetizes the intermediate coercivity fraction softer than 0.5 T and is called the medium coercivity axis. The last field of 0.1 T (associated to  $M(x)$ ) applied normal to the two first directions saturates the low coercivity fraction and is called the low coercivity axis. A sharp

decrease in the magnetization of a rock indicates the unblocking temperature of a phase, which is slightly lower than its Curie temperature (Lowrie, 1990).

## APPENDIX C: THERMAL MODELLING

We consider the cooling of a semi-infinite dyke of a half-thickness  $h$  (in m), governed by the Fourier law of heat conduction (in 1D):

$$\frac{dT}{dt} = K \left( \frac{\partial^2 T}{\partial x^2} \right) \quad (\text{Eq. IV-3})$$

where a solution is:

$$\frac{T - T_s}{T_0 - T_s} = \frac{1}{2} \left[ \operatorname{erf} \left( \frac{h - x}{2\sqrt{K \cdot t}} \right) + \operatorname{erf} \left( \frac{h + x}{2\sqrt{K \cdot t}} \right) \right] \quad (\text{Eq. IV-4})$$

that is equal to:

$$T = \frac{1}{2} \left[ \operatorname{erf} \left( \frac{h - x}{2\sqrt{K \cdot t}} \right) + \operatorname{erf} \left( \frac{h + x}{2\sqrt{K \cdot t}} \right) \right] \cdot (T_0 - T_s) + T_s \quad (\text{Eq. IV-5})$$

$T$  is the temperature (K),  $T_0$  the initial temperature of the dyke,  $T_s$  the initial temperature of the host-rock,  $t$  the time (s),  $x$  the distance from the center of the dyke (m) and  $K$  the thermal diffusivity of rocks (in  $\text{m}^2 \cdot \text{s}^{-1}$ ) is defined as :

$$K = \frac{k}{c \cdot \rho} \quad (\text{Eq. IV-6})$$

with  $k$  the thermal conductivity ( $\text{W} \cdot \text{m}^{-1} \cdot \text{K}^{-1}$ ),  $c$  the specific heat ( $\text{J} \cdot \text{kg}^{-1} \cdot \text{K}^{-1}$ ) and  $\rho$  the density ( $\text{kg} \cdot \text{m}^{-3}$ ).

Contact metamorphism records the maximal temperature suffered by the host-rock ( $T_{max}$ ) that is time and distance dependent, but without high-precision dating of metamorphism, only variations in distance are meaningful. We can therefore consider that  $T_{max}$  is reached when:

$$\left( \frac{dT}{dt} \right)_x = 0 \quad (\text{Eq. IV-7})$$

This implies that the temperature is maximal when  $t$  is:

$$t = \sqrt{\frac{x/h}{\ln \left( \frac{x/h + 1}{x/h - 1} \right)}} \quad (\text{Eq. IV-8})$$

This equation have solutions only for  $x/h < 1$ , therefore not in the dyke. The Eq. VI-8 has to be used in the Eq. VI-5 giving the temperature in function of distance.



---

*CHAPITRE V*

---

Le chapitre V vise à contraindre en temps l'histoire de refroidissement et d'exhumation des unités austroalpines de Campo et de Grosina. Ceci est réalisé grâce à une synthèse des âges publiés sur les deux unités, complétée par l'acquisition de nouveaux âges  $^{40}\text{Ar}/^{39}\text{Ar}$  sur amphibole, muscovite et biotite. Une première campagne d'échantillonnage et de préparation, précédant le début de mon travail de thèse, a été réalisée par G. Mohn. En revanche, j'ai procédé à toutes les étapes de collecte, de préparation et de séparation de la deuxième campagne. Les deux séries de mesures isotopiques présentées dans ce travail ont été effectuées personnellement lors de deux séjours prolongés à la Vrije Universiteit d'Amsterdam, partiellement financés par une bourse d'excellence « Eole » du réseau franco-néerlandais de l'enseignement et la recherche (RFN-FNA).

Ce chapitre est organisé en trois parties :

- Dans un premier temps, une brève synthèse de l'évolution géologique, tectonique et géochronologique des nappes austroalpines, et plus précisément des unités de Campo et de Grosina, place l'étude dans son contexte.
- Dans un second temps, les âges nouvellement acquis sont présentés.
- Dans un troisième temps, la discussion des résultats s'organise en trois parties où la validité et l'interprétation des âges sont clarifiées, mettant en valeur les potentiels effets que l'intrusion mafique aurait causé sur le système  $^{40}\text{Ar}/^{39}\text{Ar}$  dans l'encaissant. Ensuite, les nouveaux âges et les âges préexistants sont utilisés pour contraindre l'évolution des unités de Campo et de Grosina, en terme de vitesse de refroidissement, d'exhumation et de réchauffement. Cette partie s'appuie sur des modélisations de diffusion de l'argon dans les micas, à l'aide du programme DiffArgP (Warren *et al.*, 2011), modifié à partir de DiffArg (Wheeler, 1996). Enfin, un modèle d'évolution des deux unités est proposé en fin de chapitre, tentant d'intégrer les âges et les observations de terrain faites lors des campagnes réalisées au cours des étés 2011, 2012 et 2013.

Ce chapitre sera complété par une étude plus poussée de l'évolution structurale et pétrologique de Campo et de Grosina, lors de travaux postérieurs à ceux de thèse.

# **EXHUMATION, COOLING AND DEFORMATION HISTORY IN THE ADRIATIC RIFTED MARGIN NECKING ZONE: THE CAMPO/GROSINA SECTION (SE-SWITZERLAND AND N-ITALY)**

B. Petri<sup>1,2</sup>, G. Mohn<sup>3</sup>, J. R. Wijbrans<sup>2</sup>, G. Manatschal<sup>1</sup>, M. Beltrando<sup>4</sup>

<sup>1</sup>Ecole et Observatoire des Sciences de la Terre, Institut de Physique du Globe de Strasbourg – CNRS UMR7516, Université de Strasbourg, 1 rue Blessig, F–67084, Strasbourg Cedex, France

<sup>2</sup>Vrije Universiteit, Department of Geology and Geochemistry, de Boelelaan 1085, 1081HV Amsterdam, The Netherlands

<sup>3</sup>Département Géosciences et Environnement, Université de Cergy-Pontoise, 5, mail Gay Lussac, Neuville-sur-Oise, 95031 Cergy-Pontoise Cedex

<sup>4</sup>Departimento di Scienze della Terra, Università di Torino, Via Valperga Caluso 35, 10125 Torino, Italy

## **ABSTRACT**

The cooling and exhumation of the Campo unit and the overlying Grosina unit, separated by the Eita shear zone are explored by the acquisition of  $^{40}\text{Ar}/^{39}\text{Ar}$  ages on hornblende, muscovite and biotite. New geochronological data on the Grosina unit present  $^{40}\text{Ar}/^{39}\text{Ar}$  ages between 273 and 261 Ma for muscovite, and between 248 and 246 Ma for biotite. The Campo unit shows clearly younger ages between 210 and 177 Ma on hornblende (poorly constrained), between 186 and 176 Ma on muscovite and between 174 and 171 Ma on biotite. Numerous data were discarded due to frequent excess  $^{40}\text{Ar}$  on amphiboles, probably associated to the emplacement of the gabbro with a high  $^{40}\text{Ar}/^{36}\text{Ar}$  ratio in Permian times. These new ages, together with a compilation of existing ages obtained with different chronometers (U–Pb, Sm–Nd, Rb–Sr, K–Ar,  $^{40}\text{Ar}/^{39}\text{Ar}$ ) and performed on different lithologies from both the Campo and the Grosina units allow to estimate cooling rates for these units. The new results shows that both Campo and Grosina units underwent a cooling rate around 10°C/Ma in Permian time. The Grosina unit, being in a shallower crustal level, did not record the Jurassic cooling, reaching up to 50°C/Ma in the Campo unit. The notable difference in cooling rates between the Permian and Jurassic events attests of a cooling without being associated to an exhumation in Permian times, whereas the Campo unit cooled rapidly in Jurassic times, associated to an exhumation and an emplacement in shallow crustal levels. The latter tectonic event was probably achieved through shearing along the Eita shear zone separating the Campo unit from the overlying Grosina unit. These results bring new constrains on the strain evolution and the thermal budget of mid crustal levels during late orogenic extension and subsequent rifting.

## 1. INTRODUCTION

The mechanisms leading to extreme lithospheric thinning during rifting remain an open question (Huismans & Beaumont, 2011; Lavier & Manatschal, 2006; Ranero & Perez-Gussinye, 2010; Weinberg *et al.*, 2007). In present-day rifted margins, this extreme thinning is recorded within the so-called “necking zones”, at the transition between the 30 km thick proximal margin, and the 10 km thick distal/hyper-extended margin (Mohn *et al.*, 2012; Tugend *et al.*, 2014). Currently, little is known about how this “tapper-like” structure forms and evolves during lithospheric thinning (Osmundsen & Redfield, 2011). In particular, the characterization of the nature of the basement as well as the intra-crustal deformation within the necking zone remains difficult to address in present-day rifted margins. In order to characterize processes active in the continental basement during its thinning, constraining the evolution of the basement before, during and after the rifting is critical. Such critical information can be documented in fossil remnants of margins, preserved in orogens. In the Alpine belt, remnants of the Jurassic rifted margins surrounding the Alpine Tethys were documented (Decandia & Elter, 1972; Froitzheim & Eberli, 1990; Lemoine *et al.*, 1986; Manatschal, 2004). Notably, distinct portions of the pre-rift lithosphere were exhumed by the rifting and the subsequent Alpine orogeny. Such exhumed portions crop out in the Austroalpine nappes.

Before Mesozoic riftings in general, the Western European realm underwent a polyphase evolution. After the Variscan orogeny, the former orogenic domain suffered a Late-Carboniferous to Early-Permian magmatic and metamorphic activity in a complex tectono-metamorphic environment (e.g. Henk, 1999; Lorenz & Nicholls, 1976; Malavieille, 1993; Ménard & Molnar, 1988). The lower continental crust was formed at that time by mafic magmatic underplating and associated contact-metamorphism (Costa & Rey, 1995; Rey, 1993) producing granulites that are typically considered as post-orogenic (with near-isobaric cooling, IBC-granulite of Harley, 1989). In the Austroalpine realm, such IBC-granulites were documented in relics of the Adriatic distal rifted margin, in the Malenco nappe (Müntener *et al.*, 2000) along with a Permian mafic underplated gabbro (Hermann *et al.*, 2001). Both represent the lowermost crustal section during the Permian in the Alpine realm, as it is in contact with the sub-continental mantle (Hermann *et al.*, 1997). Mid-crustal granulites were described further East, closely associated to a Permian gabbroic complex (Braga *et al.*, 2001; Koenig, 1964; Tribuzio *et al.*, 1999). Both attest of a Permian mafic magmatism pulse, also described in the Southern, Central and Western Alps (see e.g. Spalla *et al.*, 2014) and in some cases responsible for a granulite facies metamorphism. More and more studies attest that such high-grade rocks were already placed in shallow crustal levels or even at the seafloor during late stages of Jurassic rifting, before the onset of Alpine (*sensu lato*) compressional tectonics (Beltrando *et al.*, 2013; Mohn *et al.*, 2012; Müntener &

Hermann, 2001; Vielzeuf & Kornprobst, 1984).

The aim of this work is to characterize the nature as well as the temperature-time evolution of the Adriatic necking zone basement from the Variscan to post-Variscan extension through the Jurassic rifting. More precisely, the goal is (1) to track a possible Permian exhumation, and (2) characterize the Jurassic exhumation of the middle-crust during the rifting. To do so, we will synthetize structural and petrological observations for both Grosina and Campo units preserving the remnants of the Adriatic necking zone and constrain their temporal and thermal evolution with  $^{40}\text{Ar}/^{39}\text{Ar}$  dating combined to a compilation of published ages.

## 2. TECTONIC, GEOCHRONOLOGICAL AND GEOLOGICAL FRAMEWORK

### 2.1 The evolution of the Austroalpine domain

#### 2.1.1 Variscan and post-Variscan evolution

In the Austroalpine realm, the Variscan orogenic evolution is mostly documented in the Ulten area, where crustal units reach peak metamorphic conditions at 350–325 Ma (U-Th-Pb on monazite; Langone *et al.*, 2011). In the West, amphibolite-facies metamorphism is documented but remains yet undated (Bianchi Potenza *et al.*, 1978a; Büchi, 1994; Halmes, 1991; Pace, 1966). In contrast, this western part and especially the Bernina unit develops a well-constrained Carboniferous plutonism of calc-alkaline affinity (Rageth, 1984; Spillmann & Büchi, 1993; Von Quadt *et al.*, 1994) with associated volcanics (Mercolli, 1989).

During the Permian, the continental crust was strongly affected by a magmatic and metamorphic episode that deeply modified its lithological composition and crustal architecture (Fig. V-1a).

In the upper crust, alkaline felsic magmas were emplaced and extruded between 295 and 288 Ma (Büchi, 1987; Spillmann & Büchi, 1993; Von Quadt *et al.*, 1994). It is yet unclear in the study area if the volcanic rocks are filling basins.

In the same age range, intermediate levels (middle crust) were intruded by both mafic bodies (Tribuzio *et al.*, 1999) and granitoïds (Bockemühl & Pfister, 1985; Guglielmin & Notarpietro, 1997). Locally, the intrusions are rimed by a migmatitic contact aureole that may reach granulite-facies conditions in xenoliths (Braga *et al.*, 2003; Braga *et al.*, 2001).

The lower crust was affected during the Permian by mafic underplating during emplacement of gabbros of tholeiitic affinity associated with felsic granulites (Hermann *et al.*, 2001; Hermann *et al.*, 1997; Müntener *et al.*, 2000), indicating a emplacement and contact metamorphism at around 10 kbar. The emplacement of these gabbros occurred at 281-278 Ma (U-Pb on zircon; Hansmann *et al.*, 2001).

### **2.1.2 Jurassic rifting history**

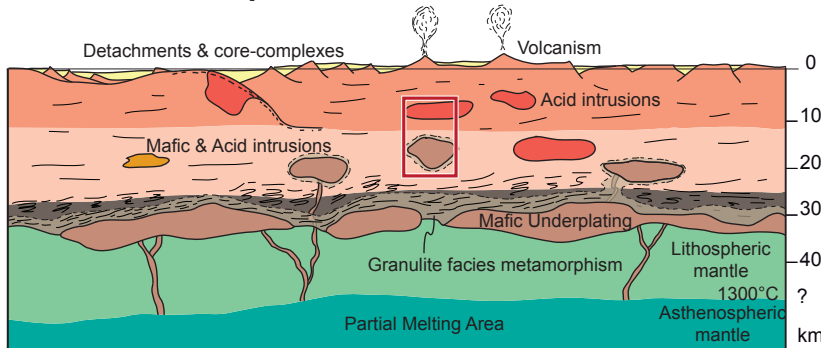
This pre-rift lithospheric architecture was disrupted in Jurassic times by a rifting event that led to the opening of the Alpine Tethys and the formation of the Adriatic rifted margin. Following Mohn *et al.* (2012), this process occurred in three stages.

- (1) The stretching phase (220-185 Ma, Fig. V-1b) during the formation of basins bounded by high-angle normal faults over the complete rift domain (Eberli, 1988). The related normal faults are typically listric and rooted in mid-crustal levels (Bertotti, 1991). During this stage, extension in the upper-crust is decoupled from deformation in the lower crust. The subcontinental mantle and the lower crust start to be exhumed and cooled at that time, as recorded by  $^{40}\text{Ar}/^{39}\text{Ar}$  ages on amphibole (Müntener, 1997; Villa *et al.*, 2000).
- (2) The thinning phase (185-175 Ma, Fig. V-1c) when extension localized within the future distal margin (Froitzheim & Eberli, 1990), and the Briançonnais domain starts to be uplifted (Decarlis *et al.*, 2013; Lemoine *et al.*, 1986). The basement starts to be exhumed at the surface by “thinning” faults and the crustal thickness of the distal domain is thinned below 10 km, by complete obliteration of the middle-crust. In the intermediate necking zone, mid-crustal levels are also expected to be exhumed along thinning faults.
- (3) The exhumation phase initiates (175-165 Ma, Fig. V-1d) when the crust in the distal domain has been thinned below 10 km and is entirely brittle. Detachments faults cut into the lower crust and the mantle enabling its exhumation to the seafloor (e.g. Mohn *et al.*, 2012). The exhumation faults are cutting through a crustal section that has been thinned during the previous thinning phase.

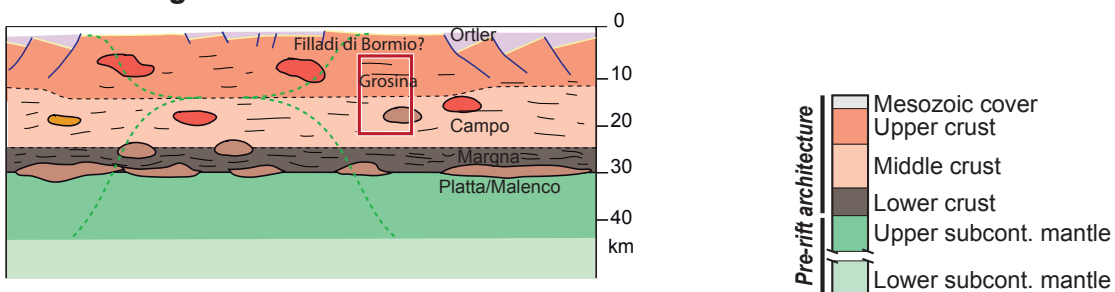
---

**Fig. V-1:** Tectonic evolution model of the European and Adriatic rifted margins during the opening of the Alpine Tethys. (a) pre-rift crustal section mainly affected by the Permian lithospheric extension (290-240 Ma) affected by the three-stages rifting with (b) the stretching phase (220-190 Ma), (c) the thinning phase (180-175 Ma) and (d) the exhumation phase (175-161 Ma), lately reactivated during the Alpine compression (< 100 Ma). Modified after (Mohn *et al.*, 2010) and Mohn *et al.* (2012), see text for details. Note the relative position of the unit position before and after the rifting.

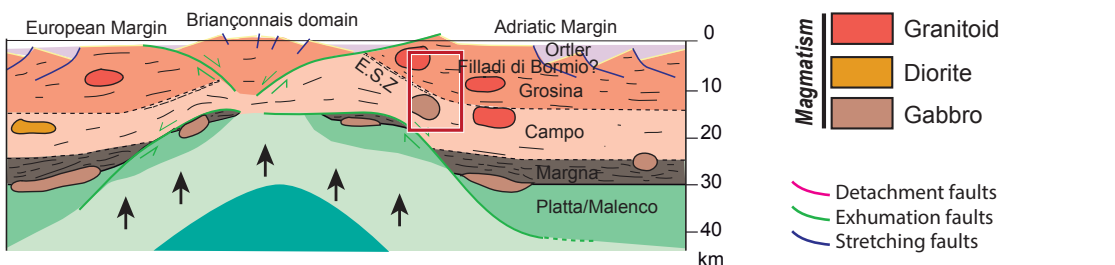
(a) **Permian lithospheric extension 290-240 Ma**



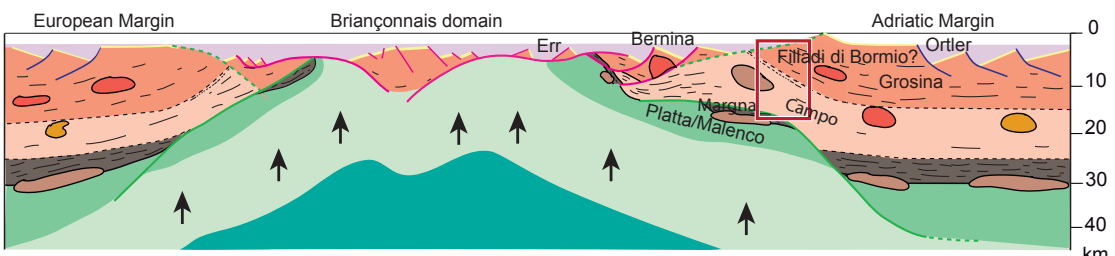
(b) **Stretching 220-190 Ma**



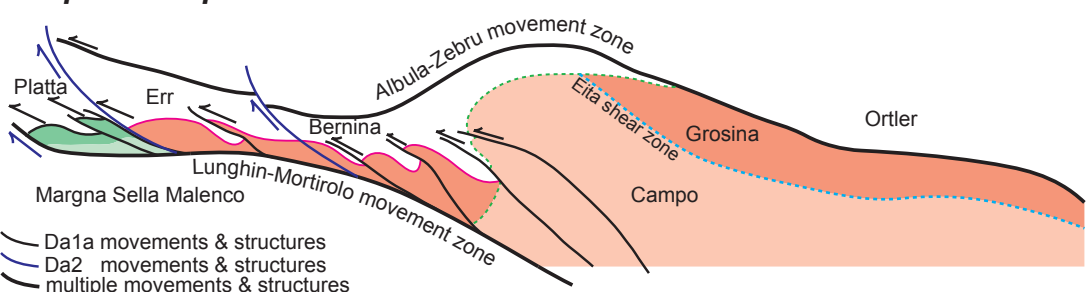
(c) **Thinning 180-175 Ma**



(d) **Exhumation 175-161 Ma**



(e) **Alpine compression <100 Ma**



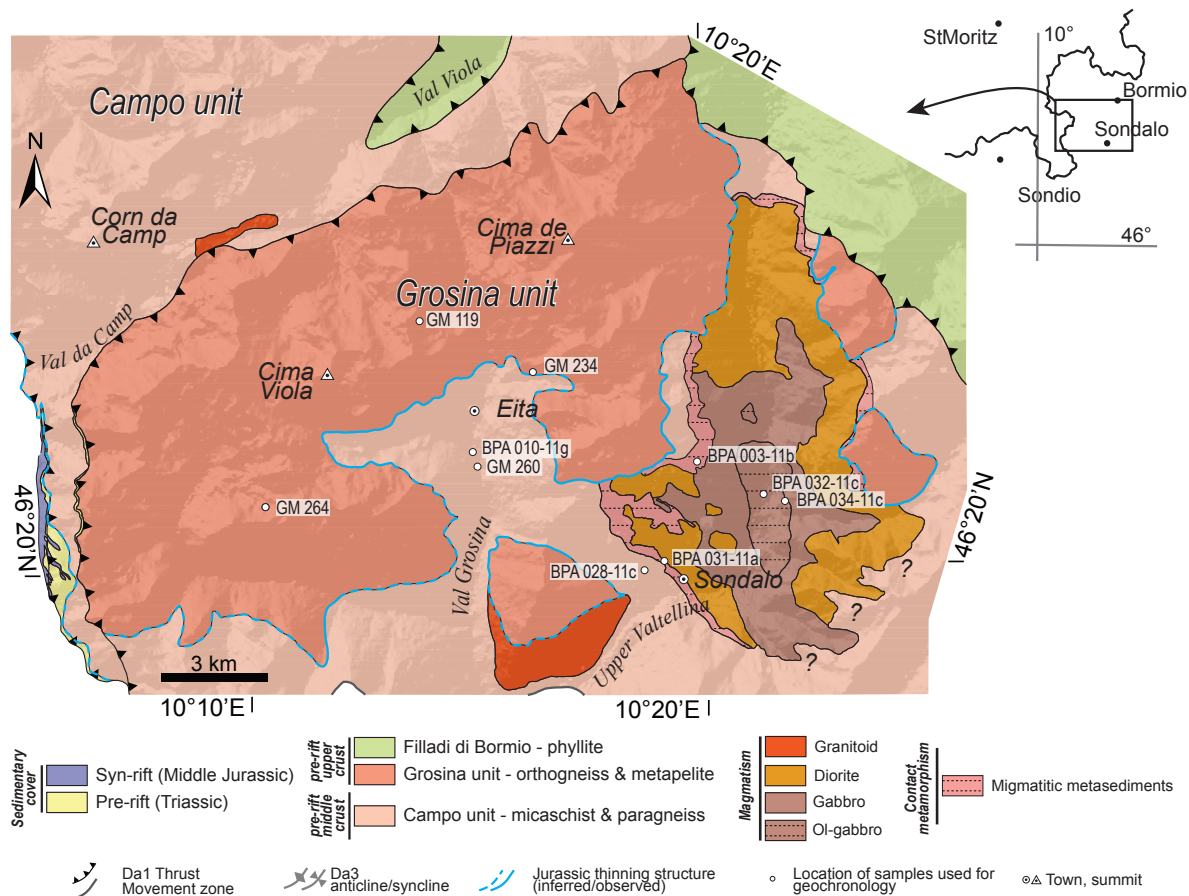


**Fig. V-2:** Geological map of the study area compiled from maps of Del Moro & Notarpietro (1987), Del Moro et al. (1999), Mohn et al. (2011), the 1:10,000 and 1:25,000 geological maps of Italy and personal observations. Location of samples used for geochronology is indicated.

The final architecture of the hyper-extended margin is the result of the superposition of all extensional phases on the inherited pre-rift crust. As a consequence of thinning and exhumation, rock units that were prior to rifting on top of each other, were juxtaposed and occurred at the end of the rifting one next to each other. The evolution of the thinning and exhumation is documented by the  $P-T-t$  evolution of these rocks as well as by the syn-tectonic sediments associated with these events at the surface. In this work, we are mainly focusing on the evolution of the middle crust from the pre-rift Permian stage to the Jurassic rifting. These rocks were exhumed in between the distal and the proximal domains, in the so-called “necking” zone recorded in the Grosina-Campo units.

### 2.1.3 Alpine reactivation

From Late Cretaceous onward, the Jurassic margin architecture was reactivated and disrupted by Alpine compression (Fig. V-1e). The stacking of the nappes occurred from Late Cretaceous till Tertiary times, by multistage thrusting of proximal domains over more distal domains of the margin. The first major deformation phase, the Da1 phase (Trupchun phase of Froitzheim *et al.*, 1994) consists of a W- to NW-directed thrusting occurring between 100 and 76 Ma (see Froitzheim *et al.*, 1994; Handy *et al.*, 1996), and related to the coeval closure of the Meliata-Vardar domain further west and the onset of the closure of the Alpine Tethys (Froitzheim *et al.*, 1996; Mohn *et al.*, 2011; Schmid *et al.*, 2008). The second phase, the Da2 phase (Duncan-Ela phase of Froitzheim *et al.*, 1994) is an extensional phase developing normal faults and associated recumbent folds (Froitzheim, 1992; Froitzheim *et al.*, 1994; Handy *et al.*, 1993) during Late Cretaceous times (80-67 Ma, Handy *et al.*, 1996). The third phase, the Da3 phase (Blaisun phase of Froitzheim *et al.*, 1994) is expressed by large-scale upright open-folds with sub-horizontal E-W trending axis in upper greenschist facies conditions (Hermann & Müntener, 1992). Da3 has been estimated to be Eocene in age (Mohn *et al.*, 2011) and is associated with the continental collision between Adria and Europe (Schmid *et al.*, 1996). The complete nappe stack is finally deformed by movement along the Engadine Line and the Insubric Line, both related to the Periadriatic fault system (Schmid *et al.*, 1989; Schmid & Froitzheim, 1993).

## 2.2 The Campo–Grosina units

The study area encompasses the Campo–Grosina units, separated by the flat-lying Eita shear zone (Figs V-2 & V-3a, Meier, 2003; Mohn *et al.*, 2012). The units are part of the middle Austroalpine domain (following the classification of Mohn *et al.*, 2011), cropping out in the SE-Switzerland and N-Italy.

The hanging wall of the Eita shear zone, the Grosina unit, is essentially made of Bt-orthogneiss (also known as “Cristallino di Grosina”, Fig. V-3b), associated with garnet–staurolite–bearing metapelites (Bianchi Potenza *et al.*, 1978a; Bianchi Potenza *et al.*, 1978b). Orthogneisses are derived from Ordovician protoliths (see references in Boriani *et al.*, 2005; Trommsdorff *et al.*, 2005; Mohn, unpublished data) preserved from subsequent deformation phases in few locations (e.g. Fig. V-4a). The structural evolution of the Grosina unit, although not yet well constrained, involves (1) a sub-vertical foliation (Sg1) only locally preserved due to the pervasive overprinting during the development of (2) a sub-horizontal planar fabric (Sg2) formed at amphibolite-facies associated with a well-defined lineation with a NW-SE trend (Fig. V-3b). Locally, this foliation is crosscut by weakly deformed Grt-bearing granodiorite (Fig.

V-3c) of unknown age but with a paragenesis and textures similar to rocks from the Permian Sondalo gabbro. Orthogneisses, metasediments and granodioritic dykes are deformed by sporadic greenschist facies shear zones, especially approaching the Eita shear zone in which chlorite-rich orthogneisses present (3) a sub-horizontal Sg3 fabric (Fig. V-3cd). This new fabric is parallel to the Sg2 fabric and shows a similar NW-SE trending lineation. The complete section is crosscut by undated and undeformed basic dykes (andesite?), probably similar to those described in the underlying Campo basement (Bianchi Potenza *et al.*, 1985) and related to the magmatism along the Peri-Adriatic system. Mohn *et al.* (2012) presented the only ages available for the Grosina basement with  $^{40}\text{Ar}/^{39}\text{Ar}$  dating on muscovite, ranging between 273 and 260 Ma (see Fig. V-11c).

The Campo basement, located in the footwall of the Eita shear zone, contains amphibolite-facies metasediments derived from an Ordovician protolith (Bergomi & Boriani, 2012) with paragneiss, micaschist, and minor intercalations of marble and amphibolite. The unit is affected by a metamorphism up to 6 kbar/650°C probably during the Variscan orogeny, along with the development of a N-W steeply dipping foliation (Sc1) lately reworked by a N-E trending sub-vertical Sc2 fabric (Fig. V-3aef; see *chapter III*). It was subsequently intruded by numerous plutons in the Permian (300–270 Ma, U-Pb on Zrn and Sm-Nd ages; Bachmann & Grauert, 1981; Del Moro *et al.*, 1981; Tribuzio *et al.*, 1999; see Fig. V-11a), with associated contact metamorphism up to granulite-facies around the Sondalo gabbro (Braga *et al.*, 2003; Braga *et al.*, 2001), and the development of high-temperature Sc3 fabric around the intrusion. Locally, undeformed Permian pegmatitic dykes crosscut the Sc2 foliation (Fig. V-3ef; Sölva *et al.*, 2003). Rb–Sr ages on muscovite from pegmatites and granitoids range between 277 and 251 Ma and between 263 and 97 Ma on biotite (see Table V-4 for references; Fig. V-11b).  $^{40}\text{Ar}/^{39}\text{Ar}$  and K–Ar ages from different lithologies are spanning between 217 and 187 Ma for muscovite and from 189 to 122 Ma for biotite (Fig. V-11c).

## 2.3 The Eita shear zone

The contact between the Grosina and the Campo basement is marked by a subhorizontal shear zone that can be mapped continuously over more than 20 km (the Eita shear zone, Meier, 2003; Mohn *et al.*, 2012). In the vicinity of the shear zone, the Sc2 planar fabric of the Campo unit is tilted by Fc4 recumbent folding with E-W trending axes and a shallow W-dipping axial plane, deforming also the Permian pegmatites (Fig. V-3e). This shear zone was interpreted as a late-Cretaceous Alpine thrust (Meier, 2003). However, based on dating and field observations, Mohn *et al.* (2012) interpreted this structure as a Jurassic extensional shear zone active during the rifting (200–180 Ma) with a possible Alpine reactivation.

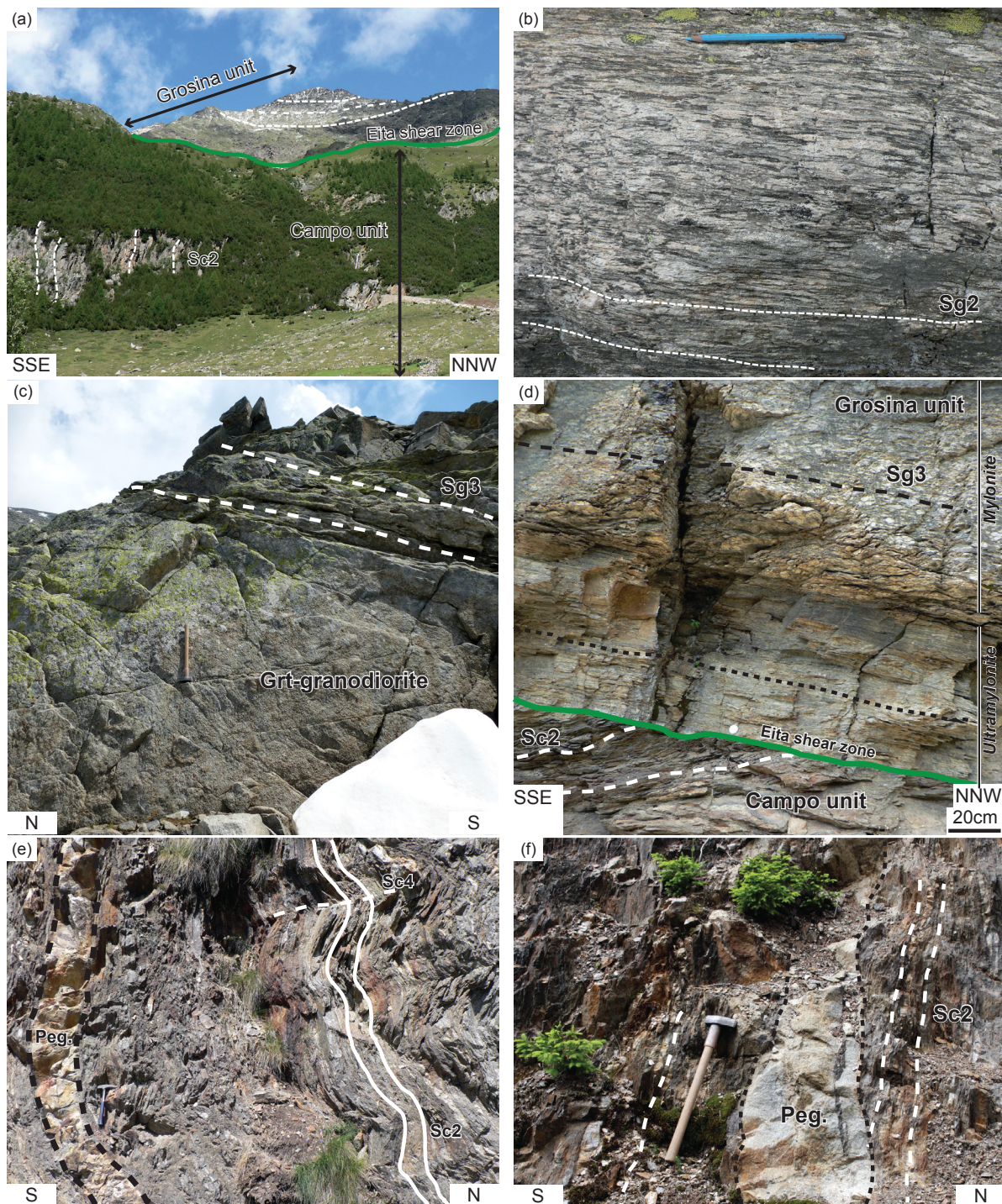


**Fig. V-3:** Field photographs. (a) Panoramic view of the Campo/Grosina units close to the Eita village. Note the vertical  $Sc_2$  foliation of the Campo unit and the flat lying foliation of the Grosina unit. Grosina unit: (b) Mylonitic orthogneiss showing the sub-horizontal amphibolite-facies  $Sg_2$  foliation; (c) garnet bearing granodiorite of unknown age presenting the greenschist facies  $Sg_3$  foliation. (d) Contact between the Campo metasediments with tilted  $Sc_2$  foliation and the Grosina orthogneiss with  $Sg_3$  greenschist facies fabric along the Eita shear zone. Campo unit: (e) Micaschist and pegmatitic dykes presenting  $Fc_4$  folds; (f) pegmatitic dyke cross-cutting the  $Sc_2$  planar fabric of metasediments.

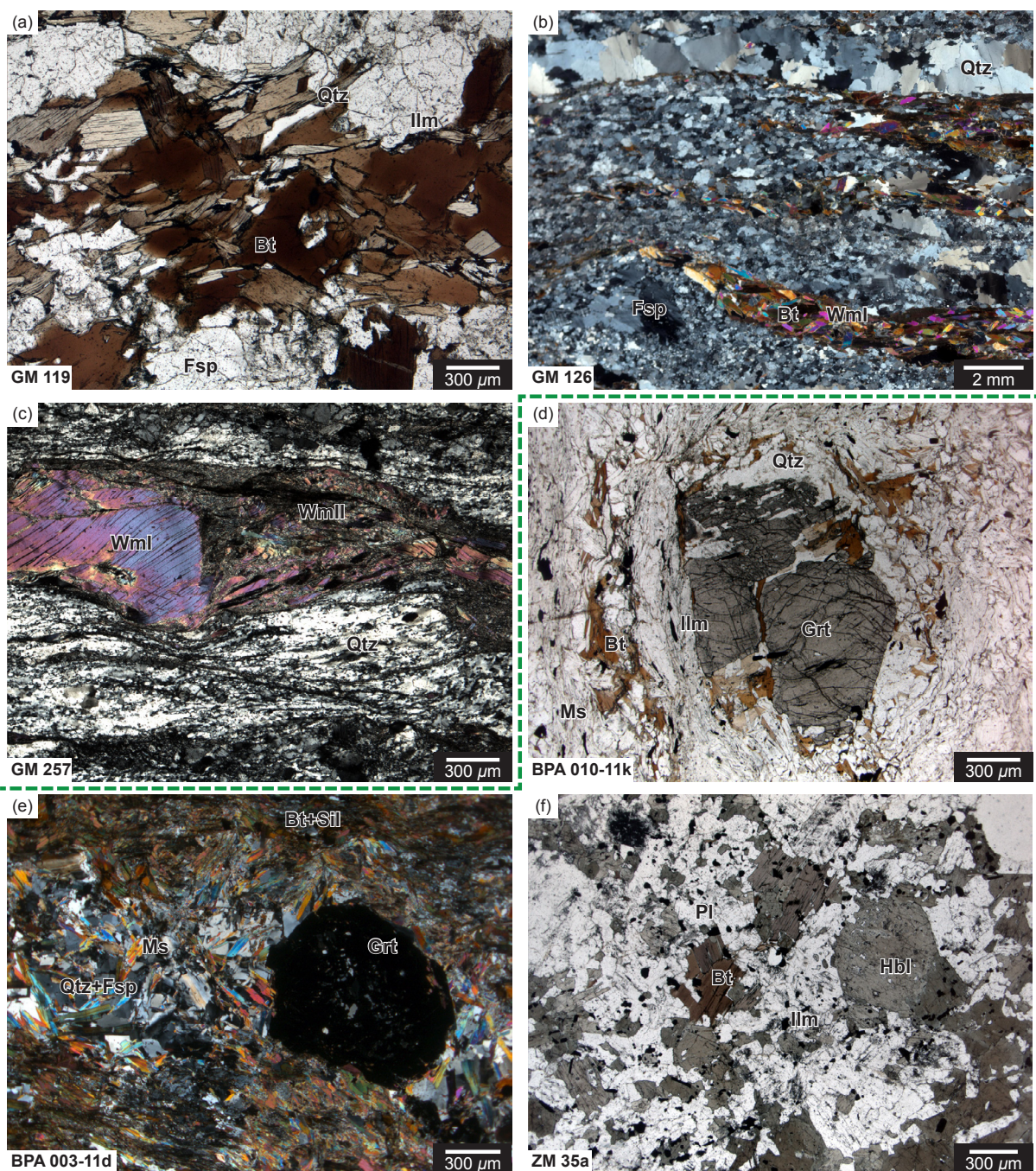


**Fig. V-4:** Photomicrographs illustrating various lithologies for (a-c) the Grosina unit and (d-f) the Campo unit. (a) Undeformed granodiorite with preserved magmatic biotites. (b) Amphibolite-facies mylonitic orthogneiss with metamorphic biotite and white mica I. Note the quartz recrystallization through grain-boundary migration. (c) Greenschist facies recrystallization of porphyroclastic white mica I into white mica II. (d) Garnet-bearing micaschist with metamorphic biotite and muscovite. (e) Garnet-sillimanite-biotite migmatite in the contact aureole of the Sondalo gabbro, with post-peak crystallization of muscovite in quartz-feldspar-garnet leucosome. (f) Magmatic hornblende and biotite from a diorite from the Sondalo pluton.

The Campo–Grosina units is thrust during late-Cretaceous (Trupchun phase of Froitzheim *et al.*, 1994) by the overlying Filladi di Bormio unit (Fig. V-2). This unit is made of prograde greenschist facies metapelites of unknown age (Boriani *et al.*, 2011; Chiesa *et al.*, 2010; Gregnanin, 1980). At the contact with the Campo unit, micaschist from the Campo unit are retrogressed into greenschist facies rocks (Andreatta, 1952).

### 3. $^{40}\text{Ar}/^{39}\text{Ar}$ GEOCHRONOLOGY

Former geochronological investigations were performed focused on the limit between the Campo and the Grosina basement (Eita shear zone, Meier, 2003; Mohn *et al.*, 2012). In contrast, the precise characterization of exhumation and cooling history of these units with modern dating techniques were lacking. We selected amphibole, muscovite and biotite grains from various lithologies in both units to carry out  $^{40}\text{Ar}/^{39}\text{Ar}$  step-heating dating (sample locations indicated in Fig. V-2). Raw analytical results are provided in Table V-1 for muscovite, Table V-2 for biotite and Table V-3 for hornblende. Results are represented as step-release spectra and inverse isochrons in Figs V-7, V-8, V-9 and V-10, where errors are reported at  $2\sigma$  (95% level of confidence). Mineral abbreviations follows IUGS recommendations after Siivola & Schmid (2007).

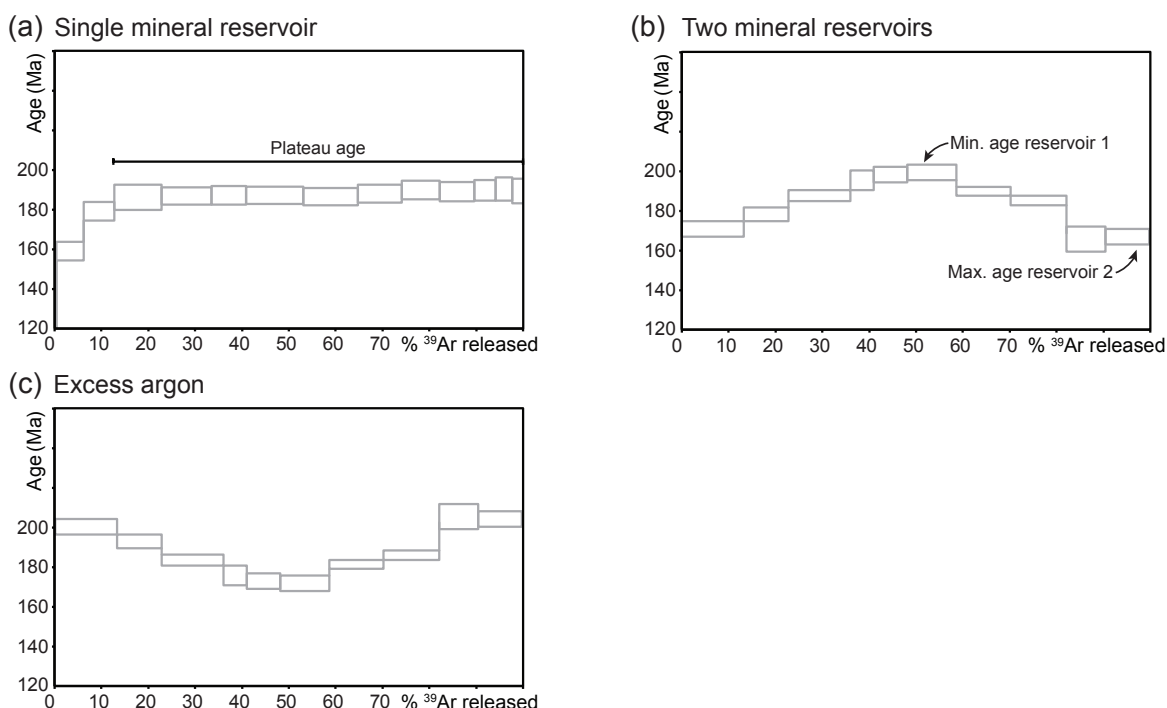


**Fig. V-5:** Synthetic plateau ages illustrating (a) a single mineral reservoir, (b) a bell shape spectrum with two mineral reservoirs releasing their trapped Ar in a narrow T-range for the oldest mineral 1 and in a wider T-range for the youngest mineral 2 (after Wijbrans & McDougall, 1986), and (c) a saddle-shape spectrum due to extraneous  $^{40}\text{Ar}$  incorporation ( $^{40}\text{Ar}$ -excess).

### 3.1 Analytical procedure

Multigrain  $^{40}\text{Ar}/^{39}\text{Ar}$  isotopic analyses were performed on muscovite, biotite and amphibole by laser step-heating at the Faculty of Earth and Life Sciences, VU Amsterdam. Mineral were separated at the mineral separation laboratory of the Faculty of Earth and Life Sciences, VU Amsterdam after crushing, sieving between 250 and 500  $\mu\text{m}$  and cleaning ultrasonically with demineralized water. Desired minerals were concentrated using a vibrating table, heavy liquids, and amagnetic separator to be finally selected by hand picking under the binocular. Minerals packages wrapped in Al-foil were co-irradiated with DRA sanidine standard packages wrapped in Cu-foil packages as fluence monitor at the NRG-Petten HFS facility in the Netherlands for 18 hours.

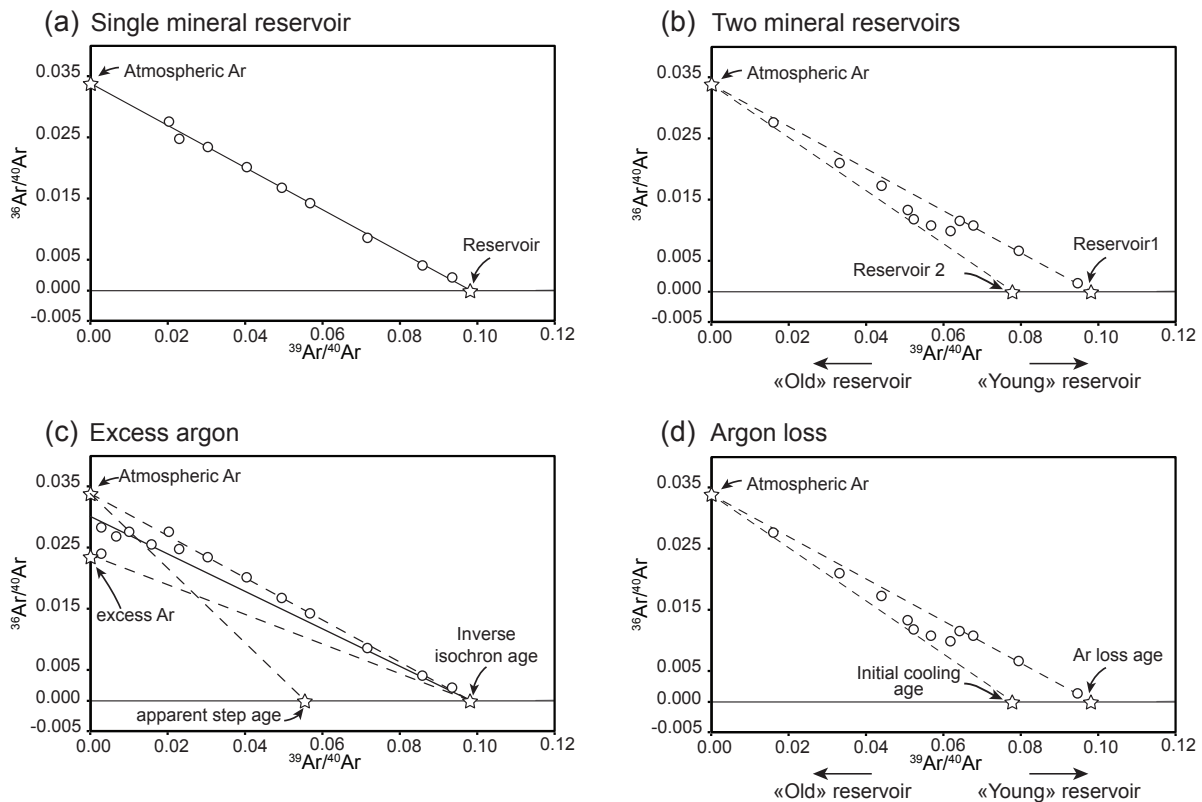


**Fig. V-6:**  $^{39}\text{Ar}/^{40}\text{Ar}$  versus  $^{36}\text{Ar}/^{40}\text{Ar}$  synthetic plots (inverse isochrons) illustrating dispersion of incremental heating data in different scenarios. (a) A single mineral reservoir mixed with extraneous Ar (here atmosphere), data will spread between the two end-members. (b) A two mineral reservoir where data will spread in a triangle defined by the extraneous Ar reservoir (here atmosphere) and the two radiogenic Ar reservoir representing the two Ar-bearing phases. (c) A case of excess argon where data will spread between the reservoir end-member and two extraneous argon reservoir represented here by the atmospheric Ar and third reservoir responsible for excess Ar. (d) A case of Ar loss corresponding to a partial reopening of the system to argon that will younger measured points with respect to the “true” age; data will spread between the extraneous argon reservoir (here atmosphere), the mineral reservoir and the reopening age. In the cases (a) and (b), the best-fit line will intersect the  $^{36}\text{Ar}/^{40}\text{Ar}$  axis in an intermediate position between the two extraneous Ar reservoirs, but will constrain the “real” reservoir age by the inverse isochron method. Modified after Beltrando et al. (2009) and Kuiper (2002).

Measurements were performed after *ca.* 6 months to allow  $^{37}\text{Ar}$  decay in Ca-rich amphiboles. Samples were pre-heated to *ca.* 200°C to remove undesirable atmospheric argon. Total fusion and step-heating, for standards and samples, respectively, were carried out by a Synrad CO<sub>2</sub> laser combined to a Raylease scan-head system to scan to totality of the mounted grains. Isotopic ratios were evaluated using a MAP 215-50 mass spectrometer with both secondary electron multiplier and Faraday collector. Blanks were measured every two (muscovite and biotite) or four (amphibole) samples measurements and before and after each experiment. Mass discrimination was made through  $^{40}\text{Ar}/^{36}\text{Ar}$  air pipette aliquots measurement.

Ages were calculated using ArArCalc (Koppers, 2002) using the decay constants of Steiger & Jäger (1977), the atmospheric  $^{40}\text{Ar}/^{39}\text{Ar}$  ratio of  $298.56 \pm 0.1\%$  (Lee *et al.*, 2006). For each sample, the J irradiation parameter was determined through linear interpolation between each standard. Standard calibration of 24.99 Ma from Wijbrans *et al.* (1995) was used for VU89 experiments whereas calibration of 25.42 Ma from Kuiper *et al.* (2008) was used for experiments VU97D.

### 3.2 Sample description and $^{40}\text{Ar}/^{39}\text{Ar}$ results

We selected two samples from the Grosina basement and eight samples from the Campo basement including granodiorite, diorite, amphibolites and metapelites (photomicrographs of samples are reported as Appendix). In most of cases, the obtained ages were too disturbed to define “plateau” ages that normally require at least three consecutive steps within their  $2\sigma$  errors containing more than 70% of the total released  $^{39}\text{Ar}$ . In case of suspected excess argon shown e.g. by old ages in the beginning of the spectrum, the inverse isochron method was used, allowing the identification of the extraneous source of argon (Beltrando *et al.*, 2009; Kuiper, 2002; McDougall & Harrison, 1999). Each experiment is presented in Figs V-7, V-8, V-9 and V-10 with its step-release spectrum and associated inverse isochron diagram.

#### 3.2.1 Grosina basement

*Muscovite GM264 (experiment VU89-G2)* [46.34994°N; 10.17277°E]: was separated from a Bt–Ms micaschist with minor garnet content. The structural position of the sample is unknown. The highly perturbed step-release spectra give a total age of  $262 \pm 3$  Ma, whereas the inverse isochron age is  $261 \pm 2$  Ma (Fig. V-7a). With such a perturbed spectrum, it is safer to use the inverse isochron age.

*Biotite GM264 (experiment VU89-G4)* [46.34994°N; 10.17277°E] : comes from the same sample than the previous experiment. 15 of the 21 steps define a sub-plateau at  $246 \pm 1$  Ma, coeval with the total fusion age (Fig. V-8b). As the spectrum is quite rough, the isochron age of  $245 \pm 2$  Ma should be used rather than the “plateau” or total fusion age.

*Biotite GM119 (experiment VU97D-B9)* [46.39640°N; 10.23004°E] : was separated from a granodiorite that showed only minor overprinting by the Dg2 deformation and still preserving its magmatic structure and minerals (Bt–Pl–Kfs–Qtz; Fig. V-4a). 8 out of 14 measurements define a “sub-plateau” at  $280 \pm 3$  Ma (Fig. V-8a). In the inverse isochron, points are reasonably well grouped close to the  $^{36}\text{Ar}/^{40}\text{Ar} = 0$  line but present a trend pointing to excess argon. Moreover, ages are decreasing with the increasing laser power usually indicating biotite–chlorite intermixing resulting in  $^{39}\text{Ar}$  recoil from biotite to chlorite during irradiation (Lo & Onstott, 1989; Ruffet *et al.*, 1991). It is therefore recommended to use the inverse isochron age of  $246 \pm 13$  Ma.

### **3.2.2 Campo basement**

*Biotite 034-11c (experiment VU97D-B8)* [46.34941°N; 10.36257°E] : was concentrated from a garnet-bearing granodiorite in the center of the Sondalo gabbro, in the vicinity of a metapelitic xenolith. Ages become progressively older during the experiment, pointing to a partial argon loss. 8 out of 14 steps define an age of  $216 \pm 2$  Ma, with a total fusion age of  $212 \pm 2$  Ma (Fig. V-8c). The inverse isochron shows scattered data points, with an inverse isochron at  $214 \pm 3$  Ma. This age is older than expected, potentially due to excess  $^{40}\text{Ar}$ .

*Biotite 031-11a (experiment VU97D-B6)* [46.33479°N; 10.31815°E] : was concentrated from a garnet-bearing granodiorite in the rim of the Sondalo gabbro, sampled close to a metapelitic xenolith. The rock preserves its magmatic structure and mineralogy, with euhedral plagioclase and interstitial amphibole and biotite. 7 consecutive steps selected from 14 steps constrain a reasonable plateau of  $173 \pm 2$  Ma with a MSWD = 0.7, totaling more than 70% of the released  $^{39}\text{Ar}$  (Fig. V-8d). Despite the spread of data in the inverse isochron diagram, the plateau age is reasonable in the sense of Baksi (2006). The total fusion age is  $170 \pm 2$  Ma and the inverse isochron age is  $171 \pm 2$  Ma.

*Hornblende 031-11a (experiment VU97D-B5)* [46.33479°N; 10.31815°E] : was separated from the same sample as the previous experiment. The spectrum is highly disturbed, with much older ages in the beginning of the experiment indicating excess argon (Fig. V-10b). On an inverse isochron plot, data can be bracketed between an old and a young envelope, with

**Table V-1:**  $^{40}\text{Ar}/^{39}\text{Ar}$  isotopic data for muscovites.

Step number	Power (W)	$^{40}\text{Ar}/^{39}\text{Ar}$ ± 1 $\sigma$	$^{37}\text{Ar}/^{39}\text{Ar}$ ± 1 $\sigma$	$^{36}\text{Ar}/^{39}\text{Ar}$ ± 1 $\sigma$	K/Ca	$^{40}\text{Ar}^*$ (%)	$^{39}\text{Ar}_K$ (%)	$^{40}\text{Ar}^*/^{39}\text{Ar}_K$ ± 1 $\sigma$	Age (Ma) ± 2 $\sigma$
<b>Ms GM264 (experiment VU89-G2) [46.34994°N; 10.17277°E]</b>									
J = 0.00327810 ± 0.00000820									
11M0513A	1.25	55.53 ± 0.08	0.04 ± 0.01	0.02 ± 0.00	11.01	87.01	3.78	48.32 ± 0.08	265.27 ± 0.87
11M0513B	1.50	50.64 ± 0.06	0.02 ± 0.00	0.01 ± 0.00	23.86	96.46	8.66	48.85 ± 0.06	267.95 ± 0.62
11M0513D	1.75	48.21 ± 0.06	0.05 ± 0.01	0.00 ± 0.00	8.23	98.48	3.65	47.48 ± 0.06	260.96 ± 0.64
11M0513E	2.00	48.60 ± 0.07	0.03 ± 0.01	0.00 ± 0.00	12.34	97.90	4.85	47.58 ± 0.07	261.47 ± 0.71
11M0513F	2.25	48.65 ± 0.06	0.03 ± 0.01	0.00 ± 0.00	15.26	97.63	5.55	47.49 ± 0.06	261.05 ± 0.60
11M0513G	2.50	49.73 ± 0.06	0.01 ± 0.01	0.00 ± 0.00	28.94	97.35	7.55	48.41 ± 0.06	265.74 ± 0.64
11M0513H	2.70	49.91 ± 0.06	0.01 ± 0.00	0.00 ± 0.00	37.92	97.88	10.03	48.85 ± 0.06	267.98 ± 0.61
11M0513J	3.20	49.37 ± 0.07	0.08 ± 0.01	0.00 ± 0.00	5.70	98.05	1.17	48.41 ± 0.08	265.73 ± 0.82
11M0513K	3.60	48.81 ± 0.08	0.02 ± 0.01	0.00 ± 0.00	17.81	97.99	1.32	47.83 ± 0.08	262.75 ± 0.83
11M0513L	4.60	48.31 ± 0.06	0.04 ± 0.01	0.00 ± 0.00	11.74	98.69	5.28	47.68 ± 0.07	261.99 ± 0.67
11M0513M	5.60	47.99 ± 0.06	0.03 ± 0.01	0.00 ± 0.00	14.44	97.71	4.37	46.90 ± 0.06	257.99 ± 0.64
11M0513N	6.20	46.92 ± 0.06	0.04 ± 0.01	0.00 ± 0.00	9.99	97.36	3.31	45.68 ± 0.06	251.75 ± 0.63
11M0513O	6.80	47.05 ± 0.06	0.04 ± 0.01	0.00 ± 0.00	9.57	97.98	3.22	46.10 ± 0.06	253.90 ± 0.65
11M0513P	7.60	47.87 ± 0.06	0.05 ± 0.01	0.00 ± 0.00	9.29	98.54	4.93	47.17 ± 0.06	259.39 ± 0.61
11M0513Q	8.00	46.39 ± 0.06	0.06 ± 0.01	0.00 ± 0.00	7.72	98.40	3.91	45.65 ± 0.06	251.59 ± 0.63
11M0513R	8.00	48.43 ± 0.06	0.03 ± 0.02	0.00 ± 0.00	14.58	98.43	3.48	47.67 ± 0.06	261.96 ± 0.66
11M0513S	8.50	47.35 ± 0.06	0.00 ± 0.00	0.00 ± 0.00	252.64	99.57	14.45	47.14 ± 0.06	259.24 ± 0.59
11M0513T	9.50	49.02 ± 0.06	0.07 ± 0.01	0.00 ± 0.00	6.50	99.02	3.12	48.54 ± 0.06	266.37 ± 0.65
11M0513U	10.50	49.80 ± 0.06	0.03 ± 0.01	0.00 ± 0.00	17.02	99.40	4.46	49.50 ± 0.06	271.29 ± 0.65
11M0513V	Fusion	48.29 ± 0.06	0.04 ± 0.03	0.00 ± 0.00	11.06	99.11	2.91	47.86 ± 0.07	262.94 ± 0.69

 $^{40}\text{Ar}^*$  indicates radiogenic  $^{40}\text{Ar}$ .

Plateau age 261.7 ± 2.7

Total fusion age 262.3 ± 1.2

Inverse isochron age 260.9 ± 2.1

Step number	Power (W)	$^{40}\text{Ar}/^{39}\text{Ar}$ ± 1 $\sigma$	$^{37}\text{Ar}/^{39}\text{Ar}$ ± 1 $\sigma$	$^{36}\text{Ar}/^{39}\text{Ar}$ ± 1 $\sigma$	K/Ca	$^{40}\text{Ar}^*$ (%)	$^{39}\text{Ar}_K$ (%)	$^{40}\text{Ar}^*/^{39}\text{Ar}_K$ ± 1 $\sigma$	Age (Ma) ± 2 $\sigma$
<b>Ms GM260 (experiment VU89-G1) [46.35939°N; 10.25048°E]</b>									
J = 0.00327810 ± 0.00000820									
11M0512A	1.25	46.96 ± 0.09	0.04 ± 0.01	0.06 ± 0.00	10.72	62.16	1.26	29.19 ± 0.12	164.86 ± 1.29
11M0512B	1.50	35.12 ± 0.05	0.10 ± 0.01	0.01 ± 0.00	4.25	92.94	5.22	32.65 ± 0.05	183.42 ± 0.55
11M0512D	1.75	32.54 ± 0.05	0.05 ± 0.01	0.00 ± 0.00	8.82	96.31	1.37	31.34 ± 0.05	176.43 ± 0.59
11M0512E	2.00	32.68 ± 0.04	0.01 ± 0.01	0.00 ± 0.00	30.90	96.00	2.55	31.38 ± 0.05	176.62 ± 0.54
11M0512F	2.25	33.34 ± 0.04	0.03 ± 0.00	0.00 ± 0.00	16.86	97.24	3.97	32.43 ± 0.04	182.24 ± 0.48
11M0512G	2.50	33.85 ± 0.04	0.01 ± 0.00	0.00 ± 0.00	29.88	97.71	8.34	33.08 ± 0.04	185.72 ± 0.42
11M0512H	2.70	33.57 ± 0.04	0.00 ± 0.00	0.00 ± 0.00	188.74	97.31	6.31	32.67 ± 0.04	183.55 ± 0.43
11M0512I	2.90	33.22 ± 0.04	0.02 ± 0.00	0.00 ± 0.00	19.31	97.38	5.55	32.35 ± 0.04	181.83 ± 0.44
11M0512L	4.60	33.11 ± 0.04	0.02 ± 0.01	0.00 ± 0.00	18.11	98.07	4.19	32.47 ± 0.04	182.49 ± 0.47
11M0512M	5.60	32.68 ± 0.04	0.03 ± 0.00	0.00 ± 0.00	15.78	98.01	8.49	32.03 ± 0.04	180.13 ± 0.42
11M0512N	6.20	33.00 ± 0.04	0.03 ± 0.01	0.00 ± 0.00	15.92	98.00	6.74	32.34 ± 0.04	181.77 ± 0.44
11M0512O	6.80	33.07 ± 0.04	0.01 ± 0.01	0.00 ± 0.00	79.41	97.35	5.55	32.19 ± 0.04	180.98 ± 0.43
11M0512P	7.60	32.45 ± 0.04	0.06 ± 0.02	0.00 ± 0.00	6.94	96.74	3.28	31.40 ± 0.05	176.74 ± 0.51
11M0512Q	8.00	32.47 ± 0.04	0.04 ± 0.01	0.00 ± 0.00	11.91	98.22	4.15	31.89 ± 0.04	179.38 ± 0.44
11M0512R	8.00	32.64 ± 0.04	0.04 ± 0.02	0.00 ± 0.00	9.78	97.46	2.82	31.81 ± 0.05	178.95 ± 0.52
11M0512S	8.00	32.60 ± 0.04	0.00 ± 0.00	0.00 ± 0.00	115.79	99.16	13.71	32.32 ± 0.04	181.69 ± 0.42
11M0512T	8.50	33.71 ± 0.04	0.00 ± 0.00	0.00 ± 0.00	90.51	98.42	5.43	33.18 ± 0.04	186.26 ± 0.45
11M0512U	9.50	33.82 ± 0.04	0.02 ± 0.01	0.00 ± 0.00	28.45	97.73	5.37	33.05 ± 0.04	185.60 ± 0.43
11M0512V	Fusion	33.84 ± 0.04	0.00 ± 0.01	0.00 ± 0.00	122.14	98.96	5.70	33.49 ± 0.04	187.91 ± 0.47

 $^{40}\text{Ar}^*$  indicates radiogenic  $^{40}\text{Ar}$ .

Plateau age 182.1 ± 1.7

Total fusion age 182.2 ± 0.9

Inverse isochron age 181.9 ± 1.9

**Table V-1: (Continued)**

Step number	Power (W)	$^{40}\text{Ar}/^{39}\text{Ar} \pm 1\sigma$	$^{37}\text{Ar}/^{39}\text{Ar} \pm 1\sigma$	$^{36}\text{Ar}/^{39}\text{Ar} \pm 1\sigma$	K/Ca	$^{40}\text{Ar}^* (\%)$	$^{39}\text{Ar}_K (\%)$	$^{40}\text{Ar}^*/^{39}\text{Ar}_K \pm 1\sigma$	Age (Ma) $\pm 2\sigma$
<b>Ms 028-IIc (experiment VU97D-B3) [46.33248°N; 10.31080°E]</b>									
J = 0.00472220 ± 0.00002467									
13M0070A	1.25	26.08 ± 0.03	0.00 ± 0.00	0.02 ± 0.00	201.31	82.53	10.79	21.53 ± 0.04	174.65 ± 0.58
13M0070B	1.50	23.95 ± 0.03	0.00 ± 0.00	0.01 ± 0.00	465.09	93.20	24.85	22.32 ± 0.03	180.76 ± 0.43
13M0070C	1.75	23.05 ± 0.03	0.00 ± 0.00	0.01 ± 0.00	497.15	93.44	24.52	21.54 ± 0.03	174.75 ± 0.41
13M0070D	2.00	23.82 ± 0.03	0.00 ± 0.00	0.01 ± 0.00	3378	88.89	10.16	21.17 ± 0.03	171.90 ± 0.48
13M0070E	2.35	24.25 ± 0.03	0.00 ± 0.00	0.01 ± 0.00	142.05	86.00	6.82	20.86 ± 0.04	169.48 ± 0.55
13M0070F	2.70	26.43 ± 0.03	0.00 ± 0.00	0.02 ± 0.00	218.46	76.72	3.42	20.27 ± 0.06	164.94 ± 0.86
13M0070G	3.05	27.62 ± 0.04	0.01 ± 0.00	0.02 ± 0.00	72.94	74.76	3.12	20.65 ± 0.06	167.83 ± 0.90
13M0070H	3.50	30.41 ± 0.04	-0.01 ± 0.00	0.03 ± 0.00	141.12	66.79	1.93	20.31 ± 0.09	165.22 ± 1.37
13M0070I	4.00	30.18 ± 0.04	0.00 ± 0.00	0.03 ± 0.00	126.09	67.47	2.16	20.36 ± 0.08	165.62 ± 1.23
13M0070J	4.65	29.94 ± 0.04	0.00 ± 0.00	0.03 ± 0.00	86.96	69.29	2.31	20.75 ± 0.08	168.61 ± 1.19
13M0070L	6.65	25.60 ± 0.03	0.00 ± 0.00	0.01 ± 0.00	377.65	83.44	7.33	21.36 ± 0.04	173.37 ± 0.60
13M0070M	8.00	30.07 ± 0.05	0.02 ± 0.00	0.04 ± 0.00	19.05	62.87	1.76	18.91 ± 0.09	154.28 ± 1.39
13M0070N	Fusion	22.21 ± 0.04	-0.02 ± 0.01	0.01 ± 0.00	18.93	90.92	0.83	20.20 ± 0.10	164.34 ± 1.50

$^{40}\text{Ar}^*$  indicates radiogenic  $^{40}\text{Ar}$ .

<b>Plateau age</b>	175.8 ± 4.3
<b>Total fusion age</b>	174.0 ± 1.7
<b>Inverse isochron age</b>	178.5 ± 5.4

Step number	Power (W)	$^{40}\text{Ar}/^{39}\text{Ar} \pm 1\sigma$	$^{37}\text{Ar}/^{39}\text{Ar} \pm 1\sigma$	$^{36}\text{Ar}/^{39}\text{Ar} \pm 1\sigma$	K/Ca	$^{40}\text{Ar}^* (\%)$	$^{39}\text{Ar}_K (\%)$	$^{40}\text{Ar}^*/^{39}\text{Ar}_K \pm 1\sigma$	Age (Ma) $\pm 2\sigma$
<b>Ms 003-IIb (experiment VU97D-B1) [46.35977°N; 10.33070°E]</b>									
J = 0.00475400 ± 0.00001937									
13M0069A	1.25	29.61 ± 0.02	0.00 ± 0.00	0.01 ± 0.00	429.65	92.21	23.00	27.31 ± 0.03	220.19 ± 0.41
13M0069B	1.50	28.87 ± 0.03	0.00 ± 0.00	0.01 ± 0.00	774.90	93.46	26.53	26.98 ± 0.04	217.71 ± 0.54
13M0069C	1.75	31.97 ± 0.03	0.00 ± 0.00	0.02 ± 0.00	135.09	84.53	15.42	27.03 ± 0.03	218.07 ± 0.51
13M0069D	2.00	36.75 ± 0.03	0.00 ± 0.00	0.03 ± 0.00	759.47	72.47	9.95	26.64 ± 0.05	215.10 ± 0.76
13M0069E	2.35	66.48 ± 0.07	0.00 ± 0.00	0.14 ± 0.00	96.28	39.96	3.80	26.57 ± 0.17	214.58 ± 2.54
13M0069F	2.70	51.36 ± 0.07	0.00 ± 0.00	0.08 ± 0.00	95.65	52.88	8.16	27.16 ± 0.13	219.10 ± 2.01
13M0069G	3.05	155.80 ± 0.30	-0.01 ± 0.01	0.44 ± 0.00	95.65	16.46	1.41	25.64 ± 0.49	207.53 ± 7.54
13M0069H	3.50	141.95 ± 0.27	-0.02 ± 0.01	0.39 ± 0.00	95.65	18.87	1.58	26.78 ± 0.43	216.19 ± 6.57
13M0069I	4.00	144.32 ± 0.30	0.01 ± 0.00	0.40 ± 0.00	54.39	17.87	1.50	25.79 ± 0.46	208.65 ± 7.05
13M0069J	4.65	98.06 ± 0.16	0.04 ± 0.00	0.24 ± 0.00	11.24	26.34	2.47	25.83 ± 0.28	208.97 ± 4.23
13M0069L	6.65	82.94 ± 0.11	0.03 ± 0.00	0.20 ± 0.00	13.61	30.48	4.74	25.28 ± 0.20	204.74 ± 3.13
13M0069M	8.00	122.04 ± 0.30	0.09 ± 0.01	0.35 ± 0.00	4.59	14.15	1.06	17.26 ± 0.46	142.31 ± 7.24
13M0069N	Fusion	41.67 ± 0.16	0.24 ± 0.03	0.05 ± 0.00	1.82	65.36	0.39	27.24 ± 0.36	219.69 ± 5.40

$^{40}\text{Ar}^*$  indicates radiogenic  $^{40}\text{Ar}$ .

<b>Plateau age</b>	217.4 ± 2.0
<b>Total fusion age</b>	216.2 ± 1.7
<b>Inverse isochron age</b>	217.8 ± 1.9

**Table V-2:**  $^{40}\text{Ar}/^{39}\text{Ar}$  isotopic for biotites.

Step number	Power (W)	$^{40}\text{Ar}/^{39}\text{Ar}$ ± 1σ	$^{37}\text{Ar}/^{39}\text{Ar}$ ± 1σ	$^{36}\text{Ar}/^{39}\text{Ar}$ ± 1σ	K/Ca	$^{40}\text{Ar}^* (\%)$	$^{39}\text{Ar}_K (\%)$	$^{40}\text{Ar}^*/^{39}\text{Ar}_K$ ± 1σ	Age (Ma) ± 2σ
<b>Bt GM260 (experiment VU89-G3) /46.35939°N; 10.25048°E/</b>									
J = 0.00327810 ± 0.00000820									
11M0509A	1.25	842.55 ± 2.95	-0.08 ± 0.06	2.75 ± 0.01	3.56	0.30	30.02	± 3.71	169.34 ± 39.91
11M0509B	1.50	87.20 ± 0.16	0.01 ± 0.01	0.18 ± 0.00	37.50	38.11	1.88	33.23 ± 0.27	186.54 ± 2.90
11M0509D	1.75	75.39 ± 0.22	0.09 ± 0.06	0.15 ± 0.00	4.64	41.99	0.22	31.66 ± 0.39	178.13 ± 4.20
11M0509E	2.00	58.53 ± 0.11	0.05 ± 0.04	0.09 ± 0.00	8.89	54.60	0.53	31.95 ± 0.22	179.72 ± 2.34
11M0509F	2.25	49.85 ± 0.07	0.01 ± 0.01	0.06 ± 0.00	34.30	63.20	1.08	31.51 ± 0.13	177.32 ± 1.41
11M0509G	2.50	44.55 ± 0.06	0.02 ± 0.01	0.04 ± 0.00	24.30	73.26	2.30	32.64 ± 0.08	183.37 ± 0.91
11M0509H	2.70	42.71 ± 0.05	-0.01 ± 0.01	0.03 ± 0.00	24.25	75.86	2.49	32.40 ± 0.08	182.12 ± 0.83
11M0509I	2.90	47.89 ± 0.06	-0.01 ± 0.01	0.05 ± 0.00	24.25	67.01	2.37	32.09 ± 0.10	180.47 ± 1.06
11M0509K	3.60	36.26 ± 0.08	-0.01 ± 0.04	0.02 ± 0.00	24.25	85.89	0.36	31.14 ± 0.16	175.37 ± 1.74
11M0509L	4.60	51.30 ± 0.07	0.03 ± 0.02	0.07 ± 0.00	14.93	62.17	2.34	31.90 ± 0.12	179.42 ± 1.26
11M0509M	5.60	51.12 ± 0.06	0.00 ± 0.01	0.07 ± 0.00	97.05	61.06	7.20	31.21 ± 0.10	175.74 ± 1.08
11M0509N	6.20	43.45 ± 0.05	0.03 ± 0.00	0.04 ± 0.00	15.66	70.29	6.87	30.54 ± 0.07	172.14 ± 0.80
11M0509O	6.80	41.25 ± 0.05	0.01 ± 0.01	0.04 ± 0.00	35.01	73.55	5.12	30.34 ± 0.07	171.03 ± 0.76
11M0509P	7.60	41.64 ± 0.05	0.02 ± 0.01	0.04 ± 0.00	28.47	72.27	5.52	30.09 ± 0.07	169.72 ± 0.76
11M0509Q	8.60	42.23 ± 0.05	0.01 ± 0.00	0.04 ± 0.00	67.86	71.62	7.02	30.24 ± 0.07	170.54 ± 0.80
11M0509R	9.60	43.53 ± 0.05	0.01 ± 0.01	0.05 ± 0.00	66.80	69.33	6.95	30.18 ± 0.07	170.21 ± 0.81
11M0509S	8.00	35.64 ± 0.08	0.00 ± 0.00	0.02 ± 0.00	66.80	85.03	42.42	30.31 ± 0.07	170.89 ± 0.80
11M0509T	9.60	34.74 ± 0.06	0.05 ± 0.03	0.02 ± 0.00	9.41	82.21	0.86	28.56 ± 0.09	161.43 ± 0.97
11M0509U	10.50	35.58 ± 0.04	0.01 ± 0.01	0.02 ± 0.00	68.27	81.61	3.36	29.03 ± 0.06	164.00 ± 0.60
11M0509V	Fusion	34.51 ± 0.06	-0.01 ± 0.02	0.02 ± 0.00	68.27	84.25	0.82	29.08 ± 0.09	164.26 ± 0.97

 $^{40}\text{Ar}^*$  indicates radiogenic  $^{40}\text{Ar}$ .

Plateau age 170.7 ± 1.1

Total fusion age 172.3 ± 0.9

Inverse isochron age 170.7 ± 1.9

Step number	Power (W)	$^{40}\text{Ar}/^{39}\text{Ar}$ ± 1σ	$^{37}\text{Ar}/^{39}\text{Ar}$ ± 1σ	$^{36}\text{Ar}/^{39}\text{Ar}$ ± 1σ	K/Ca	$^{40}\text{Ar}^* (\%)$	$^{39}\text{Ar}_K (\%)$	$^{40}\text{Ar}^*/^{39}\text{Ar}_K$ ± 1σ	Age (Ma) ± 2σ
<b>Bt 264 (experiment VU89-G4) /46.34994°N; 10.17277°E/</b>									
J = 0.00327810 ± 0.00000820									
11M0510A	1.25	82.66 ± 0.15	-0.04 ± 0.02	0.13 ± 0.00	11.30	52.40	1.20	43.31 ± 0.25	239.53 ± 2.62
11M0510B	1.50	57.90 ± 0.09	0.01 ± 0.01	0.04 ± 0.00	35.68	77.49	3.85	44.86 ± 0.11	247.54 ± 1.12
11M0510D	1.75	50.93 ± 0.13	-0.01 ± 0.03	0.02 ± 0.00	3.00	88.37	0.81	45.01 ± 0.17	248.29 ± 1.71
11M0510E	2.00	49.25 ± 0.07	-0.01 ± 0.01	0.02 ± 0.00	6.95	90.28	1.77	44.46 ± 0.10	245.45 ± 0.98
11M0510F	2.25	50.13 ± 0.07	0.03 ± 0.01	0.02 ± 0.00	16.02	88.68	3.54	44.46 ± 0.08	245.44 ± 0.83
11M0510G	2.50	50.70 ± 0.06	0.00 ± 0.01	0.02 ± 0.00	96.99	88.54	4.96	44.89 ± 0.07	247.65 ± 0.74
11M0510H	2.70	49.89 ± 0.06	0.03 ± 0.02	0.02 ± 0.00	15.67	90.79	4.84	45.30 ± 0.07	249.77 ± 0.74
11M0510I	2.90	49.76 ± 0.06	-0.01 ± 0.01	0.02 ± 0.00	27.98	90.25	4.94	44.91 ± 0.07	247.76 ± 0.73
11M0510J	3.10	50.53 ± 0.19	0.85 ± 0.12	0.02 ± 0.00	0.51	88.70	0.23	44.85 ± 0.32	247.44 ± 3.35
11M0510K	3.60	48.85 ± 0.12	-0.02 ± 0.05	0.01 ± 0.00	0.51	93.27	0.51	45.56 ± 0.17	251.13 ± 1.70
11M0510L	4.60	47.69 ± 0.08	-0.01 ± 0.01	0.01 ± 0.00	12.32	94.25	3.08	44.95 ± 0.09	247.97 ± 0.90
11M0510M	5.60	48.61 ± 0.06	0.02 ± 0.02	0.01 ± 0.00	26.78	91.74	6.73	44.59 ± 0.07	246.14 ± 0.68
11M0510N	6.20	47.23 ± 0.06	0.11 ± 0.01	0.01 ± 0.00	3.85	94.02	6.89	44.41 ± 0.06	245.21 ± 0.63
11M0510O	6.80	46.69 ± 0.06	0.00 ± 0.00	0.01 ± 0.00	18.12	95.55	6.30	44.61 ± 0.06	246.22 ± 0.61
11M0510P	7.60	46.34 ± 0.06	0.00 ± 0.01	0.01 ± 0.00	190.09	95.52	6.42	44.26 ± 0.06	244.42 ± 0.61
11M0510Q	8.00	46.66 ± 0.06	0.03 ± 0.01	0.01 ± 0.00	12.70	95.31	6.78	44.47 ± 0.06	245.52 ± 0.62
11M0510R	8.00	46.51 ± 0.08	0.04 ± 0.02	0.01 ± 0.00	10.02	96.73	5.38	44.99 ± 0.08	248.21 ± 0.83
11M0510S	8.00	46.17 ± 0.06	0.01 ± 0.01	0.01 ± 0.00	70.54	96.51	27.12	44.56 ± 0.06	245.97 ± 0.59
11M0510T	8.50	46.89 ± 0.09	0.01 ± 0.02	0.01 ± 0.00	75.61	93.14	2.62	43.67 ± 0.10	241.38 ± 1.01
11M0510U	10.50	47.21 ± 0.08	0.06 ± 0.02	0.01 ± 0.00	7.22	94.49	1.33	44.61 ± 0.10	246.23 ± 1.02
11M0510V	Fusion	46.71 ± 0.10	-0.01 ± 0.04	0.01 ± 0.00	7.22	94.29	0.70	44.04 ± 0.14	243.28 ± 1.41

 $^{40}\text{Ar}^*$  indicates radiogenic  $^{40}\text{Ar}$ .

Plateau age 246.5 ± 1.4

Total fusion age 246.2 ± 1.2

Inverse isochron age 245.1 ± 1.5

**Table V-2: (Continued)**

Step number	Power (W)	$^{40}\text{Ar}/^{39}\text{Ar}$ ± 1σ	$^{37}\text{Ar}/^{39}\text{Ar}$ ± 1σ	$^{36}\text{Ar}/^{39}\text{Ar}$ ± 1σ	K/Ca	$^{40}\text{Ar}^* (\%)$	$^{39}\text{Ar}_K (\%)$	$^{40}\text{Ar}^*/^{39}\text{Ar}_K$ ± 1σ	Age (Ma) ± 2σ
<b>Bt GM119 (experiment VU97D-B9) [46.39640°N; 10.23004°E]</b>									
J = 0.00463130 ± 0.00002177									
13M0075A	1.25	41.12 ± 0.05	0.00 ± 0.00	0.02 ± 0.00	86.82	89.15	3.69	36.66 ± 0.06	282.93 ± 0.90
13M0075B	1.50	37.60 ± 0.05	0.00 ± 0.00	0.00 ± 0.00	126.44	97.59	7.22	36.69 ± 0.05	283.13 ± 0.70
13M0075C	1.75	37.49 ± 0.04	0.00 ± 0.00	0.00 ± 0.00	157.31	98.95	15.04	37.10 ± 0.04	286.03 ± 0.62
13M0075D	2.00	36.90 ± 0.04	0.00 ± 0.00	0.00 ± 0.00	146.92	99.30	11.08	36.64 ± 0.04	282.79 ± 0.63
13M0075E	2.35	36.67 ± 0.04	0.00 ± 0.00	0.00 ± 0.00	149.27	99.28	10.02	36.41 ± 0.05	281.12 ± 0.64
13M0075F	2.70	36.70 ± 0.04	0.00 ± 0.00	0.00 ± 0.00	99.20	99.30	13.45	36.44 ± 0.04	281.37 ± 0.64
13M0075G	3.05	36.29 ± 0.04	0.01 ± 0.00	0.00 ± 0.00	70.80	99.19	10.74	35.99 ± 0.04	278.14 ± 0.63
13M0075H	3.50	36.51 ± 0.04	0.01 ± 0.00	0.00 ± 0.00	38.72	99.12	8.86	36.19 ± 0.05	279.55 ± 0.66
13M0075I	4.00	35.98 ± 0.04	0.01 ± 0.00	0.00 ± 0.00	50.88	99.13	6.92	35.67 ± 0.05	275.85 ± 0.66
13M0075J	4.65	36.20 ± 0.05	0.01 ± 0.00	0.00 ± 0.00	35.49	98.98	6.23	35.83 ± 0.05	276.98 ± 0.70
13M0075K	5.40	35.81 ± 0.05	0.02 ± 0.00	0.00 ± 0.00	23.35	98.79	3.10	35.38 ± 0.05	273.73 ± 0.78
13M0075L	6.65	36.79 ± 0.06	0.02 ± 0.00	0.00 ± 0.00	18.59	98.15	1.43	36.11 ± 0.09	279.00 ± 1.28
13M0075M	8.00	35.28 ± 0.05	0.04 ± 0.00	0.00 ± 0.00	10.39	98.21	1.45	34.65 ± 0.08	268.49 ± 1.13
13M0075N	Fusion	39.58 ± 0.08	0.05 ± 0.01	0.01 ± 0.00	8.22	93.24	0.77	36.91 ± 0.13	284.68 ± 1.80
$^{40}\text{Ar}^*$ indicates radiogenic $^{40}\text{Ar}$ .									
								<b>Plateau age</b>	280.4 ± 3.4
								Total fusion age	280.8 ± 2.5
								Inverse isochron age	246.1 ± 12.6
<b>Bt 034-I1c (experiment VU97D-B8) [46.34941°N; 10.36257°E]</b>									
J = 0.00464220 ± 0.00001996									
13M0074A	1.25	43.09 ± 0.06	0.02 ± 0.00	0.08 ± 0.00	26.33	46.88	3.08	20.20 ± 0.13	161.71 ± 2.03
13M0074B	1.50	31.19 ± 0.04	0.01 ± 0.00	0.02 ± 0.00	34.88	82.11	8.48	25.61 ± 0.05	202.68 ± 0.72
13M0074C	1.75	29.88 ± 0.03	0.01 ± 0.00	0.01 ± 0.00	30.71	88.92	10.77	26.57 ± 0.04	209.82 ± 0.60
13M0074D	2.00	29.59 ± 0.03	0.01 ± 0.00	0.01 ± 0.00	33.88	91.44	12.74	27.05 ± 0.04	213.44 ± 0.56
13M0074E	2.35	29.97 ± 0.04	0.01 ± 0.00	0.01 ± 0.00	54.35	90.78	14.11	27.20 ± 0.04	214.54 ± 0.57
13M0074F	2.70	30.48 ± 0.04	0.02 ± 0.00	0.01 ± 0.00	27.49	89.43	12.91	27.26 ± 0.04	214.97 ± 0.61
13M0074G	3.05	31.36 ± 0.04	0.02 ± 0.00	0.01 ± 0.00	27.80	88.00	8.05	27.60 ± 0.05	217.48 ± 0.67
13M0074H	3.50	30.33 ± 0.04	0.01 ± 0.00	0.01 ± 0.00	30.50	90.97	10.60	27.60 ± 0.04	217.47 ± 0.59
13M0074I	4.00	31.99 ± 0.04	0.02 ± 0.00	0.01 ± 0.00	18.96	86.61	5.32	27.70 ± 0.05	218.27 ± 0.80
13M0074J	4.65	30.24 ± 0.04	0.03 ± 0.00	0.01 ± 0.00	12.72	90.49	8.67	27.37 ± 0.04	215.78 ± 0.63
13M0074K	5.40	35.30 ± 0.05	0.09 ± 0.01	0.03 ± 0.00	4.85	76.60	2.38	27.05 ± 0.09	213.37 ± 1.39
13M0074L	6.65	39.44 ± 0.09	0.08 ± 0.01	0.05 ± 0.00	5.32	62.71	1.44	24.73 ± 0.15	196.08 ± 2.26
13M0074M	8.00	38.58 ± 0.07	0.16 ± 0.01	0.05 ± 0.00	2.72	59.67	1.17	23.02 ± 0.16	183.18 ± 2.47
13M0074N	Fusion	29.75 ± 0.13	0.11 ± 0.03	0.01 ± 0.00	3.97	92.94	0.28	27.66 ± 0.40	217.92 ± 5.94
$^{40}\text{Ar}^*$ indicates radiogenic $^{40}\text{Ar}$ .									
								<b>Plateau age</b>	215.7 ± 2.2
								Total fusion age	211.6 ± 1.7
								Inverse isochron age	214.4 ± 2.9
<b>Bt 031-IIa (experiment VU97D-B6) [46.33479°N; 10.31815°E]</b>									
J = 0.00467480 ± 0.00001905									
13M0073A	1.25	45.84 ± 0.05	0.01 ± 0.00	0.09 ± 0.00	32.22	44.81	4.33	20.54 ± 0.12	165.43 ± 1.83
13M0073B	1.50	44.21 ± 0.04	0.01 ± 0.00	0.08 ± 0.00	38.10	47.48	5.84	20.99 ± 0.11	168.89 ± 1.62
13M0073C	1.75	46.20 ± 0.04	0.01 ± 0.00	0.08 ± 0.00	55.42	46.27	7.32	21.38 ± 0.10	171.84 ± 1.50
13M0073D	2.00	42.81 ± 0.04	0.01 ± 0.00	0.07 ± 0.00	53.98	50.15	8.28	21.47 ± 0.09	172.53 ± 1.35
13M0073E	2.35	57.35 ± 0.05	0.02 ± 0.00	0.12 ± 0.00	25.97	37.33	9.22	21.40 ± 0.13	172.05 ± 1.96
13M0073F	2.70	69.09 ± 0.07	0.05 ± 0.00	0.16 ± 0.00	9.09	31.11	9.87	21.50 ± 0.16	172.74 ± 2.52
13M0073G	3.05	79.51 ± 0.08	0.03 ± 0.00	0.20 ± 0.00	13.59	27.14	8.43	21.58 ± 0.20	173.40 ± 3.04
13M0073H	3.50	73.60 ± 0.07	0.03 ± 0.00	0.18 ± 0.00	13.72	29.57	10.51	21.77 ± 0.17	174.81 ± 2.66
13M0073I	4.00	84.47 ± 0.09	0.02 ± 0.00	0.21 ± 0.00	17.51	25.59	10.57	21.61 ± 0.21	173.63 ± 3.23
13M0073J	4.65	106.43 ± 0.13	0.03 ± 0.00	0.29 ± 0.00	12.82	19.57	7.89	20.83 ± 0.29	167.65 ± 4.46
13M0073K	5.40	111.27 ± 0.12	0.05 ± 0.00	0.31 ± 0.00	8.73	18.25	6.90	20.31 ± 0.30	163.60 ± 4.66
13M0073L	6.65	120.45 ± 0.12	0.07 ± 0.00	0.34 ± 0.00	6.54	16.65	6.82	20.06 ± 0.34	161.71 ± 5.21
13M0073M	8.00	159.79 ± 0.22	0.10 ± 0.00	0.48 ± 0.00	4.14	11.72	3.62	18.73 ± 0.48	151.43 ± 7.42
13M0073N	Fusion	27.32 ± 0.10	0.21 ± 0.03	0.02 ± 0.00	2.06	76.97	0.40	21.03 ± 0.32	169.16 ± 4.87
$^{40}\text{Ar}^*$ indicates radiogenic $^{40}\text{Ar}$ .									
								<b>Plateau age</b>	172.6 ± 1.5
								Total fusion age	169.9 ± 1.6
								Inverse isochron age	171.2 ± 1.6

**Table V-2: (Continued)**

Step number	Power (W)	$^{40}\text{Ar}/^{39}\text{Ar}$ ± 1σ	$^{37}\text{Ar}/^{39}\text{Ar}$ ± 1σ	$^{36}\text{Ar}/^{39}\text{Ar}$ ± 1σ	K/Ca	$^{40}\text{Ar}^* (\%)$	$^{39}\text{Ar}_K (\%)$	$^{40}\text{Ar}^*/^{39}\text{Ar}_K$ ± 1σ	Age (Ma) ± 2σ
<b>Br 028-11c (experiment VU97D-B4) [46.33248°N; 10.31080°E]</b>									
J = 0.00469590 ± 0.00002454									
13M0071A	1.25	38.26 ± 0.04	0.01 ± 0.00	0.06 ± 0.00	70.75	56.08	5.20	21.45 ± 0.08	173.16 ± 1.17
13M0071B	1.50	31.16 ± 0.03	0.00 ± 0.00	0.03 ± 0.00	164.30	69.58	10.83	21.68 ± 0.04	174.93 ± 0.65
13M0071C	1.75	33.37 ± 0.03	0.00 ± 0.00	0.04 ± 0.00	156.56	64.04	9.56	21.37 ± 0.05	172.51 ± 0.81
13M0071D	2.00	39.05 ± 0.03	0.00 ± 0.00	0.06 ± 0.00	264.92	55.25	6.10	21.58 ± 0.07	174.10 ± 1.11
13M0071E	2.35	35.89 ± 0.03	0.00 ± 0.00	0.05 ± 0.00	190.12	58.35	9.57	20.94 ± 0.06	169.22 ± 0.90
13M0071F	2.70	34.42 ± 0.03	0.00 ± 0.00	0.04 ± 0.00	304.06	62.80	13.22	21.62 ± 0.05	174.43 ± 0.77
13M0071G	3.05	38.00 ± 0.03	0.01 ± 0.00	0.06 ± 0.00	85.94	56.66	11.32	21.53 ± 0.06	173.79 ± 0.94
13M0071H	3.50	42.89 ± 0.04	0.00 ± 0.00	0.07 ± 0.00	263.18	50.87	7.79	21.82 ± 0.08	175.99 ± 1.23
13M0071I	4.00	45.30 ± 0.04	0.01 ± 0.00	0.08 ± 0.00	74.74	47.81	7.13	21.66 ± 0.09	174.76 ± 1.37
13M0071J	4.65	48.23 ± 0.05	0.01 ± 0.00	0.09 ± 0.00	47.46	45.57	6.35	21.98 ± 0.10	177.21 ± 1.52
13M0071K	5.40	57.37 ± 0.07	0.01 ± 0.00	0.12 ± 0.00	30.31	37.33	4.39	21.42 ± 0.13	172.90 ± 2.03
13M0071L	6.65	63.90 ± 0.07	0.01 ± 0.00	0.15 ± 0.00	59.92	32.33	4.42	20.66 ± 0.16	167.05 ± 2.44
13M0071M	8.00	61.82 ± 0.07	0.04 ± 0.00	0.14 ± 0.00	10.88	32.01	3.35	19.79 ± 0.15	160.30 ± 2.40
13M0071N	Fusion	23.74 ± 0.05	-0.03 ± 0.01	0.01 ± 0.00	10.81	88.30	0.76	20.96 ± 0.12	169.36 ± 1.82
$^{40}\text{Ar}^*$ indicates radiogenic $^{40}\text{Ar}$ .									
								<b>Plateau age</b>	174.3 ± 1.9
								Total fusion age	173.1 ± 1.8
								Inverse isochron age	173.6 ± 2.1

**Table V-3:**  $^{40}\text{Ar}/^{39}\text{Ar}$  isotopic data for amphiboles.

Step number	Power (W)	$^{40}\text{Ar}/^{39}\text{Ar} \pm 1\sigma$	$^{37}\text{Ar}/^{39}\text{Ar} \pm 1\sigma$	$^{36}\text{Ar}/^{39}\text{Ar} \pm 1\sigma$	K/Ca	$^{40}\text{Ar}^* (\%)$	$^{39}\text{Ar}_K (\%)$	$^{40}\text{Ar}^*/^{39}\text{Ar}_K \pm 1\sigma$	Age (Ma) $\pm 2\sigma$
<b>Hbl GM234 (experiment VU89-G5) [46.38335°N; 10.27098°E]</b>									
J = 0.00327810 $\pm 0.00000820$									
11M0514F	2.25	76665 $\pm$ 23969	9.14 $\pm$ 7.42	255.91 $\pm$ 80	0.05	1.36	0.01	1053.13 $\pm$ 478.78	2694 $\pm$ 1272
11M0514G	2.50	6720 $\pm$ 110	1.68 $\pm$ 0.80	22.15 $\pm$ 0.37	0.26	2.61	0.09	175.91 $\pm$ 29.48	821.40 $\pm$ 221.13
11M0514H	2.70	8442 $\pm$ 203	2.52 $\pm$ 1.24	27.59 $\pm$ 0.67	0.17	3.43	0.06	289.94 $\pm$ 37.42	1205.22 $\pm$ 226.93
11M0514I	2.90	3089 $\pm$ 38	0.69 $\pm$ 0.21	10.21 $\pm$ 0.13	0.63	2.31	0.13	71.52 $\pm$ 13.77	379.99 $\pm$ 131.95
11M0514J	3.20	1599 $\pm$ 59	4.94 $\pm$ 2.87	5.29 $\pm$ 0.20	0.09	2.27	0.01	36.46 $\pm$ 11.97	203.67 $\pm$ 126.44
11M0514K	3.60	2770 $\pm$ 69	1.13 $\pm$ 0.76	9.30 $\pm$ 0.24	0.38	0.80	0.02	22.14 $\pm$ 14.87	126.39 $\pm$ 163.99
11M0514L	4.60	3960 $\pm$ 59	3.36 $\pm$ 0.98	13.04 $\pm$ 0.20	0.13	2.71	0.08	107.73 $\pm$ 17.59	545.62 $\pm$ 153.73
11M0514M	5.60	1428 $\pm$ 7	2.13 $\pm$ 0.35	4.53 $\pm$ 0.03	0.20	6.31	0.36	90.28 $\pm$ 6.05	467.68 $\pm$ 55.19
11M0514N	6.20	736.07 $\pm$ 2.12	1.45 $\pm$ 0.12	2.32 $\pm$ 0.01	0.30	6.85	0.53	50.46 $\pm$ 3.10	276.18 $\pm$ 31.47
11M0514O	6.80	318.93 $\pm$ 0.73	0.89 $\pm$ 0.08	0.97 $\pm$ 0.00	0.48	10.49	0.97	33.48 $\pm$ 1.31	187.89 $\pm$ 13.99
11M0514P	7.60	427.97 $\pm$ 0.79	1.86 $\pm$ 0.11	1.31 $\pm$ 0.01	0.23	9.62	1.15	41.24 $\pm$ 1.74	228.73 $\pm$ 18.17
11M0514Q	8.60	357.61 $\pm$ 0.60	2.21 $\pm$ 0.13	1.07 $\pm$ 0.00	0.19	11.52	1.75	41.25 $\pm$ 1.42	228.82 $\pm$ 14.80
11M0514R	9.50	321.22 $\pm$ 0.52	3.10 $\pm$ 0.17	0.97 $\pm$ 0.00	0.14	10.44	2.32	33.60 $\pm$ 1.29	188.53 $\pm$ 13.77
11M0514S	9.50	95.30 $\pm$ 0.25	3.87 $\pm$ 0.21	0.18 $\pm$ 0.00	0.11	43.48	45.80	41.56 $\pm$ 0.33	230.40 $\pm$ 3.38
11M0514T	9.50	78.83 $\pm$ 0.10	5.48 $\pm$ 0.29	0.13 $\pm$ 0.00	0.08	50.01	23.37	39.58 $\pm$ 0.19	220.09 $\pm$ 1.99
11M0514U	10.50	86.20 $\pm$ 0.10	4.85 $\pm$ 0.26	0.19 $\pm$ 0.00	0.09	34.68	9.20	30.00 $\pm$ 0.26	169.22 $\pm$ 2.80
11M0514V	13.00	67.46 $\pm$ 0.09	3.52 $\pm$ 0.19	0.14 $\pm$ 0.00	0.12	38.67	5.59	26.15 $\pm$ 0.20	148.40 $\pm$ 2.22
11M0514X	16.00	53.40 $\pm$ 0.07	2.69 $\pm$ 0.15	0.11 $\pm$ 0.00	0.16	41.98	4.93	22.46 $\pm$ 0.15	128.18 $\pm$ 1.71
11M0514Y	Fusion	54.01 $\pm$ 0.07	2.41 $\pm$ 0.13	0.11 $\pm$ 0.00	0.18	40.50	3.65	21.92 $\pm$ 0.16	125.16 $\pm$ 1.77

 $^{40}\text{Ar}^*$  indicates radiogenic  $^{40}\text{Ar}$ .

 Plateau age  $157.9 \pm 26.4$ 

 Total fusion age  $211.2 \pm 2.1$ 

 Inverse isochron age  $135.5 \pm 19.8$ 

Step number	Power (W)	$^{40}\text{Ar}/^{39}\text{Ar} \pm 1\sigma$	$^{37}\text{Ar}/^{39}\text{Ar} \pm 1\sigma$	$^{36}\text{Ar}/^{39}\text{Ar} \pm 1\sigma$	K/Ca	$^{40}\text{Ar}^* (\%)$	$^{39}\text{Ar}_K (\%)$	$^{40}\text{Ar}^*/^{39}\text{Ar}_K \pm 1\sigma$	Age (Ma) $\pm 2\sigma$
<b>Hbl 03I-IIa (experiment VU97D-B5) [46.33479°N; 10.31815°E]</b>									
J = 0.00468530 $\pm 0.00002179$									
13M0078A	1.25	20560 $\pm$ 988	-2.35 $\pm$ 0.36	65.45 $\pm$ 3.15		5.93	0.01	1220.11 $\pm$ 84.76	3436 $\pm$ 213
13M0078B	1.50	631.56 $\pm$ 1.20	1.09 $\pm$ 0.03	1.96 $\pm$ 0.01	0.39	8.27	0.78	52.27 $\pm$ 1.85	395.18 $\pm$ 25.13
13M0078C	1.75	295.69 $\pm$ 0.45	3.19 $\pm$ 0.10	0.83 $\pm$ 0.00	0.13	17.23	1.40	51.06 $\pm$ 0.80	386.95 $\pm$ 10.90
13M0078D	2.00	224.28 $\pm$ 0.28	3.37 $\pm$ 0.11	0.58 $\pm$ 0.00	0.13	23.13	2.41	52.00 $\pm$ 0.57	393.36 $\pm$ 7.71
13M0078E	2.35	151.01 $\pm$ 0.18	4.25 $\pm$ 0.14	0.35 $\pm$ 0.00	0.10	31.72	4.29	48.05 $\pm$ 0.35	366.28 $\pm$ 4.77
13M0078F	2.70	104.63 $\pm$ 0.12	4.46 $\pm$ 0.14	0.23 $\pm$ 0.00	0.10	36.69	6.43	38.51 $\pm$ 0.23	299.26 $\pm$ 3.28
13M0078G	3.05	88.64 $\pm$ 0.11	5.28 $\pm$ 0.17	0.17 $\pm$ 0.00	0.08	42.92	10.43	38.18 $\pm$ 0.18	296.92 $\pm$ 2.56
13M0078H	3.50	68.63 $\pm$ 0.08	5.96 $\pm$ 0.19	0.11 $\pm$ 0.00	0.07	51.94	11.92	35.79 $\pm$ 0.12	279.68 $\pm$ 1.77
13M0078I	4.00	47.78 $\pm$ 0.05	5.65 $\pm$ 0.18	0.06 $\pm$ 0.00	0.08	62.34	15.59	29.90 $\pm$ 0.07	236.55 $\pm$ 1.10
13M0078J	4.65	47.11 $\pm$ 0.05	5.87 $\pm$ 0.19	0.06 $\pm$ 0.00	0.07	63.23	15.53	29.91 $\pm$ 0.07	236.62 $\pm$ 1.06
13M0078K	5.40	41.94 $\pm$ 0.04	5.19 $\pm$ 0.17	0.05 $\pm$ 0.00	0.08	63.91	11.79	26.90 $\pm$ 0.06	214.15 $\pm$ 0.93
13M0078L	6.65	39.75 $\pm$ 0.04	5.64 $\pm$ 0.18	0.04 $\pm$ 0.00	0.08	69.36	10.51	27.68 $\pm$ 0.06	219.99 $\pm$ 0.83
13M0078M	8.00	41.48 $\pm$ 0.04	5.90 $\pm$ 0.19	0.05 $\pm$ 0.00	0.07	63.29	5.67	26.36 $\pm$ 0.07	210.10 $\pm$ 1.01
13M0078N	Fusion	45.79 $\pm$ 0.05	5.07 $\pm$ 0.17	0.08 $\pm$ 0.00	0.08	49.73	3.26	22.85 $\pm$ 0.09	183.50 $\pm$ 1.40

 $^{40}\text{Ar}^*$  indicates radiogenic  $^{40}\text{Ar}$ .

 Plateau age  $228.5 \pm 16.7$ 

 Total fusion age  $258.4 \pm 2.3$ 

 Inverse isochron age  $175.7 \pm 12.8$ 

Step number	Power (W)	$^{40}\text{Ar}/^{39}\text{Ar} \pm 1\sigma$	$^{37}\text{Ar}/^{39}\text{Ar} \pm 1\sigma$	$^{36}\text{Ar}/^{39}\text{Ar} \pm 1\sigma$	K/Ca	$^{40}\text{Ar}^* (\%)$	$^{39}\text{Ar}_K (\%)$	$^{40}\text{Ar}^*/^{39}\text{Ar}_K \pm 1\sigma$	Age (Ma) $\pm 2\sigma$
<b>Hbl 010-IIg (experiment VU97D-B2) [46.36312°N; 10.24878°E]</b>									
J = 0.00473810 $\pm 0.00002203$									
13M0077A	1.25	5041 $\pm$ 76	8.23 $\pm$ 0.30	12.74 $\pm$ 0.20	0.05	25.35	0.14	1284.96 $\pm$ 23.13	3533 $\pm$ 56
13M0077B	1.50	536 $\pm$ 2	9.96 $\pm$ 0.32	1.14 $\pm$ 0.01	0.04	37.46	0.62	202.21 $\pm$ 1.54	1212 $\pm$ 13
13M0077C	1.75	231.36 $\pm$ 0.41	12.47 $\pm$ 0.39	0.35 $\pm$ 0.00	0.03	55.64	2.33	129.86 $\pm$ 0.47	865.09 $\pm$ 5.01
13M0077D	2.00	133.71 $\pm$ 0.17	13.25 $\pm$ 0.42	0.14 $\pm$ 0.00	0.03	70.91	5.90	95.70 $\pm$ 0.21	674.61 $\pm$ 2.45
13M0077E	2.35	102.07 $\pm$ 0.11	13.74 $\pm$ 0.44	0.08 $\pm$ 0.00	0.03	77.42	12.85	79.79 $\pm$ 0.14	578.51 $\pm$ 1.79
13M0077F	2.70	79.83 $\pm$ 0.08	13.47 $\pm$ 0.43	0.05 $\pm$ 0.00	0.03	84.33	21.64	67.95 $\pm$ 0.11	503.55 $\pm$ 1.39
13M0077G	3.05	66.64 $\pm$ 0.07	13.56 $\pm$ 0.43	0.04 $\pm$ 0.00	0.03	84.14	13.24	56.61 $\pm$ 0.10	428.66 $\pm$ 1.28
13M0077H	3.50	69.50 $\pm$ 0.07	13.54 $\pm$ 0.44	0.04 $\pm$ 0.00	0.03	84.23	11.81	59.10 $\pm$ 0.10	445.36 $\pm$ 1.31
13M0077I	4.00	71.28 $\pm$ 0.07	13.24 $\pm$ 0.43	0.04 $\pm$ 0.00	0.03	83.55	11.57	60.12 $\pm$ 0.10	452.17 $\pm$ 1.33
13M0077J	4.65	69.07 $\pm$ 0.07	13.35 $\pm$ 0.43	0.03 $\pm$ 0.00	0.03	87.19	6.89	60.79 $\pm$ 0.10	456.62 $\pm$ 1.36
13M0077K	5.40	58.03 $\pm$ 0.08	13.10 $\pm$ 0.43	0.03 $\pm$ 0.00	0.03	87.04	4.22	50.97 $\pm$ 0.11	390.26 $\pm$ 1.54
13M0077L	6.65	64.85 $\pm$ 0.07	12.89 $\pm$ 0.42	0.03 $\pm$ 0.00	0.03	88.70	5.13	58.04 $\pm$ 0.10	438.32 $\pm$ 1.33
13M0077M	8.00	49.63 $\pm$ 0.09	13.15 $\pm$ 0.43	0.03 $\pm$ 0.00	0.03	84.33	2.02	42.24 $\pm$ 0.13	329.12 $\pm$ 1.85
13M0077N	Fusion	45.98 $\pm$ 0.09	13.14 $\pm$ 0.43	0.03 $\pm$ 0.00	0.03	82.16	1.64	38.13 $\pm$ 0.16	299.58 $\pm$ 2.27

 $^{40}\text{Ar}^*$  indicates radiogenic  $^{40}\text{Ar}$ .

 Plateau age  $445.2 \pm 12.9$ 

 Total fusion age  $509.9 \pm 4.2$ 

Inverse isochron age

**Table V-3: (Continued)**

Step number	Power (W)	$^{40}\text{Ar}/^{39}\text{Ar}$ ± 1 $\sigma$	$^{37}\text{Ar}/^{39}\text{Ar}$ ± 1 $\sigma$	$^{36}\text{Ar}/^{39}\text{Ar}$ ± 1 $\sigma$	K/Ca	$^{40}\text{Ar}^* (\%)$	$^{39}\text{Ar}_K (\%)$	$^{40}\text{Ar}^*/^{39}\text{Ar}_K$ ± 1 $\sigma$	Age (Ma) ± 2 $\sigma$
<b>Hbl 032-IIc (experiment VU97D-B7) [46.35123°N; 10.35480°E]</b>									
J = 0.00465330 ± 0.00001815									
13M0094A	1.25	48798 ± 27026	-0.51 ± 0.64	164.37 ± 91		0.47	0.01	227.15 ± 240.77	1301 ± 1965
13M0094B	1.50	7113 ± 857	-0.05 ± 0.11	23.74 ± 2.86	1.46	1.39	0.06	99.02 ± 32.19	684 ± 370
13M0094C	1.75	25202 ± 3556	0.36 ± 0.83	84.68 ± 12	1.19	0.72	0.01	180.49 ± 111.27	1100 ± 1015
13M0094D	2.00	22333 ± 2828	0.76 ± 0.56	73.70 ± 9.34	0.56	2.48	0.02	554.26 ± 117.23	2300 ± 550
13M0094E	2.35	18264 ± 1844	2.13 ± 0.39	57.59 ± 5.82	0.20	6.83	0.03	1249.20 ± 145.92	3462 ± 360
13M0094F	2.70	12862 ± 1032	3.08 ± 0.35	38.60 ± 3.10	0.14	11.32	0.03	1458.82 ± 127.34	3703 ± 275
13M0094G	3.05	32051 ± 3082	22.77 ± 2.28	86.72 ± 8.35	0.02	20.06	0.01	6537.19 ± 649.24	6219 ± 347
13M0094H	3.50	8568 ± 155	11.39 ± 0.26	22.27 ± 0.41	0.04	23.20	0.09	2004.61 ± 46.11	4212 ± 75
13M0094I	4.00	4599 ± 46	8.65 ± 0.13	11.96 ± 0.13	0.05	23.13	0.16	1070.57 ± 18.54	3227 ± 52
13M0094J	4.65	1014 ± 3	6.66 ± 0.05	2.47 ± 0.01	0.06	28.23	1.16	287.78 ± 3.18	1533 ± 23
13M0094K	5.40	358.06 ± 0.59	6.02 ± 0.04	0.79 ± 0.00	0.07	34.62	3.52	124.52 ± 1.01	824.59 ± 10.78
13M0094L	6.65	204.66 ± 0.33	5.87 ± 0.04	0.39 ± 0.00	0.07	43.54	8.30	89.49 ± 0.53	628.06 ± 6.26
13M0094M	8.00	121.02 ± 0.19	5.73 ± 0.04	0.19 ± 0.00	0.07	55.04	14.51	66.89 ± 0.26	488.85 ± 3.38
13M0094N	Fusion	71.83 ± 0.12	5.39 ± 0.03	0.07 ± 0.00	0.08	71.96	72.09	51.90 ± 0.13	390.27 ± 1.77
$^{40}\text{Ar}^*$ indicates radiogenic $^{40}\text{Ar}$ .									
								<b>Plateau age</b>	428.6 ± 96.3
								Total fusion age	493.2 ± 3.8
								Inverse isochron age	344.2 ± 7.6

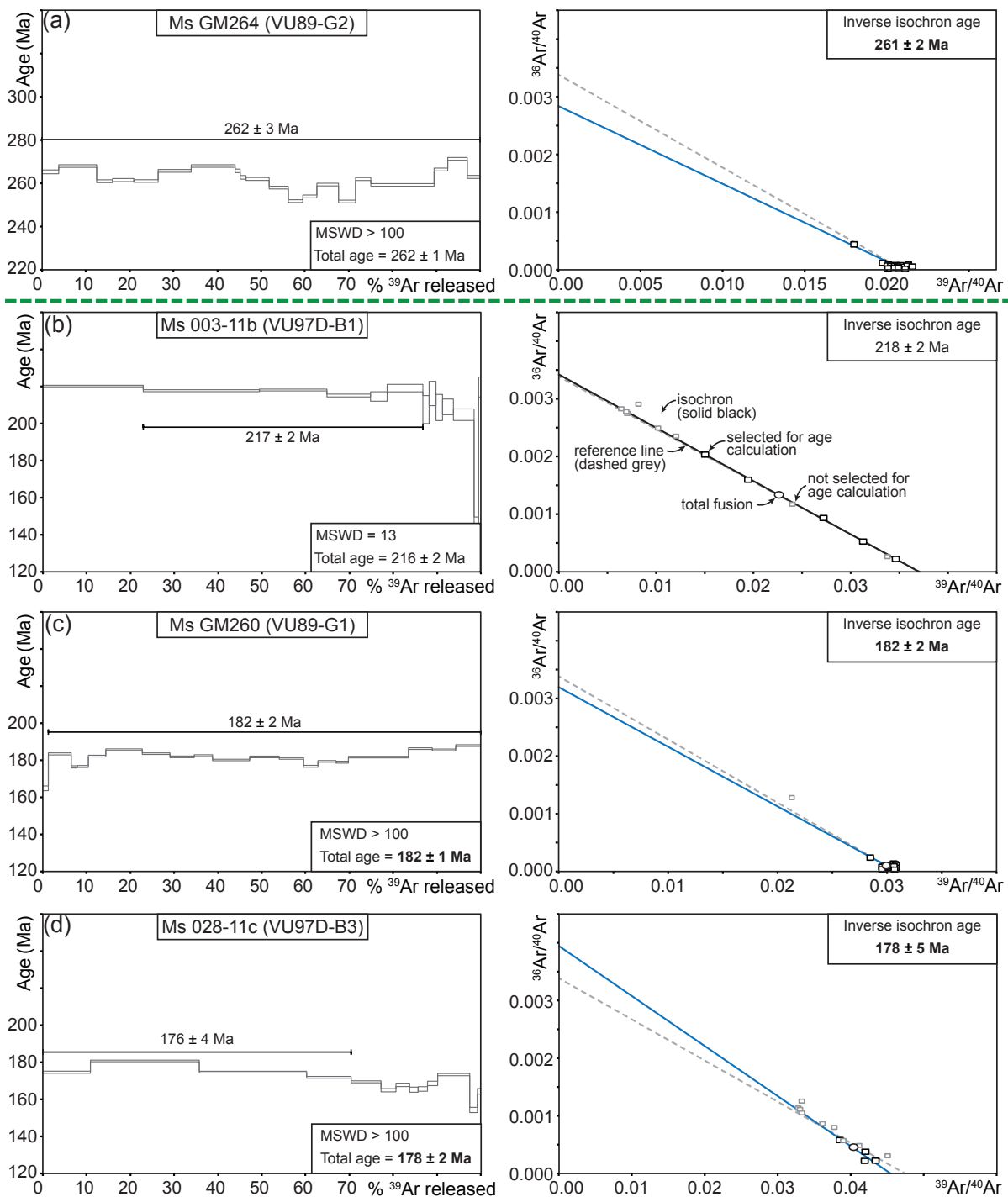


**Fig. V-7:**  $^{40}\text{Ar}/^{39}\text{Ar}$  step-release spectra and inverse isochron plots for muscovite from (a) the Grosina unit and (b-d) the Campo unit. Steps used to determine the “plateau” ages (if possible) are indicated by the horizontal black lines. Ages in bold and blue indicate the most reliable age between “plateau” age, total fusion age and inverse isochron age. Sample locations are shown in Fig. V-2. Analysed mineral, sample and experiment (in brackets) name are indicated (top side) along with the mean square weighted deviation (MSWD) of the “plateau” age and the total fusion age (bottom right-hand side). Ages were regressed using ArArCalc (Koppers, 2002).

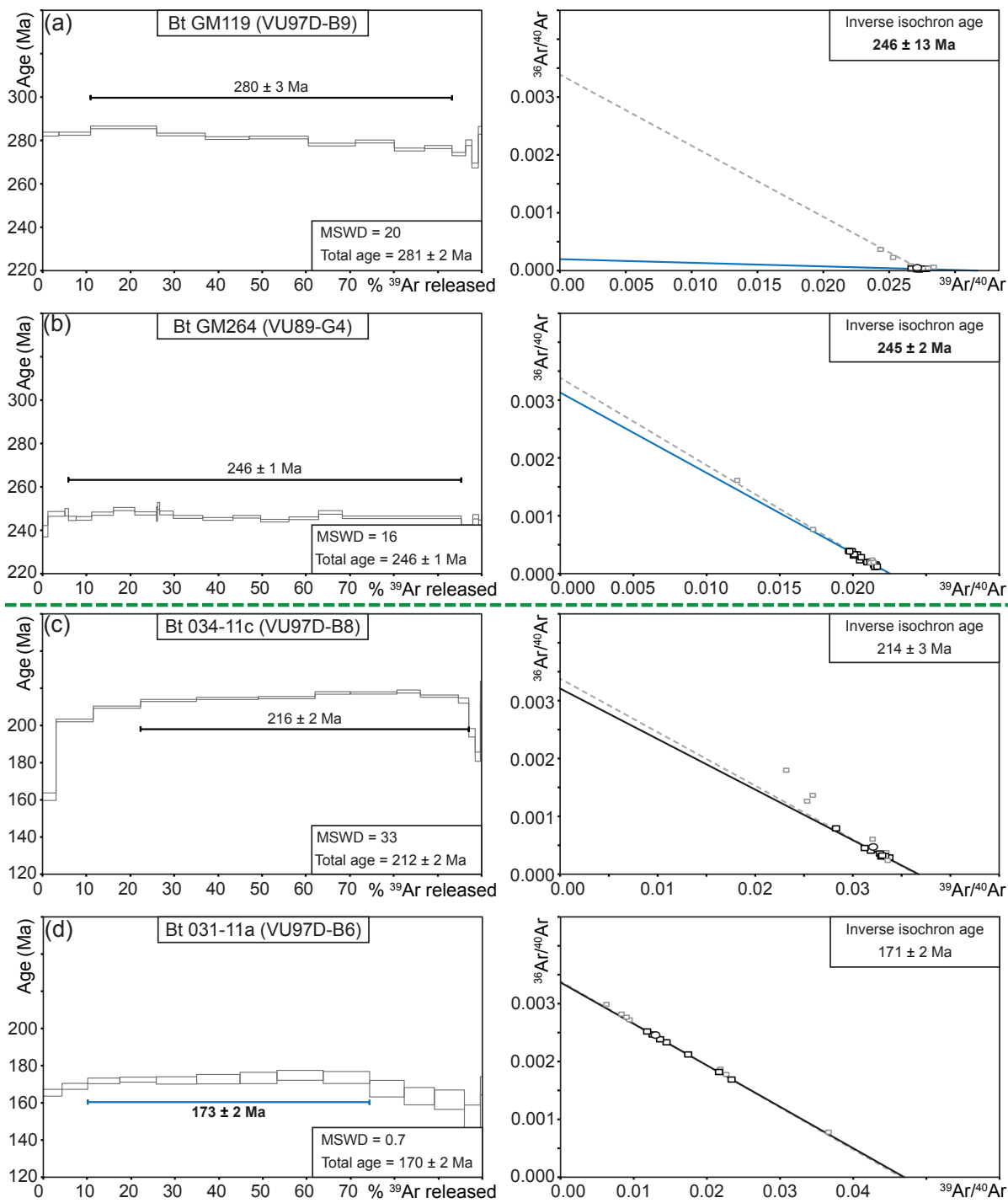


**Fig. V-8:**  $^{40}\text{Ar}/^{39}\text{Ar}$  step-release spectra and inverse isochron plots for biotite from (a,b) the Grosina unit and (c,d) the Campo unit. Steps used to determine the “plateau” ages (if possible) are indicated by the horizontal black lines. Ages in bold and blue indicate the most reliable age between “plateau” age, total fusion age and inverse isochron age. Sample locations are shown in Fig. V-2. Analysed mineral, sample and experiment (in brackets) name are indicated (top side) along with the mean square weighted deviation (MSWD) of the “plateau” age and the total fusion age (bottom right-hand side). Ages were regressed using ArArCalc (Koppers, 2002).

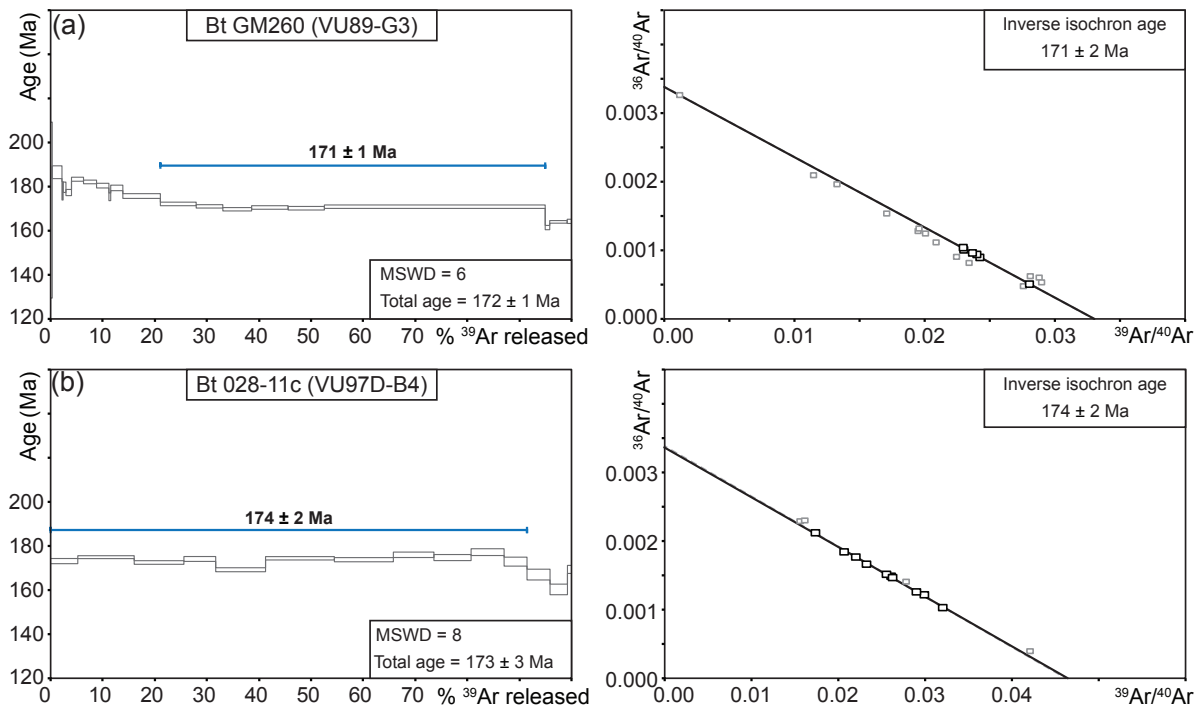


**Fig. V-9:**  $^{40}\text{Ar}/^{39}\text{Ar}$  step-release spectra and inverse isochron plots for biotite from the Campo unit. Steps used to determine the “plateau” ages (if possible) are indicated by the horizontal black lines. Ages in bold and blue indicate the most reliable age between “plateau” age, total fusion age and inverse isochron age. Sample locations are shown in Fig. V-2. Analysed mineral, sample and experiment (in brackets) name are indicated (top side) along with the mean square weighted deviation (MSWD) of the “plateau” age and the total fusion age (bottom right-hand side). Ages were regressed using ArArCalc (Koppers, 2002).

respectively, inverse isochron ages of  $210 \pm 4$  Ma and  $177 \pm 13$  Ma.

*Muscovite 003-11b (experiment VU97D-B1)* [46.35977°N; 10.33070°E] : was separated from a restitic part of a migmatite, in the contact aureole of the Sondalo gabbro. The sample present the Sc3 foliation, and muscovite grows without any shape-preferred orientation after the main deformation and metamorphic peak in leucosomes. 5 consecutive steps taken from 13 steps constrain an age of  $217 \pm 2$  Ma close to the total fusion age of  $217 \pm 2$  Ma (Fig. V-7b). Data are very scattered on an inverse isochron plot, and indicate an age of  $218 \pm 2$  Ma, indicating a strong mixing between air and radiogenic argon. This may suggest weathered muscovite (e.g. illitization; de Jong *et al.*, 2001) but only one radiogenic  $^{40}\text{Ar}$  source and air can be identified on the inverse isochron plot. Alternatively, this unique age older than expected is potentially due to excess  $^{40}\text{Ar}$ .

*Muscovite GM260 (experiment VU89-G1)* [46.35939°N; 10.25048°E] : was separated from a garnet-bearing micaschist presenting the main Sc2 foliation of the Campo basement. 18 consecutive steps loosely define an age of  $182 \pm 2$  Ma, coeval with the total fusion age of  $182 \pm 1$  Ma (Fig. V-7c). Inverse isochron confirms that the sample contains only one argon reservoir with a minor air component and gives a good age of  $182 \pm 2$  Ma. As the spectrum is rough, it is

safier to consider the total fusion or inverse isochron age.

*Biotite GM260 (experiment VU89-G3)* [46.35939°N; 10.25048°E] : was separated from the same sample as the muscovite in the previous experiment. The decreasing age indicates a probable chloritized biotite (Lo & Onstott, 1989). 6 out of 20 steps defines a “sub-plateau” age of  $171 \pm 1$  Ma close to the total fusion age of  $172 \pm 1$  Ma and the inverse isochron age of  $171 \pm 2$  Ma (Fig. V-9a). The inverse isochron plot points to a quite strong contribution of air in the biotite, again pointing to probably chloritization of the mineral. This age therefore must be used with caution.

*Muscovite 028-11c (experiment VU97D-B3)* [46.33248°N; 10.31080°E] : was separated from a micaschist in the vicinity of the Sondalo gabbro. It presents the Sc3 fabric defined by the shape-preferred orientation of minerals. 4 consecutive steps loosely define an age of  $176 \pm 4$  Ma, with a total fusion age of  $178 \pm 2$  Ma (Fig. V-7d). On the inverse isochron, data are well grouped and define an age of  $178 \pm 5$  Ma. In the view of the disturbed step-released spectrum, the inverse isochron age should be preferred.

*Biotite 028-11c (experiment VU97D-B4)* [46.33248°N; 10.31080°E] : was separated from the same sample as the muscovite in the previous experiment. 10 consecutive steps out of 14 steps define a sub-plateau age of  $174 \pm 2$  Ma and a total fusion age of  $173 \pm 3$  Ma (Fig. V-9b). The inverse isochron present scattered data but with an expected age of  $174 \pm 2$  Ma.

*Hornblende 010-11g (experiment VU97D-B2)* [46.36312°N; 10.24878°E] : was separated from an amphibolite presenting fresh hornblende aligned in the Sc2 fabric. Isotopic measurement shows strong excess  $^{40}\text{Ar}$  in the mineral (Fig. V-10a). Both total fusion age of  $510 \pm 4$  Ma and inverse isochron age of  $283 \pm 90$  Ma are geologically meaningless due to the high excess argon content.

*Hornblende 032-11c (experiment VU97D-B7)* [46.35123°N; 10.35480°E] : was selected from a amphibole-bearing gabbro in the center of the Sondalo gabbro, preserving the magmatic structure and minerals. Isotopic measurement shows strong excess  $^{40}\text{Ar}$  in the mineral (Fig. V-10c). Both total fusion age of  $493 \pm 4$  Ma and inverse isochron age of  $344 \pm 8$  Ma are older than the emplacement age determined by Sm–Nd or U–Pb (Bachmann & Grauert, 1981; Tribuzio *et al.*, 1999) and are consequently useless for geochronological purposes.

*Hornblende GM234 (experiment VU89-G5)* [46.38335°N; 10.27098°E] : was separated from an amphibolite with hornblende aligned in the Sc2 fabric. Isotopic measurement shows strong excess  $^{40}\text{Ar}$  in the mineral (Fig. V-10d). Both total fusion age of  $493 \pm 4$  Ma and inverse

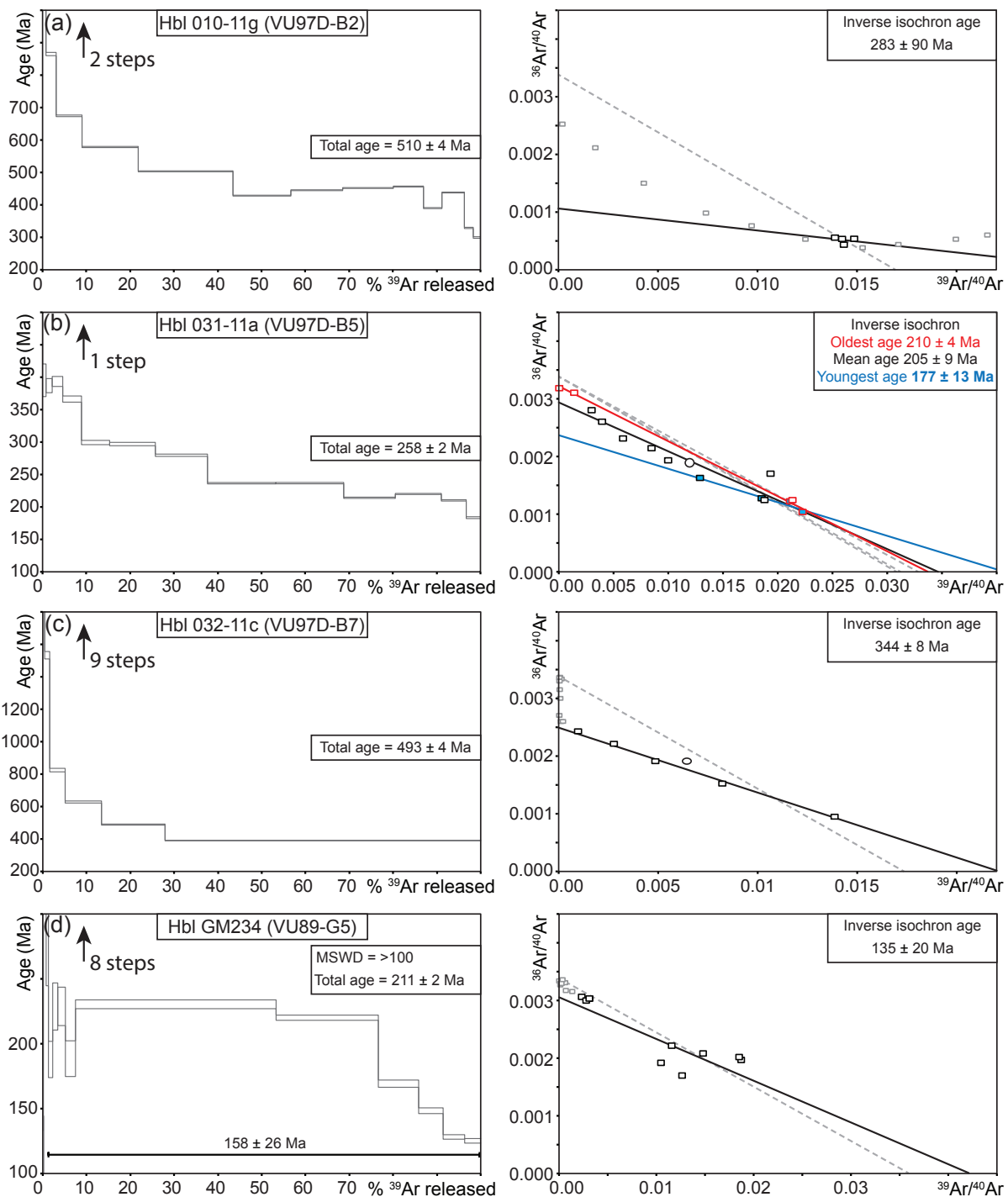


**Fig. V-10:**  $^{40}\text{Ar}/^{39}\text{Ar}$  step-release spectra and inverse isochron plots for hornblende from the Campo unit. Steps used to determine the “plateau” ages (if possible) are indicated by the horizontal black lines. Ages in bold and blue indicate the most reliable age between “plateau” age, total fusion age and inverse isochron age. Sample locations are shown in Fig. V-2. Analysed mineral, sample and experiment (in brackets) name are indicated (top side) along with the mean square weighted deviation (MSWD) of the “plateau” age and the total fusion age (bottom right-hand side). Ages were regressed using ArArCalc (Koppers, 2002).

isochron age of  $135 \pm 20$  Ma are geologically meaningless.

## 4. DISCUSSION ON AGES

### 4.1 Significance of the measured ages

The results of the  $^{40}\text{Ar}/^{39}\text{Ar}$  experiments made on different lithologies from the Campo unit highlight the moderate to strong extraneous incorporation of  $^{40}\text{Ar}$  in some samples, in particular in hornblendes. We synthetize below the geologically consistent results and subsequently discuss the excess argon problem.

#### 4.1.1 $^{40}\text{Ar}/^{39}\text{Ar}$ ages on amphibole and micas

The Grosina and Campo units have apparently undergone contrasting evolutions (Fig. V-11c). The Grosina unit shows consistent muscovite ages between 273 and 261 Ma significantly older than the biotite ages at 248–246 Ma. In contrast, the Campo basement has a poorly constrained amphibole age (between  $210 \pm 4$  and  $177 \pm 13$  Ma) partly overlapping muscovite ages spanning between 182 and 176 Ma. Similar muscovite ages of the Campo basement farther south were dated by Meier (2003) at  $188 \pm 4$  Ma. Dated biotite separates from the Campo basement are slightly younger, ranging between 174 and 171 Ma ( $\pm 1\text{--}2$  Ma). The Figure V-12 shows that the Campo unit has ages significantly younger than the Grosina unit. The transition between the two basements, separated in the field by the Eita shear zone, is characterized by a sharp change in  $^{40}\text{Ar}/^{39}\text{Ar}$  ages (Fig. V-12). In both basements, minerals were separated from high-temperature assemblages inferred to be at least Carboniferous or Permian in age. Therefore, we assume that they are recording the cooling rather than the crystallization of minerals.

#### 4.1.2 Possible reasons for excess $^{40}\text{Ar}$

$^{40}\text{Ar}/^{39}\text{Ar}$  dating relies on the assumption that the system was initially open above the “closure temperature”, where argon is expected to leave the host mineral in an infinite reservoir. This should occur for long term stagnation in the middle and lower continental crust at normal temperature and pressure (e.g. Warren *et al.*, 2012). We suggest that some of our samples present excess-Ar based on: (1) amphibole sampled in and around the Permian Sondalo gabbro have older  $^{40}\text{Ar}/^{39}\text{Ar}$  ages than the age of intrusion of the pluton determined by U–Pb on zircon and Sm–Nd ages (Bachmann & Grauert, 1981; Tribuzio *et al.*, 1999), and (2) few mica ages are inconsistent with respect to the other dated samples coming from the same unit.

We suggest that excess-Ar was mobilized due to the heat introduced into the unit by

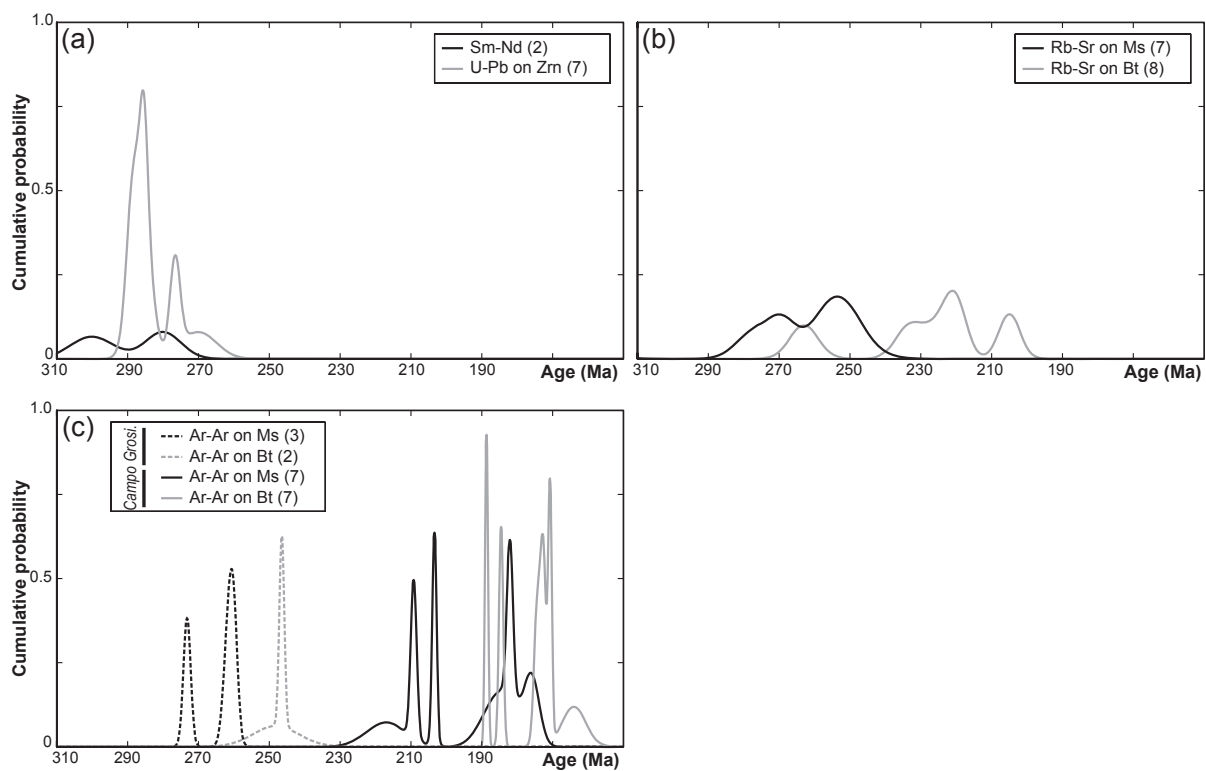


**Fig. V-11:** Cumulative probability histogram of (a) crystallization (Sm-Nd and U-Pb) ages of the Sondalo gabbro, (b) Rb-Sr ages on muscovite and biotite from the Campo unit and (c)  $^{40}\text{Ar}/^{39}\text{Ar}$  and K-Ar ages on muscovite and biotite from the Grosina and the Campo units from both bibliography and present work. The complete dataset is provided in Table V-4.

the mantle-derived mafic intrusion that disturbed the  $^{40}\text{Ar}/^{39}\text{Ar}$  ratio for amphibole and micas. As the mafic magma was generated in the mantle, it has a low K-content and therefore a low radiogenic Ar-production. Therefore, it has a  $^{40}\text{Ar}/^{36}\text{Ar}$  ratio of the mantle (Sarda *et al.*, 1985; Staudacher *et al.*, 1989; Trieloff *et al.*, 1997). The high  $^{40}\text{Ar}/^{36}\text{Ar}$  of the magma is the first possible source of excess-Ar in the pluton. The second possible source may be related to the intrusion of the Sondalo gabbro in a K-rich environment. Although Ar is expected to leave the mineral lattice and diffuse out of the mineral, the higher environmental Ar inhibited this process and eventually triggered back diffusion from the external reservoir into the mineral. This process can even affect the country rock few meters around the intrusion (Hyodo & York, 1993). As the analyzed disturbed minerals are up to 5 km from the intrusion, it questions the extent of the gabbro below the nowadays outcropping surface, or the ability of a postulated excess  $^{40}\text{Ar}$  “wave” to affect the host.

The amphiboles were significantly more affected by excess-Ar than the micas, probably due to the more sensitive character of amphibole due to a low  $^{40}\text{K}$  content and therefore a lower internal radiogenic  $^{40}\text{Ar}$  concentration (Kelley, 2002). Otherwise micas are likely affected by

extraneous argon incorporation due to the higher partition coefficient between extraneous fluids and micas (Kelley, 2002).

Biotite age from the sample BPA 034-11c is *ca.* 40 Ma older than other dated biotites from the Campo basement. Similarly, the muscovite age from the sample BPA 003-11b is ca. 30 Ma older than other dated muscovites. The older “sub-plateau” age presented in Figures V-7b and V-8c may be due to extraneous  $^{40}\text{Ar}$  incorporation homogeneously distributed in the biotite lattice (Foland, 1983; McDougall & Harrison, 1999) eventually brought by fluids (Kelley,

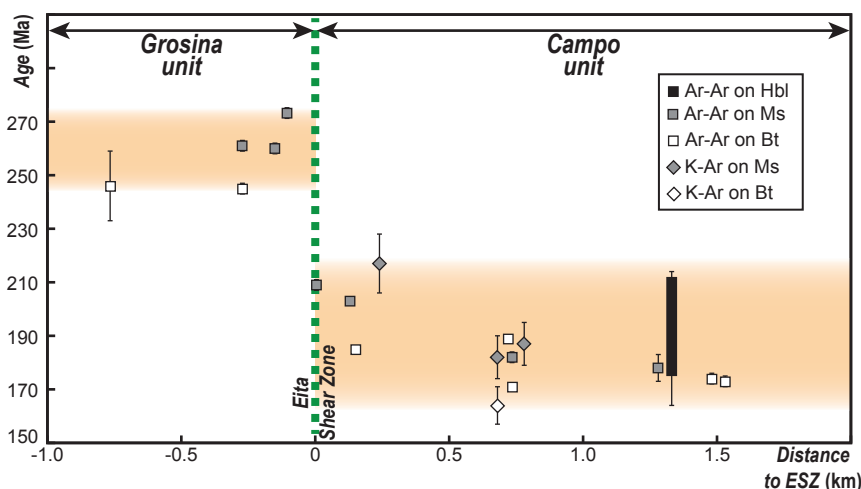


**Fig. V-12:** Time versus distance diagram representing the spatial distribution of the ages with respect to the sub-horizontal Eita shear zone. Errors are represented at a  $2\sigma$  level of confidence.

2002). Nevertheless, a possible alternative explanation may be brought by the temperature-time evolution of the unit, as discussed in a further section with diffusion modelling.

#### 4.2 Exhumation and cooling history of the Campo and Grosina basements

These new ages, together with a compilation of published U–Pb, Sm–Nd, Rb–Sr, K–Ar and  $^{40}\text{Ar}/^{39}\text{Ar}$  ages performed on both the Grosina and Campo basements (see Fig. V-11 and Table V-4), constitute a consistent dataset to estimate the respective cooling history using the notion of rapid or slow cooling. Commonly, the cooling history is inferred from the difference in age of two chronometers with different temperature-dependent closure of the isotopic system. Overlapping or comparable ages record a rapid cooling whereas disparate ages may attest of a slow cooling. In addition, this history may be estimated by calculating the cooling rate, but has to be used with caution, as closure temperatures may be sensitive to other parameters such as the cooling rate itself, the mineral chemistry, the mineral size... In this study, geochronological data are linked to the closure temperature of the probed chronometer/mineral system (Fig. V-13) using for  $^{40}\text{Ar}/^{39}\text{Ar}$ : 500°C for hornblende (Harrison, 1982), 400°C for muscovite (Harrison *et*

**Table V-4:** Compilation of pre-Alpine ages from the Campo/Grosina area (N-limb of the Mortirolo anticline, completed after Meier, 2003).

Lat (°N)	Lon (°E)	Local. prec.	Reference	Sample	Lithology	Unit	Area	Method	Mineral	Age (Ma)	Err. (2σ)
<i>Campo unit, U-Pb and Sm-Nd ages</i>											
46.347	10.349	Mid	Tribuzio <i>et al.</i> , 1999	SO5/1	Troctolite	Campo	Sondalo Gabbro	Sm-Nd	WR-Min	300	12
46.348	10.349	Mid	Tribuzio <i>et al.</i> , 1999	SO5/11	Norite	Campo	Sondalo Gabbro	Sm-Nd	WR-Amp-Pl	280	10
46.322	10.353	Mid	Bachmann & Grauert, 1981	?	Diorite	Campo	Sondalo gabbro	U-Pb	Zrn	270	
46.396	10.342	High	This study	M28B73	Diorite	Campo	Vendrello	U-Pb	Zrn	289	4
46.360	10.311	High	This study	GM 601	Diorite	Campo	Above Alto	U-Pb	Zrn	285	2
46.345	10.325	High	This study	M1B14	Diorite	Campo	Above Sondalo	U-Pb	Zrn	285	6
46.360	10.331	High	This study	BPA 003-12d	Migmatite	Campo	Alto	U-Pb	Zrn	288	5
46.360	10.331	High	This study	BPA 003-12c	Migmatite	Campo	Alto	U-Pb	Zrn	289	4
46.394	10.343	High	This study	BPA 109-12c	Migmatite	Campo	Vendrello	U-Pb	Zrn	277	3
<i>Campo unit, Rb-Sr ages</i>											
46.347	10.350	Mid	Tribuzio <i>et al.</i> , 1999	SO5/1	Troctolite	Campo	Sondalo Gabbro	Rb-Sr	Pl-Amp	266	10
46.348	10.350	Mid	Tribuzio <i>et al.</i> , 1999	SO5/11	Norite	Campo	Sondalo Gabbro	Rb-Sr	Pl-Amp	269	16
46.430	10.170	Low	Del Moro & Notarpietro, 1987	PB2	Granitoids	Campo	Pizzo Bianco	Rb-Sr	Ms	277	10
46.311	10.288	Low	Del Moro & Notarpietro, 1987	VR1	Granitoids	Campo	Vernuga	Rb-Sr	Ms	269	8
46.328	10.336	Mid	Bachmann & Grauert, 1981	?	Ms-pegmatite	Campo	Sant'Agnese	Rb-Sr	Ms	257	
46.322	10.352	Mid	Bachmann & Grauert, 1981	?	Ms-pegmatite	Campo	Mondadizza	Rb-Sr	Ms	251	
46.343	10.271	Low	Hanson <i>et al.</i> , 1966	10-M	Ms-pegmatite	Campo	Val Grosina	Rb-Sr	Ms	252	15
46.362	10.249	Mid	Thöni, 1981	T 946	Pegmatite	Campo	Val Grosina	Rb-Sr	Ms	329	15
46.430	10.170	Low	Del Moro & Notarpietro, 1987	PB2	Granitoids	Campo	Pizzo Bianco	Rb-Sr	Bt	263	8
46.275	10.164	Low	Del Moro & Notarpietro, 1987	VF6	Granitoids	Campo	Val Ferrata	Rb-Sr	Bt	220	6
46.264	10.157	Mid	Del Moro <i>et al.</i> , 1981	VA 2	Granitoids	Campo	Val Ferrata	Rb-Sr	Bt	224	8
46.414	10.149	Low	Del Moro & Notarpietro, 1987	V6	Granitoids	Campo	Val Viola	Rb-Sr	Bt	205	6
46.414	10.149	Low	Del Moro & Notarpietro, 1987	V12	Granitoids	Campo	Val Viola	Rb-Sr	Bt	233	8
46.311	10.288	Low	Del Moro & Notarpietro, 1987	VR1	Granitoids	Campo	Vernuga	Rb-Sr	Bt	127	4
46.314	10.288	Mid	Del Moro <i>et al.</i> , 1981	VA 79-4	Granitoids	Campo	Vernuga	Rb-Sr	Bt	107	4
46.362	10.249	Mid	Thöni, 1981	T 946	Pegmatite	Campo	Val Grosina	Rb-Sr	Bt	97	4
<i>Grosina unit, Ar-Ar ages</i>											
46.350	10.173	High	This study	GM264	Micaschist	Grosina	Above Val de Sach	Ar-Ar	Ms	261	2
46.388	10.254	High	Mohn <i>et al.</i> , 2012	Sample 208	Chl-Orthogneiss	Grosina	ESZ (100m from)	Ar-Ar	Ms	260	2
46.387	10.253	High	Mohn <i>et al.</i> , 2012	Sample 257	Chl-Orthogneiss	Grosina	ESZ(1m from)	Ar-Ar	Ms	273	2
46.396	10.230	High	This study	GM119	Bt-orthogneiss	Grosina	Bt-zone	Ar-Ar	Bt	246	13
46.350	10.173	High	This study	GM264	Micaschist	Grosina	Above Val de Sach	Ar-Ar	Bt	245	2
<i>Campo unit, Ar-Ar and K-Ar ages</i>											
46.335	10.318	High	This study	BPA31-11a	Diorite	Campo	Sondalo	Ar-Ar	Hbl	210	4
46.332	10.311	High	This study	BPA28-11c	Micaschist	Campo	Sommacologna	Ar-Ar	Ms	177	13
46.359	10.250	High	This study	GM260	Micaschist	Campo	Eita valley	Ar-Ar	Ms	178	5
46.363	10.325	High	Mohn <i>et al.</i> , 2012	Sample 17	Granitoid dyke	Campo	ESZ (1m from)	Ar-Ar	Ms	182	2
46.383	10.271	High	Mohn <i>et al.</i> , 2012	Sample 233	Deformed pegmatite	Campo	ESZ	Ar-Ar	Ms	203	1
46.343	10.271	Low	Hanson <i>et al.</i> , 1966	10-M	Ms-pegmatite	Campo	Val Grosina	K-Ar	Ms	209	2
46.362	10.249	Mid	Thöni, 1981	T 946	Pegmatite	Campo	Val Grosina	K-Ar	Ms	217	11
46.353	10.251	Mid	Thöni, 1981	T 945	Micaschist	Campo	Val Grosina	K-Ar	Ms	182	8
46.332	10.311	High	This study	BPA28-11c	Micaschist	Campo	Sommacologna	Ar-Ar	Bt	187	8
46.335	10.318	High	This study	BPA31-11a	Diorite	Campo	Sondalo	Ar-Ar	Bt	174	2
46.359	10.250	High	This study	GM260	Micaschist	Campo	Eita valley	Ar-Ar	Bt	173	2
46.363	10.325	High	Mohn <i>et al.</i> , 2012	Sample 32	Banded migmatite	Campo	Migmatitic aureole	Ar-Ar	Bt	185	1
46.358	10.331	High	Mohn <i>et al.</i> , 2012	Sample 6	Leucosome	Campo	Migmatitic aureole	Ar-Ar	Bt	189	1
46.362	10.249	Mid	Thöni, 1981	T 946	Pegmatite	Campo	Val Grosina	K-Ar	Bt	164	7
46.353	10.251	Mid	Thöni, 1981	T 945	Micaschist	Campo	Val Grosina	K-Ar	Bt	122	6

al., 2009), 300°C for biotite (Harrison *et al.*, 1985); for Rb–Sr: 500°C for muscovite (Jäger *et al.*, 1967), 450°C for amphibole and 300°C for biotite (Dodson, 1973; Jäger *et al.*, 1967). U–Pb and Sm–Nd ages are expected to record the crystallization of the rock. We consider here that these ages record the cooling of the rock below 800°C being roughly when the crystallization of felsic magmas occurs. Cooling rates were calculated for each chronometer pair per sample in order to rule out potential spatial variations of the geothermal gradient (e.g. Mancktelow &

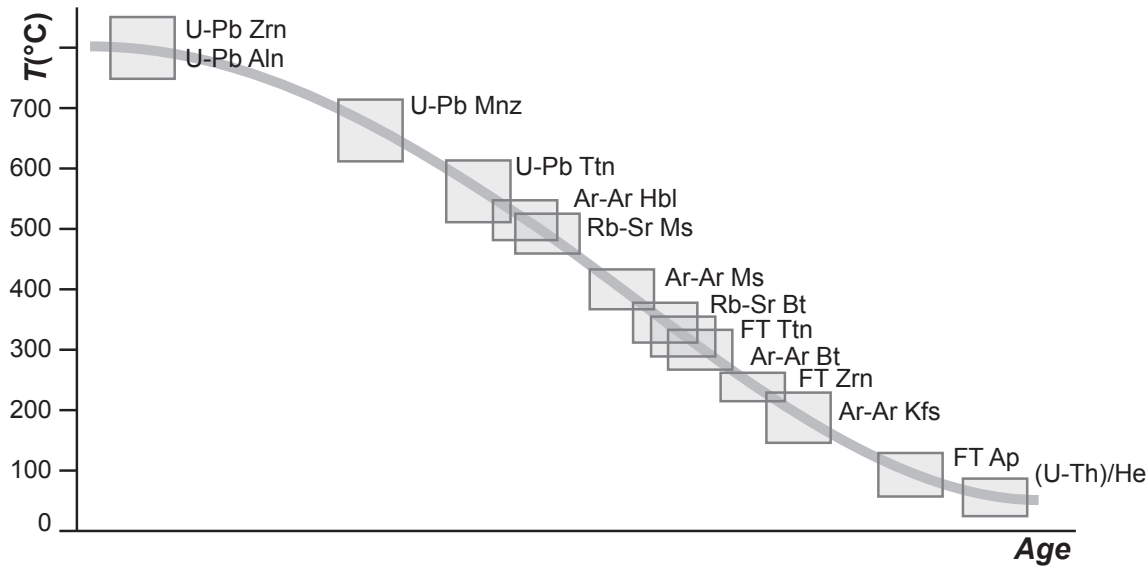


**Fig. V-13:** Synthetic T-t path presenting the closure temperature of different thermo-chronometers (modified after Spear, 1993).

Grasemann, 1997). Results are presented in Figure V-14b. Two distinct cooling “events” can be identified from the data presented in Figures V-11 and V-14: a Permio-Triassic cooling, and a subsequent Jurassic cooling.

#### 4.2.1 Permian cooling

The difference between Sm–Nd and Rb–Sr ages (11 and 34 Ma of difference for samples SO5/11 and SO5/1, respectively) from the Campo unit led Tribuzio *et al.* (1999) and Braga *et al.* (2001) to conclude that rocks from the Sondalo gabbro cooled slowly at a rate of 10°C/Ma after the emplacement in Permian times, but faster immediately after the intrusion. This is confirmed by the Rb–Sr ages on muscovite being 14 Ma older than Rb–Sr ages on biotite (sample PB2 of Del Moro & Notarpietro, 1987) and 35 Ma older than K–Ar ages on muscovite (Sample 10-M of Hanson *et al.*, 1966). The spread of Rb–Sr ages also support a slow cooling (see Fig. V-11b), if they do not correspond to mixed ages possibly done through partial reopening. The cooling history of the Grosina basement is only documented by  $^{40}\text{Ar}/^{39}\text{Ar}$  dating with a gap of 16 Ma between muscovite and biotite from the sample GM 264 (Figs V-7a

& V-8b). Estimated cooling rates for samples collected in the Grosina and the Campo units are similar and around 10°C/Ma and even lower for samples 10-M (of Hanson *et al.*, 1966) and GM 264. We can conclude, following such similarities, that the Campo–Grosina units record the same cooling “event” in Permian to Triassic times that is characterized by low cooling rates in the same range than those described in Ivrea (~5 °C/Ma, Siegesmund *et al.*, 2008).

#### **4.2.2 Jurassic cooling**

The Jurassic cooling is only recorded in the Campo basement by the  $^{40}\text{Ar}/^{39}\text{Ar}$  system. The new hornblende, muscovite and biotite ages presented in this study span in a narrow temporal range with ca. 4 Ma difference between hornblende and biotite (sample BPA 031-11a) and between muscovite and biotite (sample BPA 028-11c). It points to a rapid cooling of the Campo basement, with estimated rates reaching up to 45°C/Ma. Such rapid cooling is also indicated by the near-constant age of consecutive steps for biotites, translated by the lower MSWD values of the “plateau” ages between the Permian cooling stage (Grosina unit) and the Jurassic cooling stage (Campo unit, Figs V-8 & V-9).

#### **4.2.3 Cooling with or without exhumation?**

The cooling of samples and more generally of basement units can be achieved through two end-member processes. The first option is that the sample remains at the same depth, but the crustal section cools, the geothermal gradient decreases and isotherms are deepening. Such way of cooling may result in low cooling rates like those derived from Permian/Triassic times. Low cooling rates below 10°C/Ma are consistent with a conductive cooling of the lithosphere after the Permian high-temperature phase and associated thermal subsidence occurring in Mesozoic times (Ziegler *et al.*, 2004). Moreover, it seems that such cooling rates are characteristics for post-orogenic systems (Busch *et al.*, 1996; Dunlap, 2000). In the Ivrea section, rates are even slightly lower (Siegesmund *et al.*, 2008), potentially due to the protracted magmatic activity in Triassic times in the Southern Alps (e.g. Cassinis *et al.*, 2008; Schaltegger & Brack, 2007). In contrast, rocks can be exhumed to shallower and cooler crustal levels, implying a role of tectonic deformation. With such mechanism, cooling rates are expected to be high, which seems to be characteristic of units affected by the Jurassic rifting (e.g. Beltrando *et al.*, 2013; Bertotti *et al.*, 1999).

#### **4.2.4 Only cooling or re-heating and cooling?**

The estimates of the Grosina unit indicate that this unit was initially at  $T > 400^\circ\text{C}$  before 260 Ma, as indicated by the youngest  $^{40}\text{Ar}/^{39}\text{Ar}$  ages on muscovite. The youngest  $^{40}\text{Ar}/^{39}\text{Ar}$  ages on biotite from the Grosina unit indicates that in Triassic times, at the end of the

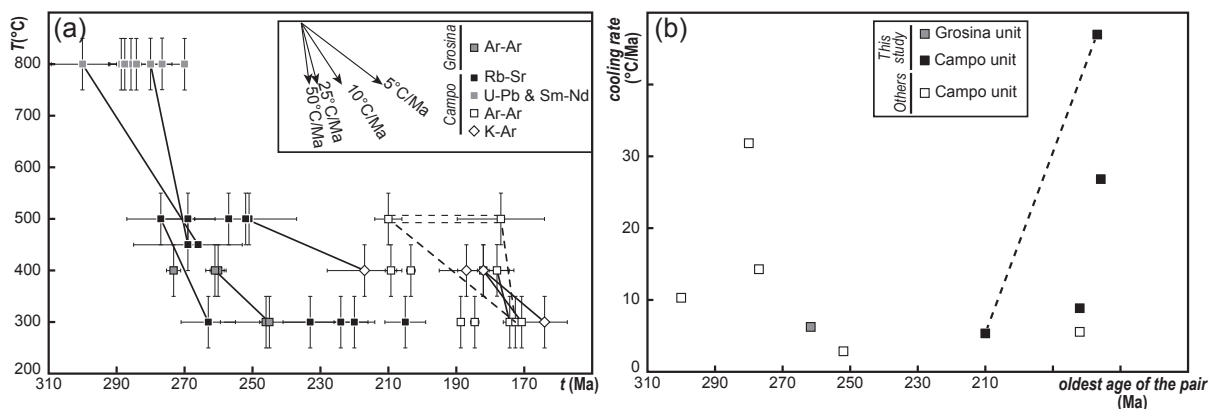


**Fig. V-14:** (a) Temperature ( $T$ ) versus time ( $t$ ) diagram for the different thermo-chronometers for the Grosina and the Campo units. Arrows represent different cooling rate. Error bars are plotted at  $2\sigma$  level of confidence for ages, and are arbitrarily plotted at  $\pm 50^\circ\text{C}$  to denote the uncertainty in closure temperature determination. (b) Calculated cooling rates for samples having different thermo-chronometers represented in function of the oldest age of the different thermo-chronometers. Dotted line indicates the poorly constrained cooling-rate range for sample BPA 031-11a (relying on the amphibole age). The complete dataset is provided in Table V-4. See text for details.

Permian cooling stage, the unit was at temperatures lower than  $300^\circ\text{C}$  at an unknown depth, and was never subsequently re-open. At the onset of the Jurassic cooling event, around 190–185 Ma, the temperature of the Campo basement was between 400 and  $500^\circ\text{C}$ , as indicated by the oldest  $^{40}\text{Ar}/^{39}\text{Ar}$  age of muscovite and eventually by the  $^{40}\text{Ar}/^{39}\text{Ar}$  age of amphibole. The unit was subsequently cooled rapidly to reach temperatures lower than  $300^\circ\text{C}$  after *ca.* 170 Ma, as pointed by the youngest  $^{40}\text{Ar}/^{39}\text{Ar}$  on biotite age. Such a temperature–time path is at odds with the presence of Rb–Sr ages on biotite older than 185 Ma, as their closure temperature should be close to  $300^\circ\text{C}$  (Dodson, 1973; Jäger *et al.*, 1967). Moreover with such fast cooling rates,  $^{40}\text{Ar}/^{39}\text{Ar}$  and K–Ar ages on muscovite and biotite should be encompassed in a narrow time window, not older than 190 Ma for muscovite and older than 180 Ma for biotite.

Therefore, two theoretical scenarios can be envisaged. The first scenario (Fig. V-15ac) involves one single cooling from 500 to  $470^\circ\text{C}$  from Triassic (250 Ma) to Jurassic times (185 Ma), not intersected by re-heating periods, and subsequently exhumed at near-surface conditions ( $50^\circ\text{C}$ , 0.5 kbar) from 185 to 165 Ma, in agreement with the expected fast cooling rates during Jurassic rifting. In such a context, old ages may be due to different closure temperature of minerals due to different grains size, different chemistry, etc. The second scenario (Fig. V-15bd) involves a first Triassic cooling stage continuous to the Permian thermal high, to reach  $270^\circ\text{C}$  in the Triassic, before the onset of rifting. Such a temperature is in line with expected temperatures at the onset of rifting by taking a geothermal gradient of  $25^\circ\text{C}/\text{km}$  suggested by lower crustal environmental conditions at that time (Müntener *et al.*, 2000). Subsequently, the argon system is re-open in Jurassic times from 190 to 185 Ma, followed by a rapid cooling associated to

the exhumation at near surface conditions (50°C, 0.5 kbar) around 165 Ma. In such context, old ages should be regarded as mixed ages between Permo-Triassic cooling and Jurassic re-opening/cooling. In order to test both hypotheses, we modelled the diffusion of argon in micas with DiffArgP (Warren *et al.*, 2011), a version of DiffArg (Wheeler, 1996) implemented with the *P*-dependent diffusion of muscovite (Harrison *et al.*, 2009).

The first model (Fig. V-15e) preserves old ages ( $> 200$  Ma) in the core of big muscovite, whereas small muscovite grains will preserve only ages around 190 Ma, due to the initially slow cooling. This scenario explains the presence of old muscovite ages in the Campo unit as e.g. the  $217 \pm 11$  Ma of Hanson *et al.* (1966). Conversely, biotite present systematically the same age of 180 Ma with any modelled grain size, and that is not consistent with the  $216 \pm 2$  Ma of the biotite from sample BPA 034-11c. Such pattern is due to the fast cooling between 180 and 165 Ma, allowing closure of the crystal in a narrow time range with respect to the argon system. In this context, the Rb–Sr ages older than  $^{40}\text{Ar}/^{39}\text{Ar}$  ages on biotite implies that the closure temperature of Rb–Sr is higher than the proposed value of 300°C. This model implies also to maintain a high geothermal gradient in Triassic time, inconsistent with the lack of potential thermal support by magmatism in the Austroalpine realm, in contrast to the Southern Alps domain. Moreover, it does not fit with the aggradation of shallow-marine sediments at the surface during Triassic times, suggesting subsidence, i.e. either cooling or thinning of the crust).

The second model (Fig. V-15f) with 400°C as peak temperature allows big biotites to preserve ages older than 200 Ma, whereas muscovite is only mildly affected by diffusion, keeping its initial cooling age close to 250 Ma. Higher peak temperature allows partial resetting of muscovite, already visible with 450°C, but with such conditions, biotites are totally re-open and would not preserve old ages, not even for big grains. This model is supported by the supposed geothermal gradient at the onset of rifting in line with the shallow-marine sedimentation in upper crustal levels. Moreover, the re-heating of crustal units during rifting was already described (e.g. Clerc & Lagabrielle, 2014). This model explains well the existence of  $^{40}\text{Ar}/^{39}\text{Ar}$  on biotite ages older than 200 Ma (e.g. sample BPA 034-11c), but is unable to reconcile the measured muscovite ages.

Neither one of the two end-member models fits perfectly with the measured ages. Whereas the first model explains the spread in muscovite ages it does not explain the old ages of biotite and the second model is supported by more geological observations but is unable to explain old and young ages for both muscovite and biotite. The actual temperature-time evolution should lie between the two modelled end-members. We suggest that potentially, one problem may arise from strong differences in mineral chemistry, e.g. for the magmatic biotite of sample BPA 034-11c, that shift the closure of the system to higher temperatures. Another

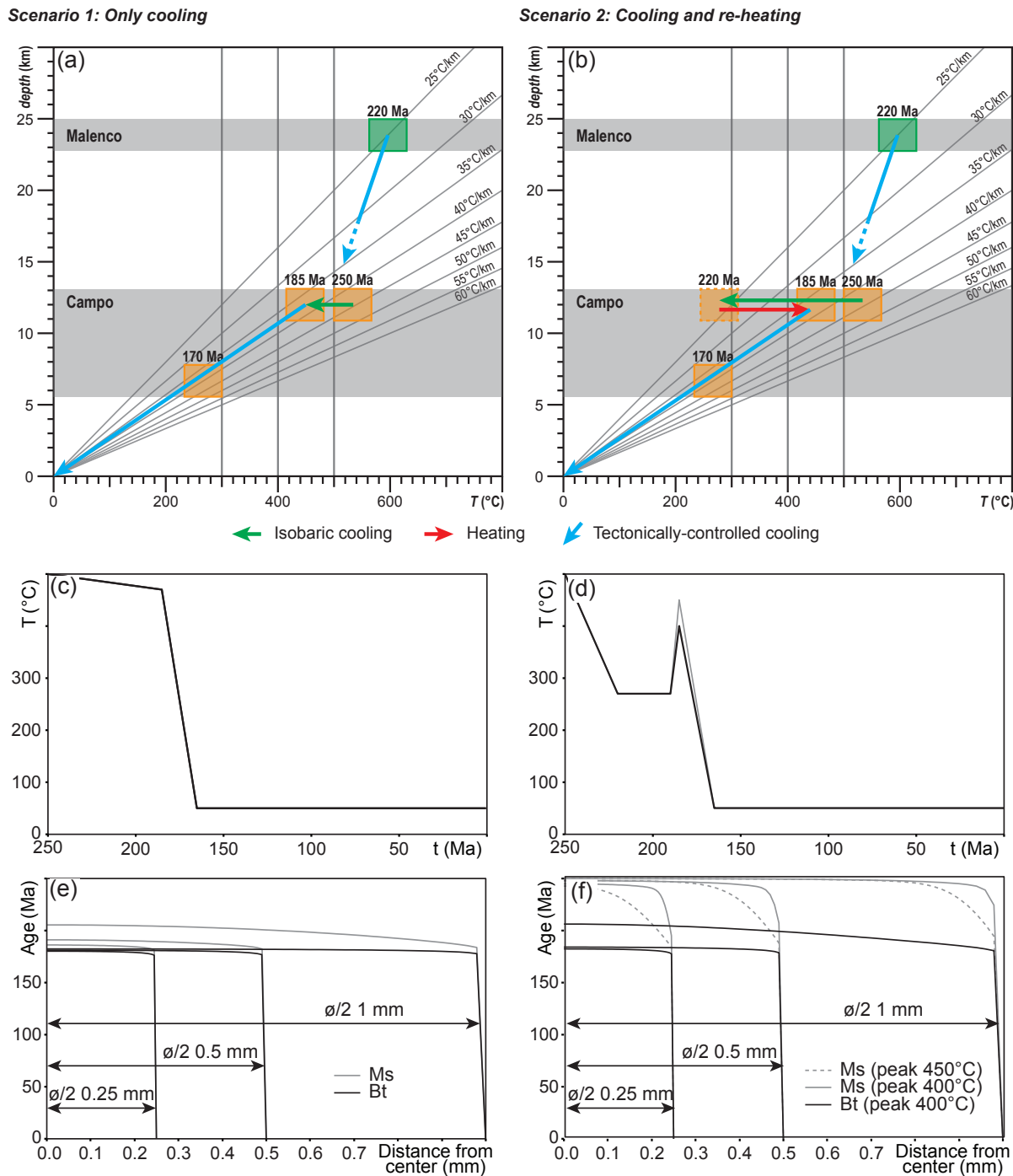


**Fig. V-15:** Two possible scenario of temperature–time–depth evolution for the Campo unit corresponding to (a) one cooling from Triassic to Jurassic times or (b) a Triassic cooling followed by a late-Triassic heating and Jurassic cooling and exhumation. For each thermal evolution (c,d), diffusion of argon in muscovite and biotite is presented for different grain size (e,f). Diffusion was calculated using DiffArgP (Warren et al., 2011; Wheeler, 1996) with initial conditions of 4 kbar/500°C and final exhumation after 185 Ma to reach 0.5 kbar/50°C with one continuous cooling (case 1) or with a re-heating event (case 2). P–T evolution of the Malenco unit is from Müntener et al. (2000).

explanation could also be strong lateral variations in temperature in a rifted margin context (e.g. Scheck-Wenderoth & Maystrenko, 2008).

## **5. EVOLUTIONARY MODEL OF THE FORMATION OF NECKING ZONE**

Our results suggest that the basements of the Adriatic margin, nowadays preserved in the Austroalpine units, records a polyphase tectonic history characterized notably by a Permian post-orogenic cooling, and the subsequent Jurassic thinning. Based on information from the Grosina unit, the Campo unit, and additional data from the Austroalpine and Upper Penninic nappes (Fig. V-16), we propose a polyphase evolutionary model for the formation of the Adriatic necking zone from Permian to Jurassic times.

### **5.1 Post-orogenic evolution**

After deformations associated to the Variscan orogeny, a transient high geothermal gradient was developed (Schuster & Stüwe, 2008) by heat: (1) conducted from the hot rising asthenospheric mantle leading to its partial melting (Müntener *et al.*, 2004; Rampone *et al.*, 1996; Rampone *et al.*, 1998) and/or (2) advected in all crustal levels due to the emplacement of mafic magmas (e.g. Sinigoi *et al.*, 2011). The “high-temperature regime” ceased at *ca.* 260 Ma in the lower crust of the Austroalpine domain (Hermann & Rubatto, 2003), after the emplacement of the lower crustal Braccia gabbro and the mid-crustal Sondalo gabbro (Hansmann *et al.*, 2001; Hermann *et al.*, 2001; Tribuzio *et al.*, 1999). The end of the “high-temperature regime” is also indicated by the conductive cooling of the Grosina unit (Fig. V-17a). Whereas the tectonic activity seems to have stopped in Permian time, the thermal subsidence resulted first in aggradating sequences (overfilling of Permian basins) and eventually in the transgression and development of shallow-marine carbonate platforms during the Triassic.

The amphibolite facies Sg2 foliation of the Grosina unit is crosscut by a granodioritic dyke only affected by Dg3 deformations. Therefore, amphibolite facies Sg1 and Sg2 are older than the dyke supposed to be of Permian age. Therefore, we suggest that both Sg1 and Sg2 fabrics are unrelated to the cooling of the Grosina unit during late-Permian to Triassic times or to the subsequent rifting history. The  $^{40}\text{Ar}/^{39}\text{Ar}$  chronometer was “closed” in the Grosina unit for both muscovite and biotite at the onset of the Jurassic rifting while it was still open in the

Campo unit. Therefore, the depth of the Grosina unit had to lie at the beginning of rifting (late Triassic/earliest Jurassic) at a shallower crustal level (upper crust) comparing with the Campo unit that had to lie at temperatures  $> 300^{\circ}\text{C}$ , i.e. in the ductile middle crust.

## 5.2 Rifting evolution

The thermal regime of rifted margins is essentially controlled by heat supply from lithospheric thinning, and by the intimately associated exhumation and cooling of rocks and emplacement of magma. For magma-poor margins, the temporal variations in the thermal gradient is controlled by a competition between lithospheric and crustal thinning/exhumation processes, which may vary in time and space.

### 5.2.1 Rifting phase I (stretching phase): 220–185 Ma

The first stage of the rifting is characterized in the upper crust by a deformation distributed across the future proximal and distal domains (Fig. V-17b). In the Austroalpine, this rift phase is characterized by the formation of high-angle normal faults cutting through the Triassic platform (Fig. V-16), and the synchronous deposition of the Allgäu syn-rift formation (Eberli, 1988; Froitzheim & Eberli, 1990). Some of these faults are listric and rooted in the

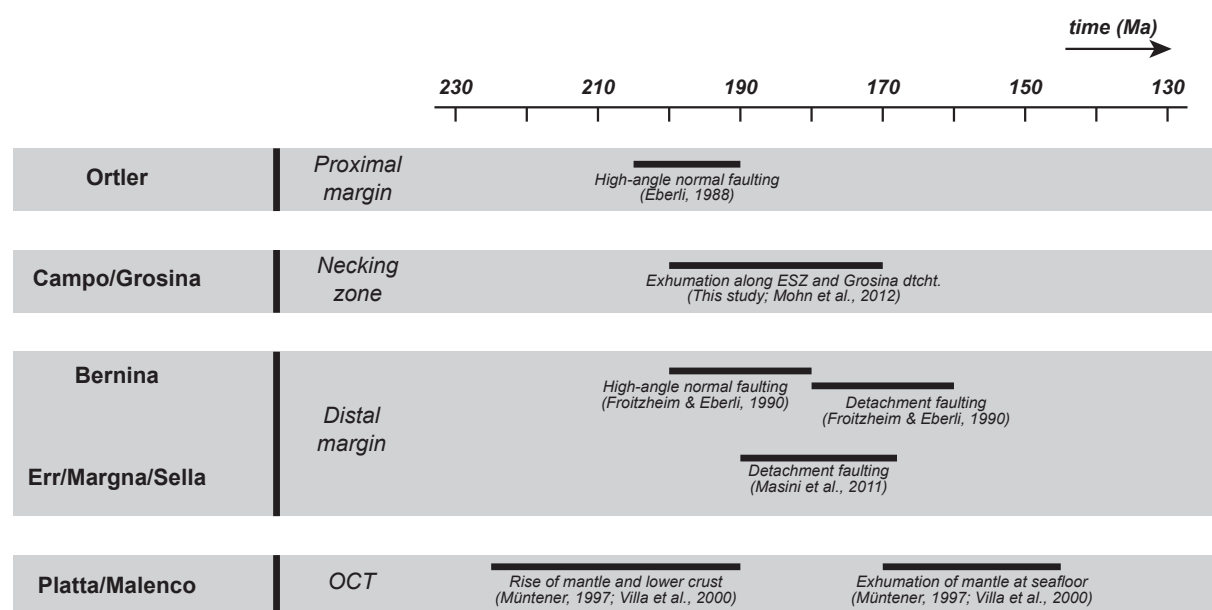


**Fig. V-16:** Compilation of tectonic phase ages from the Adriatic margin in the Austroalpine realm. See text for discussion.

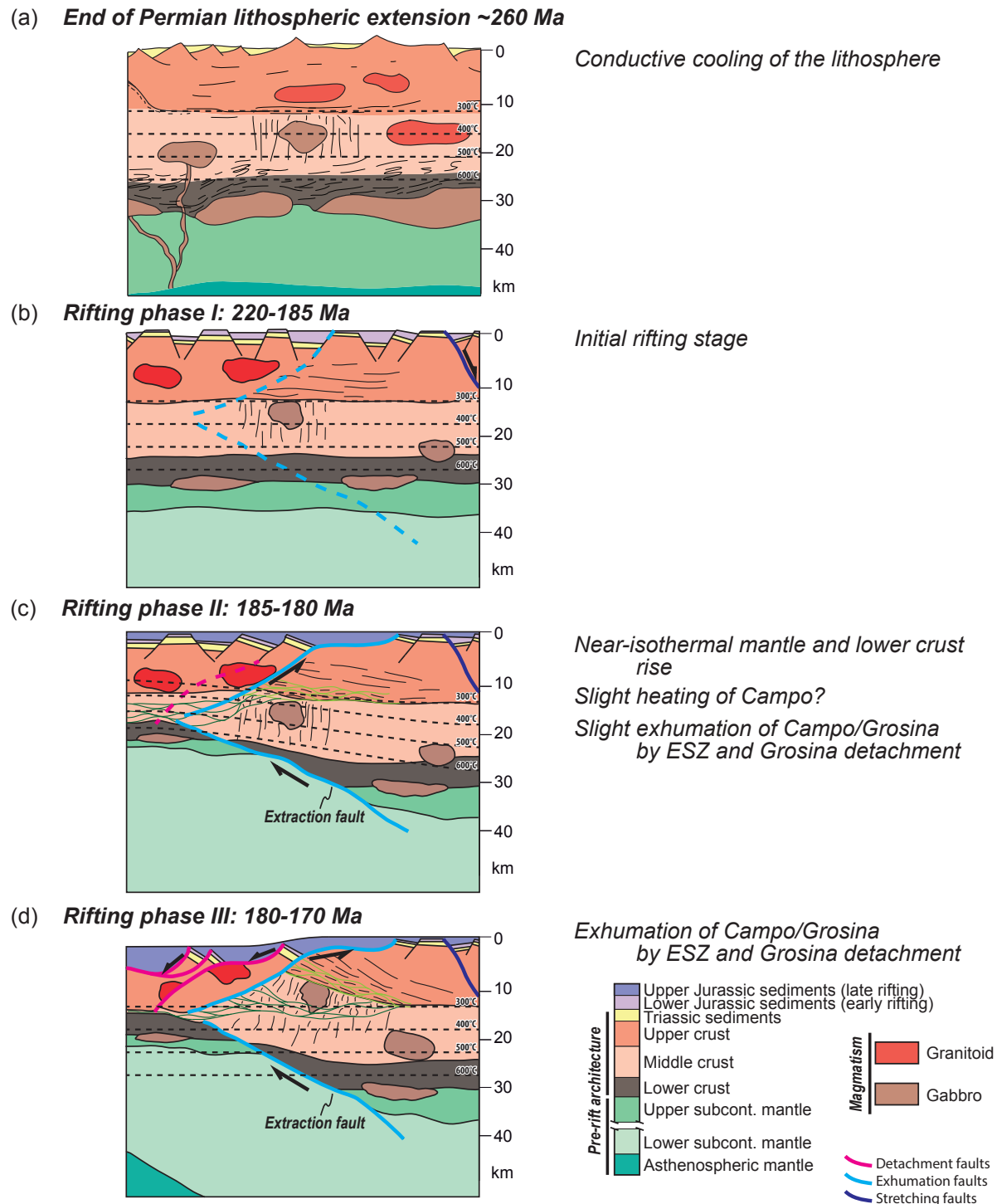


**Fig. V-17:** Evolutionary model of the formation of a necking zone of the Adriatic margin in the Austroalpine domain. (a) ~260 Ma: End of the Permian lithospheric extension. (b) 220–190 Ma: Initial stage with formation of high-angle normal faults. (c) 190–180 Ma: Rise of the mantle and lower crust by thinning of the middle-crust in the distal domain, formation of the necking zone and Eita shear zone, heating of the Campo unit. (d) 180–170 Ma: Exhumation and cooling of the Campo and Grosina unit along the Eita shear zone and Grosina detachment.

middle crust, indicating that extension in the upper-crust was decoupled from deformation in the middle and lower crust (Mohn *et al.*, 2012). Mantle and lower crustal units start to rise and cool, as attested by the first  $^{40}\text{Ar}/^{39}\text{Ar}$  ages on amphibole in the Malenco unit (Müntener, 1997; Villa *et al.*, 2000).

### 5.2.2 Rifting phase II (thinning phase): 185–180 Ma

At the end of the first phase, sub-continental mantle and lower crust are decompressed and exhumed at shallower levels (~15–20 km). Such exhumation is interpreted to be achieved through shearing along extraction faults (e.g. the Margna shear-zone, juxtaposing lower-crustal units in the distal margin to mid-crustal unit in the necking zone (Fig. V-17c). The near-isothermal decompression of deep seated units indicates that they were still reasonably hot at that time. Potentially, the heat of the footwall made of exhumed lower crust and mantle is able to heat adjacent mid-crustal units in the hanging wall of the extraction fault (e.g. Campo unit in Fig. V-17c). This may support a high geothermal gradient in the necking zone at this stage of rifting, and eventually may allow a slight temperature increase and potential resetting of some chronometers.

In the Grosina unit, the Sg2 foliation is locally transposed by a Sg3 fabric in greenschist facies, also found at the contact between the Campo and the Grosina basement (e.g. Eita shear zone in Fig. V-17c). This deformation affects granodiorite dykes of supposed Permian age in the Grosina basement, and also the Permian pegmatites at the top of the Campo basement (dated by Sölna *et al.*, 2003), constraining an upper limit around 255–250 Ma for the greenschist facies deformation. The dating of a pseudotachylite vein at  $84 \pm 1.5$  Ma by Meier (2003) suggested that the Eita shear zone was a major Late Cretaceous Alpine thrust. Alternatively, Mohn *et al.* (2012) interpreted the structure as an extensional shear zone associated to the Jurassic rifting with eventually a reactivation during the Alpine orogeny. The new data presented in this study indicate that the Campo basement has younger  $^{40}\text{Ar}/^{39}\text{Ar}$  ages (200–170 Ma) than the structurally overlying Grosina basement (273–245 Ma), and that the Campo unit was exhumed during Jurassic time along a Jurassic extensional structure. Accordingly to the ideas of Mohn *et al.* (2012), we suggest that part of the Jurassic deformation is accommodated along the Eita shear zone, but also along the numerous greenschist facies structures that sporadically affects the Grosina basement and possibly along the Grosina detachment (Fig. V-17c). This

interpretation, which is based on geochronological data is also supported by the thrusting of the Filladi di Bormio over the Campo–Grosina units during late-Cretaceous times (Trupchun phase of Froitzheim *et al.*, 1994), suggesting that the Grosina unit was lying over the Campo unit before onset of Alpine deformation.

Following the diffusion modelling presented in figure (V-15), the spread of  $^{40}\text{Ar}/^{39}\text{Ar}$  ages on muscovite from the Campo unit may be explained by different grain sizes during either a slow cooling due to a slow exhumation during the phase I. Alternatively, we favor an exhumation where heat is maintained by the exhumation of the neighboring “hotter” lower crust and sub-continental mantle, and eventually by shear-induced heating (e.g. Burg & Gerya, 2005). In the necking zone, thinning is accommodated by formation of amphibolite to greenschist facies structures, represented by the Eita shear zone and associated structures described in the Grosina basement. Therefore, we suggest that the thinning of the continental crust is partly accommodated by a complex set of anastomosing shear zones. At that time, the strain is highly partitioned, as these shear zones did not affect the Campo unit. Eventually, we suggest that this may be due to a strong inherited mechanical anisotropy. Indeed, the Grosina unit showed before the rifting the strong Sg2 planar fabric which may be preferentially reactivated during rifting while the Campo unit with the subvertical foliation was only weakly affected by the Jurassic deformation. At the end of the phase II, the Campo unit was rapidly cooled and exhumed by the synchronous activity of the Eita shear zone and the Grosina detachment.

### **5.2.3 Rifting phase III (exhumation): 180-170 Ma**

At this stage, extensional deformation was localized in the future distal margin (Fig. V-17d). When the continental crust was extremely thinned ( $\sim 10$  km), detachment faults (Err and Bernina detachments) were able to cut through the residual brittle continental crust, exhuming parts of the lower crust and the sub-continental mantle to the seafloor (Froitzheim & Eberli, 1990; Masini *et al.*, 2011; Müntener, 1997; Villa *et al.*, 2000). Exhumation occurs during the deposition of the Salüver formation in the distal domain (Masini *et al.*, 2011). From the Margna-Sella units, it can be shown that the continental crust in the most distal margin is made of pre-rift upper and lower crust preserving Permian sediments and pre-rift lower crust with Permian

gabbro and granulites, without evidence of pre-rift mid crustal rocks in-between (e.g. Müntener & Hermann, 2001). This suggests that exhumation post-dates a previous phase of rifting (phase II) during which the crust was thinned to  $< 10\text{ km}$  by thinning and locale omission of the ductile middle crust.

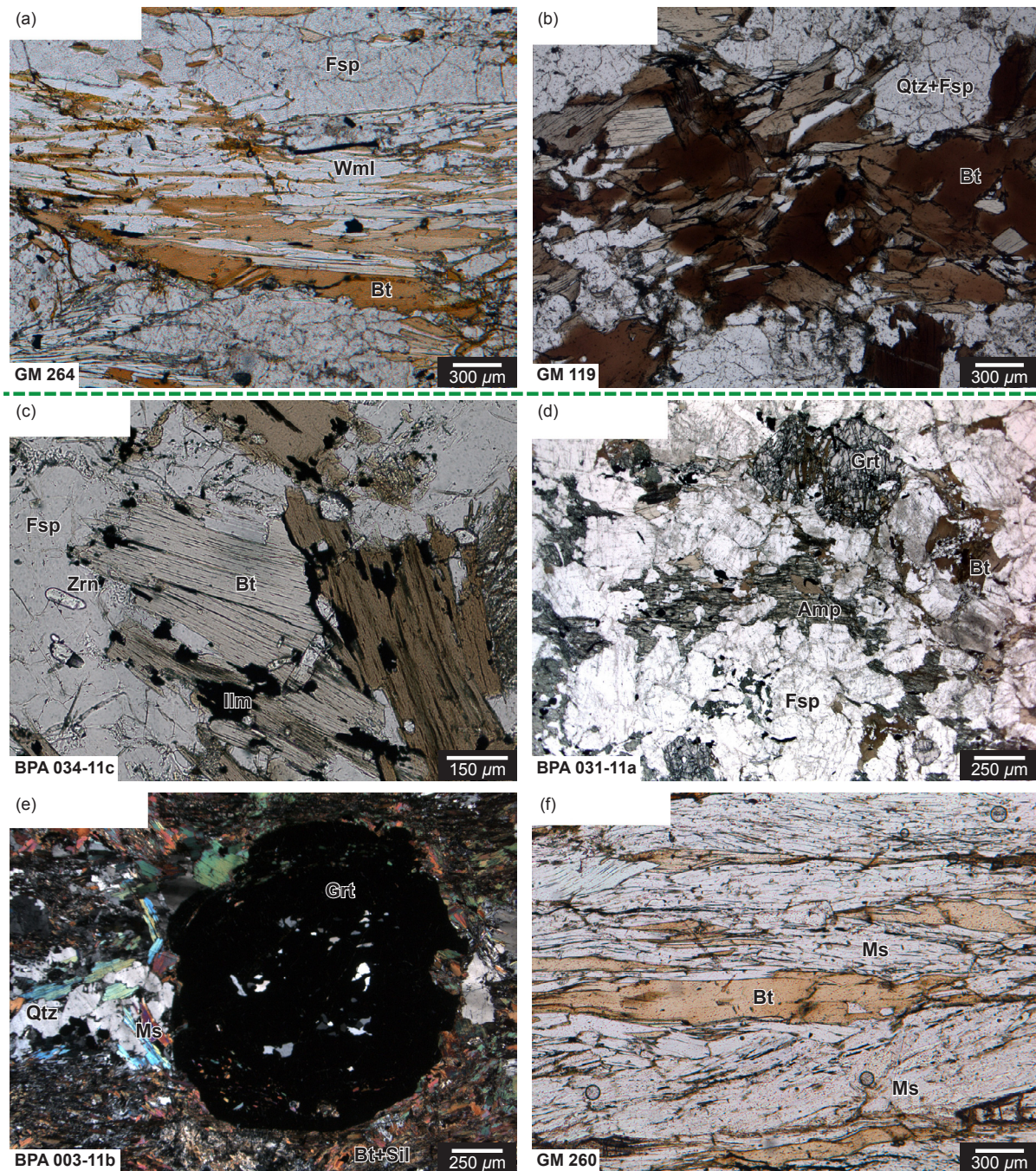
## **6. CONCLUSION**

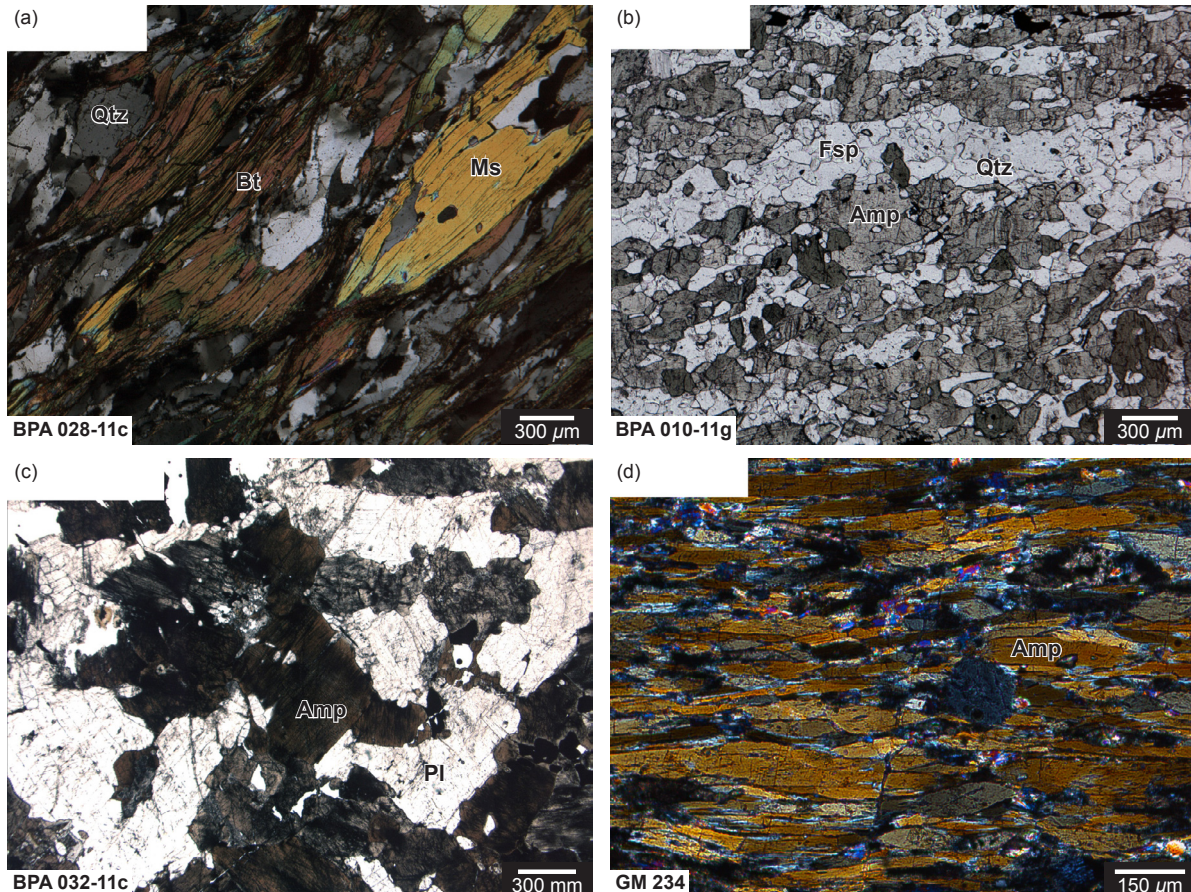
New  $^{40}\text{Ar}/^{39}\text{Ar}$  ages and a compilation of ages from the literature define two cooling gradients in the Campo/Grosina units from the Austroalpine domain (SE-Switzerland, N-Italy). (1) A Permian cooling gradient was initiated before 275 Ma (oldest  $^{40}\text{Ar}/^{39}\text{Ar}$  on muscovite from the Grosina unit) and ended after 245 Ma (youngest  $^{40}\text{Ar}/^{39}\text{Ar}$  on biotite from the Campo unit), leaving the  $^{40}\text{Ar}/^{39}\text{Ar}$  chronometer closed in the Grosina unit and open in the Campo unit. It is recorded in both Campo and Grosina units. Its slow cooling rate indicates cooling without or with a slight exhumation of the units, typical for the cooling of the lithosphere dominated by conduction at the end of the Permian high-temperature phase. (2) A Jurassic cooling rate is recorded in the Campo unit. It is characterized by a rapid cooling initiated before 180 Ma (oldest muscovite dated by  $^{40}\text{Ar}/^{39}\text{Ar}$  in this study) and terminated after 170 Ma (youngest biotite dated by  $^{40}\text{Ar}/^{39}\text{Ar}$  in this study). Such a fast cooling is attributed to tectonic exhumation due to the activity of shear zones and detachment at the top of the Campo and/or Grosina unit (e.g. Eita Shear zone and/or Grosina detachment) during the Jurassic opening of the Alpine Tethys and associated formation of the Adriatic continental margin and more particularly its necking zone.

## **ACKNOWLEDGMENTS**

B. P. benefited from an excellence scholarship “Eole” from the French-Dutch network (RFN-FNA). Roel van Elsas and Klaudia Kuiper are particularly thanked for the mineral separation and preparation, respectively. M.-E. Epin and P. Wernert are gratefully thanked for their assistance on the field during the sampling campaign.

**APPENDIX: PHOTOMICROGRAPHS OF SAMPLES DATED WITH THE  $^{40}\text{Ar}/^{39}\text{Ar}$  METHOD**







---

*CHAPITRE VI*

---



## DISCUSSION GÉNÉRALE

Ce travail de thèse a eu pour but de caractériser les processus post-orogéniques et leurs conséquences pour l'architecture de la lithosphère continentale. Les stades tardi- à post-orogéniques de l'orogénèse varisque en Europe de l'ouest sont caractérisés par une intense activité magmatique, métamorphique et tectonique, en particulier du Carbonifère supérieur au Permien inférieur. Les effets sont importants, à toutes les échelles et à tous les niveaux de la lithosphère continentale, des bassins superficiels au manteau profond (Fig. VI-2). Cette lithosphère, préservant des indices de processus post-orogéniques, est accessible dans les Alpes. En effet, ces niveaux ont été exhumés grâce aux différentes phases extensives mésozoïques, puis compressives du Crétacé au Tertiaire. Ainsi, la mise en place d'intrusions mafiques permianes est reportée dans les Alpes, non seulement en base de la croûte continentale (Hermann *et al.*, 1997; Quick *et al.*, 1994), mais également dans la croûte continentale moyenne et supérieure (Monjoie *et al.*, 2005; Tribuzio *et al.*, 2009; Tribuzio *et al.*, 1999). Alors que la mise en place de ces intrusions de croûte inférieure a été le sujet de nombreuses études depuis plusieurs décennies (voir *chapitre I*), le fonctionnement des systèmes magmatiques plus superficiels demeure peu contraint.

Ainsi, ce travail de thèse concerne un système magmatique et métamorphique permien de croûte moyenne, le gabbro de Sondalo qui se met en place dans l'unité de Campo (nappes austroalpines) dans une phase tardi- à post-orogénique. La compréhension de son fonctionnement a été établie en trois niveaux :

- la compréhension de l'évolution métamorphique de l'encaissant du gabbro de Sondalo, loin, au contact, et dans le pluton (*chapitre III*) ;
- la compréhension des mécanismes d'ascension et de mise en place du gabbro dans la croûte moyenne (*chapitres III et IV*) ;
- la compréhension des systèmes d'exhumation du gabbro, de son encaissant et des unités avoisinantes (*chapitres III, IV et V*).

Ce dernier chapitre a pour but de discuter les résultats et de les intégrer dans un contexte général, permettant de discuter les processus post-orogéniques mais également leur importance pour les phases de déformations postérieures.

## 1. QUEL EST LE LIEN ENTRE MAGMATISME ET MÉTAMORPHISME LORS DE L’ÉVOLUTION TARDI- À POST-OROGÉNIQUE ? (CHAPITRE III)

Dans les Alpes, le Permien est connu pour un épisode métamorphique de haute température et moyenne pression, dont le lien avec des intrusions de magmas mafiques n'est pas systématique (Schuster & Stüwe, 2008). Les métasédiments de l'unité de Campo enregistrent un trajet  $P-T$  associé à l'orogénèse varisque au Carbonifère, daté entre 350 et 325 Ma dans la zone voisine d'Ulten (Langone *et al.*, 2011). Ces métasédiments sont équilibrés dans le faciès des amphibolites (micaschistes à grenat et staurotide, équilibrés à 6 kbar/600°C), lors du développement des foliations Sc1 et Sc2 (Fig. VI-1a). L'unité de Campo est ensuite exhumée dans des niveaux crustaux intermédiaires (~ 4 kbar soit ~12 km de profondeur) entre 310 et 290 Ma avant l'intrusion du gabbro permien de Sondalo (Fig. VI-1b). Cette exhumation est éventuellement associée aux déformations Dc2 dans l'unité de Grosina. La mise en place durant le Permien (289–285 Ma, âges U–Pb sur zircon) du pluton mafique de Sondalo est responsable d'un métamorphisme de haute température, dont l'intensité augmente en s'approchant du pluton, des roches loin de l'encaissant dans l'unité de Campo (à 4 kbar) aux xénolites de l'encaissant incorporés par le pluton (Fig. VI-1c). Une auréole migmatitique est développée autour du gabbro de Sondalo, par fusion partielle de l'encaissant métasédimentaire. Dans cette auréole, les échantillons suivent une évolution contrastée, en étant soit (1) uniquement exhumés (de 6 kbar/750°C à 5 kbar/725°C), soit (2) tout d'abord enfouis (de 4,5 kbar/500°C à 5,2 kbar/800°C) pour être finalement décomprimés sous 4,8 kbar (Fig. VI-1d). Ces déplacements verticaux sont associés au développement d'une foliation de haute température entourant le pluton dans l'auréole métamorphique de contact (Sc4). Lors de l'intrusion, des xénolites dérivés de l'encaissant sont incorporés. Le métamorphisme dans ces roches atteint le faciès des granulites (5,5 kbar/930°C) avant qu'elles soient finalement exhumées à 4 kbar pendant la déformation Dc4 (Fig. VI-1d). En revanche, loin de l'intrusion, le métamorphisme est indiqué par la cristallisation statique d'andalousite et de cordiérite.

La relation complexe entre magmatisme et métamorphisme décrite dans la croûte moyenne, avec la présence d'une auréole migmatitique et de xénolites granulitiques, est également observée dans les systèmes plus profonds de la croûte inférieure (p. ex. Redler *et al.*, 2012; Redler *et al.*, 2013). L'augmentation de chaleur est responsable d'un métamorphisme, à la limite entre le métamorphisme de contact et le métamorphisme régional, affectant des unités qui parfois ne présentent pas de gabbros, comme documenté par exemple dans les Alpes (Schuster & Stüwe, 2008). La chaleur nécessaire au métamorphisme régional est advectée dans la croûte continentale par les gabbros eux-mêmes (p. ex. Annen *et al.*, 2006). De plus, l'état thermique particulièrement élevé du manteau, inhérent à sa fusion partielle, participe au réchauffement de

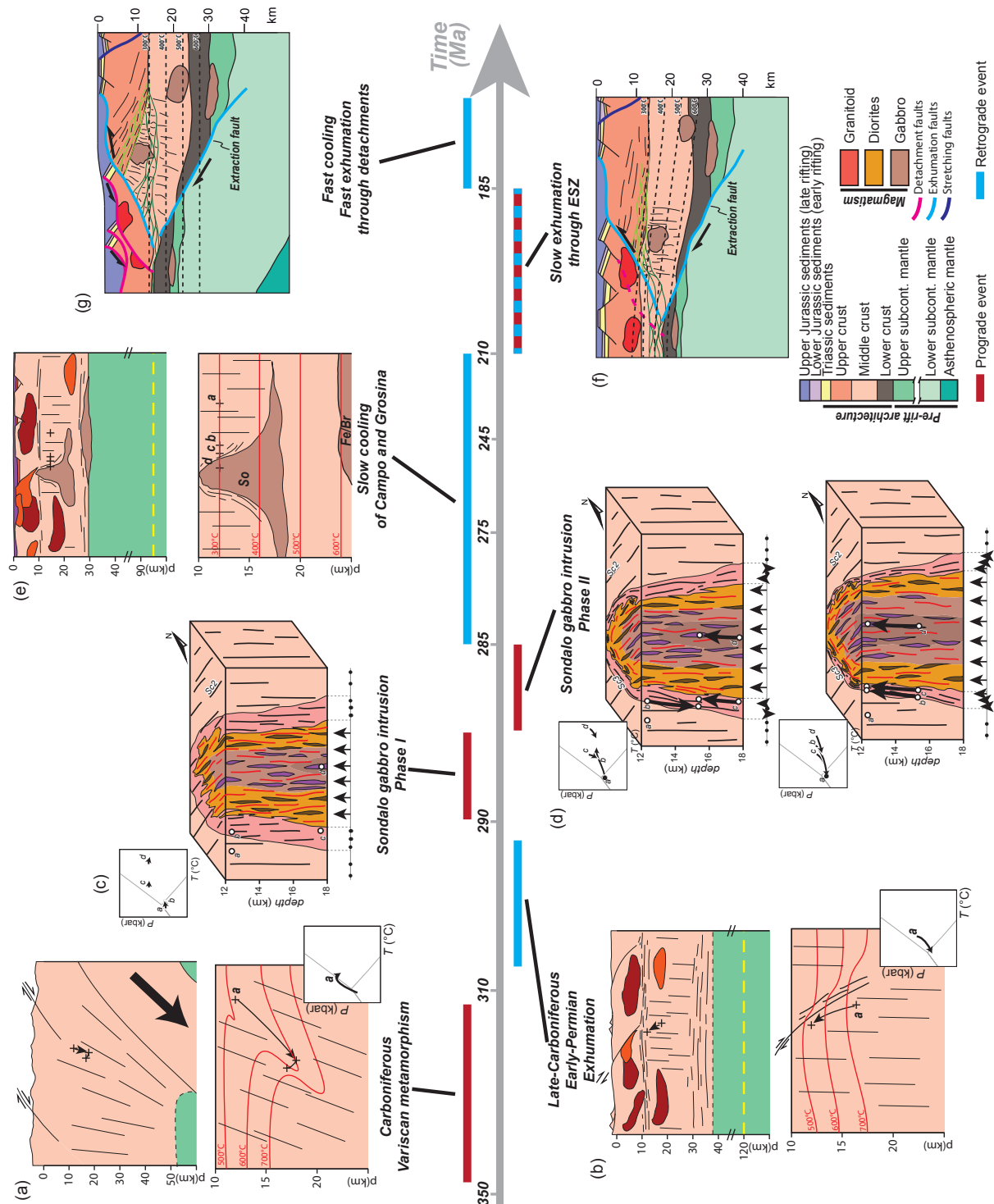


**Fig. VI-1:** Synthèse de l'évolution des unités de Campo et de Grosina du Carbonifère au Jurassique. Voir texte et chapitres précédents pour détails.

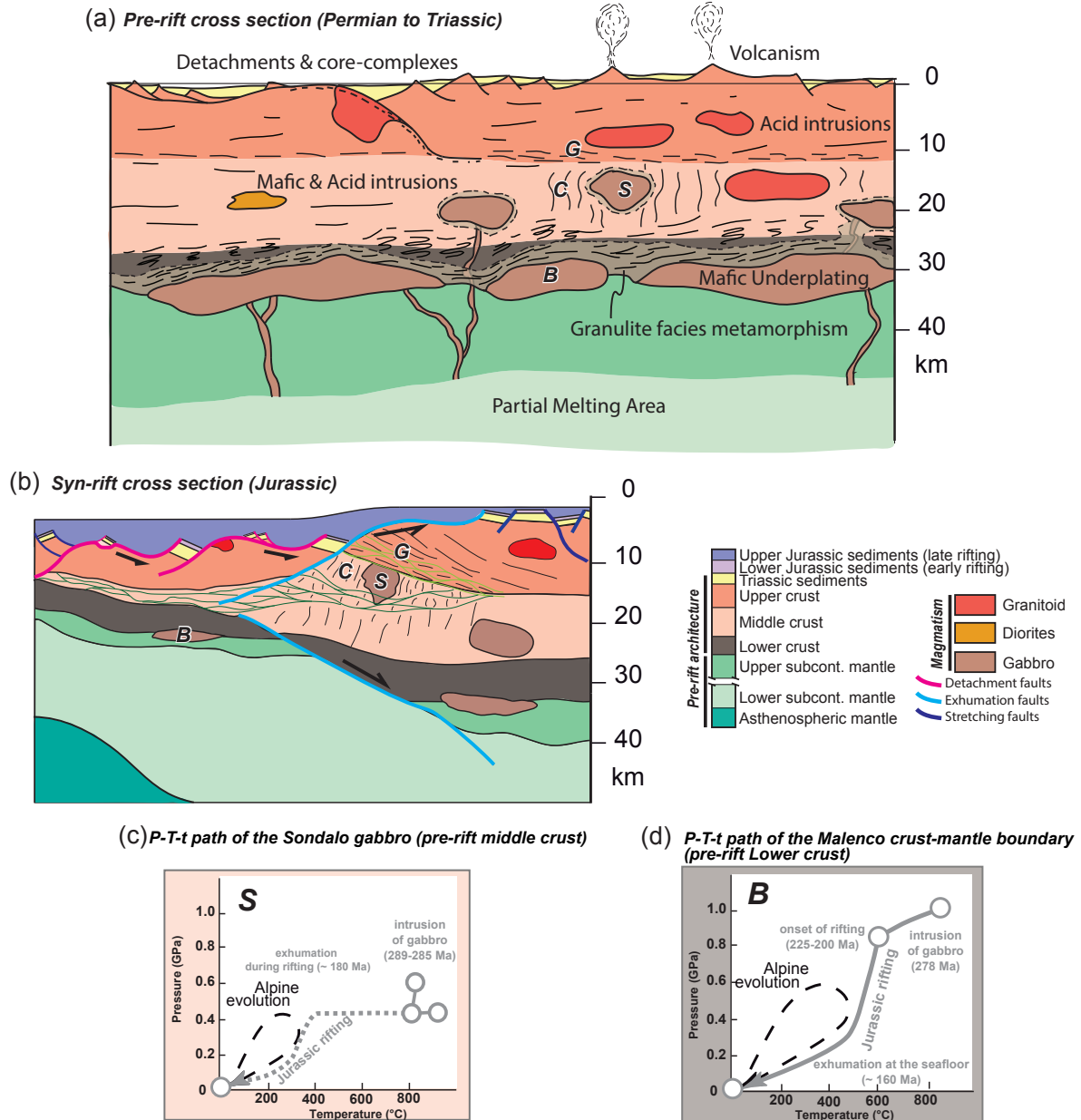


**Fig. VI-2:** (a) Coupe schématique de la croûte continentale au Permien, dans les nappes austroalpines. Modifiée d'après Mohn et al. (2012). (b) Coupe schématique syn-rift le long de la marge adriatique au Jurassique. Voir chapitre V pour détails. S : Sondalo ; G : Grosina ; C : Campo ; B : Braccia. Les trajets P-T-t de (c) Sondalo sont de cette étude et (d) de Malenco/Braccia sont de Müntener et al. (2000).

la croûte continentale par conduction.

Cependant, si la relation entre le métamorphisme régional préexistant et le métamorphisme de contact, associé à la mise en place des gabbros, est assez claire dans l'unité de croûte moyenne étudiée, elle demeure en revanche assez floue dans la croûte inférieure. En effet, dans la zone d'Ivrée, la majeure partie des corps mafiques s'est mise en place dans une unité encaissante ayant déjà subi un métamorphisme dans le faciès des granulites (Barboza *et al.*, 1999). Certains auteurs associent ce métamorphisme à des injections de liquides mafiques plus anciennes que le corps mafique principal (p. ex. Peressini *et al.*, 2007). Dans ce contexte, le métamorphisme de haute température permien serait plus ou moins dans la continuité des chemins  $P-T$  d'exhumation post-orogéniques (Barboza & Bergantz, 2000). Ainsi, le sous-plaquage mafique serait synchrone de l'exhumation de l'unité encaissante (*kinzigite formation*). Cette évolution contraste notablement avec celle de l'unité de Campo, où les pressions enregistrées par les roches encaissantes loin du pluton stagnent à 4 kbar avant, pendant et après l'intrusion, ce qui suggère que le magma mafique se met en place dans une croûte déjà exhumée à la fin de l'orogénèse varisque.

En conclusion, l'amincissement du manteau lithosphérique au Permien est responsable d'un magmatisme mafique mis en place dans la croûte continentale, ainsi que d'un état thermique mantellique particulièrement élevé. Tous deux causent un métamorphisme de haute température décrit dans plusieurs localités en Europe de l'ouest ; toutefois la contribution relative de chacun reste difficile à déterminer, en particulier dans les unités crustales les plus profondes.

## 2. QUELLE EST LA DYNAMIQUE DE MISE EN PLACE DES INTRUSIONS MAFIQUES PERMIENNES ? (CHAPITRES III & IV)

La dynamique d'ascension et de mise en place des magmas mafiques dans la croûte continentale, en dehors des corps mafiques sous-plaqués, reste assez peu documentée. Les relations entre structures magmatiques et métamorphiques d'une part et paragénèses métamorphiques d'autre part indiquent que l'intrusion du gabbro de Sondalo a été opérée en deux phases distinctes, entre 289 et 285 Ma ( $\pm 4\text{--}6$ , âges U–Pb sur zircon), caractérisées par des comportements rhéologiques différents des roches encaissantes de l'unité de Campo. Dans un premier temps (Fig. VI-1c & VI-3b), le liquide magmatique a utilisé et flué le long de la foliation sub-verticale préexistante de l'unité de Campo (Sc2), produisant une foliation magmatique parallèle à Sc2. Les très faibles déformations de l'encaissant métapélitique indiquent que l'ascension du magma a été réalisée par dyking. Ce processus a également été proposé pour la mise en place de magmas mafiques denses dans la croûte inférieure (Rutter *et al.*, 1993). Dans un second temps (Fig. VI-1d & VI-3c), le cœur du pluton est exhumé « en masse », entraînant

les xénolites équilibrés à 6 kbar dans des niveaux moins profonds (~12 km, 4 kbar). Ce transfert est réalisé par cisaillement dans l’auréole métamorphique de contact devenue ductile, pendant la formation de la foliation entourant le pluton (Sc3), mais également dans les parties externes du pluton, comme indiqué par la transposition des foliations magmatiques dans ces zones. Ainsi, lors de cette deuxième phase intrusive, le magma profite de l’adoucissement rhéologique dans l’auréole métamorphique de contact pour atteindre des niveaux plus superficiels.

Les corps mafiques mis en place dans la croûte inférieure présentent de nombreuses déformations synchrones ou postérieures à leur mise en place et sont dès lors décrits comme syn-extensifs (Handy & Streit, 1999; Quick *et al.*, 1994; Zibra, 2006). D’une manière générale, les zones de cisaillement sont particulièrement liées aux intrusions magmatiques, soit parce qu’elles créent l’espace nécessaire à leur mise en place (Rosenberg, 2004), soit inversement parce que le magma les localise (Hollister & Crawford, 1986). De même, bassins sédimentaires, activité volcanique et éventuellement détachements sont fréquemment associés dans la croûte supérieure (Cassinis *et al.*, 1995; Froitzheim *et al.*, 2008; Lago *et al.*, 2004). En revanche, dans les niveaux intermédiaires étudiés, l’absence de déformations sub-solidus permianes empêche toute association directe entre l’intrusion et la déformation tectonique. La tectonique peut au contraire jouer un rôle dans la mobilisation du magma dans la croûte inférieure, afin de permettre son ascension (Fig. VI-3, p. ex. Handy & Streit, 1999). Dans des niveaux superficiels, elle participe éventuellement à l’ouverture des structures le long desquelles le magma percole la croûte – comme par exemple lors de la première phase de l’intrusion du gabbro de Sondalo – mais sa contribution demeure peu contrainte.

À l’opposé des corps mafiques de croûte inférieure qui documentent plutôt des transferts horizontaux de magma (voir p. ex. Rutter *et al.*, 1993), les structures magmatiques du gabbro de Sondalo mettent en évidence un déplacement vertical de magma au travers de la croûte continentale. Une étude géochimique pourrait potentiellement augmenter la compréhension des systèmes magmatiques permians, et en particulier le lien entre les liquides peu différenciés (p. ex. le corps mafique d’Ivrée), et les liquides plus différenciés documentés dans les unités plus superficielles (p. ex. Serie dei Laghi). Dans ce contexte, il reste à déterminer si le gabbro de Sondalo pourrait représenter un intermédiaire magmatique entre les intrusions peu différenciées et différenciées.

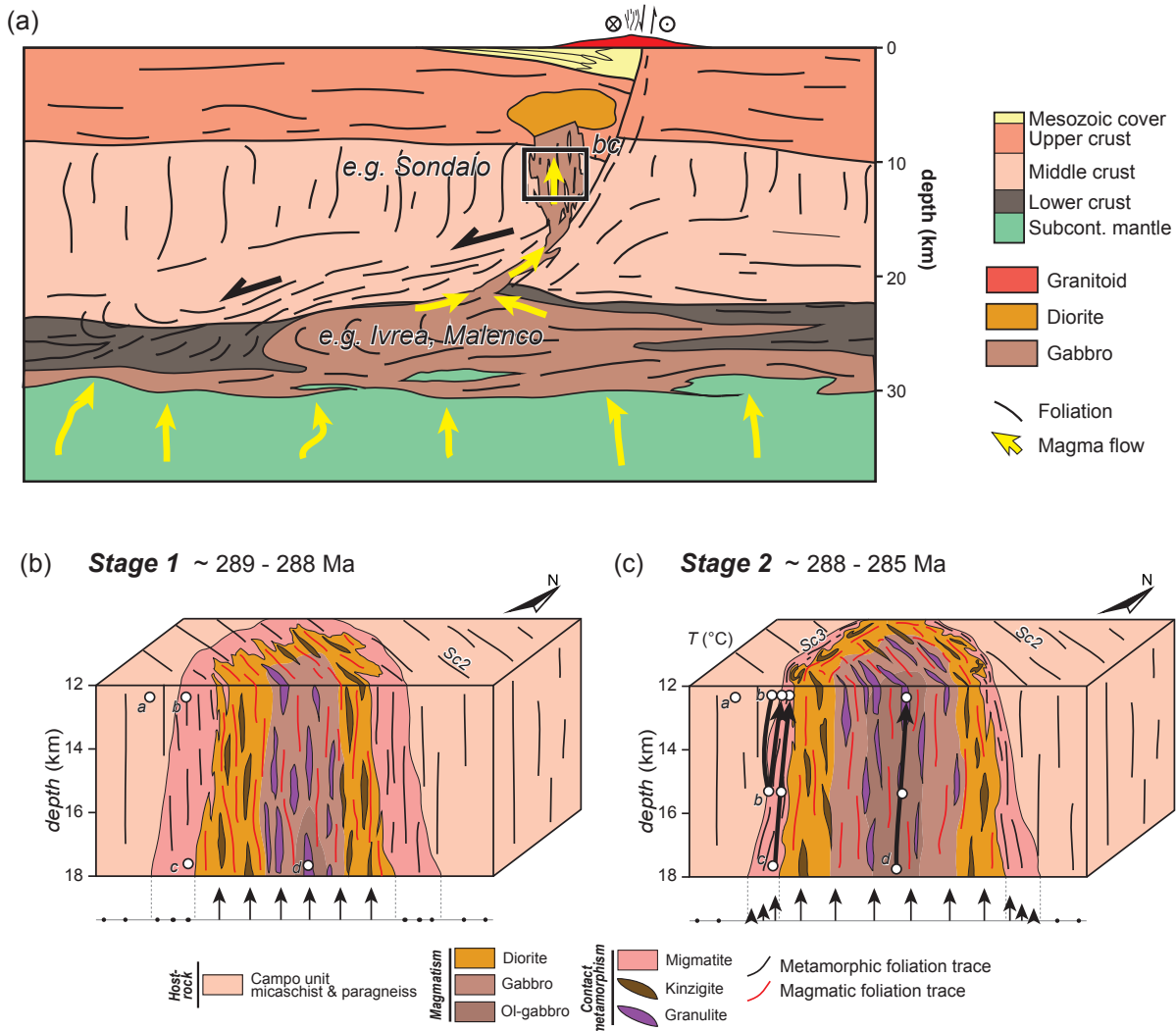


**Fig. VI-3:** Modèle synthétique représentant l'ascension du magma mafique au travers de la croûte continentale. Le magma est extrait de corps mafiques de la croûte inférieure par des zones de cisaillement d'échelle crustale. Modifié d'après Handy & Streit (1999) et Rutter et al. (1993). Le schéma n'est horizontalement pas à l'échelle. (b) Modèle schématique de mise en place du pluton de Sondalo où le magma profite de l'anisotropie mécanique de l'encaissant ( $Sc_2$ ) pour remonter et (c) où le centre du pluton remonte en-masse avec les xénolites lors du développement de la foliation  $Sc_3$  dans l'auréole métamorphique de contact et éventuellement dans la zone bordière du pluton. Voir chapitre IV pour détails.

### **3. QUELS SONT LES SYSTÈMES D’EXHUMATION DES INTRUSIONS PERMIENNES, DE LEUR FORMATION AU RIFTING MÉSOZOÏQUE ? (CHAPITRES III, IV & V)**

L’étude de la formation des bassins sédimentaires dans les Alpes mettent en évidence au moins deux phases de rifting importantes, avec au moins une phase permienne, et une phase jurassique. La relation entre ces phases de rifting a été très discutée (p. ex., Müntener *et al.*, 2000). Il a été proposé que soit (1) le rifting évolue de manière continue du Permien au Jurassique jusqu’à l’ouverture de la Téthys alpine, soit (2) le rifting permien est indépendant du rifting jurassique. Les résultats du *chapitre V* ont permis de contraindre leur rôle relatif dans l’exhumation de Campo et de l’unité sus-jacente de Grosina. Après l’intrusion du gabbro de Sondalo et le métamorphisme de haute température qui y est associé, les roches de l’unité de Campo et de Grosina vont refroidir en plusieurs étapes, permettant de caractériser les deux évènements.

#### **3.1 Le refroidissement permien**

Le refroidissement permien est particulièrement lent ( $\leq 10^{\circ}\text{C/Ma}$ ), comme documenté dans l’unité de Grosina par les âges  $^{40}\text{Ar}/^{39}\text{Ar}$  sur muscovites, bien plus anciens que sur biotite (Fig. VI-1e). Dans l’unité de Campo, il est indiqué par les âges Sm–Nd et Rb–Sr réalisés sur le gabbro (Braga *et al.*, 2001; Tribuzio *et al.*, 1999). Le refroidissement est initié à partir de 275 Ma (plus vieil âge  $^{40}\text{Ar}/^{39}\text{Ar}$  sur muscovite) et se prolonge au moins jusque 245 Ma (plus jeunes âges  $^{40}\text{Ar}/^{39}\text{Ar}$  sur biotite). Pour l’unité de Campo comme pour l’unité de Grosina, il est interprété comme indépendant de toute exhumation tectonique. En d’autres mots, ces résultats montrent que les unités n’ont pas subi d’exhumation tectonique majeure lors du Permien et du Trias. Ainsi, ces unités ont vraisemblablement séjourné longtemps dans les niveaux crustaux dans lesquels ils se trouvaient au Permien inférieur.

Dès lors, après l’évènement permien de haute-température, le refroidissement a probablement eu lieu par conduction thermique, provoquant la subsidence thermique et les bassins *sags* (p. ex. Ziegler *et al.*, 2004; Ziegler *et al.*, 2006), et la fin des conditions de haute température dans la croûte inférieure dans l’Austroalpin (Hermann & Rubatto, 2003).

Ces résultats renforcent un peu plus l’idée selon laquelle les granulites permianes associées au magmatisme mafique représentent des marqueurs fiables de la position des différents niveaux crustaux avant les différents évènements post-permiens (p. ex. rifting jurassique, orogénèse alpine). Elles peuvent ainsi aider à la reconstruction de l’architecture pré-mésozoïque des unités déformées.

Il est important de noter que dans les Alpes du sud et de l'est, l'activité magmatique se poursuit. La continuité des processus magmatiques associée à une subsidence plus importante dans les Alpes de l'est est à relier avec les ouvertures au Permien et au Trias de la Neotéthys, puis des bassins de Meliata et de Vardar (Schmid *et al.*, 2008; Stampfli & Kozur, 2006).

### 3.2 Le refroidissement jurassique

Ces roches sont affleurantes dans l'Austroalpine, exhumées le long de la marge adriatique lors du rifting jurassique de la Téthys alpine, bien distinct des événements permiens. Ce rifting est principalement enregistré par les chronomètres dans l'unité de Campo, avec la présence d'âges  $^{40}\text{Ar}/^{39}\text{Ar}$  jurassiques sur muscovite et biotite quasiment identiques. Le refroidissement de l'unité de Campo est initié avant 182 Ma (plus vieil âge  $^{40}\text{Ar}/^{39}\text{Ar}$  sur muscovite) et continue après 171 Ma (plus jeune âge  $^{40}\text{Ar}/^{39}\text{Ar}$  sur biotite). Les vitesses de refroidissement de l'unité, atteignant jusque 50°C/Ma, semblent typiques des systèmes exhumés tectoniquement lors du rifting. Les unités de Campo et de Grosina représentent un domaine transitionnel entre la marge proximale et la marge distale : la zone d'étranglement (ou necking zone, Mohn *et al.*, 2012). Dans les premiers stades de la formation de cette zone d'étranglement (Fig. VI-1f), l'unité de Campo est légèrement exhumée par cisaillement le long de la zone de cisaillement d'Eita et le long de nombreuses structures associées qui se trouvent dans l'unité de Grosina. Le système est alors supporté thermiquement par l'ascension de la croûte inférieure et du manteau sous-continentale (Malenco). En effet, ces portions profondes de la croûte continentale pré-rift commencent à être exhumées dès 210 Ma (Villa *et al.*, 2000) et vont suivre une exhumation quasiment isotherme (Fig. VI-2bd, Müntener *et al.*, 2000), amenant la chaleur dans les niveaux plus superficiels. La zone d'étranglement est finalement formée lors de l'exhumation de Campo et de Grosina, rapidement opérée par le jeu de failles d'extraction comme par exemple le détachement de Grosina (Fig. VI-1f & VI-2bc).

A partir de la fin du Crétacé, les structures de la marge continentale vont être réactivées par la compression Alpine, détaillées par Froitzheim *et al.* (1994) et Mohn *et al.* (2011).

Par conséquent, dans les unités de Campo et de Grosina, ainsi que dans les unités plus profondes (Müntener *et al.*, 2000), il semble que la phase de rifting permienne représente un événement indépendant du rifting jurassique. En revanche, cette distinction vue dans les Alpes centrales n'est peut-être pas aussi évidente dans les Alpes du sud et de l'est.

## **4. L'EXTENSION POST-OROGÉNIQUE PERMIENNE : QUEL CONTEXTE GÉODYNAMIQUE ?**

### **4.1 Dynamique lithosphérique permienne**

#### **4.1.1 Évolution des bassins**

Les stades finaux de l'orogénèse varisque sont marqués par l'ouverture de bassins sédimentaires syn-convergents au Carbonifère, bassins qui deviennent plus nombreux à partir du début du Permien, dans un régime tectonique transtensif (Fig. VI-4a, Arthaud & Matte, 1977; Burg *et al.*, 1994; Lorenz & Nicholls, 1976). Cette évolution indique que les reliefs s'aplanissent progressivement. La morphologie des bassins est différente selon leur position par rapport à l'ancien orogène : nombreux, fins et allongés dans les anciennes parties internes, ils sont plus larges dans les parties externes (Fig. VI-4a). Que ce soit au nord ou au sud, les bassins sont progressivement connectés sans jeu de faille (McCann *et al.*, 2006), c'est-à-dire par subsidence thermique (p. ex. Ziegler *et al.*, 2004; Ziegler *et al.*, 2006), comme cela est également suggéré par les âges  $^{40}\text{Ar}/^{39}\text{Ar}$  dans les nappes austroalpines (*chapitre V*). Ainsi, pendant le Permien inférieur, l'asthénosphère était probablement peu profonde dans tout le domaine ouest européen, jusque dans le sud de la Norvège.

La présence de bassins contemporains en dehors de la chaîne ne peut pas être expliquée par l'effondrement gravitaire, mais implique que les forces tectoniques soient transtensives à extensives (p. ex. Henk, 1999). Cette tectonique résulte des mouvements différentiels entre les blocs Gondwana et Laurussia, également responsables des nombreux décrochements documentés au Permien en Europe de l'ouest (Arthaud & Matte, 1977). L'éventuelle contribution de l'effondrement gravitaire dépend de l'épaisseur originelle de la croûte continentale, épaisseur qui est actuellement difficile à estimer alors que la topographie du domaine orogéniques reste soumise à discussions (voir p. ex. Franke, 2012).

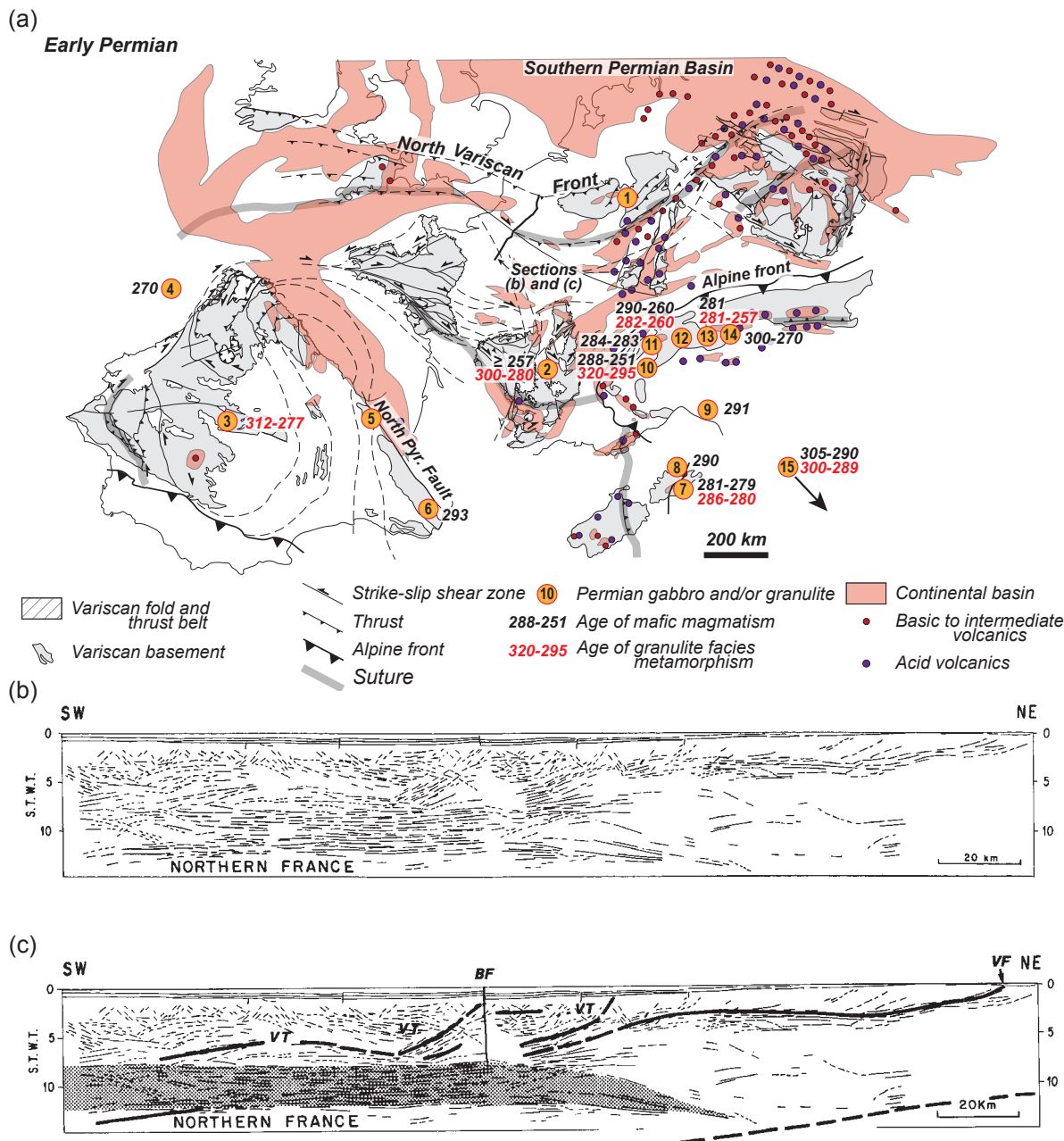


**Fig. VI-4:** Carte des bassins sédimentaires, des volcanites, des gabbros et des granulites datés (ou supposés) du Permien inférieur (290-260 Ma) d'après Burg et al. (1994), Cassinis et al. (2012), Châteauneuf (1989), Feys (1989) et Lorenz & Nicholls (1976). 1 – Massif de l'Eifel (e.g. Loock et al., 1990) ; 2 – Massif Central (Beaunit, Costa & Rey, 1995; Downes et al., 1991; Féménias et al., 2003) ; 3 – Système Central Espagnol (Fernández-Suárez et al., 2006; Villaseca et al., 2007) ; 4 – Marge Ibérique (site ODP 1069, Manatschal et al., 2001) ; 5 – Massif d'Ursuya (Vielzeuf, 1984; Vielzeuf & Kornprobst, 1984) ; 6 – Norite de Treilles (Vielzeuf & Pin, 1991) ; 7 – Massif de Santa Lucia (Paquette et al., 2003; Rossi et al., 2006) ; 8 – Gabbro de Bocca di Tenda (Cocherie et al., 2005; Tribuzio et al., 2009) ; 9 – Monte Ragola (Meli et al., 1996) ; 10 – Ivrea (Peressini et al., 2007; Pin, 1986) ; 11 – Sassa, Sermenta et Mont Collon (Baletti et al., 2012; Bussy et al., 1998; Monjoie et al., 2007) ; 12 – Complexe de Gruf (Galli et al., 2012) ; 13 – Malenco (Hansmann et al., 2001; Hermann & Rubatto, 2003) ; 14 – gabbro de Sondalo (Bachmann & Grauert, 1981; Tribuzio et al., 1999) ; 15 – Calabre (Caggianelli et al., 2013; Schenk, 1981). Schéma de la chaîne varisque modifié d'après Martínez Catalán (2011) et Ballèvre et al. (2014). (bc) Coupe sismique profonde du nord de la France avec (b) son interprétation. BF – Faille de Bray ; VF – Front Varisque ; VT – Chevauchement varisque. Gris : croûte inférieure litéée. D'après Bois et al. (1989).

#### 4.1.2 Activité mantellique

Après l'orogénèse varisque, les ophiolites alpines documentent une fusion partielle particulièrement poussée au Permien (Müntener *et al.*, 2004; Rampone *et al.*, 1996; Rampone *et al.*, 1998). Les liquides mafiques extraits se retrouvent sous la forme de plutons sous-plaqués dans les unités continentales affleurant dans les Alpes et dans les Pyrénées (p. ex. Hermann *et al.*, 1997; Voshage *et al.*, 1990), que ce soit dans les unités « européennes » comme « adriatiques » (Fig. VI-4a, Paquette *et al.*, 2003; Rossi *et al.*, 2006; Zibra, 2006). Certains auteurs prolongent le sous-plaquage sous l'ensemble de l'ancien domaine orogénique, hypothèse basée sur la présence d'une croûte inférieure fortement réfléchitive dans les coupes sismiques (Fig. VI-4bc, Bois *et al.*, 1989; Costa & Rey, 1995; Rey, 1993). Ceci est confirmé par la présence de granulites felsiques et mafiques – remontées par le volcanisme tertiaire et quaternaire (Fig. VI-4a, p. ex. Downes *et al.*, 1990; Fernández-Suárez *et al.*, 2006) – qui pré servent dans certains cas leur structures magmatiques (Berger *et al.*, 2007; Féménias *et al.*, 2003; Féménias *et al.*, 2005). Ces magmas s'épanchent également en surface avec un remplissage des bassins sédimentaires, parfois par des laves et tuffs volcaniques (Fig. VI-4a, p. ex. Cassinis *et al.*, 1995), dans les parties internes, mais également externes de l'ancien orogène (Timmerman, 2004). Principalement mafique et alcalin dans les bassins nord et sud permien, les laves deviennent progressivement felsiques et calco-alcalines vers le sud (Fig. VI-4a, Bonin, 1988; Timmerman, 2004). De fait, bien que la présence de corps sous-plaqués dans les bassins externes à la chaîne varisque soit encore débattue (bassin nord permien, Ebbing *et al.*, 2005; Thybo & Artemieva, 2013; Timmerman *et al.*, 2009), le même évènement magmatique semble affecter tout le domaine européen.

### 4.2 Différences de l'évolution post-orogénique entre les parties internes et parties externes de l'orogène varisque

Dans ce contexte, la différence de magmatisme permo-carbonifère soulevée par Bonin (1988) – plutôt alcalin dans les parties externes, plutôt calco-alcalin dans les parties internes – est expliquée par l'enrichissement prolongé du manteau sous le domaine orogénique par le jeu des diverses subductions associées à la convergence continentale. Progressivement, les magmas alcalins ou tholeiitiques vont dominer partout en Europe, marquant un changement progressif de la source mantellique (Bonin, 1988; Bonin *et al.*, 1998). La répartition géographique du volcanisme felsique et basique (Fig. VI-4a) peut être expliquée par la rhéologie de la croûte continentale. Les résultats du *chapitre III* et des modélisations de Gerya & Burg (2007) ont montré que l'ascension de magma mafique au travers de la croûte continentale est très sensible au comportement rhéologique de cette dernière : une croûte froide et fragile va favoriser leur ascension vers des niveaux crustaux peu profonds, à la différence d'une croûte inférieure trop

chaude et ductile qui va les bloquer. Ainsi, les parties internes de l’orogène, dans lesquelles des dômes migmatitiques sont documentés à 300 Ma (Ledru *et al.*, 2001), inhibent potentiellement l’ascension des magmas mafiques, à la différence des bassins permiens nord et sud dans les parties varisques externes.

Cette différence notable d’état thermique de la croûte est également aperçue dans le « style » de rifting développé. Alors que le mode de déformation des parties externes semble se rapprocher d’un rift classique, avec la formation de bassins assez larges réutilisant des structures lithosphériques d’ordre majeur (Ebbing *et al.*, 2005; McCann *et al.*, 2006), la présence de nombreux bassins étroits et allongés (Fig. VI-4a, Burg *et al.*, 1994; McCann *et al.*, 2006) est plutôt semblable au rifting diffus de Buck (1991). En théorie, ce dernier déforme une croûte continentale particulièrement chaude (et éventuellement sur-épaisse), à l’opposé des riftings étroits qui se développent dans des domaines mécaniquement plus résistants, donc typiquement plus froids (Buck, 1991; Buck *et al.*, 1999).

#### 4.3 Analogie entre la province du *Basin and Range* et la dynamique permienne en Europe

Les situations géodynamiques lors de l’effondrement des chaînes orogéniques ne sont pas exactement similaires durant le Permien en Europe et actuellement dans le *Basin and Range*. Dans la première, l’orogène est majoritairement bordé de continents, alors que dans la seconde, une marge active persiste le long de tout le domaine orogénique. En revanche, de nombreux points communs persistent. En plus de ceux soulevés dans le contexte de cette étude (chapitre I), le style de déformation lors de l’extension tardive à post-orogénique reste particulièrement semblable (Malavieille, 1993).

L’extension dans les anciennes parties internes de l’orogène varisque atteint 35 % ( $\beta = 1.35$ , Henk, 1993) et forme de nombreux bassins, qui peuvent se révéler assez profonds mais toujours fluviatiles (Fig. VI-4, p. ex. Courel *et al.*, 1986; Henk, 1993). Les quelques intrusions mafiques documentées qui se mettent en place à la base de la croûte montrent des pressions conformes avec une épaisseur de croûte continentale normale (30-36 km pour Braccia, > 25 km pour le complexe mafique d’Ivrée, Demarchi *et al.*, 1998; Müntener *et al.*, 2000) et dont l’évolution rétrograde suit un refroidissement isobarique (au moins pour le gabbro de Braccia, Müntener *et al.*, 2000). Ces résultats sont confirmés par les coupes sismiques actuelles au travers des portions de croûte continentale peu affectées par les évènements post-Permiens, documentant un Moho restant autour de 30 km de profondeur (Bois *et al.*, 1989; Rey, 1993). Ces résultats suggèrent qu’à la fin du Permien, la croûte continentale a une épaisseur d’environ 30 km impliquant soit (1) un faible amincissement crustal durant le Permien, soit (2) que cet

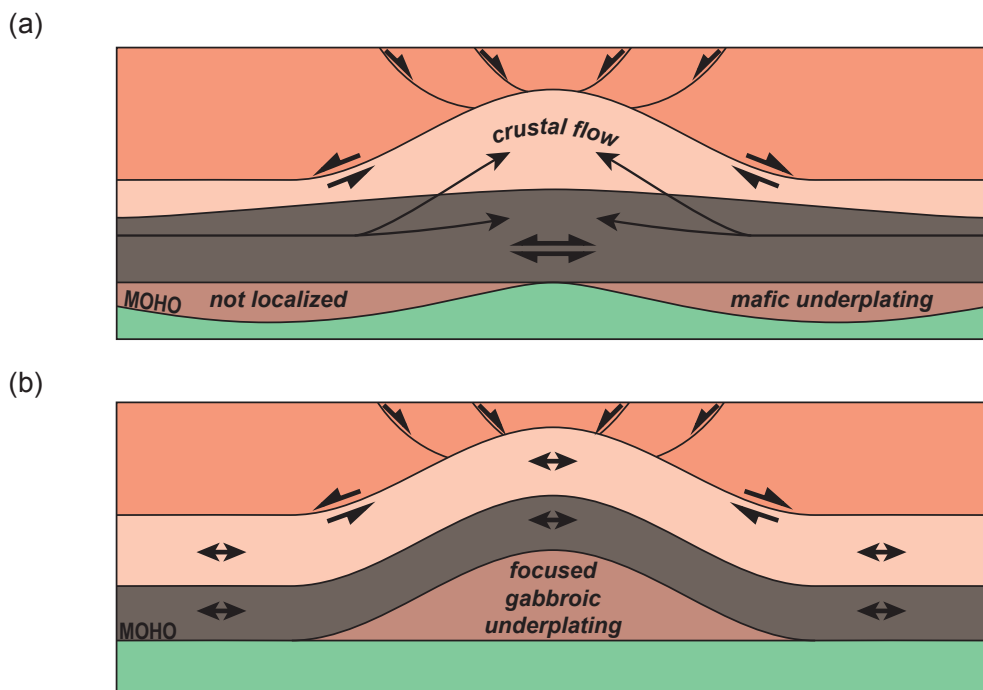


**Fig. VI-5:** Modèle conceptuel d'évolution de la croûte continentale lors de déformations extensives sans exhumation du Moho impliquant soit (a) un fluage de la croûte et une mise en place non localisée de gabbros, soit (b) un fluage limité de la croûte compensé par une mise en place localisée de gabbros. Modifié d'après Block & Royden (1990).

amincissement a été compensé par des additions de magmas issus de la fusion partielle du manteau (c.-à-d. du sous-plaquage).

La situation est similaire dans la province du *Basin and Range*, où malgré l'extension estimée à 100 % voir localement plus ( $\beta = 2-3$ , Wernicke *et al.*, 1982; Zoback & Zoback, 1980), la croûte continentale n'est pas amincie sous 30 km (p. ex. Zandt *et al.*, 1995). Cette relation est expliquée par une combinaison entre fluage de la croûte inférieure (Fig. VI-5a) et mise en place de magmas dérivés du manteau (Fig. VI-5b, Block & Royden, 1990), formant des corps magmatiques sous-plaqués (Jarchow *et al.*, 1993; Thybo & Artemieva, 2013; Wendlandt *et al.*, 1993). Des mécanismes de déformation similaires ont éventuellement été actifs pendant l'événement tardif-carbonifère à permien, avec tantôt un fluage de la croûte continentale (Costa & Rey, 1995; Rey, 1993), tantôt des intrusions mafiques localisées (Hermann *et al.*, 2001; Quick *et al.*, 1994). Spatialement et temporellement, le rôle relatif des deux processus peut changer, avec peut-être un fluage de la croûte favorisé pendant les stades initiaux et dans les parties internes de l'orogène, où la croûte continentale serait encore partiellement fondu après la phase orogénique (Vanderhaeghe & Teyssier, 2001). Ces processus permettant une extension crustale avec un amincissement limité pourraient expliquer la formation de dômes migmatitiques, comme par exemple le Velay (Ledru *et al.*, 2001), mais restent actuellement difficiles à évaluer.

## 5. QUELLE EST L'INFLUENCE DE L'ARCHITECTURE CRUSTALE OU LITHOSPÉRIQUE HÉRITÉE DES ÉVÈNEMENTS POST-OROGÉNIQUES SUR LES RIFTS MÉSOZOÏQUES ?

Alors que les modèles d'amincissement lithosphérique utilisent fréquemment une architecture crustale pré-rift simplifiée et litée (Fig. VI-6a), les synthèses de l'introduction et du chapitre I montrent que les processus tardi- à post-orogéniques complexifient l'architecture de la croûte continentale. Ainsi, la tectonique permienne, associée à son magmatisme et son métamorphisme, a un effet important sur la composition et la structure de la lithosphère européenne et donc sur sa rhéologie (Fig. VI-6b). Ces déformations peuvent avoir un contrôle (à petite échelle) sur la localisation des déformations postérieures (p. ex. Manatschal *et al.*, 2014).

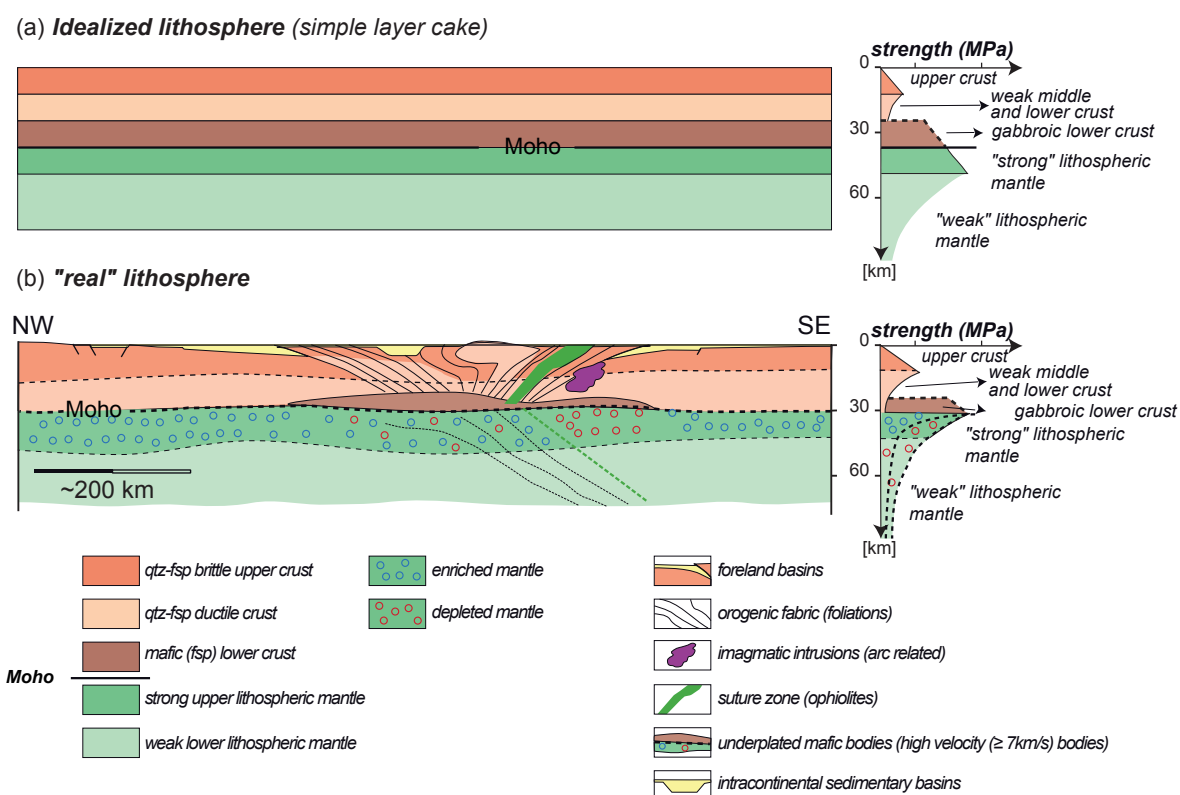


**Fig. VI-6:** Coupe schématique de la lithosphère ayant (a) une architecture litée simpliste et (b) une architecture plus réaliste avec la représentation de différents éléments hérités des processus orogéniques. Modifié d'après Manatschal *et al.* (2014).

En profondeur, la présence de l'asthénosphère à des profondeurs particulièrement faibles déclenche sa fusion partielle, ce qui appauvrit le manteau en éléments volatiles et le déhydrate. Ceci a une conséquence importante sur sa rhéologie (Fig. VI-6b). Le potentiel de localisation/délocalisation de la déformation de ce processus est certain, mais en mesurer l'extension géographique demeure assez difficile. De plus, la fusion partielle du manteau précédant les riftings mésozoïques rend le manteau moins fertile, réduisant le budget de magma pouvant être produit ultérieurement. Le caractère magmatique ou non magmatique d'une marge continentale hyper-étirée peut éventuellement en dépendre.

La sismique réfraction dans les marges passives actuelles documentent fréquemment des corps de haute vitesse en base de croûte, certaines fois interprétés comme hérités d'un épisode de sous-plaquage pré-rift (p. ex. Nirrengarten *et al.*, 2014). Comme démontré dans ce manuscrit, ils sont potentiellement mis en place lors des processus tardi- à post-orogéniques. Ils impliquent un changement rhéologique certain dans la croûte inférieure, et éventuellement de portions crustales plus superficielles. Les effets sur la localisation de la déformation peuvent être visibles par exemple dans l'Austroalpin, où les structures varisques et permianes sont préservées, malgré des déformations mésozoïques et cénozoïques documentées dans l'unité sus-jacente de Grosina, suggérant que le gabbro de Sondalo puisse représenter un corps « rigide ». Éventuellement, le métamorphisme associé à ce contexte géodynamique peut, de manière similaire au processus mantellique, rendre les lithologies crustales moins fertiles, et ainsi produire une quantité de liquide granitiques limitée lors d'évènements métamorphiques de haute température documentés lors des riftings mésozoïques (Clerc & Lagabrielle, 2014)

À la surface, les nombreux bassins bordés par des failles et ouverts au travers de l'ancien domaine orogénique peuvent constituer un héritage de type structural susceptible d'être réactivé par les déformations mésozoïques. Par exemple, l'ouverture de la Tethys alpine réactive dans le domaine briançonnais un bassin permo-carbonifère (Courel *et al.*, 1986). Même si cet héritage ne va pas contraindre la position du rift à grande échelle, il peut – au moins localement – contrôler la formation de bassins extensifs (p. ex. Autin *et al.*, 2013).

Ainsi, durant les évènements post-orogéniques, certains processus affaiblissent les domaines affectés (p. ex. formation de bassins), alors que d'autres le renforcent (essentiellement le magmatisme mafique rigidifiant particulièrement le manteau et la croûte inférieure). Le rôle de l'héritage issu des évènements post-orogéniques est certainement très important dans les processus de rifting ; savoir s'il servira à localiser ou à délocaliser la déformation restera une question de proportion relative entre les différents processus.

---

## *CONCLUSION*

---



La fin d'une phase orogénique est marquée par une intense activité tectonique, magmatique et métamorphique, lors de la formation d'une croûte continentale équilibrée à partir d'une croûte orogénique par définition sur-épaisse. Chaque processus actif pendant cette période va modifier d'une manière plus ou moins pérenne et plus ou moins profonde l'architecture de la croûte continentale, ce qui influera sur les systèmes de rift postérieurs. Ce travail a ainsi visé à comprendre le fonctionnement de certains de ces processus post-orogéniques.

En Europe de l'ouest, le stade terminal de l'orogénèse dévono-carbonifère varisque a lieu de la fin du Carbonifère au début du Permien (voir *chapitres I & VI*). La tectonique transtensive est marquée par la présence de structures décrochantes au travers de tout l'ancien domaine orogénique. Des bassins intracontinentaux sont ouverts, que ce soit dans les parties internes comme dans les parties externes de l'ancien orogène varisque. Ces bassins sont très fréquemment associés à une forte activité volcanique. Dans la croûte continentale, des magmas mafiques sont mis en place sous forme de plutons gabbroïques, le plus souvent sous-plaqués, mais atteignant également des niveaux plus superficiels. Ils sont fréquemment associés à un métamorphisme de contact de haute température, et occasionnellement à un métamorphisme régional. Les températures élevées du manteau sous-continental, responsables de sa fusion partielle, impliquent une asthénosphère particulièrement peu profonde dans tout le domaine ouest européen. L'extension géographique de cet évènement est indiquée par plusieurs facteurs : la présence suspectée de corps sous-plaqués, que ce soit dans les parties internes comme externes de l'ancienne orogène varisque ; la couverture géographique du volcanisme ; la formation de bassins *sags* par subsidence thermique dès la fin du Permien inférieur. Toutes les parties de cette croûte continentale vont être plus ou moins déformés et utilisés lors des phases mésozoïques de rifting, par exemple lors de la formation de la Téthys alpine ou de l'océan Atlantique.

Les travaux présentés dans ce manuscrit se concentrent principalement un système magmatique, métamorphique et tectonique de croûte moyenne, afin d'étudier les relations entre magmatisme mafique et métamorphisme, de documenter les mécanismes d'ascension et de mise en place de magmas mafiques dans des niveaux crustaux intermédiaires, et enfin de caractériser les systèmes d'exhumation de ces roches. Ainsi, cette étude s'est focalisée sur les nappes austroalpines (SE de la Suisse, N de l'Italie), où l'unité métasédimentaire de Campo est intrudée par le gabbro de Sondalo durant le Permien.

L'unité de Campo a suivi une évolution prograde varisque selon un gradient métamorphique barrovien pendant le Carbonifère, évolution associée à la formation des foliations Sc1 et Sc2 (voir *chapitre III*). Le cadre géodynamique de cette évolution orogénique reste à contraindre. Par la suite, l'unité de Campo a été positionnée dans des niveaux crustaux intermédiaires à environ 12 km de profondeur (4 kbar), avant la mise en place de gabbros mafiques dans l'unité de Campo.

L'intrusion du gabbro de Sondalo, effectuée entre 289 et 285 Ma (âges U–Pb sur zircon), a tout d'abord profité de l'anisotropie mécanique procurée par la foliation Sc2 de l'unité de Campo lors de son ascension (voir *chapitre IV*). La chaleur amenée par le magma mafique est responsable d'un métamorphisme dans les roches encaissantes, avec la formation d'une auréole migmatitique (jusqu'à 5,2/6 kbar pour 750/800 °C) autour du pluton et l'incorporation de xénolites dérivés de l'unité de Campo, où le métamorphisme atteint le faciès des granulites (5,5 kbar/930°C). La deuxième phase de l'intrusion est caractérisée par une remontée *en-masse* du cœur du pluton, juxtaposant toutes les roches aujourd'hui à l'affleurement, à 12 km de profondeur (4 kbar). Cette ascension est opérée au travers de cisaillements réalisés dans l'auréole métamorphique de contact, lors de la formation de la foliation Sc3, ainsi qu'au travers de cisaillements dans les parties externes du pluton. Les déformations dans l'unité cessent avec les conditions de haute température, indiquant que les déformations tectoniques ne sont pas directement liées à la mise en place du magma. Ce gabbro dans des niveaux intermédiaire, peut aider, grâce à plus de contrainte géochimique, à comprendre le système magmatique et en particulier le lien entre les magmas non différenciés et différenciés dans un contexte post-orogénique.

Après les évènements de haute température durant le Permien, l'unité de Campo et son unité sus-jacente de Grosina suivent un refroidissement particulièrement lent comme indiqué par les âges  $^{40}\text{Ar}/^{39}\text{Ar}$  dans l'unité de Grosina (entre 275 et 245 Ma) et les âges Rb–Sr dans l'unité de Campo (voir *chapitre V*). Les vitesses de refroidissement particulièrement faibles indiquent que les unités ont refroidi en profondeur à partir du Permien, sans être exhumées. Ces interprétations sont en accord avec la subsidence thermique enregistrée aux mêmes époques en Europe.

Par la suite, les unités de Campo et de Grosina sont exhumées lors de la formation de la marge adriatique associée à l'ouverture de la Téthys alpine au Jurassique (voir *chapitre V*). Dans un premier temps, entre 210 et 180 Ma, l'unité de Campo est légèrement exhumée par le biais de zones de cisaillement dans et à la base de l'unité de Grosina, équilibrant localement les roches dans le facies des schistes verts. Les âges  $^{40}\text{Ar}/^{39}\text{Ar}$  de l'unité de Campo indiquent des vitesses de refroidissement particulièrement élevées, pouvant être expliquées par une exhumation tectonique des roches. Ainsi, cette exhumation a été opérée par le jeu de failles d'extractions (p. ex. le détachement de Grosina), dans les stades finaux de la formation de la zone d'étranglement.

Intégrés aux évolutions de différentes parties de la croûte, ces résultats permettent de décrire un modèle (1) d'évolution tectonique, magmatique et métamorphique lors des événements post-orogéniques permiens en Europe de l'ouest (*chapitres I, III, IV & VI*), et (2) de formation des zones d'étranglement dans les marges continentales hyper-étirées (*chapitre V & VI*). Cependant certaines zones d'ombres subsistent, par exemple sur les relations entre extension et exhumation dans la croûte, ainsi qu'entre tectonique et magmatisme.



---

## *RÉFÉRENCES*

---



- ALVAREZ, W., COCOZZA, T. & WEZEL, F. C., 1974. Fragmentation of the Alpine orogenic belt by microplate dispersal. *Nature*, **248**(5446), 309-314.
- ANDREATTA, C., 1952. Polymetamorphose und Tektonik in der Ortlergruppe. *Neues Jahrbuch für Mineralogie Monatshefte*, 13-28.
- ANNEN, C., 2011. Implications of incremental emplacement of magma bodies for magma differentiation, thermal aureole dimensions and plutonism–volcanism relationships. *Tectonophysics*, **500**(1–4), 3-10.
- ANNEN, C., BLUNDY, J. D. & SPARKS, R. S. J., 2006. The Genesis of Intermediate and Silicic Magmas in Deep Crustal Hot Zones. *Journal of Petrology*, **47**(3), 505-539.
- ANNEN, C. & SPARKS, R. S. J., 2002. Effects of repetitive emplacement of basaltic intrusions on thermal evolution and melt generation in the crust. *Earth and Planetary Science Letters*, **203**(3–4), 937-955.
- ARMIJO, R., TAPONNIER, P., MERCIER, J. L. & TONG-LIN, H., 1986. Quaternary extension in Southern Tibet: field observations and tectonic implications. *Journal of Geophysical Research*, **91**(B14), 13803-13872.
- ARTHAUD, F. & MATTE, P., 1977. Late Paleozoic strike-slip faulting in the southern Europe and northern Africa: Result of a right-lateral shear zone between the Appalachians and the Urals. *Geological Society of America Bulletin*, **88**(9), 1305-1320.
- ARZI, A. A., 1978. Critical phenomena in the rheology of partially melted rocks. *Tectonophysics*, **44**(1–4), 173-184.
- ASHWORTH, J. R., 1975. Staurolite at anomalously high grade. *Contributions to Mineralogy and Petrology*, **53**(4), 281-291.
- AUTIN, J., BELLAHSEN, N., LEROY, S., HUSSON, L., BESLIER, M.-O. & D'ACREMONT, E., 2013. The role of structural inheritance in oblique rifting: Insights from analogue models and application to the Gulf of Aden. *Tectonophysics*, **607**(0), 51-64.
- AVOUAC, J. P. & BUROV, E. B., 1996. Erosion as a driving mechanism of intracontinental mountain growth. *Journal of Geophysical Research*, **101**(B8), 17747-17769.
- BACHMANN, G. & GRAUERT, B., 1981. Radiometrische Alterbestimmungen des Gabbro von Sondalo. Oberes Velltin, Intalienische Alpen. *Fortschritte der Mineralogie*, **59**(1), 11-13.
- BAKSI, A. K., 2006. Guidelines for assessing the reliability of the 40Ar/39Ar plateau ages: Application to ages relevant to hotspot tracks. Available at: <http://www.mantleplumes.org/ArAr.html>
- BALETTI, L., ZANONI, D., SPALLA, M. I. & GOSSO, G., 2012. Structural and petrographic map of the Sassa gabbro complex (Dent Blanche nappe, Austroalpine tectonic system, Western Alps, Italy). *Journal of Maps*, **8**, 413-430.
- BALLÈVRE, M., MARTÍNEZ CATALÁN, J. R., LÓPEZ-CARMONA, A., PITRA, P., ABATI, J., FERNÁNDEZ, R. D., DUCASSOU, C., ARENAS, R., BOSSE, V., CASTIÑEIRAS, P., FERNÁNDEZ-SUÁREZ, J., GÓMEZ BARREIRO, J., PAQUETTE, J.-L., PEUCAT, J.-J., POUJOL, M., RUFFET, G. & SÁNCHEZ MARTÍNEZ, S., 2014. Correlation of the nappe stack in the Ibero-Armorican arc across the Bay of Biscay: a joint French–Spanish project. *Geological Society, London, Special Publications*, **405**.
- BARBOZA, S. A. & BERGANTZ, G. W., 2000. Metamorphism and Anatexis in the Mafic Complex Contact Aureole, Ivrea Zone, Northern Italy. *Journal of Petrology*, **41**(8), 1307-1327.
- BARBOZA, S. A., BERGANTZ, G. W. & BROWN, M., 1999. Regional granulite facies metamorphism in the Ivrea zone: Is the Mafic Complex the smoking gun or a red herring? *Geology*, **27**(5), 447-450.

- BECQ-GIRAUDON, J.-F. & VAN DEN DRIESSCHE, J., 1994. Dépôts périglaciaires dans le Stéphano-Autunien du Massif Central: témoin de l'effondrement gravitaire d'un haut plateau hercynien. *Comptes Rendus de l'Académie des Sciences - Series IIA - Earth and Planetary Science*, **318**, 675-682.
- BELTRANDO, M., LISTER, G. S., FORSTER, M., DUNLAP, W. J., FRASER, G. & HERMANN, J., 2009. Dating microstructures by the  $^{40}\text{Ar}/^{39}\text{Ar}$  step-heating technique: Deformation-pressure-temperature-time history of the Penninic Units of the Western Alps. *Lithos*, **113**(3-4), 801-819.
- BELTRANDO, M., RUBATTO, D., COMPAGNONI, R. & LISTER, G., 2007. Was the Valaisan basin floored by oceanic crust? Evidence of Permian magmatism in the Versoysen unit (Valaisan domain, NW Alps). *Ophioliti*, **32**(2), 85-99.
- BELTRANDO, M., ZIBRA, I., MONTANINI, A. & TRIBUZIO, R., 2013. Crustal thinning and exhumation along a fossil magma-poor distal margin preserved in Corsica: A hot rift to drift transition? *Lithos*, **168-169**(0), 99-112.
- BENCIOLINI, L., POLI, M. E., VISONÀ, D. & ZANFERRARI, A., 2006. Looking inside Late Variscan tectonics: structural and metamorphic heterogeneity of the Eastern Southalpine Basement (NE Italy). *Geodinamica Acta*, **19**(1), 17-32.
- BENN, K. & ALLARD, B., 1989. Preferred mineral orientations related to magmatic flow in ophiolite layered gabbros. *Journal of Petrology*, **30**(4), 925-946.
- BERGER, J., FÉMÉNIAS, O., COUSSAERT, N., MERCIER, J.-C. & DEMAFFE, D., 2007. Cumulating processes at the crust-mantle transition zone inferred from Permian mafic-ultramafic xenoliths (Puy Beaunit, France). *Contributions to Mineralogy and Petrology*, **153**(5), 557-575.
- BERGOMI, M. A. & BORIANI, A., 2012. Late Neoproterozoic - Early Paleozoic accretion of the Southalpine and Austroalpine basements of Central Alps (Italy). *Géologie de la France*, **1**, 69.
- BERTOTTI, G., 1991. Early Mesozoic extension and Alpine shortening in the western Southern Alps: The geology of the area between Lugano and Menaggio (Lombardy, northern Italy). *Memorie di scienze geologiche*, **43**, 17-123.
- BERTOTTI, G., SEWARD, D., WIJBRANS, J., TER VOORDE, M. & HURFORD, A. J., 1999. Crustal thermal regime prior to, during, and after rifting: A geochronological and modeling study of the Mesozoic South Alpine rifted margin. *Tectonics*, **18**(2), 185-200.
- BIANCHI POTENZA, B., CARIMATI, R., POTENZA, R. & TESTA, B., 1985. Considerazioni cronologiche sul filone trachitico di Sondalo (Lombardia, Valtellina). *Atti della Società di Scienze Naturali e del Museo Civico di Storia Naturale di Milano*, **120**(8-4), 141-144.
- BIANCHI POTENZA, B., GORLA, L. & NOTARPIETRO, A., 1978a. La «formazione di Valle Grosina»: revisione dei suoi aspetti petrografici in un nuovo contesto geologico II. Gli «gneiss minimi». *Rendiconti Società Italiana di Mineralogia e Petrologia*, **34**(2), 371-385.
- BIANCHI POTENZA, B., GORLA, L. & NOTARPIETRO, A., 1978b. La «formazione di Valle Grosina»: revisione dei suoi aspetti petrografici in un nuovo contesto geologico III: gli «gneiss occhiadini». *Rendiconti Società Italiana di Mineralogia e Petrologia*, **34**(2), 387-401.
- BIRD, P., 1979. Continental delamination and the Colorado plateau. *Journal of Geophysical Research*, **84**(B13), 7561-7571.
- BLOCK, L. & ROYDEN, L. H., 1990. Core complex geometries and regional scale flow in the lower crust. *Tectonics*, **9**(4), 557-567.
- BOCKEMÜHL, C., 1988. *Der Marteller Granit (Südtirol, Italien): Petrographi, Geochemie, Altersbestimmungen*, University of Basel, unpublished dissertation.

- BOCKEMÜHL, C. & PFISTER, H., 1985. Geologie der Serottini-Intrusion (Campo-Kristallin, Val Camonica, Italien). *Schweizerische mineralogische und petrographische Mitteilungen*, **65**, 79-94.
- BOEKHOUT, F., SPIKINGS, R., SEMPLER, T., CHIARADIA, M., ULIANOV, A. & SCHALTEGGER, U., 2012. Mesozoic arc magmatism along the southern Peruvian margin during Gondwana breakup and dispersal. *Lithos*, **146–147**(0), 48-64.
- BOHLEN, S. R., 1991. On the formation of granulites. *Journal of Metamorphic Geology*, **9**, 223-229.
- BOIS, C., PINET, B. & ROURE, F., 1989. Dating lower crustal features in France and adjacent areas from deep seismic profiles. In: *Properties and Processes of Earth's Lower Crust* Geophys. Monogr. Ser., pp. 17-31, AGU, Washington, DC.
- BONIN, B., 1988. From orogenic to anorogenic environments: evidence from associated magmatic episodes. *Schweizerische mineralogische und petrographische Mitteilungen*, **68**, 301-311.
- BONIN, B., AZZOUNI-SEKKAL, A., BUSSY, F. & FERRAG, S., 1998. Alkali-calcic and alkaline post-orogenic (PO) granite magmatism: petrologic constraints and geodynamic settings. *Lithos*, **45**(1–4), 45-70.
- BONIN, B., BRÄNDLEIN, P., BUSSY, F., DESMONS, J., EGGENBERGER, U., FINGER, F., GRAF, K., MARRO, C., MERCOLLI, I., OBERHÄNSLI, R., PLOQUIN, A., VON QUADT, A., VON RAUMER, J., SCHALTEGGER, U., STEYRER, H. P., VISONÀ, D. & VIVIER, G., 1993. Late Variscan Magmatic Evolution of the Alpine Basement. In: *Pre-Mesozoic Geology in the Alps* (eds von Raumer, J. F. & Neubauer, F.), pp. 171-201, Springer Berlin Heidelberg.
- BORIANI, A., BERGOMI, M. & GIOBBI, E., 2005. Relationships between late-Variscan strike-slip faults and the emplacement of intrusive magmas in the South Alpine and in the Upper-Austroalpine basement of Central Alps. *Geophysical Research Abstracts*, **7**, 11051.
- BORIANI, A., BINI, A. & BERRA, F., 2011. Note illustrative della Carta Geologica d'Italia alla scala 1:50.000, Foglio 56 Sondrio. *Servizio Geologico d'Italia, ISPRA*, 242 p.
- BORIANI, A., BURLINI, L. & SACCHI, R., 1990. The Cossato-Mergozzo-Brissago Line and the Pogallo Line (Southern Alps, Northern Italy) and their relationships with the late-Hercynian magmatic and metamorphic events. *Tectonophysics*, **182**(1–2), 91-102.
- BORIANI, A. & GIOBBI, E., 2004. Does the basement of western southern Alps display a tilted section through the continental crust? A review and discussion. *Periodico di Mineralogia*, **73**, 5-22.
- BORIANI, A., TRAVERSI, G., DEL MORO, A. & NOTARPIETRO, A., 1982. Il «granito di Brusio» (Val Poschiavo - Svizzera): caratterizzazioni chimiche, petrologiche e radiometriche. *Rendiconti Società Italiana di Mineralogia e Petrologia*, **38**(1), 97-108.
- BORRADAILLE, G. J. & JACKSON, J. A., 2010. Structural geology, petrofabrics and magnetic fabrics (AMS, AARM, AIRM). *Journal of Structural Geology*, **32**, 1519-1551.
- BORRADAILLE, G. J., 1988. Magnetic susceptibility, petrofabrics and strain. *Tectonophysics*, **156**, 1-20.
- BORRADAILLE, G. J. & HENRY, B., 1997. Tectonic applications of magnetic susceptibility and its anisotropy. *Earth-Science Reviews*, **42**, 49-93.
- BORSI, S., FERRARA, G., PAGANELLI, L. & SIMBOLI, G., 1968. Isotopic age measurements of the M. Monzoni intrusive complex. *Mineralogica et Petrographica Acta*, **14**, 171-183.
- BOUCHEZ, J.-L., 2000. Anisotropie de susceptibilité magnétique et fabrique des granites. *Comptes Rendus de l'Académie des Sciences - Series IIA - Earth and Planetary Science*, **330**(1), 1-14.

- BOUSQUET, R., OBERHÄNSLI, R., SCHMID, S. M., BERGER, A., WIEDERKEHR, M., ROBERT, C., MÖLLER, A., ROSENBERG, C. L., KOLLER, F., MOLLI, G. & ZEILINGER, G., 2012. *Metamorphic framework of the Alps*, CCGM/CGMW. <http://www.geodynalphs.org>.
- BRAGA, R., CALLEGARI, A., MESSIGA, B., OTTOLINI, L., RENNA, M. R. & TRIBUZIO, R., 2003. Origin of prismatic minerals from the Sondalo granulites (Central Alps, northern Italy). *European Journal of Mineralogy*, **15**, 393-400.
- BRAGA, R., GIACOMINI, F., MESSIGA, B. & TRIBUZIO, R., 2001. The Sondalo Gabbroic Complex (Central Alps, Northern Italy): Evidence for Emplacement of Mantle-Derived Melts into Amphibolite Facies Metapelites. *Physics and Chemistry of the Earth, Part A: Solid Earth and Geodesy*, **26**(4-5), 333-342.
- BRAGA, R., MASSONNE, H.-J. & MORTEN, L., 2007. An early metamorphic stage for the Variscan Ulten Zone gneiss (NE Italy): evidence from mineral inclusions in kyanite. *Mineralogical magazine*, **71**(6), 691-702.
- BRAGA, R. & MASSONNE, H. J., 2008. Mineralogy of inclusions in zircon from high-pressure crustal rocks from the Ulten Zone, Italian Alps. *Periodico di Mineralogia*, **77**(3), 43-64.
- BROWN, M., 1994. The generation, segregation, ascent and emplacement of granite magma: the migmatite-to-crustally-derived granite connection in thickened orogens. *Earth-Science Reviews*, **36**, 83-130.
- BROWN, M., 2007. Crustal melting and melt extraction, ascent and emplacement in orogens: mechanisms and consequences. *Journal of the Geological Society*, **164**(4), 709-730.
- BRUN, J.-P., SOKOUTIS, D. & VAN DEN DRIESSCHE, J., 1994. Analogue modeling of detachment fault systems and core complexes. *Geology*, **22**(4), 319-322.
- BÜCHI, H., 1987. Geologie und Petrographie der Bernina IX. Das Gebiet zwischen Pontresina und dem Morteratschgletscher. *Unpublished Diplomarbeit, University of Zürich*.
- BÜCHI, H., 1994. Der variskische Magmatismus in der östlichen Bernina. *Schweizerische mineralogische und petrographische Mitteilungen*, **74**, 359-371.
- BUCK, W. R., 1991. Modes of continental lithospheric extension. *Journal of Geophysical Research: Solid Earth*, **96**(B12), 20161-20178.
- BUCK, W. R., LAVIER, L. & POLIAKOV, A. N. B., 1999. How to make a rift wide. *Philosophical Transactions of the Royal Society of London. Series A: Mathematical, Physical and Engineering Sciences*, **357**(1753), 671-693.
- BURG, J.-P. & GERYA, T., 2005. The role of viscous heating in Barrovian metamorphism of collisional orogens: thermomechanical models and application to the Le Pontine Dome in the Central Alps. *Journal of Metamorphic Geology*, **23**, 75-95.
- BURG, J.-P., VAN DEN DRISSCHE, J. & BRUN, J.-P., 1994. Syn- to post-thickening extension in the Variscan Belt of Western Europe: Modes and structural consequences. *Géologie de la France*, **3**, 33-51.
- BUSCH, J. P., VAN DER PLUIJM, B. A., HALL, C. M. & ESSEN, E. J., 1996. Listric normal faulting during postorogenic extension revealed by  $^{40}\text{Ar}/^{39}\text{Ar}$  thermochronology near the Robertson Lake shear zone, Grenville orogen, Canada. *Tectonics*, **15**(2), 387-402.
- BUSSY, F. & HERNANDEZ, J., 1997. Short-lived bimodal magmatism at 307 Ma in the Mont-Blanc/Aiguilles-Rouges area: a combination of decompression melting, basaltic underplating and crustal fracturing. *Quaderni Geodinamica Alpina e Quaternaria, Milano*, **4**, 22.
- BUSSY, F., SARTORI, M. & THÉLIN, P., 1996. U-Pb zircon dating in the middle Penninic basement of the Western Alps (Valais, Switzerland). *Schweizerische mineralogische und petrographische Mitteilungen*, **76**, 81-84.
- BUSSY, F., VENTURINI, G., HUNZIKER, J. & MARTINOTTI, G., 1998. U-Pb ages of magmatic rocks of the western Austroalpine Dent-Blanche-Sesia Unit. *Schweizerische mineralogische und petrographische Mitteilungen*, **78**, 163-168.

- CAGGIANELLI, A., PROSSER, G., FESTA, V., LANGONE, A. & SPIESS, R., 2013. From the upper to the lower continental crust exposed in Calabria. 86° Congresso Nazionale della Società Geologica Italiana - Arcavacata di Rende (CS), 2012. *Geological Field Trips (GFT)*, **5**(1.2).
- CALLEGARI, A. & BRACK, P., 2002. Geological map of the Tertiary Adamello batholith (Northern Italy). Explanatory notes and legend. *Memorie di scienze geologiche*, **54**, 19-49.
- CAMPA, G., GIACOMINI, F. & GIGLIA, A., 1997. *Carta Geologica del versante sinistro della Valtellina tra la Val di Scala e la Valle delle Presure (Sondrio)*, Scala 1:10.000, University of Pavia, unpublished master thesis.
- CAMPIGLIO, C. & POTENZA, R., 1964. Facies dioritiche collegate con il gabbro di Sondalo (Alta Valtellina): studio geologico-petrografico. *Atti della Società di Scienze Naturali e nel Museo Civico di Storia Naturale di Milano*, **103**(4), 325-343.
- CAMPIGLIO, C. & POTENZA, R., 1966. Le facies oliviniche del gabbro di Sondalo (Alta Valtellina, Lombardia). *Atti della Società di Scienze Naturali e nel Museo Civico di Storia Naturale di Milano*, **105**(1), 102-122.
- CAMPIGLIO, C. & POTENZA, R., 1967. Facies a pirosseno rombico del gabbro di Sondalo (Alta Valtellina). *Atti della Società di Scienze Naturali e nel Museo Civico di Storia Naturale di Milano*, **106**, 193-208.
- CAÑÓN-TAPIA, E. & CHÁVEZ-ÁLVAREZ, M. J., 2004. Theoretical aspects of particle movement in flowing magma: implications for the anisotropy of magnetic susceptibility of dykes. *Geological Society, London, Special Publications*, **238**, 227-249.
- CAPUZZO, N. & WETZEL, A., 2004. Facies and basin architecture of the Late Carboniferous Salvan-Dorénaz continental basin (Western Alps, Switzerland/France). *Sedimentology*, **51**(4), 675-697.
- CASSINIS, G., CORTESOGNO, L., GAGGERO, L., PEROTTI, C. R. & BUZZI, L., 2008. Permian to Triassic geodynamic and magmatic evolution of the Brescian Prealps (eastern Lombardy, Italy). *Bollettino della Società Geologica Italiana*, **123**(3), 501-518.
- CASSINIS, G., PEROTTI, C. & RONCHI, A., 2012. Permian continental basins in the Southern Alps (Italy) and peri-mediterranean correlations. *International Journal of Earth Sciences*, **101**(1), 129-157.
- CASSINIS, G., TOUTIN-MORIN, N. & VIRGILI, C., 1995. A General Outline of the Permian Continental Basins in Southwestern Europe. In: *The Permian of Northern Pangea* (eds Scholle, P., Peryt, T. & Ulmer-Scholle, D.), pp. 137-157, Springer Berlin Heidelberg.
- CERMAK, V. & RYBACH, L., 1982. Thermal conductivity and specific heat of minerals and rocks (ed Angenheister, G.) *Landolt-Börnstein - Group V Geophysics*.
- CHÂTEAUNEUF, J. J., 1989. Esquisse paléogéographique du Permien de l'Europe de l'Ouest. *Synthèse Géologique des Bassins Permiens Français: Mémoire du Bureau de Recherches Géologiques et Minières*, **128**.
- CHIESA, S., MICHELI, P., CARIBONI, M., TOGNINI, P., MOTTA, D., LONGHIN, M., ZAMBOTTI, G., MARCATO, E. & FERRARIO, A., 2010. Note illustrative della Carta Geologica d'Italia alla scala 1:50.000, Foglio 41 Ponte di Legno. *Servizio Geologico d'Italia, ISPRA*, 160 p.
- CHOPIN, F., CORSINI, M., SCHULMANN, K., EL HOUICHA, M., GHENNE, J.-F. & EDEL, J. B., 2014. Tectonic evolution of the Rehamna metamorphic dome (Morocco) in the context of the Alleghanian-Variscan orogeny. *Tectonics*, **33**(6), 1154-1177.
- CLARK, C., FITZSIMONS, I. C. W., HEALY, D. & HARLEY, S. L., 2011. How Does the Continental Crust Get Really Hot? *Elements*, **7**(4), 235-240.

- CLARK, C., KIRKLAND, C. L., SPAGGIARI, C. V., OORSCHOT, C., WINGATE, M. T. D. & TAYLOR, R. J., 2014. Proterozoic granulite formation driven by mafic magmatism: An example from the Fraser Range Metamorphics, Western Australia. *Precambrian Research*, **240**(0), 1-21.
- CLARK, D. A. & TONKIN, C., 1994. Magnetic anomalies due to pyrrhotite: examples from the Cobar area, N.S.W., Australia. *Journal of Applied Geophysics*, **32**(1), 11-32.
- CLEMENS, J. D. & MAWER, C. K., 1992. Granitic magma transport by fracture propagation. *Tectonophysics*, **204**(3–4), 339-360.
- CLERC, C. & LAGABRIELLE, Y., 2014. Thermal control on the modes of crustal thinning leading to mantle exhumation: Insights from the Cretaceous Pyrenean hot paleomargins. *Tectonics*, **33**(7), 1340-1359.
- COCHERIE, A., ROSSI, P., FANNING, C. M. & GUERROT, C., 2005. Comparative use of TIMS and SHRIMP for U-Pb zircon dating of A-type granites and mafic tholeiitic layered complexes and dykes from the Corsican Batholith (France). *Lithos*, **82**(1–2), 185-219.
- COFFIN, M. F. & ELDHOLM, O., 1994. Large igneous provinces: crustal structure, dimensions, and external consequences. *Reviews of Geophysics*, **32**(1), 1-36.
- COGGON, R. & HOLLAND, T. J. B., 2002. Mixing properties of phengitic micas and revised garnet-phengite thermobarometers. *Journal of Metamorphic Geology*, **20**(7), 683-696.
- COLLINS, W. J. & SAWYER, E. W., 1996. Pervasive granitoid magma transfer through the lower-middle crust during non-coaxial compressional deformation. *Journal of Metamorphic Geology*, **14**, 565-579.
- CORRADINI, M., NOTARPIETRO, A. & POTENZA, R., 1973. L'assetto geologico degli gneiss di valle grosina nell'alta Valtellina (Sondrio, Italia). *Atti della Società di Scienze Naturali e del Museo Civico di Storia Naturale di Milano*, **114**(2), 135-151.
- COSTA, S. & REY, P., 1995. Lower crustal rejuvenation and growth during post-thickening collapse: Insights from a crustal cross section through a Variscan metamorphic core complex. *Geology*, **23**(10), 905-908.
- COUREL, L., DONSIMONI, M. & MERCIER, D., 1986. La place du charbon dans la dynamique des systèmes sédimentaires des bassins houillers intramontagneux. *Mémoires de la Société géologique de France*, **149**, 37-50.
- CRUDEN, A. R., KOYI, H. & SCHMELING, H., 1995. Diapiric basal entrainment of mafic into felsic magma. *Earth and Planetary Science Letters*, **131**(3–4), 321-340.
- DAVIES, J. H. & VON BLANCKENBURG, F., 1995. Slab breakoff: A model of lithosphere detachment and its test in the magmatism and deformation of collisional orogens. *Earth and Planetary Science Letters*, **129**, 85-102.
- DE JONG, K., FÉRAUD, G., RUFFET, G., AMOURIC, M. & WIJBRANS, J. R., 2001. Excess argon incorporation in phengite of the Mulhacén Complex: submicroscopic illitization and fluid ingress during late Miocene extension in the Betic Zone, south-eastern Spain. *Chemical Geology*, **178**(1–4), 159-195.
- DEBON, F., GUERROT, C., MÉNOT, R. P., VIVIER, G. & COCHERIE, A., 1998. Late Variscan granites of the Belledonne massif (French Western Alps): an Early Visean magnesian plutonism. *Schweizerische mineralogische und petrographische Mitteilungen*, **78**, 67-85.
- DEBON, F. & LEMMET, M., 1999. Evolution of Mg/Fe Ratios in Late Variscan Plutonic Rocks from the External Crystalline Massifs of the Alps (France, Italy, Switzerland). *Journal of Petrology*, **40**(7), 1151-1185.
- DECANDIA, F. A. & ELTER, P., 1972. La zone ofiolitifera del Bracco nel settore compreso tra Levanto e la Val Graveglia (Appennino Ligure). *Memorie della Società Geologica Italiana*, **11**, 503-530.

- DECARLIS, A., DALLAGIOVANNA, G., LUALDI, A., MAINO, M. & SENO, S., 2013. Stratigraphic evolution in the Ligurian Alps between Variscan heritages and the Alpine Tethys opening: A review. *Earth-Science Reviews*, **125**, 43-68.
- DEL MORO, A., MARTIN, S. & PROSSER, G., 1999. Migmatites of the Ulten Zone (NE Italy), a Record of Melt Transfer in Deep Crust. *Journal of Petrology*, **40**(12), 1803-1826.
- DEL MORO, A. & NOTARPIETRO, A., 1987. Rb-Sr Geochemistry of some Hercynian granitoids overprinted by eo-Alpine metamorphism in the Upper Valtellina, Central Alps. *Schweizerische mineralogische und petrographische Mitteilungen*, **67**, 295-306.
- DEL MORO, A., NOTARPIETRO, A. & POTENZA, R., 1981. Revisione del significato strutturale e geocronologico delle masse intrusive minori dell'Alta Valtellina: risultati preliminari. *Rendiconti Società Italiana di Mineralogia e Petrologia*, **38**(1), 89-96.
- DEL MORO, A. & VISONÀ, D., 1982. The epiplutonic Hercynian Complex of Bressanone (Brixen, Eastern Alps, Italy): Petrologic and radiometric data. *Neues Jahrbuch für Mineralogie Abhandlungen*, **145**(1), 66-85.
- DEMARCHI, G., QUICK, J. E., SINIGOI, S. & MAYER, A., 1998. Pressure gradient and original orientation of a lower-crustal intrusion in the Ivrea-Verbano zone, Northern Italy. *Journal of Geology*, **106**, 609-622.
- DENÈLE, Y., LAUMONIER, B., PAQUETTE, J.-L., OLIVIER, P., GLEIZES, G. & BARBEY, P., 2014. Timing of granite emplacement, crustal flow and gneiss dome formation in the Variscan segment of the Pyrenees. *Geological Society, London, Special Publications*, **405**.
- DEWEY, J. F., 1988. Extensional collapse of orogens. *Tectonics*, **7**(6), 1123-1139.
- DOBLAS, M., OYARZUN, R., LÓPEZ-RUIZ, J., CEBRIÁ, J. M., YOUBI, N., MAHECHA, V., LAGO, M., POCOVÍ, A. & CABANIS, B., 1998. Permo-Carboniferous volcanism in Europe and northwest Africa: a superplume exhaust valve in the centre of Pangaea? *Journal of African Earth Sciences*, **26**(1), 89-99.
- DODSON, M., 1973. Closure temperature in cooling geochronological and petrological systems. *Contributions to Mineralogy and Petrology*, **40**(3), 259-274.
- DOWNES, H., DUPUY, C. & LEYRELOUP, A. F., 1990. Crustal evolution of the Hercynian belt of Western Europe: Evidence from lower-crustal granulitic xenoliths (French Massif Central). *Chemical Geology*, **83**(3-4), 209-231.
- DOWNES, H., KEMPTON, P. D., BRIOT, D., HARMON, R. S. & LEYRELOUP, A. F., 1991. Pb and O isotope systematics in granulite facies xenoliths, French Massif Central: implications for crustal processes. *Earth and Planetary Science Letters*, **102**(3-4), 342-357.
- DUNLAP, W. J., 2000. Nature's diffusion experiment: The cooling-rate cooling-age correlation. *Geology*, **28**(2), 139-142.
- EBBING, J., AFEWORK, Y., OLESEN, O. & NORDGULEN, Ø., 2005. Is there evidence for magmatic underplating beneath the Oslo Rift? *Terra Nova*, **17**(2), 129-134.
- EBERLI, G. P., 1988. The evolution of the southern continental margin of the Jurassic Tethys Ocean as recorded in the Allgäu Formation of the Austroalpine Nappes of Graubünden (Switzerland). *Eclogae Geologicae Helvetiae*, **81**(1), 175-214.
- ENGLAND, P. C. & THOMPSON, A., 1986. Some thermal and tectonic models for crustal melting in continental collision zones. *Geological Society, London, Special Publications*, **19**(1), 83-94.
- FAURE, M., 1995. Late orogenic carboniferous extensions in the Variscan French Massif Central. *Tectonics*, **14**(1), 132-153.
- FAURE, M., LARDEAUX, J.-M. & LEDRU, P., 2009. A review of the pre-Permian geology of the Variscan French Massif Central. *Comptes Rendus Géoscience*, **341**(2-3), 202-213.

- FÉMÉNIAS, O., COUSSAERT, N., BINGEN, B., WHITEHOUSE, M., MERCIER, J.-C. C. & DEMAFFE, D., 2003. A Permian underplating event in late- to post-orogenic tectonic setting. Evidence from the mafic–ultramafic layered xenoliths from Beaunit (French Massif Central). *Chemical Geology*, **199**(3–4), 293–315.
- FÉMÉNIAS, O., OHNSTETTER, D., COUSSAERT, N., BERGER, J. & DEMAFFE, D., 2005. Origin of micro-layering in a deep magma chamber: Evidence from two ultramafic–mafic layered xenoliths from Puy Beaunit (French Massif Central). *Lithos*, **83**(3–4), 347–370.
- FERNÁNDEZ-SUÁREZ, J., ARENAS, R., JEFFRIES, T. E., WHITEHOUSE, M. J. & VILLASECA, C., 2006. A U-Pb study of zircons from a lower crustal granulite xenolith of the Spanish Central System: a record of Iberian lithospheric evolution from the Neoproterozoic to the Triassic. *Journal of Geology*, **114**(4), 471–783.
- FERRANDO, S., LOMBARDO, B. & COMPAGNONI, R., 2008. Metamorphic history of HP mafic granulites from the Gesso-Stura Terrain (Argentera Massif, Western Alps, Italy). *European Journal of Mineralogy*, **20**(5), 777–790.
- FEYS, R., 1989. Introduction. *Synthèse Géologique des Bassins Permiens Français: Mémoire du Bureau de Recherches Géologiques et Minières*, **128**, 17–22.
- FLOOD, R. H. & VERNON, R. H., 1978. The Cooma Granodiorite, Australia: An example of in situ crustal anatexis? *Geology*, **6**, 81–84.
- FOLAND, K. A., 1983. 40Ar/39Ar incremental heating plateaus for biotites with excess argon. *Chemical Geology*, **41**(0), 3–21.
- FOUNTAIN, D. M., 1976. The Ivrea—Verbano and Strona-Ceneri Zones, Northern Italy: A cross-section of the continental crust—New evidence from seismic velocities of rock samples. *Tectonophysics*, **33**(1–2), 145–165.
- FOUNTAIN, D. M., 1989. Growth and modification of lower continental crust in extended terrains: The Role of extension and magmatic underplating. In: *Properties and Processes of Earth's Lower Crust Geophys. Monogr. Ser.*, pp. 287–299, AGU, Washington, DC.
- FOUNTAIN, D. M. & SALISBURY, M. H., 1981. Exposed cross-sections through the continental crust: implications for crustal structure, petrology, and evolution. *Earth and Planetary Science Letters*, **56**(0), 263–277.
- FRANKE, W., 2012. Comment on Dörr and Zulauf: Elevator tectonics and orogenic collapse of a Tibetan-style plateau in the European Variscides: the role of the Bohemian shear zone. *Int J Earth Sci (Geol Rundsch)* (2010) **99**: 299–325. *International Journal of Earth Sciences*, **101**, 2027–2034.
- FRANKE, W., 2014. Topography of the Variscan orogen in Europe: failed—not collapsed. *International Journal of Earth Sciences*, **103**(5), 1471–1499.
- FREI, R., BIINO, G. G. & PROSPERT, C., 1995. Dating a Variscan pressure-temperature loop with staurolite. *Geology*, **23**(12), 1095–1098.
- FROITZHEIM, N., 1992. Formation of recumbent folds during synorogenic crustal extension (Austroalpine nappes, Switzerland). *Geology*, **20**, 923–926.
- FROITZHEIM, N., DERKS, J. F., WALTER, J. M. & SCIUNNACH, D., 2008. Evolution of an Early Permian extensional detachment fault from synintrusive, mylonitic flow to brittle faulting (Grassi Detachment Fault, Orobic Anticline, southern Alps, Italy). *Geological Society, London, Special Publications*, **298**(1), 69–82.
- FROITZHEIM, N. & EBERLI, G. P., 1990. Extensional detachment faulting in the evolution of a Tethys passive continental margin, Eastern Alps, Switzerland. *Geological Society of America Bulletin*, **102**(9), 1297–1308.
- FROITZHEIM, N., SCHMID, S. M. & CONTI, P., 1994. Repeated change from crustal shortening to orogen-parallel extension in the Austroalpine units of Graubünden. *Eclogae Geologicae Helvetiae*, **87**(2), 559–612.

- FROITZHEIM, N., SCHMID, S. M. & FREY, M., 1996. Mesozoic paleogeography and the timing of eclogite-facies metamorphism in the Alps: A working hypothesis. *Eclogae Geologicae Helvetiae*, **89**(1), 81-110.
- GALLI, A., LE BAYON, B., SCHMIDT, M., BURG, J.-P. & REUSSER, E., 2013. Tectonometamorphic history of the Gruf complex (Central Alps): exhumation of a granulite–migmatite complex with the Bergell pluton. *Swiss Journal of Geosciences*, **106**(1), 33-62.
- GALLI, A., LE BAYON, B., SCHMIDT, M. W., BURG, J. P., REUSSER, E., SERGEEV, S. A. & LARIONOV, A., 2012. U–Pb zircon dating of the Gruf Complex: disclosing the late Variscan granulitic lower crust of Europe stranded in the Central Alps. *Contributions to Mineralogy and Petrology*, **163**(2), 353-378.
- GANGULY, J., 1972. Staurolite Stability and Related Parageneses: Theory, Experiments, and Applications. *Journal of Petrology*, **13**(2), 335-365.
- GAPAIS, D., PÊCHER, A., GILBERT, E. & BALLÈVRE, M., 1992. Synconvergence spreading of the higher Himalaya crystalline in Ladakh. *Tectonics*, **11**(5), 1045-1056.
- GAZZOLA, D., GOSSO, G., PULCRANO, E. & SPALLA, M. I., 2000. Eo-Alpine HP metamorphism in the Permian intrusives from the steep belt of the central Alps (Languard-Campo nappe and Tonale Series). *Geodinamica Acta*, **13**, 149-167.
- GEOFFROY, L., CALLOT, J. P., AUBOURG, C. & MOREIRA, M., 2002. Magnetic and plagioclase linear fabric discrepancy in dykes: a new way to define the flow vector using magnetic foliation. *Terra Nova*, **14**, 183-190.
- GERDES, A., WÖRNER, G. & HENK, A., 2000. Post-collisional granite generation and HT-LP metamorphism by radiogenic heating: the Variscan South Bohemian Batholith. *Journal of the Geological Society*, **157**(3), 577-587.
- GERYA, T. & BURG, J. P., 2007. Intrusion of ultramafic magmatic bodies into the continental crust: Numerical simulation. *Physics of the Earth and Planetary Interiors*, **160**, 124-142.
- GLAZNER, A. F. & BARTLEY, J. M., 2006. Is stoping a volumetrically significant pluton emplacement process? *Geological Society of America Bulletin*, **118**(9/10), 1189-1195.
- GODARD, G., MARTIN, S., PROSSER, G., KIENAST, J. R. & MORTEN, L., 1996. Variscan migmatites, eclogites and garnet-peridotites of the Ulten zone, Eastern Austroalpine system. *Tectonophysics*, **259**(4), 313-341.
- GORLA, L. & POTENZA, R., 1975. La “Formazione della Punta di Pietra Rossa” auct.: Revisione del suo significato nel contesto geologico delle Alpi Centrali. *Bollettino della Società Geologica Italiana*, **94**, 177-183.
- GOSSO, G., MESSIGA, B. & SPALLA, M. I., 1995. Dumortierite-kyanite relics within the HT-LP country rocks of the SOndalo Gabbro: a record of extension related to uplift of HP-rocks. *Abstract 55, presented at the IOS International Ophiolite Symposium, Pavia 1995*.
- GOSSO, G., SALVI, F., SPALLA, M. I. & ZUCALI, M., 2004. Map of deformation partitioning in the polydeformed and polymetamorphic Austroalpine basement of the Central Alps (Upper Valtellina and Val Camonica, Italy). In: *Mapping Geology in Italy* (eds Pasquare, G., Venturini, C. & Gropelli, G.), pp. 291-300, APAT, Roma.
- GRAUERT, B., HÄNNY, R. & SOPTRAJANOVA, G., 1974a. Geochronology of a polymetamorphic and anatetic gneiss region: The moldanubicum of the area Lam-Deggendorf, eastern Bavaria, Germany. *Contributions to Mineralogy and Petrology*, **45**(1), 37-63.
- GRAUERT, B., SEITZ, M. G. & SOPTRAJANOVA, G., 1974b. Uranium and lead gain of detrital zircon studied by isotopic analyses and fission-track mapping. *Earth and Planetary Science Letters*, **21**(4), 389-399.
- GREGNANIN, A., 1980. Metamorphism and magmatism in the Western Italian Tyrol. *Rendiconti Società Italiana di Mineralogia e Petrologia*, **36**(1), 49-64.

- GREVEL, K.-D., NAVROTSKY, A., FOCKENBERG, T. & MAJZLAN, J., 2002. The enthalpy of formation and internally consistent thermodynamic data of Mg-staurolite. *American Mineralogist*, **87**(4), 397-404.
- GUGLIELMIN, M. & NOTARPIETRO, A., 1997. Hercynian granitoids of the Northern Valtellina: the granodiorites l.s. and diorites of the Val Viola Pass. *Mineralogica et Petrographica Acta*, **40**, 1-9.
- GUILLONG, M., MEIER, D. L., ALLAN, M. M., HEINRICH, C. A. & YARDLEY, B. W. D., 2008. SILLS: A MATLAB-based program for the reduction of laser ablation ICP-MS data of homogeneous materials and inclusions. *Mineralogical Association of Canada Short Course 40*, 328-333.
- GUIRAUD, M., POWELL, R. & REBAY, G., 2001. H<sub>2</sub>O in metamorphism and unexpected behaviour in the preservation of metamorphic mineral assemblages. *Journal of Metamorphic Geology*, **19**(4), 445-454.
- GUNTLI, R. & LINIGER, M., 1989. Metamorphose in der Magma-Decke im Bereich Piz da la Margna und Piz Fedoz (Oberengadin). *Schweizerische mineralogische und petrographische Mitteilungen*, **69**, 289-301.
- GUTIÉRREZ-ALONSO, G., MURPHY, J. B., FERNÁNDEZ-SUÁREZ, J., WEIL, A. B., FRANCO, M. P. & GONZALO, J. C., 2011. Lithospheric delamination in the core of Pangea: Sm-Nd insights from the Iberian mantle. *Geology*, **39**(2), 155-158.
- HALMES, C., 1991. *Petrographische und geochemische Untersuchungen am Err-Kristallin zwischen St. Moritz und dem Val Bever (Engadin, Graubünden)*, University of Bern, Lizentiararbeit.
- HANDY, M., HERWEGH, M. & REGLI, C., 1993. Tektonische Entwicklung der westlichen Zone von Samedan (Oberhalbstein, Graubünden, Schweiz). *Eclogae Geologicae Helvetiae*, **86**(3), 785-817.
- HANDY, M. R., HERWEG, M., KAMBER, B. S., TIETZ, R. & VILLA, I. M., 1996. Geochronologic, petrologic and kinematic constraints on the evolution of the Err-Platta boundary, part of a fossil continent-ocean suture in the Alps (eastern Switzerland). *Schweizerische mineralogische und petrographische Mitteilungen*, **76**, 453-474.
- HANDY, M. R., M. SCHMID, S., BOUSQUET, R., KISSLING, E. & BERNOLLI, D., 2010. Reconciling plate-tectonic reconstructions of Alpine Tethys with the geological-geophysical record of spreading and subduction in the Alps. *Earth-Science Reviews*, **102**(3-4), 121-158.
- HANDY, M. R. & STREIT, J. E., 1999. Mechanics and mechanisms of magmatic underplating: inferences from mafic veins in deep crustal mylonite. *Earth and Planetary Science Letters*, **165**(3-4), 271-286.
- HANSMANN, W., MÜNTENER, O. & HERMANN, J., 2001. U-Pb zircon geochronology of a tholeiitic intrusion and associated migmatites at a continental crust-mantle transition, Val Malenco, Italy. *Schweizerische mineralogische und petrographische Mitteilungen*, **81**, 239-255.
- HANSON, G. N., EL TAHAWI, M. R. & WEBER, W., 1966. K-Ar and Rb-Sr ages of pegmatites in the South Central Alps. *Earth and Planetary Science Letters*, **1**, 407-413.
- HARLEY, S. L., 1989. The origins of granulites: a metamorphic perspective. *Geological Magazine*, **126**(3), 215-247.
- HARRISON, T. M., 1982. Diffusion of 40Ar in hornblende. *Contributions to Mineralogy and Petrology*, **78**(3), 324-331.
- HARRISON, T. M., CÉLÉRIER, J., AIKMAN, A. B., HERMANN, J. & HEIZLER, M. T., 2009. Diffusion of 40Ar in muscovite. *Geochimica et Cosmochimica Acta*, **73**(4), 1039-1051.
- HARRISON, T. M., DUNCAN, I. & McDougall, I., 1985. Diffusion of 40Ar in biotite: Temperature, pressure and compositional effects. *Geochimica et Cosmochimica Acta*, **49**(11), 2461-2468.

- HARTLEY, A. J. & OTAVA, J., 2001. Sediment provenance and dispersal in a deep marine foreland basin: the Lower Carboniferous Culm Basin, Czech Republic. *Journal of the Geological Society*, **158**(1), 137-150.
- HASALOVÁ, P., ŠTÍPSKÁ, P., POWELL, R., SCHULMANN, K., JANOUŠEK, V. & LEXA, O., 2008. Transforming mylonitic metagranite by open-system interactions during melt flow. *Journal of Metamorphic Geology*, **26**(1), 55-80.
- HASALOVÁ, P., WEINBERG, R. F. & MACRAE, C., 2011. Microstructural evidence for magma confluence and reusage of magma pathways: implications for magma hybridization, Karakoram Shear Zone in NW India. *Journal of Metamorphic Geology*, **29**, 875-900.
- HAUZENBERGER, C. A., HÖLLER, W. & HOINKES, G., 1996. Transition from eclogite to amphibolite-facies metamorphism in the Austroalpine Ulten Zone. *Mineralogy and Petrology*, **58**(3-4), 111-130.
- HEEREMANS, M., FALEIDE, J. I. & LARSEN, B. T., 2004a. Late Carboniferous-Permian of NW Europe: an introduction to a new regional map. *Geological Society, London, Special Publications*, **223**(1), 75-88.
- HEEREMANS, M., TIMMERMAN, M. J., KIRSTEIN, L. A. & FALEIDE, J. I., 2004b. New constraints on the timing of late Carboniferous-early Permian volcanism in the central North Sea. *Geological Society, London, Special Publications*, **223**(1), 177-193.
- HENK, A., 1993. Late orogenic basin evolution in the Variscan Internides: the Saar-Nahe Basin, southwest Germany. *Tectonophysics*, **223**, 273-290.
- HENK, A., 1999. Did the Variscides collapse or were they torn apart?: A quantitative evaluation of the driving forces for post-convergent extension in central Europe. *Tectonics*, **18**(5), 774-792.
- HENK, A., VON BLANCKENBURG, F., FINGER, F., SCHALTEGGER, U. & ZULAUF, G., 2000. Syn-convergent high-temperature metamorphism and magmatism in the Variscides: a discussion of potential heat sources. *Geological Society, London, Special Publications*, **179**(1), 387-399.
- HERMANN, J. & MÜNTENER, O., 1992. Strukturelle Entwicklung im Grenzbereich zwischen dem penninischen Malenco-Ultramafit und dem Unterostalpin (Magna- und Sella-Decke). *Schweizerische mineralogische und petrographische Mitteilungen*, **72**, 225-240.
- HERMANN, J., MÜNTENER, O. & GÜNTHER, D., 2001. Differentiation of Mafic Magma in a Continental Crust-to-Mantle Transition Zone. *Journal of Petrology*, **42**(1), 189-206.
- HERMANN, J., MÜNTENER, O., TROMMSDORFF, V., HANSMANN, W. & PICCARDO, G. B., 1997. Fossil crust-to-mantle transition, Val Malenco (Italian Alps). *Journal of Geophysical Research: Solid Earth*, **102**(B9), 20123-20132.
- HERMANN, J. & RUBATTO, D., 2003. Relating zircon and monazite domains to garnet growth zones: age and duration of granulite facies metamorphism in the Val Malenco lower crust. *Journal of Metamorphic Geology*, **21**(9), 833-852.
- HIGGINS, M., 1991. The origin of laminated and massive anorthosite, Sept Iles layered intrusion, Québec, Canada. *Contributions to Mineralogy and Petrology*, **106**(3), 340-354.
- HOLLAND, T. & POWELL, R., 2003. Activity-composition relations for phases in petrological calculations: an asymmetric multicomponent formulation. *Contributions to Mineralogy and Petrology*, **145**(4), 492-501.
- HOLLAND, T. J. B. & POWELL, R., 1998. An internally consistent thermodynamic data set for phases of petrological interest. *Journal of Metamorphic Geology*, **16**(3), 309-343.
- HOLLISTER, L. S. & CRAWFORD, M. L., 1986. Melt-enhanced deformation: A major tectonic process. *Geology*, **14**, 558-561.
- HOSKIN, P. W. O. & SCHALTEGGER, U., 2003. The composition of zircon and igneous and metamorphic petrogenesis. *Reviews in Mineralogy and Geochemistry*, **53**(1), 27-62.

- HOUSEMAN, G. A., MCKENZIE, D. P. & MOLNAR, P., 1981. Convective instability of a thickened boundary layer and its relevance for the thermal evolution of continental convergent belts. *Journal of Geophysical Research*, **86**(B7), 6115-6132.
- HROUDA, F., 1982. Magnetic anisotropy of rocks and its application in geology and geophysics. *Geophysical Surveys*, **5**, 37-82.
- HROUDA, F., CHLUPÁČOVÁ, M. & REJL, L., 1971. The mimetic fabric of magnetite in some foliated granodiorites, as indicated by magnetic anisotropy. *Earth and Planetary Science Letters*, **11**(1-5), 381-384.
- HROUDA, F. & KAHAN, Š., 1991. The magnetic fabric relationship between sedimentary and basement nappes in the High Tatra Mountains, N. Slovakia. *Journal of Structural Geology*, **13**(4), 431-442.
- HUISMANS, R. & BEAUMONT, C., 2011. Depth-dependent extension, two-stage breakup and cratonic underplating at rifted margins. *Nature*, **473**(7345), 74-78.
- HUPPERT, H. E. & SPARKS, R. S. J., 1988. The generation of granitic magmas by intrusion of basalt into continental crust. *Journal of Petrology*, **29**(3), 599-624.
- HYODO, H. & YORK, D., 1993. The discovery and significance of a fossilized radiogenic argon wave (argonami) in the Earth's crust. *Geophysical Research Letters*, **20**(1), 61-64.
- INDARES, A., WHITE, R. W. & POWELL, R., 2008. Phase equilibria modelling of kyanite-bearing anatetic paragneisses from the central Grenville Province. *Journal of Metamorphic Geology*, **26**(8), 815-836.
- JACKSON, S., 2008. LAMTRACE data reduction software for LA-ICP-MS. In: *Laser Ablation ICP-MS in the Earth Sciences: Current Practices and Outstanding Issues. Short Course Series*, **40**. (ed Sylvester, P.), pp. 305-307, Mineral Association of Canada.
- JÄGER, E., NIGGLI, E. & WENK, E., 1967. Rb-Sr Altersbestimmungen an Glimmern der Zentralalpen. *Beiträge zur Geologischen Karte der Schweiz NF134*, **Bern**, 1-67.
- JAGOUTZ, O., MÜNTENER, O., BURG, J. P., ULMER, P. & JAGOUTZ, E., 2006. Lower continental crust formation through focused flow in km-scale melt conduits: The zoned ultramafic bodies of the Chilas Complex in the Kohistan island arc (NW Pakistan). *Earth and Planetary Science Letters*, **242**(3-4), 320-342.
- JARCHOW, C. M., THOMPSON, G. A., CATCHINGS, R. D. & MOONEY, W. D., 1993. Seismic evidence for active magmatic underplating under the Basin and Range province, Western United States. *Journal of Geophysical Research*, **98**(B12), 22095-22108.
- JELINEK, V., 1977. The statistical theory of measuring anisotropy of magnetic susceptibility of rocks and its application. *Geofyzika, Brno*, **87**, 1-87.
- KELLEY, S., 2002. Excess argon in K-Ar and Ar-Ar geochronology. *Chemical Geology*, **188**(1-2), 1-22.
- KERRICK, D. M., 1990. *The Al<sub>2</sub>SiO<sub>5</sub> polymorphs*. Mineralogical Society of America. Washington, DC.
- KIRSTEIN, L. A., DAVIES, G. R. & HEEREMANS, M., 2006. The petrogenesis of Carboniferous-Permian dyke and sill intrusions across northern Europe. *Contributions to Mineralogy and Petrology*, **152**(6), 721-742.
- KOENIG, M. A., 1964. *Geologisch-petrographische Untersuchungen im oberen Veltlin*, PhD thesis, Universität Zurich.
- KOPPERS, A. A. P., 2002. ArArCALC-software for 40Ar/39Ar age calculations. *Computers & Geosciences*, **28**(5), 605-619.
- KRAINER, K., 1993. Late- and Post-Variscan Sediments of the Eastern and Southern Alps. In: *Pre-Mesozoic Geology in the Alps* (eds von Raumer, J. F. & Neubauer, F.), pp. 537-564, Springer Berlin Heidelberg.

- KRIEGSMAN, L. M. & HENSEN, B. J., 1998. Back reaction between restite and melt: Implications for geothermobarometry and pressure-temperature paths. *Geology*, **26**(12), 1111-1114.
- KUIPER, K. F., DEINO, A., HILGEN, F. J., KRIEGSMAN, W., RENNE, P. R. & WIJBRANS, J. R., 2008. Synchronizing Rock Clocks of Earth History. *Science*, **320**(5875), 500-504.
- KUIPER, Y. D., 2002. The interpretation of inverse isochron diagrams in  $^{40}\text{Ar}/^{39}\text{Ar}$  geochronology. *Earth and Planetary Science Letters*, **203**, 499-506.
- LADENHAUF, C., ARMSTRONG, R., KONZETT, R. & MILLER, C., 2001. The timing of pre-Alpine high-pressure metamorphism in the Eastern Alps: constraints from U-Pb SHRIMP dating of eclogite zircons from the Austroalpine Silvretta nappe. *Journal of Conference Abstracts (EUG XI)*, **6**, 600.
- LAGO, M., ARRANZ, E., POCOVÍ, A., GALÉ, C. & GIL-IMAZ, A., 2004. Permian magmatism and basin dynamics in the southern Pyrenees: a record of the transition from late Variscan transtension to early Alpine extension. *Geological Society, London, Special Publications*, **223**(1), 439-464.
- LAGROIX, F. & BORRADAILE, G. J., 2000. Magnetic fabric interpretation complicated by inclusions in mafic silicates. *Tectonophysics*, **325**(3–4), 207-225.
- LANGONE, A., BRAGA, R., MASSONNE, H.-J. & TIEPOLO, M., 2011. Preservation of old (prograde metamorphic) U-Th-Pb ages in unshielded monazite from the high-pressure paragneisses of the Variscan Ulten Zone (Italy). *Lithos*, **127**(1–2), 68-85.
- LARDEAUX, J. M. & SPALLA, M. I., 1991. From granulites to eclogites in the Sesia zone (Italian Western Alps): a record of the opening and closure of the Piedmont ocean. *Journal of Metamorphic Geology*, **9**(1), 35-59.
- LATTARD, D., ENELMANN, R., KONTNY, A. & SAUERZAPF, U., 2006. Curie temperatures of synthetic titanomagnetites in the Fe-Ti-O system: Effects of composition, crystal chemistry, and thermomagnetic methods. *Journal of Geophysical Research: Solid Earth*, **111**, 1-18.
- LÄUFER, A., HUBICH, D. & LOESCHKE, J., 2001. Variscan geodynamic evolution of the Carnic Alps (Austria/Italy). *International Journal of Earth Sciences*, **90**(4), 855-870.
- LAVIER, L. L. & MANATSCHAL, G., 2006. A mechanism to thin the continental lithosphere at magma-poor margins. *Nature*, **440**(7082), 324-328.
- LEDRU, P., COURRIOUX, G., DALLAIN, C., LARDEAUX, J. M., MONTEL, J. M., VANDERHAEGHE, O. & VITEL, G., 2001. The Velay dome (French Massif Central): melt generation and granite emplacement during orogenic evolution. *Tectonophysics*, **342**(3–4), 207-237.
- LEE, J.-Y., MARTI, K., SEVERINGHAUS, J. P., KAWAMURA, K., YOO, H.-S., LEE, J. B. & KIM, J. S., 2006. A redetermination of the isotopic abundances of atmospheric Ar. *Geochimica et Cosmochimica Acta*, **70**(17), 4507-4512.
- LEECH, M. L., 2001. Arrested orogenic development: eclogitization, delamination, and tectonic collapse. *Earth and Planetary Science Letters*, **185**, 149-159.
- LEMOINE, M., BAS, T., ARNAUD-VANNEAU, A., ARNAUD, H., DUMONT, T., GIDON, M., BOURBON, M., DE GRACIANSKY, P.-C., RUDKIEWICZ, J.-L., MEGARD-GALLI, J. & TRICART, P., 1986. The continental margin of the Mesozoic Tethys in the Western Alps. *Marine and Petroleum Geology*, **3**(3), 179-199.
- LIBOUREL, G., 1985. *Le complexe de Santa Lucia di Mercurio (Corse): Ultramafites mantelliques, intrusion basique stratifiée, paragneiss granulitique. Un équivalent possible des complexes de la zone d'Ivrée*, PhD Thesis, Université Paul Sabatier de Toulouse.
- LIBOUREL, G., 1988. Le complexe de Santa-Lucia di Mercurio (Corse): un équivalent possible des complexes de la Zone d'Ivrée. *Comptes Rendus de l'Académie des Sciences - Series IIA - Earth and Planetary Science*, **307**, 1225-1230.

- LINCK, G., 1899. Die Pegmatite des Oberen Veltlin. *Jenaischen Zeitschrift für Naturwissenschaft*, 345-360.
- LINNEN, R. L. & KEPPLER, H., 2002. Melt composition control of Zr/Hf fractionation in magmatic processes. *Geochimica et Cosmochimica Acta*, **66**(18), 3293-3301.
- LISTER, J. R. & KERR, R. C., 1991. Fluid-mechanical models of crack propagation and their application to magma transport in dykes. *Journal of Geophysical Research: Solid Earth*, **96**(B6), 10049-10077.
- LO, C.-H. & ONSTOTT, T. C., 1989. <sup>39</sup>Ar recoil artifacts in chloritized biotite. *Geochimica et Cosmochimica Acta*, **53**(10), 2697-2711.
- LOOCK, G., STOSCH, H. G. & SECK, H. A., 1990. Granulite facies lower crustal xenoliths from the Eifel, West Germany: petrological and geochemical aspects. *Contributions to Mineralogy and Petrology*, **105**(1), 25-41.
- LORENZ, V. & NICHOLLS, I. A., 1976. The Permocarboniferous Basin and Range Province of Europe. An Application op Plate Tectonics. In: *The Continental Permian in Central, West, and South Europe* (ed Falke, H.) *Nato Advanced Study Institutes Series*, pp. 313-342, Springer Netherlands.
- LORENZ, V. & NICHOLLS, I. A., 1984. Plate and intraplate processes of Hercynian Europe during the late paleozoic. *Tectonophysics*, **107**(1-2), 25-56.
- LOWRIE, W., 1990. Identification of ferromagnetic minerals in a rock by coercivity and unblocking temperature properties. *Geophysical Research Letters*, **17**(2), 159-162.
- LUCAS, S. B. & ST-ONGE, M. R., 1995. Syn-tectonic magmatism and the development of compositional layering, Ungava Orogen (northern Quebec, Canada). *Journal of Structural Geology*, **17**(4), 475-491.
- LUDWIG, K. R., 2012. *Isoplot v. 3.75: A Geochronological Toolkit for Microsoft Excel.*, Special Publication No. 5. Berkeley Geochronology Center, Berkeley, 75 pp.
- MAGGETTI, M. & FLISCH, M., 1993. Evolution of the Silvretta Nappe. In: *Pre-Mesozoic Geology in the Alps* (eds von Raumer, J. F. & Neubauer, F.), pp. 469-484, Springer Berlin Heidelberg.
- MAHAN, K. H., BARTLEY, J. M., COLEMAN, D. S., GLAZNER, A. F. & CARL, B. S., 2003. Sheeted intrusion of the synkinematic McDoogle pluton, Sierra Nevada, California. *Geological Society of America Bulletin*, **115**(12), 1570-1582.
- MAHAR, E. M., BAKER, J. M., POWELL, R., HOLLAND, T. J. B. & HOWELL, N., 1997. The effect of Mn on mineral stability in metapelites. *Journal of Metamorphic Geology*, **15**(2), 223-238.
- MAIR, V. & SCHUSTER, R., 2003. New geochronological data from the austroalpine Ortler crystalline in the Martell Valley (Southern Tyrol, Italy). *Mitteilung Österreichische Mineralogische Gesellschaft*, **148**, 215-217.
- MALAVIEILLE, J., 1993. Late orogenic extension in mountain belts: insights from the Basin and Range and the late Paleozoic Variscan belt. *Tectonics*, **12**(5), 1115-1130.
- MALAVIEILLE, J., GUIHOT, P., COSTA, S., LARDEAUX, J. M. & GARDIEN, V., 1990. Collapse of the thickened Variscan crust in the French Massif Central: Mont Pilat extensional shear zone and St. Etienne Late Carboniferous basin. *Tectonophysics*, **177**(1-3), 139-149.
- MANATSCHAL, G., 2004. New models for evolution of magma-poor rifted margins based on a review of data and concepts from West Iberia and the Alps. *International Journal of Earth Sciences*, **93**(3), 432-466.
- MANATSCHAL, G., FROITZHEIM, N., RUBENACH, M. & TURRIN, B. D., 2001. The role of detachment faulting in the formation of an ocean-continent transition: insights from the Iberia Abyssal Plain. *Geological Society, London, Special Publications*, **187**(1), 405-428.

- MANATSCHAL, G., LAVIER, L. & CHENIN, P., 2014. The role of inheritance in structuring hyperextended rift systems: Some considerations based on observations and numerical modeling. *Gondwana Research*(in press).
- MANCKTELOW, N. S., 2008. Tectonic pressure: Theoretical concepts and modelled examples. *Lithos*, **103**(1–2), 149-177.
- MANCKTELOW, N. S. & GRASEMANN, B., 1997. Time-dependent effects of heat advection and topography on cooling histories during erosion. *Tectonophysics*, **270**(3–4), 167-195.
- MARTÍNEZ CATALÁN, J. R., 2011. Are the oroclines of the Variscan belt related to late Variscan strike-slip tectonics? *Terra Nova*, **23**, 241-247.
- MASINI, E., MANATSCHAL, G., MOHN, G., GHENNE, J.-F. & LAFONT, F., 2011. The tectono-sedimentary evolution of a supra-detachment rift basin at a deep-water magma-poor rifted margin: the example of the Samedan Basin preserved in the Err nappe in SE Switzerland. *Basin Research*, **23**(6), 652-677.
- MATTE, P., 1986. Tectonics and plate tectonics model for the Variscan belt of Europe. *Tectonophysics*, **126**(2–4), 329-374.
- MATTE, P., 2001. The Variscan collage and orogeny (480-290 Ma) and the tectonic definition of the Armorica microplate: a review. *Terra Nova*, **13**, 122-128.
- MATTE, P., 2006. The Southern Urals: deep subduction, soft collision and weak erosion. *Geological Society, London, Memoirs*, **32**(1), 421-426.
- McCANN, T., PASCAL, C., TIMMERMAN, M. J., KRZYWIEC, P., LÓPEZ-GÓMEZ, J., WETZEL, L., KRAWCZYK, C. M., RIEKE, H. & LAMARCHE, J., 2006. Post-Variscan (end Carboniferous-Early Permian) basin evolution in Western and Central Europe. *Geological Society, London, Memoirs*, **32**(1), 355-388.
- McCarthy, T. C. & PATIÑO DOUCE, A. E., 1997. Experimental evidence for high-temperature felsic melts formed during basaltic intrusion of the deep crust. *Geology*, **25**(5), 463-466.
- McDOUGALL, I. & HARRISON, T. M., 1999. *Geochronology and Thermochronology by the  $^{40}\text{Ar}/^{39}\text{Ar}$  method*. Oxford University Press, New York.
- McKENZIE, D., 1984. The Generation and Compaction of Partially Molten Rock. *Journal of Petrology*, **25**(3), 713-765.
- MEIER, A., 2003. *The Periadriatic Fault System in Valtellina (N-Italy) and the Evolution of the Southwestern Segment of the Eastern Alps*, PhD Thesis, ETH Zurich.
- MEISSNER, R. & MOONEY, W., 1998. Weakness of the lower continental crust: a condition for delamination, uplift, and escape. *Tectonophysics*, **296**, 47-60.
- MELI, S., MONTANINI, A., THÖNI, M. & FRANK, W., 1996. Age of mafic granulite blocks from the External Liguride Units (Northern Apennines, Italy). *Memorie di scienze geologiche*, **48**, 65-72.
- MENAND, T., 2011. Physical controls and depth of emplacement of igneous bodies: A review. *Tectonophysics*, **500**(1–4), 11-19.
- MÉNARD, G. & MOLNAR, P., 1988. Collapse of a Hercynian Tibetan Plateau into a late Palaeozoic European Basin and Range province. *Nature*, **334**(6179), 235-237.
- MERCOLLI, I., 1989. The volcanic suite of the Julier area (Grisons). Part 1: volcanic and tectonic evolution. *Schweizerische mineralogische und petrographische Mitteilungen*, **69**, 423-433.
- MILLER, C. & THÖNI, M., 1995. Origin of eclogites from the Austroalpine Ötztal basement (Tirol, Austria): geochemistry and Sm-Nd vs. Rb-Sr isotope systematics. *Chemical Geology*, **122**(1–4), 199-225.
- MILLER, C. & THÖNI, M., 1997. Eo-alpine eclogitisation of Permian MORB-type gabbros in the Koralpe (Eastern Alps, Austria): new geochronological, geochemical and petrological data. *Chemical Geology*, **137**(3–4), 283-310.

- MILLER, C., THÖNI, M., GOESSLER, W. & TESSADRI, R., 2011. Origin and age of the Eisenkappel gabbro to granite suite (Carinthia, SE Austrian Alps). *Lithos*, **125**(1–2), 434–448.
- MILLER, R. B. & PATERSON, S. R., 2001. Construction of mid-crustal sheeted plutons: Examples from the North Cascades, Washington. *Geological Society of America Bulletin*, **113**(11), 1423–1442.
- MOHN, G., MANATSCHAL, G., BELTRANDO, M., MASINI, E. & KUSZNIR, N., 2012. Necking of continental crust in magma-poor rifted margins: Evidence from the fossil Alpine Tethys margins. *Tectonics*, **31**(1), 1–28.
- MOHN, G., MANATSCHAL, G., MASINI, E. & MÜNTENER, O., 2011. Rift-related inheritance in orogens: a case study from the Austroalpine nappes in Central Alps (SE-Switzerland and N-Italy). *International Journal of Earth Sciences*, **100**(5), 937–961.
- MOHN, G., MANATSCHAL, G., MÜNTENER, O., BELTRANDO, M. & MASINI, E., 2010. Unravelling the interaction between tectonic and sedimentary processes during lithospheric thinning in the Alpine Tethys margins. *International Journal of Earth Sciences*, **99**(1), 75–101.
- MONJOIE, P., BUSSY, F., LAPIERRE, H. & PFEIFER, H.-R., 2005. Modeling of in-situ crystallization processes in the Permian mafic layered intrusion of Mont Collon (Dent Blanche nappe, western Alps). *Lithos*, **83**(3–4), 317–346.
- MONJOIE, P., BUSSY, F., SCHALTEGGER, U., MULCH, A., LAPIERRE, H. & PFEIFER, H.-R., 2007. Contrasting magma types and timing of intrusion in the Permian layered mafic complex of Mont Collon (Western Alps, Valais, Switzerland): evidence from U/Pb zircon and 40Ar/39Ar amphibole dating. *Swiss Journal of Geosciences*, **100**(1), 125–135.
- MULCH, A., ROSENAU, M., DÖRR, W. & HANDY, M., 2002. The age and structure of dikes along the tectonic contact of the Ivrea-Verbano and Strona-Ceneri Zones (southern Alps, Northern Italy, Switzerland). *Schweizerische mineralogische und petrographische Mitteilungen*, **82**, 55–76.
- MUNDIL, R., PÁLFY, J., RENNE, P. R. & BRACK, P., 2010. The Triassic timescale: new constraints and a review of geochronological data. *Geological Society, London, Special Publications*, **334**(1), 41–60.
- MÜNTENER, O., 1997. *The Malenco peridotites (Alps): Petrology and geochemistry of subcontinental mantle and Jurassic exhumation during rifting*, PhD Thesis, ETH Zurich.
- MÜNTENER, O. & HERMANN, J., 2001. The role of lower crust and continental upper mantle during formation of non-volcanic passive margins: evidence from the Alps. *Geological Society, London, Special Publications*, **187**(1), 267–288.
- MÜNTENER, O., HERMANN, J. & TROMMSDORFF, V., 2000. Cooling History and Exhumation of Lower-Crustal Granulite and Upper Mantle (Malenco, Eastern Central Alps). *Journal of Petrology*, **41**(2), 175–200.
- MÜNTENER, O., PETTKE, T., DESMURS, L., MEIER, M. & SCHALTEGGER, U., 2004. Refertilization of mantle peridotite in embryonic ocean basins: trace element and Nd isotopic evidence and implications for crust–mantle relationships. *Earth and Planetary Science Letters*, **221**(1–4), 293–308.
- MÜNTENER, O. & PICCARDO, G. B., 2003. Melt migration in ophiolitic peridotites: the message from Alpine-Apennine peridotites and implications for embryonic ocean basins. *Geological Society, London, Special Publications*, **218**(1), 69–89.
- MURALI, A. V., PARTHASARATHY, R., MAHADEVAN, T. M. & DAS, M. S., 1983. Trace element characteristics, REE patterns and partition coefficients of zircons from different geological environments—A case study on Indian zircons. *Geochimica et Cosmochimica Acta*, **47**(11), 2047–2052.

- MUTTONI, G., KENT, D. V., GARZANTI, E., BRACK, P., ABRAHAMSEN, N. & GAETANI, M., 2003. Early Permian Pangea ‘B’ to Late Permian Pangea ‘A’. *Earth and Planetary Science Letters*, **215**(3–4), 379-394.
- NELSON, K. D., 1992. Are crustal thickness variations in old mountain belts like the Appalachians a consequence of lithospheric delamination? *Geology*, **20**, 498-502.
- NICOLAS, A., 1992. Kinematics in Magmatic Rocks with Special Reference to Gabbros. *Journal of Petrology*, **33**(4), 891-915.
- NIMIS, P. & MORTEN, L., 2000. P-T evolution of ‘crustal’ garnet peridotites and included pyroxenites from Nonsberg area (upper Austroalpine), NE Italy: from the wedge to the slab. *Journal of Geodynamics*, **30**(1–2), 93-115.
- NIRRENGARTEN, M., GERNIGON, L. & MANATSCHAL, G., 2014. Lower crustal bodies in the Møre volcanic rifted margin: Geophysical determination and geological implications. *Tectonophysics(in press)*.
- NOTARPIETRO, A. & DE CAPITANI, L., 1985a. Contributo alla conoscenza delle plutoniti austridiche dell’Alta Valtellina: Il granito del Pizzo Bianco. *Rendiconti Società Italiana di Mineralogia e Petrologia*, **40**, 353-363.
- NOTARPIETRO, A. & DE CAPITANI, L., 1985b. Contributo alla conoscenza delle plutoniti austridiche dell’Alta Valtellina: Il granito di Val Ferrata. *Rendiconti Società Italiana di Mineralogia e Petrologia*, **40**, 365-375.
- NOTARPIETRO, A. & GORLA, L., 1981. Contributo alla conoscenza delle formazioni Austridiche nell’alta e media Valtellina. Variazioni petrochimiche nella formazione di Valle Grosina. *Rendiconti Società Italiana di Mineralogia e Petrologia*, **37**(2), 755-791.
- O’BRIEN, P. J. & RÖTZLER, J., 2003. High-pressure granulites: formation, recovery of peak conditions and implications for tectonics. *Journal of Metamorphic Geology*, **21**, 3-20.
- ONCKEN, O., PLESCH, A., WEBER, J., RICKEN, W. & SCHRADER, S., 2000. Passive margin detachment during arc-continent collision (Central European Variscides). *Geological Society, London, Special Publications*, **179**(1), 199-216.
- OSMUNDSEN, P. T. & REDFIELD, T. F., 2011. Crustal taper and topography at passive continental margins. *Terra Nova*, **23**, 349-361.
- PACE, F., 1966. Studio petrografico dell’alta Val Viola (Sondrio). *Atti della Società di Scienze Naturali e del Museo Civico di Storia Naturale di Milano*, **1**, 43-60.
- PADOVANO, M., ELTER, F. M., PANDELI, E. & FRANCESCHELLI, M., 2012. The East Variscan Shear Zone: new insights into its role in the Late Carboniferous collision in southern Europe. *International Geology Review*, **54**(8), 957-970.
- PAQUETTE, J.-L., MÉNOT, R.-P., PIN, C. & ORSINI, J.-B., 2003. Episodic and short-lived granitic pulses in a post-collisional setting: evidence from precise U-Pb zircon dating through a crustal cross-section in Corsica. *Chemical Geology*, **198**(1–2), 1-20.
- PATERSON, S. R. & FOWLER JR, T. K., 1993. Re-examining pluton emplacement processes. *Journal of Structural Geology*, **15**(2), 191-206.
- PATERSON, S. R. & MILLER, R. B., 1998. Mid-crustal magmatic sheets in the Cascades Mountains, Washington: implications for magma ascent. *Journal of Structural Geology*, **20**(9-10), 1345-1363.
- PATERSON, S. R. & VERNON, R. H., 1995. Bursting the bubble of ballooning plutons: A return to nested diapirids emplaced by multiple processes. *Geological Society of America Bulletin*, **107**(11), 1356-1380.
- PATERSON, S. R., VERNON, R. H. & FOWLER, T. K., 1991. Aureole tectonics. *Reviews in Mineralogy and Geochemistry*, **26**(1), 673-722.

- PATERSON, S. R., VERNON, R. H. & TOBISCH, O. T., 1989. A review of criteria for the identification of magmatic and tectonic foliations in granitoids. *Journal of Structural Geology*, **11**(3), 349-363.
- PATIÑO DOUCE, A. & JOHNSTON, A. D., 1991. Phase equilibria and melt productivity in the pelitic system: implications for the origin of peraluminous granitoids and aluminous granulites. *Contributions to Mineralogy and Petrology*, **107**(2), 202-218.
- PEARCE, G. W. & FUETEN, F., 1989. An intensive study of magnetic susceptibility anisotropy of amphibolite layers of the Thompson Belt, North Manitoba. *Tectonophysics*, **162**(3-4), 315-329.
- PEARCE, N. J. G., PERKINS, W. T., WESTGATE, J. A., GORTON, M. P., JACKSON, S. E., NEAL, C. R. & CHENERY, S. P., 1997. A compilation of new and published major and trace element data for NIST SRM 610 and NIST SRM 612 glass reference materials. *Geostandards and geoanalytical research*, **21**(1), 115-144.
- PERESSINI, G., QUICK, J. E., SINIGOI, S., HOFMANN, A. W. & FANNING, M., 2007. Duration of a Large Mafic Intrusion and Heat Transfer in the Lower Crust: a SHRIMP U-Pb Zircon Study in the Ivrea-Verbano Zone (Western Alps, Italy). *Journal of Petrology*, **48**(6), 1185-1218.
- PETFORD, N., CRUDEN, A. R., MCCAFFREY, K. J. W. & VIGNERESSE, J.-L., 2000. Granite magma formation, transport and emplacement in the Earth's crust. *Nature*, **408**, 669-673.
- PETFORD, N., KERR, R. C. & LISTER, J. R., 1993. Dike transport of granitoid magmas. *Geology*, **21**, 845-848.
- PETRI, B. & SKRZYPEK, E., 2013. *TCWizard Matlab Package - Help File, 26/04/2013 Update.*, Online report, University of Strasbourg. Available at: [http://eost.unistra.fr/fileadmin/upload/EOST/Benoit\\_Petri/software1/TCWizard\\_HelpFile.pdf](http://eost.unistra.fr/fileadmin/upload/EOST/Benoit_Petri/software1/TCWizard_HelpFile.pdf)
- PIN, C., 1986. Datation U-Pb sur zircons à 285 M.a. du complexe gabbro-dioritique du Val Sesia-Val Mastallone et âge tardい-hercynien du métamorphisme granulitique de la zone Ivrea-Verbano (Italie). *Comptes Rendus de l'Académie des Sciences. Série 2. Sciences de la Terre et des planètes*, **9**, 827-830.
- PITRA, P., POUJOL, M., VAN DEN DRIESSCHE, J., POILVET, J.-C. & PAQUETTE, J.-L., 2012. Early Permian extensional shearing of an Ordovician granite: The Saint-Eutrope "C/S-like" orthogneiss (Montagne Noire, French Massif Central). *Comptes Rendus Géoscience*, **344**(8), 377-384.
- PLATT, J. P. & ENGLAND, P. C., 1993. Convective removal of lithosphere beneath mountain belts: thermal and mechanical consequences. *American Journal of Science*, **293**, 307-336.
- POHL, F., FROITZHEIM, N., GEISLER-WIERWILLE, T. & SCHLÖDER, O., 2014. Permian magmatism, Permian detachment faulting, and Alpine thrusting in the Orobic Anticline, southern Alps, Italy. *Geophysical Research Abstracts*, **16**, EGU2014-6542.
- POTENZA, R., 1973. A geomathematic investigation of syntecis in a gabbroic formation. *Mathematical Geology*, **5**(4), 321-339.
- POWELL, R., GUIRAUD, M. & WHITE, R. W., 2005. Truth and beauty in metamorphic phase-equilibria: conjugate variables and phase diagrams. *The Canadian Mineralogist*, **43**(1), 21-33.
- POWELL, R., HOLLAND, T. & WORLEY, B., 1998. Calculating phase diagrams involving solid solutions via non-linear equations, with examples using THERMOCALC. *Journal of Metamorphic Geology*, **16**(4), 577-588.
- QUICK, J. E., SINIGOI, S. & MAYER, A., 1994. Emplacement dynamics of a large mafic intrusion in the lower crust, Ivrea-Verbano Zone, northern Italy. *Journal of Geophysical Research*, **99**(B11), 21559-21573.

- QUICK, J. E., SINIGOI, S., NEGRINI, L., DEMARCHI, G. & MAYER, A., 1992. Synmagmatic deformation in the underplated igneous complex of the Ivrea-Verbano zone. *Geology*, **20**(7), 613-616.
- RAGETH, R., 1984. Intrusiva und Extrusiva der Bernina-Decke zwischen Morteratsch und Berninapass (Graubünden). *Schweizerische mineralogische und petrographische Mitteilungen*, **64**, 83-109.
- RAMBERG, H., 1981. *Gravity, deformation and the earth's crust, in theory, experiments and geological application*. Academic Press, London.
- RAMPONE, E., HOFMANN, A. W., PICCARDO, G. B., VANNUCCI, R., BOTTAZZI, P. & OTTOLINI, L., 1996. Trace element and isotope geochemistry of depleted peridotites from an N-MORB type ophiolite (Internal Liguride, N. Italy). *Contributions to Mineralogy and Petrology*, **123**(1), 61-76.
- RAMPONE, E., HOFMANN, A. W. & RACZEK, I., 1998. Isotopic contrasts within the Internal Liguride ophiolite (N. Italy): the lack of a genetic mantle–crust link. *Earth and Planetary Science Letters*, **163**(1–4), 175-189.
- RAMSAY, J. G., 1989. Emplacement kinematics of a granite diapir: the Chindamora batholith, Zimbabwe. *Journal of Structural Geology*, **11**(1–2), 191-209.
- RANERO, C. R. & PEREZ-GUSSINYE, M., 2010. Sequential faulting explains the asymmetry and extension discrepancy of conjugate margins. *Nature*, **468**(7321), 294-299.
- RASCH, W., 1911. Petrographische Untersuchung der dioritischen Gesteine aus dem Gabbrogebiet des oberen Veltlin. *Neues Jahrbuch für Mineralogie und Paläontologie*, **32**, 197-238.
- REBAY, G. & SPALLA, M. I., 2001. Emplacement at granulite facies conditions of the Sesia–Lanzo metagabbros: an early record of Permian rifting? *Lithos*, **58**(3–4), 85-104.
- REDLER, C., JOHNSON, T. E., WHITE, R. W. & KUNZ, B. E., 2012. Phase equilibrium constraints on a deep crustal metamorphic field gradient: metapelitic rocks from the Ivrea Zone (NW Italy). *Journal of Metamorphic Geology*, **30**(3), 235-254.
- REDLER, C., WHITE, R. W. & JOHNSON, T. E., 2013. Migmatites in the Ivrea Zone (NW Italy): Constraints on partial melting and melt loss in metasedimentary rocks from Val Strona di Omegna. *Lithos*, **175–176**(0), 40-53.
- RENNE, P. R., SCOTT, G. R., GLEN, J. M. G. & FEINBERG, J. M., 2002. Oriented inclusions of magnetite in clinopyroxene: Source of stable remanent magnetization in gabbros of the Messum Complex, Namibia. *Geochemistry Geophysics Geosystems*, **3**(12), 1-11.
- REY, P., 1993. Seismic and tectono-metamorphic characters of the lower continental crust in Phanerozoic areas: A consequence of post-thickening extension. *Tectonics*, **12**(2), 580-590.
- REY, P., VANDERHAEGHE, O. & TEYSSIER, C., 2001. Gravitational collapse of the continental crust: definition, regimes and modes. *Tectonophysics*, **342**(3–4), 435-449.
- RICHTER, C., KELSO, P. & MACLOED, C. J., 1996. Magnetic fabrics and sources of magnetic susceptibility in lower crustal and upper mantle rocks from Hess Deep. In: *Proceedings of the Ocean Drilling Program, Scientific Results* (eds Mével, C., Gillis, K. M. & Allan, J. F.), pp. 393-403, 147, Ocean Drilling Program, College Station, Texas.
- ROCHETTE, P., 1987. Metamorphic control of the magnetic mineralogy of black shales in the Swiss Alps: toward the use of “magnetic isogrades”. *Earth and Planetary Science Letters*, **84**(4), 446-456.
- ROCHETTE, P., AUBOURG, C. & PERRIN, M., 1999. Is this magnetic fabric normal? A review and case studies in volcanic formations. *Tectonophysics*, **307**, 219-234.
- ROCHETTE, P., JACKSON, M. & AUBOURG, C., 1992. Rock magnetism and the interpretation of anisotropy of magnetic susceptibility. *Reviews of Geophysics*, **30**(3), 209-226.

- ROSCHER, M. & SCHNEIDER, J. W., 2006. Permo-Carboniferous climate: Early Pennsylvanian to Late Permian climate development of central Europe in a regional and global context. *Geological Society, London, Special Publications*, **265**(1), 95-136.
- ROSENBERG, C. L., 2004. Shear zones and magma ascent: A model based on a review of the Tertiary magmatism in the Alps. *Tectonics*, **23**(3).
- ROSSI, P., COCHERIE, A., FANNING, C. M. & DELOULE, É., 2006. Variscan to eo-Alpine events recorded in European lower-crust zircons sampled from the French Massif Central and Corsica, France. *Lithos*, **87**(3–4), 235-260.
- ROYDEN, L. & KEEN, C. E., 1980. Rifting process and thermal evolution of the continental margin of Eastern Canada determined from subsidence curves. *Earth and Planetary Science Letters*, **51**(2), 343-361.
- RUBATTO, D., 2002. Zircon trace element geochemistry: partitioning with garnet and the link between U-Pb ages and metamorphism. *Chemical Geology*, **184**(1–2), 123-138.
- RUBATTO, D., FERRANDO, S., COMPAGNONI, R. & LOMBARDO, B., 2010. Carboniferous high-pressure metamorphism of Ordovician protoliths in the Argentera Massif (Italy), Southern European Variscan belt. *Lithos*, **116**(1–2), 65-76.
- RUBATTO, D., SCHALTEGGER, U., LOMBARDO, B., COLOMBO, F. & COMPAGNONI, R., 2001. Complex Paleozoic magmatic and metamorphic evolution in the Argentera Massif (Western Alps) resolved with U-Pb dating. *Schweizerische mineralogische und petrographische Mitteilungen*, **81**, 213-228.
- RUDNICK, R. L. & FOUNTAIN, D. M., 1995. Nature and composition of the continental crust: a lower crustal perspective. *Reviews of Geophysics*, **33**(3), 267-309.
- RUFFET, G., FÉRAUD, G. & AMOURIC, M., 1991. Comparison of 40Ar-39Ar conventional and laser dating of biotites from the North Trégor Batholith. *Geochimica et Cosmochimica Acta*, **55**(6), 1675-1688.
- RUTTER, E., BRODIE, K. & EVANS, P. J., 1993. Structural geometry, lower crustal magmatic underplating and lithospheric stretching in the Ivrea-Verbano zone, northern Italy. *Journal of Structural Geology*, **15**(3-5), 647-662.
- SANDIFORD, M., 1989. Horizontal structures in granulite terrains: A record of mountain building or mountain collapse? *Geology*, **17**(5), 449-452.
- SARDA, P., STAUDACHER, T. & ALLÈGRE, C. J., 1985. 40Ar36Ar in MORB glasses: constraints on atmosphere and mantle evolution. *Earth and Planetary Science Letters*, **72**(4), 357-375.
- SATO, K., SANTOSH, M. & TSUNOGAE, T., 2010. High P-T phase relation of magnesian ( $Mg0.7Fe0.3$ ) staurolite compositon in the system  $FeO-MgO-Al2O3-SiO2-H2O$ : Implications for prograde high-pressure history of ultrahigh-temperature metamorphic rocks. *American Mineralogist*, **95**(1), 177-184.
- SAWYER, E. W., CESARE, B. & BROWN, M., 2011. When the Continental Crust Melts. *Elements*, **7**(4), 229-234.
- SCHALTEGGER, U., 1994. Unravelling the pre-Mesozoic history of Aar and Gotthard massifs (Central Alps) by isotopic dating - a review. *Schweizerische mineralogische und petrographische Mitteilungen*, **74**, 41-51.
- SCHALTEGGER, U., ABRECHT, J. & CORFU, F., 2003. The Ordovician orogeny in the Alpine basement: constraints from geochronology and geochemistry in the Aar Massif (Central Alps). *Schweizerische mineralogische und petrographische Mitteilungen*, **83**, 183-195.
- SCHALTEGGER, U. & BRACK, P., 2007. Crustal-scale magmatic systems during intracontinental strike-slip tectonics: U, Pb and Hf isotopic constraints from Permian magmatic rocks of the Southern Alps. *International Journal of Earth Sciences*, **96**(6), 1131-1151.

- SCHALTEGGER, U. & CORFU, F., 1995. Late Variscan “Basin and Range” magmatism and tectonics in the Central Alps: evidence from U-Pb geochronology. *Geodinamica Acta*, **8**(2), 82-98.
- SCHALTEGGER, U., FANNING, C. M., GÜNTHER, D., MAURIN, J. C., SCHULMANN, K. & GEBAUER, D., 1999. Growth, annealing and recrystallization of zircon and preservation of monazite in high-grade metamorphism: conventional and in-situ U-Pb isotope, cathodoluminescence and microchemical evidence. *Contributions to Mineralogy and Petrology*, **134**(2-3), 186-201.
- SCHALTEGGER, U. & GEBAUER, D., 1999. Pre-Alpine geochronology of the Central, Western and Southern Alps. *Schweizerische mineralogische und petrographische Mitteilungen*, **79**, 79-87.
- SCHECK-WENDEROTH, M. & MAYSTRENKO, Y., 2008. How warm are passive continental margins? A 3-D lithosphere-scale study from the Norwegian margin. *Geology*, **36**(5), 419-422.
- SCHENK, V., 1981. Synchronous uplift of the lower crust of the Ivrea Zone and of Southern Calabria and its possible consequences for the Hercynian orogeny in Southern Europe. *Earth and Planetary Science Letters*, **56**, 305-320.
- SCHMID, R. & WOOD, B. J., 1976. Phase relationships in granulitic metapelites from the Ivrea-Verbano zone (Northern Italy). *Contributions to Mineralogy and Petrology*, **54**(4), 255-279.
- SCHMID, S., BERNOLLI, D., FÜGENSCHUH, B., MATENCO, L., SCHEFER, S., SCHUSTER, R., TISCHLER, M. & USTASZEWSKI, K., 2008. The Alpine-Carpathian-Dinaridic orogenic system: correlation and evolution of tectonic units. *Swiss Journal of Geosciences*, **101**(1), 139-183.
- SCHMID, S., FÜGENSCHUH, B., KISSLING, E. & SCHUSTER, R., 2004. Tectonic map and overall architecture of the Alpine orogen. *Eclogae Geologicae Helvetiae*, **97**(1), 93-117.
- SCHMID, S. M., AEBLI, H. R., HELLER, F. & ZINGG, A., 1989. The role of the Periadriatic Line in the tectonic evolution of the Alps. *Geological Society, London, Special Publications*, **45**, 153-171.
- SCHMID, S. M. & FROITZHEIM, N., 1993. Oblique slip and block rotation along the Engadine line. *Eclogae Geologicae Helvetiae*, **86**(2), 569-593.
- SCHMID, S. M. & HAAS, R., 1989. Transition from near-surface thrusting to Intrabasement Decollement, Schlinig Thrust, eastern Alps. *Tectonics*, **8**(4), 697-718.
- SCHMID, S. M., PFIFFNER, O. A., FROITZHEIM, N., SCHÖNBORN, G. & KISSLING, E., 1996. Geophysical-geological transect and tectonic evolution of the Swiss-Italian Alps. *Tectonics*, **15**(5), 1036-1064.
- SCHULMANN, K. & JEŽEK, J., 2012. Some remarks on fabric overprints and constrictional AMS fabrics in igneous rocks. *International Journal of Earth Sciences*, **101**, 705-714.
- SCHULZ, B. & VON RAUMER, J., 1993. Syndeformational Uplift of Variscan High-pressure Rocks (Col de Bérard, Aiguilles Rouges Massif, Western Alps). *Zeitschrift der Deutschen Geologischen Gesellschaft*, **144**, 104-120.
- SCHUSTER, R., SCHARBERT, S., ABART, R. & FRANK, W., 2001. Permo-Triassic extension and related HT/LP metamorphism in the Austroalpine-Southalpine realm. *Mitteilungen der Geologie und Bergbau Studenten Österreichs*, **44**, 111-141.
- SCHUSTER, R. & STÜWE, K., 2008. Permian metamorphic event in the Alps. *Geology*, **36**(8), 603-606.
- SCOTT, D. R. & STEVENSON, D. J., 1986. Magma ascent by porous flow. *Journal of Geophysical Research: Solid Earth*, **91**(B9), 9283-9296.
- SELVERSTONE, J., 2005. Are the Alps collapsing? *Annual Review of Earth and Planetary Sciences*, **33**(1), 113-132.

- SIEGESMUND, S., LAYER, P., DUNKL, I., VOLLBRECHT, A., STEENKEN, A., WEMMER, K. & AHRENDT, H., 2008. Exhumation and deformation history of the lower crustal section of the Valstrona di Omegna in the Ivrea Zone, southern Alps. *Geological Society, London, Special Publications*, **298**(1), 45-68.
- SIVOLA, J. & SCHMID, R., 2007. Recommendations by the IUGS Subcommission on the Systematics of Metamorphic Rocks: List of mineral abbreviations. Web version 01.02.07. (<http://www.bgs.ac.uk/scmr/home.html>).
- SINIGOI, S., QUICK, J. E., DEMARCI, G. & KLÖTZLI, U., 2011. The role of crustal fertility in the generation of large silicic magmatic systems triggered by intrusion of mantle magma in the deep crust. *Contributions to Mineralogy and Petrology*, **162**(4), 691-707.
- SKRZYPEK, E., TABAUD, A. S., EDEL, J. B., SCHULMANN, K., COCHERIE, A., GUERROT, C. & ROSSI, P., 2012. The significance of Late Devonian ophiolites in the Variscan orogen: a record from the Vosges Klippen Belt. *International Journal of Earth Sciences*, **101**(4), 951-972.
- SNOKE, A. W., KALAKAY, T. J., QUICK, J. E. & SINIGOI, S., 1999. Development of a deep-crustal shear zone in response to syntectonic intrusion of mafic magma into the lower crust, Ivrea–Verbano zone, Italy. *Earth and Planetary Science Letters*, **166**(1–2), 31-45.
- SOLANO, J. M. S., JACKSON, M. D., SPARKS, R. S. J. & BLUNDY, J., 2014. Evolution of major and trace element composition during melt migration through crystalline mush: Implications for chemical differentiation in the crust. *American Journal of Science*, **314**(5), 895-939.
- SÖLVA, H., THÖNI, M. & HABLER, G., 2003. Dating a single garnet crystal with very high Sm/Nd ratios (Campo basement unit, Eastern Alps). *European Journal of Mineralogy*, **15**, 35-42.
- SPALLA, M. I., CARMINATI, E., CERIANI, S., OLIVA, A. & BATTAGLIA, D., 1999. Influence of deformation partitioning and metamorphic re-equilibration on P-T path reconstruction in the pre-Alpine basement of central Southern Alps (Northern Italy). *Journal of Metamorphic Geology*, **17**(3), 319-336.
- SPALLA, M. I., ZANONI, D., MAROTTA, A. M., REBAY, G., RODA, M., ZUCALI, M. & GOSSO, G., 2014. The transition from Variscan collision to continental break-up in the Alps: insights from the comparison between natural data and numerical model predictions. *Geological Society, London, Special Publications*, **405**.
- SPEAR, F. S., 1993. *Metamorphic phase equilibria and pressure-temperature-time paths*, Mineralogical Society of America, Washington, D. C.
- SPEAR, F. S., KOHN, M. J. & CHENEY, J. T., 1999. P-T paths from anatetic pelites. *Contributions to Mineralogy and Petrology*, **134**(1), 17-32.
- SPILLMANN, P. & BÜCHI, H. J., 1993. The Pre-Alpine Basement of the Lower Austro-Alpine Nappes in the Bernina Massif (Grisons, Switzerland; Valtellina, Italy). In: *Pre-Mesozoic Geology in the Alps* (eds von Raumer, J. F. & Neubauer, F.), pp. 457-467, Springer Berlin Heidelberg.
- STACEY, J. S. & KRAMERS, J. D., 1975. Approximation of terrestrial lead isotope evolution by a two-stage model. *Earth and Planetary Science Letters*, **26**(2), 207-221.
- STAMPFLI, G. M., 1996. The Intra-Alpine terrain: A Paleotethyan remnant in the Alpine Variscides. *Eclogae Geologicae Helvetiae*, **89**(1), 13-42.
- STAMPFLI, G. M., HOCHARD, C., VÉRARD, C., WILHEM, C. & VONRAUMER, J., 2013. The formation of Pangea. *Tectonophysics*, **593**(0), 1-19.
- STAMPFLI, G. M. & KOZUR, H. W., 2006. Europe from the Variscan to the Alpine cycles. *Geological Society, London, Memoirs*, **32**(1), 57-82.

- STAMPFLI, G. M., MOSAR, J., MARQUER, D., MARCHANT, R., BAUDIN, T. & BOREL, G., 1998. Subduction and obduction processes in the Swiss Alps. *Tectonophysics*, **296**(1–2), 159-204.
- STAUB, R., 1946. Geologische Karte der Berninagruppe und ihrer Umgebung im Oberengadin, Bergell, Val Malenco, Puschlav und Livigno, scale 1:50,000. *Speziale Karte 118, Schweizerische Geologische Kommission*.
- STAUDACHER, T., SARDÀ, P., RICHARDSON, S. H., ALLÈGRE, C. J., SAGNA, I. & DMITRIEV, L. V., 1989. Noble gases in basalt glasses from a Mid-Atlantic Ridge topographic high at 14°N: geodynamic consequences. *Earth and Planetary Science Letters*, **96**(1–2), 119-133.
- STEIGER, R. J. & JÄGER, E., 1977. Subcommission on geochronology: Convention on the use of decay constants in geo- and cosmochronology. *Earth and Planetary Science Letters*, **36**, 359-362.
- STEPANOV, A. S. & HERMANN, J., 2013. Fractionation of Nb and Ta by biotite and phengite: Implications for the “missing Nb paradox”. *Geology*.
- STIPP, M., STÜNITZ, H., HEILBRONNER, R. & SCHMID, S. M., 2002. The eastern Tonale fault zone: a “natural laboratory” for crystal plastic deformation of quartz over a temperature range from 250 to 700 °C. *Journal of Structural Geology*, **24**, 1861-1884.
- ŠTÍPSKÁ, P. & POWELL, R., 2005. Does ternary feldspar constrain the metamorphic conditions of high-grade meta-igneous rocks? Evidence from orthopyroxene granulites, Bohemian Massif. *Journal of Metamorphic Geology*, **23**(8), 627-647.
- SUN, S.-s. & McDONOUGH, W. F., 1989. Chemical and isotopic systematics of oceanic basalts: implications for mantle composition and processes. *Geological Society, London, Special Publications*, **42**(1), 313-345.
- THÉLIN, P., SARTORI, M., BURRI, M., GOUFFON, Y. & CHESSEX, R., 1993. The Pre-Alpine Basement of the Briançonnais (Wallis, Switzerland). In: *Pre-Mesozoic Geology in the Alps* (eds von Raumer, J. F. & Neubauer, F.), pp. 297-315, Springer Berlin Heidelberg.
- THÖNI, M., 1981. Degree and evolution of the alpine metamorphism in the Austroalpine unit W of the Hohe Tauern in the light of K/Ar and Rb/Sr age determination on micas. *Jahrbuch der Geologischen Bundesanstalt*, **124**(1), 111-174.
- THÖNI, M., 1999. A review of geochronological data from the Eastern Alps. *Schweizerische mineralogische und petrographische Mitteilungen*, **79**, 209-230.
- THÖNI, M. & JAGOUTZ, E., 1992. Some new aspects of dating eclogites in orogenic belts: Sm-Nd, Rb-Sr, and Pb-Pb isotopic results from the Austroalpine Saualpe and Koralpe type-locality (Carinthia/Styria, southeastern Austria). *Geochimica et Cosmochimica Acta*, **56**(1), 347-368.
- THÖNI, M., MOTTANA, A., DELITATA, M. C., DE CAPITANI, L. & LIBORIO, G., 1992. The Val Biandino composite pluton: A late Hercynian intrusion into the South-Alpine metamorphic basement of the Alps (Italy). *Neues Jahrbuch für Mineralogie Monatshefte*, **12**, 545-554.
- THYBO, H. & ARTEMIEVA, I. M., 2013. Moho and magmatic underplating in continental lithosphere. *Tectonophysics*, **609**(0), 605-619.
- TIMMERMAN, M. J., 2004. Timing, geodynamic setting and character of Permo-Carboniferous magmatism in the foreland of the Variscan Orogen, NW Europe. *Geological Society, London, Special Publications*, **223**(1), 41-74.
- TIMMERMAN, M. J., HEEREMANS, M., KIRSTEIN, L. A., LARSEN, B. T., SPENCER-DUNWORTH, E.-A. & SUNDVOLL, B., 2009. Linking changes in tectonic style with magmatism in northern Europe during the late Carboniferous to latest Permian. *Tectonophysics*, **473**(3–4), 375-390.

- TOBISCH, O. T., McNULTY, B. A. & VERNON, R. H., 1997. Microgranitoid enclave swarms in granitic plutons, central Sierra Nevada, California. *Lithos*, **40**(2–4), 321-339.
- TRIBUZIO, R., RENNA, M. R., BRAGA, R. & DALLAI, L., 2009. Petrogenesis of Early Permian olivine-bearing cumulates and associated basalt dykes from Bocca di Tenda (Northern Corsica): Implications for post-collisional Variscan evolution. *Chemical Geology*, **259**(3–4), 190-203.
- TRIBUZIO, R., THIRLWALL, M. F. & MESSIGA, B., 1999. Petrology, mineral and isotope geochemistry of the Sondalo gabbroic complex (Central Alps, Northern Italy): implications for the origin of post-Variscan magmatism. *Contributions to Mineralogy and Petrology*, **136**(1–2), 48-62.
- TRIELOFF, M., WEBER, H. W., KURAT, G., JESSBERGER, E. K. & JANICKE, J., 1997. Noble gases, their carrier phases, and argon chronology of upper mantle rocks from Zabargad Island, Red Sea. *Geochimica et Cosmochimica Acta*, **61**(23), 5065-5088.
- TROMMSDORFF, V., MONTRASIO, A., HERMANN, J., MÜNTENER, O., SPILLMANN, P. & GIERÉ, R., 2005. The Geological Map of Valmalenco. *Schweizerische mineralogische und petrographische Mitteilungen*, **85**, 1-13.
- TRÜMPY, R., 1975. Penninic-Austroalpine boundary in the Swiss Alps: a presumed former continental margin and its problems. *American Journal of Science*, **279**, 209-238.
- TRÜMPY, R., 1980. *Geology of Switzerland: An outline of the geology of Switzerland*. Wepf & Co., Basel and New York.
- TUGEND, J., MANATSCHAL, G., KUSZNIR, N. J., MASINI, E., MOHN, G. & THINON, I., 2014. Formation and deformation of hyperextended rift systems: Insights from rift domain mapping in the Bay of Biscay-Pyrenees. *Tectonics*, **23**(7), 1239-1276.
- TUMIATI, S., THÖNI, M., NIMIS, P., MARTIN, S. & MAIR, V., 2003. Mantle–crust interactions during Variscan subduction in the Eastern Alps (Nonsberg–Ulten zone): geochronology and new petrological constraints. *Earth and Planetary Science Letters*, **210**(3–4), 509-526.
- TURNER, S., SANDIFORD, M. & FODEN, J., 1992. Some geodynamic and compositional constraints on “postorogenic” magmatism. *Geology*, **20**(10), 931-934.
- ULIANOV, A., MÜNTENER, O., SCHALTEGGER, U. & BUSSY, F., 2012. The data treatment dependent variability of U-Pb zircon ages obtained using mono-collector, sector field, laser ablation ICPMS. *Journal of Analytical Atomic Spectrometry*, **27**(4), 663-676.
- VAN DEN DRIESEN, J. & BRUN, J. P., 1991-1992. Tectonic evolution of the Montagne Noire (french Massif Central): a model of extensional gneiss dome. *Geodinamica Acta*, **5**(1–2), 85-99.
- VAN DEN EECKHOUT, B., GROCOTT, J. & VISSERS, R., 1986. On the role of diapirism in the segregation, ascent and final emplacement of granitoid magmas—discussion. *Tectonophysics*, **127**(1–2), 161-166.
- VAN WEES, J. D., STEPHENSON, R. A., ZIEGLER, P. A., BAYER, U., McCANN, T., DADLEZ, R., GAUPP, R., NARKIEWICZ, M., BITZER, F. & SCHECK, M., 2000. On the origin of the Southern Permian Basin, Central Europe. *Marine and Petroleum Geology*, **17**(1), 43-59.
- VANDERHAEGHE, O., 2001. Melt segregation, pervasive melt migration and magma mobility in the continental crust: the structural record from pores to orogens. *Physics and Chemistry of the Earth, Part A: Solid Earth and Geodesy*, **26**(4–5), 213-223.
- VANDERHAEGHE, O., 2012. The thermal–mechanical evolution of crustal orogenic belts at convergent plate boundaries: A reappraisal of the orogenic cycle. *Journal of Geodynamics*, **56–57**(0), 124-145.
- VANDERHAEGHE, O. & TEYSSIER, C., 2001. Partial melting and flow of orogens. *Tectonophysics*, **342**(3–4), 451-472.

- VERNON, R. H., 2000. Review of microstructural evidence of magmatic and solid-state flow. *Electronic Geosciences*, **5**(2), 1-23.
- VIELZEUF, D., 1984. *Relations de phases dans le faciès granulite et implication sédodynamiques. L'exemple des granulites des Pyrénées*, PhD Thesis, Université de Clermont II.
- VIELZEUF, D. & HOLLOWAY, J., 1988. Experimental determination of the fluid-absent melting relations in the pelitic system. *Contributions to Mineralogy and Petrology*, **98**(3), 257-276.
- VIELZEUF, D. & KORNPROBST, J., 1984. Crustal splitting and the emplacement of Pyrenean Iherzolites and granulites. *Earth and Planetary Science Letters*, **67**, 87-96.
- VIELZEUF, D. & MONTEL, J., 1994. Partial melting of metagreywackes. Part I. Fluid-absent experiments and phase relationships. *Contributions to Mineralogy and Petrology*, **117**(4), 375-393.
- VIELZEUF, D. & PIN, C., 1989. Geodynamic implications of granulitic rocks in the Hercynian belt. *Geological Society, London, Special Publications*, **43**(1), 343-348.
- VIELZEUF, D. & PIN, C., 1991. Granulites orthodérivées d'âge tardi-hercynien; exemple de la norite de Treilles, Corbières (Aude, France). *Bulletin de la société géologique de France*, **162**(6), 1057-1066.
- VILLA, I. M., HERMANN, J., MÜNTENER, O. & TROMMSDORFF, V., 2000.  $^{39}\text{Ar}$ - $^{40}\text{Ar}$  dating of multiply zoned amphibole generations (Malenco, Italian Alps). *Contributions to Mineralogy and Petrology*, **140**(3), 363-381.
- VILLASECA, C., OREJANA, D., PATERSON, B. A., BILLSTROM, K. & PÉREZ-SOBA, C., 2007. Metaluminous pyroxene-bearing granulite xenoliths from the lower continental crust in central Spain: their role in the genesis of Hercynian I-type granites. *European Journal of Mineralogy*, **19**(4), 463-477.
- VON BLANCKENBURG, F., 1992. Combined high-precision chronometry and geochemical tracing using accessory minerals: applied to the Central-Alpine Bergell intrusion (central Europe). *Chemical Geology*, **100**(1-2), 19-40.
- VON QUADT, A., GRÜNENFELDER, M. & BÜCHI, H., 1994. U-Pb zircon ages from igneous rocks of the Bernina nappe system (Grisons, Switzerland). *Schweizerische mineralogische und petrographische Mitteilungen*, **74**, 373-382.
- VON RAUMER, J. F., FINGER, F., VESELÁ, P. & STAMPFLI, G. M., 2014. Durbachites-Vaugnerites – a geodynamic marker in the central European Variscan orogen. *Terra Nova*, **26**(2), 85-95.
- VON RAUMER, J. F. & NEUBAUER, F., 1993. History of Geological Investigations in the Pre-Triassic Basement of the Alps. In: *Pre-Mesozoic Geology in the Alps* (eds von Raumer, J. F. & Neubauer, F.), pp. 55-63, Springer Berlin Heidelberg.
- VOSHAGE, H., HOFMANN, A. W., MAZZUCHELLI, M., RIVALENTI, G., SINIGOI, S., RACZEK, I. & DEMARCI, G., 1990. Isotopic evidence from the Ivrea Zone for a hybrid lower crust formed by magmatic underplating. *Nature*, **347**(6295), 731-736.
- VOSHAGE, H., HUNZIKER, J. C., HOFMANN, A. W. & ZINGG, A., 1987. A Nd and Sr isotopic study of the Ivrea zone, Southern Alps, N-Italy. *Contributions to Mineralogy and Petrology*, **97**(1), 31-42.
- WARREN, C. J., KELLEY, S. P., SHERLOCK, S. C. & McDONALD, C. S., 2012. Metamorphic rocks seek meaningful cooling rate: Interpreting  $^{40}\text{Ar}/^{39}\text{Ar}$  ages in an exhumed ultra-high pressure terrane. *Lithos*, **155**, 30-48.
- WARREN, C. J., SHERLOCK, S. C. & KELLEY, S. P., 2011. Interpreting high-pressure phengite  $^{40}\text{Ar}/^{39}\text{Ar}$  laserprobe ages: an example from Saih Hatait, NE Oman. *Contributions to Mineralogy and Petrology*, **161**(6), 991-1009.

- WATERS, D. J., 2001. The significance of prograde and retrograde quartz-bearing intergrowth microstructures in partially melted granulite-facies rocks. *Lithos*, **56**(1), 97-110.
- WEIL, A. B., GUTIÉRREZ-ALONSO, G., JOHNSTON, S. T. & PASTOR-GALÁN, D., 2013. Kinematic constraints on buckling a lithospheric-scale orocline along the northern margin of Gondwana: A geologic synthesis. *Tectonophysics*, **582**(0), 25-49.
- WEINBERG, R. F., 1996. Ascent mechanism of felsic magmas: news and views. *Earth and Environmental Science Transactions of the Royal Society of Edinburgh*, **87**(1-2), 95-103.
- WEINBERG, R. F., 1999. Mesoscale pervasive felsic magma migration: alternatives to dyking. *Lithos*, **46**, 393-410.
- WEINBERG, R. F. & PODLADCHIKOV, Y. Y., 1994. Diapiric ascent of magmas through power law crust and mantle. *Journal of Geophysical Research: Solid Earth*, **99**(B5), 9543-9559.
- WEINBERG, R. F. & PODLADCHIKOV, Y. Y., 1995. The rise of solid-state diapirs. *Journal of Structural Geology*, **17**(8), 1189-1195.
- WEINBERG, R. F., REGENAUER-LIEB, K. & ROSENBAUM, G., 2007. Mantle detachment faults and the breakup of cold continental lithosphere. *Geology*, **35**(11), 1035-1038.
- WELLS, P. R. A., 1980. Thermal models for the magmatic accretion and subsequent metamorphism of continental crust. *Earth and Planetary Science Letters*, **46**, 253-265.
- WENDLANDT, E., DEPAOLO, D. J. & SCOTT BALDRIDGE, W., 1993. Nd and Sr isotope chronostratigraphy of Colorado Plateau lithosphere: implications for magmatic and tectonic underplating of the continental crust. *Earth and Planetary Science Letters*, **116**(1-4), 23-43.
- WERNICKE, B., SPENCER, J. E., BURCHFIELD, B. C. & GUTH, P. L., 1982. Magnitude of crustal extension in the southern Great Basin. *Geology*, **10**(10), 499-502.
- WHEELER, J., 1996. Diffarg: A program for simulating argon diffusion profiles in minerals. *Computers & Geosciences*, **22**(8), 919-929.
- WHITE, R. W., POMROY, N. E. & POWELL, R., 2005. An in situ metatexite–diatexite transition in upper amphibolite facies rocks from Broken Hill, Australia. *Journal of Metamorphic Geology*, **23**(7), 579-602.
- WHITE, R. W. & POWELL, R., 2002. Melt loss and the preservation of granulite facies mineral assemblages. *Journal of Metamorphic Geology*, **20**(7), 621-632.
- WHITE, R. W., POWELL, R. & HALPIN, J. A., 2004. Spatially-focussed melt formation in aluminous metapelites from Broken Hill, Australia. *Journal of Metamorphic Geology*, **22**(9), 825-845.
- WHITE, R. W., POWELL, R. & HOLLAND, T. J. B., 2007. Progress relating to calculation of partial melting equilibria for metapelites. *Journal of Metamorphic Geology*, **25**(5), 511-527.
- WHITMARSH, R., BESLIER, M. & WALLACE, P., 1998. Leg 173. *Proc. ODP, Init. Rep.*, **173**, 493.
- WHITNEY, D. L., TEYSSIER, C., REY, P. & BUCK, W. R., 2012. Continental and oceanic core complexes. *Geological Society of America Bulletin*.
- WIEDENBECK, M., ALLÉ, P., CORFU, F., GRIFFIN, W. L., MEIER, M., OBERLI, F., VON QUADT, A., RODDICK, J. C. & SPIEGEL, W., 1995. Three natural zircon standards for U-Th-Pb, Lu-Hf, trace element and ree analyses. *Geostandards and geoanalytical research*, **19**(1), 1-23.
- WIJBRANS, J. R. & McDougall, I., 1986.  $^{40}\text{Ar}/^{39}\text{Ar}$  dating of white micas from an Alpine high-pressure metamorphic belt on Nacos (Greece): the resetting of the argon isotopic system. *Contributions to Mineralogy and Petrology*, **93**, 186-194.
- WIJBRANS, J. R., PRINGLE, M. S., KOPPERS, A. A. P. & SCHEVEERS, R., 1995. Argon geochronology of small samples using the Vulkaan argon laserprobe. *Proceedings of the Koninklijke Nederlandse Akademie van weten schappen - Biological chemical geological physical and medical sciences*, **98**, 185-218.

- WILSON, J. T., 1966. Did the Atlantic close and then re-open? *Nature*, **211**, 676-681.
- WILSON, M., NEUMANN, E.-R., DAVIES, G. R., TIMMERMAN, M. J., HEEREMANS, M. & LARSEN, B. T., 2004. Permo-Carboniferous magmatism and rifting in Europe: introduction. *Geological Society, London, Special Publications*, **223**(1), 1-10.
- XIONG, X., KEPPLER, H., AUDÉTAT, A., NI, H., SUN, W. & LI, Y., 2011. Partitioning of Nb and Ta between rutile and felsic melt and the fractionation of Nb/Ta during partial melting of hydrous metabasalt. *Geochimica et Cosmochimica Acta*, **75**(7), 1673-1692.
- YAOUANCQ, G. & MACLOED, C. J., 2000. Petrofabric investigation of gabbros from the Oman ophiolite: comparison between AMS and rock fabric. *Marine Geophysical Researches*, **21**, 289-305.
- ŽÁK, J., VERNER, K. & TÝCOVÁ, P., 2008. Multiple magmatic fabrics in plutons: an overlooked tool for exploring interactions between magmatic processes and regional deformation? *Geological Magazine*, **145**(04), 537-551.
- ZANDT, G., MYERS, S. C. & WALLACE, T. C., 1995. Crust and mantle structure across the Basin and Range–Colorado plateau boundary at 37°N latitude and implications for Cenozoic extensional mechanism. *Journal of Geophysical Research*, **100**(B6), 10529-10548.
- ZANETTI, A., MAZZUCHELLI, M., SINIGOI, S., GIOVANARDI, T., PERESSINI, G. & FANNING, M., 2013. SHRIMP U-Pb Zircon Triassic Intrusion Age of the Finero Mafic Complex (Ivrea–Verbano Zone, Western Alps) and its Geodynamic Implications. *Journal of Petrology*, **54**(11), 2235-2265.
- ZIBRA, I., 2006. *Late-hercynian granitoid plutons emplaced along a deep crustal shear zone. A case study from the S. Lucia nappe (Alpine Corsica, France)*, PhD Thesis, Università di Pisa.
- ZIBRA, I., KRUHL, J. H., MONTANINI, A. & TRIBUZIO, R., 2012. Shearing of magma along a high-grade shear zone: Evolution of microstructures during the transition from magmatic to solid-state flow. *Journal of Structural Geology*, **37**(0), 150-160.
- ZIEGLER, P. A., SCHUMACHER, M. E., DÈZES, P., VAN WEES, J.-D. & CLOETINGH, S., 2004. Post-Variscan evolution of the lithosphere in the Rhine Graben area: constraints from subsidence modelling. *Geological Society, London, Special Publications*, **223**(1), 289-317.
- ZIEGLER, P. A., SCHUMACHER, M. E., DÈZES, P., VAN WEES, J.-D. & CLOETINGH, S., 2006. Post-Variscan evolution of the lithosphere in the area of the European Cenozoic Rift System. *Geological Society, London, Memoirs*, **32**(1), 97-112.
- ZOBACK, M. L. & ZOBACK, M., 1980. State of stress in the conterminous United States. *Journal of Geophysical Research: Solid Earth (1978–2012)*, **85**(B11), 6113-6156.
- ZWART, H. J., 1962. On the determination of the polymetamorphic mineral associations, and its application to the bosost area (central Pyrenees). *Geologische Rundschau*, **52**, 38-65.



---

## *ANNEXES*

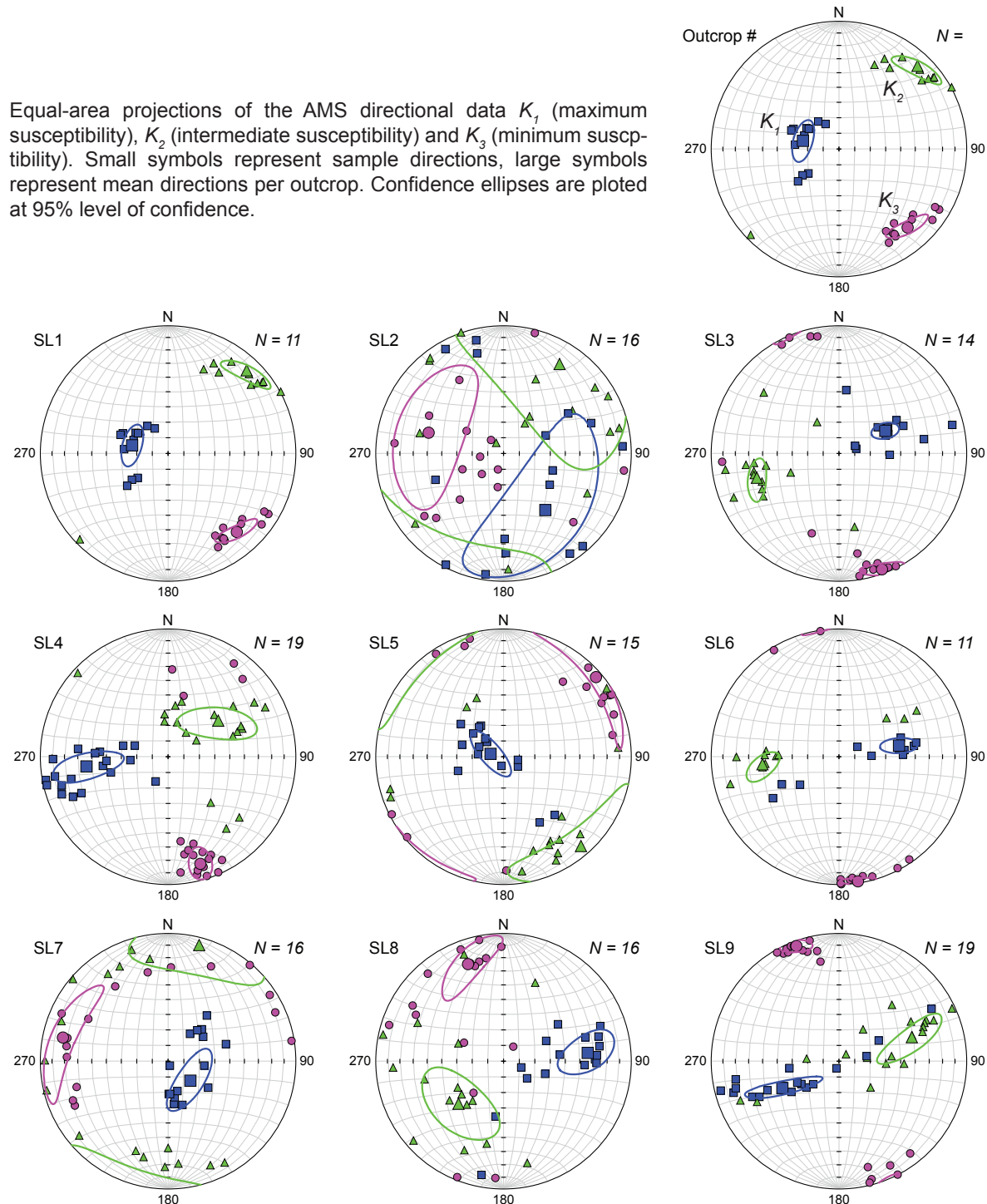
---

## **TABLE DES MATIÈRES**

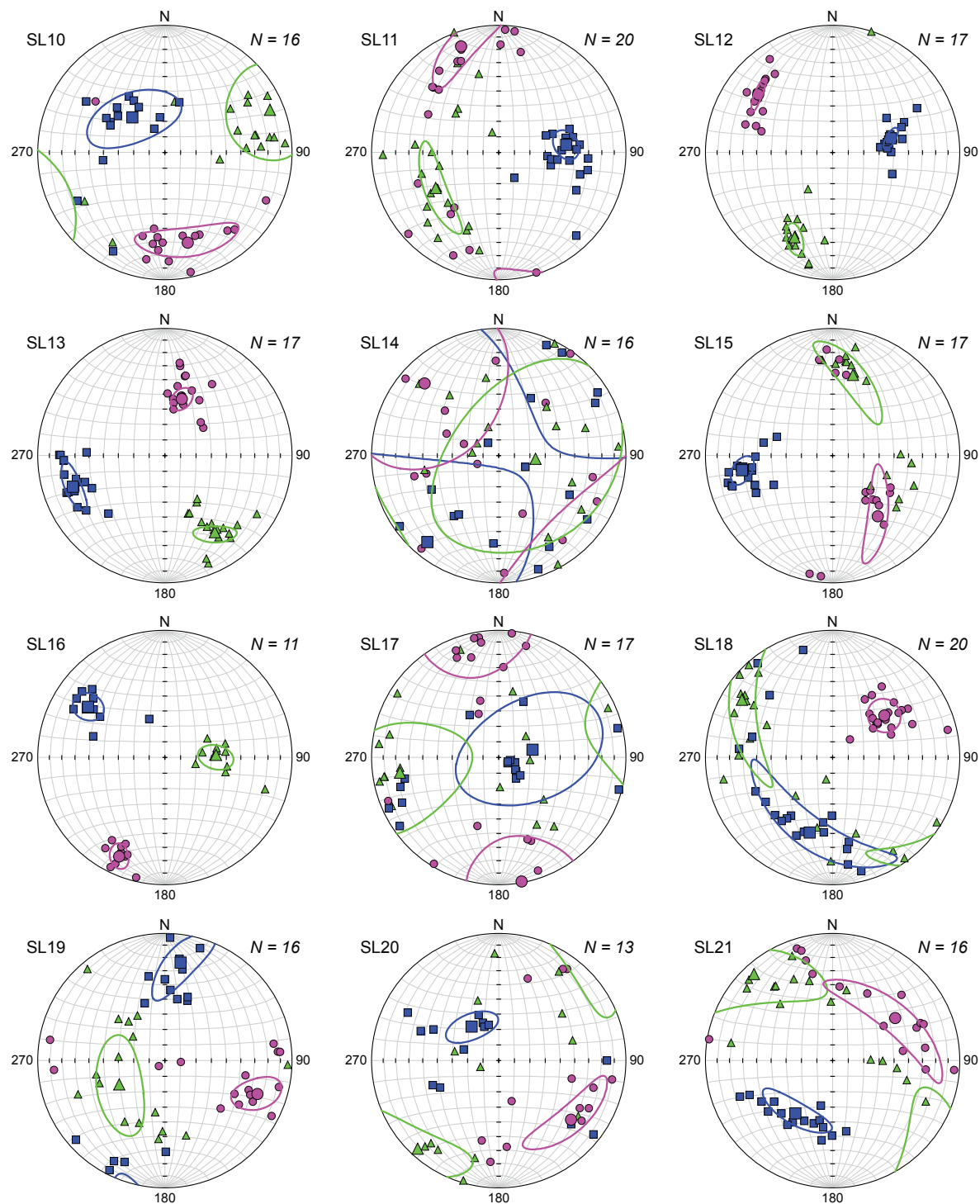
<i>Annexe 1: Orientations des axes de susceptibilités magnétiques</i>	249
<i>Annexe 2: Coordonnées géographiques des localités étudiées: Unité de Campo</i>	255
<i>Annexe 3: Coordonnées géographiques des localités étudiées: Gabbro de Sondalo</i>	258
<i>Annexe 4: Coordonnées géographiques des localités étudiées: Gabbro de Sondalo (ASM)</i>	259
<i>Annexe 5: Carte géologique et structurale du gabbro de Sondalo</i>	261
<i>Annexe 6: Carte litho-tectonique des nappes austroalpines et pénniques supérieures</i>	263

**Annexe 1: Orientations des axes de susceptibilités magnétiques**

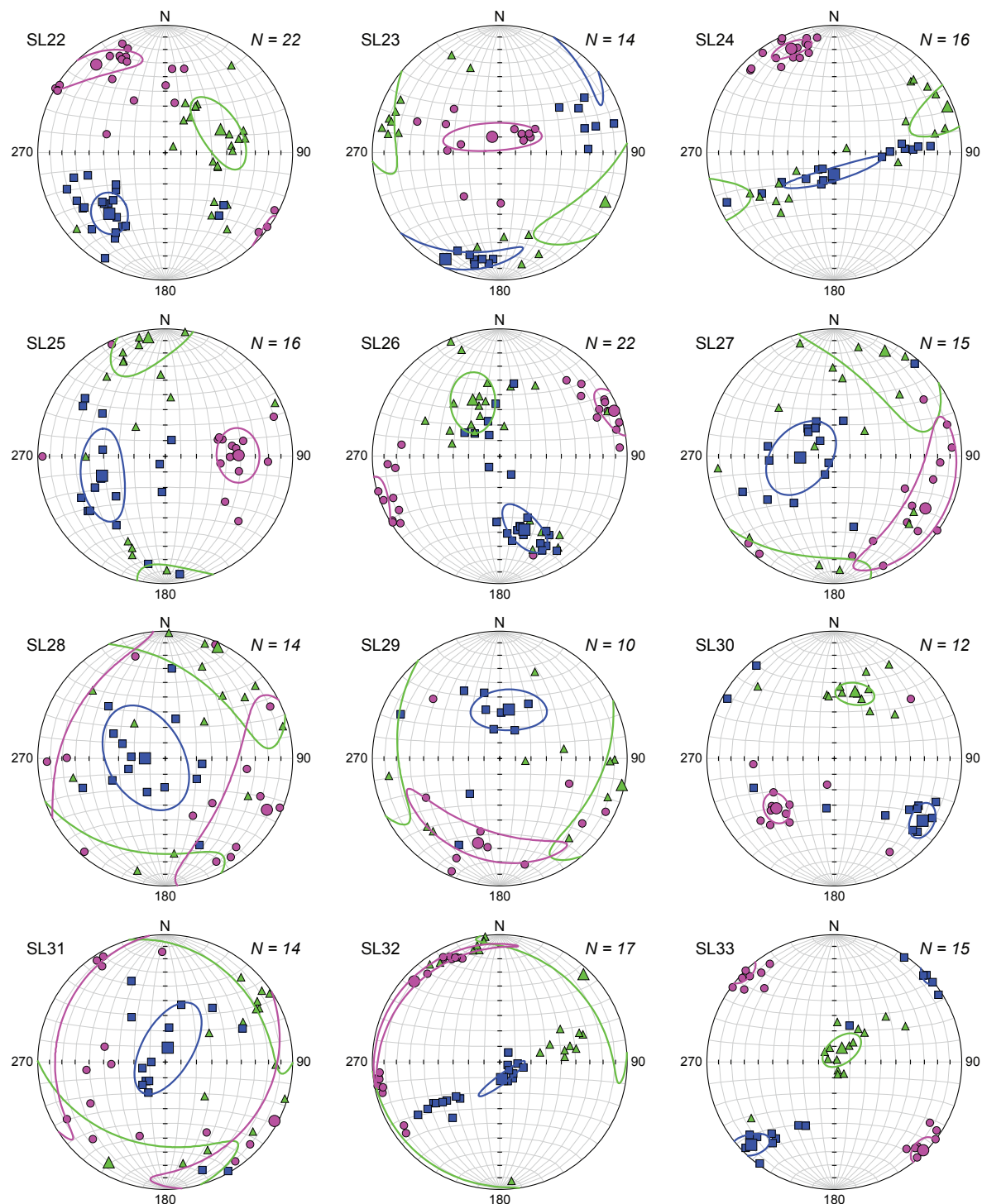
Equal-area projections of the AMS directional data  $K_1$  (maximum susceptibility),  $K_2$  (intermediate susceptibility) and  $K_3$  (minimum susceptibility). Small symbols represent sample directions, large symbols represent mean directions per outcrop. Confidence ellipses are plotted at 95% level of confidence.



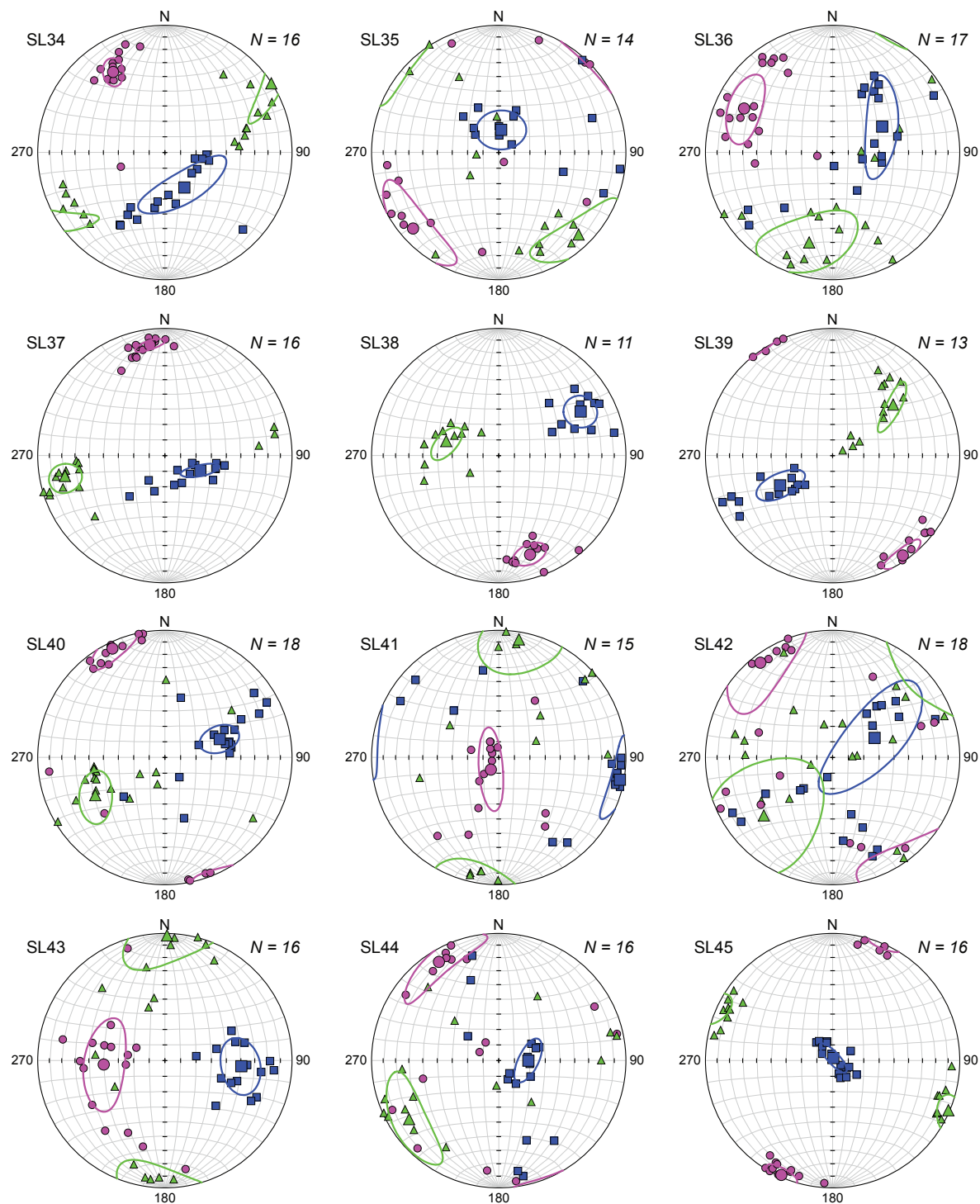
*Annexe 1: (suite)*



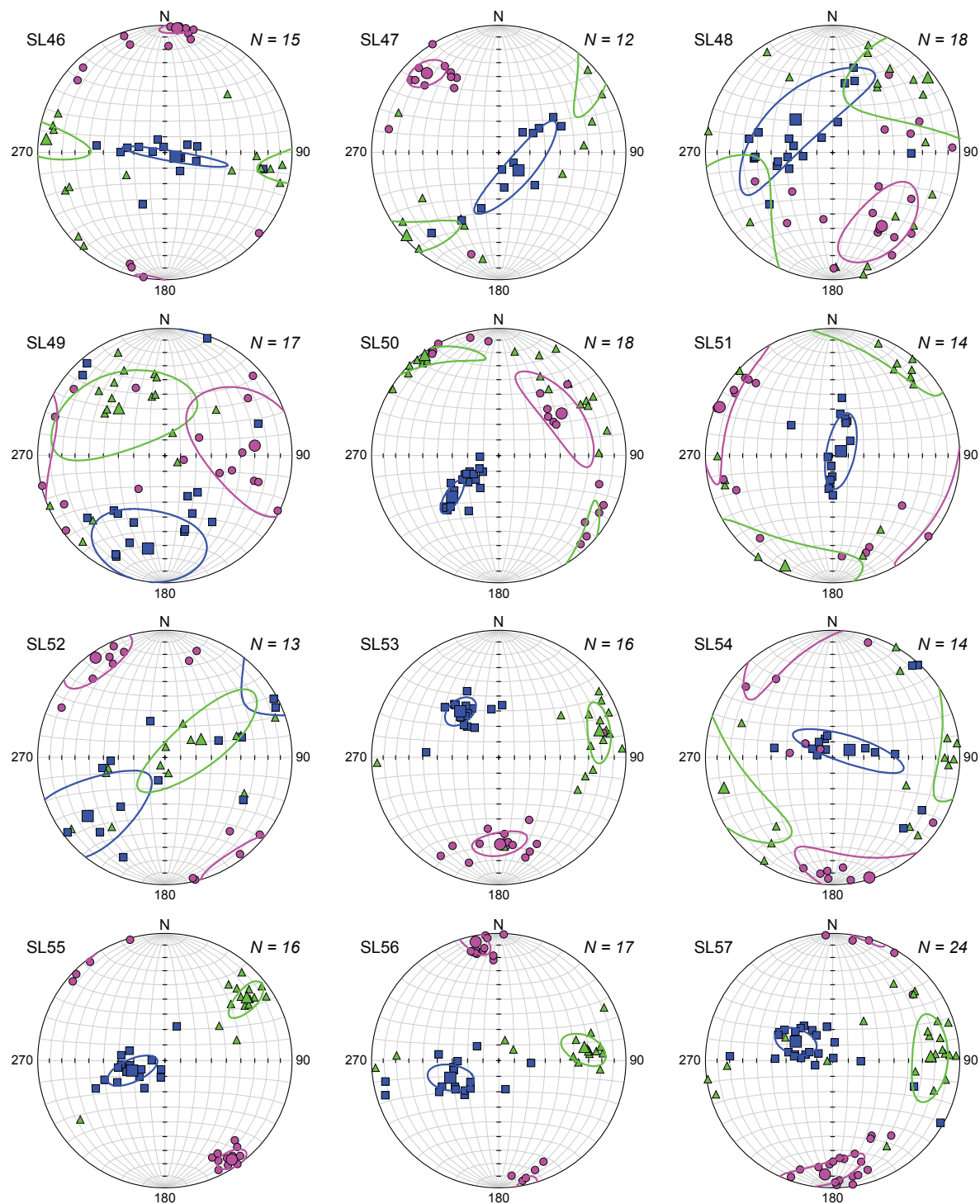
**Annexe 1: (suite)**



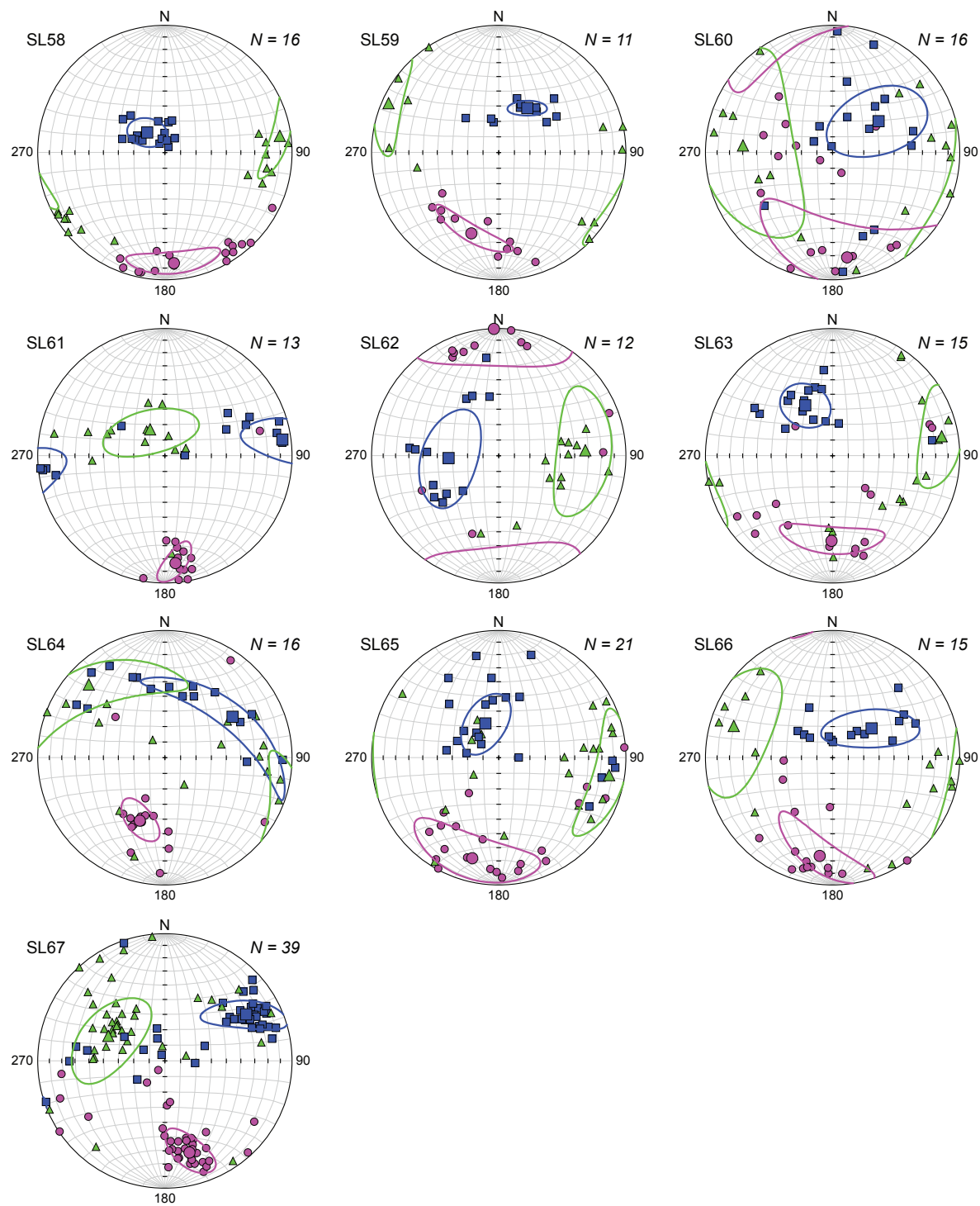
*Annexe 1: (suite)*



*Annexe 1: (suite)*



*Annexe 1: (suite)*



*Annexe 2: Coordonnées géographiques des localités étudiées:Unité de Campo*

Localité	X_UTM_32N	Y_UTM_32N	Localité	X_UTM_32N	Y_UTM_32N
BPA001	602878	5134072	BPA045	595455	5125825
BPA002	602318	5135020	BPA046	595449	5126692
BPA003	602369	5134882	BPA047	595461	5127140
BPA004	602443	5134466	BPA048	595342	5127554
BPA005	602557	5134368	BPA049	594896	5127632
BPA006	602593	5134330	BPA050	595012	5127377
BPA007	602714	5133807	BPA051	594494	5127423
BPA008	602953	5133712	BPA052	595514	5129058
BPA009	601388	5134786	BPA053	591736	5129286
BPA010	596061	5135152	BPA054	591699	5130018
BPA011	596021	5135291	BPA055	591723	5130257
BPA012	596183	5136287	BPA056	595208	5130172
BPA013	596265	5137607	BPA057	593496	5130557
BPA014	601954	5133214	BPA058	593511	5131006
BPA015	602817	5133798	BPA059	593750	5131017
BPA016	602793	5133896	BPA060	593852	5131104
BPA017	602879	5134072	BPA061	596377	5133813
BPA018	602832	5134176	BPA062	596314	5134196
BPA019	602730	5134136	BPA063	596016	5135601
BPA020	602611	5134316	BPA064	595744	5136561
BPA021	602334	5133388	BPA065	597014	5137320
BPA022	591727	5143074	BPA066	596891	5129132
BPA023	591336	5142178	BPA067	596780	5128307
BPA024	590138	5119355	BPA068	596719	5129413
BPA025	594342	5121628	BPA069	596594	5129589
BPA026	596455	5126481	BPA070	600363	5130903
BPA027	599352	5129396	BPA071	600533	5131343
BPA028	600888	5131824	BPA072	604518	5136935
BPA029	601003	5131880	BPA073	603204	5138868
BPA030	601181	5131921	BPA074	603199	5139081
BPA031	601450	5132090	BPA075	603157	5137705
BPA032	604239	5133964	BPA076	603080	5138535
BPA033	605549	5133721	BPA077	601054	5132012
BPA034	604840	5133773	BPA078	600840	5132311
BPA035	607710	5132953	BPA079	601291	5132776
BPA036	608555	5133839	BPA080	601216	5131640
BPA037	607170	5133312	BPA081	600829	5134570
BPA038	592031	5121015	BPA082	601176	5134415
BPA039	595514	5123022	BPA083	601759	5134841
BPA040	601825	5132702	BPA084	602055	5136422
BPA041	602208	5132760	BPA085	602192	5136704
BPA042	595660	5125558	BPA086	601825	5137290
BPA043	595701	5125671	BPA087	602002	5137607
BPA044	595501	5125825	BPA088	601626	5137884

*Annexe 2: (suite)*

<b>Localité</b>	<b>X_UTM_32N</b>	<b>Y_UTM_32N</b>	<b>Localité</b>	<b>X_UTM_32N</b>	<b>Y_UTM_32N</b>
BPA089	589401	5149646	BPA133	603093	5138992
BPA090	589665	5148798	BPA134	604543	5137205
BPA091	590015	5147856	BPA135	603809	5130477
BPA092	591016	5146172	BPA136	601870	5123956
BPA093	590233	5146617	BPA137	604494	5123085
BPA094	607856	5132794	BPA138	605186	5123188
BPA095	612010	5135933	BPA139	589207	5122767
BPA096	610878	5135853	BPA140	595028	5138218
BPA097	588319	5140626	BPA141	603078	5140656
BPA098	588228	5141136	BPA142	596780	5135243
BPA099	590821	5142020	BPA143	597513	5133666
BPA100	599135	5129394	BPA144	597732	5133098
BPA101	598931	5129455	BPA145	598199	5132723
BPA102	588518	5122711	BPA146	598506	5133396
BPA103	588577	5122789	BPA147	605915	5139978
BPA104	589106	5122721	BPA148	585722	5139586
BPA105	602332	5133643	BPA149	584225	5140491
BPA106	602878	5134073	BPA150	584040	5140856
BPA107	602730	5134136	BPA151	584493	5140332
BPA108	603128	5133892	BPA152	594462	5135657
BPA109	603276	5138702	BPA153	594368	5135570
BPA110	604482	5137255	BPA154	593551	5135211
BPA111	604199	5138448	BPA155	590090	5133993
BPA112	604873	5137703	BPA156	592889	5135357
BPA113	601643	5133249	BPA157	595854	5140284
BPA114	606491	5133711	BPA158	596509	5140349
BPA115	605706	5133766	BPA159	597323	5140243
BPA116	604101	5130987	BPA160	597124	5140148
BPA117	604084	5135151	BPA161	595986	5139880
BPA118	605730	5140859	BPA162	603158	5131525
BPA119	605824	5139907	BPA163	603225	5131448
BPA120	605316	5139568	BPA164	603638	5131719
BPA121	605278	5139399	BPA165	603384	5131571
BPA122	605919	5139996	BPA166	603656	5131774
BPA123	602167	5131980	BPA167	603758	5131982
BPA124	602476	5131903	BPA168	603787	5132342
BPA125	602886	5131418	BPA169	603847	5132593
BPA126	603068	5131471	BPA170	604131	5133867
BPA127	605416	5133277	BPA171	603716	5133777
BPA128	605537	5132818	BPA172	601162	5134276
BPA129	605313	5132538	BPA173	604093	5134311
BPA130	602651	5130527	BPA174	604380	5135648
BPA131	604708	5133345	BPA175	605987	5140083
BPA132	604865	5133361	BPA176	606138	5139837

*Annexe 2: (suite)*

<b>Localité</b>	<b>X_UTM_32N</b>	<b>Y_UTM_32N</b>
BPA177	613779	5136929
BPA178	611480	5135212
BPA179	603936	5134400
BPA180	600860	5134900
BPA181	596858	5140056
BPA182	604635	5133942
BPA183	604607	5133736
BPA184	604655	5133601
BPA185	604755	5133785
BPA186	605010	5134185
BPA187	601804	5138343
BPA188	602267	5137560
BPA189	602250	5137624
BPA190	602099	5137979
BPA191	602628	5139762
BPA192	601629	5133051
BPA193	597570	5133547
BPA194	597988	5132884
BPA195	598263	5132726
BPA196	599190	5132923
BPA197	599090	5133178
BPA198	599214	5133280
BPA199	599522	5133342
BPA200	599566	5133393
BPA201	602734	5134100
BPA202	601261	5132831
BPA203	601188	5132786
BPA204	600787	5132693
BPA205	604361	5129610
BPA206	604638	5129530
BPA207	604710	5129454
BPA208	601398	5134583

**Annexe 3: Coordonnées géographiques des localités étudiées: Gabbro de Sondalo**

Localité	X_UTM_32N	Y_UTM_32N	Localité	X_UTM_32N	Y_UTM_32N
ZM 01	602335	5133389	ZM 45	601645	5133249
ZM 02	602362	5133550	ZM 46	602836	5132197
ZM 03	602514	5133624	ZM 47	606555	5133859
ZM 04	602611	5133679	ZM 48	607138	5133336
ZM 05	602680	5133715	ZM 49	605701	5133769
ZM 06	602809	5133800	ZM 50	605548	5133716
ZM 07	602756	5133796	ZM 51	604878	5135189
ZM 08	602763	5133870	ZM 52	605035	5135152
ZM 09	602832	5134176	ZM 53	604713	5133345
ZM 10	602632	5134288	ZM 54	604238	5133965
ZM 11	602475	5134464	ZM 55	604134	5131289
ZM 12	602369	5134882	ZM 56	604204	5130749
ZM 13	602622	5133392	ZM 57	604029	5130424
ZM 14	602766	5133463	ZM 58	604371	5136383
ZM 15	602921	5133620	ZM 59	604142	5135427
ZM 16	603036	5133672	ZM 60	604125	5135212
ZM 17	603091	5133810	ZM 61	605729	5140860
ZM 18	603126	5133887	ZM 62	605440	5139665
ZM 19	603027	5134313	ZM 63	605277	5139396
ZM 20	603155	5134774	ZM 64	605917	5139993
ZM 21	603213	5136027	ZM 65	601678	5132240
ZM 22	603197	5135500	ZM 66	602166	5131981
ZM 23	603349	5135246	ZM 67	602478	5131904
ZM 24	603432	5135085	ZM 68	603019	5131447
ZM 25	603465	5134876	ZM 69	605462	5132809
ZM 26	603199	5139081	ZM 70	605311	5132542
ZM 27	603208	5138975	ZM 71	605405	5132486
ZM 28	603204	5138868	ZM 72	605573	5132349
ZM 29	603274	5138718	ZM 73	602651	5130527
ZM 30	603091	5138996	ZM 74	603809	5130477
ZM 31	603080	5138535			
ZM 32	603008	5138464			
ZM 33	603035	5138381			
ZM 34	602968	5138301			
ZM 35	603086	5138296			
ZM 36	603091	5138000			
ZM 37	603190	5137614			
ZM 38	604541	5137212			
ZM 39	604474	5137262			
ZM 40	604625	5137474			
ZM 41	604885	5137703			
ZM 42	604197	5138448			
ZM 43	604295	5138486			
ZM 44	604150	5138605			

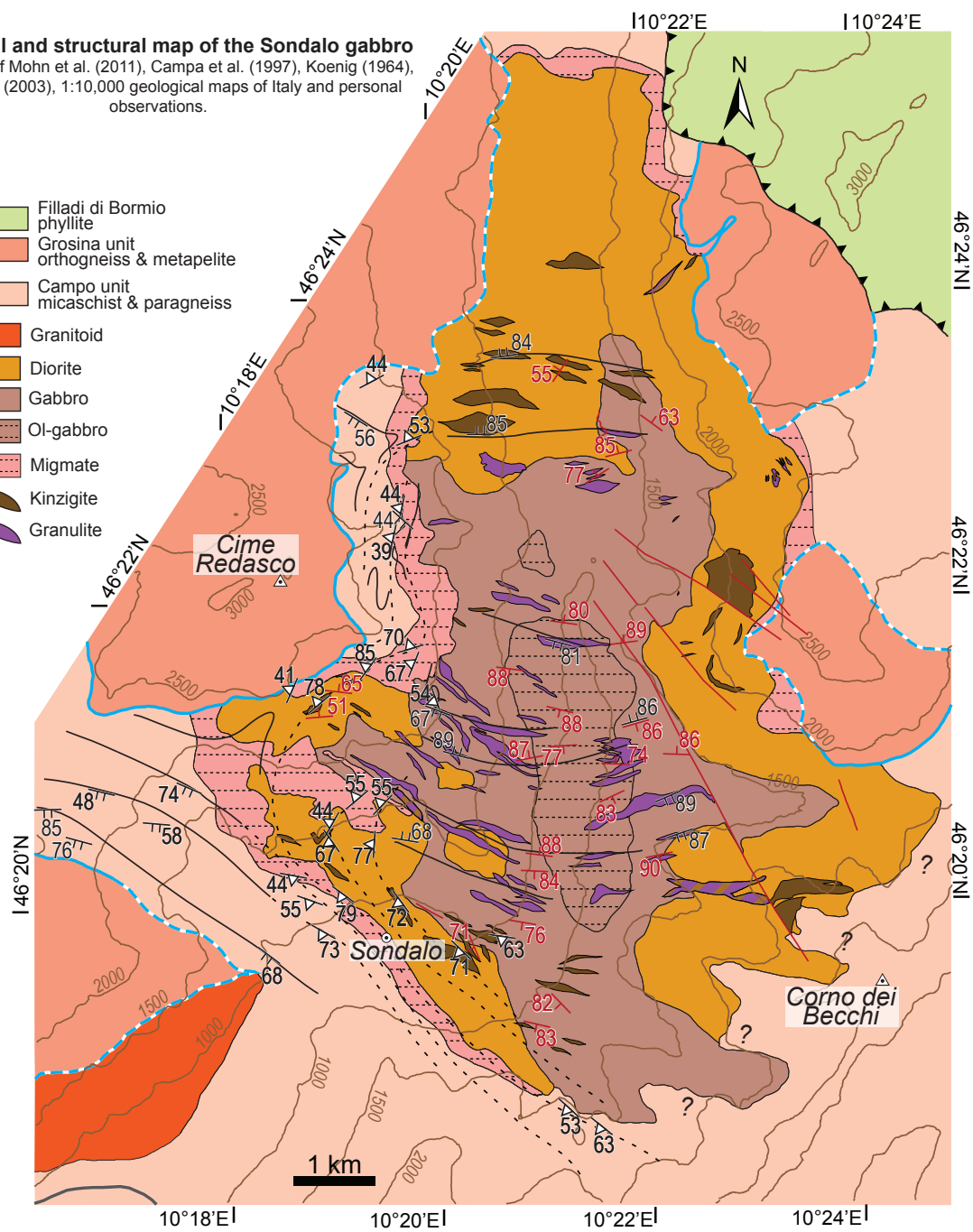
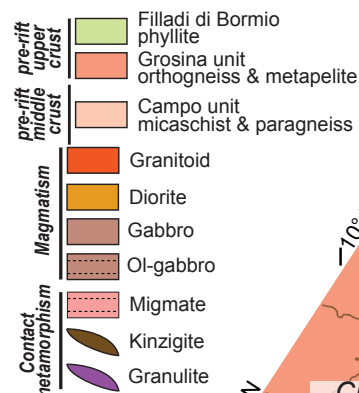
*Annexe 4: Coordonnées géographiques des localités étudiées: Gabbro de Sondalo (ASM)*

<b>Localité</b>	<b>X_UTM_32N</b>	<b>Y_UTM_32N</b>	<b>Localité</b>	<b>X_UTM_32N</b>	<b>Y_UTM_32N</b>
SL01	604083	5138488	SL45	603098	5138992
SL02	604196	5139313	SL46	603101	5138311
SL03	604686	5137455	SL47	603219	5137640
SL04	604504	5137139	SL48	604084	5131258
SL05	604380	5136414	SL49	602646	5133486
SL06	604145	5135443	SL50	603060	5133762
SL07	604310	5134102	SL51	603063	5134352
SL08	604661	5133320	SL52	603135	5134790
SL09	604870	5133360	SL53	602956	5135967
SL10	605604	5134126	SL54	603257	5135933
SL11	605551	5133721	SL55	603308	5135317
SL12	604652	5134030	SL56	603485	5134846
SL13	603761	5130502	SL57	603723	5134471
SL14	601677	5132239	SL58	603936	5134400
SL15	602862	5132189	SL59	605098	5136705
SL16	602418	5131951	SL60	605102	5136259
SL17	602634	5133388	SL61	605344	5136372
SL18	602234	5133569	SL62	605633	5136714
SL19	602718	5133734	SL63	605911	5136874
SL20	602727	5134028	SL64	606338	5137352
SL21	602532	5134421	SL65	605669	5137514
SL22	601408	5134724	SL66	605230	5137861
SL23	601226	5134673	SL67	604808	5137491
SL24	601039	5134466			
SL25	601283	5134392			
SL26	603030	5131427			
SL27	604245	5130880			
SL28	604870	5130598			
SL29	605331	5130346			
SL30	605770	5130255			
SL31	603955	5130335			
SL32	606492	5133143			
SL33	605666	5132934			
SL34	605444	5132803			
SL35	605317	5132507			
SL36	605569	5132350			
SL37	605930	5132404			
SL38	606099	5132061			
SL39	605220	5133177			
SL40	604878	5135189			
SL41	605030	5135140			
SL42	605353	5135138			
SL43	605065	5135376			
SL44	605008	5134875			



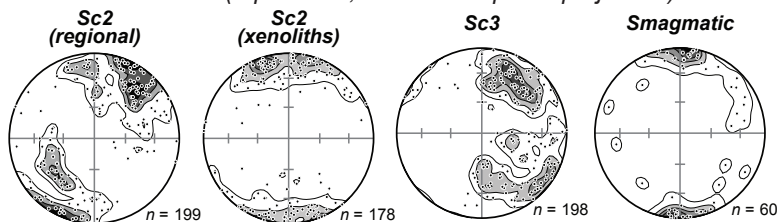
**Annexe 5: Carte géologique et structurale du gabbro de Sondalo**

**Geological and structural map of the Sondalo gabbro**  
 compilation of Mohn et al. (2011), Campa et al. (1997), Koenig (1964),  
 Braga et al. (2003), 1:10,000 geological maps of Italy and personal  
 observations.



- <sup>89</sup> Sc2, interpretative Sc2 trace
- △<sup>39</sup> Sc3, interpretative Sc3 trace
- <sup>88</sup> Smagmatic
- ✓ Da1 Thrust
- Movement zone
- Jurassic thinning structure (inferred/observed)
- Fault
- Location of samples used for pictures and petrology
- △ Town, summit
- AMS stations

**Planar structures (equal-area, lower hemisphere projection)**

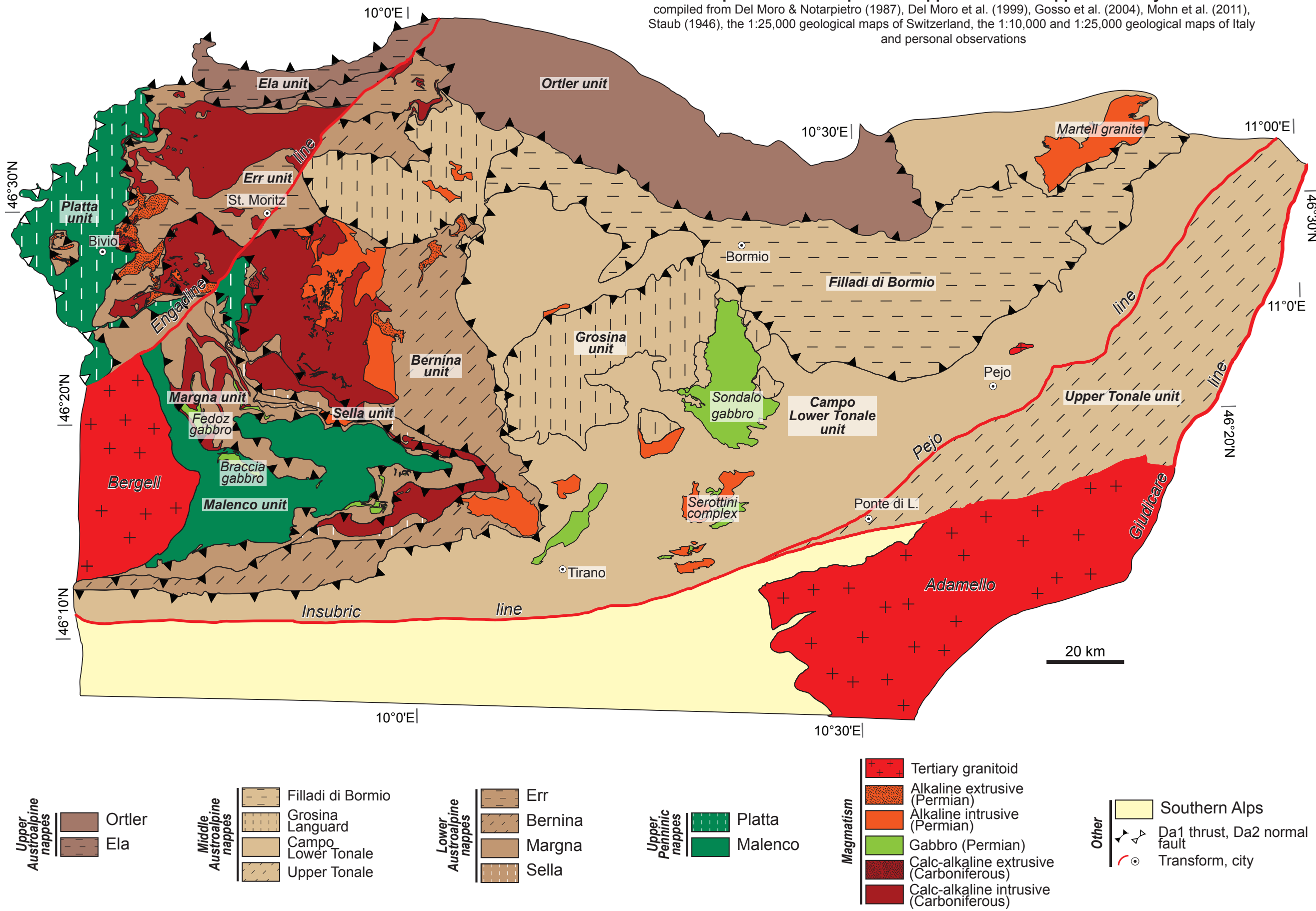




## Annexe 6: Carte litho-tectonique des nappes austroalpines et penniques supérieures

## Litho-tectonic map of the Austroalpine and upper-Penninic nappes in N-Italy and SE-Switzerland

compiled from Del Moro & Notarpietro (1987), Del Moro et al. (1999), Goso et al. (2004), Mohn et al. (2011), Staub (1946), the 1:25,000 geological maps of Switzerland, the 1:10,000 and 1:25,000 geological maps of Italy and personal observations





---

# *GUIDE D'EXCURSION*

---



# **THE EVOLUTION OF THE CAMPO AND GROSINA UNITS IN THE AUSTROALPINE NAPPES (N-ITALY): FROM THE VARISCAN OROGEN TO THE JURASSIC RIFTING**

B. Petri<sup>1,2</sup>, G. Mohn<sup>3</sup>, G. Manatschal<sup>1</sup>, and M. Beltrando<sup>4</sup>

<sup>1</sup> Ecole et Observatoire des Sciences de la Terre, Institut de Physique du Globe de Strasbourg – CNRS UMR7516, Université de Strasbourg, 1 rue Blessig, F-67084, Strasbourg Cedex, France

<sup>2</sup> Vrije Universiteit, Department of Geology and Geochemistry, de Boelelaan 1085, 1081HV Amsterdam, The Netherlands

<sup>3</sup> Département Géosciences et Environnement, Université de Cergy-Pontoise, 5, mail Gay Lussac, Neuville-sur-Oise, 95031 Cergy-Pontoise Cedex

<sup>4</sup> Dipartimento di Scienze della Terra, Università di Torino, Via Valperga Caluso 35, 10125 Torino, Italy

## **ABSTRACT**

The Campo-Grosina units preserve a polyphase tectonic history spanning the Carboniferous Variscan orogeny, the Permian post-Variscan extension, the Jurassic rifting and eventually the Alpine orogeny. The tectonic, magmatic and the metamorphic evolution of both units during this complex history are illustrated in this fieldtrip. Pre-Permian metamorphic fabrics are exposed in the upper part of the Grosina basement characterized by a gently NW-dipping foliation formed at amphibole facies conditions. The Campo basement is regionally characterized by a pre-Permian steeply dipping NW–SE trending fabric formed at amphibolite-facies conditions, as suggested by the presence of garnet–staurolite micaschists. During the Permian, the Campo basement was intruded by several magmatic bodies, including the Sondalo gabbroic complex. A new high-temperature fabric was developed in the contact aureole of this intrusion. The Grosina and Campo units are separated by a regional tectonic contact, labelled "Eita shear zone". Greenschist facies mylonites are associated with shearing along this interface both in the Campo and Grosina basement rocks. The main phase of activity of the Eita shear zone is ascribed to Jurassic rifting, based on geochronological data, and it was likely followed by Alpine reactivation.

## 1. INTRODUCTION

The Austroalpine units in SE Switzerland and N-Italy consist of a stack of several nappe systems emplaced during the late Cretaceous, sampling remnants of the former Jurassic Adriatic rifted margins (e.g. Trümpy, 1975; Froitzheim & Eberli, 1990; Froitzheim *et al.*, 1994; Manatschal & Nievergelt, 1997; Mohn *et al.*, 2011). While the Lower and Upper Austroalpine nappe systems (in the sense of Mohn *et al.*, 2011), where the relics of the former Adriatic distal and proximal rifted margins are preserved, have been extensively studied, the “Middle Austroalpine” Campo-Grosina units, sampling the necking zone of the former Adriatic margin, remain relatively poorly investigated (see the PhD theses of Koenig, 1964; Meier, 2003; Schudel, 1965). The Campo-Grosina units lie in a critical position in the Austroalpine nappe stack: to the West, they overlie the Lower Austroalpine nappe system (i.e. Bernina unit) while to the North-East, they are overthrust by the Upper Austroalpine nappe system (i.e. Filladi di Bormio, Ortler nappes, Fig. 1). Considerations based on their present-day position in the nappe stack, combined with litho-stratigraphic and geochronological data, led Mohn *et al.* (2011; 2012) to suggest that the Campo-Grosina units sample the Adriatic necking zone, where major crustal thinning was accommodated during Jurassic rifting.

The Campo-Grosina units consist of a 3 km thick portion of polymetamorphosed basement rocks with rarely preserved Mesozoic cover rocks – the only possible occurrence has been reported by Staub (1946) in Val Poschiavo. The Grosina unit is separated from the underlying Campo unit by the Eita shear zone (Meier, 2003). The latter can be mapped continuously over more than 20 km, residing at the same structural level. The Campo unit consists mainly of amphibolite-facies metasediments (garnet-staurolite metapelites, biotite-muscovite paragneisses, amphibolites and silicate-bearing marbles) recording a multiphase pre-Alpine tectonic history (Meier, 2003). During the Permian, the Campo basement was affected by a major magmatic and metamorphic event characterized by the emplacement of felsic and mafic plutons (Del Moro & Notarpietro, 1987; Meier, 2003; Tribuzio *et al.*, 1999). Within this context, the Sondalo gabbroic complex was emplaced at mid-crustal depths ( $0.6 \pm 0.2$  GPa,  $900^\circ\text{C}$ , Braga *et al.*, 2003; Braga *et al.*, 2001) at 280-300 Ma (Sm-Nd mineral isochron, Tribuzio *et al.*, 1999). The gabbroic complex is concentrically zoned from Ol-gabbro in the core to gabbronorite and finally diorite in the rim, and contains numerous host-rock xenoliths. Similarly to the Campo unit, the Grosina basement records a multi-stage metamorphic and deformation history. This basement is mainly composed of variably deformed biotite and chlorite orthogneiss associated with sillimanite-biotite gneiss, garnet-biotite micaschists, andalusite micaschists and diopside-bearing calc-silicates.

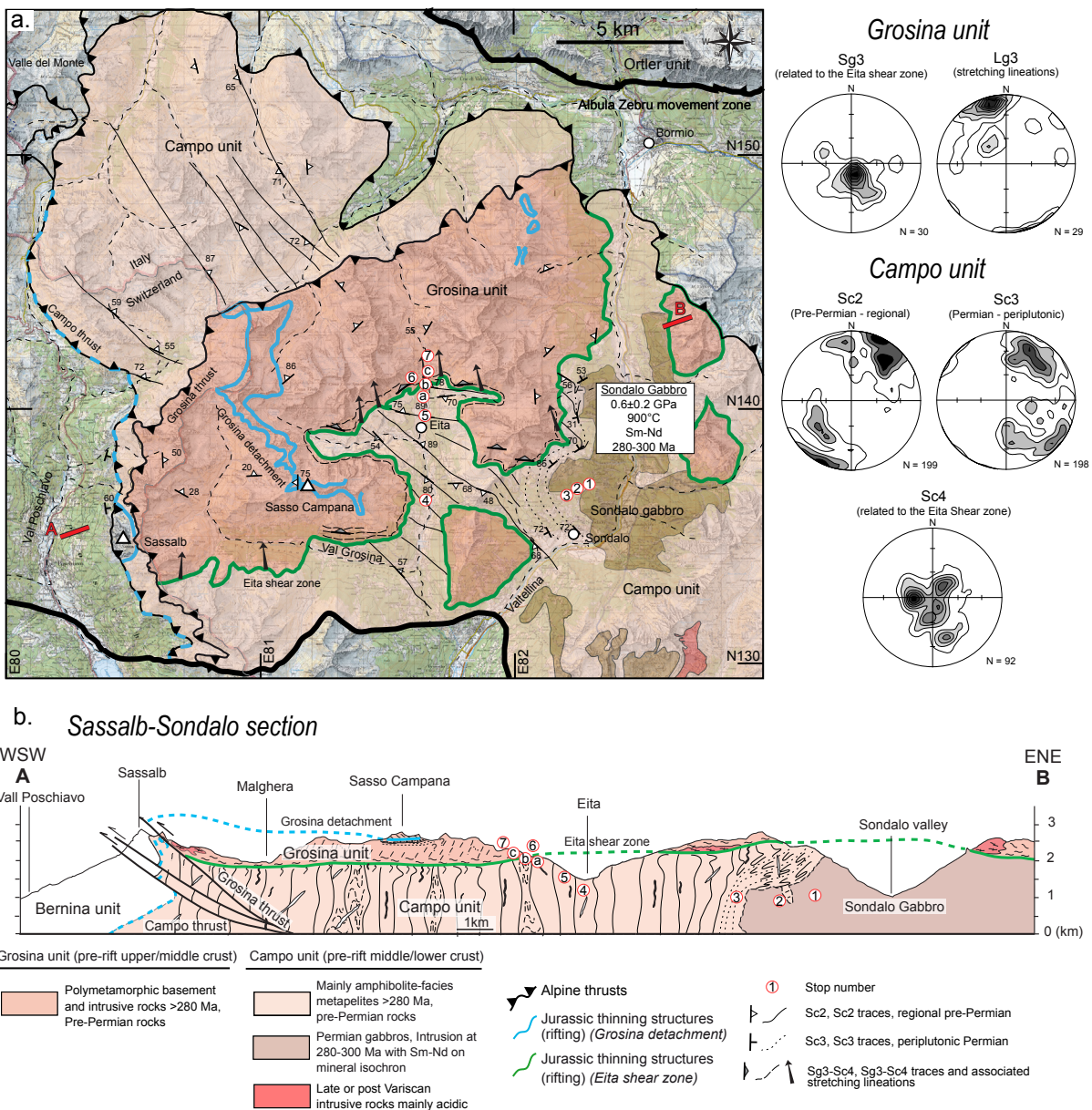


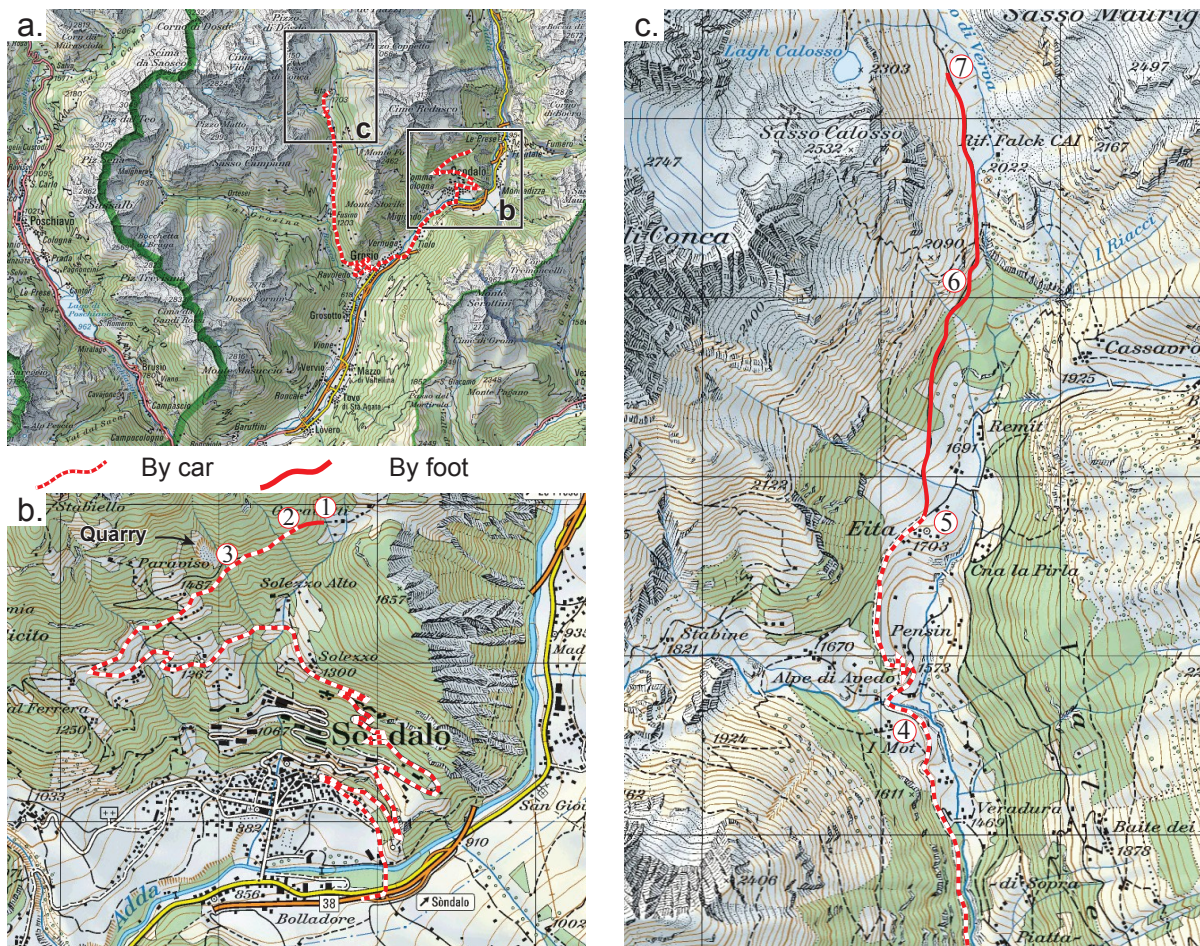
**Fig. 1:** a) Simplified tectonic map of the Campo-Grosina units in SE-Switzerland and N-Italy. Map compiled from Staub (1946), Bonsignore et al. (1969), Montrasio (1969), Meier (2003) and Mohn et al. (2012) and own observations. Orientations of structural elements in the study area are presented in lower hemisphere Schmidt (equal area) projection. b) Geological cross-section across the Campo-Grosina units. Note that the trace of the cross-section is indicated on the map. Localization of the excursion stops are indicated on the map and on the cross section.

The aim of this one day field trip is twofold: 1) to document the main lithologies, structures, fabrics and metamorphic mineral assemblages of the Campo-Grosina units in Valtellina and Val Grosina and 2) to familiarize the participants with the complex tectono-metamorphic history recorded by the Campo-Grosina basement rocks during the Variscan orogeny, the Permian post-Variscan extension, the Jurassic rifting and the Alpine orogeny.

## 2. LOGISTICS

This field trip is held in the North of Italy. The first part of the field trip takes place in the Upper Valtellina, above the city of Sondalo, while the second part is held in the Val Grosina, farther west (Fig. 2). From Switzerland, the Valtellina is accessible driving to the South, through the Val Poschiavo. From Italy, the city of Sondalo can be reached following the main SS38 road (Lago di Como, Sondrio). From there, drive through the town following the signs to the Albergo Rezia hotel (see map on Fig. 2). Upon reaching the hotel, follow Via Mazzini up to the quartz quarry. After the entrance of the quarry, continue straight on the track (Please note that the track is in bad condition) for approximately 50-100m before parking your vehicle to the right. Please note that trucks from the quarry use the road during the week, making car access sometimes difficult.

The second part of the field trip is located in Val Grosina. Drive back to Sondalo, then follow the SS38 until the Grosio exit. Turn right to enter in Grosio, then drive across the town and, upon reaching the town center, turn left in Via Valorsa, towards Val Grosina, Fusino, Eita. Starting from Fusino you will be driving on a toll road and a 3 € fee is to be paid at the entrance of the village. Several stops are located along this road before reaching the village of Eita.



Recommended topographic maps are:

- Passo del Bernina, 1:50000, Carta nazionale della Svizzera, Foglio 269

For geological maps, see:

- Carta Geologica d'Italia 1:50000, sheets 023 (Livigno), 024 (Bormio), 040 (Tirano) and 041 (Ponte di Legno).

### 3. FIELD OBSERVATIONS

Hereafter, used mineral abbreviations follow recommendations of IUGS (Siivola & Schmid, 2007). Structural framework is described as follows: “D” stands for a deformation event responsible for the development of folds “F” and schistosity “S”, “c” refers to the Campo unit and “g” to the Grosina unit and numbering refers to the relative chronological sequence of deformations/fabrics determined from field and microstructural observations. Outcrop locations are given in UTM coordinates.

#### **Stop 1: Sondalo gabbro (X: 602334; Y:5133388)**

After parking next to the quarry, which will be visited at Stop 2, walk up on the gravel road and cross another gravel road to the left to reach the first outcrop. Stop 1 is dedicated to the preserved magmatic assemblage of the Sondalo gabbroic complex (here an Hbl-gabbro). Here grayish plagioclase, brown amphibole and rare biotite can be observed (Fig. 3a). Locally a steeply dipping E-W striking magmatic fabric is observed, characterized by the shape preferred orientation of plagioclase and interstitial amphibole (Fig. 3a). This steep fabric is only partly developed in this outcrop but can be seen higher up or farther towards the center of the pluton.

Under the microscope, the gabbro displays a medium grained intersertal texture. Spaces between subeuhedral laths of labradoritic plagioclase ( $An_{70}-An_{50}$ ) are filled with red-brown amphibole (Ti-pargasite) bearing inclusions of clinopyroxene (Fig. 3b). Most of the (rare) biotites are rimmed by secondary chlorite.

---

**Fig. 2:** Topographic map showing the excursion stops. a) General topographic map of the area, b) and c) respectively topographic maps of the Sondalo area and Val Grosina. Red dotted lines indicate roads suitable for driving, while red lines indicate footpaths.

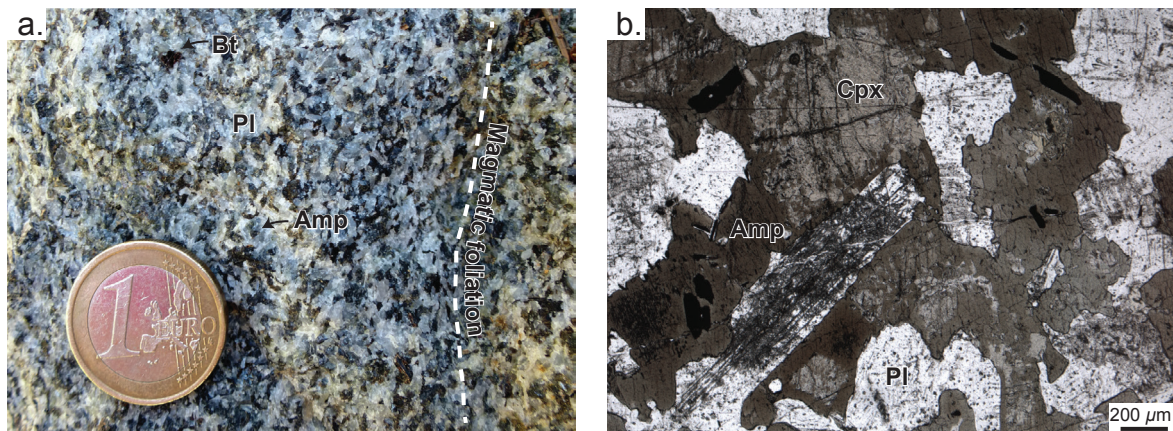


**Fig. 3:** Stop 1: the Sondalo gabbro. a) Field photograph and b) photomicrographs. The gabbro consists of plagioclase, biotite and amphibole. Locally, a steep magmatic fabric is weakly developed.

### Stop 2: Diorite/xenolith contact (X:601954; Y:5133214)

Walk back towards the car, using the same gravel road. The cliff in front of the car park preserves the contact between the Sondalo gabbro and a roof pendant of the Campo country rock, consisting of migmatitic metapelites and amphibolites (Fig. 4a).

The Sondalo gabbroic complex is rimmed by dioritic bodies of variable thickness. The medium-coarse grained diorite is mainly composed of brown amphibole, biotite and plagioclase.

Mingling patterns between two generations/types of magma with distinct grain size and mineralogy can be seen locally (Fig. 4b,c). The fine grained diorite shows chilled margins and consists mainly of small amphiboles (~100  $\mu\text{m}$ ) with few plagioclase laths, reaching locally 1mm in length, and biotites (Fig. 4c). In thin-section, the diorite contains sub-euhedral andesine-type plagioclase laths ( $\text{An}_{45}-\text{An}_{35}$ ), brown amphibole locally rimming clinopyroxene core (visible with a hand lens), interstitial biotite and rare magmatic garnet (Fig. 4d). Interstitial biotites are more frequent than at the previous stop and are clearly forming as late stage crystallization products (locally around amphibole grains).

In contrast, the medium grained felsic type is principally made of large subeuhedral plagioclase and to a lesser extent amphibole, chloritized biotite and rare anhedral quartz along grain boundaries (Fig. 4c).

The Campo country rock displays a high temperature (HT) metamorphic aureole of few hundred meters around the Sondalo gabbroic complex (Fig. 4e,f). This contact metamorphism is responsible for the anatexis of host metapelite and amphibolite both in the aureole and in the xenoliths within the pluton.

In migmatitic metapelites, the leucosome consists of quartz, K- and alkali feldspar, garnet and biotite whereas the melanosome is made of biotite, sillimanite and garnet.

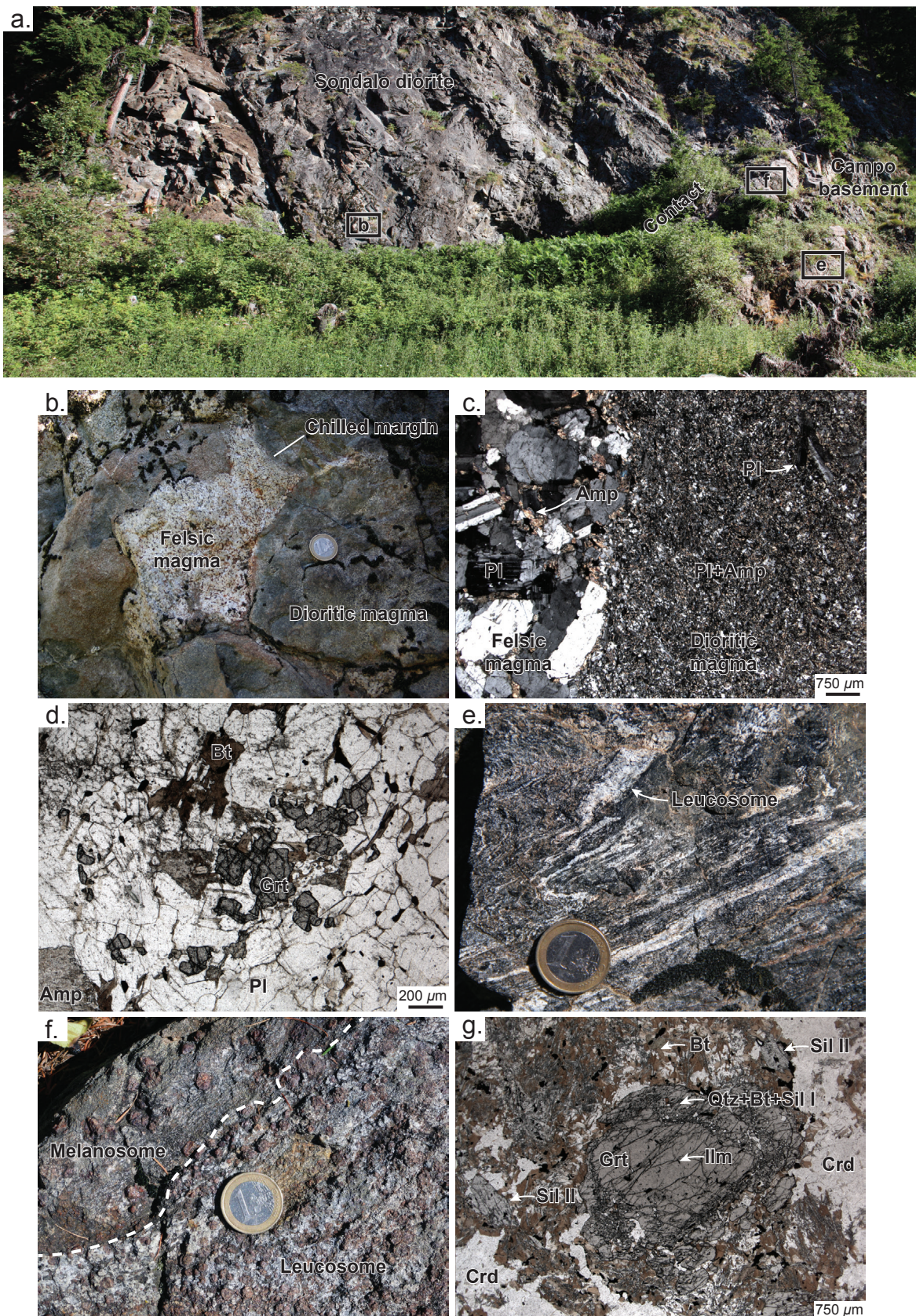


**Fig. 4:** Stop 2: The diorite/xenolith contact. a) General view of the outcrop with the contact between the diorite and a metapelitic xenolith of host rock. b) and c) Magma mingling between diorite and a more felsic magma. d) Felsic magma, e) Migmatitic amphibolite, f) Migmatitic metapelites and g) Melanosome of a migmatitic metapelite.

Most of the host-rock xenoliths within the pluton show an internal foliation and a xenolith/magmatic rocks contact parallel to the regional Sc2 foliation found in the country rock (Fig. 1). In contrast, a Sc3 HT fabric could be identified at the margins of the magmatic body (please note that the older fabrics Sc1 and Sc2 will be described in the following stops). This Sc3 HT foliation is rimming the pluton and variably transposes the main Sc2 foliation (Fig. 1). In this outcrop, metapelites display Sc3 HT fabric that is gently to steeply dipping to the South-West. This fabric is defined by the shape preferred orientation of leucocratic aggregates as well as sillimanite and biotite.

Under the microscope, the melanocratic metapelite shows a porphyroblastic texture and contains sillimanite I displaying a marked shape preferred orientation, large garnet (up to 5 mm), cordierite, ilmenite and biotite (Fig. 4g). Garnet shows inclusions of ilmenite in the core while the rim bears rounded inclusions of biotite and quartz and, in the outermost parts, sillimanite I (Fig. 4g). This inclusion-rich garnet rim is interpreted as related to HT metamorphic growth during contact metamorphism. The garnet core, instead, is inherited from a previous metamorphic event (that will be described in Stop 4). Sillimanite II is randomly oriented and commonly found within biotite aggregates (Fig. 4g). This metamorphic assemblage is typical for the upper-amphibolite facies melanosomes (i.e. kinzigites) generally found at the pluton margins. Peak contact metamorphic assemblage consisting of cordierite, garnet, hercynite and sillimanite is observed in xenoliths attesting granulite facies conditions.

Amphibolite layers are classically found within the Campo basement. In this stop, they are strongly folded and show alternation of dark-brown amphibole layers with plagioclase-rich layers interpreted as probable leucosomes (Fig. 4e). The leucocratic layers consist essentially of plagioclase, and small clinopyroxene rimmed by amphibole while the melosome is made of brown amphiboles. Both leucosome and melosome have an equigranular texture.

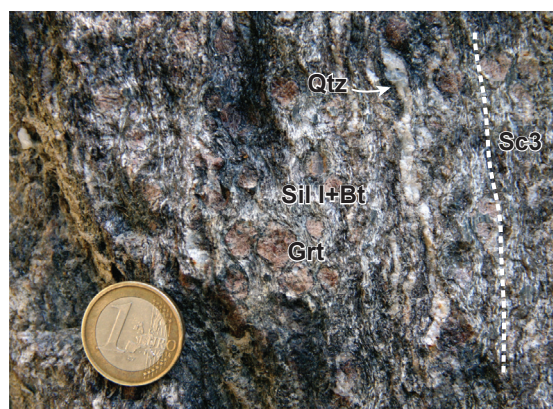


**Fig. 5:** Stop 3: The host rock contact metamorphism. Field photograph of a kinzigite (garnet–biotite–sillimanite metapelite).

### Stop 3: Contact metamorphism in the Campo metapelites (X:601629; Y:5133051)

Walking down on the gravel road, until entrance of the underground quartz quarry, where the typical mineral assemblage indicative of contact metamorphism of the Campo metapelites is exposed. Upper-amphibolite metapelites (kinzigites) characteristically consist of a biotite-sillimanite-garnet assemblage interlayered with quartz lenses. Sillimanite and biotite aggregates wrapped around garnet are aligned in the HT Sc3 fabric, which dips steeply to the north-east. In this stop, the Sc3 fabric is parallel to the pre-existing Sc2 fabric. Therefore evidences for transposition, such as folds, are hardly visible but are observed at the north-eastern margin of the pluton.

### Stop 4: The Campo basement (X:596061; Y:5135152)

The second part of this field trip takes place in Val Grosina (Fig. 2). Stop 4 is located along the road to Eita (see the logistic part above) at the crossing between the main road and a secondary road, to the left, going up to few houses. In Val Grosina, the regional amphibolite facies metamorphism of the Campo basement is not affected by the contact metamorphism related to the Sondalo gabbro (Fig. 1). This basement is largely made of metasediments which consist of micaschists and paragneiss locally associated with amphibolites and rare marbles.

At this stop the steeply dipping, NW-SE striking Sc2 regional fabric of the Campo basement can be observed. This fabric is defined by the preferred orientation of micas, amphiboles and quartz lenses. Close to isoclinal Fc2 folds affecting interlayered metapelite-paragneiss-quartz lenses are observed locally (Fig. 6a). The folded layering, hereafter labelled Sc1 is highly transposed in this locality but is well preserved farther north in Val Viola–Val da Camp.

In Val Grosina, the Campo metapelites consist of muscovite, biotite, quartz, garnet, ilmenite, minor plagioclase and sillimanite (Fig. 6c,d). In thin section, porphyroblastic garnets show inclusions of ilmenite oriented at high angle with respect to the main Sc2 fabric observed in the rock matrix. Therefore, garnet growth is considered as syn- to post- Sc1.

Notably, the regional Sc2 fabric is locally cross-cut by pegmatite dikes ranging in thickness from several centimeters up to one meter (Fig. 6a). These pegmatite dikes consist of quartz, K-feldspar, white mica and tourmaline and have Jurassic K–Ar ages (on muscovite and biotite; Thöni, 1981). They have been dated further to the north by Sölva *et al.* (2003) with the Sm/Nd method on a magmatic garnet, suggesting a Late Permian-Early Triassic crystallization ages of  $255\pm3$  Ma and  $250\pm3$  Ma respectively for the garnet core and the garnet rim.

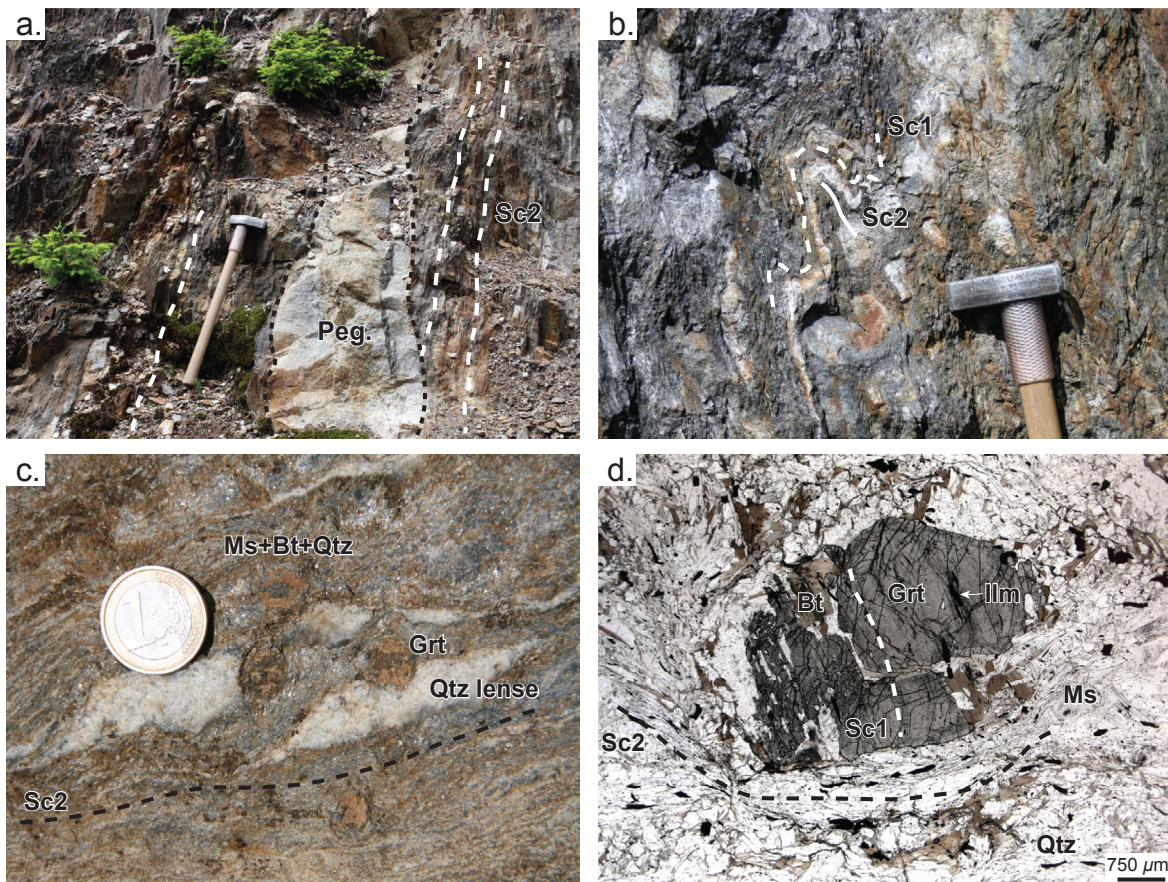


**Fig. 6:** Stop 4: The regional Campo metapelites. a) Tur-bearing pegmatite cross-cutting the regional Campo fabric (Sc2) of the Campo basement. b) Close to isoclinal fold preserving the relics of the Sc1 fabric. c) Zoom on the garnet micaschists, d) Garnet micaschist.

### Stop 5: The Campo basement and its pegmatites: a general view of the Campo and Grosina units (X:596105; Y:5136310)

Reaching the village of Eita, park the car by the church. Stop 5 is located on the hill just above the church. The steep Sc2 regional fabric of the Campo basement, discordantly crosscut by the Late Permian-Early Triassic pegmatite dikes, can be seen here (Fig. 7b). Locally, this steep Sc2 fabric is overprinted by later Dc4 deformation characterized by plurimetric recumbent open folds. Dc4 structures become more and more pervasive on the way to the next stops.

A landscape view of the Campo-Grosina units is available from here. The angular unconformity between the steep regional Sc2 Campo fabric and the relatively flat Sg2-Sg3 fabrics visible in the overlying Grosina unit can be seen in the cliff to the north-west (Figs. 1, 7a). The two units are separated by the Eita shear zone (Meier, 2003) which will be the main topics of the next stops.

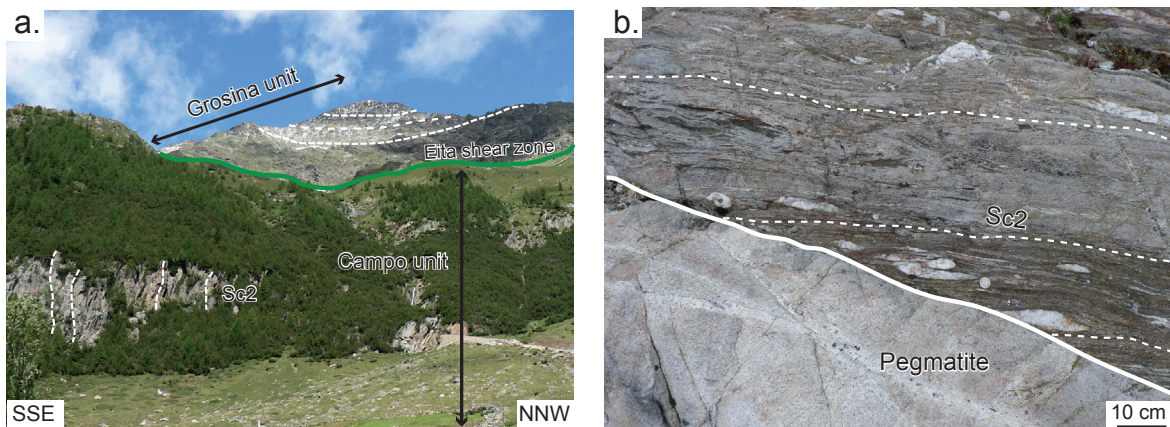


**Fig. 7:** Stop 5: a) A general view of the Campo and the Grosina units: the overlying Grosina unit is separated from the underlying Campo unit by the Eita shear zone. Note the angular discordance between the steep fabric of Campo and the relatively flat fabric of Grosina. b) A pegmatite dyke crosscut the regional Sc2 fabric of the Campo basement.

### Stops 6a,b,c: The Eita shear zone (X:596265; Y:5137607)

#### Stop 6a: Campo basement in the vicinity of the Eita shear zone

From the village of Eita, follow the gravel path heading north on the western side of the valley. A cross section through the Campo and Grosina units can be seen along the path. A few hundred meters from the village of Eita, approaching the tectonic contact (i.e. the Eita shear zone), the regional steep fabric of the Campo basement is gradually overprinted by a new Dc4 deformation associated to a finite strain gradient. This new deformation leads to transposition of the regional Sc2 fabric and is characterized by recumbent Fc4 folds with E-W trending axes and a shallow W-dipping axial plane, locally associated to a spaced cleavage (Fig. 8a,b). Towards the contact, a gradual increase of the amplitude associated with a decrease of the wavelength of the Fc4 folds is observed. Locally Late Permian-Early Triassic pegmatites or aplitic dykes in the Campo basement are deformed and folded in the vicinity (~30 m) of the contact with the Grosina unit, indicating that this deformation (Dc4) is younger than Permian (Fig. 8a). Approaching the contact, the Sc2 Campo fabric, which in metapelites consists of muscovite, biotite, garnet, quartz and plagioclase, is folded and overprinted by a retrograde greenschist facies metamorphism.

Under the microscope, the greenschist fabric is characterized by: 1) the stability of chlorite and white mica in Fc4 fold hinges whereas biotite, garnet and sillimanite are destabilized (Fig. 8b), 2) kinking of porphyroclastic white micas and 3) the undulose extinction associated to sub-grain rotation recrystallization of quartz.

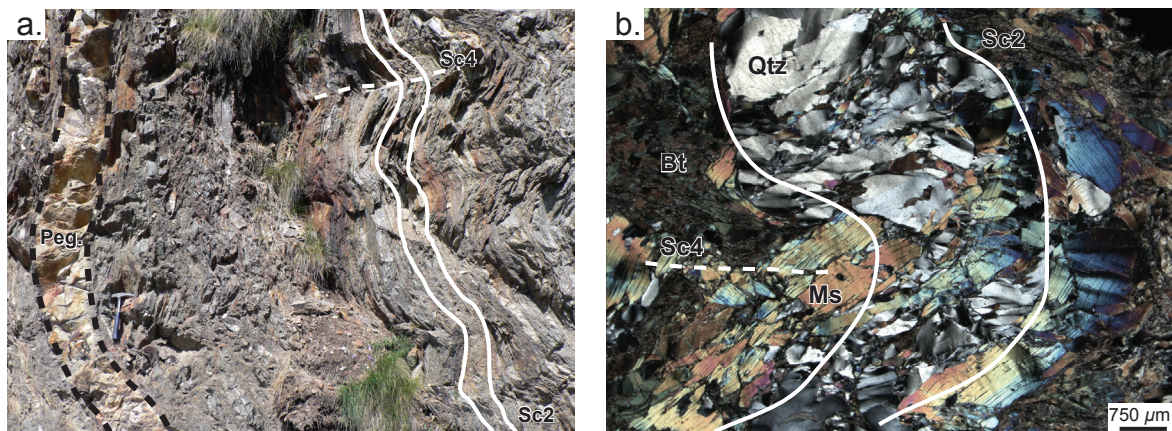


**Fig. 8:** Stop 6a: The Campo basement in the vicinity of the Eita shear zone. a) Pegmatite dyke and the Sc2 fabric of Campo show open recumbent fold (Fc4). b) Micaschist from the Campo unit showing mica kinks in the hinge zone of an Fc4 fold.

#### Stop 6b: The contact - Eita Shear Zone s.s. (pseudotachylite)

At the contact, the Sc2 Campo fabric is sub-parallel to the shear zone boundary, as a consequence of shearing and the transposition into parallelism with Sc4.

The contact *sensu stricto* is marked by a pseudotachylite vein bearing many angular host-rock clasts associated with numerous shear bands, previously described by Meier (2003) (Fig. 9d). The angular clasts consist mainly of strongly recrystallized quartz mylonite (Fig. 9d) suggesting that the mylonitic deformation is either cogenetic or predate the formation of the pseudotachylite veins.

The overlying Grosina orthogneiss is characterized by a pervasive ultramylonitic fabric (Sg3) for *ca.* 1 m. This shear fabric is characterized by a shallow north-dipping orientation containing a NNW-SSE trending mineral stretching lineation. In thin section, the ultramylonite consists of fine grained ( $\sim \mu\text{m}$ ) quartz, white mica II and clay minerals, with rare quartz porphyroclasts (Fig. 9d). Locally, this pervasive ultramylonitic fabric is cataastically deformed producing angular clasts of randomly oriented quartz mylonite (Fig. 9c). Up-section, the transition from an ultramylonite to mylonite is accompanied by an increase in grain size (Fig. 9a,b).

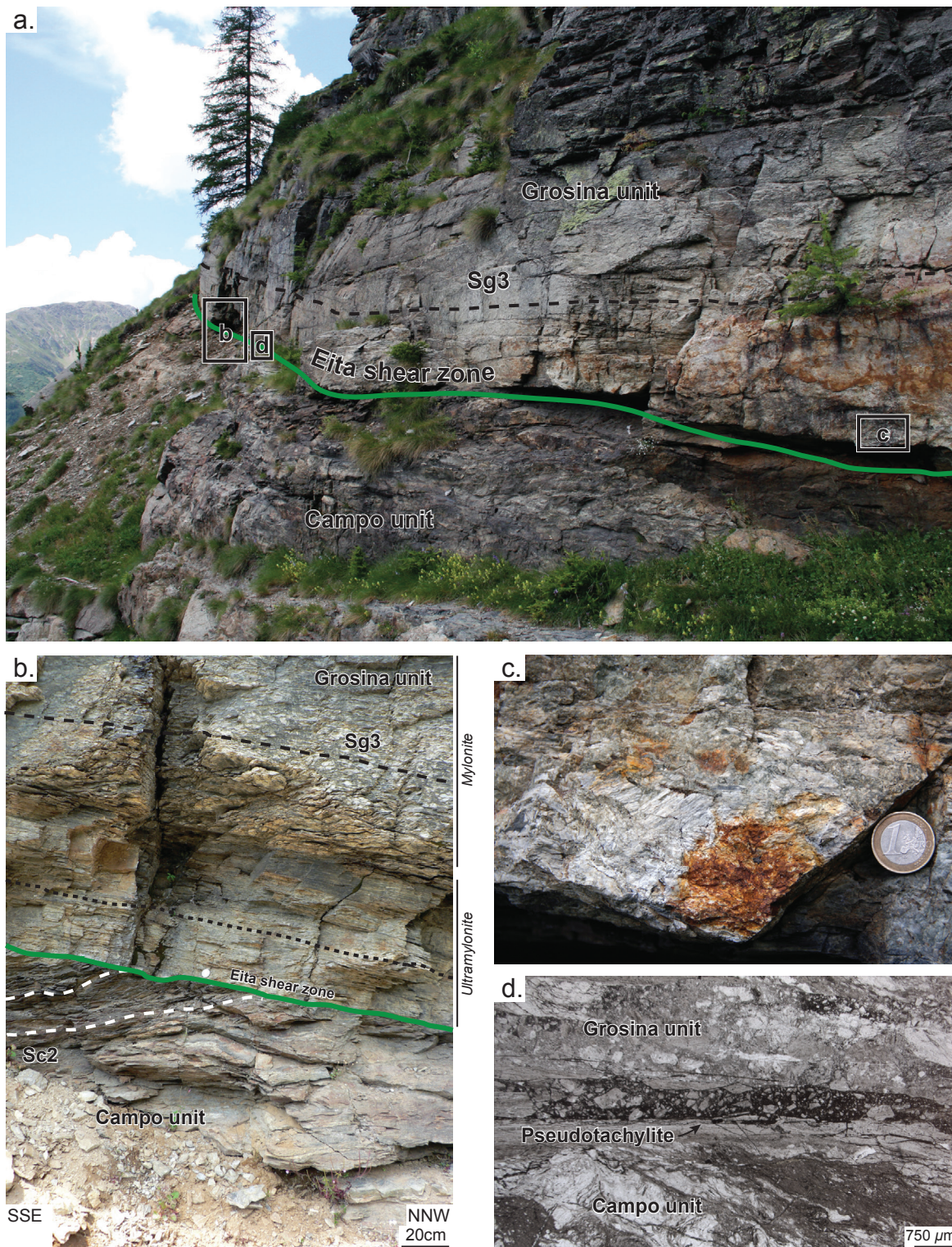


**Fig. 9:** Stop 6b: The Eita shear zone ss. a) The Eita shear zone separating the underlying Campo from the overlying Grosina units. b) Zoom on the Eita shear zone. The Campo Sc2 fabric is parallelized to the shear zone boundary, drag of the Sc2 fabric indicates a top to the NNW sense of shear. The Grosina basement is affected by the Sg3 shear fabric passing up-section from an ultramylonite to mylonite. c) Cataclasite at the contact with angular clasts of quartz mylonite. d) The contact injected by a pseudotachylite vein with angular elements.

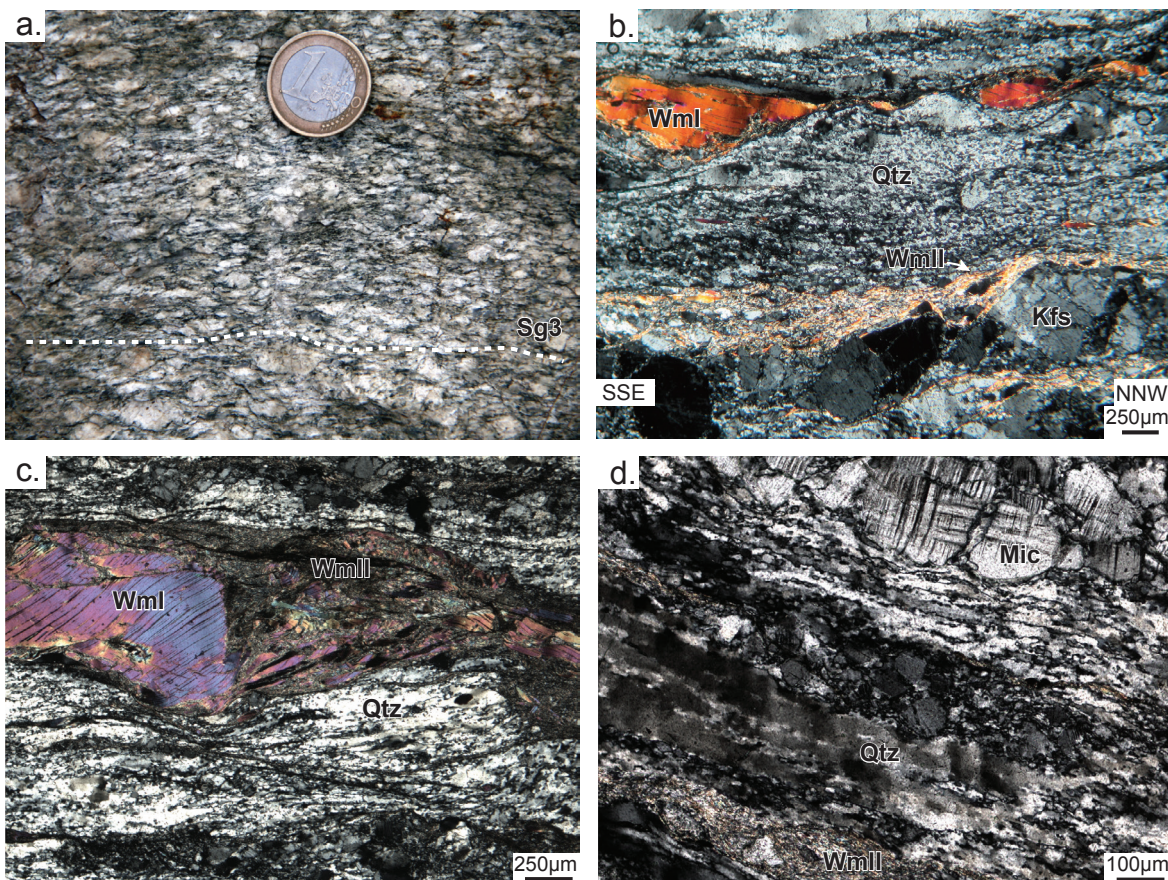


**Fig. 10:** Stop 6c: The Grosina basement in the vicinity of the Eita shear zone. a) Greenschist-facies orthogneiss of the Grosina basement showing feldspar porphyroclasts. b) The pervasive green schist facies fabric (Sg3) of the Grosina basement. Please note the semi-brittle deformation of the Grosina orthogneiss characterized by the dynamic recrystallization of quartz and the brittle deformation of feldspar c) Large porphyroclastic white mica I recrystallizing into fine-grained white mica II, into the foliation. Quartz display subgrain rotation and possibly bulging recrystallization associated with shear bands, d) Greenschist facies mylonite. Alkali-feldspar; made up-section by microcline (Mic), formed polycrystalline aggregates. Fine-grained quartz shows dominant subgrain rotation recrystallization, locally associated with still preserved quartz ribbons. Fine-grained white mica (Wm II) forms narrow aggregates parallel to the shear fabric.

#### **Stop 6c: The Grosina basement in the vicinity of the Eita shear zone**

For a thickness of ca. 200 m from the contact with the Campo unit, the Grosina basement consists of an orthogneiss pervasively deformed in green schist facies conditions (Fig. 10a). The orthogneiss is characterized by a well-defined gently to moderately North-dipping Sg3 foliation, locally associated with a NNW-SSE stretching lineation defined by elongated porphyroclastic feldspar.

This shear fabric consists of quartz, white mica II, chlorite wrapping around porphyroclastic K-feldspar, plagioclase and white mica I (Fig. 10b). Mylonitic deformation is associated with the dynamic recrystallization of quartz. The newly recrystallized fine-grained quartz show a strong preferred orientation oblique with respect to elongated ribbons and the shear plane, characteristic of subgrain rotation recrystallization. Locally, remnants of porphyroclastic quartz show undulose extinctions with evidence of bulging recrystallization

along grain boundaries (Fig. 10d). Porphyroclastic white mica I is pervasively kinked and it displays undulose extinction, while fine-grained white mica II lies on the foliation plane (Fig. 10c). K-feldspar and plagioclase are heavily fractured and fragmented. However, feldspars form inequigranular aggregates indicating probably a previous stage of dynamic recrystallization at higher temperature (Fig. 10d). The evidence of dynamic recrystallization of quartz, brittle deformation of feldspar and the growth of chlorite and white mica, indicate that shearing took place at temperature in the order of 350-400°C.

### Stop 7: The Bt-orthogneiss of the Grosina unit (X:586370; Y:5138650)

Continue on the gravel road towards the North up to a small lake (please note that the lake is not drawn on the Swiss topographic map). The loose blocks near the lake provide an overview of the biotite-bearing orthogneisses located in the upper part of the Grosina unit (Fig. 11).

These orthogneisses show a pervasive fabric associated with a strong prolate strain as suggested by the grain shapes of feldspar and quartz. In outcrop, a well-defined mineral stretching lineation, marked by quartz and feldspar, trends NNW-SSE, similarly to the greenschist facies mylonites close to the Eita shear zone. In thin section, this shear fabric is defined by quartz, plagioclase, K-feldspar, biotite, white mica and titanite. Quartz grains display irregular shape, size and grain boundaries suggesting recrystallization through grain boundary migration. In contrast, porphyroclastic K-feldspar and plagioclase record the presence of recrystallized bulges at boundaries suggesting a bulging recrystallization process as well as local sub-grain recrystallization. Therefore, in contrast to the lower part of the Grosina unit close to the Eita shear zone, the upper part preserves evidence of higher grade deformation at amphibolite facies conditions.

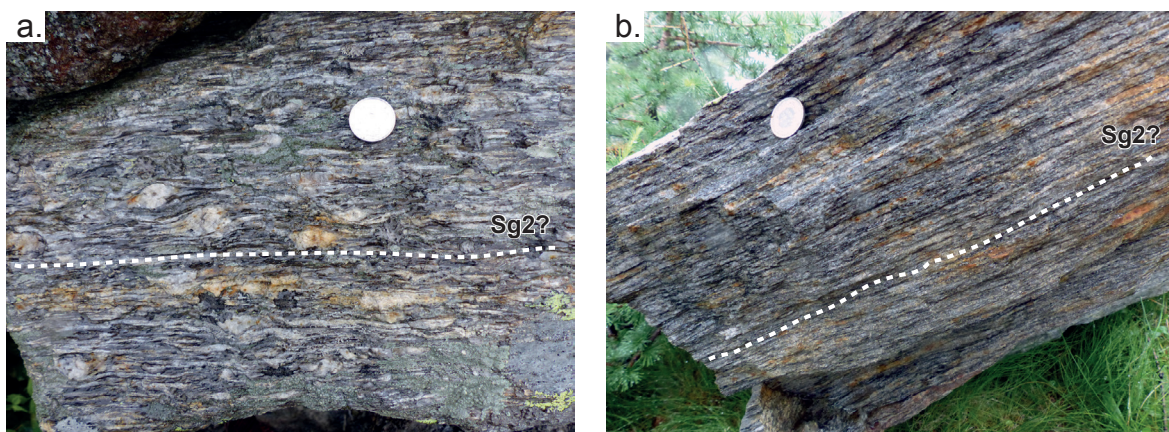


**Fig. 11:** Loose blocks of Bt-orthogneiss from the Grosina unit near the lake showing a) an augengneiss texture and b) a mylonitic texture (see text for details) with possibly Sg2 amphibolite-facies foliation.

## **4. TECTONO-METAMORPHIC EVOLUTION**

The Campo-Grosina units lie in a critical position in the Austroalpine nappe stack sampling the transition between the proximal and distal margins: the former Adriatic necking zone. Therefore, the understanding of the tectonic history of these units may represent an opportunity to characterize crustal thinning processes during the Jurassic rifting but also to investigate the Permian post-Variscan extension and the Variscan history.

### **Paleozoic evolution of the Campo-Grosina units**

Several generations of pre-Permian structures have been documented in the Campo basement. Although Sc1 fabric is generally partly to completely transposed by Dc2 deformation, mineral assemblages associated with Sc1 are still preserved, at least locally. Sc1 is interpreted as evidence of a prograde metamorphic evolution following a barrovian metamorphic gradient, leading to garnet growth. Staurolite stability within Sc1 is then followed by sillimanite formation during Dc2 deformation.

The precise timing of these tectono-metamorphic events remains, at the moment, loosely constrained. Late Permian-Early Triassic pegmatite dikes (Figs. 6,7, Stops 4,5) cross-cut the Sc2 fabric thus suggesting that the tectono-metamorphic evolution outlined here is pre-Permian in age. Importantly, the Campo unit displays similarities with the basement of the Southern Alps and, to the East, the Ulten zone metasediments in terms of lithological composition and tectono-metamorphic evolution (on the exception that the Ulten metasediments does not record the subsequent Permian HT metamorphism, and contains lenses of mantle-derived peridotites). There, the prograde history is bracketed by U–Th–Pb monazite ages between 351 and 343 Ma whereas post-peak thermal relaxation was achieved between 330–326 Ma (Langone *et al.*, 2011).

During the Permian, the Campo basement underwent a major heating event associated with the emplacement of numerous plutonic bodies, including the Sondalo gabbro. Emplacement of the latter pluton generated a HT contact metamorphic aureole in the country rock (Figs. 3,4,5, Stops 1,2,3), associated with melting of the host rock metapelites. As a result, migmatitic metasediments rim the pluton. Contact metamorphism and melting are associated to the development of the new Sc3 fabric. In the center of the pluton, host-rock xenoliths records granulite-facies metamorphism. Braga *et al.* (2001; 2003), based on metamorphic investigations on the contact metamorphism, proposed an emplacement of the gabbro at 0.4–0.6 GPa suggesting that the Campo basement was residing in a mid-crustal position during the Permian.

In contrast, the Paleozoic history of the Grosina unit is less constrained. The timing of the pervasive deformation at amphibolite facies conditions recorded in the upper part of the Grosina unit and visible in the loose blocks of Stop 7 is still poorly constrained.  $^{40}\text{Ar}/^{39}\text{Ar}$  dating on porphyroclastic muscovite from orthogneiss equilibrated in greenschist facies conditions in the lower part of the Grosina unit yielded ages of *ca.* 260 Ma, interpreted as cooling ages (Mohn *et al.*, 2012). These results suggest that the deformation in amphibolite facies is older than 260 Ma.

Notably, Permian heating was related to the collapse of the Variscan orogen, associated to lithospheric thinning (e.g. Malaveille, 1993; Ménard & Molnar, 1988; Wilson *et al.*, 2004) and/or to a westward propagation of the Neotethys rift system (e.g. Schuster *et al.*, 2001; Schuster & Stüwe, 2008). Evidence for this Permian thermal event is widespread through the entire Alpine belt and linked to a high geothermal gradient. This HT metamorphism has a strong cogenetic link with the emplacement of magmatic intrusions at all crustal levels (e.g. Schuster & Stüwe, 2008). In this framework, Campo-Grosina units are of particular interest, recording the evolution of mid-crustal levels during the Permian post-orogenic event.

### Jurassic evolution of the Campo-Grosina units

In the vicinity of the Eita shear zone, both the Campo and Grosina basements were overprinted by greenschist facies metamorphism (Sc4 in Campo and Sg3 in Grosina). However, the deformation style and the thickness of the overprinted area vary considerably. The Campo basement was only affected in the uppermost 30-40m, while the Grosina basement was overprinted over more than 200m. This discrepancy may be attributed to the different orientation of pre-existing mineral fabrics in the Campo unit, characterized by a vertical Sc2 fabric, with respect to the relatively flat Sg2 fabric of the Grosina basement.

Meier (2003), based on  $^{40}\text{Ar}/^{39}\text{Ar}$  dating of a pseudotachylite at  $84 \pm 2$  Ma, interpreted this shear zone as a major Alpine thrust fault active during the late Cretaceous. However based on an extensive geochronological survey of the Campo and Grosina units and the Eita shear zone by the  $^{40}\text{Ar}/^{39}\text{Ar}$  technique, Mohn *et al.* (2012) proposed that the Eita shear zone is an extensional structure mainly active during Jurassic rifting and possibly reactivated during the Alpine orogeny. This interpretation is mainly based on the following arguments:

- 1) The Eita shear zone separates the Grosina basement with late-Permian white mica cooling ages ( $>260$  Ma) from the Campo basement showing younger cooling ages (205-183 Ma) (for further details, see Mohn *et al.*, 2012). These ages bracket the time of activity of the interface between the Campo and Grosina units.

2) The Campo and Grosina basements are over-thrusted in Val di Rezzalo by the Filladi di Bormio unit during an early Alpine deformation phase (Trupchun phase of Froitzheim *et al.*, 1994) suggesting that the juxtaposition of Campo-Grosina units must be pre-Alpine. Therefore, the Eita shear zone is interpreted as major decoupling horizon developed at the brittle-ductile transition during the Jurassic.

### **Alpine evolution of the Campo-Grosina units**

The Alpine overprint in the Campo-Grosina units is relatively minor and deformations are essentially localized in discrete (meter scale) greenschist facies shear zones. The Alpine overprint increases southward approaching of the Insubric line (Gazzola *et al.*, 2000; Meier, 2003). The Eita shear zone may have been reactivated during the Alpine orogeny, as suggest by Meier (2003). However, following the lines of evidence discussed in the previous section, this reworking should be minor. At regional scale, the Campo-Grosina units are affected by large wavelength folding with ENE-SWS trending fold axes probably during the Tertiary (Froitzheim *et al.*, 1994; Meier, 2003). Such folding may explain the variation in altitude of the Eita shear zone across the region.

## **5. CONCLUSION**

The Campo-Grosina units preserved the relics of a complex tectono-metamorphic and magmatic history documenting the transition from the Variscan orogeny to the Permian post-Variscan extension, and eventually to the Jurassic rifting. The Campo basement depicts mainly the Paleozoic history providing key insights on mid-crustal processes during the Permian post-Variscan extension. In contrast, the lower part of the Grosina unit has been significantly overprinted by retrograde deformation. This deformation may represent a witness of crustal thinning processes during the Jurassic rifting in necking zones. Eventually, the Campo-Grosina units represent an ideal natural laboratory to investigate the complex interactions between the Permian post-orogenic extension and subsequent Jurassic rifting leading to the opening of the Alpine Tethys.

## **ACKNOWLEDGMENTS**

B. Petri benefited from financial support from the University of Strasbourg and the excellence scholarship “Eole” from the French-Dutch network (RFN-FNA). N.S. Mancktelow is thanked for helpful discussions and R. Braga for his informal review.

## REFERENCES

- BONSIGNORE, G., BORGO, A., GELATI, R., MONTRASIO, A., POTENZA, R., POZZI, R., RAGNI, U. & SCHIAVINATO, G., 1969. Note illustrative della Carta Geologica d'Italia alla scala 1:100.000, Foglio 8 Bormio. *Servizio Geologico d'Italia, Ministero dell'Industria, del Commercio e dell'Artigianato - Direzione Generale delle Miniere*, 123 p.
- BRAGA, R., CALLEGARI, A., MESSIGA, B., OTTOLINI, L., RENNA, M. R. & TRIBUZIO, R., 2003. Origin of prismaticine from the Sondalo granulites (Central Alps, northern Italy). *European Journal of Mineralogy*, **15**, 393-400.
- BRAGA, R., GIACOMINI, F., MESSIGA, B. & TRIBUZIO, R., 2001. The Sondalo Gabbroic Complex (Central Alps, Northern Italy): Evidence for Emplacement of Mantle-Derived Melts into Amphibolite Facies Metapelites. *Physics and Chemistry of the Earth, Part A: Solid Earth and Geodesy*, **26**(4-5), 333-342.
- DEL MORO, A. & NOTARPIETRO, A., 1987. Rb-Sr Geochemistry of some Hercynian granitoids overprinted by eo-Alpine metamorphism in the Upper Valtellina, Central Alps. *Schweizerische mineralogische und petrographische Mitteilungen*, **67**, 295-306.
- FROITZHEIM, N. & EBERLI, G. P., 1990. Extensional detachment faulting in the evolution of a Tethys passive continental margin, Eastern Alps, Switzerland. *Geological Society of America Bulletin*, **102**(9), 1297-1308.
- FROITZHEIM, N., SCHMID, S. M. & CONTI, P., 1994. Repeated change from crustal shortening to orogen-parallel extension in the Austroalpine units of Graubünden. *Eclogae Geologicae Helvetiae*, **87**(2), 559-612.
- GAZZOLA, D., GOSSO, G., PULCRANO, E. & SPALLA, M. I., 2000. Eo-Alpine HP metamorphism in the Permian intrusives from the steep belt of the central Alps (Languard-Campo nappe and Tonale Series). *Geodinamica Acta*, **13**, 149-167.
- KOENIG, M. A., 1964. *Geologisch-petrographische Untersuchungen im oberen Veltlin*, PhD thesis, Universität Zurich.
- LANGONE, A., BRAGA, R., MASSONNE, H.-J. & TIEPOLO, M., 2011. Preservation of old (prograde metamorphic) U-Th-Pb ages in unshielded monazite from the high-pressure paragneisses of the Variscan Ulten Zone (Italy). *Lithos*, **127**(1-2), 68-85.
- MALAVIEILLE, J., 1993. Late orogenic extension in mountain belts: insights from the Basin and Range and the late Paleozoic Variscan belt. *Tectonics*, **12**(5), 1115-1130.
- MANATSCHAL, G. & NIEVERGELT, P., 1997. A continent-ocean transition recorded in the Err and Platta nappes (Eastern Switzerland). *Eclogae Geologicae Helvetiae*, **90**, 3-27.
- MEIER, A., 2003. *The Periadriatic Fault System in Valtellina (N-Italy) and the Evolution of the Southwestern Segment of the Eastern Alps*, PhD Thesis, ETH Zurich.
- MÉNARD, G. & MOLNAR, P., 1988. Collapse of a Hercynian Tibetan Plateau into a late Palaeozoic European Basin and Range province. *Nature*, **334**(6179), 235-237.
- MOHN, G., MANATSCHAL, G., BELTRANDO, M., MASINI, E. & KUSZNIR, N., 2012. Necking of continental crust in magma-poor rifted margins: Evidence from the fossil Alpine Tethys margins. *Tectonics*, **31**(1), 1-28.
- MOHN, G., MANATSCHAL, G., MASINI, E. & MÜNTENER, O., 2011. Rift-related inheritance in orogens: a case study from the Austroalpine nappes in Central Alps (SE-Switzerland and N-Italy). *International Journal of Earth Sciences*, **100**(5), 937-961.
- MONTRASIO, A., 1969. Carta geologica d'Italia, foglio 19, Tirano, scale 1:100000. *Servizio Geologico d'Italia, Rome*.
- SCHUDEL, W., 1965. *Geologie der Val Grosina, Provinz Sondrio, Italia*, PhD Thesis, ETH Zurich.

- SCHUSTER, R., SCHARBERT, S., ABART, R. & FRANK, W., 2001. Permo-Triassic extension and related HT/LP metamorphism in the Austroalpine-Southalpine realm. *Mitteilungen der Geologie und Bergbau Studenten Österreichs*, **44**, 111-141.
- SCHUSTER, R. & STÜWE, K., 2008. Permian metamorphic event in the Alps. *Geology*, **36**(8), 603-606.
- SIVOLA, J. & SCHMID, R., 2007. Recommendations by the IUGS Subcommission on the Systematics of Metamorphic Rocks: List of mineral abbreviations. Web version 01.02.07. (<http://www.bgs.ac.uk/scmr/home.html>).
- SÖLVA, H., THÖNI, M. & HABLER, G., 2003. Dating a single garnet crystal with very high Sm/Nd ratios (Campo basement unit, Eastern Alps). *European Journal of Mineralogy*, **15**, 35-42.
- STAUB, R., 1946. Geologische Karte der Berninagruppe und ihrer Umgebung im Oberengadin, Bergell, Val Malenco, Puschlav und Livigno, scale 1:50,000. *Speziale Karte 118, Schweizerische Geologische Kommission*.
- THÖNI, M., 1981. Degree and evolution of the alpine metamorphism in the Austroalpine unit W of the Hohe Tauern in the light of K/Ar and Rb/Sr age determination on micas. *Jahrbuch der Geologischen Bundesanstalt*, **124**(1), 111-174.
- TRIBUZIO, R., THIRLWALL, M. F. & MESSIGA, B., 1999. Petrology, mineral and isotope geochemistry of the Sondalo gabbroic complex (Central Alps, Northern Italy): implications for the origin of post-Variscan magmatism. *Contributions to Mineralogy and Petrology*, **136**(1-2), 48-62.
- TRÜMPY, R., 1975. Penninic-Austroalpine boundary in the Swiss Alps: a presumed former continental margin and its problems. *American Journal of Science*, **279**, 209-238.
- WILSON, M., NEUMANN, E.-R., DAVIES, G. R., TIMMERMAN, M. J., HEEREMANS, M. & LARSEN, B. T., 2004. Permo-Carboniferous magmatism and rifting in Europe: introduction. *Geological Society, London, Special Publications*, **223**(1), 1-10.



## ***LISTE DES FIGURES***

### **INTRODUCTION**

<b><i>Fig. 1:</i></b> Modèle d'évolution simplifié d'un cycle de Wilson.	24
<b><i>Fig. 2:</i></b> Modèles d'effondrement gravitaire d'un orogène.	27
<b><i>Fig. 3:</i></b> Évolution théorique du géotherme orogénique à post-orogénique.	29

### **CHAPTER I**

<b><i>Fig. I-1:</i></b> Reconstruction palinspatique de l'orogène varisque.	34
<b><i>Fig. I-2:</i></b> Schéma de la chaîne varisque en Europe de l'ouest.	35
<b><i>Fig. I-3:</i></b> Carte des structures tardi-varisques.	37
<b><i>Fig. I-4:</i></b> Carte des bassins et volcanites carbonifères (315 – 305 Ma).	39
<b><i>Fig. I-5:</i></b> Carte des bassins et volcanites carbonifères à permiens (305 – 260 Ma).	40
<b><i>Fig. I-6:</i></b> Synthèse non exhaustive des gabbros et granulites permiens.	43
<b><i>Fig. I-7:</i></b> Coupe sismique profonde du nord de la France.	44

### **CHAPTER II**

<b><i>Fig. II-1:</i></b> Cartes litho-tectoniques des domaines alpins et austroalpins.	48
----------------------------------------------------------------------------------------	----

### **CHAPTER III**

<b><i>Fig. III-1:</i></b> Litho-tectonics map of the Alpine and Austroalpine domains.	58
<b><i>Fig. III-2:</i></b> Geological and structural maps of the Campo/Grosina units.	61
<b><i>Fig. III-3:</i></b> Synthetic block across the Eita valley.	63
<b><i>Fig. III-4:</i></b> Field photographs of metasediments structures.	64
<b><i>Fig. III-5:</i></b> Field photographs of mineral relationships in metasediments.	66
<b><i>Fig. III-6:</i></b> Microphotographs showing the paragenetic relationships in metapelites.	67
<b><i>Fig. III-7:</i></b> Microphotographs showing the paragenetic relationships in metapelites.	70
<b><i>Fig. III-8:</i></b> Crystallization-deformation relationships of the metapelites.	72
<b><i>Fig. III-9:</i></b> Garnet compositional profiles for modelled samples.	73
<b><i>Fig. III-10:</i></b> $P-T$ pseudosection for micaschist sample BPA 099-12a (micaschist).	77
<b><i>Fig. III-11:</i></b> $P-T$ pseudosection for micaschist sample BPA 003-11 (kinzigite).	79
<b><i>Fig. III-12:</i></b> $P-T$ pseudosection for micaschist sample BPA 002-11d (kinzigite).	80
<b><i>Fig. III-13:</i></b> $P-T$ pseudosection for micaschist sample BPA 018-11 (granulite).	83
<b><i>Fig. III-14:</i></b> Sketches summarizing the inferred $P-T$ paths.	85
<b><i>Fig. III-15:</i></b> Schematic evolution of the Campo unit.	88

## CHAPTER IV

<b>Fig. IV-1:</b> Litho-tectonics map of the Alpine and Austroalpine domains.	97
<b>Fig. IV-2:</b> Geological and structural maps of the Sondalo gabbro.	100
<b>Fig. IV-4:</b> Field photographs of mafic rocks.	102
<b>Fig. IV-5:</b> Photomicrographs of magmatic rocks.	106
<b>Fig. IV-7:</b> Conventional Concordia age diagrams and zircon CL images(diorites).	108
<b>Fig. IV-8:</b> Conventional Concordia age diagrams and zircon CL images(metasediments).	110
<b>Fig. IV-9:</b> REE and trace element composition for diorite M28B73.	111
<b>Fig. IV-10:</b> REE and trace element composition for diorite M1B14.	112
<b>Fig. IV-11:</b> REE and trace element composition for metasediments.	113
<b>Fig. IV-12:</b> Synthesis of magnetic mineralogy determination.	120
<b>Fig. IV-13:</b> AMS parameters diagrams.	124
<b>Fig. IV-14:</b> AMS parameters maps.	125
<b>Fig. IV-15:</b> Averaged AMS parameters / textures relationship.	127
<b>Fig. IV-16:</b> Maps of magnetic and magmatic fabrics.	128
<b>Fig. IV-17:</b> Histograms of magnetic and magmatic fabrics orientations.	129
<b>Fig. IV-18:</b> Evolutionary of the emplacement of the Sondalo gabbro.	134
<b>Fig. IV-19:</b> 1D thermal model of the intrusion.	137
<b>Fig. IV-20:</b> Synthetic model of ascent of magma through the crust.	140

## CHAPTER V

<b>Fig. V-1:</b> Tectonic evolution model of the European and Adriatic rifted margins.	153
<b>Fig. V-2:</b> Geological map of the Campo/Grosina units.	154
<b>Fig. V-3:</b> Field photographs of structural relations between the Campo/Grosina units.	157
<b>Fig. V-4:</b> Photomicrographs of lithologies from the Campo/Grosina units.	158
<b>Fig. V-5:</b> Synthetic step-release spectra.	159
<b>Fig. V-6:</b> $^{39}\text{Ar}/^{40}\text{Ar}$ versus $^{36}\text{Ar}/^{40}\text{Ar}$ synthetic plots.	160
<b>Fig. V-7:</b> $^{40}\text{Ar}/^{39}\text{Ar}$ diagrams for muscovite.	170
<b>Fig. V-8:</b> $^{40}\text{Ar}/^{39}\text{Ar}$ diagrams for biotite.	171
<b>Fig. V-9:</b> $^{40}\text{Ar}/^{39}\text{Ar}$ diagrams for biotite from the Campo unit.	172
<b>Fig. V-10:</b> $^{40}\text{Ar}/^{39}\text{Ar}$ diagrams for hornblende from the Campo unit.	174
<b>Fig. V-11:</b> Cumulative probability histogram ages in the Campo/Grosina units.	177
<b>Fig. V-13:</b> Synthetic T-t path.	179
<b>Fig. V-14:</b> Temperature/time diagrams and calculated cooling rates.	181
<b>Fig. V-15:</b> Argon diffusion modelling of temperature–time–depth evolutions.	183
<b>Fig. V-16:</b> Tectonic phases in the Austroalpine realm.	185
<b>Fig. V-17:</b> Evolutionary model of the formation of a necking zone.	186

## CHAPTER VI

<b>Fig. VI-1:</b> Synthèse de l'évolution des unités de Campo et de Grosina.	197
<b>Fig. VI-2:</b> Trajets $P-T-t$ de la croûte moyenne et de la croûte inférieure.	198
<b>Fig. VI-3:</b> Modèle synthétique rdascension du magma mafique.	201
<b>Fig. VI-4:</b> Carte des bassins, volcanites, gabbros et granulites permiens.	205
<b>Fig. VI-5:</b> Evolution schématique de la croûte continentale de l'extension.	208
<b>Fig. VI-6:</b> Différences entre croûte continentale simplifiée et réelle.	209

## FIELD GUIDE

<b>Fig. 1:</b> Simplified tectonic map and cross-section of the Campo-Grosina units.	269
<b>Fig. 2:</b> Topographic map showing the excursion stops.	270
<b>Fig. 3:</b> Stop 1: the Sondalo gabbro.	272
<b>Fig. 4:</b> Stop 2: The diorite/xenolith contact.	273
<b>Fig. 5:</b> Stop 3: The host rock contact metamorphism.	274
<b>Fig. 6:</b> Stop 4: The regional Campo metapelites.	275
<b>Fig. 7:</b> Stop 5: The Campo basement.	276
<b>Fig. 8:</b> Stop 6a: The Campo basement in the vicinity of the Eita shear zone.	277
<b>Fig. 9:</b> Stop 6b: The Eita shear zone ss.	279
<b>Fig. 10:</b> Stop 6c: The Grosina basement in the vicinity of the Eita shear zone.	280
<b>Fig. 11:</b> Loose blocks of Bt-orthogneiss from the Grosina unit.	281

## ***LISTE DES TABLEAUX***

### **CHAPTER III**

<b>Table III-1:</b> Representative mineral analysis (BPA 099-12a and BPA003-11a).	74
<b>Table III-2:</b> Representative mineral analysis (BPA 002-11d and BPA 018-11a).	75
<b>Table III-3:</b> Major element concentration used for mineral equilibria modelling.	76

### **CHAPTER IV**

<b>Table IV-1:</b> U–Pb isotopic data for zircon (magmatic samples).	114
<b>Table IV-2:</b> U–Pb isotopic data for zircon (metamorphic samples).	115
<b>Table IV-3:</b> U, Th and trace element (REE) concentration (magmatic samples).	116
<b>Table IV-4:</b> U, Th and trace element (REE) concentration (metamorphic samples).	117
<b>Table IV-5:</b> Anisotropy of Magnetic Susceptibility data.	122

### **CHAPTER V**

<b>Table V-1:</b> $^{40}\text{Ar}/^{39}\text{Ar}$ isotopic data for muscovites.	163
<b>Table V-2:</b> $^{40}\text{Ar}/^{39}\text{Ar}$ isotopic for biotites.	165
<b>Table V-3:</b> $^{40}\text{Ar}/^{39}\text{Ar}$ isotopic data for amphiboles.	168
<b>Table V-4:</b> Compilation of pre-Alpine ages from the Campo/Grosina area.	178

## **TABLE DES MATIÈRES**

RÉSUMÉ ÉTENDU	5
EXTENDED ABSTRACT	9
REMERCIEMENTS	13
SOMMAIRE	19
INTRODUCTION	23
<b>1. Les processus tardi- à post-orogéniques</b>	25
<b>2. Implications pour l'architecture de la croûte continentale</b>	28
2.1 Modifications thermiques	28
2.2 Modifications lithologiques	28
<b>3. Les éléments clés</b>	29
CHAPITRE I: CONTEXTE	31
<b>1. Orogénèse varisque</b>	33
1.1 Convergences et subductions dévono-carbonifères	33
1.2 Collision carbonifère	35
<b>2. Évolution tardi- à post-orogénique</b>	36
2.1 Évolution des bassins sédimentaires	38
2.2 Évolution magmatique	41
2.3 Évolution métamorphique	42
2.4 Cadre géodynamique	44
CHAPITRE II: CADRE ET MÉTHODOLOGIE	45
<b>1. Questions soulevées</b>	47
<b>2. Où y répondre ?</b>	47
<b>3. Comment y répondre</b>	49
<b>4. Plan du mémoire de thèse</b>	50
CHAPITRE III: MÉTAMORPHISME POST-VARISQUE DANS LES ALPES	53
Abstract	55
<b>1. Introduction</b>	56
<b>2. Geological setting</b>	57
2.1 Evidence for Variscan orogeny	57
2.2 Evidence for the post-Variscan evolution in the upper and lower crust	59
2.3 Evidence for the post-Variscan evolution in the middle crust	60
<b>3. Structural evolution</b>	62
3.1 Regional Sc1 and Sc2 fabrics	62
3.2 Regional Sc2 fabric preserved in the pluton	63
3.3 Syn-intrusion Sc3 fabric	63
3.4 Evidence for rift-related and Alpine deformations	65

<b>4. Petrography and mineral chemistry</b>	65
4.1 Regional micaschists and paragneiss	66
4.2 Migmatitic metapelite in contact aureole	68
4.3 Migmatitic and granulitic metapelites in xenoliths	71
<b>5. Mineral equilibria modelling</b>	76
5.1 Modelling strategy	76
5.2 Regional metamorphism: pseudosection for sample BPA 099-12a	77
5.3 Contact metamorphism: pseudosection for sample BPA 003-11a	78
5.4 Contact metamorphism: pseudosection for sample BPA 002-11d	81
5.5 Contact metamorphism: pseudosection for sample BPA 018-11a	82
<b>6. Discussion</b>	84
6.1 P-T-d evolution of the Campo unit	84
<i>6.1.1 Regional evolution</i>	84
<i>6.1.2 Evolution of metasediments in and around the pluton</i>	84
6.2 Implications for the geodynamic evolution of the Austroalpine domain	87
<i>6.2.1 Variscan tectono-metamorphic evolution</i>	87
<i>6.2.2 Late-Variscan tectono-metamorphic evolution</i>	87
<b>7. Conclusion</b>	90
<b>Acknowledgments</b>	90
CHAPITRE IV: MISE EN PLACE D'UN GABBRO EN CROÛTE MOYENNE	91
<b>Abstract</b>	93
<b>1. Introduction</b>	94
<b>2. Geological setting</b>	96
<b>3. Petrology and structure of the Campo unit</b>	99
<b>4. Petrography and magmatic structures of the Sondalo gabbro</b>	100
4.1 The Sondalo gabbro	100
4.2 Petrography	101
4.3 Magmatic fabric	101
<b>5. Geochronology</b>	104
5.1 Samples description	105
<i>5.1.1 Magmatic rocks</i>	105
<i>5.1.2 Migmatitic metasediments</i>	106
5.2 Zircon morphology and internal structure	107
5.3 U-Pb results	107
5.4 U, Th, Hf and trace element geochemistry of zircon	109
<i>5.4.1 Magmatic rocks</i>	109
<i>5.4.2 Migmatitic metasediments</i>	118

<b>6. Anisotropy of Magnetic Susceptibility</b>	119
6.1 AMS Methods	119
6.2 Magnetic mineralogy results	120
6.3 Bulk susceptibility	121
6.4 Magnetic fabric parameters	124
6.5 Magnetic foliation and lineation	126
<b>7. Discussion</b>	129
7.1 Timing of pluton emplacement and contact metamorphism	129
7.1.1 <i>Magmatic rocks</i>	129
7.1.2 <i>Metamorphic rocks</i>	130
7.1.3 <i>Synthesis</i>	131
7.2 Magmatic and magnetic fabrics	131
7.3 Magma ascent mechanisms	133
7.3.1 <i>Stage 1: magma flow along host-rock anisotropy</i>	133
7.3.2 <i>Stage 2: rise of the core of the pluton</i>	135
7.3.3 <i>Stage 3: late-magmatic activity</i>	136
7.4 Discussion with a simple thermal model	136
7.4.1 <i>Results</i>	136
7.4.2 <i>Implication on the contact aureole</i>	138
7.5 Implications for intrusion dynamics	138
7.5.1 <i>Stage 1</i>	138
7.5.2 <i>Stage 2</i>	139
7.6 Implications for the Permian post-Variscan extension	140
<b>8. Conclusions</b>	141
<b>Acknowledgments</b>	141
<b>Appendix A: Geochronology: methods</b>	142
<b>Appendix B: Anisotropy of magnetic susceptibility: methods</b>	142
<b>Appendix C: Thermal modelling</b>	144
<b>CHAPITRE V: EXHUMATION ET REFROIDISSEMENT PENDANT LE RIFTING</b>	147
<b>Abstract</b>	149
<b>1. Introduction</b>	150
<b>2. Tectonic, geochronological and geological framework</b>	151
2.1 The evolution of the Austroalpine domain	151
2.1.1 <i>Variscan and post-Variscan evolution</i>	151
2.1.2 <i>Jurassic rifting history</i>	152
2.1.3 <i>Alpine reactivation</i>	155
2.2 The Campo–Grosina units	155
2.3 The Eita shear zone	156

<b>3. <math>^{40}\text{Ar}/^{39}\text{Ar}</math> geochronology</b>	159
3.1 Analytical procedure	160
3.2 Sample description and $^{40}\text{Ar}/^{39}\text{Ar}$ results	161
3.2.1 <i>Grosina basement</i>	161
3.2.2 <i>Campo basement</i>	162
<b>4. Discussion on ages</b>	175
4.1 Significance of the measured ages	175
4.1.1 $^{40}\text{Ar}/^{39}\text{Ar}$ ages on amphibole and micas	175
4.1.2 Possible reasons for excess $^{40}\text{Ar}$	175
4.2 Exhumation and cooling history of the Campo and Grosina basements	177
4.2.1 <i>Permian cooling</i>	179
4.2.2 <i>Jurassic cooling</i>	180
4.2.3 <i>Cooling with or without exhumation?</i>	180
4.2.4 <i>Only cooling or re-heating and cooling?</i>	180
<b>5. Evolutionary model of the formation of necking zone</b>	184
5.1 Post-orogenic evolution	184
5.2 Rifting evolution	185
5.2.1 <i>Rifting phase I (stretching phase): 220–185 Ma</i>	185
5.2.2 <i>Rifting phase II (thinning phase): 185–180 Ma</i>	187
5.2.3 <i>Rifting phase III (exhumation): 180–170 Ma</i>	188
<b>6. Conclusion</b>	189
<b>Acknowledgments</b>	189
<b>Appendix: Photomicrographs of dated samples</b>	190
<b>CHAPITRE VI: DISCUSSION GÉNÉRALE</b>	193
<b>1. Quel est le lien entre magmatisme et métamorphisme ?</b>	196
<b>2. Quelle est la dynamique de mise en place des intrusions mafiques ?</b>	199
<b>3. Quels sont les systèmes d'exhumation ?</b>	202
3.1 Le refroidissement permien	202
3.2 Le refroidissement jurassique	203
<b>4. L'extension post-orogénique permienne : quel contexte géodynamique ?</b>	204
4.1 Dynamique lithosphérique permienne	204
4.1.1 <i>Évolution des bassins</i>	204
4.1.2 <i>Activité mantellique</i>	206
4.2 Différences entre les parties internes et externes de l'orogène varisque	206
4.3 Analogie avec la province du Basin and Range	207
<b>5. Quelle est l'influence de l'architecture lithosphérique sur les rifts ?</b>	209
<b>Conclusion</b>	211

RÉFÉRENCES	217
ANNEXES	247
GUIDE D'EXCURSION	265
<b>Abstract</b>	267
<b>1. Introduction</b>	268
<b>2. Logistics</b>	270
<b>3. Field observations</b>	271
Stop 1: Sondalo gabbro	271
Stop 2: Diorite/xenolith contact	272
Stop 3: Contact metamorphism in the Campo metapelites	275
Stop 4: The Campo basement	275
Stop 5: The Campo basement and its pegmatites	276
Stops 6a,b,c: The Eita shear zone	277
<i>Stop 6a: Campo basement</i>	277
<i>Stop 6b: The contact - Eita Shear Zone s.s.</i>	278
<i>Stop 6c: The Grosina basement</i>	280
Stop 7: The Bt-orthogneiss of the Grosina unit	281
<b>4. Tectono-metamorphic evolution</b>	282
Paleozoic evolution of the Campo-Grosina units	282
Jurassic evolution of the Campo-Grosina units	283
Alpine evolution of the Campo-Grosina units	284
<b>5. Conclusion</b>	284
<b>Acknowledgments</b>	284
<b>References</b>	285
LISTE DES FIGURES	288
LISTE DES TABLEAUX	291
TABLE DES MATIÈRES	292
RÉSUMÉ	298
ABSTRACT	298



# Formation et exhumation des granulites Permianes

## Établir les conditions pre-rift et déterminer l'histoire de l'exhumation syn-rift

### Résumé

Le stade final de l'orogénèse varisque (310–270 Ma) est caractérisé par une intense activité tectonique, magmatique et métamorphique. Pendant le Permien, des intrusions acides et basiques se mettent en place dans tous les niveaux crustaux et sont associées à un métamorphisme de contact de haute température. Tous ces processus modifient à toutes les échelles l'architecture de la lithosphère continentale, ce qui influera potentiellement sur les déformations postérieures. Ces roches seront éventuellement exhumées lors des riftings mésozoïques. Alors que la plupart des études concernent la formation des bassins superficiels permiens ou l'évolution magmatique et métamorphique de la croûte profonde, l'évolution des niveaux crustaux intermédiaires reste peu décrite.

Ainsi, cette étude a visé à contraindre les processus tectoniques, magmatiques et métamorphiques actifs dans la croûte moyenne, du Permien à l'exhumation des roches pendant les riftings mésozoïques, en se focalisant sur un gabbro permien dans les nappes austroalpines (Italie du nord, sud-est de la Suisse). L'évolution du gabbro de Sondalo, mis en place dans l'unité de Campo, est examinée en combinant géologie structurale, pétrologie magmatique et métamorphique, et géochronologie.

Les résultats de cette étude (1) apportent des contraintes sur les relations thermiques et mécaniques entre le pluton et l'encaissant pendant sa mise en place dans la croûte moyenne, (2) décrivent les mécanismes d'ascension de magmas mafiques au travers de la croûte continentale et (3) documentent l'exhumation et le refroidissement de l'unité de Campo et de l'unité sus-jacente de Grosina pendant la formation de la marge riftée adriatique.

*Mots clefs:* Évolution post-orogénique, rifting, Alpes, Campo, Grosina, nappes austroalpines, Varisque, Permien

### Abstract

The final stage of the Variscan orogeny (310–270 Ma) is characterized by an intense tectonic, magmatic and metamorphic event. During the Permian, acid and mafic intrusions were emplaced at all crustal levels and associated to high-temperature contact metamorphism. All these processes modify at different scales the lithospheric architecture, potentially influencing subsequent deformations. Eventually, these rocks are exhumed during Mesozoic rifting phases. While most of the studies focus either on the formation of Permian basins or on the lower crustal magmatic and metamorphic evolution, the characterization of the middle crust is lacking.

Therefore, this study aims to unravel tectonic, magmatic and metamorphic processes active at mid-crustal levels from the Permian to the exhumation of the rocks during the Mesozoic riftings by focusing on a Permian gabbro in the Austroalpine nappes (N-Italy, SE-Switzerland). The evolution of the Sondalo gabbro, emplaced in the Campo unit, is examined by combining structural geology, magmatic and metamorphic petrology, and geochronology.

The results of this study bring constrains on (1) the thermal and mechanical relationship between the pluton and the host rock during its emplacement in the middle crust, (2) the mechanisms of mafic magmas ascent through the continental crust and (3) the exhumation and cooling history of the Campo unit and the overlying Grosina unit during the formation of the Adriatic rifted margin.

*Keywords:* Post-orogenic evolution, rifting, Alps, Campo, Grosina, Austroalpine nappes, Variscan, Permian